SEISMIC BEHAVIOR OF GEOSYNTHETIC REINFORCED RETAINING STRUCTURES WITH COHESIVE BACKFILLS

by

İsmail Emrah Kılıç

B.S., Civil Engineering, Boğaziçi University, 2006

M.S., Civil Engineering, Boğaziçi University, 2008

Submitted to the Institute for Graduate Studies in
Science and Engineering in partial fulfillment of
the requirements for the degree of
Doctor of Philosophy

Graduate Program in Civil Engineering

Boğaziçi University

2015

ACKNOWLEDGEMENTS

In the first place, I would like to express my sincere gratitude to my thesis supervisor, Prof. Erol Güler for his helpful suggestions, guidance, continuous support and encouragement. And also I am very grateful to Assoc. Prof. Ayşe Edinçliler for her guidance and support for this thesis especially during the really tough shaking table experiments in the Kandilli earthquake research laboratory. I would also thank to Assoc. Prof. Özer Çincioğlu and Assoc. Prof. İsmail Hakkı Aksoy for their valuable suggestions throughout the preparation of this thesis.

I would also thank to Prof Gülay Altay because of her support and encouragement starting from the early years of my graduate study that are beyond words. I am very grateful to Assoc. Prof. Hilmi Luş for his helpful suggestions during this thesis and for his support and encouragement during my graduate study.

I would like to thank my dear colleague and team mate Cihan Cengiz for his endless support and encouragement during this study. Without his support, it was not possible for me to accomplish this thesis.

I would like to thank Ahmet Korkmaz and Oktay Çırağ from Kandilli earthquake research laboratory for their incredible support during the experiments. I would like to thank all my friends in the department and in the soil mechanics laboratory; Tarık Tufan, Emirhan Sancak, Abdullah Akça, Onur Pehlivan, Tahir Erdem Öztürk, Ayşe Aydın, Belgin Özgül, Yener Aydın, Ümit Melep and Kadir Gündoğdu for their inexpressible support during this study. Many heartfelt thanks go to all my friends supported me during my whole study, Emrah Karabulut, Ekin Özer, Caner Bölükbaş, Anıl Yıldız, Rahman Shahshenas, Pelin Boyacıoğlu, Sevilay Çakır, Tunay Çarpar, Fethi Güllü, Yiğit Can Altan, Ulvi Berat Şensoy, Selahattin Akalp and my elder brothers Ufuk Şahin, Yavuz Tokmak and Emin Çiftçi. Also I would also like to thank Istanbul Teknik Engineering and Industry Company for their supports.

And finally I would like to thank my dear parents Gülten Kılıç and Mehmet Özalp Kılıç for their endless support, encouragement and love they gave during my life.

This thesis has been supported by Boğaziçi University Scientific Research Project with the project code 7481.

I would also like to thank TÜBİTAK BİDEB (The Scientific and Technological Research Council of Turkey) for their support during my graduate study with the national scholarship programme for Ph.D. students (2211).

ABSTRACT

SEISMIC BEHAVIOR OF GEOSYNTHETIC REINFORCED RETAINING STRUCTURES WITH COHESIVE BACKFILLS

In this study, seismic performance of geosynthetic-reinforced modular block retaining walls backfilled with cohesive, fine grained clay-sand soil mixture was investigated. Four model walls were constructed and shaking table tests performed for three 1/2 scaled (wall height 190 cm) and one 1/4 scaled model walls were evaluated to investigate the effects of backfill type, the influence of reinforcement length and the scaling effects. Scaled versions of the recorded El Centro and Kobe earthquakes were applied to the model walls. Polyester geogrids were used in the tests with a vertical spacing of 20 cm. Reinforcement length to wall height ratio was 0.8 (for one model 0.6 was used). A 12.5^o battered facing was constructed with modular hollow concrete blocks. Model walls were instrumented by 8 accelerometers, located on facing and on backfill surface. 8 laser displacement transducers were used and 15 strain gages were located on three geogrid layers at top, mid and bottom heights of wall. Maximum and permanent displacements on front wall, acceleration amplification ratios on front wall and inside the backfill, strain values to calculate tensile loads on reinforcements and visual observations for facing and backfill surface were the results of this test to evaluate the performance of cohesive backfilled model wall. No stability problem was occurred under extreme seismic loading. Any indication of failure was not observed except minimal residual deformations on the facing during base excitations. And acceptable tension cracks were observed on the backfill surface after final seismic motions. As a result it can be said that; the model walls with cohesive backfill performed well under seismic loading conditions when compared with granular backfills and checked with the limit design values described in previous studies.

ÖZET

KOHEZYONLU DOLGU KULLANILMIŞ GEOSENTETİK DONATILI İSTİNAT DUVARLARININ SİSMİK PERFORMANSI

Bu çalışmada geosentetik donatılı modüler blok öncepheli istinat duvarlarının kilkum karışımı kohezyonlu zemin dolgusu kullanılması durumdaki sismik performansları incelenmiştir. Üç adet ½ oranında (duvar yüksekliği 190 cm) ve bir adet ¼ oranında ölçeklendirilmiş model duvar, dolgu zemini özelliği, donatı uzunluğu ve ölçeklendirme etkisini incelemek amacıyla sarsma masası testlerine tabi tutulmuştur. Modellere ölçeklendirilmiş El Centro ve Kobe depremi sismik yük olarak tatbik edilmiştir. Donatı olarak polyester geogridler 20 cm düşey aralıklarla kullanılmıştır. Donatı uzunluğunun duvar boyuna oranı 0.8'dir (bir duvar modeli için 0.6 kullanılmıştır). Ön cephe 12.5° eğimli olacak şekilde içi boşluklu modüler bloklar kullanılarak inşa edilmiştir. 8 adet ivmeölçer ön cephede ve dolgu üst yüzeyinde konumlandırılmıştır. 8 adet lazer deplasman ölçer duvar ön cephesine ve sarsma masası üzerine yerleştirilmiştir. Toplamda 15 adet gerinim ölçer en alt, orta ve en üst donatı katmanlarına yerleştirilmiştir. Maksimum ve kalıcı önyüz deplasmanları, önyüzde ve dolgu içindeki ivme amplifikasyonları, donatı çekme kuvvetlerinin hesaplandığı gerinim değerleri ve önyüz ile dolgu yüzeyinde yapılan görsel incelemeler; model duvarların performansının değerlendirilmesi için kullanılmış olan deney sonuçlarıdır. Oldukça yüksek deprem yükleri altında dahi duvarlarda bir stabilite problemi gözlemlenmemiştir. Makul düzeydeki kalıcı önyüz deformasyonları haricinde herhangi bir göçme emaresi gözlemlenmemiştir. Son deprem yüklerinden sonra kohezyon dolgulu model duvarların üst yüzeylerinde kabul edilebilir çekme çatlakları oluşmuştur. Sonuç olarak kohezyonlu dolgu kullanılmış model duvarların; granüler dolgulu model duvarlar ile kıyaslandığında ve önceki çalışmalardaki sınır tasarım değerleriyle karşılaştırıldığında oldukça iyi bir deprem performansı gösterilmiştir.

TABLE OF CONTENTS

LIST OF FIGURES

LIST OF TABLES

LIST OF SYMBOLS

a	Maximum ground acceleration coefficient
a_m	Maximum horizontal acceleration coefficient in reinforced soil wall
c	Soil cohesion
$C_{\|c\|}$	Coefficient of curvature
C_u	Coefficient of uniformity
E	Modulus of Elasticity
F_T	Total force applied by the retained fill on the back of reinforced zone
H	Wall Height
K_A	Active coefficient of earth pressure
K_{AE}	Total seismic earth pressure coefficient
K_P	Passive coefficient of earth pressure
$k_{\|c\|}$	Critical acceleration
k_h	Horizontal seismic coefficient
k_v	Vertical seismic coefficient
L	Reinforcement length
L_a	Length of reinforcement in front of critical surface
L_e	Length of embedment in the resisting zone
P_A	Active static earth pressure resultant force
P_{AE}	Total dynamic active earth force
PI	Plasticitiy index
P_I	Inertia force
P_R	Resisting force
q_{ult}	Ultimate bearing capacity
S_v	Spacing between reinforcement layers
t	Time
T_a	Allowable tensile force per unit width of reinforcement
T_{max}	Maximum tension force per unit width of wall

W_a	Weight of active zone
z	Depth
α	Angle of failure plane
β	Angle of backfill slope
γ	Unit weight
φ	Internal friction angle
δ	Mobilized interface friction angle
θ	Seismic inertia angle
ε	Strain
λ	Scaling factor
μ	Soil-reinforcement friction coefficient
σ_1	Vertical principal stress
σ_3	Lateral confining stress
σ_H	Horizontal stress
σ_v	Vertical stress
τ	Shear stress
ΔK_{dyn}	Incremental dynamic active earth pressure coefficient
ΔP_{dyn}	Incremental dynamic component of PAE

LIST OF ACRONYMS/ABBREVIATIONS

AASHTO	American Association of State Highway and Transportation Officials
FHWA	Federal Highway Administration
NCMA	National Concrete Masonry Association
PGA	Peak ground acceleration

1. INTRODUCTION

1.1. General

Geosynthetic-reinforced soil walls (GRS walls) have been used widely for approximately thirty years and reinforced retaining walls are preferred to conventional retaining wall systems because of the factors including cost-efficiency, aesthetics, simple construction techniques, higher performance, much more durability and the ability to adapt to different site conditions. The major disadvantage of GRS walls is the necessity of good quality granular materials specified as the backfill soil by design guideline recommendations. This requirement affects negatively the low cost benefit. In practice fine grained soils and marginal cohesive soils can be employed as backfill material with proper drainage measures; that leads to cost savings and new soil reinforcement applications. However since the literature does not cover such backfill materials, the behavior of such walls cannot be designed for. Engineers observe that using marginal, cohesive soils provide good results. However this observation is usually made under static loading conditions. However it is not known how such walls will behave under earthquake loading conditions. Therefore in this research we wanted to determine how these walls behave under earthquake loading by making a series of shaking table tests.

Successful seismic performances of GRS walls have been verified with a lot of evidences observed at the site during large earthquakes and reported in the literature. In practice, limit-equilibrium analysis is used in the design of GRS walls and seismic stability is evaluated using pseudo-static methods. This approach cannot determine the amount of deformation and efficiency of reinforcements under considered seismic forces so using a performance based design approach by which deformations can be specified may be helpful. For backfill usage with a percentage of fines providing cohesion it can be mentioned that; there are strong recommendations for the use of granular material by various design agencies and no general design methodology is arranged for the use of cohesive backfill soil, while there are lots of applications on the site and strong experimental evidences that fine grained cohesive backfill soil can perform well. The

deficiency in the literature about the seismic performance of GRS walls with cohesive backfill is the main reason that makes this study essential.

Guler *et al.*, (2007), performed numerical analysis on reinforced soil walls with cohesive backfill under construction loads and Guler *et al.*, (2012), also evaluated seismic performance by numerical analysis; these two studies are ended up with good performance of cohesive backfill and these numerical studies provided a basis for this study that investigated the seismic performance with physical testing (reduced scale shaking table tests) of model walls. This study included several stages as literature review, laboratory calibration tests, shaking table tests and evaluation of the results of shaking table tests.

For literature review study; a general definition for the reinforced soil, design recommendations by Federal Highway Administration (FHWA) and National Concrete Masonry Association (NCMA) and general design approaches including limit-equilibrium methodology, pseudo-static analysis, displacement methods and finite element/finite difference methods were reviewed. Previous shaking table test studies conducted for GRS walls and reinforced slopes were searched to have an opinion about the methodology and results of these similar studies.

Before the shaking table tests, a parametric study was performed in the geotechnical laboratory to comprehend the properties of the cohesive and granular backfill soil and to decide the percentage of fines used in the cohesive backfill. This study was performed to obtain soil classification and plasticity properties and the strength characteristics (including triaxial tests) of backfill soils. Scaling laws, was examined which constitute similarity between the model and prototype, include selecting materials that were used in the tests such as modular blocks and geogrid reinforcements. Also calibration study for the instrumentation was completed for accelerometers, displacement transducers and strain gauges on reinforcements.

In this study, a series of reduced-scale shaking table tests were conducted using the shaking table at the Kandilli Observatory and Earthquake Research Institute (KOERI)

of Boğaziçi University. In order to evaluate seismic performance, four different setups were constructed as; first was the benchmark model that was ½ scaled and had granular backfill, second and third model walls were also ¼ scaled but had cohesive backfill soil only difference with these identical walls was reinforcement lengths, geogrid length to height ratio (L/H) was 0.8 for the second wall while 0.6 for the third wall and the fourth wall was ¼ scaled, exactly half scaled version of the second wall. Scaled versions of the recorded El Centro and Kobe earthquakes at different amplitudes were applied to the model walls.

Results recorded during the shaking table tests were grouped as, the maximum and permanent displacements on the front wall, acceleration amplification ratios on the front wall and inside the backfill and strain values implying the tensile loads on the reinforcements. As a conclusion, these results of the shaking table tests were analyzed and evaluated to investigate the effects of backfill type (one granular backfill setup was tested as a control sample) on the seismic behavior of the model walls as the foremost outcome. Then the comparison of the second of third walls was evaluated for the influence of reinforcement length and finally the investigation of the results for second and fourth wall indicated the scaling effects on seismic behavior. Also, to check the limit equilibrium approaches the obtained tensile load results from reinforcements were compared with the design recommendations by the Federal Highway Administration (FHWA) the National Concrete Masonry Association (NCMA).

2. GENERAL INFORMATION AND LITERATURE REVIEW

2.1. General Information

2.1.1. Definition and Historical Development

Soil retaining structures can be classified as externally stabilized and internally stabilized systems according to their retaining mechanisms. Figure 2.1 shows some retaining wall types including cantilever, braced, tied back, etc. Externally stabilized systems have external structural walls, constructed with high stiffness and/or high unit weight materials, which create a resisting force against the lateral earth pressure of the backfill soil. The external structure does not work effectively until the entire backfill soil starts yielding and reaches its critical state (active or passive states) where soil pressure produces an overall driving force (Holtz, 2002).

The internally stabilized systems consist of soil layers partitioned during construction of entire soil mass with horizontal reinforcement layers. These reinforcement layers stabilize the soil mass by extending beyond the potential reinforcement surfaces, and confine the local yielding of nearby layer (Holtz, 2002).

For the design and construction of foundations, embankment slopes and earth retaining structures, the use of reinforced soil is a recent development. Reinforced soil is a tensional strengthened construction that uses metallic rods, strips, geotextiles and geogrids as reinforcement material and these composite reinforced backfills are also named as mechanically stabilized earth walls.

Retaining structures have been constructed since the prehistoric times of mankind, defensive walls and religious monuments were the first examples of soil retaining systems. Later times as the size, especially the height of these structures started to increase; the lateral earth pressure generated from the mass of backfill caused stability

problems (Kerisel, 1992). To oppose this pressure, rocks and stone blocks with a larger volume and mass in front of the backfill soil were used. After that people realized that reinforcing the backfill soil would be a solution for lateral earth pressure. Lots of examples can be introduced for the application of soil reinforcement phenomena. Improving the strength of clay bricks with straws as reinforcement; sticks and dicks employed to increase the strength of mud structures; bamboo or wooden mesh used for erosion and landslide control can be presented as primitive examples of reinforced soil (FHWA, 2009).

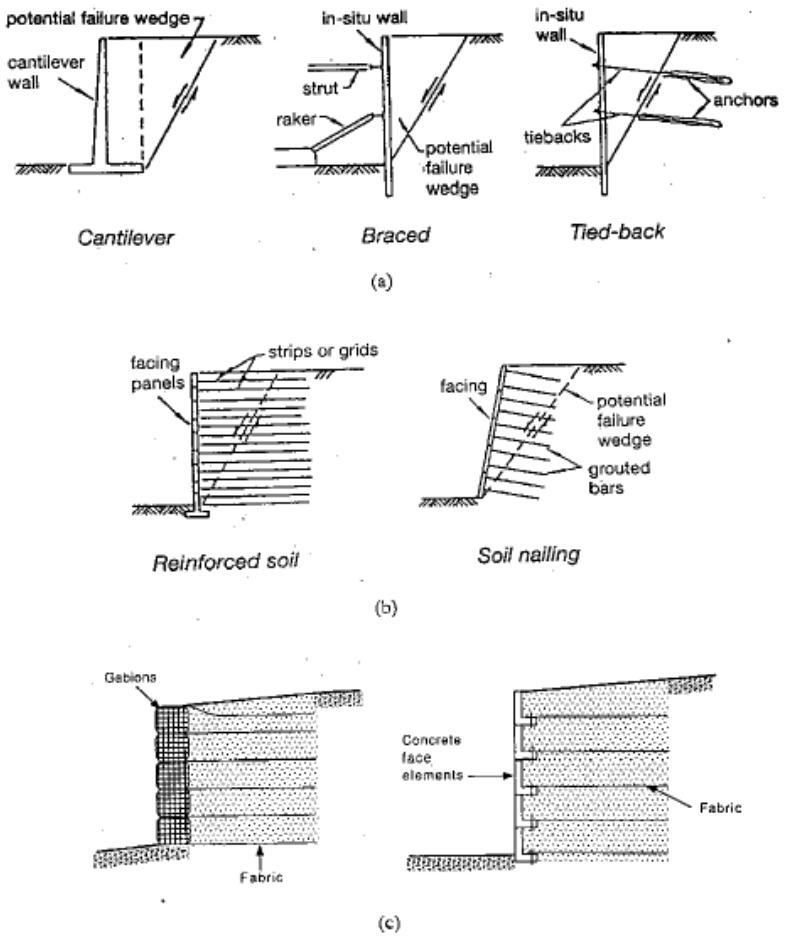

Figure 2.1. Retaining Wall System Uxamples (Jones, 1997).

However the present concept of analysis and design of soil reinforcement for retaining wall construction was developed by a French engineer Henri Vidal in the early 1960s. The French Road Research Laboratory has done comprehensive research on the use of reinforced earth as a construction material in which steel strip reinforcement is

used. The first reinforced wall example of this technology in the United States was built in 1972 on California State Highway (FHWA, 2009).

Figure 2.2 shows the components of a geosynthetic reinforced retaining wall as retained backfill, foundation (natural) soil, reinforced (mechanically stabilized) soil, reinforcement, facing element and leveling pad.

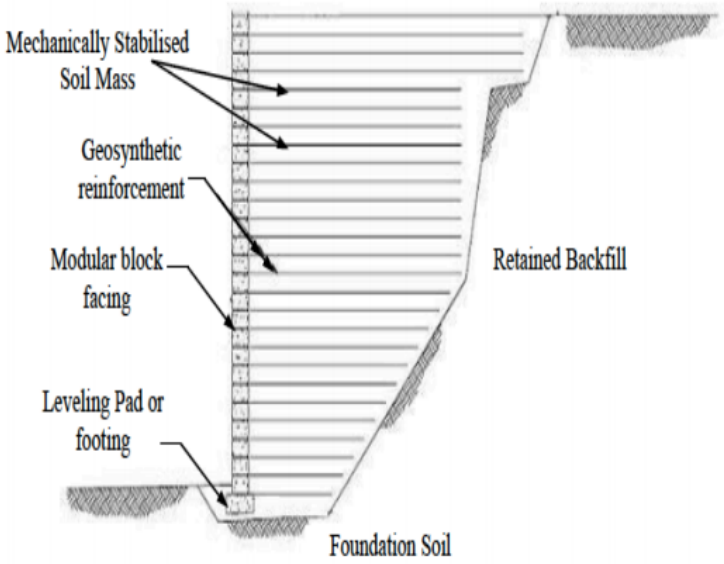

Figure 2.2. Components of a GRS-RW (Güler and Enünlü, 2009).

Foundation soil is the soil under the retained and stabilized fill that supports the entire system. Foundation soil has to be investigated for soil characteristics as bearing capacity, settlement potential, and drainage characteristic and if these features cannot meet the valid regulations; soil improvement work can be carried out. Retained backfill, located between reinforced soil and natural soil, is the compacted soil for fills but for cut walls may be the undisturbed soil. Stabilized soil mass is constructed as one layer compacted fill and one layer reinforcement; the main internal retaining system principle arises from the interaction between soil and reinforcement so this internal surface friction angle has to be high as possible. Also for the efficient reinforcement effect and compaction effort, grains size distribution and moisture content has to be regulated. No organic or harmful materials are allowed in the reinforced and retained fill. Reinforcement units are the inclusions that stabilize the soil by their tensile strength;

steel strips, geotextile (geogrid, geosynthetic) layers are employed generally as inclusion. Facing unit is a part of reinforcement system that keeps soil together between inclusions, is used to provide stability using dead weight and visual enrichment of the wall. Footing generally consists of crushed stone or unreinforced concrete; it is main task is to distribute the weight of facing units over a wider area and to obtain a level surface during construction. (Güler and Enünlü, 2009).

2.1.2. Performance of Reinforced Soil Structures

Placement of reinforcement into the backfill soil increases the tensile strength of soil and it generates a shear resistance at the interface by friction; these two effects are the beneficial actions behind the reinforced soil idea. This idea leads to use of geosynthetics as reinforcement material in various applications as retaining walls, highway embankment slopes, bridge abutments, seawalls and industrial bulk storage facilities.

MSE walls have many advantages over conventional externally stabilized retaining walls and these advantages or reasons to use reinforced soil retaining walls can be summarized as follows.

i) Flexibility of MSE walls is one of their greatest advantages. Flexibility makes them capable of tolerating large deformations due to poor subsoil foundation conditions and do not need rigid foundation supports (FHWA, 2009). Flexible behavior also prevents the crack generation that can be caused of differential settlements of subsoil. Also very small lateral earth pressure is activated at the backfill soil, compared to conventional retaining walls (Güler and Selek, 2014).
ii) Geosynthetics have higher resistance to corrosion and chemical resistance than steel reinforcement (FHWA, 2009).
iii) Simple and rapid construction provides less site preparation, appropriate for every soil condition. There is no need for very talent labor and less manpower and construction equipment is required (FHWA, 2009). Various shapes and textures for design of facing elements provide aesthetic aspects. Construction steps and finished work examples are illustrated in Figure 2.3 and Figure 2.4.

Figure 2.3. Scenes from Construction Steps of MSEWs (Tencate, 2012).

Figure 2.4. Examples of MSEW Applications (Tencate, 2012).

iv) The most important factor to prefer reinforced earth systems and geosynthetics as reinforcing material is economical aspect. Geosynthetic reinforced soil structure is cost effective because it requires less construction time, it is less dependent to weather conditions, the earthwork volume be probably reduced when compared to conventional reducing structures (Holtz, 2002). Material and labor costs can be said as other important cost reduction factors.

The cost of conventional retaining walls increase in accordance with rising height of the retaining wall and with increasing preventions for poor subsoil conditions. Ko-

erner *et al.*, (1998) performed a survey which included four wall types (gravity walls, crib-bin walls, MSE walls metal reinforcement, MSE walls geosynthetic reinforcement) that was studied and responded by 40 states of U. S. Departments of Transportation. In this manner, this survey reflects a wide national study of thousands of walls which were publicly funded. The result from the survey is illustrated in Figure 2.5 and the differences become even more apparent. Gravity walls and crib/bin walls are pretty clearly more expensive than MSE walls. Also crib/bin walls are rarely constructed over 7 m. in height. Although a convergence can be observed as the wall height increases, geosynthetic reinforced MSE walls are the least expensive of all wall categories.

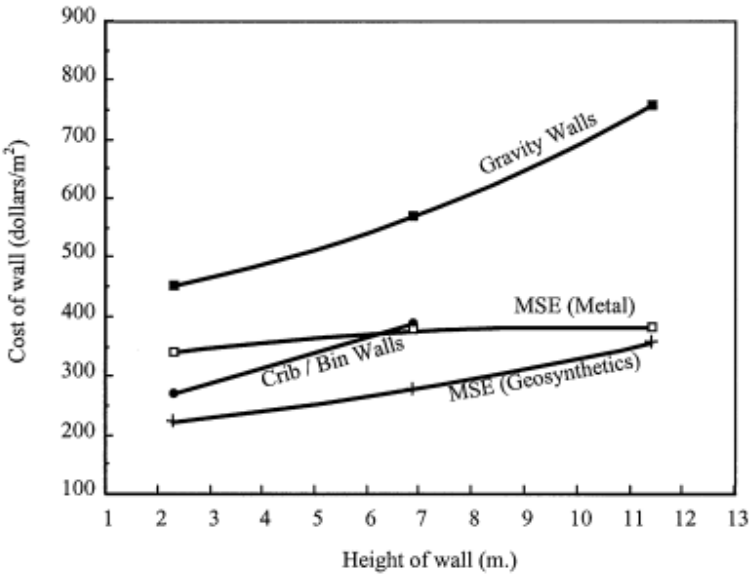

Figure 2.5. Cost for Four Types of Retaining Walls (Koerner, 1998).

To talk about disadvantages for MSE walls it can be said that they need a large volume for the reinforced backfill to fix reinforcements which can mean a relatively large earthwork and again for the backfill good quality granular fill is required which can induce an extra cost (FHWA, 2009).

2.1.3. Mechanism of Reinforced Soil Structures

Reinforced soil structure mechanism based on the principle that the soil's tension capacity is improved by the reinforcements. There are two concepts to explain the

fundamentals of this mechanism; discrete system and composite material approach.

For the discrete system; when the soil starts yielding shear forces developed in the unstable soil mass is transferred to the reinforcement layers that will provide a shear strength according to its axial tensile capacity; as it can be seen in Figure 2.6. This shear transfer has two beneficial results the developed shear stress starts to decrease and does not reach its critical limit state and the lateral earth pressures generated by reinforced soil mass is decreased. Internal shear transfer from soil to inclusion can follow two ways; friction developed from normal stress acting on the shear plane and adhesion that is an interfacial force formed between surfaces of two different materials (Hausmann, 1990).

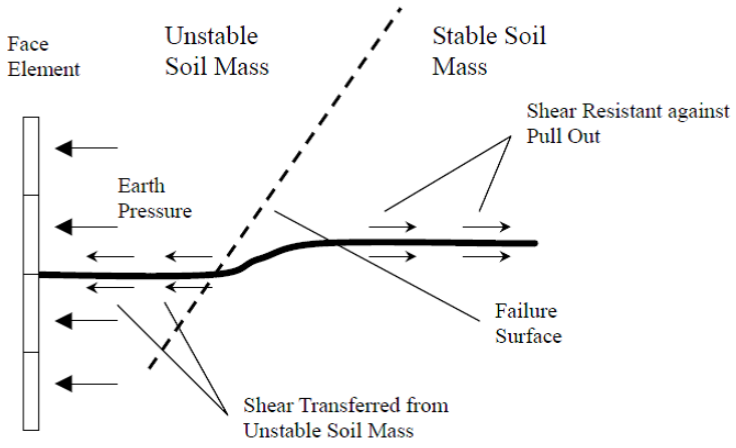

Figure 2.6. Reinforcing Soil Mechanism Discrete System Approach (Hausmann, 1990).

Reinforced soil mass can be considered as a composite system for another way to explain the mechanism using Mohr Coulomb failure criteria. As it can be seen in Figure 2.7, Mohr circle 0 represents the soil at initial condition and with increasing vertical stress Mohr circle changes to circle 1 that represents the failure condition of unreinforced soil. If the soil is reinforced Mohr circle 2 will be obtained with two possible failure envelopes. The extra vertical stress that the soil can take while reinforcement will be the difference between σ_{11} and σ_{21}. Line B and C are two assumed failure envelopes. Line B means that the friction angle of the reinforced soil does not

change and the increase in the strength is caused by the additional cohesion induced from reinforcement, C_{comp}. On the other hand, Line C suggests a higher friction angle for the reinforced soil mass caused by inclusion effect (Hausmann, 1990). Boyle (1995) conducted experiments with Unit Cell Device (UCD) to verify these two hypothesis and the test data indicates the increasing friction angle (Line C) concept. Boyle (1995) also found that the tensile stress on the reinforcement while straining increases the lateral earth pressure on the soil layer that increases its strength by confinement effect.

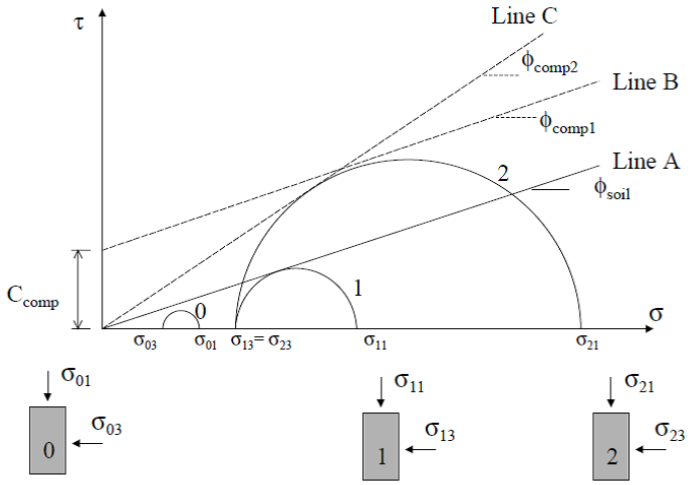

Figure 2.7. Reinforcing Soil Mechanism Composite Material Approach (Hausmann, 1990).

For failure mechanism of the reinforced system; at low confining pressures failure occurs due to slippage of reinforcement out from soil, when the confining pressure is high, rupture of the reinforcement may take place for failure.

2.2. Design of MSE Walls

Design methods and concepts are improved and suggested for reinforced soil structures and MSE wall systems, since reinforced soil concept can find place in geotechnical applications considerably in recent years. For the design concepts practiced for several years, a general consensus has been reached for the components of a design aspect as; working stress analyses, limit equilibrium analyses and deformation evaluations.

Working stress analyses can be defined simply as determining the location and properties of inclusions and calculating the stress in the reinforced soil using strength properties of the soil and inclusion (FHWA, 2001).

Limit equilibrium analyses are employed for the design of MSE walls since static lateral force equilibrium equations cannot reach a solution because the soil strength properties are nonlinear, lateral force and stress distribution are indeterminate. To overcome the indeterminacy for equilibrium equations, a "limit" potential failure or slip surface is determined; this surface may be inside, outside or partially inside/outside of the stabilized soil mass. This approach is named as "limit equilibrium analysis" and it serves to solve equilibrium by taking the shear strength of the material as the shear forces acting along the potential failure surface. In this approach, factors applied to the material strength are used to ensure that the assumed failure will not take place or in other words factor of safety recommendations are employed to decrease the deformation values which are assumed at the verge of failure to tolerable values (Güler and Enünlü, 2009). So limit equilibrium analyses approach is insufficient to determine the nonlinear behavior of soil mass, where the stress-strain analysis, deformation analysis and different types of material models are employed.

Deformation analyses are employed to observe the performance of the structure with respect to horizontal and vertical displacements and to evaluate the effect of deformations on the inclusions. Vertical deformation analyses are carried out with conventional differential settlement calculations, which are analyzed longitudinally along the wall face and transversely from the wall face to the end of reinforced soil mass. On the other hand horizontal calculations are not easy to determine and less certain for the performed analysis, so they are examined approximately (FHWA, 2001).

Major design and construction guidelines accepted in a general agreement are as following, National Concrete Masonry Association (NCMA) design manual, Federal Highway Association (FHWA) design and construction guidelines and AASHTO guidelines for design.

For design consideration, external and internal stability of the MSE wall is evaluated at all appropriate strength limit states of the reinforced soil mass under static lateral load effects and under dynamic conditions as vehicle impact and seismic loading.

In external stability evaluation, the reinforced soil zone and the facing column are considered as a monolithic gravity structure. Sliding, overturning about the toe (limiting eccentricity) and foundation bearing capacity are the three potential failure mechanisms considered in the external stability evaluation of MSE walls which is similar to that used for conventional reinforced gravity structures.

Internal stability analyses for geosynthetic reinforced soil walls are dependent on three fundamental characteristics; one of them is the soil reinforcement-interaction meaning that the resistance to pullout of geosynthetic reinforcement layers from the anchorage zone and to slide along a reinforcement layer. And the other two characteristics are the tensile resistance and durability of the reinforcing material. During the mobilization the structural integrity of the reinforced zone has to be preserved with respect to over-stressing of reinforcement within the reinforced zone (FHWA, 2009).

Facing stability analyses are performed to assure that the facing column is stable at all elevations above the toe of the wall and to ensure that over-stressing is prevented at the connections between facing units and reinforcement layers (Güler and Enünlü, 2009).

External and internal modes of failure are represented entirely in Figure 2.8 and corresponding minimum recommended factors of safety for static and seismic design are given in Table 2.1.

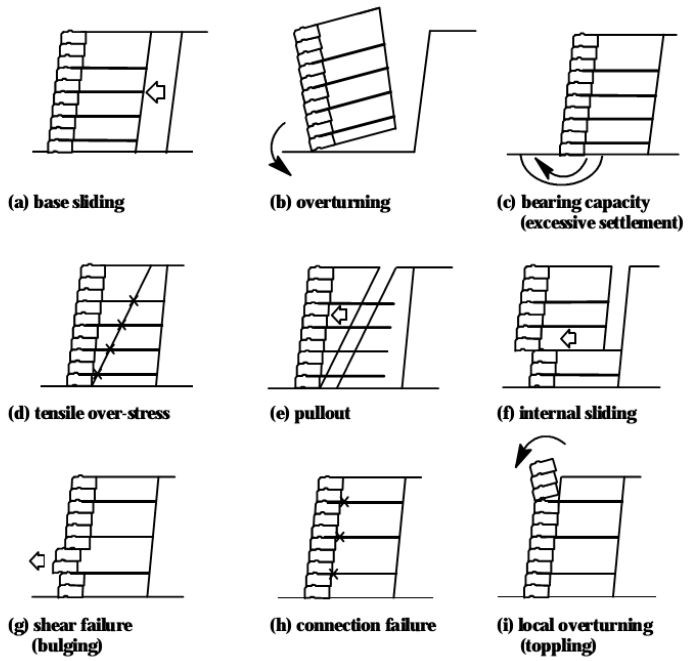

Figure 2.8. Modes of Failure for External, Internal and Facing Stability (Bathurst and Cai, 1995).

Table 2.1. Minimum Factor of Safety for Design of MSE Walls (Bathurst, 1998).

Failure Mode		Static	Seismic
Base Sliding	FS_{sl}	1.5	1.1
Overturning	FS_{ot}	1.5	1.1
Bearing Capacity	FS_{bc}	2	1.5
Global Stability	FS_{gl}	1.3-1.5	1.1
Tensile over stress	FS_{os}	1	1
Pullout	FS_{po}	1.5	1.1
Internal Sliding	FS_{sli}	1.5	1.1
Shear (bulging)	FS_{sc}	1.5	1.1
Connection	FS_{cs}	1.5	1.1
Local Overturning	FS_{otl}	1.5	1.1
Crest Toppling	FS_{otc}	1.5	1.1

2.2.1. Static Lateral Earth Pressure

Static earth pressures, active and passive pressures on retaining structures are developed according to the movement of the wall. The minimum possible horizontal pressure case implying the active earth pressure occurs when a wall rotates about its base and away from the backfill at an amount on the order of 0.001 to 0.003 radian (a top deflection of 0.001 to 0.003H, where H is the wall height). As the wall moves away, horizontal stresses decrease and shear stresses increase until shear failure occurs because the vertical stresses caused by the weight of the backfill are carried by shear strength. If the wall moves toward the backfill, horizontal stresses increase and shear stresses first decrease and then increase to a maximum at failure. Active pressure condition can generate higher horizontal stresses, because the horizontal stress along the shear plane is resisted by both shear stress and vertical stress components. Much larger wall rotations, 0.02 to 0.2 radians, are required to develop passive pressure or maximum possible horizontal pressure, than active case. Rankine theory (1857) and Coulomb theory (1776) are the two widely used approaches in most of the practices.

Coulomb theory, as it can be seen in Figure 2.9, can be employed to predict soil thrust on walls arising from irregular backfill slopes, surcharge loads on the backfill surface, and seepage forces, in contrast to Rankine theory. The most important difference is that; a unique failure angle is derived for every design condition at Coulomb wedge theory whereas Rankine theory fixes the internal failure plane.

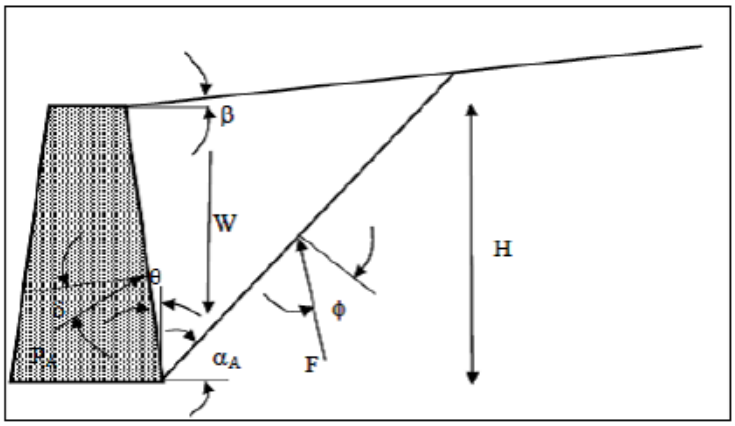

Figure 2.9. Active Earth Pressure Coulomb Wedge Theory (Başbuğ, 2011).

2.2.2. Seismic Design of MSE Walls

Analytical and numerical analyses for the seismic design of the MSE walls can be examined under three categories;

- pseudo static methods that originated from Monobe - Okabe approach
- displacement methods that varied from Newmark sliding block analysis
- dynamic finite element, finite difference methods

2.2.3. Pseudo Static Methods

Pseudo-static methods are originated from conventional limit-equilibrium methods of analysis for retaining structures in which assumed horizontal and vertical components of ground acceleration are employed as destabilizing body forces.

Monobe-Okabe method is an established approach in geotechnical engineering that is an extension of Coulomb wedge analysis. Total active earth force, PAE, generated by the backfill soil can be calculated as follows;

$$P_{AE} = \frac{1}{2}(1 \pm k_v)K_{AE}\gamma H^2 \tag{2.1}$$

where γ is the unit weight of the soil, H is the height of the wall.

The application of total active earth force on the facing column of a segmental retaining wall is illustrated in Figure 2.10.

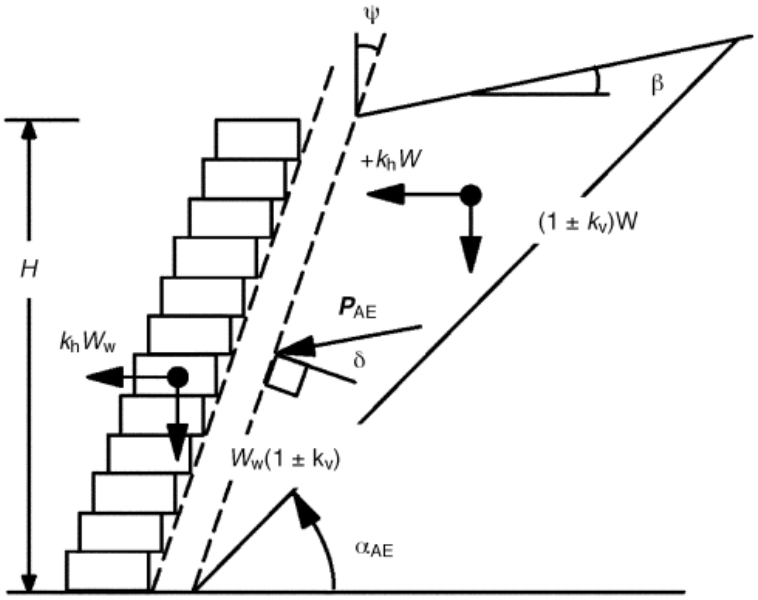

Figure 2.10. Forces and Geometry of a Segmental Retaining wall for Pseudo-static Analysis (Bathurst *et al.*, 2002).

Seed and Whitman (1970), seperated P_{AE} into two components as, P_A defining the static earth force component and ΔP_{dyn} representing incremental dynamic earth force component. K_{AE} can also be decomposed in the same manner into K_A, the static active earth pressure coefficient and ΔK_{dyn}, the incremental dynamic earth pressure coefficient.

$$P_{AE} = P_A + \Delta P_{dyn} \tag{2.2}$$

$$(1 \pm k_v)K_{AE} = K_A + \Delta K_{dyn} \tag{2.3}$$

Okabe and Zarrabi reported closed form approximate solutions for, α_{AE}, the location of the critical planar surface from the horizontal, which also means the assumed active failure plane within the soil mass and the retained soil, as follows.

$$\alpha_{AE} = \phi - \theta + \tan^{-1}\left(\frac{-A_\alpha + D_\alpha}{E_\alpha}\right) \tag{2.4}$$

where;

$$A_\alpha = \tan(\phi - \theta + \beta) \tag{2.5}$$

$$B_\alpha = 1/\tan(\phi - \theta + \psi) \tag{2.6}$$

$$C_\alpha = \tan(\delta + \theta - \psi) \tag{2.7}$$

$$D_\alpha = \sqrt{A_\alpha[A_\alpha + B_\alpha][B_\alpha C_\alpha + 1]} \tag{2.8}$$

$$E_\alpha = 1 + [C_\alpha(A_\alpha + B_\alpha)] \tag{2.9}$$

Bathurst and Cai (1995) recommended the active earth pressure distribution shown in Figure 2.11 for external, internal and facing stability calculations of reinforced segmental retaining walls based on a review of the literature for conventional gravity retaining walls.

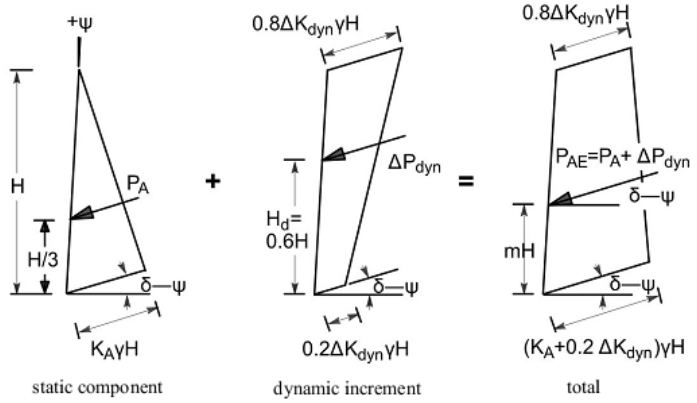

Figure 2.11. Active Earth Pressure Distribution (Bathurst and Cai, 1995).

This distribution is agreed and used in FHWA guidelines for external stability calculations. In the absence of seismic effects, the distribution becomes the triangular active static distribution due to soil weight.

Selection of seismic coefficients has been searched widely in literature and a general agreement has not been stated. In conventional pseudo-static methods of analysis, the choice of horizontal seismic coefficient, k_h, is correlated with the horizontal peak ground acceleration, a_h, in a simple manner. Bathurst and Hatami (1998), indicated that seismic coefficients depend on a number of factors, as; wall height, wall toe boundary (degree of toe restraint), base acceleration intensity, ratio of ground motion predominant frequency to wall fundamental frequency, soil properties and, to a lesser extent, the reinforcement stiffness. The following equation for k_h and a_h relation proposed by Segrestin and Bastick (1988) is used by current FHWA guidelines.

$$k_h = \frac{a_h}{g}\left(1.45 - \frac{a_h}{g}\right) \tag{2.10}$$

Seed and Whitman (1970), proposed that disregarding the vertical component of seismic coefficient, k_v, is a reasonable assumption for conventional gravity structures using pseudo-static methods for design. Wolfe *et al.*, (1978), examined reduced-scale model reinforced earth walls using shaking table tests to study the effect of combined horizontal and vertical ground acceleration on the seismic stability. They suggested that the vertical component of seismic motion may be ignored in terms of seismic stability design. These conclusions can also be criticized to be applied to GRS walls. Engineering judgment must be employed in the selection of vertical and horizontal seismic coefficients, because significant vertical accelerations may occur at sites located at short epicentral distances.

2.2.4. External Stability

As it was mentioned before during external stability analysis the reinforced soil is supposed as a rigid coherent body. Figure 2.12 represents the geometry of a inclined

backfill soil with lateral earth pressures acting on surface where the inclusion ends.

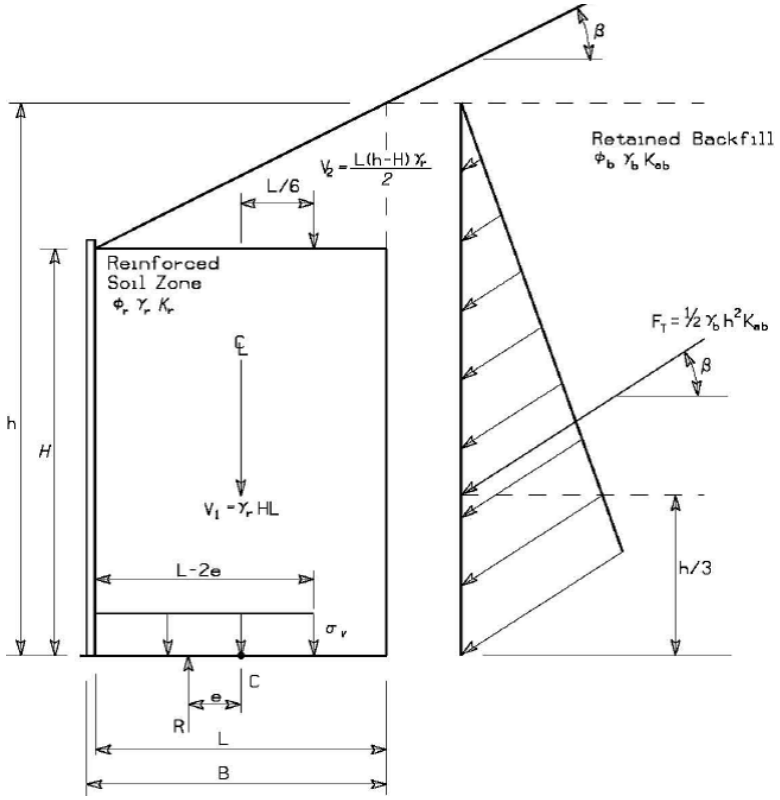

Figure 2.12. Calculation of Sliding, Eccentricity and Bearing Check of an Inclined Backfill Soil (FHWA, 2009).

As it is illustrated in Figure 2.12, to compute vertical stress, sv, at the base of the wall, total applied lateral force from the retained soil fill, KT, behind the reinforced zone will be calculated as following.

$$F_T = \frac{1}{2} K_a \, \gamma_f \, h^2 \tag{2.11}$$

where γ_f is the unit weight of retained fill, h is the height of reinforced zone from base.

To provide overturning stability, eccentricity in the reinforced zone obtained from following equation has to be smaller than L/6 limit value. If it exceeds the limit, reinforcement length should be increased.

$$e = \frac{F_T \cos\beta \ \frac{h}{3} - F_T \sin\beta \ \frac{L}{2} - V_2 \frac{L}{6}}{V_1 + V_2 + F_T \sin\beta} \tag{2.12}$$

where e is the eccentricity, L is the reinforcement length, V_1 is the weight of the reinforced soil zone, V_2 is the weight of inclined zone over reinforced soil zone.

Also vertical stress, σ_v, at the base of the wall will be calculated with horizontal and vertical loads as in Equation 2.13, surcharge loads can also be added for the geometry illustrated in Figure 2.12.

$$\sigma_v = \frac{V_1 + V_2 + F_T \sin\beta}{L - 2e} \tag{2.13}$$

Sliding stability analysis will be carried out by ensuring the factor of safety, which is the ratio of the resisting forces to the driving forces, is greater than the limit value 1.5 (FHWA, 2009). Factor of safety for sliding stability, resisting and driving forces can be calculated as follows.

$$FS_{sliding} = \frac{\sum horizontal\ resisting\ forces}{\sum horizontal\ driving\ forces} = \frac{\sum P_n}{\sum P_d} \geq 1.5 \tag{2.14}$$

$$P_d = F_T \cos\beta \tag{2.15}$$

$$P_n = (V_1 + V_2 + F_T \sin\beta)\mu \tag{2.16}$$

where μ is the coefficient of friction at the base.

The coefficient of friction at the base of reinforced soil is decided by taking the minimum of these three: internal friction angle of the retained fill, internal friction angle of the reinforced soil and the soil-reinforcement friction angle.

After the static effects for the external stability analyses are determined, seismic effects will be investigated with pseudo-static analysis similar to conventional gravity structures.

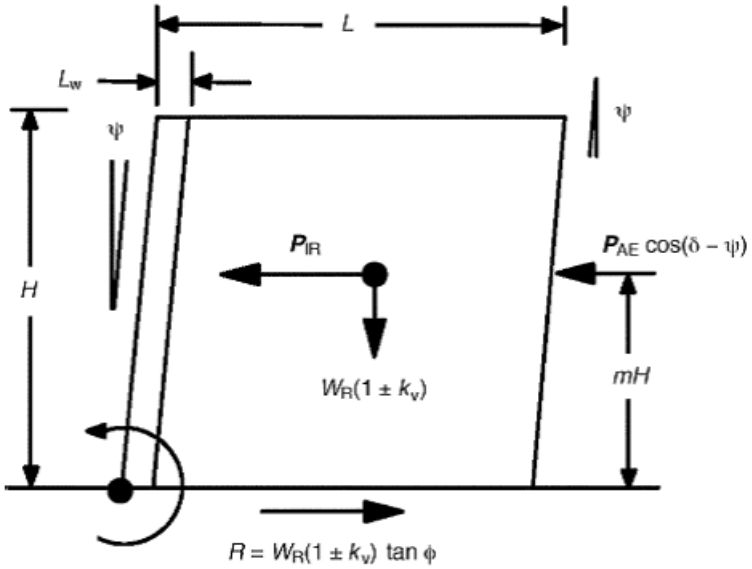

Figure 2.13. Geometry and Forces for External Stability Calculations (Bathurst *et al.*, 2002).

Figure 2.13 illustrates the simplified geometry and horizontal forces assumed in external stability calculations for the segmental retaining wall case. Resisting load in factor of safety equation for base sliding and overturning is determined by, W_R, the weight of the reinforced zone plus the weight of the facing column. The inertial force due to the gravity mass, P_{IR}, can be obtained by the following expression proposed by Cai and Bathurst (1995).

$$P_{IR} = \eta \, k_h \, \gamma H^2 \tag{2.17}$$

where η is taken as 0.6 based on recommendations for reinforced walls that use steel reinforcement.

Limiting the acting point of the resultant mass, W_R, within L/3 of the base midpoint ensures the overturning stability of the reinforced mass for walls subject to seismic effects. FHWA (1996) guideline for geosynthetic-reinforced walls also does not include overturning as a potential failure mode for external stability.

2.2.5. Internal Stability

Internal failure of GRS walls can occur in two different mechanisms. The tensile forces in the reinforcements or the shear forces in the case of rigid reinforcements increase to values over their tensile strength capacity so that failure becomes by elongation or breakage of reinforcements which can cause large movements and/or possible collapse of the structure. The other possible mechanism is failure by pullout, which occurs when the tensile forces in the reinforcement become larger than the pullout resistance (FHWA, 2009).

The procedure for internal stability design consists of determining the maximum tensile forces, their location along critical slip surfaces and the resistance provided by the reinforcements both in pullout capacity and tensile strength. The critical slip surface is expected to coincide with the maximum tensile forces line in each reinforcement layer.

Selection of soil reinforcement type is another issue, inclusions are either inextensible (mostly metallic) or extensible (mostly polymeric materials). The shape and location of the critical failure surface is based upon reinforcement structure and theoretical studies. This critical failure surface suggested in FHWA recommendations are approximately bilinear in the case of inextensible reinforcements (Figure 2.14), approximately linear in the case of extensible reinforcements (Figure 2.15), and both passes through the toe of the wall (FHWA, 2009).

Methodology for internal stability calculation consists of calculating the maximum tensile forces in the reinforcements and checking the breakage and pullout failure potential at these tensile forces for static and dynamic loading conditions.

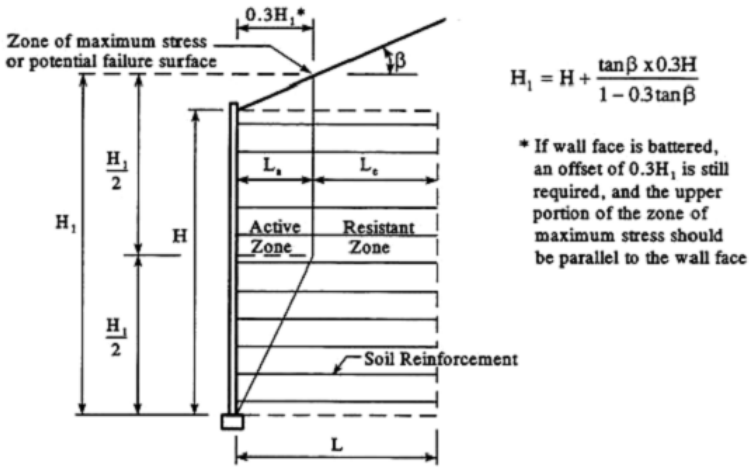

Figure 2.14. Location of Assumed Failure Surface for Inextensible Reinforcement (FHWA, 2009).

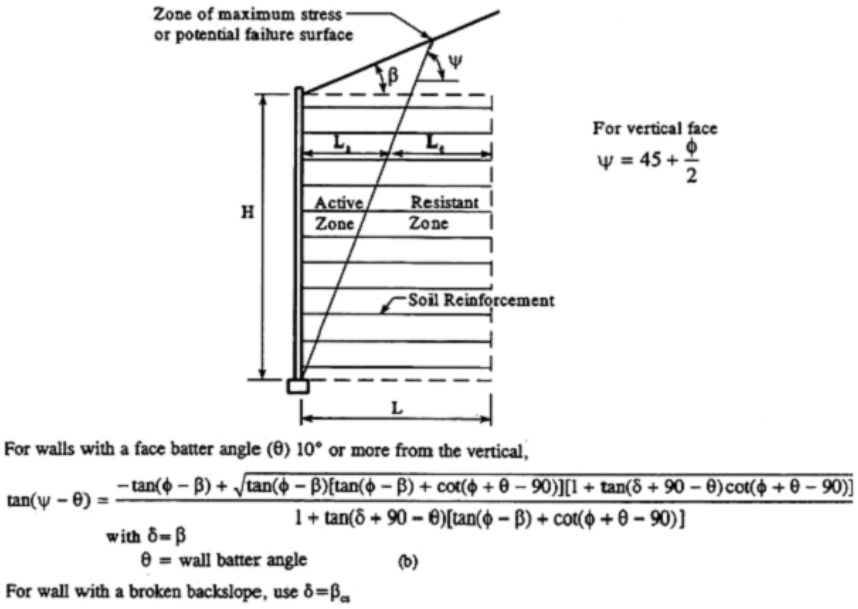

Figure 2.15. Location of Assumed Failure Surface for Extensible Reinforcement (FHWA, 2009).

More reinforcement in the upper portion of the wall is required for stability when uniform reinforcement length and spacing is used for the full height of the wall. Therefore varying the reinforcement density with depth can result a cost saving. The maximum vertical spacing of reinforcement should be limited to two times of the block depth, for walls constructed with modular blocks (FHWA, 2009). For internal stability analysis, the distribution of horizontal stress, σ_H, is established with Equation 2.19

and the point at which failure line intersects the inclusion for each reinforcement level is determined. Lateral active earth pressure coefficient K_a is obtained using a Coulomb earth pressure relationship and it is simplified to Rankine's equation for a vertical wall with horizontal backfill. The coefficient K_r always equals to K_a for geosynthetic reinforcement at any ground depth.

$$K_a = \tan^2(45 - \frac{\phi}{2}) \tag{2.18}$$

$$\sigma_H = K_r \, \sigma_V + \Delta\sigma_H \tag{2.19}$$

where $\Delta\sigma_H$ is the horizontal stress increment due to any horizontal concentrated surcharge, σ_v is the total vertical stress including soil self-weight and any vertical surcharge.

Maximum tension force in each reinforcement layer for unit width of the wall can be calculated as following:

$$T_{\max} = \sigma_H \, S_v \tag{2.20}$$

where S_v is the vertical reinforcement spacing.

Now, the suitable strength of reinforcement and number of discrete reinforcement layers for the vertical reinforcement layout can be selected. Stability with respect to the breakage will be ensured when the maximum tension force, T_{max}, does not exceed the limiting value, T_a, the allowable tensile strength of the reinforcement (FHWA, 2009).

Stability according to pullout failure should be checked with the following equation for each layer, as pullout resistance and/or tensile loads may change for each

reinforcement layer.

$$T_{\max} \leq \frac{1}{FS_{PO}} F^{*} \gamma \, Z_p \, L_e \, C \, R_c \, \alpha \tag{2.21}$$

where FS_{PO} is the safety factor against pullout, should be greater than or equal to 1.5, C is taken as 2 for strip, grid, and sheet type reinforcement, α is the scale correction factor, $F*$ is the pullout resistance factor, R_c is the coverage ratio, γZ_p is the overburden pressure including distributed dead load surcharges, L_e is the length of inclusion in the resisting zone.

From above equation; length of inclusion in the resisting zone, L_e, can be calculated, also considering FHWA recommendations as illustrated in Figure 2.14 and Figure 2.15 (FHWA, 2009).

The total length of the reinforcement, L, can be found with sum of, L_e and L_a; L_a length of reinforcement in the active zone can be found with:

$$L_a = (H - Z) \tan(45 - \frac{\phi}{2}) \tag{2.22}$$

where Z is the depth to the reinforcement level.

To check the internal stability under seismic loading, FHWA recommends the addition of dynamic increments calculated at each reinforcement layer to the tensile force comes from static influence. Pseudo-static methods for walls, assumes that the internal earth pressure is distributed such that each reinforcement layer carry a portion of the integrated earth pressure over a tributary area, S_v. FHWA guideline suggests the procedure shown in Figure 2.16 to get reinforcement forces for over-stressing (breakage) and pullout calculations. In this method, Rankine earth pressure theory is used with a Rankine failure plane (α=45+φ/2) for vertical walls, to calculate the static earth force, P_A, Bathurst *et al.*, 2002. The dynamic earth force is calculated as;

$$\Delta P_{dyn} = k_H \, W_A \tag{2.23}$$

where W_A is the weight of the static internal failure wedge.

The distribution of the dynamic tensile reinforcement load increment, ΔT_{dyn}; that will be added to static tensile force to find total tension load, T_i; is distributed regarding the anchorage lengths in the resistance zone according to Equation 2.24.

$$\Delta T_{dyn\,i} = \Delta P_{dyn}\, L_{ai} / \sum_{j=1}^{N} L_{aj} \tag{2.24}$$

where L_a is the anchorage length.

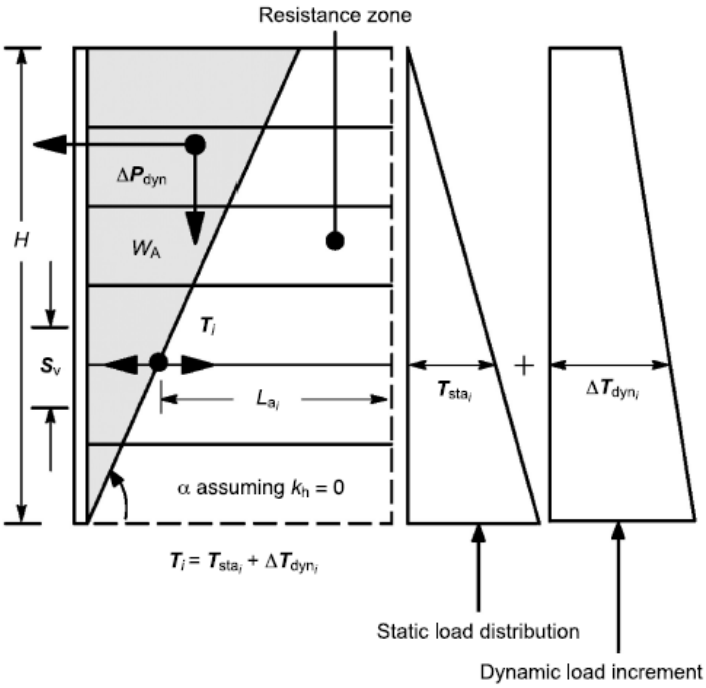

Figure 2.16. Seismic Effects for Internal Stability Check (Bathurst *et al.*, 2002).

Various methods are employed for internal stability analysis; two-part wedge failure mechanism as illustrated in Figure 2.17 and log spiral failure mechanism shown in Figure 2.18 are preferred approaches (Bathurst *et al.*, 2002).

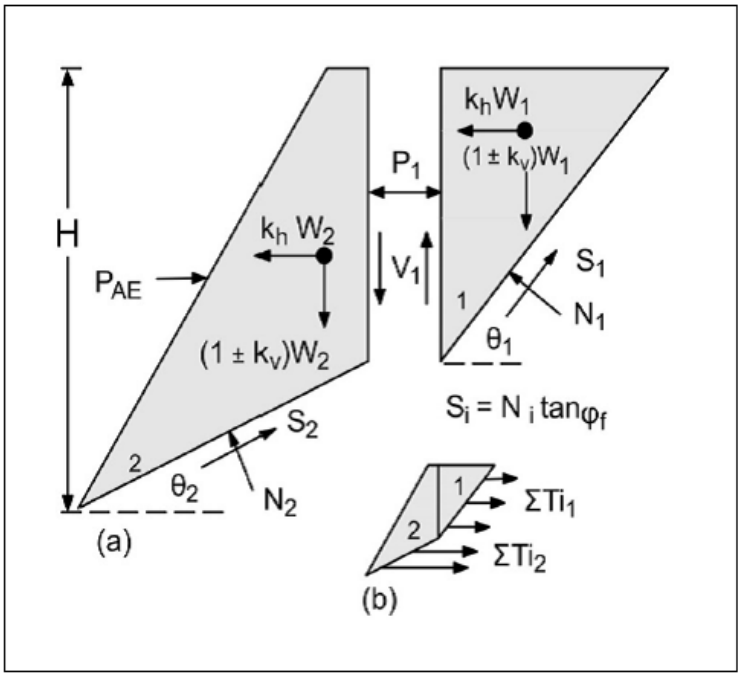

Figure 2.17. Two Part Failure Wedge Analysis (Bathurst *et al.*, 2002).

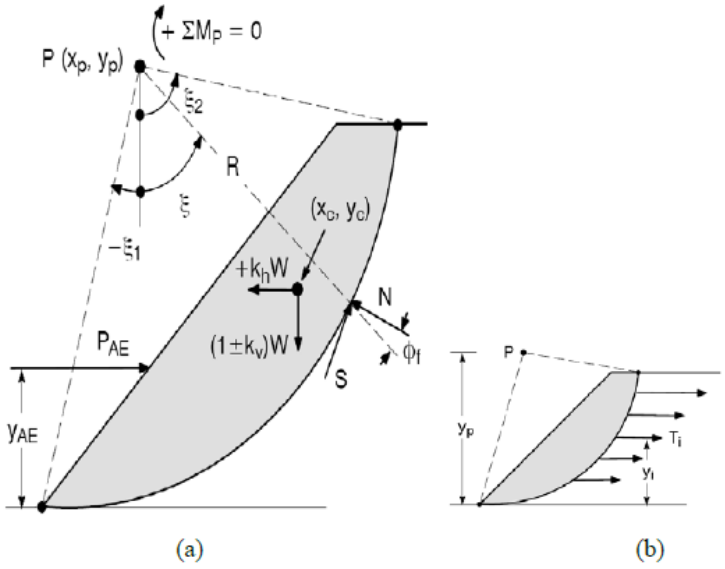

Figure 2.18. Log Spiral Analysis (Bathurst *et al.*, 2002).

2.2.6. Newmark's Sliding Block Displacement Analysis

Pseudo-static analysis based on limit equilibrium methods do not include deformations and displacements which sometimes reach to undesirable values that can also

be defined as failure. Newmark's theory regards the potential sliding body as a rigid monolithic mass under the influence of seismic forces. Each time the seismic force induced on the body (plus the existing static force) overcomes the available resistance strength along a potential sliding shear surface, permanent displacement of the mass develops and accumulates stepwise.

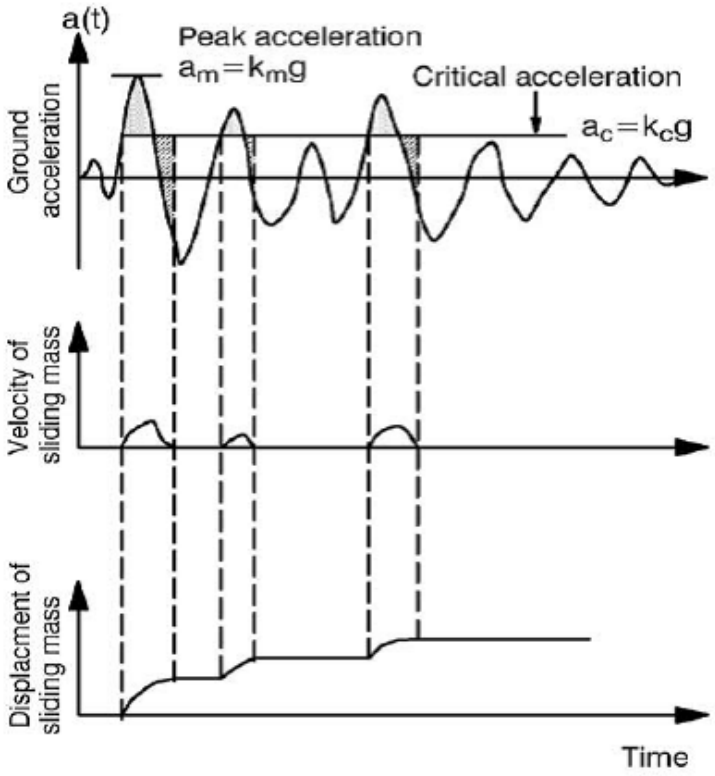

Figure 2.19. Newmark's Method to Calculate Permanent Displacements (Bathurst *et al.*, 2002).

The critical acceleration, $k_{|c|}$, to initiate sliding or shear failure should be determined for each translation failure mechanism to employ Newmark's method. The value of $k_{|c|}$ can be determined from pseudo-static analysis by searching for values of k_h that give a factor of safety of one. As it can be seen in Figure 2.19, the critical acceleration is determined on the horizontal ground acceleration record from the site and double integration is performed to calculate cumulative displacements; where g is the gravitational constant, a(t) is the horizontal ground acceleration function with time t, $am = k_m$ g is the peak value of a(t), and $a_{|c|} = k_{|c|}$ g is the critical horizontal

acceleration of the sliding block. The permanent displacement under seismic action is calculated by integrating those portions of the acceleration time history graph that are above the critical acceleration and those portions that are below until the relative velocity between the sliding mass and the sliding base reduces to zero, for a given ground acceleration time history and a known critical acceleration of the sliding mass (Bathurst *et al.*, 2002).

Newmark's double integration method and Bathurst and Cai's mean upper bound method are used to calculate permanent displacements. Figure 2.20 is used to obtain non-dimensionalized displacement in terms of $d/(v_m^2/k_{mg})$ for critical acceleration ratio by given methods.

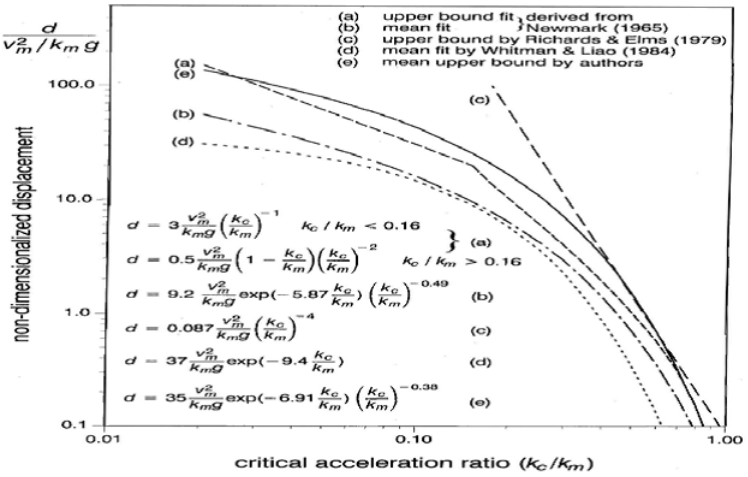

Figure 2.20. Non-dimensionalized Displacement in Terms of $d/(v_m^2/k_{mg})$ Versus Critical Acceleration Ratio (Bathurst and Cai, 1996).

2.3. Seismic Performance of Reinforced Soil Structures in Literature

In the literature, behavior and characteristics of GRS structures under seismic loads have been searched in every respect including laboratory tests for soil-reinforcement interaction, analytical and FEM models representing reinforced soil structure, scaled laboratory models tested with centrifuge or shaking table and site surveys. Koseki *et al.*, (2006) summarized the seismic performance of GRS structures including site case histories for reinforced soil structure performances in recent earthquakes.

Sandri (1994) made a site inspection for reinforced modular block retaining walls higher than 4.5 m in Los Angeles area after 1994 Northridge earthquake. This inspection shows that no visual damage was observed on 9 0f 11 structures located within 23 to 113 km of epicenter.

After 1995 Kobe earthquake in the study of Tatsuoka (1997) it was found out that GRS wall with a full-height rigid facing was damaged insignificantly, displacements of 20 cm at the top and 10 cm at the bottom was recorded. This 5.8 m GRS wall had the same performance with a conventional retaining wall at the same location and equipped with a very expensive support system including bored piles. After the Kobe earthquake Nishimura *et al.*, (1996) surveyed 10 geogrid reinforced soil walls with different heights and steepened slopes. All the structures survived with small deformations, even during the earthquake peak ground acceleration range changing between 0.3 to 0.7 g.

The study of Koseki and Hayano (2000) after 1999 Chi Chi earthquake, addressed the importance of reinforcement spacing with some examples. Excessive deformation on the facing and reinforcement rupture was observed at a reinforced segmental retaining wall with 80 cm reinforcement spacing, whereas the deformations remained limited for the retaining walls with 60 cm spacing.

After 2001 El Salvador earthquake with a magnitude of 7.6, a large number of retaining walls damaged which were not built in compliance with seismic design guidelines, where the others constructed in an ordered way survived with minor damages. The main problems met for the damaged walls were the additional overturning loads at the top of the wall developed by the masonry privacy fences placed at the top of the wall and extension of the top unreinforced (gravity) portion of the walls added after construction. Cutting reinforcements behind the wall to attach subsurface utilities was also a major cause of failure (Race and del Cid, 2001).

2.3.1. Review for Marginal Backfill Examples

Successful performances of properly designed and constructed reinforced walls with marginal (including cohesive) backfills were observed during earthquakes. During these seismic actions no significant signs of structural distress or movements have been noted. Also an embankment built using a clay backfill and reinforced with nonwoven geotextiles performed good during the experience of a relatively large earthquake motion (Nakamura *et al.*, 1988). Thus, it is clear that use of fine grained marginal soils as backfill material with proper design will lead to important cost savings, new soil reinforcement applications and also utilization of materials such as nearly saturated cohesive soils and mine wastes; which would otherwise require disposal in construction projects. The high transportation costs of the granular backfill material may be as much as the half of the total cost and substantial costs generated from the disposal of unused cohesive soils has to be added; on the other hand reinforcement materials account for a relatively small portion of the total cost. For an example of a 6 m high reinforced earth wall the portions of the total cost was noted as 17% for reinforced elements, 25% for facing, 40% for the granular fill, 15% the parapets and foundation and 3% represented the earthwork (Mitchell and Zornberg, 1995).

Reduced-scale models and full-scale models of reinforced soil structures that used fine grained soils as backfill have been built to help to observe the feasibility of soil reinforcement interaction.

To investigate the performance of these walls by using cohesive fills, a full scale experimental reinforced wall was constructed by the Transport and Road Research Laboratory, U.K. (Murray and Boden, 1979). The wall was built as a vertical sided 6 m high embankment, with three layers of different fill materials each constituted about one-third of the height. At the lowest level a wet cohesive fill was placed, in the middle layer granular fill was used and a cohesive fill at lower moisture content was placed in the upper section; various different types of impermeable reinforcing elements (seven types) and four types of facing panels were used as in Figure 2.21. Pore water pressures during the construction and six months later were monetarized and it was seen that

relatively high excess pore water pressures generated in the lower wet sandy clay layer. In the first two years after construction of the fill material large horizontal movements and vertical settlements were observed. Measured vertical settlements were up to 50 mm just behind the facing panels and up to 40 mm were recorded in the middle of the embankment. Along various reinforcement types no preferential drainage was observed and also for vertical settlements walls supported by metallic or plastic reinforcements created a little difference when compared with other reinforcement types.

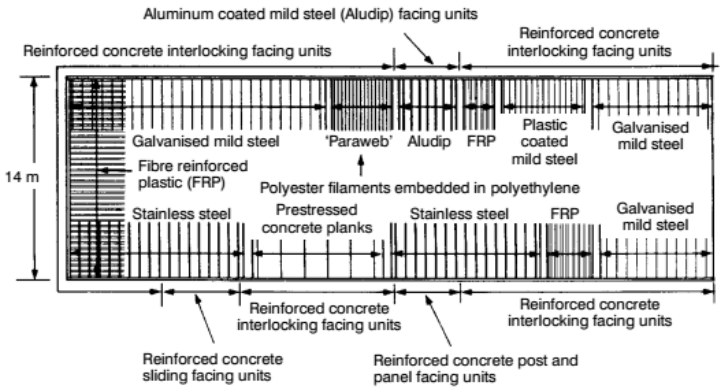

Figure 2.21. Transport and Road Research Laboratory (TRRL) experimental Reinforced Wall (Murray and Boden, 1979).

The Devon test fill, built in Alberta, Canada is a 12 m high test embankment that was constructed as three sections reinforced with different geogrid materials and one unreinforced section. Silty clay that was compacted at wet of optimum was used as fill material to get significant deformations and geogrid strains and to comprehend their relation with pore water pressure generation. The instrumentation was placed within the embankment as shown in Figure 2.22. The construction period was resulted in 26 months; first a 3 m fill was placed then another 3 m fill was placed and finally with a 6 m fill the construction period was completed. The pore water pressures increased in direct response to the loading during the fill placement periods. During embankment construction the embankment underwent vertical and horizontal deformation which generated strain in geogrids. During winter shut down significant settlements were reported as the pore water pressures dissipated. The increase of effective stress made the soil stronger, the geogrids were not subjected to much additional load and the

measured strains decreased slightly. After the embankment reached the fill height of 12 m, an increase in the pore water pressure was observed which was attributed to shear deformations occurring within the embankment and to migration of pore water pressures from the center of embankment to the slope face. Within this study it was understood that generated pore water pressures affected the performance of the monitored reinforced structure significantly and lateral and vertical displacements were closely related to the generation and dissipation of pore water pressures (Sego *et al.*, 1990).

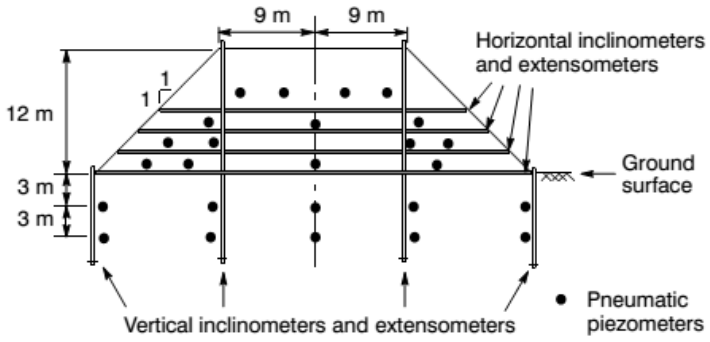

Figure 2.22. Instrumentation in Devon test fill (Sego *et al.*, 1990).

Five full scale field test embankments were constructed in Japan to examine the effect of nonwoven geotextile reinforcements on the stability and deformation of clay embankments and to investigate the stabilizing function of structural facing elements in steep reinforced clay embankments (Tatsuoka and Yamauchi, 1986; Tatsuoka *et al.*, 1990). A volcanic ash clay called Kanto loam that had a degree of saturation of 83 to 90% was used as backfill for these geotextile reinforced embankments which ranged in height from 4 to 5.5 m. The test embankments performed satisfactorily when they were subjected to heavy rainfalls and earthquakes. When the embankment was exposed to rainfall a high degree of suction was occurred in the geotextile reinforced zones (U1, U3, U4 and U6) and positive pore water pressures were generated in the unreinforced zone (U2 and U5) as in Figure 2.23; where limit equilibrium analysis showed that suction in the backfill material contributes significantly to the stability of the clayey slopes. After the rainfall rapid pore water pressure dissipation was observed through geotextile layers where they worked effective as a drainage layer. With the observa-

tion that any notable displacement would not occur under natural heavy rainfall, the embankment was subjected to a heavy artificial rainfall. Then, several large cracks appeared only in the unreinforced fill behind the reinforced zones. The three main modes of deformation took place as; rotation about the toe, sliding along a shear band and local compression near the toe. Any cracks or slip surfaces did not appear in the reinforced zones which indicated that the nonwoven geotextiles were effective in reinforcing the cohesive backfill. The stability of reinforced soils can be increased by using facing structures with various kinds of rigidities as local rigidity, overall axial rigidity and overall bending rigidity. The slope faces of these structures were either wrapped around with nonwoven geotextiles; which caused the larger deformations to be occurred among the other facing types, covered with discrete concrete panels or constructed with the aid of gabions. In this study it was observed that the use of full height continuous rigid facing would be effective in reducing the deformations in clay reinforced walls.

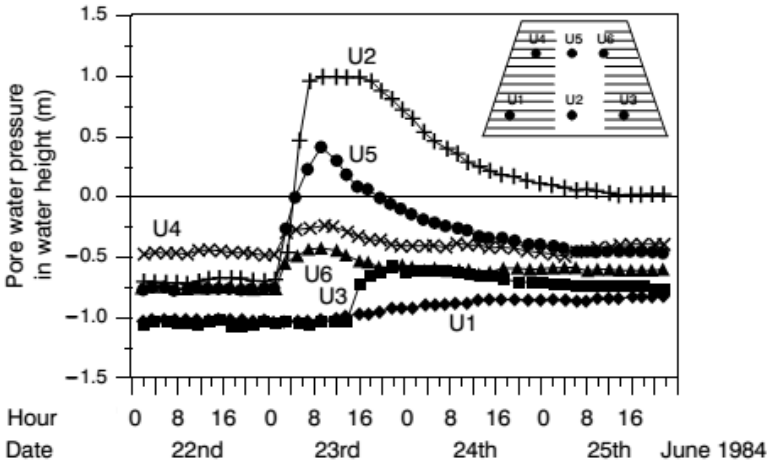

Figure 2.23. Variation of Pore Water Pressures During Rainfall in a Clay Embankment Reinforced with Nonwoven Geotextiles (Tatsuoka and Yamauchi, 1986).

The first geotextile reinforced wall was built by French Highway Administration in Rouen in which weathered chalk, silt and fire stone were used as backfill material. The wall was 4 m high and 20 m long and was founded on very compressible peat with a water content of 300%. Nonwoven geotextile layers were extended 5 to 6 m behind the wall face and geotextile layers wrapping around 0.5 m thick backfill layers formed

the wall face. An inclinometer located in the reinforced fill measured a total settlement of 1.1 m and differential settlements of 250 mm over a length of 3 m and 20 mm lateral deformations were occurred on the wall face.

Centrifuge models of geotextile reinforced and unreinforced vertical walls comprised kaolin clay as backfill at its plastic limits were built by Goodings (1990). The models were reinforced with variable vertical spacing and length, where each layer of soil was compacted using a pressure of 200 kPa. In lightly reinforced walls, two modes of failure were observed as, opening of a tension crack followed by overturning and geotextile breakage. Opening of a tension crack followed by the development of an inclined sliding failure surface that appeared on the wall face was the failure type emerged at intermediate to heavily reinforced models as it is shown in Figure 2.24. Failures occurred by geotextile breakage; did not by pullout in all cases. Models were also generated with backfills in which sand was mixed with different percentages of sand as well as different natural soils. In all tested models reinforcement represented a significant beneficial effect when equivalent height reinforced and unreinforced models were compared. It was also noted that increasing number of reinforcement layers increased the reinforcement effectiveness.

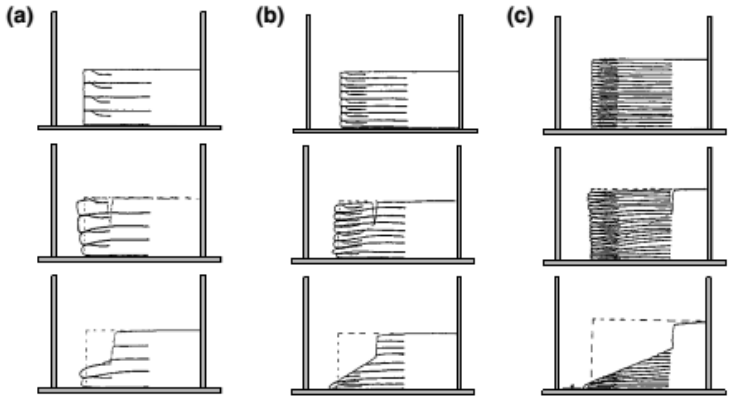

Figure 2.24. Failure Modes for Centrifuge Models (a) Lightly Reinforced Model; (b) Intermediate Reinforced Model; (c) Heavily Reinforced Model (Goodings, 1990).

2.3.2. Shaking Table Tests

Advantages as economic concerns and beneficial control over parameters make the shaking table tests most preferred testing method especially for the dynamic loading conditions despite their deficiencies in terms of scaling effects and boundary conditions. A twenty year summary for the shaking table tests performed to investigate seismic behavior of geosynthetic reinforced retaining walls is reported in that chapter.

Japan is an outstanding country for earthquake resistant design due to availability of test facilities. In order to establish design specifications two main Japanese agencies, Japan Railway Technical Research Institute (Murata *et al.*, 1994) and Public Works Research Institute (Matsuo *et al.*, 1998) conducted the pioneer model tests. JR Wall was constructed as 2.5 m high, ½ scaled back to back type model wall, had a gabion/rigid concrete panel facing wall, strength of geogrid reinforcement was decreased to one-third of the prototype, reinforcement length to wall height ratio was 0.4 and backfill was dry sand. Horizontal sinusoidal waves and scaled earthquake results up to 0.5 g at 3.4 Hz were applied as base acceleration. The main results obtained from these test were increase in reinforcement loads due to base excitation were very small and increased towards the facing wall. Sinusoidal wave excitation created greater deformation compared to scaled earthquake records. Amplification results were similar for the reinforced zone that behaved as a monolithic body and unreinforced zone and these values could reach up to 1.5 at wall top. PWRI model walls had height of 1 and 1.4 m with incremental and propped wall facing types, reinforcement length to wall height ratio was 0.4 and 0.7, and effects of facing slope (vertical and battered) was also investigated during the tests. A sinusoidal base acceleration with stepwise increasing amplitudes at 5 Hz was conducted also with scaled ground motions. Recorded ground motions resulted with higher margin of safety for tested walls compared to sinusoidal base excitations. Even the predicted factor of safety was less than one, any failure case was observed for model walls. It was also observed the most effective way to reduce to wall deformation was increasing the reinforcement length ratio L/H. An unexpected result was also obtained as the horizontal displacements at the top of the walls were greater for continuous panel facing than discrete facing wall.

After 1995 Kobe earthquake a study was conducted by Koseki *et al.*, (1998) including tilting and shaking table tests on both conventional and geosynthetic reinforced model walls. Propped panel was used as facing for reinforced wall and phosphor-bronze strips were used as geogrid reinforcement with L/H=0.4 ratio. A sinusoidal excitation with stepwise increasing amplitude at 5 Hz was used as ground base motion. Within the experiments, overturning was observed as the main failure mode for both conventional and reinforced walls but model walls were placed on a soft foundation (200 mm thick, Toyura sand) that might be the reason for overturning was supposed as the main failure mode. This observation contributed to FHWA (1996) guidelines with a new recommendation that the overturning failure mode should not be ignored when the wall was seated on a soft foundation. In reinforced soil walls, shear deformation was observed in the reinforced zones and it was recommended that the effects of this deformation should be taken into account for displacement calculations. Steeper failure plane angles were generated in all model walls compared to the estimated values obtained with pseudo static methods.

Tatsuoka *et al.*, (1998) also carried out tilting and shaking table tests on various reduced scale model walls. Different failure patterns were observed during the tests as straight failure plane for unreinforced backfills and two part wedge for reinforced backfills and this observation inspired the opinion that a different pseudo static method should be used for the design of reinforced wall. According the test results it was obtained that the critical k_h value could not totally control the failure plane angle.

The study, of Bathurst *et al.*, (1996) in which seismic performance of model reinforced segmental retaining walls were examined, focused on the effect of interface shear properties on the facing column stability in terms of the measured front wall displacements. The model was 1/6 scaled version of the prototype with 240 cm length, 102 cm height and 140 cm width, the backfill was a standard laboratory silica #40 sand, HDPE geogrid was used as reinforcement at five layers. Four model walls differed from each other according to facing batter (vertical or inclined 8 degrees), block-block and block-geosynthetic interfaces (fixed and frictional). Interfaces gained their shear capacity directly from sliding resistance were named as frictional type while the other

interfaces were fixed at some locations to attain higher shear capacity. The amplitude of the base input was incrementally increased up to 0.4 g where the input frequency was kept constant at 5 Hz. As a conclusion it was reported the resistance of the retaining wall system was improved by increasing the shear capacity from frictional to fixed type interfaces and by increasing the wall batter. Measured accelerations did not show a uniform distribution throughout the soil wall system. Critical accelerations used in pseudo static analysis could be obtained from the measured accelerations at the middle of the wall and at the top of the backfill surface because they gave accurate estimations. Tensile loads occurred on the reinforcements were quite lower than the tensile capacities.

The studies of El Emam and Bathurst (2004 and 2005) pointed out that in the previous work the forces developed against the facing column and transferred to the wall toe had not been measured. In this study, model walls with the same geometry (Figure 2.25) of previous work were constructed with different facing panel toe boundary conditions (hinged or sliding), reinforcement layer (length, spacing and axial stiffness) and facing panel configurations (panel thickness (mass) and inclination angle). A large number of instruments were located on 14 different model walls measuring toe forces, wall displacements, reinforcement strains and acceleration-time responses at selected locations. During the base input motion the reinforcement load was observed as greatest at the back of the facing panel (at the connections). The amplitude and duration of the base excitation were the key parameters that affected the magnitudes of the permanent lateral displacements of the front facing. Also, larger permanent displacements of facing panels were recorded with sliding toe compared with hinged toe. At the end of construction the restrained toe could take approximately 50% of the earth force acting behind the facing panel and for base accelerations greater than 0.4 g more than 50% of the total earth force was attracted by the toe. Toe vertical loads measured at the base of the front facing were higher that the weight of the facing, probable cause of this situation was the down-drag forces generated at the back of wall face. Tensile load distributions along the reinforcements were more uniform compared with the estimated triangular distribution in pseudo static design methods. Difference in amplification values measured in the sand backfill and on the front facing attributed

to the fact that the structure did not work as a monolithic body.

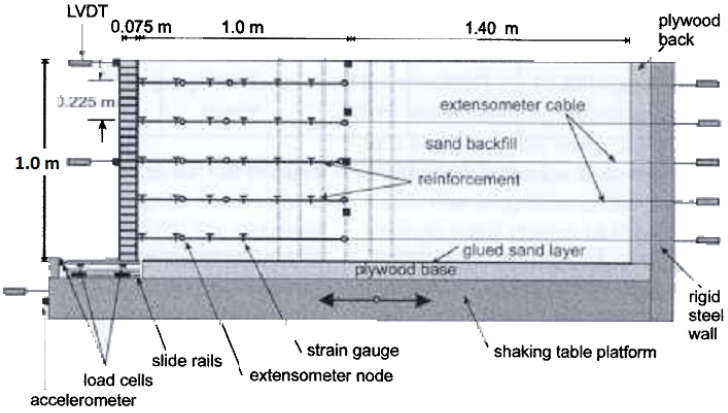

Figure 2.25. Configuration of Model Wall and Instrumentation Layout (El Emam and Bathurst, 2004).

Ling *et al.*, (2005) examined shaking table tests for three modular block front facing geosynthetic reinforced retaining wall systems, the model walls had 2.8 m height, 2 m width and 4 m depth and the front face constructed with concrete blocks had a batter of 12o as illustrated in Figure 2.26. Fine sand at a moisture content of 9.5% was used as backfill and polyester (PET) geogrid with ultimate strength of 35 kN/m was selected as reinforcement, for Wall 1 and 2 geogrid length to wall height ratio was 0.73 while for Wall 3 it was 0.6, and the vertical spacing between consecutive reinforcement layers were 60 cm for Wall 1 and reduced to 40 cm for Wall 2 and Wall 3. Block to block interface shear was strengthened by front end lips added to blocks that prevent direct outward relative slippage of consecutive blocks. Model walls were instrumented to be able to get data from front facing displacements, backfill surface settlements, reinforcement strains, accelerations at front facing and backfill, vertical and horizontal earth pressures during seismic excitation. Two excitations were applied in each test which was the scaled versions of Kobe earthquake, the first one was scaled to 0.4 g and the second was scaled to 0.8 g, for Wall 3 both horizontal and vertical accelerations were applied to the model. Model walls performed well during seismic motions, for 0.4 g they showed negligible deformations, for 0.86 g maximum lateral displacements of the front wall reached 100 mm which was also quite lower than the limit values. As a conclusion, increasing the length of top reinforcement layer,

reducing vertical reinforcement spacing and grouting the top two blocks to create a firm reinforcement connection were the main actions to provide a better wall performance. For reinforcements it was noted that the bottom layers experienced largest peak force during second shaking. A larger settlement occurred in the unreinforced zone indicating the lateral sliding of the reinforced zone as a coherent body. It has to be also noted that the backfill contained no fine material and in the private sector the amount of fines used may exceed 35% so the further study should also be aimed at that issue.

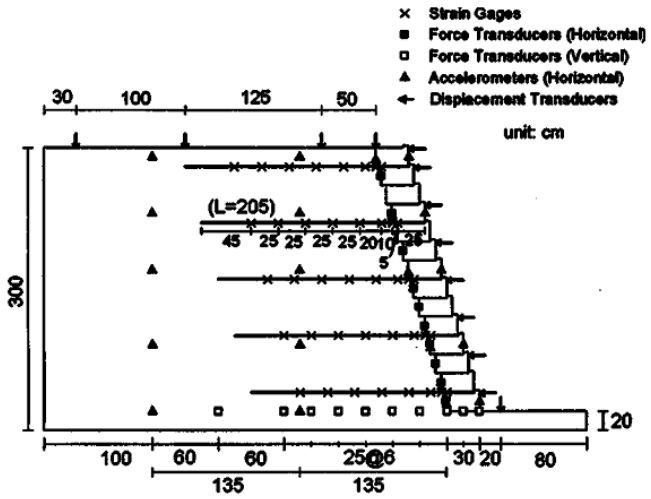

Figure 2.26. Model Wall Layout and Instrumentation (Ling *et al.*, 2005).

Ling *et al.*, (2012) proposed shaking table test results for seismic performance of three geosynthetic reinforced segmental retaining wall systems that had the same configuration with the previous 2005 study but in that study fine grained low-quality backfill was used. The backfill soil mixture was silty sand with plasticity index 7.4. Again the 0.4 g and 0.8 g scaled versions of Kobe earthquake was used as base input motion but four excitations were applied to each wall; last three had amplitude of 0.8 g to examine the effects of possible subsequent earthquakes. L/H ratios were 0.6 for each three models, where vertical reinforcement spacing was 40 cm for Wall 1 and 80 cm for Wall 2 and 3; and the lip of the all blocks was removed in Wall 3. Model walls with the low quality backfill performed better than the sandy backfill equivalents in the previous study under the same earthquake loadings. Horizontal displacements of the front facing, lateral earth pressure and reinforcement tensile loads were all measured less than the previously tested sandy wall. No tension cracks were observed behind

the reinforced soil because of the combination of apparent cohesion and the longer top reinforcement. Lesser tensile load development on geogrids was an expected result because of the apparent cohesion. Also in the static condition the geogrids were not functioned because the apparent cohesion alone would be enough to hold a vertical wall of certain height. Local shear failure in the front part of the backfill resulting in toppling was observed as failure mechanism. It also should be noted that; true cohesion and soil matrix suction are the sources of apparent cohesion and its value can vary with the soil moisture content; so precautions should be taken for the seepage of surface water into the backfill soil and counting on its long-term value should be conservatively considered.

Watanabe *et al.*, (2003) conducted a series of shaking table tests with wall models of 50 cm high with a level backfill that was consisted of very dense dry sand layers. For base input motion, scaled versions of Kobe earthquake record was applied to the model walls with 0.1g increments consequently. Final wall geometry, soil deformations and internal soil failure planes can be seen in Figure 2.27; for conventional type walls base sliding and overturning failure modes were observed, in GRS walls overturning mode was predominant. A simple shear mode of failure was observed in reinforced backfills which was different form the direct sliding mechanism, in which the reinforced backfill works as a coherent body, assumed in limit equilibrium analyses. A local toe failure was also observed in conventional retaining walls because the normal bearing stress at the toe of the rigid footing decreased when the wall displaced about 20 mm resulted in loss of bearing capacity at the toe. Hence the wall loads of reinforced soil retaining wall was spread over a wider base, local toe failure was not observed. Stabilizing effect of reinforcement layers on wall facing deformations induced the good performance of reinforced retaining walls. The development of largest tensile loads in the uppermost reinforcement layers can be related with resistance of the facing wall against overturning. This observation about the distribution of reinforcement loads under seismic loading was not comparable with the static loading case where the maximum tensile loads generated on the lower layers.

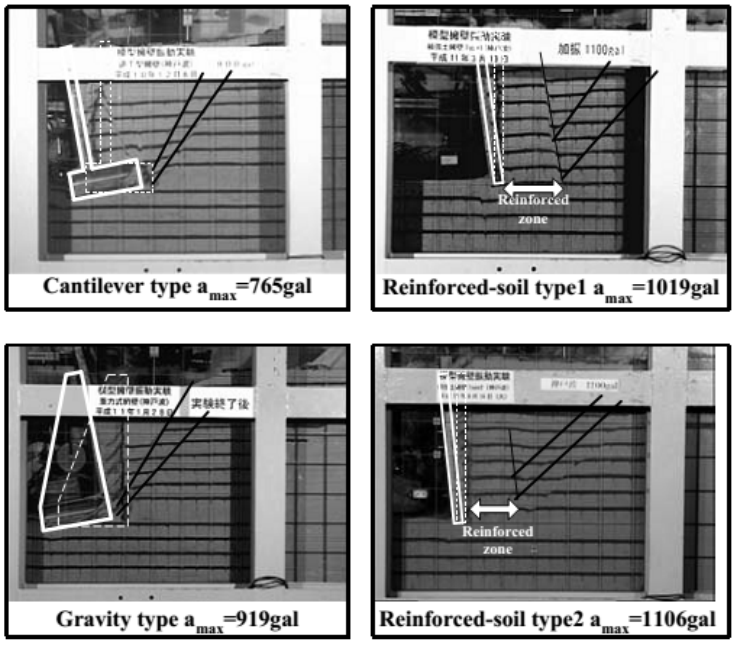

Figure 2.27. Final Wall Geometry, Soil Deformations and Internal Soil Failure Planes of Model Wall Systems (Watanabe *et al.*, 2003).

Kong *et al.*, (2009) conducted a series of shaking table tests to investigate seismic behavior of model slopes with 1.3 m height, 3.60 m length and 0.8 m width constructed with a slope ratio of 1:1.6. The study investigated the efficiency of slope stability improvement by reinforcing the slope with geogrids and the effect of reinforcement length and density on the potential slip failure surface and yield acceleration according to the test results. Data obtained from test results offered an insight to failure mechanism of side slope under seismic excitation.

Huang *et al.*, investigated the dynamic behavior of reinforced slopes with two studies in terms of horizontal acceleration response (2010) and horizontal displacement response (2011) by conducting uniaxial shaking table tests on 480 mm high geosynthetic reinforced model slopes with a slope angle of 60^o. Simple sinusoidal wave loads at specified frequency, consisting of step-wise increased horizontal peak ground acceleration were used as the horizontal input ground motions. It was reported that in the test results the horizontal peak ground acceleration, the wave frequency and the cumulative permanent displacement of the slope; affected both the horizontal acceler-

ation response at the crest and the lateral slope displacement in the first study. At certain levels of input accelerations, related with the development of major slip planes in the slope mass; amplification state to a de-amplification state transitions were observed and it was also mentioned that this transition was also related with the plastic slope displacement and the total slope height (D_{max}/H_t) ratio. In the second study the effects of horizontal peak ground acceleration and wave frequencies on the seismic displacement of the slope were searched. For geosynthetic reinforced slopes subjected to a relatively intensive input base acceleration of 0.4-0.6 g, or subjected to a maximum wall displacement greater than 1.9-3.9% of the wall height; there was not any amplified acceleration response was measured at the crest of the slope.

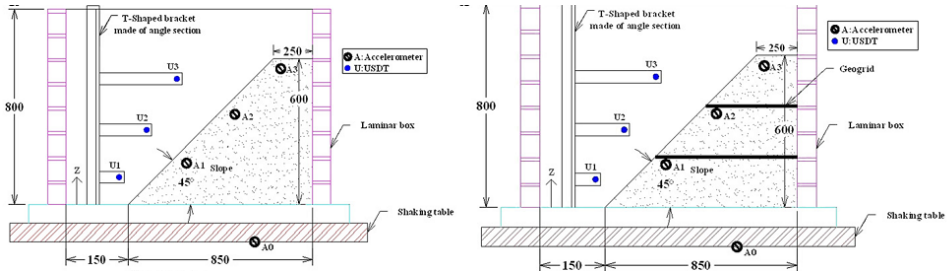

Figure 2.28. Unreinforced and Reinforced Clayey Sand Slopes (Srilatha *et al.*, 2013).

Srilatha *et al.*, (2013) conducted a series of shaking table tests to study the effect of frequency of base excitation on the dynamic response of unreinforced and geogrid reinforced soil slopes. Slopes were constructed inside a laminar box, using clayey sand with a total slope height of 600 mm with a base width of 850 mm with two slope angles 45^o and 60^o as can be seen in Figure 2.27. The frequency of shaking varied between 2 Hz, 5 Hz and 7 Hz where the amplitude of acceleration was kept as 0.3g. Further displacements were measured for unreinforced slopes compared with reinforced slopes at all frequency levels. Reinforced slopes showed lesser displacements compared to unreinforced slopes at all frequency levels. Accelerations were amplified more at the top of the slopes, also higher displacements were recorded at the corresponding upper parts. The acceleration and displacement response of the system exhibited an increasing trend with increasing frequency but this increase was not proportional with the changing frequency. Dramatic increase for slope displacements occurred at 7 Hz while the slope displaced insignificantly at frequencies 2 and 5 Hz.

Wang *et al.*, (2015) conducted large scale shaking table tests to investigate the seismic response of geogrid reinforced and unreinforced soil retaining wall models with saturated sand backfill constructed in a laminar shear box and the dimensions of the rigid walls were 1.7 m length, 0.7 m height and 5 m width. Accelerations, lateral displacements of the wall, settlement of backfill sand, excess pore water pressures in the backfill sand and strains on geogrids were evaluated, regarding the effects of different ground motions. Three seismic waves obtained from earthquake records were applied in the tests, representing three different wave characteristics as one near-field, one far-field and one middle-far-field seismic wave. Results from tests implied that seismic waves from far and mid-far field has to be considered, they had greater effect on the seismic behavior compared to near field seismic waves. Although the backfill sand was saturated, geogrid reinforcement could make an effective contribution to the seismic resistance. Geogrid layers also accelerated the dissipation of excess pore water pressure resulted in decrease of the excess pore water pressure development. Lateral displacements of reinforced walls were measured as lower than the unreinforced walls. Reinforcements also took place in decreasing the surface settlement of the backfill this result was obtained by both the comparisons of reinforced and unreinforced walls and reinforced versus unreinforced zones in a wall model. The strains on the mid layer geogrids were recorded as highest indicating their important role in seismic stability of retaining walls, also the geogrid-front facing connections took an active role for seismic design.

In the study of Güler and Enünlü (2009) uniaxial shaking table tests were performed to investigate the seismic performance of ½ scaled geosynthetic reinforced retaining wall models with modular block facing that was constructed in a rigid box container had the dimensions of 1.9 m height, 2.8 m length and 0.5 m width. Sinusoidal harmonic waves and scaled El Centro earthquake records were applied as base motion and test results were obtained including front face displacements, amplification of accelerations on front wall and at top of backfill and strains on geogrids. Two reinforcement lengths were compared as design parameter during the tests, tested geogrid length to wall height ratios were 0.9 and 0.6. As a result no permanent deformations were observed on the model walls confirming the successful performance of reinforced

retaining walls. The models with shorter reinforcements were subjected to larger deformations and larger tensile loads were measured on the geogrids, compared with the models with longer geogrids. And also shallower internal failure surfaces (decreasing inclination of failure line form horizontal) were observed for model walls with shorter reinforcements implying less stiff walls. The maximum average tensile strains observed in the geotextile reinforcements were observed at points which are close to the potential failure surface predicted by Rankine theory.

Güler and Selek (2014) performed shaking table test of eight geosynthetic reinforced model walls that are illustrated in Figure 2.29. (four of them were 2 m high ½ scaled, three of them were 2 m high ¼ scaled, one of them was 1 m high ¼ scaled). It was reported in the results that reinforcement length and vertical spacing between reinforcement layers did not affect the acceleration amplifications significantly and also the reinforcement lengths meeting the minimum requirements of FHWA design procedures, did not have an important effect on front face displacements. Decreasing the geotextile length and increasing the vertical spacing resulted in an increase on reinforcement tensile strains. Potential failure planes created by drawing a line passing through the locus where maximum strain was occurred along the geogrid and they were compared with the Rankine theory's estimated failure planes as illustrated in Figure 2.30.

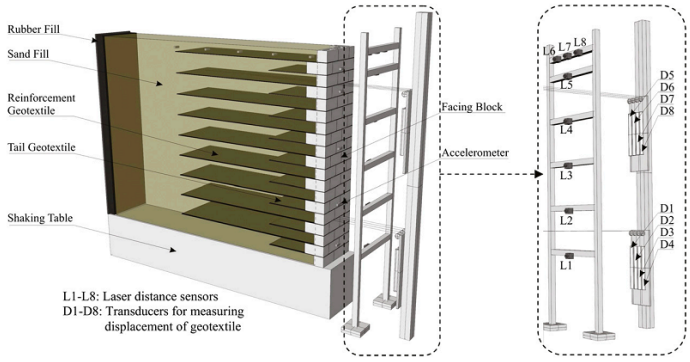

Figure 2.29. Shaking Table Test Setup and Instrumentation Layout (Güler and Selek, 2014).

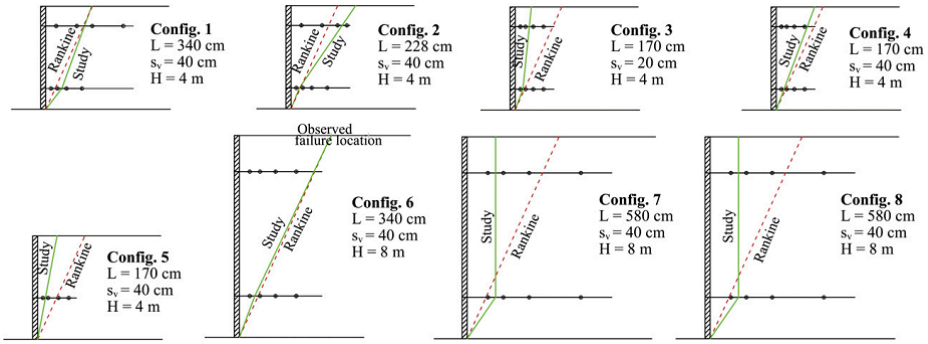

Figure 2.30. Potential Failure Planes Obtained From Maximum Strains and Rankine Theory Prediction (Güler and Selek, 2014).

Başbuğ (2011) conducted shaking table tests for four ½ scaled and 1.9 m high geogrid reinforced retaining walls with modular block facing. Model walls were exposed to scaled El Centro, Izmit and Sakarya earthquake records consecutively, as base input excitation. During the study, the influence of the parameters as backfill soil type (gravel and sand), wall inclination (vertical and 6^o inclined), reinforcement length (L/H=0.47 and 0.7) and reinforcement stiffness; on the seismic performance of model walls was investigated. As a conclusion, model walls constructed considering the current design procedures performed successfully under seismic loading conditions. Even at the extreme seismic loading conditions (peak accelerations at 0.97g) no stability problem was observed for the model walls and the permanent displacements and maximum deformations at those loading conditions were stay lower than considerable limits.

2.3.3. Finite Element Analysis

Nowadays, numerical analysis methods are being able to simulate the behavior of reinforced retaining walls and slopes under seismic loading conditions with the help of improving comprehensive and complicated material models that are also compatible with dynamic conditions. In this manner, this improvement leads to obtain the behavior and seismic response of the structures according to various parameters and design criteria; within a cost and time effective way. Compared to conventional limit

equilibrium calculation methods, finite element analysis take into account force equilibrium condition, strain stress relationships, material models with seismic properties and interface relations between materials those resulted in a more rigorous approach. Despite the advanced modelling skills, the assumptions and idealism of numerical analysis are still drawbacks, compared with the physical test results. Then, the validation analyses based upon well accepted physical model test studies have an important place in the reliability of finite element models. However, a finite element study does not take place in the concept of this thesis, a summary is done below for the important physically validated finite element model analyses accomplished in the literature.

Bathurst and Hatami (1998) carried out a numerical model of an idealized reinforced retaining wall with 6 m height, having a rigid panel facing and six reinforcement layers. Numerical results obtained by the finite difference program FLAC pointed out that a base that allows the sliding of wall and soil or a constrained base just allowed to rotate only about the toe had an influence on the seismic response of the wall. And also it was observed that the reinforcement stiffness and reinforcement length had an impact on seismic behavior and the tension loads and their distribution on the reinforcements.

El Emam *et al.*, (2004) made numerical analysis of a 1 meter high retaining wall model with panel facing, by the finite difference program FLAC, validated with the results of previous shaking table test study. Numerical model established for two different toe restriction types, estimated the results of the physical tests successfully in terms of front facing displacements, tensile loads on reinforcements and facing toe reaction forces.

In the study of Ling *et al.*, (2005) a numerical model of a 6 m high, modular block facing, geosynthetic reinforced retaining wall was prepared via the finite element program Diana-Swaydne, in accordance with the results of the shaking table test study accomplished in 2005. A plastic soil material model was developed to describe the backfill and foundation soil. With this numerical study, the effects of backfill properties, seismic motion and reinforcement layout on the seismic behavior of reinforced retaining wall was investigated. It was found that the permanent deformations and

the tensile loads developed on reinforcements were in the allowable limits although the tensile loads were twice larger than the tensile loads measured after construction. Less acceleration amplifications were observed within the more plastically deformed backfills. Although different reinforcement lengths caused various lateral displacements and vertical settlements of the backfill top, they did not make a significant difference in amplification ratios. Decreasing reinforcement lengths and increasing vertical spacing between reinforcements, caused an increase in developed tensile loads and lateral soil pressures.

In their study, Lee *et al.*, (2010) reported the results of numerical simulation of full full-scale geosynthetic-reinforced soil walls that were exposed to seismic loading by shaking table tests in the study of Ling *et al.*, (2005). Numerical models were generated by the program LS-DYNA and material models were defined according to the available laboratory data. In the study numerical model results were compared with the test data for parameters including wall displacement, backfill settlement, lateral earth pressure, reinforcement tensile load, acceleration amplifications in reinforced soil zone and in retained soil zone. It was seen that not all of these calculated results match up with test data but there was quite similarity for the lateral earth pressure and horizontal displacement results.

Ling *et al.*, (2010) presented the results of simulated numerical model of a geosynthetic reinforced retaining wall and for validation of the model they made use of the data from the shaking table tests that they conducted at 2005. It was found that, when the calculated results and data from the tests compared; the results were quite similar in terms of front facing deformations, tensile loads on reinforcements and horizontal and vertical time history records.

Güler *et al.*, (2007) established a finite element model of a 3.6 m high modular block facing reinforced retaining wall with the program Plaxis and for the confirmation of this model, instrumented full scale wall model results of Bathurst *et al.*, (2000) were used, including horizontal wall facing displacements, and toe and foundation reactions data. Finite element models were generated for different combinations of reinforcement

spacing, reinforcement length and backfill soil. The φ-c reduction method, (a special shear strength reduction technique up to failure) was used to simulate to find the safety factors at failure conditions. For models with granular backfills, locations of shear strain concentration at the end of the construction phase were similar with the failure planes estimated with the limit equilibrium-based design methods. Lower tensile loads were developed in the reinforcements for walls with cohesive backfill compared with walls with granular backfill. For cohesive backfill, no shear strain concentrations were observed in the numerical models at the end of construction indicating that for that wall geometry and reinforcement layout no internal failure mechanism was developed under working load conditions.

Güler *et al.*, (2012) evaluated the seismic performance of a 6 m high geosynthetic reinforced retaining wall with modular block facing, with finite element analysis after validating the results of numerical model with the data obtained from the full scale shaking table test study of Ling *et al.*, (2005). It was found that the increase in the amplitude of the base motion, increase the lateral displacements of the front wall in the same direction but not with the same increase rate. The potential failure plane locations predicted by finite element analysis agreed well with the results of the limit equilibrium analysis. As an important result of the study it was found that when cohesive soil was used instead of granular soil as backfill, the wall deformations were decreased at a rate of 50%. This result indicated that if proper drainage and compaction conditions were established, cohesive soils could be used as a proper backfill material.

3. METHODOLOGY

In this chapter, methodology about construction, instrumentation and monitoring of three 1/2 and one 1/4 reduced-scale model walls are presented. As it was noted before Setup1 is a 1/2 scaled model with granular backfill that is accepted as a benchmark test, Setup 2 is identical with the first setup but the backfill is cohesive soil, Setup 3 has the same material and geometric properties with the second setup but geogrid length L/H ratio is different, Setup 4 is a 1/4 scaled model which is exactly the half scaled version of second setup with the same cohesive backfill.

First of all, because the setups in this study are scaled models of the prototype, scaling conditions for the setups are explained. Then the shaking table system and instrumentation including accelerometers, laser displacement transducers and strain gages are introduced in details. For the next part the main constitutive materials as backfill soil, geogrids and modular blocks are introduced; characteristic soil material properties of backfill soil types (both granular and cohesive) were determined with laboratory work which is also mentioned in details. Finally model configurations including model geometry and also location of instrumentations are presented and illustrated and important details of the construction period is explained and illustrated. Dynamic excitations applied on model walls are presented as well.

3.1. Scaling Law for Model Walls

For the model tests the scaling ratio was determined as big as possible to the extent permitted by the carrying capacity (10 tons) and dimensions (3 m x 3 m) of the shaking table system. Maximum height of the model wall was calculated according to these load and dimension constraints (weight of the steel container box was subtracted) and the dimensions of the scaled model was determined as 190 cm height, 280 cm depth and 50 cm width, these dimensions are 1/4 scaled version of the prototype. Then to create a condition of similarity between the model and prototype the scaling law has to be valid. And Buckingham's π theorem was used in this study as the method for

reducing the number of dimensional (experimental) variables into a smaller number of dimensionless groups.

According to the above stated scaling law the height of the geosynthetic reinforced wall was designated as the independent parameter, which was henceforth named as N. All the other relevant geometrical dimensions, strength parameters, and physical quantities; where applicable, were determined according to the scaling law. The quantities which are described without units, is exempt from the scaling law. These quantities were: Rankine active earth pressure coefficient, K_a, the angle of internal friction of the soil, ϕ_{soil}, and the strain. The scaling factors used in this study which relate the geometric dimensions and other relevant physical quantities to their real-life counterparts are tabulated in Table 3.1. It should be noted here that the tensile strength capacity of the geosynthetic reinforcement alongside with the compressive strength capacity of the modular facing block were not scaled for practical reasons.

Table 3.1. Scaling Factors Used in This Study.

Quantity	Theoretical Ratio (Prototype/Ratio)	Study (1/2 scaled)	Study (1/4 scaled)
Height (H)	N	2	4
Length (L)	N	2	4
Vertical spacing (S_v)	N	2	4
Block of width (w)	N	2	4
Block height (h)	N	2	4
Frequency (f)	$N\sqrt{2}$	$\sqrt{2}$	2
Time (T)	$N/\sqrt{2}$	$1/\sqrt{2}$	1/2

3.2. Setup and Instrumentation

Test wall setup covers a steel container box with a glass cover frame affixed, this container box including the model wall is fixed to shaking table. The data is recorded by two data acquisition systems to which accelerometers, displacement transducers and

strain gages are connected.

3.2.1. Shaking Table

A large shaking table facility (Figure 3.1) available at earthquake laboratory of Bogaziçi Universtiy, Kandilli Observatory and Earthquake Research Institute (KOERI) (Istanbul, Turkey) was used to simulate predetermined seismic action during the tests. Shaking table facility (ANCO R-148) manufactured by ANCO Engineering, Inc. is comprised of a loading table of 3m x 3m dimensions and payload capacity of 10 tons and a computer controlled uniaxial servo-hydraulic motor traversing the load platform to create an earthquake simulation. Digitally controlled servo-hydraulic actuator consisting of dual 3-stage Moog servo-valve, has a stroke capacity of ± 12 cm and the shaking table can be operated over an acceleration range of to 2g and frequency range of 0 to 50 Hz. Displacement time history data of the desired seismic action is transmitted to the servo-controller system from the digital control system.

Figure 3.1. Shaking Table Facility at Kandilli Earthquake Laboratory.

3.2.2. Steel Container Box and Glass Covered Frame

The steel container soil box illustrated in Figure 3.2 was utilized for the test; is rectangular in cross-section, with inside dimensions 1,9 m (height) x 2,8 m (length) x 0,53 m (width), with a design weight of approximately 2.3 tons, designed to be installed on the shaking table. During study the full height of the container was not used in all

scaled models, the height of this retaining wall was 1 m and lengths was 1.4 m as the fourth test model wall.

Figure 3.2. Steel Container Box with Glass Covered Frame Fixed on Shaking Table.

A glass covered light-weight steel frame was fastened in front of the open face of the container as a precaution for the collapse of front wall during test. The frame weights 150 kg, lightweight steel was chosen regarding the weight capacity of the shaking. A high strength glass that can endure the impact of facing elements was chosen also to allow visual observation during tests. Also, the laser displacement sensors were attached inside the steel frame so the frame and container worked as a monolithic system, that led to more accurate relative displacement data obtained from the laser sensors. Glass covered frame is shown in Figure 3.3 and general sketch of the system and setup is given in Figure 3.4.

3.2.3. Accelerometers

The number of accelerometers was agreed upon the available channels of data acquisition system, a total number of 8 accelerometers were used for each setup. One accelerometer was fixed on shaking table to record base acceleration; five accelerometers were located on front wall and two submerged accelerometers embedded in at the top of backfill at the level of top geogrid one was located 50 cm away from the end of modular block and the other was located 50 cm in front of the EPS board.

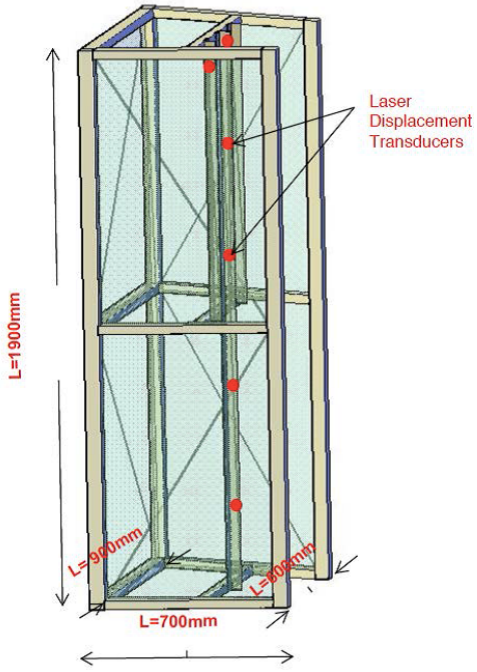

Figure 3.3. Glass Covered Steel Frame (Başbuğ, 2011).

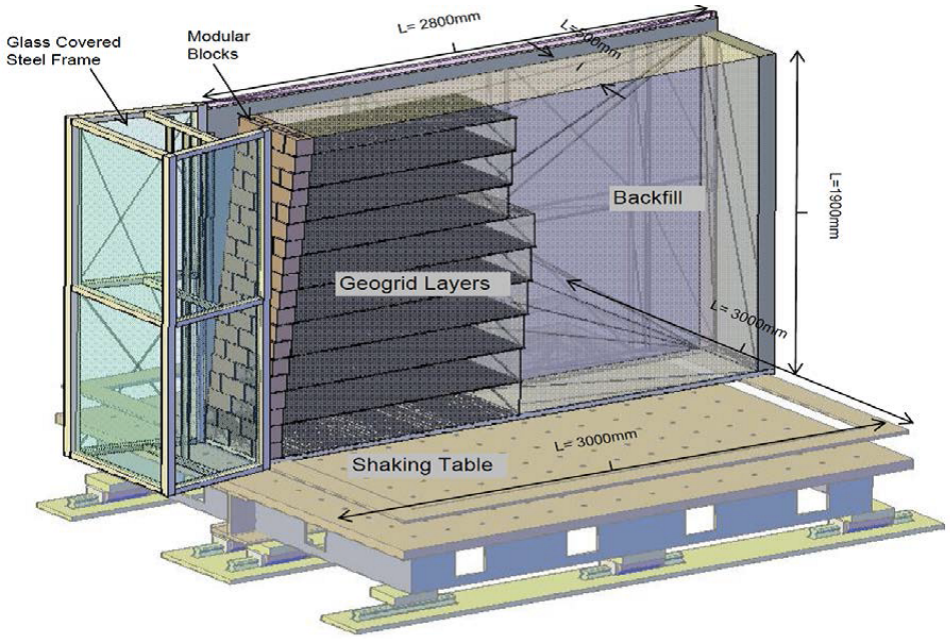

Figure 3.4. General View for the Setup and Shaking Table (Başbuğ, 2011).

Accelerometers were manufactured by "PCB Piezotronics Inc." and model no was "3801G3FB3G". Accelerometers are of capacitive type, which have +/- 3g acceleration measurement capacity, an average of 1000mV/g sensitivity and a frequency range of 0 to 100 Hz. The two submersible accelerometers were DYTRAN 3217A, which have

50 g acceleration range, an average of 100mV/g sensitivity, a frequency range of 1 to 10000 Hz and submersible to 175 psi. In tests they were adjusted at 5ms (200 Hz) as measurement time.

Accelerometers were manufactured by "PCB Piezotronics Inc." and model no was "3801G3FB3G". Accelerometers are of capacitive type, which have +/- 3g acceleration measurement capacity, an average of 1000mV/g sensitivity and a frequency range of 0 to 100 Hz. The two submersible accelerometers were DYTRAN 3217A, which have 50 g acceleration range, an average of 100mV/g sensitivity, a frequency range of 1 to 10000 Hz and submersible to 175 psi. In tests they were adjusted at 5ms (200 Hz) as measurement time.

3.2.4. Laser Displacement Sensors

Laser displacement transducers were attached to the steel frame that can be accepted as a coherent system with steel container box so that the measured displacements reflected the relative deformation of the front wall and more accurate results could be taken. Seven laser displacement transducers were located against the front wall, two of them were recording top block's displacement because this relative movement was the most critical displacement value for the wall behavior and one transducer was set on the shaking table as a feedback displacement measurement for the base excitation applied by the servo-controlled actuator. Laser displacement sensors were of type ODSL8-V/4-400-S-12 from Leuze Electronic. They have a displacement measurement range from 2 to 40 cm with 0.1 mm of precision measurement ability. In tests they were adjusted at 5ms (200 Hz) of measurement time.

3.2.5. Strain Gauges

One of the most important parts of this study was to measure the local strains on geogrids during dynamic excitation. For that reason, strain gages produced especially for plastic materials and configured to minimize the effect of gage tightening; were utilized in the experiments. The gages have 2.8 mm of gage width (it is attached to

4.5 mm width geogrid surface) and 5 mm gage length with a 120 Ω of gage resistance. The gages were produced by Kyowa and KFG-5-120-C1 is their type. Considering the total number of 16 available channels of the data acquisition system, a total of three geogrid layers each with five strain gages were instrumented. Figure 3.5 and Figure 3.6 represent the general view for model wall instrumentation, exact locations of strain gages are given in details further.

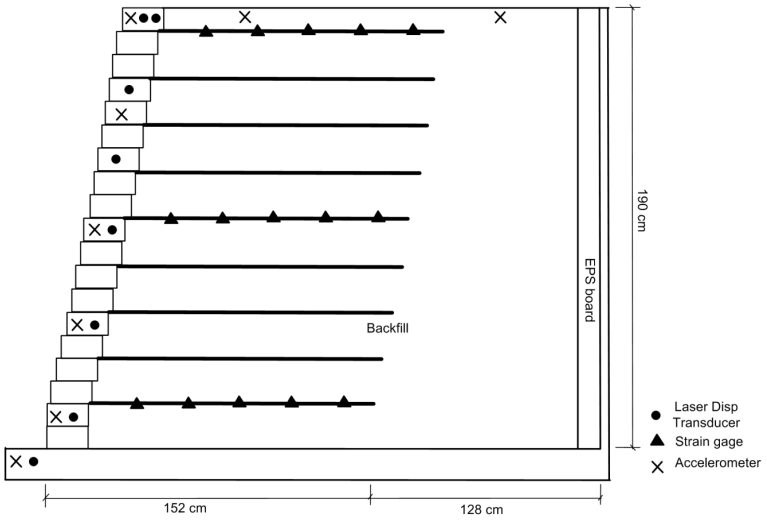

Figure 3.5. Location of Instrumentation Side View.

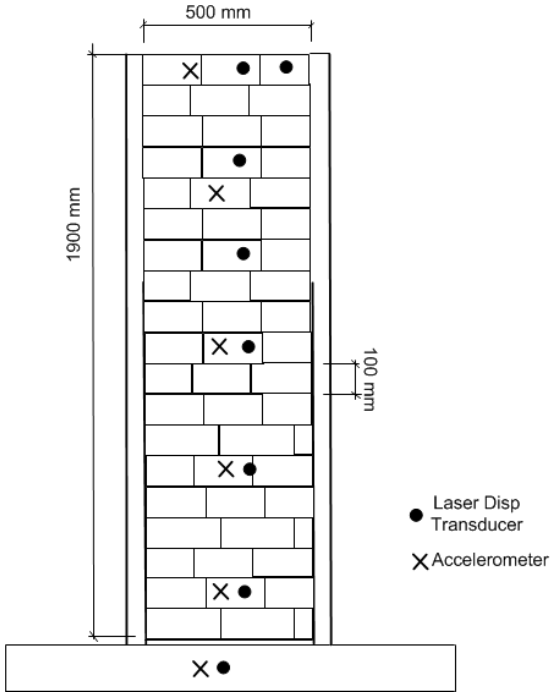

Figure 3.6. Location of Instrumentation Front View.

3.2.6. Data Acquisition System

National Instruments' PCI-6229 M Data Acquisition System was used for connection of accelerometers and laser sensors. It allows working with 16 analog input channels that have 16-bit of resolution and 250 kS/s (250000 samples per second) of sampling rate. 200 samples per second rate was adjusted for the laser sensor and accelerometer data.

For strain gage measurements Gartner Instruments' $Q_{.raxx}$ A107-16 data acquisition system box each having 16 channels was used in experiments. This system uses 16 analog input channels that have 24-bit of resolution and 10 kHz (10000 samples per second) of sampling rate. 200 samples per second rate was adjusted for the strain gage data too.

3.3. Materials

Materials used in the tests can be classified as the backfill soil (granular and cohesive), modular block for front wall, geogrid, EPS board and rubber sheet.

3.3.1. Backfill Soil

During this study two types of backfill materials was used; commercially available poorly graded sand was used as granular backfill material. 30% by weight powdered cohesive soil (kaolinite) was added to this granular backfill to constitute the other type of backfill soil. To decide the ratio of fine soil UU triaxial tests were performed for 20, 30 and 40% by weight fine ratios. To classify the granular soil sieve analysis was conducted and grain size distribution curve was obtained as shown in Figure 3.7.

The parameters that can be obtained from the Figure 3.7 are coefficient of uniformity (C_u) is 3.0 and coefficient of gradation (C_c) is 1.08 where $D_{10} = 0.25$, D_{30}=0.45 and D_{60}=0.75. Only 0.04 percent of the soil is under No. 200 sieve and these indicate that the soil is poorly graded sand (SP). The void ratio of the granular material was

obtained according to ASTM specifications as e_{max} = 0.82 (γ_d= 1.44 kg/m^3) and e_{min} = 0.58 (γ_d= 1.71 kg/m^3) (air dry, water content = 0.6%).

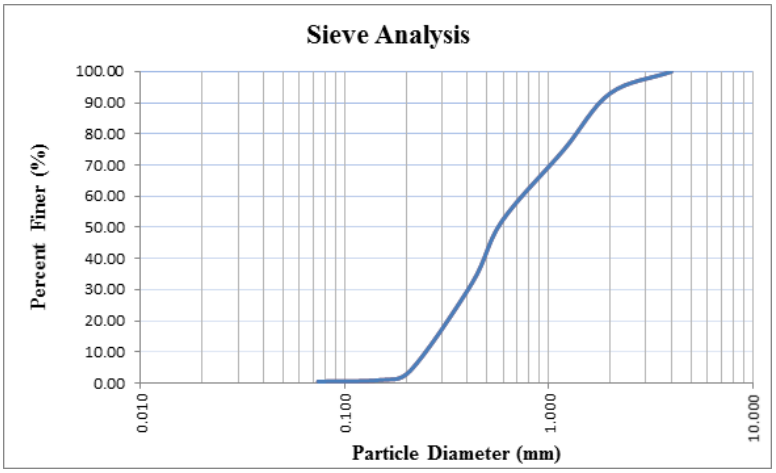

Figure 3.7. Sieve Analysis of Sand.

During our study to investigate the properties of the backfill soil types, the gradation between 4 mm and 0.075 mm was used for granular soil. To determine the plasticity index and activity for the cohesive the Cassagrande liquid limit analysis and plastic limit analysis tests were done in a bulk manner. In this bulk case granular and kaolinite were mixed by 20, 30 and 40 percent by weight respectively; all of the material was passed No. 40 sieve (0.425 mm) and the tests were repeated with different water contents. The tests were conducted to observe the plastic behavior (activity) of the mixed backfill and after the tests the cohesive backfill can be named as non-plastic for 20 and 30 percent by weight backfills. And a non-significant plasticity was determined for 40 percent by weight backfill as seen in Table 3.2 in which also the corresponding specific gravity values are also given. Specific gravity (G_s) value obtained for granular soil is 2.63.

The Proctor compaction test was also performed to find the optimum moisture content of the backfills to find out water content percentages for compaction during construction of the model walls. The results of the laboratory tests to obtain the maximum dry unit weight of compaction and the optimum moisture content can be seen in Figure 3.8. The optimum moisture content and corresponding maximum dry

unit weights for different clay contents are given in Table 3.3.

Table 3.2. Plasticity Index and Specific Gravity Values for Samples.

Sample	Liquid limit (%)	Plastic Limit (%)	Plasticitiy index (%)	Specific gravity
K20S80	np	np	np	2.633
K30S70	12	np	np	2.638
K40S60	24	17	7	2.644

Table 3.3. Optimum Moisture Content and Maximum Dry Unit Weight.

	Sand	K20S80	K30S70	K40S60
Optimum Moisture Content (%)	7.6	9.1	9.9	11.5
Max. Dry Unit Weight (kg/m3)	1.79	1.82	1.87	1.88

During the construction of model walls sand cone test were performed to determine the relative densities of the backfill material. For dry sand backfill e=0.66 was measured which corresponds to a relative density of 63% (medium dense sand) at water content of 0.5%. Therefore, the unit weight of sand used in the tests was calculated 1.55 g/cm^3. For K30 S70 backfills it is not reasonable to determine relative densities according to dry mixtures of kaolinite and sand; but dry unit weights at the backfills' water contents were measured with sand cone tests and corresponding void ratios were determined (for G_s=2.638). Compaction percentages are given relative to γ_d=1.87 g/cm^3 at water content 9.9%.

Table 3.4. Sand Cone Tests for Cohesive Model Wall Backfills.

Model wall	Setup 2	Setup 3	Setup 4
Water content (%)	9.2	9	8.9
γ_d (g/cm^3)	1.76	1.74	1.78
Void ratio	0.5	0.52	0.48
Compaction effort	0.94	0.93	0.96

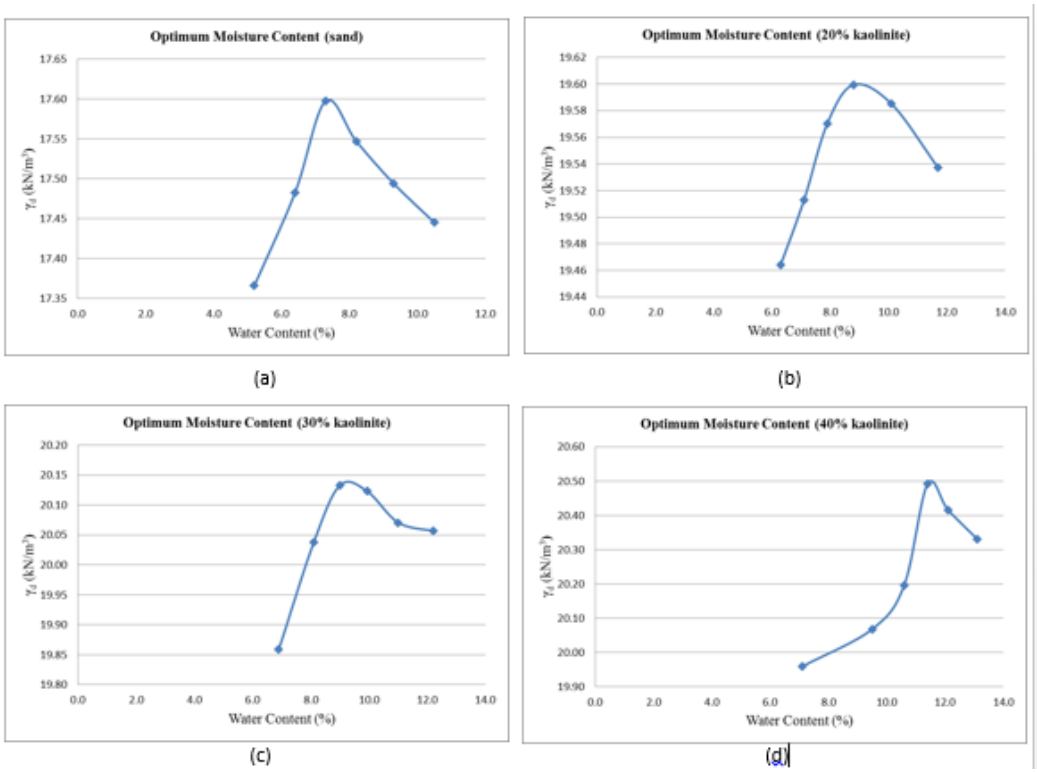

Figure 3.8. Optimum Moisture Content for Backfills a) Sand, b) K20S80, c) K30S70 and d) K40S60.

To determine the shear strength and stress-strain relationships for the backfill, triaxial tests were conducted and at the end of these tests the kaolinite-sand ratio that was determined as fine grained backfill specimen. Unconsolidated undrained triaxial test was applied to the granular "dry" sand without any fine content because dry sand was used as backfill for the threshold sample (Setup1) for model wall tests. Specimens were prepared consistent with the void ratio of dry sand backfill measured with sand cone test as e=0.66.

Unconsolidated undrained triaxial tests were conducted for specimens including kaolinite 20 (K20S80), 30 (K30S70) and 40 (K40S60) percent by weight. For UU tests the specimens were prepared at dry of optimum moisture content and the tests were performed at unsaturated conditions to reflect the real strength behaviors of the backfill soil in the large scale tests those were tried to be constructed at those moisture contents. Because the apparent cohesion was the main strength criteria for the samples, it was risky to prepare samples at wet of optimum because there would be shear strength loss when the water content was more than optimum moisture content. For the UU tests moisture contents were 8% for K20S80, 9% for K30S70 and 10% for K40S60 which were always approximately 2% lower than optimum moisture content. Samples were prepared inside a modified proctor mold to obtain three samples at similar moisture contents and compacted with similar effort. Standard proctor energy was calibrated and applied inside this larger modified mold. To take those samples from the mold three steel cylinders (5cm diameter, 12.5 cm height) attached to a stiff cap were used, these tubes were tucked into the soil, compacted in mold by compressing the stiff cap with help of concrete compression test machine. And the sample was taken out of tubes, to which Vaseline had been applied at inner surface, utilizing soil extraction apparatus used for compaction tests. UU triaxial tests were performed for unsaturated and at dry of optimum samples at 25, 50 and 75 kPa cell pressures; these cell pressures were chosen to reflect the static vertical and horizontal stresses expected in model walls (for 2 m height backfills).

It is important to keep in mind that these values are not effective strength values at undrained condition and pore water pressures were not measured because total shear strength parameters were taken into account.

In the literature, it is known that capillary cohesion influence strongly the strength and flow properties of granular materials. At low levels of water content, the water forms a discontinuous phase composed of interparticle bridges that are unevenly distributed in the bulk state. For soils with fine content the apparent cohesion term takes place, which is composed of matrix suction and true cohesion. The strength generating from apparent cohesion decreased drastically with increase in saturation. In the

literature, the unsaturated triaxial tests show that the angle of internal friction of soil effective stress is not affected by the degree of saturation, but the cohesion decreases with the degree of saturation and approaches to zero at a fully saturated condition.

The shear strength values are given at Figure 3.9 to 3.12, Mohr Coulomb failure criterion was used, and total shear strength values were measured under three different cell pressures 25, 50 and 75 kPa. Average shear strength values were calculated in terms of cohesion and internal friction angle for specimens, as given in Table 3.5. After the evaluation of results K30S70 sample was chosen to use as fine grained backfill soil because after 40 percent by weight kaolinite ratio it was observed that the granular structure was lost its effect with a smaller internal friction angle and K30S70 also can present a significant cohesive behavior that will create a difference with granular material.

Table 3.5. Internal Friction and Cohesion Values for Backfill Samples.

	Sand	K20S80	K30S70	K40S60
Internal friction angle (^{o})	39.5	33	27.5	12.5
Cohesion (kPa)	np	14	26	37

Deviatoric stress versus axial strain relationship is illustrated in Figure 3.13 and Figure 3.14, for dry sand and K30S70 cohesive backfill which were determined as backfill types used in model walls. For the material properties of the backfills a detailed numerical analysis was done and the results containing initial elastic modulus (E_0) and secant stiffness modulus (E_{50}) at different reference (cell) pressures are given in Table 3.6.

Table 3.6. Initial and Secant Elastic Modulus Values for Sand and K30S70 Backfill.

	Sand			K30S70		
Cell Pressure (kPa)	25	50	75	25	50	75
E_{50} (kPa)	7300	11100	15400	4400	6900	9200
E_0 (kPa)	11500	16700	22400	8500	10600	13800

3.3.2. Geogrids

Geogrid produced by "Istanbul Teknik Engineering and Industry Co." named as Fortex GG 40-40 was used in all model wall configurations. The ultimate tensile strength for this geogrid is 41.1 kN/m. The wide width tensile tests were performed according to DIN EN ISO 10319; the stress-strain relationship for the five test samples are shown in Figure 3.15 and Table 3.7 summarizes the strength properties of the geogrid.

Table 3.7. Properties of the Geogrid Fortex GG-40.

Ultimate Tensile Strength	Tensile Strength %2 strain	Tensile Strength %3 strain	Tensile Strength %5 strain	Strain at Nominal Tensile Strength
(kN/m)	(kN/m)	(kN/m)	(kN/m)	(%)
41.1	7.51	8.8	11.7	12.01

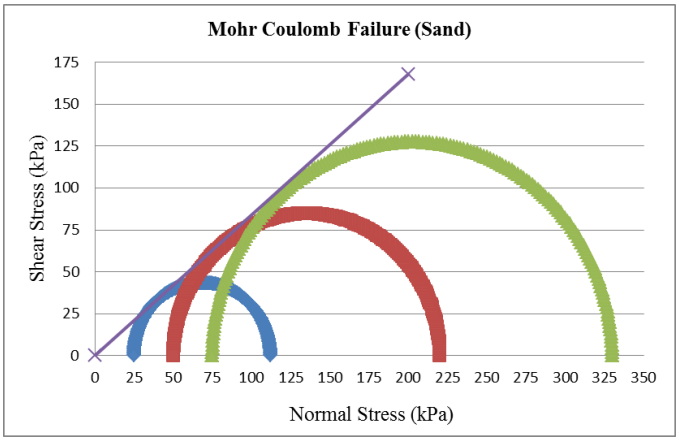

Figure 3.9. Mohr Coulomb Failure Line for Sand Backfill.

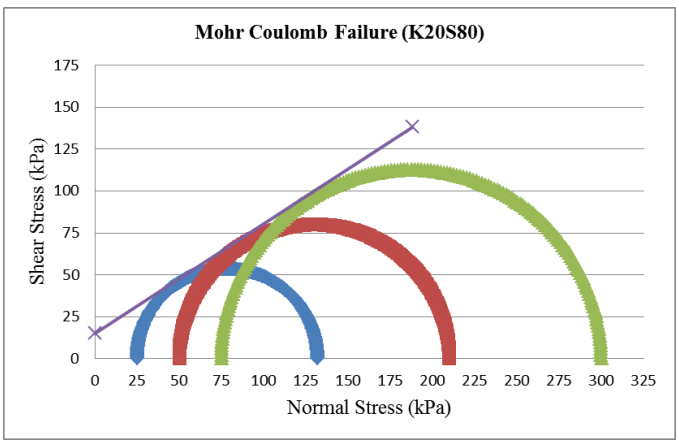

Figure 3.10. Mohr Coulomb Failure Line for K20S80 Backfill.

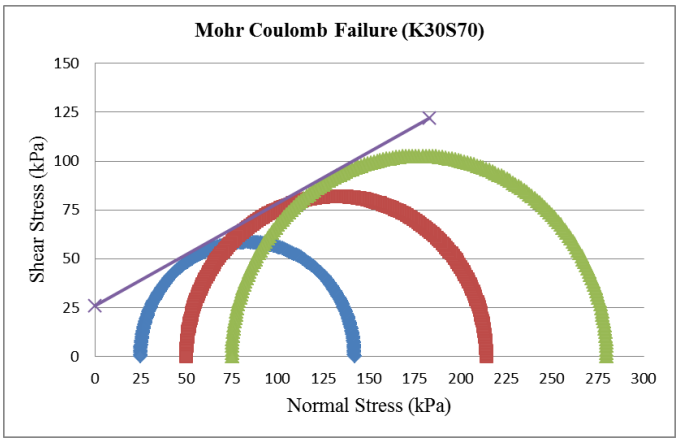

Figure 3.11. Mohr Coulomb Failure Line for K30S70 Backfill.

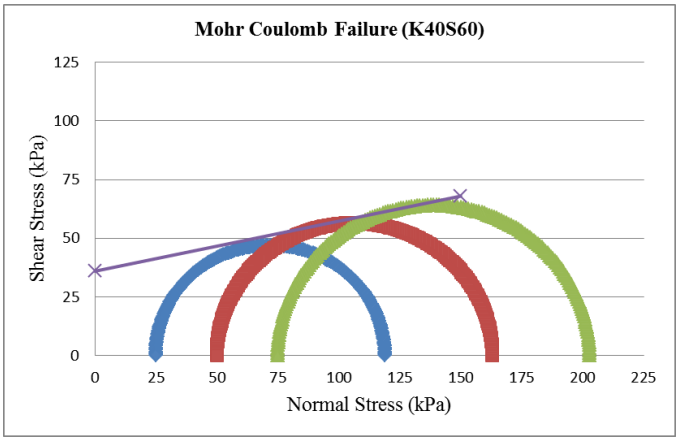

Figure 3.12. Mohr Coulomb Failure Line for K40S60 Backfill.

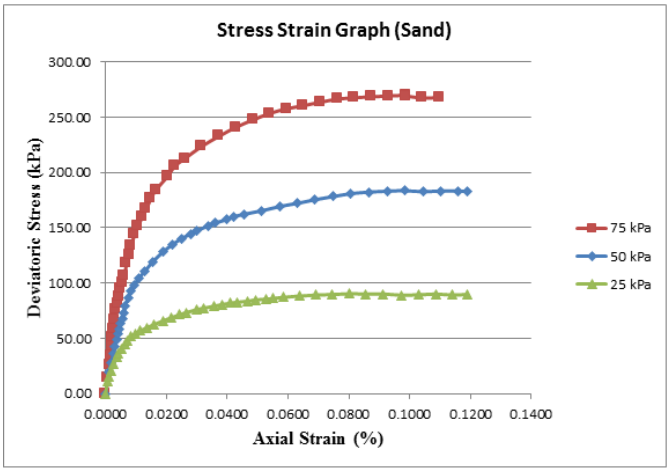

Figure 3.13. Stress Strain Relationship for Sand Backfill.

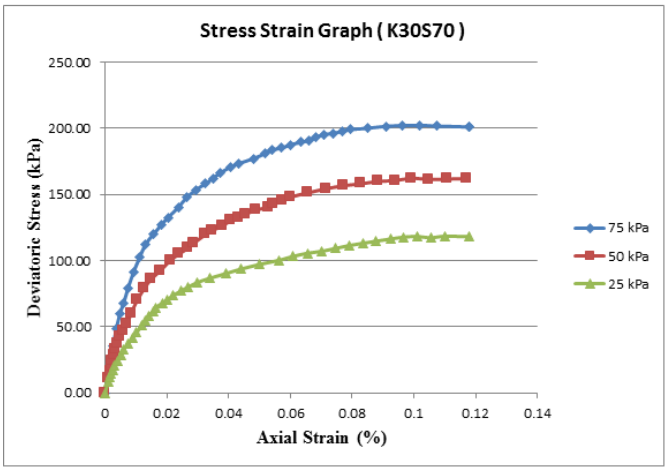

Figure 3.14. Stress Strain Relationship for K30S70 Backfill.

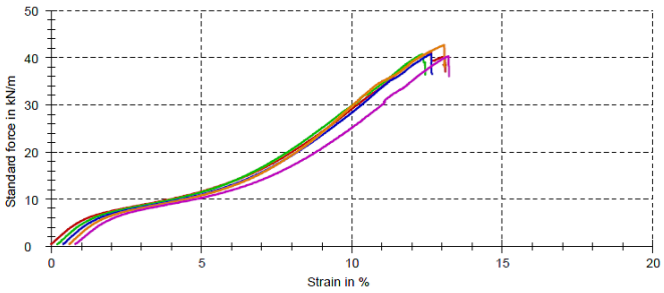

Figure 3.15. Stress-Strain Relationship for Geogrid Fortex GG 40-40 (Istanbul Teknik Engineering and Industry Co.).

For the implementation of strain gages on the geogrid surfaces, the surface was rubbed out by a cellulosic solver so the gages could stick on a smoother surface. Then the gages were adhered to that surface by an epoxy based adhesive and a compression on them was put into effect. After that the adhesive got dried, the gages were coated with high elastic RTV silicon which can resist vibration and impact. The ends of the gage were soldered to the wires of data transfer cables and again this soldered part was coated with silicon. After silicon coating was finished the cables were fixed to the geogrids with tapes and plastic clamps and the cables were put into protection covers. These steps of the application are illustrated in Figure 3.16.

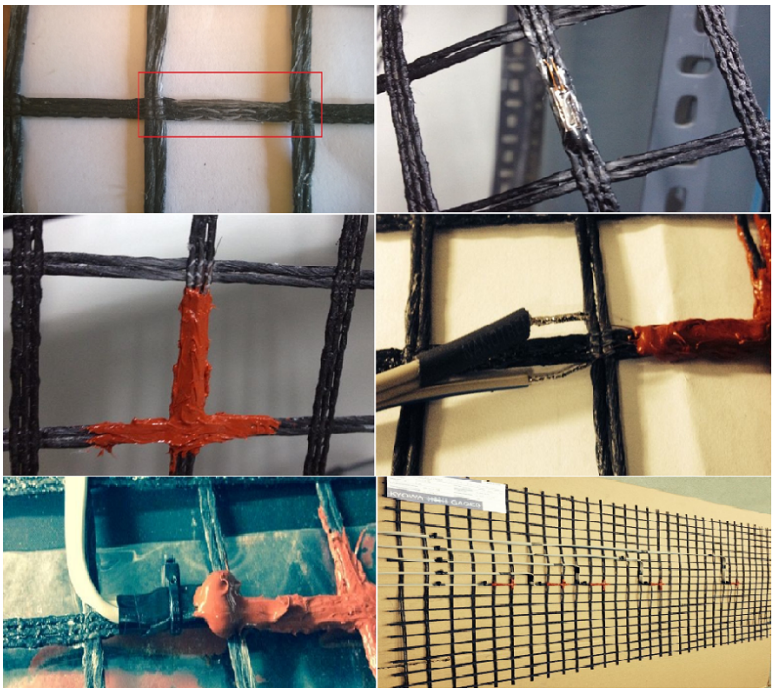

Figure 3.16. Application Process of Strain Gages Onto the Geogrids.

3.3.3. EPS Boards

EPS boards were accepted as buffer in order to absorb the possible reflecting of earthquake waves from the backside of the steel container soil box in this study. EPS boards with 10 cm. thickness and density equal to ρ=20kg/m^3 were placed at the backside of the fill.

The density and thickness were specified according to the study of Athanasopoulos *et al.*, (2007b). In their study experimental and finite element analyses were carried out to investigate the damping characteristics of the EPS boards. The finite element analyses were conducted for walls with a height of 4.0m, with EPS buffers having density 15, 20 and 25kg/m^3 and normalized thickness (according to wall width), t_r, ranging from 5% to 40%. Typical results are presented in the diagrams of Figure 3.17, indicating that isolation efficiencies, A_r, as great as 90% can be realized for shaking intensities ranging from 0.1g to 0.5g. As an observation from the diagrams, the A_r values greater than 50% require a significant increase of the thickness of the EPS inclusion (up to 40% of the wall height). Also the fact that isolation efficiency increases with

decreasing EPS density; can be seen from the diagrams, this effect is not significant. In practical applications a balance between the desired higher isolation efficiency and the undesired backfill deformations, may be established by using an optimum EPS density.

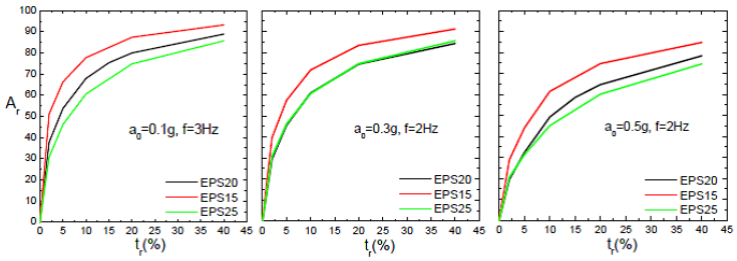

Figure 3.17. Seismic Isolation Efficiency of EPS as a Function of Thickness, Material Density and Seismic Intensity (Athanasopoulos *et al.*, 2007b).

3.3.4. Modular Blocks

In this study, two types of facing blocks were used; for the ½ scaled test walls hollow blocks with the dimensions 100 mm x 100 mm x 200 mm (height, depth, width). Because the width of wall facing is 50 cm, 100 mm x 100 mm x 100 mm one block was produced and was used for the rest 10 cm. The dimensions of the blocks can be seen in Figure 3.18. Gravel was filled in the hollow to increase the friction between block and geogrid. For the ¼ scaled test walls, non-hollow blocks with the dimensions 50 mm x 50 mm x 100 mm (height, depth, width) were used. The blocks are modular concrete blocks and modulus of elasticity of all is E=2x10^6 N/mm^2.

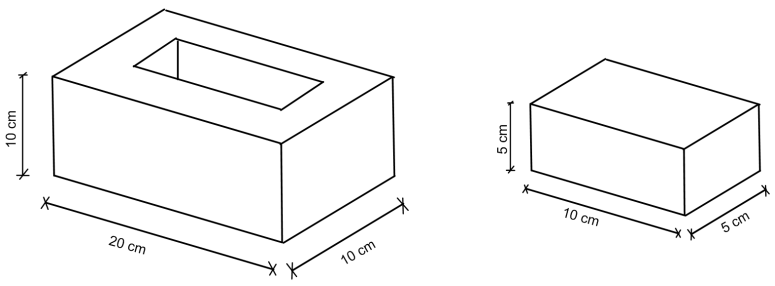

Figure 3.18. Dimensions of the Modular Blocks.

3.3.5. Rubber Sheet

The side effects in terms of friction between the steel sidewalls and backfill were eliminated by placing 6 mm thick rubber sheets on sidewalls. Rubber sheets followed the deformation of the backfill without significant resistance that could be accepted as an evidence for the soil volume pretended to be semi-infinite at sides.

3.4. Methodology for Construction and Seismic Loading

In this section, construction phase of model walls and seismic loads that the model walls were exposed to, are explained. Steel container box was placed the shaking table with the help of crane and fixed to the platform by eight bolts firmly. First of all, the inner sides of the container coated with grease oil as lubricant for the rubber sheets coating the inner side walls (Figure 3.19). After that 10 cm thick EPS board were placed in front of the back side of container. For Setup 1, "dry" sand was placed into container with 20 cm lifts, at each 20 cm lift a hand compactor was used for compaction work, and then the geogrid was placed on as the procedure is illustrated in Figure 3.20 and Figure 3.21.

The compactor's weight was 85 kg, plate dimensions were 400 mm (width) x 550 mm (length), centrifugal force was 10 kN to an effective depth of 25 cm. Modular blocks were placed in front of soil lifts, the hollows were filled with aggregates to increase friction between block and geogrid, first block was put behind the toe, which is a steel bar with a 2.5 cm height welded to the base of steel container which was a restriction for the base movement of front wall. And each modular block was put vertically but a 1-2 cm inwards to backfill and at the end an inclination of 12-13^o was created for the front wall. The uppermost blocks were the most unstable part of the front facing and they could topple during the dynamic excitation, so the upper two block layers were grouted to each other and construction bars were installed through the hollow parts of the blocks to increase stability as it can be seen in Figure 3.22.

After the construction was completed, instrumentation phase started accelerom-

eters were mounted on modular facing and two submerged accelerometers were embedded in soil at the top of the backfill. Strain gages were almost placed during construction since they were attached to three geogrid layers and data cables were taken out of the backfill through the small gaps created on modular blocks. Then the glass cover frame on which laser displacement sensors were installed, was fixed to the container the final view of instrumentation is illustrated in Figure 3.23.

Figure 3.19. Half Full Container with Dry Sand with Grease Behind Rubber Sheet.

Figure 3.20. Compaction Work.

Figure 3.21. A Geogrid Layer with Strain Gauge Instrumentation.

Figure 3.22. Grouted Top Blocks.

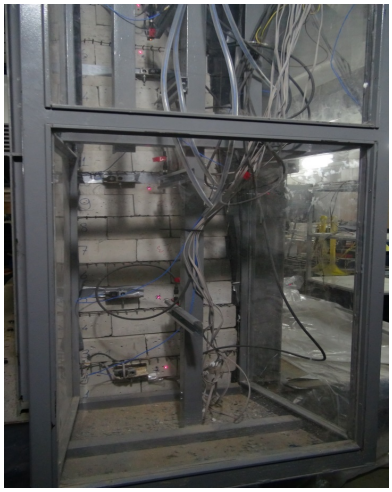

Figure 3.23. A View for Instrumentation with Glass Cover Frame.

For the wall configurations with cohesive backfill, kaolinite and sand was mixed

with 30% and 70% by weight respectively at optimum moisture content (approximately 9% water content) homogenously with the help of a small concrete mixing machine having a capacity of 140 liters.

For the Setup 4, which was the half scaled version of Setup 2 same procedure was followed same wall inclination was used in this wall model, but the geogrid lengths and block dimensions were adjusted to the scaled dimensions. In that wall configuration glass covered frame was not employed instead a frame on which laser displacement sensors were fixed was welded inside the steel container box, 20 cm in front of wall facing as it is illustrated in Figure 3.24. A steel bar was welded to the base in front of the lowest modular block layer to restrict the horizontal base movement of the wall (toe) as it can be seen in Figure 3.25 and the top two block layers were grouted to each other to avoid toppling.

Figure 3.24. Instrumentation of Setup 4.

Figure 3.25. Front View for Setup 4.

After construction phase was completed, model walls were performed under different seismic loading conditions. Two different recorded earthquakes were taken from the website of USGS El Centro and Kobe (KJMA station EW direction) earthquakes were used as base excitation. El Centro earthquake with a PGA of 0.33g and different amplitude ratios of the Kobe earthquake with a PGA of 0.82g was applied; for Kobe earthquake 50%, 75%, 100% and 125% (for Setup 4 also 150% was used) scales of amplitude (PGA) was given as different seismic loads; for those time history records same period and frequency domain was used.

Since the model walls were ½ and ¼ (Setup 4) scaled the periods of the earthquakes were decreased by $1/\sqrt{2}$ and ½ (Setup 4) respectively. According to that, applied El Centro earthquake was lasted in 23 seconds for ½ scaled models and 15.5 seconds for ¼ scaled models; Kobe earthquake was lasted in 34 seconds for ½ scaled models and 24 seconds for ¼ scaled models. Time history graphs for El Centro 100% and Kobe 100% earthquake for ½ scaled and ¼ scaled models are illustrated in Figure 3.26 to Figure 3.29 respectively. Seismic base excitations were applied to model wall in that order; El Centro100%, Kobe 50%, Kobe 75%, Kobe 100% and Kobe 125% (Kobe 150% was added for Setup 4).

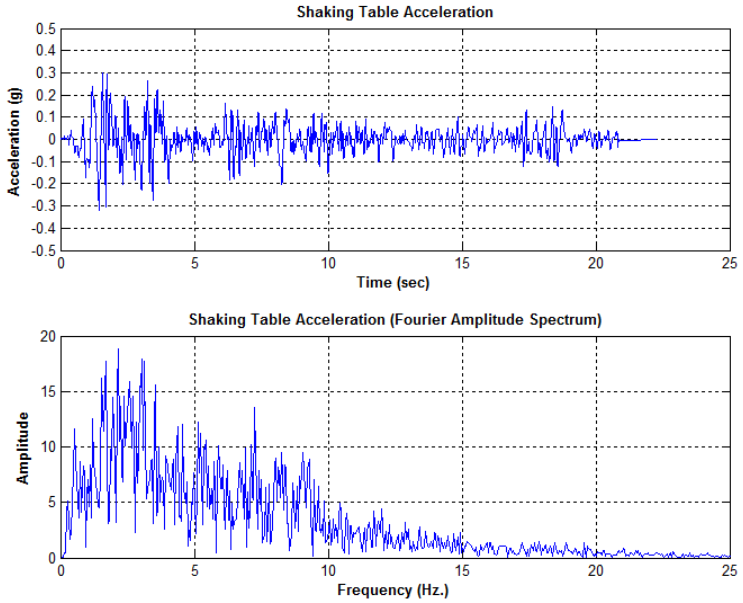

Figure 3.26. Time History Graph for El Centro 100% Earthquake, ½ Scaled Models.

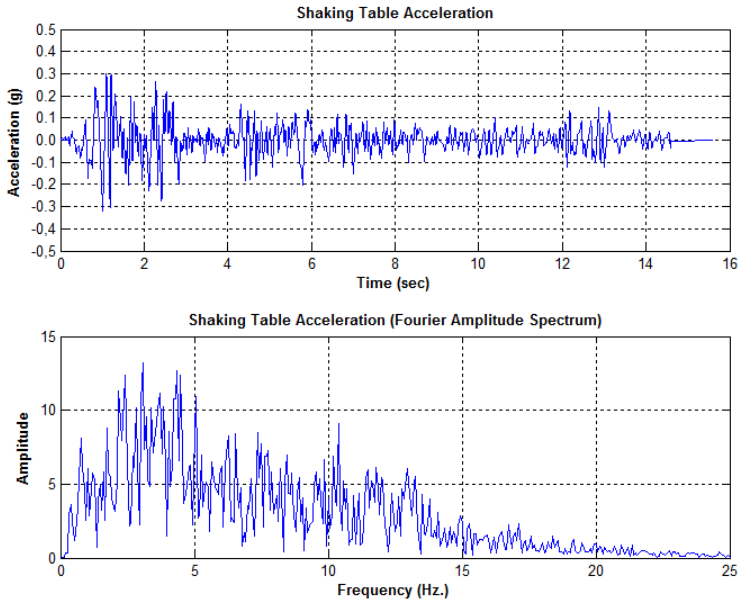

Figure 3.27. Time History Graph for El Centro 100% Earthquake, ¼ Scaled Models.

Shaking table tests were consisted of comparison of four different wall configurations with each other under different base excitations. To summarize Setup 1, Setup 2 and Setup 3 were ½ scaled model walls; Setup 4 was a ¼ scaled model wall.

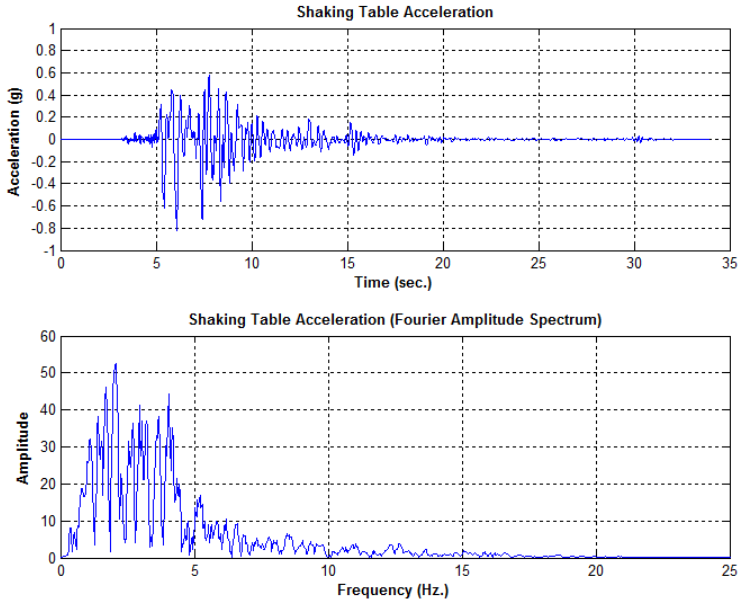

Figure 3.28. Time History Graph for Kobe 100% Earthquake, ½ Scaled Models.

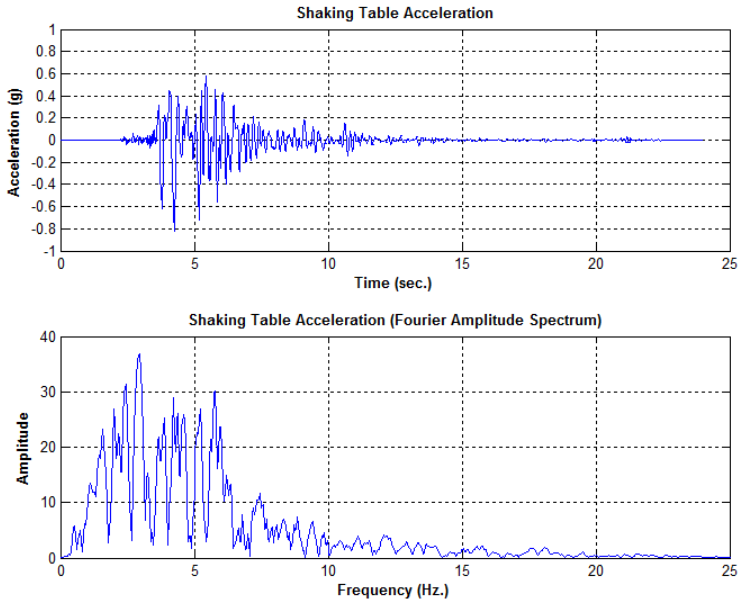

Figure 3.29. Time History Graph for Kobe 100% Earthquake, ¼ Scaled Models.

Setup 1 was a reference wall for Setup 2; Setup 1 had dry sand backfill whereas Setup 2 had K30S70 (30% kaolinite, 70% sand) backfill at optimum moisture content and all other parameters (geogrid lengths and properties, modular blocks, inclination, vertical spacing between geogrids and setup geometry) were same for Setup 1 and 2

that led an explicit comparison for the effects of backfill soil to the wall behavior and especially to have an opinion about the performance of geosynthetic reinforced walls with cohesive backfill compared to the sand backfill.

Setup 2 was a reference wall for Setup 3; they had both cohesive backfills (K30S70) and all the other parameters were same except the geogrid lengths Setup 2 had a geogrid length of 0.8H (152 cm) whereas Setup 3 had a geogrid length of 0.6H (114 cm) and Setup 3 also stand for an additional experiment for the performance of cohesive backfills.

Setup 2 was also a reference wall for Setup 4; Setup 4 was a half scaled version of Setup 2 with K30S70 backfill all the geometric properties were scaled as geogrid length (ratio is same 0.8 H, 76 cm), modular block dimensions (100x50x50 mm), wall inclination was same with Setup 2. Setup 4 was employed to find out effects of scaling on the behavior of model wall in terms of relative wall displacements and tensile loads on geogrids when compared to Setup 2.

Detailed illustration for wall configurations, including geometries and exact locations of instrumentation is given in Figure 3.30 for Setup 1 and Setup 2, Figure 3.31 for Setup 3 and Figure 3.32 for Setup 4.

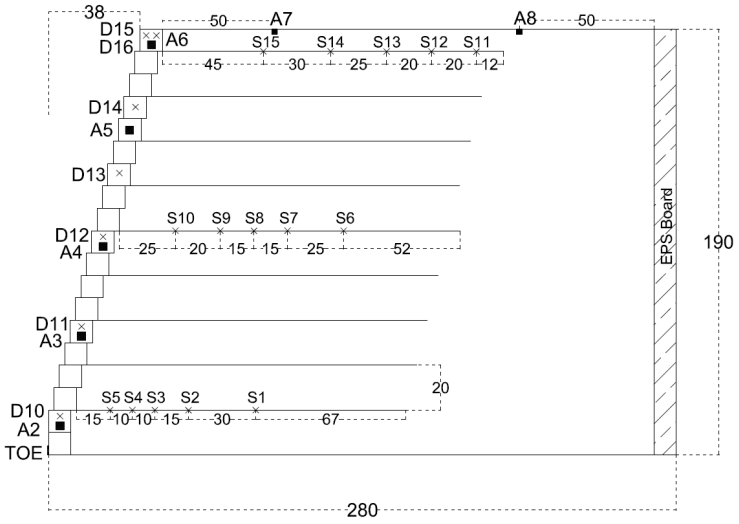

Figure 3.30. Wall Configuration and Instrumentation of Setup 1 and Setup 2.

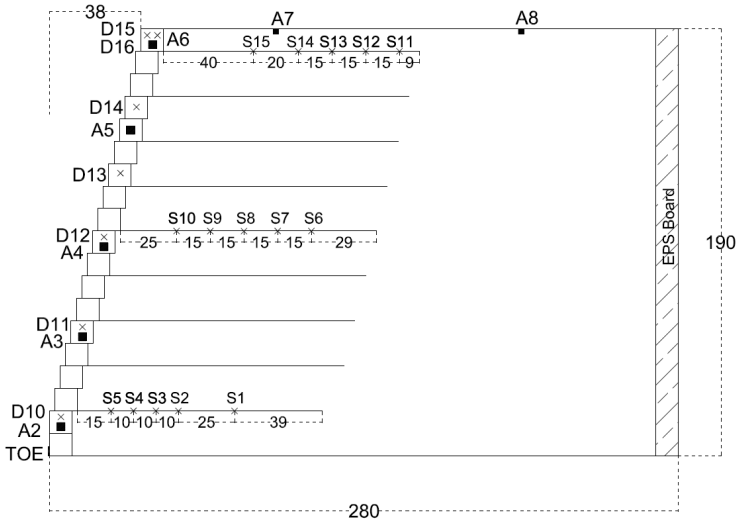

Figure 3.31. Wall Configuration and Instrumentation of Setup 3.

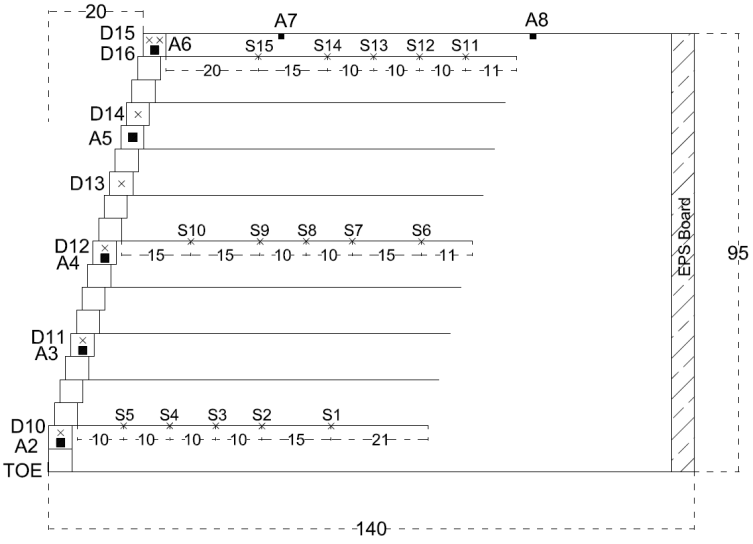

Figure 3.32. Wall Configuration and Instrumentation of Setup 4.

Figure 3.33 illustrates the final view of the setup with instrumentation for Setup 2. Figure 3.34 illustrates the preparation and control of instrumentation for Setup 4.

Figure 3.33. Final Controls Before Testing Setup 2.

Figure 3.34. Instrumentation Control for Setup 4.

4. TEST RESULTS AND EVALUATION

4.1. General

In this chapter; test results obtained from shaking table tests are presented and these results are evaluated for four model wall configurations. First of all, methods to obtain and analyzing data from these tests are explained. Then in the following chapters test results for three main parameters acceleration data, displacement data and strain data also related with tensile load values on reinforcements are reported. These test results are evaluated according to model wall types and seismic load types and compared and related to each other to understand the behavior of geosynthetic reinforced retaining walls with granular and cohesive backfill under seismic loading.

4.1.1. Data Evaluation Methods

Acceleration data and displacement data, each of them employed 8 channels, were collected with National Instruments' PCI-6229 M data acquisition system and strain values obtained from 15 channels were collected with Gartner Instruments' Q.raxx A107-16 data acquisition system. Acceleration, displacement and strain data were collected at a high sampling rate (200 Hz) that leads to more accurate results and this sampling rate reduced risks for skipping the peak points on the time history graph and aliasing distortion errors.

Using two different data loggers created some simultaneous data obtaining problems but this problem was overcame by superimposing the starting points of the motion for relative displacements and strain data which also has very similar trends of time history graphs.

Raw data obtained by the data loggers were processed by Matlab codes to convert them from millivolt versus time data to the desired dimension time history graphs. This raw data was also noise influenced data so it was hard to understand the peak

points and time dependent behavior according to time history graphs. Sudden and big increments for acceleration and displacement shifts in time domain and peaks that were not related to the input motion in frequency domain were observed caused by the noise. To get rid of noise from the data, band-pass filters were applied to the raw data that means determining a lower and upper frequency limits and extracting the raw data lower and higher then these limits. After the band-pass filter was applied sudden and meaningless peaks were get rid of in time domain and time history data gained a more clear appearance and the peaks in frequency domain which were not related with the frequencies of the input data were cleared away.

For acceleration data a band-pass filter 0.1 to 25 Hz was applied and an example for that is illustrated in Figure 4.1. High frequencies were not effective in displacement and strain data but the upper limit was also agreed as 25 Hz for them and lower limit of the band-pass filter was selected as 0.01 Hz.

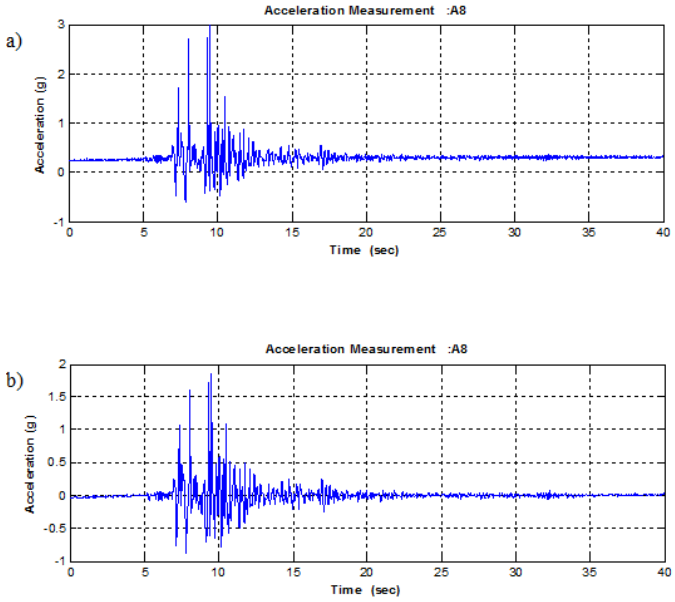

Figure 4.1. Acceleration Data a) Raw Data b) Band-pass Filtered 0.1-25 Hz.

4.1.2. Fundamental Frequency of Walls

Predominant frequencies of each wall configuration were determined according to the Fast Fourier transformed variations of acceleration time history data. In other

words the frequencies at which the peak amplitude values took place were determined for the acceleration time history graph in frequency domain and these were named as the predominant frequencies. In Section 4.2.1, Table 4.1 summarizes the predominant frequencies of the wall configurations for each base excitation, the predominant frequencies measured on shaking table (accelerometer A1) were written on that table. As an important point approximately same predominant frequencies were obtained from the accelerometers located on the front facing of model walls. So it can be noted that for ½ scaled model walls 4.02-4.05 Hz and for ¼ scaled models 5.75 Hz were the predominant frequencies for the given Kobe Earthquake.

To determine the natural frequency of the model wall is an essential step in seismic design of reinforced-soil retaining walls. Reinforced-soil retaining walls with heights lower than 10 m. are generally considered as short-period structures. The contribution of higher modes in total dynamic response of retaining wall systems are reduced by soil damping. According to this, fundamental frequency is the key parameter that controls the response of the wall to the seismic action (Hatami and Bathurst, 2000).

Formula 4.1 is an empirical formula suggested by Wu (1994) to calculate fundamental frequency f_{11} in Hz, it is used for a two dimensional, linear elastic medium of width B and height H. G is the shear modulus, Q is the density and υ is the Poisson ratio of the soil medium.

$$f_{11} = \frac{1}{4H}\sqrt{\frac{G}{Q}}\sqrt{1+\left(\frac{2}{1-\upsilon}\right)\left(\frac{H}{B}\right)^2} \tag{4.1}$$

The fundamental frequency for ½ scaled (H=1.9 m and B=2.8 m) medium-dense dry sand backfill model wall was calculated according to G_0=5640 kN/m^2 that was the average initial shear modulus taken from triaxial tests conducted at 25 and 50 kPa. And the other terms were determined as Q=1.55 kg/m3, υ=0.25 and f_{11} is found as 11.8 Hz, and the ¼ scaled models (H=0.95 m and B=1.4 m) has fundamental frequency 23.6 Hz.

For K30S70 cohesive backfill models same geometry with G0=3930 kN/m^2 that was the average initial shear modulus taken from triaxial tests conducted at 25 and 50 kPa. And the other terms were determined as Q=1.84 kg/m^3, υ=0.25 and f_{11} is found as 9.1 Hz, and the ¼ scaled models (H=0.95 m and B=1.4 m) has fundamental frequency 18.2 Hz.

According to these predominant and fundamental frequencies, it can be said that a resonant behavior is not expected for model walls and also such a behavior was not observed during the tests.

4.2. Accelerations

In this chapter horizontal accelerations measured during the tests with accelerometers located on the structure are investigated. These acceleration measurements were obtained from three main locations; the base input accelerometer on the shaking table, five accelerometers on the front face modular blocks along the wall height and two accelerometers in the backfill top (one in the reinforced zone the other in the unreinforced zone). The magnitude and distribution of the acceleration results, the peak values and amplifications are evidences for the behavior of the structure during seismic action.

4.2.1. Test Results

Acceleration test results include the peak acceleration values obtained from the accelerometers and the amplification factors for each. Amplification factors were calculated as the ratio of the maximum acceleration of the structure to the peak input base acceleration. So the peak input base acceleration gathered directly from accelerometer A1 on the shaking table is important. Figure 4.2 and Figure 4.3 illustrate two seismic data both in time and frequency domains, one is the input base acceleration data from which the corresponding horizontal displacement, put in effect by shaking table, was calculated by double integration; the other acceleration data was measured from the accelerometer on the shaking table. The data on the figures are for Kobe 100%, measured for Setup 2, it can be seen that the amplitudes of the acceleration in

time domain do not match up; for inward and outward directions peak accelerations measured as 0.936g and 0.897g instead of the applied 0.583g and 0.822g respectively. It can be noticed that the acceleration values were more compatible in "negative" direction which may also affect the behavior of test setup. And also it can be seen that dominant frequency of the input acceleration measured as 4.03 Hz whereas it was 2.1 Hz in the original record for Kobe 100% earthquake. For El Centro earthquake the original record's peak acceleration values were 0.298g and -0.320g and the predominant frequency was 2.15 Hz. As an example the measured acceleration record from the shaking table for Setup 2 had, 0.513g and -0.415g as peak acceleration data and the calculated spectral predominant frequency for this measured data was 5.4 Hz.

For all test setups these obtained input acceleration did not overlap the desired input acceleration mentioned in Section 3.4, the waveform of the accelerations coincided but they differed in amplitudes. These differences of 4 setups for every seismic action, the peak acceleration values and the predominant frequencies are given in Table 4.1. Acceleration time history data of the four setups and their corresponding Fourier amplitude spectrum are given in Appendix A.

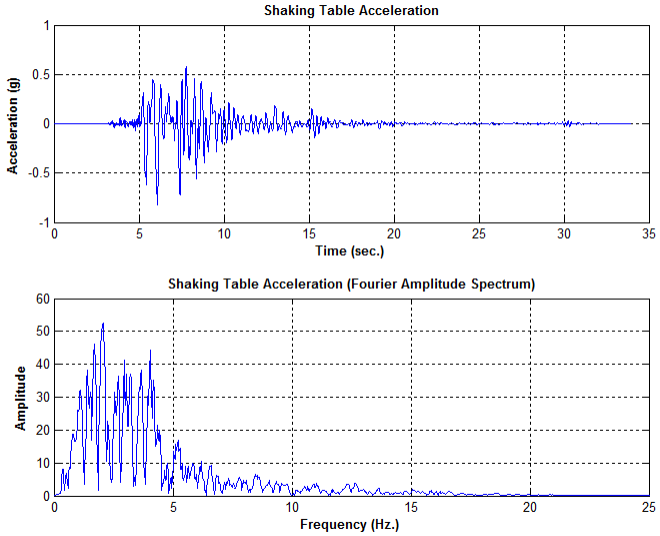

Figure 4.2. Acceleration Data Kobe 100% of the Shaking Table System Calculations.

Table 4.1. The Differences Between the Applied and Measured Base Input Accelerations.

		Measured PGA (+) direction (g)	Measured PGA (-) direction (g)	Predominant Frequency (Hz)	Desired PGA (+) direction (g)	Desired PGA (-) direction (g)	Predominant Frequency (Hz)	Acceleration difference (+) direction (%)	Acceleration difference (-) direction (%)
SETUP1	El Centro	0.515	-0.378	5.4	0.298	-0.320	2.15	73	18
	Kobe 50%	0.479	-0.563	4.02	0.292	-0.412	2.05	64	37
	Kobe 75%	0.667	-0.725	4.02	0.437	-0.617	2.05	53	17
	Kobe100%	0.926	-0.987	4.02	0.583	-0.823	2.05	59	20
SETUP2	El Centro	0.513	-0.415	5.4	0.298	-0.320	2.15	72	30
	Kobe 50%	0.53	-0.523	4.05	0.292	-0.412	2.05	82	27
	Kobe 75%	0.673	-0.694	4.03	0.437	-0.617	2.05	54	12
	Kobe100%	0.937	-0.898	4.03	0.583	-0.823	2.05	61	9
	Kobe 125%	1.166	-1.125	4.03	0.729	-1.029	2.05	60	9
SETUP3	El Centro	0.547	-0.46	5.4	0.298	-0.320	2.15	84	44
	Kobe 50%	0.52	-0.51	4.05	0.292	-0.412	2.05	78	24
	Kobe 75%	0.675	-0.705	4.05	0.437	-0.617	2.05	54	14
	Kobe100%	0.954	-0.942	4.05	0.583	-0.823	2.05	64	14
	Kobe 125%	1.21	-1.161	4.05	0.729	-1.029	2.05	66	13
SETUP4	El Centro	0.466	-0.452	4.35	0.298	-0.320	3.1	56	41
	Kobe 50%	0.614	-0.467	5.75	0.292	-0.412	2.95	111	13
	Kobe 75%	0.895	-0.676	5.75	0.437	-0.617	2.95	105	10
	Kobe100%	1.02	-0.961	5.75	0.583	-0.823	2.95	75	17
	Kobe 125%	1.233	-1.142	5.75	0.729	-1.029	2.95	69	11
	Kobe 150%	1.351	-1.401	5.75	0.875	-1.235	2.95	54	13

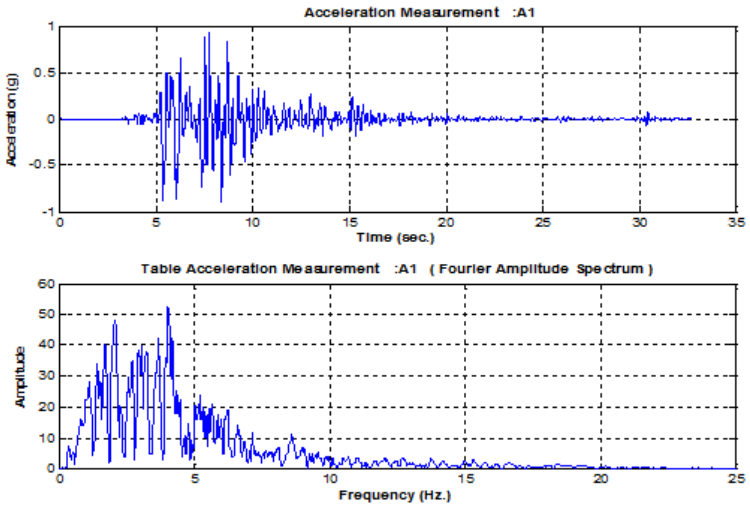

Figure 4.3. Acceleration Data Kobe 100% From Setup 2 Measured by Accelerometer on the Shaking Table A1.

Peak ground accelerations in both positive (inwards) and negative (outwards) directions and their corresponding amplification factors are given in Table 4.2 to Table 4.5 for four wall setups. Every wall setup was exposed to four to six seismic actions and they were named as different percent ratios of the earthquakes in the following figures and tables. As it was stated previously A1 is the base input acceleration, A2 to A6 accelerometers are on the front wall, A7 and A8 are in the backfill. Figure 4.4to Figure 4.7 illustrate the distribution of inwards and outwards peak acceleration values along the front wall according for four setup walls. The amplification factors according to base input acceleration of every different seismic action along the front wall for inward and outward directions are figured in Figure 4.8 to Figure 4.15.

In Table 4.2 it can be seen that, for all base excitations maximum peak acceleration values were measured by A6 accelerometer located on the top block. Maximum amplification factor was recorded as 1.861 for inwards and 1.412 for outwards where the peak acceleration value was 1.723g for inwards and -1.394g for outwards and the applied seismic action was Kobe 100% which had 0.926g and -0.987g for applied peak acceleration values. The amplification factors increased with increasing applied seismic load. Kobe 50% and El Centro 100% earthquakes were comparable because they had almost same peak acceleration values inwards but they differed in wave forms so the

amplification factors became different along the wall height the maximum amplification factor was 1.192 for El Centro 100% and 1.311 for Kobe 50% for inward direction. And the records taken from accelerometer A7 located on the top of the reinforced backfill zone and the accelerometer A8 on the unreinforced backfill show that there was not significant acceleration amplification in reinforced zone and de-amplification occurred in unreinforced backfill. For A7 maximum amplification factor was recorded as 1.152 fot inwards for Kobe 75%. Minimum de-amplification record measured by A8 was 0.814 for outwards during Kobe 75% earthquake.

Table 4.2. Peak Ground Accelerations and Amplification Ratios for Setup 1 During Seismic Actions.

SETUP 1												
	El Centro 100%				Kobe 50%				Kobe 75%			
Accelerometer No	Peak Acc. (+) (g)	Peak Acc. (-) (g)	Amplification Factor (+)	Amplification Factor (-)	Peak Acc. (+) (g)	Peak Acc. (-) (g)	Amplification Factor (+)	Amplification Factor (-)	Peak Acc. (+) (g)	Peak Acc. (-) (g)	Amplification Factor (+)	Amplification Factor (-)
A1	0.515	-0.378	1.000	1.000	0.479	-0.563	1.000	1.000	0.667	-0.725	1.000	1.000
A2	0.518	-0.374	1.006	0.989	0.538	-0.523	1.124	0.928	0.778	-0.744	1.166	1.026
A3	0.524	-0.381	1.017	1.006	0.556	-0.538	1.161	0.955	0.858	-0.780	1.286	1.076
A4	0.537	-0.386	1.043	1.020	0.568	-0.577	1.186	1.025	0.884	-0.771	1.325	1.063
A5	0.561	-0.407	1.089	1.076	0.611	-0.656	1.276	1.166	0.996	-0.825	1.493	1.138
A6	0.614	-0.438	1.192	1.158	0.628	-0.664	1.311	1.179	1.049	-0.946	1.573	1.305
A7	0.519	-0.418	1.008	1.104	0.432	-0.459	0.903	0.815	0.768	-0.752	1.152	1.038
A8	0.455	-0.412	0.883	1.089	0.490	-0.537	1.023	0.954	0.625	-0.590	0.937	0.814

	Kobe 100%			
Accelerometer No	Peak Acc. (+) (g)	Peak Acc. (-) (g)	Amplification Factor (+)	Amplification Factor (-)
A1	0.926	-0.987	1.000	1.000
A2	1.067	-1.004	1.152	1.017
A3	1.236	-1.102	1.335	1.117
A4	1.353	-1.101	1.461	1.116
A5	1.435	-1.176	1.550	1.191
A6	1.723	-1.394	1.861	1.412
A7	1.001	-0.893	1.081	0.905
A8	0.897	-0.824	0.969	0.835

Table 4.3. Peak Ground Accelerations and Amplification Ratios for Setup 2 During Seismic Actions.

SETUP 2												
	El Centro 100%				Kobe 50%				Kobe 75%			
Accelerometer No	Peak Acc. (+) (g)	Peak Acc. (-) (g)	Amplification Factor (+)	Amplification Factor (-)	Peak Acc. (+) (g)	Peak Acc. (-) (g)	Amplification Factor (+)	Amplification Factor (-)	Peak Acc. (+) (g)	Peak Acc. (-) (g)	Amplification Factor (+)	Amplification Factor (-)
A1	0.513	-0.415	1.000	1.000	0.530	-0.523	1.000	1.000	0.673	-0.694	1.000	1.000
A2	0.525	-0.420	1.023	1.012	0.546	-0.533	1.030	1.019	0.710	-0.682	1.055	0.983
A3	0.520	-0.438	1.014	1.055	0.579	-0.542	1.092	1.036	0.739	-0.711	1.098	1.024
A4	0.591	-0.450	1.153	1.084	0.587	-0.550	1.108	1.052	0.889	-0.741	1.321	1.068
A5	0.592	-0.454	1.154	1.094	0.590	-0.551	1.113	1.054	0.959	-0.773	1.425	1.114
A6	0.617	-0.465	1.202	1.120	0.648	-0.564	1.222	1.078	1.004	-0.819	1.492	1.180
A7	0.580	-0.445	1.131	1.072	0.577	-0.546	1.089	1.044	0.928	-0.787	1.379	1.134
A8	0.526	-0.383	1.026	0.924	0.527	-0.490	0.993	0.936	0.833	-0.696	1.237	1.003
	Kobe 100%				Kobe 125%							
Accelerometer No	Peak Acc. (+) (g)	Peak Acc. (-) (g)	Amplification Factor (+)	Amplification Factor (-)	Peak Acc. (+) (g)	Peak Acc. (-) (g)	Amplification Factor (+)	Amplification Factor (-)				
A1	0.937	-0.898	1.000	1.000	1.166	-1.125	1.000	1.000				
A2	0.982	-0.879	1.048	0.979	1.302	-1.146	1.117	1.018				
A3	1.074	-0.902	1.146	1.004	1.404	-1.175	1.204	1.044				
A4	1.250	-0.967	1.334	1.077	1.722	-1.315	1.477	1.169				
A5	1.318	-1.046	1.406	1.165	1.695	-1.374	1.454	1.222				
A6	1.563	-1.190	1.669	1.325	2.059	-1.672	1.766	1.486				
A7	1.522	-1.011	1.624	1.126	1.886	-1.334	1.617	1.186				
A8	1.432	-0.892	1.528	0.993	1.905	-1.130	1.634	1.004				

Table 4.4. Peak Ground Accelerations and Amplification Ratios for Setup 3 During Seismic Actions.

SETUP 3												
	El Centro 100%				Kobe 50%				Kobe 75%			
Accelerometer No	Peak Acc. (+) (g)	Peak Acc. (-) (g)	Amplification Factor (+)	Amplification Factor (-)	Peak Acc. (+) (g)	Peak Acc. (-) (g)	Amplification Factor (+)	Amplification Factor (-)	Peak Acc. (+) (g)	Peak Acc. (-) (g)	Amplification Factor (+)	Amplification Factor (-)
A1	0.547	-0.460	1.000	1.000	0.520	-0.510	1.000	1.000	0.675	-0.705	1.000	1.000
A2	0.574	-0.462	1.049	1.004	0.572	-0.516	1.100	1.012	0.739	-0.706	1.095	1.001
A3	0.561	-0.478	1.025	1.039	0.590	-0.529	1.135	1.037	0.758	-0.716	1.123	1.016
A4	0.617	-0.496	1.129	1.078	0.599	-0.558	1.152	1.094	0.883	-0.758	1.307	1.075
A5	0.626	-0.497	1.145	1.080	0.602	-0.569	1.158	1.116	0.988	-0.797	1.464	1.130
A6	0.680	-0.512	1.244	1.113	0.654	-0.583	1.258	1.143	1.046	-0.880	1.550	1.248
A7	0.626	-0.479	1.144	1.041	0.552	-0.539	1.061	1.058	0.955	-0.784	1.414	1.112
A8	0.536	-0.446	0.980	0.971	0.507	-0.464	0.974	0.910	0.819	-0.730	1.213	1.035
	Kobe 100%				Kobe 125%							
Accelerometer No	Peak Acc. (+) (g)	Peak Acc. (-) (g)	Amplification Factor (+)	Amplification Factor (-)	Peak Acc. (+) (g)	Peak Acc. (-) (g)	Amplification Factor (+)	Amplification Factor (-)				
A1	0.954	-0.942	1.000	1.000	1.210	-1.161	1.000	1.000				
A2	0.984	-0.917	1.031	0.973	1.266	-1.160	1.046	0.999				
A3	1.018	-0.987	1.067	1.048	1.437	-1.192	1.187	1.026				
A4	1.258	-0.957	1.319	1.016	1.737	-1.273	1.435	1.097				
A5	1.433	-1.078	1.502	1.145	1.900	-1.517	1.570	1.307				
A6	1.647	-1.256	1.726	1.333	2.195	-1.762	1.813	1.518				
A7	1.506	-1.006	1.579	1.068	2.071	-1.365	1.711	1.176				
A8	1.491	-0.969	1.563	1.029	1.987	-1.200	1.641	1.034				

Table 4.5. Peak Ground Accelerations and Amplification Ratios for Setup 4 During Seismic Actions.

SETUP 4												
	El Centro 100%				Kobe 50%				Kobe 75%			
Accelerometer No	Peak Acc. (+) (g)	Peak Acc. (-) (g)	Amplification Factor (+)	Amplification Factor (-)	Peak Acc. (+) (g)	Peak Acc. (-) (g)	Amplification Factor (+)	Amplification Factor (-)	Peak Acc. (+) (g)	Peak Acc. (-) (g)	Amplification Factor (+)	Amplification Factor (-)
A1	0.466	-0.452	1.000	1.000	0.614	-0.467	1.000	1.000	0.895	-0.676	1.000	1.000
A2	0.475	-0.445	1.019	0.984	0.648	-0.474	1.055	1.015	0.934	-0.669	1.044	0.990
A3	0.489	-0.484	1.049	1.070	0.680	-0.483	1.107	1.034	1.001	-0.720	1.118	1.065
A4	0.503	-0.505	1.079	1.118	0.683	-0.492	1.112	1.054	1.003	-0.729	1.121	1.078
A5	0.493	-0.495	1.058	1.096	0.671	-0.510	1.093	1.092	1.037	-0.728	1.159	1.077
A6	0.496	-0.515	1.064	1.139	0.687	-0.497	1.119	1.064	1.045	-0.743	1.168	1.099
A7	0.507	-0.492	1.087	1.088	0.679	-0.532	1.106	1.139	1.059	-0.716	1.184	1.060
A8	0.495	-0.509	1.062	1.126	0.675	-0.497	1.100	1.064	1.068	-0.722	1.193	1.068
	Kobe 100%				Kobe 125%				Kobe 150%			
Accelerometer No	Peak Acc. (+) (g)	Peak Acc. (-) (g)	Amplification Factor (+)	Amplification Factor (-)	Peak Acc. (+) (g)	Peak Acc. (-) (g)	Amplification Factor (+)	Amplification Factor (-)	Peak Acc. (+) (g)	Peak Acc. (-) (g)	Amplification Factor (+)	Amplification Factor (-)
A1	1.020	-0.961	1.000	1.000	1.233	-1.142	1.000	1.000	1.351	-1.401	1.000	1.000
A2	1.079	-0.945	1.058	0.983	1.278	-1.125	1.036	0.985	1.379	-1.369	1.021	0.977
A3	1.184	-0.984	1.161	1.024	1.403	-1.183	1.138	1.036	1.563	-1.461	1.157	1.043
A4	1.235	-0.999	1.211	1.040	1.586	-1.202	1.286	1.053	1.672	-1.471	1.238	1.050
A5	1.222	-1.036	1.198	1.078	1.643	-1.377	1.332	1.205	2.248	-1.531	1.664	1.093
A6	1.272	-1.050	1.247	1.093	1.920	-1.326	1.557	1.161	2.212	-1.838	1.637	1.312
A7	1.290	-1.036	1.265	1.078	1.895	-1.346	1.537	1.179	2.168	-1.555	1.605	1.110
A8	1.179	-1.018	1.156	1.060	1.744	-1.288	1.415	1.128	2.231	-1.601	1.652	1.143

Table 4.3includes the measured acceleration data for Setup 2 with cohesive backfill that was similar to Setup 1 with sand backfill. The amplification factors increased with increasing earthquake load and the maximum amplification factors were recorded on the top blocks. For Kobe 100% earthquake the maximum amplification factors were 1.669 for inwards and 1.325 for outwards, smaller than Setup 1 and the maximum amplification factors were measured for Kobe 125% earthquake as 1.766 inwards and 1.486 outwards. A7 accelerometer recorded that significant amplifications occurred in reinforced zone for inward direction regarding the maximum amplification factors 1.624 for Kobe 100% and 1.617 for Kobe 125%; where 1.126 for Kobe 100% and 1.186 for Kobe 125% were the amplification factors measured for outward direction with A7. Likewise through the unreinforced backfill considerable inward amplifications were observed as 1.528 for Kobe 100% and 1.634 for Kobe 125%. But at the same time, no acceleration amplification was seen inside the same unreinforced zone for outwards with respect to 0.993 and 1.004 recorded as maximum amplification values for Kobe 100% and Kobe 125%.

Table 4.4; including the peak acceleration and amplification records for Setup 3 showed similar results with the Setup 2. Setup 3 had slight higher peak acceleration and amplification values than the Setup 2 and the reason for this was Setup 3 had shorter reinforcement lengths. For Kobe 100% earthquake the maximum amplification factors were 1.726 for inwards and 1.333 for outwards, higher than Setup 2. The maximum amplification factors were measured for Kobe 125% earthquake as 1.813 for inwards and 1.518 for outwards. In reinforced and unreinforced backfill zones these two setups showed similar behavior in terms of acceleration amplification.

Peak acceleration and corresponding amplifications records of Setup 4, that was the half scaled version of Setup 2, can be seen in Table 4.5. For Kobe 100% 1.247 and 1.093, for Kobe 125% 1.557 and 1.161, for Kobe 150% 1.637 and 1.312 were the measured inward and outward amplification factors respectively. These results seemed relatively lower than the scaled version Setup 2. The peak acceleration values were 1.272g and -1.050g for Kobe 100% earthquake where they reached the values 2.212g and -1.838g during Kobe 150% earthquake. And in the reinforced and unreinforced

zones significant inward amplification records were obtained as 1.537 and 1.415 for Kobe 125% and 1.605 and 1.653 for Kobe 150%. But they did not show a remarkable amplification for acceleration for outward direction where 1.179 and 1.128 were maximum reinforced and unreinforced amplification factors for Kobe 125% and 1.110 and 1.143 were reinforced and unreinforced amplification factors for Kobe 150%. Similar to all setups highest peak accelerations and amplification factors were recorded on the top blocks. And amplification factors increased with increasing base excitation especially for Kobe 125% and Kobe 150% earthquakes which reach 1.23g and 1.35g as applied peak acceleration values inwards.

Figure 4.4 illustrates the peak acceleration values for Setup 1 for both inward and outward directions. Acceleration at zero height represents the acceleration record obtained from the accelerometer A1 located on the shaking table. And this peak acceleration value from A1 was given to compare the other peak acceleration data along the height of the wall with the base excitation. For Setup 1 it is obvious that Kobe 100% differed from the previous earthquakes in terms of acceleration magnitude in both directions. And especially for Kobe 100% earthquake it can be seen that, there was a significant increase of acceleration on top blocks.

Peak acceleration values for Setup 2 is shown by Figure 4.5 and it can be seen that after Kobe 100% earthquake there is an almost linear increase of peak acceleration values along the wall height from bottom to top block. For Kobe 100% and Kobe 125% this increase was more remarkable for inward direction similar to the trend of Setup 1.

Figure 4.6 shows the peak displacement values of Setup 3 and the almost same trend with Setup 2 was observed from the graph. For Kobe 125% earthquake peak acceleration value of top block reached 2.2g inwards where it was -1.76g outwards.

Figure 4.7 illustrates the peak acceleration values of Setup 4 in both directions. Up to Kobe 125% earthquake the acceleration distribution along the wall height was constant but especially for inward direction an increase from bottom to top blocks was observed for Kobe 125% and Kobe 150% earthquakes. The top blocks reached 1.92g

and 2.21g for Kobe 125% and Kobe 150% motions respectively.

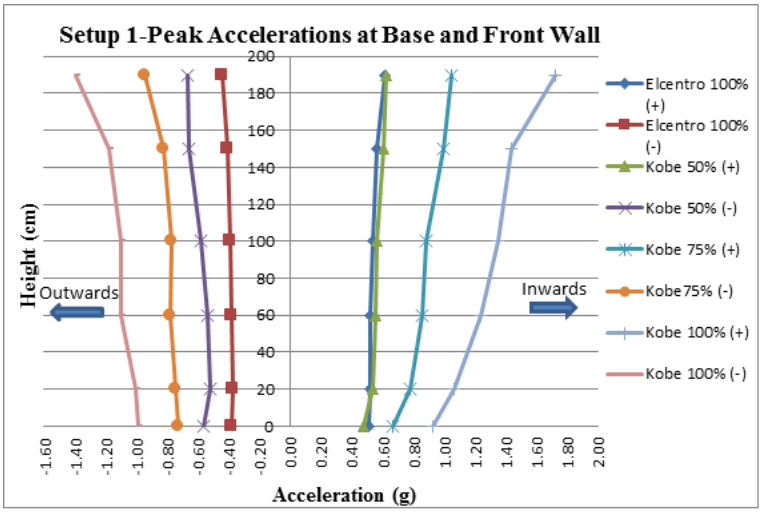

Figure 4.4. Peak Accelerations at Base and Facing of Setup 1.

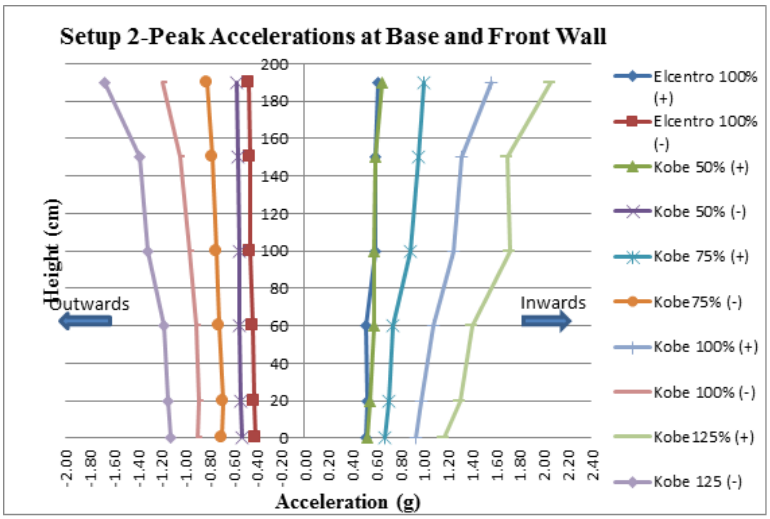

Figure 4.5. Peak Accelerations at Base and Facing of Setup 2.

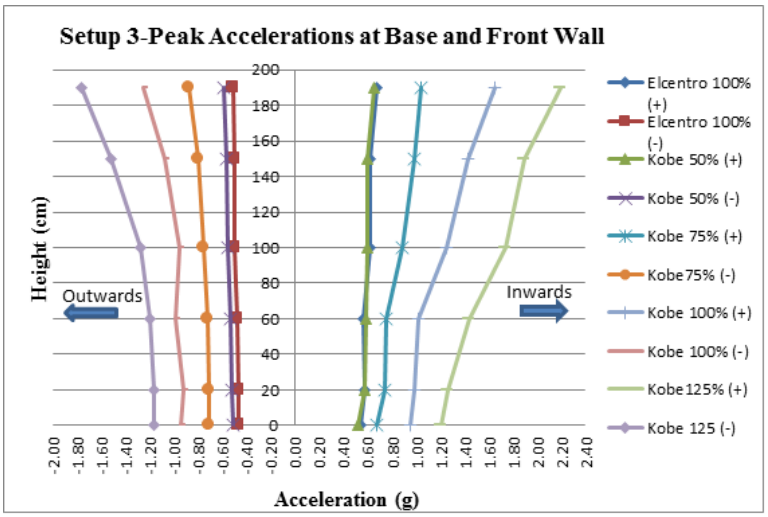

Figure 4.6. Peak Accelerations at Base and Facing of Setup 3.

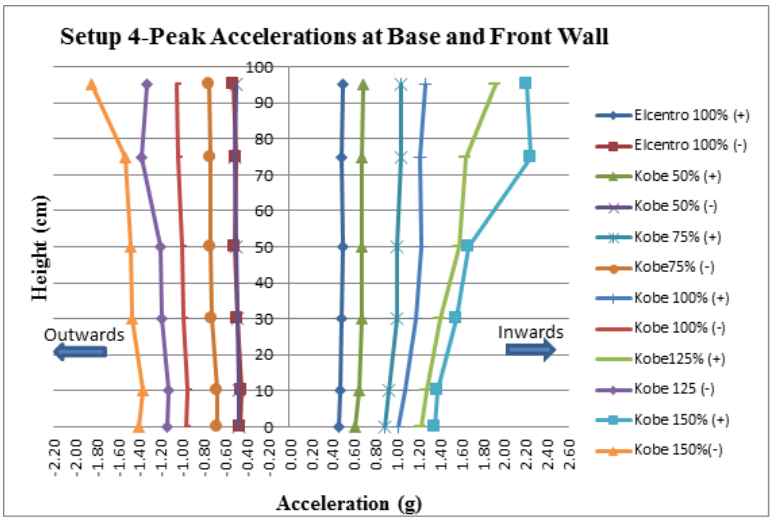

Figure 4.7. Peak Accelerations at Base and Facing of Setup 4.

Figure 4.8 and Figure 4.9 illustrates the inwards and outwards acceleration amplification values of Setup 1. The linear increase along the wall height from bottom to top was more obvious in Kobe 75% and Kobe 100% earthquakes. For Kobe 50% and El Centro 100% earthquakes de-amplification was also observed at blocks up to mid height.

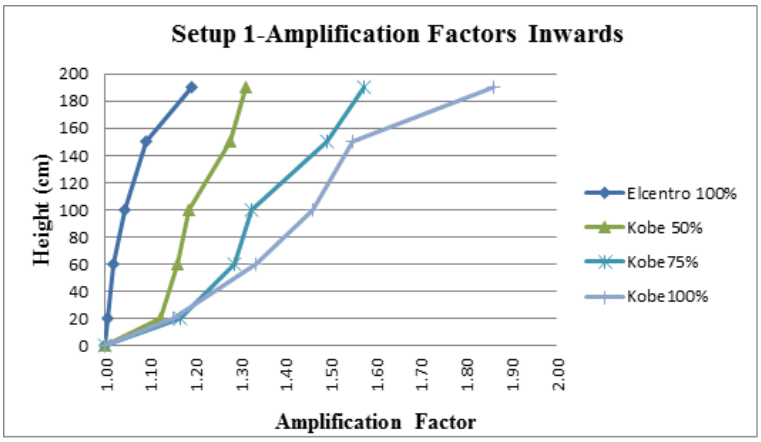

Figure 4.8. Inward Amplification Factors at Facing of Setup 1.

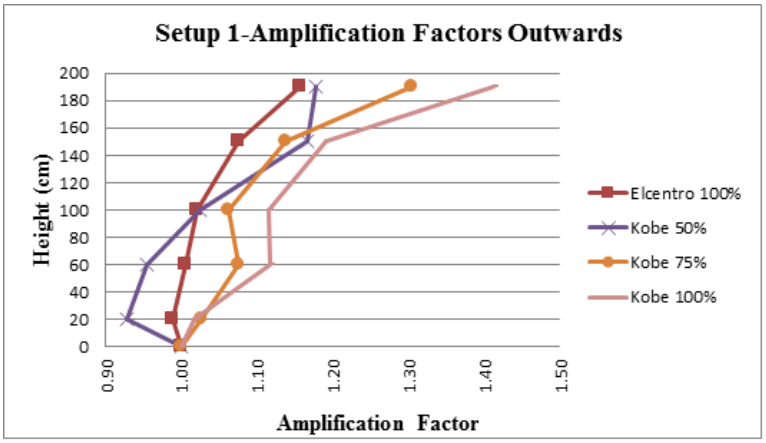

Figure 4.9. Outward Amplification Factors at Facing of Setup 1.

For Setup 2, the amplification factors through height of the front wall are illustrated in Figure 4.10 and Figure 4.11. The linear increase of amplification values along the height of the wall for Kobe 75%, 100% and 125% were more remarkable for inwards. For these earthquakes this linear increase was started over the mid height for outwards and these values were lower than the inward counterparts.

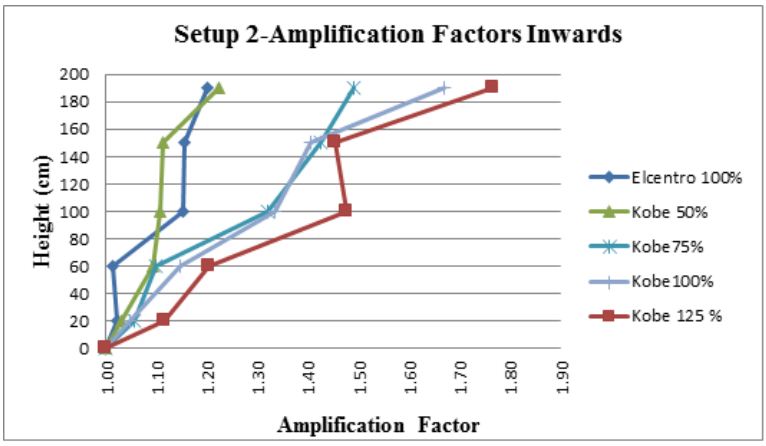

Figure 4.10. Inward Amplification Factors at Facing of Setup 2.

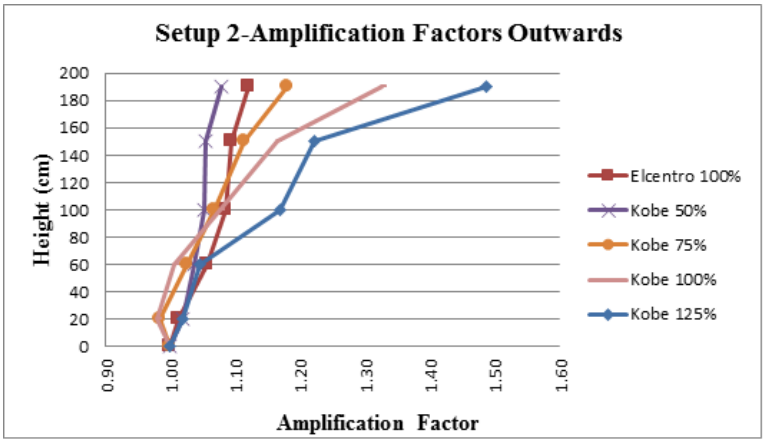

Figure 4.11. Outward Amplification Factors at Facing of Setup 2.

Figure 4.12 and Figure 4.13 illustrates the acceleration amplification factors for Setup 3 in both directions. According to figures, it can be said that amplification factor behavior of this model wall was almost same with Setup 2.

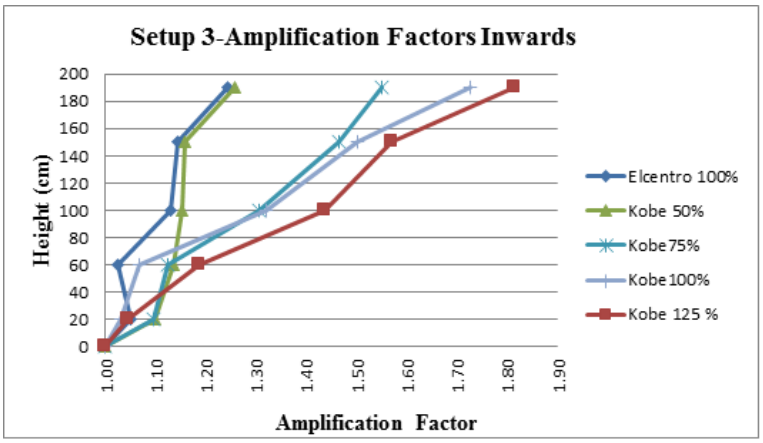

Figure 4.12. Inward Amplification Factors at Facing of Setup 3.

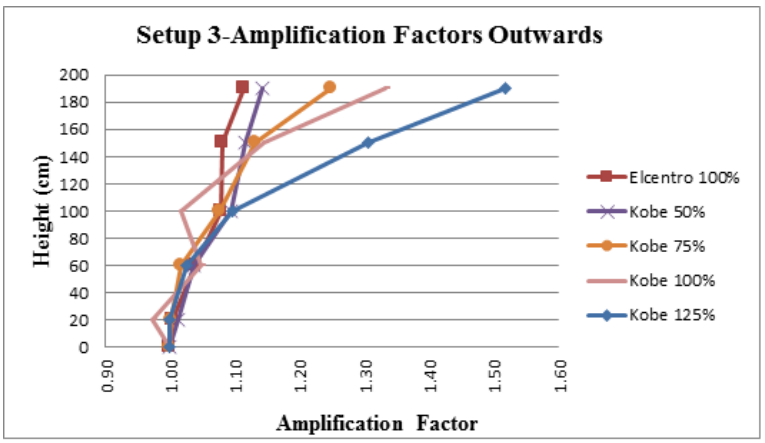

Figure 4.13. Outward Amplification Factors at Facing of Setup 3.

Figure 4.14 and Figure 4.15 illustrate the amplification factors of Setup 4 in both directions. The linear increase is more apparent for Kobe 125% earthquake and in addition that linear increase an amplification peak was generated on the wall top for Kobe 150% for inward direction. For outwards an increase along the wall height was not observed and the figured disordered behavior was only observed at Setup 4 for outwards.

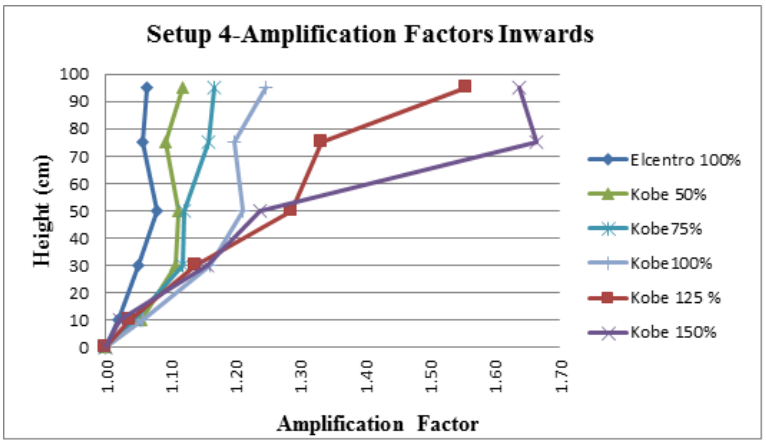

Figure 4.14. Inward Amplification Factors at Facing of Setup 4.

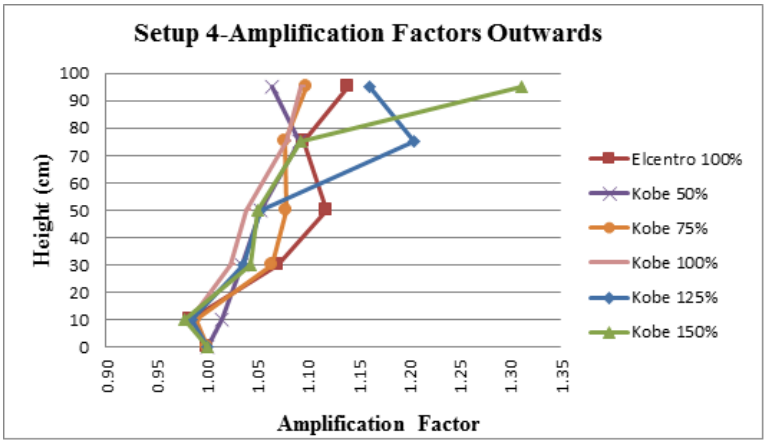

Figure 4.15. Outward Amplification Factors at Facing of Setup 4.

Figure 4.16 illustrates the amplification factors recorded on the block at the height of 150 cm of the facing for Setup 1, 2 and 3 during seismic actions. Seismic actions were given in terms of gravitational acceleration "g" on the horizontal axis. It can be seen that amplification factors for outward direction were less than inward direction.

In Figure 4.17 amplification factors recorded on facing modular blocks at 190 cm are shown for Setup 1, 2 and 3 during base excitations. In outward direction for Setup 3 amplification factor was over 1.5 and this value was around 1.3 at 150 cm. Maximum amplification factors for inward direction were 1.85 for Setup 1 and 1.81 for Setup 3 at 190 cm where these factors were around 1.55 for Setup 1 and 3 at 150 cm.

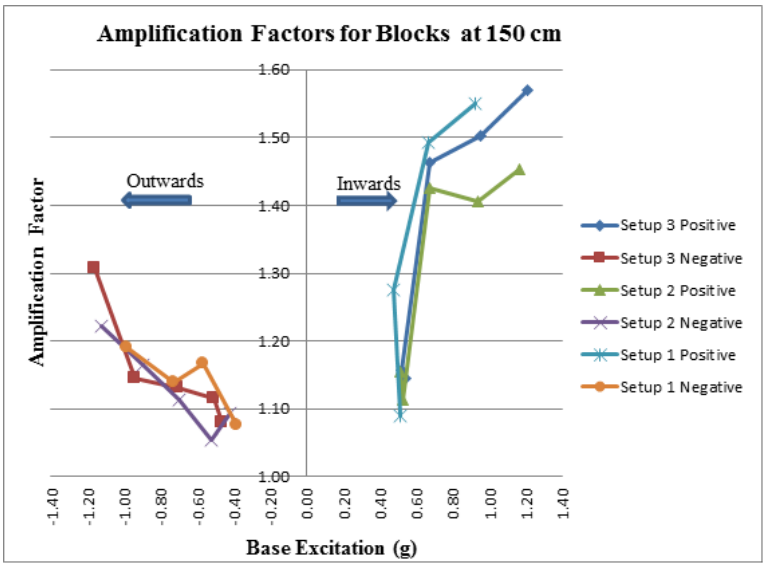

Figure 4.16. Amplification Factors on Facing Modular Blocks at 150 cm During Base Excitations.

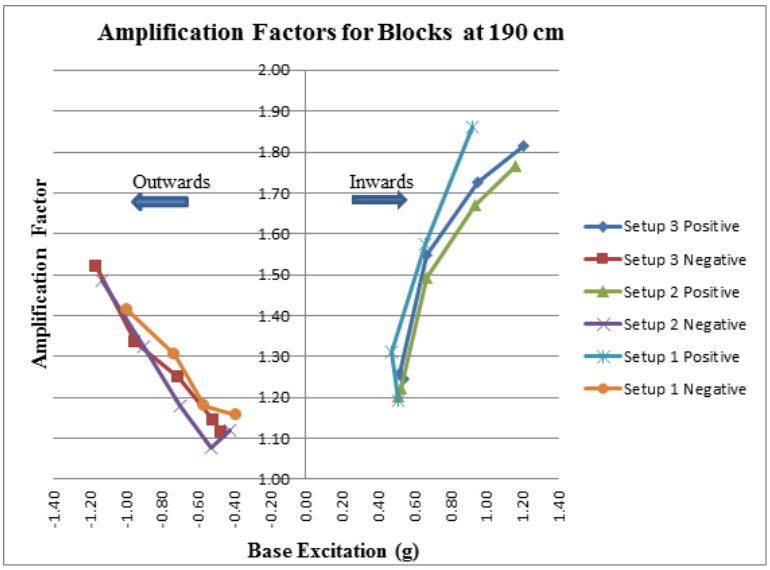

Figure 4.17. Amplification Factors on Facing Modular Blocks at 190 cm During Base Excitations.

4.2.2. Summary of the Results

The most outstanding result of the above data is that peak acceleration values and their associated amplification factors represent a great difference between positive (inwards) and negative (outwards) directions. The reason for that behavior can

probably be explained by the aimed and measured input base acceleration differences listed in Table 4.1. As an example for the Setup 3 at the top of wall the measured accelerations at the top of the wall got close to 2.2g level inwards whereas 1.76g was reached outwards at the same elevation; their amplification factors are 1.81 for inwards and 1.52 for outwards. This tendency has an effect on the relative displacements of the front wall especially on the residual displacements. Study of Ling (2003) mentioned that amplification ratio of 3 or greater, induce additional stresses to the superstructure. This limit was not exceeded in any of the tests conducted in this study.

For all setups the maximum accelerations occurred on the top of the wall of the front facing. For Setup 1 and 2 the accelerations tended to increase significantly between 150 cm and 190 cm, for Setup 3 the starting point of this increase became at 100 cm, mid height of front wall. The accelerometers for the backfill could just be located on the wall top and the amplification factors of them were lower than the factors of the front wall at the same elevation. This can be explained by the condition that the soil mass and the front wall did not move monolithically where the movement of the interior soil mass was more constrained than the front wall (Zarnani and Bathurst, 2007). While the accelerometers in the backfill were located on the wall top there was no chance to observe the change of acceleration through the inside backfill. But it was observed that the amplification factors in the reinforced zone were larger than unreinforced backfill soil. This can be attributed to the lower stiffness of the backfill zone since loose soils have better damping characteristics.

For Setup 2 and Setup 3 trends of Kobe 75%, Kobe 100% and Kobe 125% were very similar for both directions. This increase of amplification factors with increasing base excitation was also reported in the study of Matsuo *et al.*, (1998). In this study there was an increase after 0.9g for inward direction and 0.6g for outward direction but an incremental amplification increase was observed for each base input excitation. This was in contradiction with the results of the study of Başbuğ (2011) where they observed an input base acceleration value, 0.56g after which the amplification factors tended to increase significantly. Also in some references as; Ling *et al.*, (2005), Huang *et al.*, (2010) and Yang *et al.*, (2013) a critical acceleration was introduced after which the

amplification factor does not increase but rather starts to decrease with the increase of input acceleration. When the critical acceleration level is exceeded by increasing shaking intensity, it is supposed that the overall stiffness of the model decreases and damping increases. A critical acceleration threshold was not observed in that study. This may be caused by the fact that large soil shear deformations did not occur in the backfill which could have causing softening and strength degradation.

For the influence of the backfill type it can be said that the amplification factors for Kobe 100% of Setup 1 were 1.86 and 1.41 for inward and outward directions respectively at the top of the wall. For Setup 2 under the same seismic action amplification factors were 1.67 and 1.32 and for Setup 3, 1.72 and 1.33. These values suggest that the amplification factors of dry sand backfill were greater than its cohesive backfill counterparts at the modular block facing. This outcome is consistent with the relative displacements of these walls. Any difference could not be observed for the distribution of peak acceleration values of Setup2 and Setup 3. Slightly higher amplification factors were observed in the Setup 3 compared to Setup 2. This tendency was also compatible with the influence of reinforcement length on relative displacements of walls. But this result is not consistent with the observation of Allen and Bathurst (2002) who stated that the amplification factor was increased by increasing the reinforcement length and the global stiffness (sum of the layer stiffness values divided by the height of the wall). Wall models had same heights (190 cm) so when the reinforcement length was increased, the global stiffness would also increase. Relative displacement of the wall was more effective than the global stiffness for amplification, while searching the effects of reinforcement length.

For the influence of scale factor, Setup 2 and Setup 4 is taken into consideration; the amplification factors of for example Kobe 125% for Setup 2 were 1.77 and 1.49 for inward and outward directions while Setup 4's amplification factors were 1.56 and 1.16 respectively. Although there was a decrease especially for outward direction, a scaled difference ratio (the model was the half scale of Setup 2) cannot be mentioned both for peak acceleration values and amplification factors.

4.3. Horizontal Displacements

The main objective of this chapter is to investigate the effects of different base excitations on four different wall configurations. To achieve this, the relation between the base excitations and the consequent peak displacements and residual displacements in both negative and positive directions were analyzed. Along the wall height seven laser displacement transducers were located, two of them were located on the top blocks for two reasons one of them was to control the top block system could work as a coherent body and secondly to guarantee the critical top wall displacement measurement data by two sensors. One displacement transducer (D9) was located on the shaking table to record base input excitation. Displacement time history data of the wall configurations for each applied base action are given in Appendix B. For Appendix A and Appendix B it should be noted that the time axes of the tests presented in these figures differ from duration of excitations, because zero time pads were added at the beginning and end of the data. Accordingly new durations become 40 second for Kobe ½ scaled, 30 seconds for El Centro ½ scaled, 30 seconds for Kobe ¼ scaled and 25 seconds for El Centro ¼ scaled.

4.3.1. Test Results

Displacement base excitation was calculated from the desired acceleration time history data by double integration and applied to the shaking table system by a controller unit. But this excitation cannot be enforced by the shaking table exactly because of the load capacity and mechanical efficiency of the system, feedback of the base input excitation was collected from shaking table by a laser displacement transducer (D9) located on it. The ratio of the desired and collected displacements signifies degree of achievement of system and in this study more than 95% of efficiency was reached and an example for this feedback is given in Figure 4.18. It was observed that applied displacement was +70.7 mm and -86.3 mm while the measured input base displacement was +74.9 mm and -89.5 mm for Kobe 100% earthquake.

The base acceleration data from shaking table is another concern which affects the

relative displacement behavior of the setup, Setup2 Kobe 125% measured input base displacement (D9) data and its related relative displacement data is given in Figure 4.19 for bottom (D10), mid (D12) and top (D15) blocks of wall. It can be well understood from this figure that when the input base excitation and relative displacement data were overlapped (both acceleration and displacement data are collected in 200 Hz) there is a well suit situation between them. It is observed that front wall moved in opposite direction of base excitation because of the inertial forces in the beginning when the deformation started. This relation is a bit corrupted but still there is a consistency in behavior. It also should be mentioned that positive displacement values represent inward movement, while the negative displacement values represent outward movement of wall.

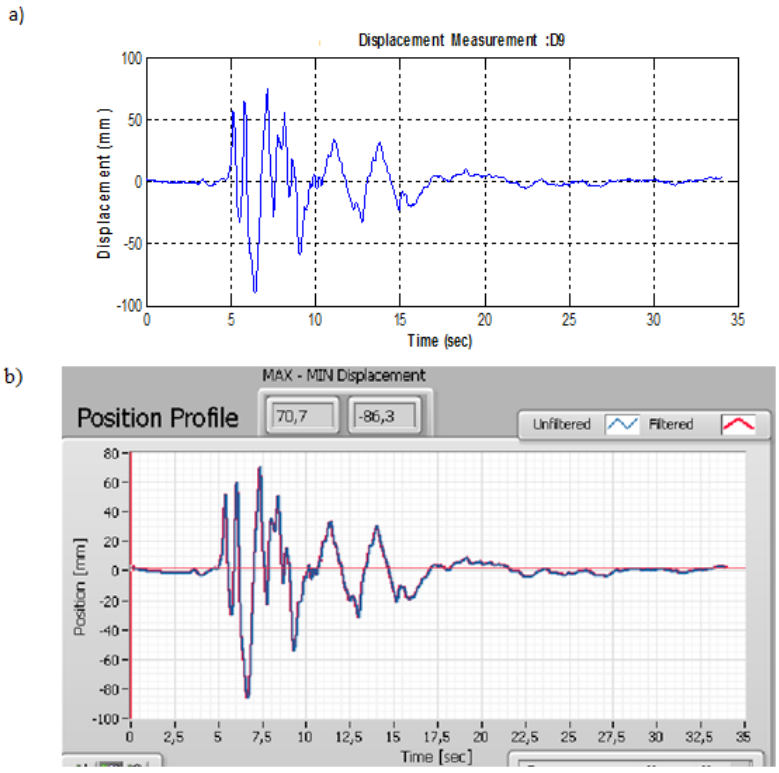

Figure 4.18. a) Measured and b) Applied Base Input Displacements, Kobe 100% Earthquake.

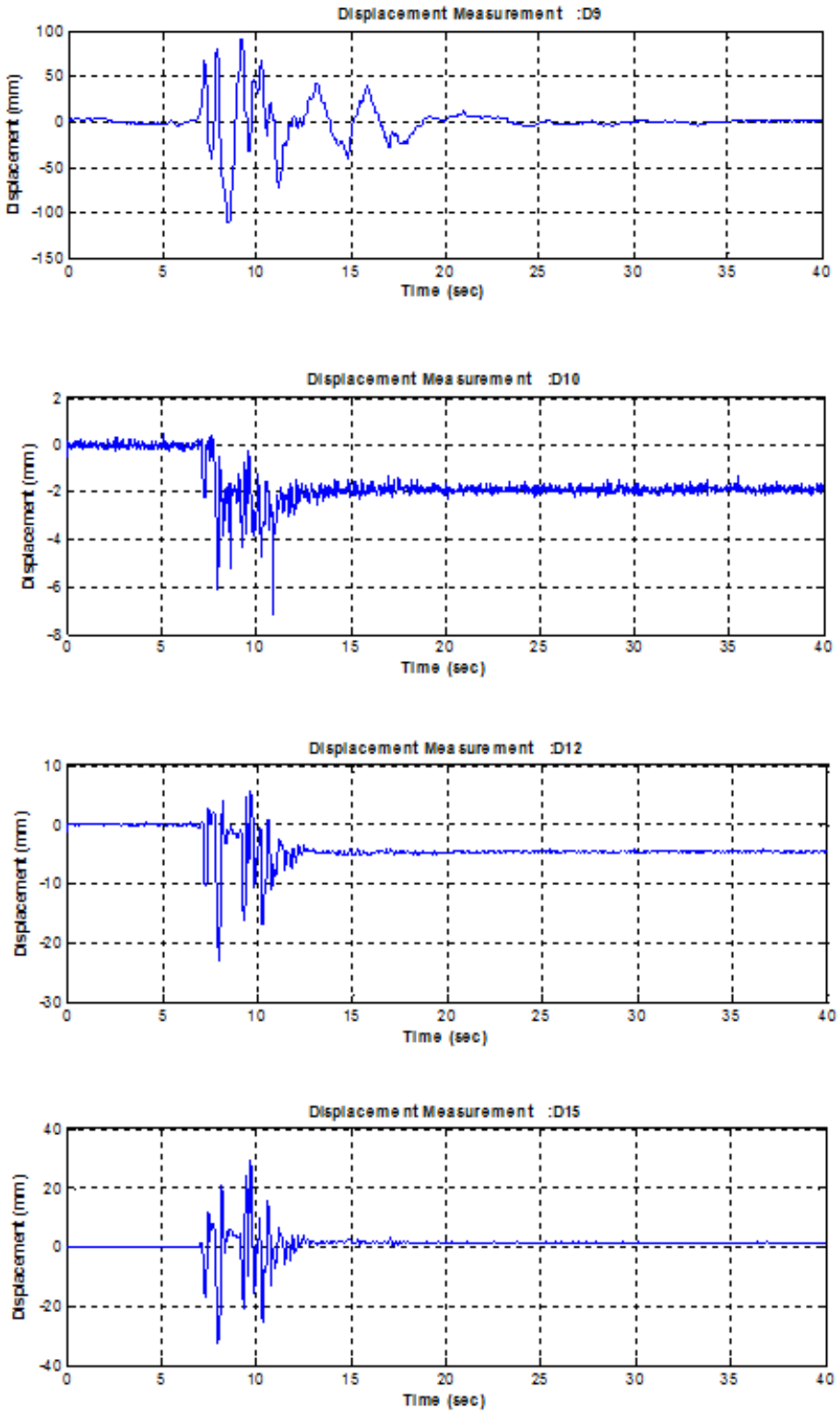

Figure 4.19. Base Input Displacement and Wall Bottom, Mid and Top Relative Displacements Kobe 125% from Setup 2.

Peak relative displacement values and base input excitations in both positive and

negative directions and also residual relative displacement values are given in Table 4.6 to Table 4.9 for all wall configurations. As it was stated previously D9 measured base input displacement, D10 to D16 measured facing displacements where D15 and D16 were located at top blocks. Figure 4.20 to Figure 4.23 illustrate the distribution of positive (inward) and negative (outward) peak relative displacement values that also means the deformation shape of walls during the seismic action. Residual displacement values along the facing for all seismic actions are figured in Figure 4.24 to Figure 4.26.

Table 4.6 reports the relative peak and residual displacements measured on modular blocks of retaining wall of Setup 1 during seismic actions. Applied seismic motion in terms of displacement was recorded by D9 laser displacement transducer on the shaking table. Displacement transducers D15 and D16 were located on the top blocks of the facing. Positive direction means the blocks moved inwards to backfill and blocks moved outwards took negative displacement values. Peak displacement values in both positive and negative directions increased with increasing base excitation amplitudes for all four setups. For El Centro 100% earthquake, it can be seen that the front blocks displaced inwards at most 8.65 mm where they displaced outwards as 1.87 mm at top and related residual displacements were +5.50 mm at the top of the wall. This behavior can be explained with the thought that, medium-dense sand that compacted during excitations became denser and stiffer. This situation resulted with settlements on top and inward movement of modular blocks. This behavior was same for Kobe 50% earthquake but peak and residual displacement values decreased by comparison. Kobe 75% and Kobe 100% earthquakes behaved almost elastically and any deformation was not observed on the facing. Maximum displacements for the top block reached 20.4 mm and -34.6 mm for Kobe 100% whereas maximum residual displacements were measured as -4.15 mm with D14 transducer.

For Setup 2, Table 4.7 represents the measured relative peak and residual displacement values along the front facing. Likewise Setup 1, peak displacement values increased along the wall height from bottom to top for each base excitation. For El Centro 100% 1.64 mm and - 0.53 mm, for Kobe 50% 1.28 mm and -1.40 mm and for Kobe 75% 3.46 mm and - 4.84 mm were the obtained peak displacements at both

directions on the top blocks, no failure indication was observed and the walls behaved elastically with almost zero residual displacements. Peak displacement values for these three earthquakes for Setup 2 with cohesive backfill were less than half of the displacement values obtained for Setup 1 with dry sand backfill. Peak displacement values for Kobe 100% earthquake as 12.69 mm and -13.22 mm for both directions were also less than the Setup 1. For Kobe 125% earthquake peak displacements were measured as 29.13 mm and -32.42 mm at the top blocks and no failure deformation was observed on the facing. At the mid height of the wall a bulging was formed with -4.60 mm residual displacement and at the top blocks residual displacement was 1.60 mm directed inwards during Kobe 125%.

For Setup 3, Table 4.8 represents the measured relative peak and residual displacement values along the front facing. For El Centro 100% 1.30 mm and - 0.78 mm, for Kobe 50% 1.34 mm and -1.49 mm and for Kobe 75% 3.90 mm and - 4.88 mm were the measured peak displacements the top blocks. These displacement values were almost similar with the Setup 2 although the reinforcement lengths were shorter in Setup 3. So this setup had a secondary meaning when it was considered as a verification test for Setup 2. Peak displacement values were measured for Kobe 100% earthquake as 14.99 mm and -14.24 mm and for Kobe 125% earthquake 31.33 mm and -34.35 mm at the top blocks and no failure deformation was observed on the facing. For Kobe 125% earthquake residual displacement at the wall mid height was -4.90 mm and at top blocks was 2.45 mm. Peak and residual displacements were slightly higher than the Setup 2 and this result can be attributed to the reinforcement lengths.

Table 4.9 represents the relative peak and residual displacements measured for Setup 4 during seismic motions. From the table, it can be seen that up to Kobe 100% earthquake the walls behave elastically, peak displacements were insignificant in both directions and no residual displacements took place. For Kobe 100% earthquake the peak displacements at the wall top was 2.22 mm and -2.33 mm which were approximately one sixth of Setup 2 which was the two times scaled version of Setup 4. Also for Setup 2 peak displacements at mid-height (at 1.00 m) corresponding to full height of Setup 4 were 6.35 mm and -9.97 mm; these values were also quite higher than wall

top displacements of Setup 4. Peak displacement values were measured for Kobe 125% earthquake as 4.02 mm and -6.07 mm and for Kobe 150% earthquake 9.47 mm and -18.00 mm at top blocks. For Setup 2 the peak displacements were 29.13 mm and -32.42 mm at top of the wall and 5.76 mm and -23.00 mm at mid-height of the wall during Kobe 125% earthquake, these results were also higher than the scaled version Setup 4. For Kobe 125% and Kobe 150% the outward displacement values were higher than the inward displacement along the full wall height. For Kobe 150% at the elevation of 60 cm peak displacements were recorded as 1.31 mm and -15.30 mm and -10.00 mm residual displacement but again the residual displacements were generated inwards as 1.30 mm. This behavior of residual displacement was consistent with the results of Kobe 125% earthquake of Setup2 and Setup 3.

Table 4.6. Peak and Residual Relative Displacements for Setup 1 During Seismic Actions.

	El Centro 100%			Kobe 50%			Kobe 75%		
Displacement Transducer No	Peak Disp. (+) (mm)	Peak Disp. (-) (mm)	Residual Disp. (mm)	Peak Disp. (+) (mm)	Peak Disp. (-) (mm)	Residual Disp. (mm)	Peak Disp. (+) (mm)	Peak Disp. (-) (mm)	Residual Disp. (mm)
D9	66.46	66.40		37.22	43.80		56.52	65.34	
D10	1.10	-0.27	0.45	0.80	-0.65	0.30	1.06	-1.45	-0.40
D11	1.35	-0.56	0.75	1.07	-0.58	0.40	1.81	-2.56	-0.90
D12	2.38	-0.64	1.20	2.19	-1.21	0.95	2.54	-4.49	-1.10
D13	3.68	-1.14	2.25	2.12	-1.64	1.25	3.59	-5.43	-1.45
D14	5.23	-2.17	4.10	3.04	-3.60	1.80	5.19	-8.13	-0.80
D15	8.37	-1.87	5.30	4.56	-3.11	2.15	8.34	-10.81	0.40
D16	8.65	-1.32	5.50	3.46	-3.21	1.55	8.07	-10.25	0.20

	Kobe 100%		
Displacement Transducer No	Peak Disp. (+) (mm)	Peak Disp. (-) (mm)	Residual Disp. (mm)
D9	75.29	89.57	
D10	0.87	-3.13	-0.80
D11	4.83	-6.62	-1.05
D12	7.90	-10.77	-1.90
D13	7.70	-15.17	-2.40
D14	8.73	-23.05	-4.15
D15	20.40	-34.60	-1.00
D16	17.74	-27.16	-0.70

Table 4.7. Peak and Residual Relative Displacements for Setup 2 During Seismic Actions.

	El Centro 100%			Kobe 50%			Kobe 75%		
Displacement Transducer No	Peak Disp. (+) (mm)	Peak Disp. (-) (mm)	Residual Disp. (mm)	Peak Disp. (+) (mm)	Peak Disp. (-) (mm)	Residual Disp. (mm)	Peak Disp. (+) (mm)	Peak Disp. (-) (mm)	Residual Disp. (mm)
D9	63.44	-65.66		37.41	-44.04		56.80	-65.28	
D10	0.53	-0.57	0.00	0.57	-0.65	-0.05	0.60	-2.35	-0.60
D11	0.91	-0.56	0.00	0.99	-1.01	-0.05	1.44	-3.38	-1.05
D12	0.85	-0.67	0.00	0.74	-1.26	-0.10	1.57	-3.99	-0.95
D13	1.03	-0.80	0.00	1.02	-1.35	-0.01	2.38	-4.01	-0.65
D14	1.46	-0.78	0.00	1.25	-1.55	-0.05	3.09	-4.49	-0.45
D15	1.64	-0.53	0.25	1.28	-1.40	-0.05	3.46	-4.84	-0.30
D16	1.25	-0.74	0.15	1.27	-1.25	0.05	3.37	-4.61	-0.25

	Kobe 100%			Kobe 125%		
Displacement Transducer No	Peak Disp. (+) (mm)	Peak Disp. (-) (mm)	Residual Disp. (mm)	Peak Disp. (+) (mm)	Peak Disp. (-) (mm)	Residual Disp. (mm)
D9	74.72	-88.39		91.99	-110.49	
D10	0.83	-2.57	-0.70	0.49	-7.05	-1.90
D11	1.88	-7.90	-2.45	2.09	-13.19	-4.00
D12	6.35	-9.97	-2.30	5.76	-23.00	-4.60
D13	9.47	-10.88	-0.90	11.40	-25.43	-3.05
D14	11.92	-13.96	0.25	21.80	-31.18	-1.10
D15	12.69	-13.22	0.45	29.13	-32.42	1.60
D16	12.38	-12.18	0.60	27.97	-31.50	1.20

Table 4.8. Peak and Residual Relative Displacements for Setup 3 During Seismic Actions.

	El Centro 100%			Kobe 50%			Kobe 75%		
Displacement Transducer No	Peak Disp. (+) (mm)	Peak Disp. (-) (mm)	Residual Disp. (mm)	Peak Disp. (+) (mm)	Peak Disp. (-) (mm)	Residual Disp. (mm)	Peak Disp. (+) (mm)	Peak Disp. (-) (mm)	Residual Disp. (mm)
D9	63.23	-65.08		37.36	-43.58		56.39	-64.27	
D10	0.85	-0.70	-0.20	0.70	-0.68	-0.10	1.26	-1.08	-0.30
D11	0.65	-0.64	-0.05	0.86	-0.87	0.00	1.59	-3.18	-0.90
D12	0.99	-0.78	-0.15	0.99	-1.20	0.05	1.92	-3.73	-1.10
D13	1.00	-0.92	-0.02	1.26	-1.30	-0.05	2.45	-4.06	-0.70
D14	1.15	-1.01	-0.10	1.08	-1.47	-0.05	3.24	-4.55	-0.40
D15	1.30	-0.78	0.00	1.34	-1.49	-0.10	3.90	-4.88	-0.25
D16	0.99	-0.72	0.00	1.30	-1.36	-0.05	3.49	-4.71	-0.20

	Kobe 100%			Kobe 125%		
Displacement Transducer No	Peak Disp. (+) (mm)	Peak Disp. (-) (mm)	Residual Disp. (mm)	Peak Disp. (+) (mm)	Peak Disp. (-) (mm)	Residual Disp. (mm)
D9	74.99	-89.48		91.55	-110.22	
D10	0.71	-4.14	-0.85	0.87	-4.50	-1.55
D11	2.20	-10.49	-2.60	2.33	-12.03	-3.75
D12	5.09	-11.32	-2.10	6.94	-24.16	-4.90
D13	8.73	-12.12	-1.55	14.05	-27.65	-2.40
D14	12.95	-13.13	0.20	23.64	-32.27	-0.40
D15	14.99	-14.24	0.60	31.33	-34.35	2.45
D16	14.49	-12.00	0.40	29.96	-32.64	2.20

Table 4.9. Peak and Residual Relative Displacements for Setup 4 During Seismic Actions.

	El Centro 100%			Kobe 50%			Kobe 75%		
Displacement Transducer No	Peak Disp. (+) (mm)	Peak Disp. (-) (mm)	Residual Disp. (mm)	Peak Disp . (+) (mm)	Peak Disp. (-) (mm)	Residual Disp. (mm)	Peak Disp. (+) (mm)	Peak Disp. (-) (mm)	Residual Disp. (mm)
D9	25.42	-37.38		18.47	-23.79		27.16	-34.81	
D10	0.62	-0.55	0.05	0.35	-0.66	0.05	0.75	-1.24	-0.15
D11	0.67	-0.55	0.05	0.74	-0.82	0.20	1.15	-1.21	0.00
D12	0.63	-0.39	0.05	0.91	-0.40	0.05	1.24	-0.81	-0.05
D13	0.58	-0.79	0.02	0.97	-0.62	0.05	1.32	-1.20	0.00
D14	0.89	-0.66	0.10	0.93	-0.85	0.00	1.62	-1.40	-0.10
D15	0.71	-0.64	0.00	0.85	-0.67	0.00	1.51	-1.09	0.05
D16	0.96	-0.52	0.05	1.29	-0.67	0.10	1.52	-1.13	-0.05
	El Centro 100%			Kobe 125%			Kobe 150%		
Displacement Transducer No	Peak Disp. (+) (mm)	Peak Disp. (-) (mm)	Residual Disp. (mm)	Peak Disp . (+) (mm)	Peak Disp. (-) (mm)	Residual Disp. (mm)	Peak Disp. (+) (mm)	Peak Disp. (-) (mm)	Residual Disp. (mm)
D9	36.66	-47.46		44.57	-58.10		53.72	-69.65	
D10	1.20	-1.93	-0.05	1.43	-1.54	0.25	0.54	-9.53	-6.70
D11	2.75	-1.95	-0.40	2.10	-4.64	-0.65	1.31	-15.30	-10.00
D12	1.78	-2.27	-0.15	4.49	-5.35	-0.90	3.37	-17.57	-8.80
D13	1.90	-2.95	-0.35	4.56	-5.79	-0.50	4.88	-18.03	-5.30
D14	2.02	-2.86	-0.40	4.99	-6.11	-0.20	7.95	-18.73	-4.05
D15	1.83	-2.48	-0.15	3.25	-5.93	-0.70	8.45	-16.61	1.30
D16	2.22	-2.33	-0.25	4.02	-6.07	-0.45	9.47	-18.00	1.15

Figure 4.20 illustrates the distribution of relative peak displacements through the height of the wall. Negative displacement values on the left hand side refer to outward displacements and the positive displacement values on the right hand side refer to inward displacements. At 190 cm two displacement values which can be seen, correspond to two top block displacements. The linear increase of displacements for outward direction was remarkable for Kobe 100% earthquake as illustrated in graph.

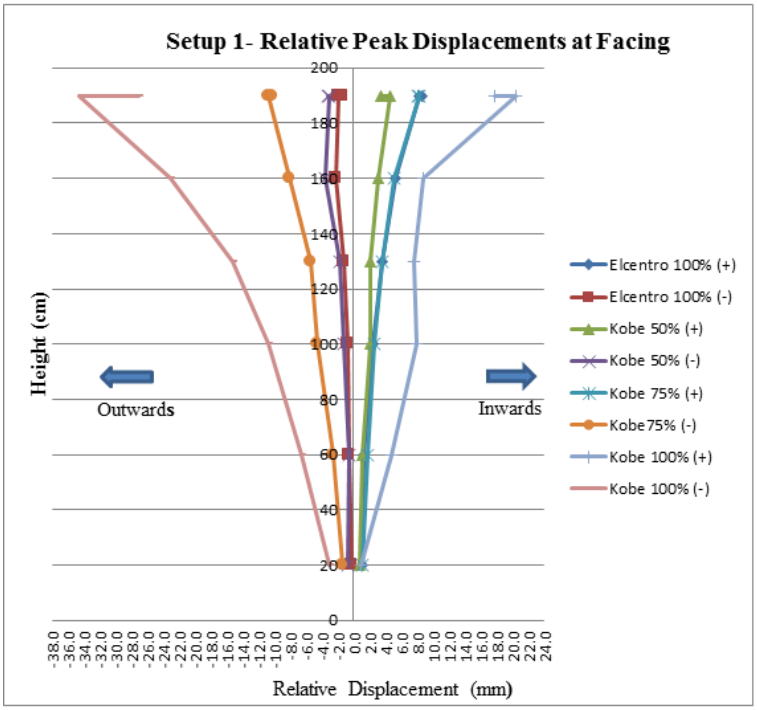

Figure 4.20. Peak Relative Displacements at Facing of Setup 1.

Figure 4.21 illustrates the relative peak displacement values of Setup 2 both for positive and negative directions. As it can be seen from the figure, displacement values for Kobe 100% and Kobe 125% were relatively higher than the previous excitations. For both Kobe 100% and Kobe 125% linear increase of displacements through the wall height started from the bottom of the wall for outward direction where the increase started remarkably from the mid-height of the wall for inward direction.

Figure 4.22 shows the relative peak displacements of Setup 3 on the facing along the wall height. The displacement trends under all seismic actions were quite similar with the Setup 2. Almost elastic behavior of the wall regarding the close peak

displacement values for inward and outward directions appears explicitly in the figure.

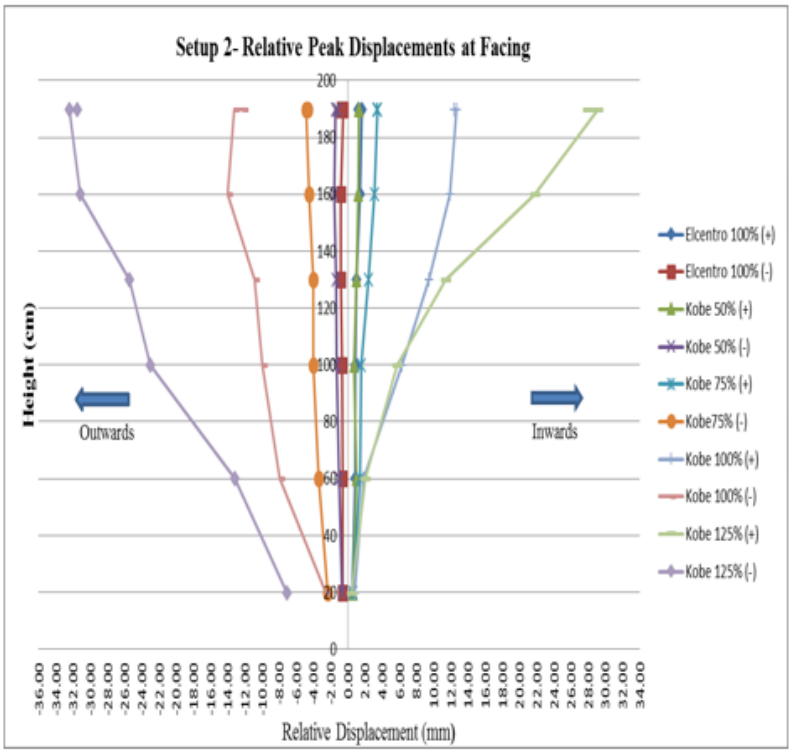

Figure 4.21. Peak Relative Displacements at Facing of Setup 2.

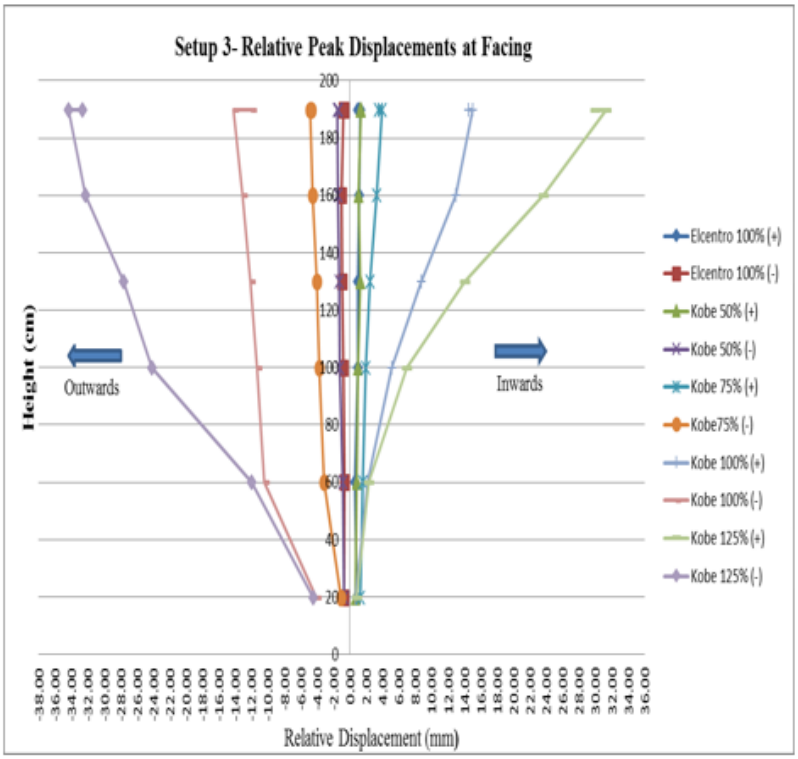

Figure 4.22. Peak Relative Displacements at Facing of Setup 3.

Figure 4.23 illustrates the relative peak displacements at facing of Setup 4 recorded during base excitations. Up to Kobe 100% earthquake measured peak displacement values were insignificant. Kobe 125% and Kobe 150% earthquakes created significant displacement values. As it can be seen from the figure the most outstanding result is the relatively high negative displacement values for Kobe 150% causing a remarkable outward movement of the modular block facing.

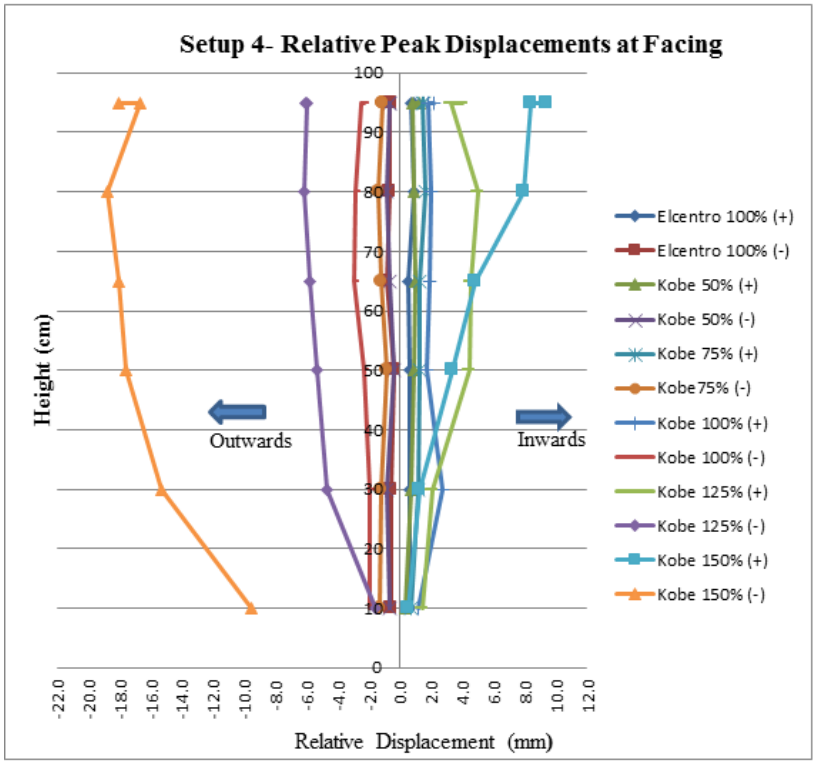

Figure 4.23. Peak Relative Displacements at Facing of Setup 4.

Figure 4.24 illustrates relative peak displacements recorded on the facing block at 160 cm for Setup 1, 2 and 3 during base excitations. Base excitations for El Centro and different amplitudes of Kobe earthquake are given in terms of gravitational acceleration at horizontal axis. It can be seen that outward displacement values were higher than inward values for each base motion. For Setup 1 there was a remarkable decrease compared to other setups for inward displacement value after 0.8g and for outwards direction Setup 1 had always higher relative displacement values than Setup 2 and 3.

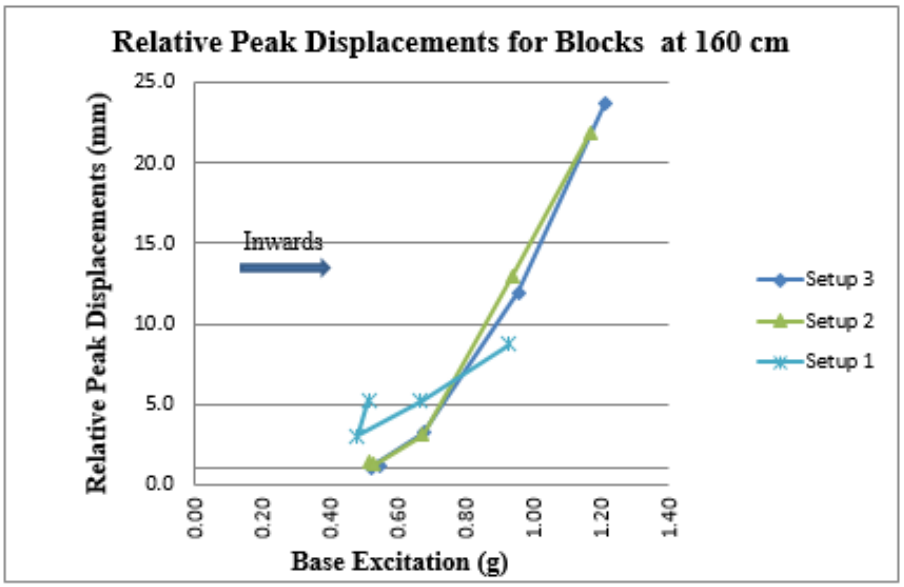

(a)

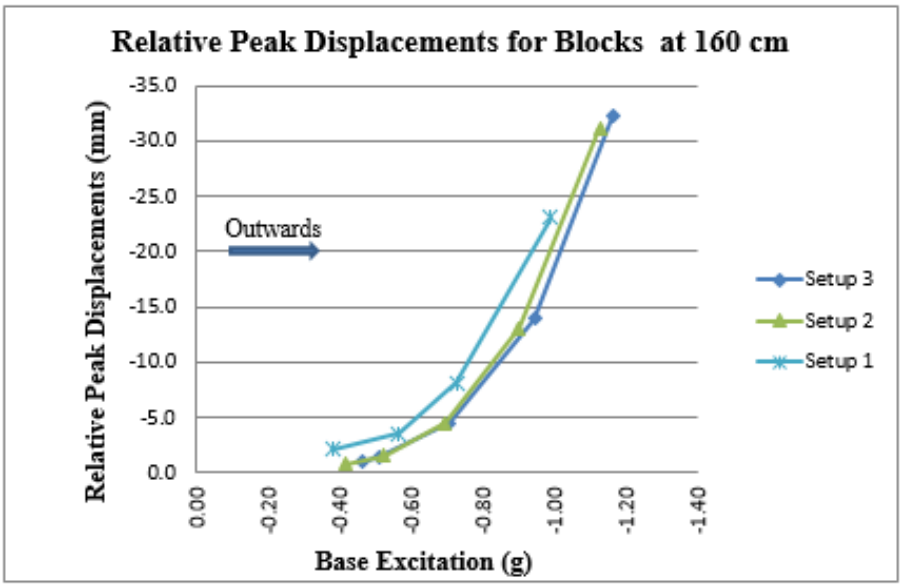

(b)

Figure 4.24. Relative Peak Displacement Values Recorded on the Modular Block at 160 cm (a) Inwards (b) Outwards.

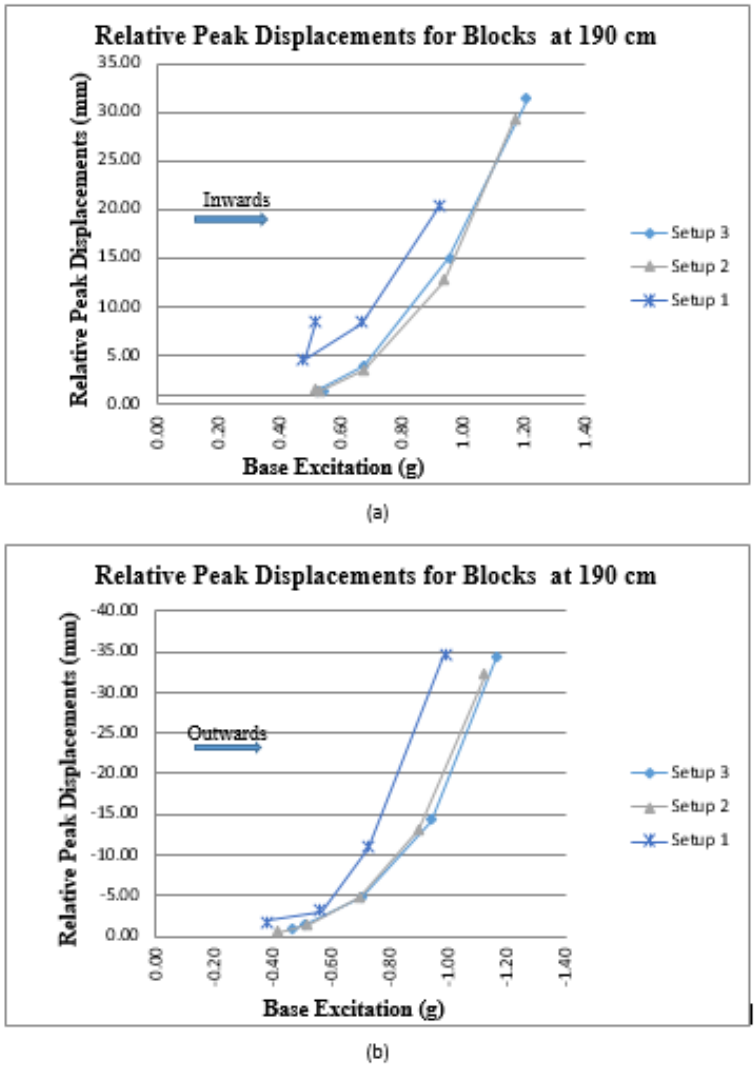

Figure 4.25. Relative Peak Displacement Values Recorded on the Modular Block at 190 cm (a) Inwards (b) Outwards.

In Figure 4.25, relative peak displacement values recorded for the top modular block at 190 cm are illustrated under seismic motions. It can be seen from the figure that both for inward and outward directions Setup 1 had higher relative displacement values during each base excitation. For inward direction Setup 2 and 3 reached and passed 30 mm relative displacement value for base excitation 1.2g (Kobe 125% earthquake). All the setups reached approximately -35 mm peak relative displacement value during Kobe 100% earthquake (0.99g) for Setup 1 and during Kobe 125% (1.15g) earthquake for Setup 2 and 3.

Figure 4.26 shows the relative residual displacement values at the facing of Setup 1 measured under seismic actions. As it can be seen from the figure, residual displacements for El Centro 100% and Kobe 50% were occurred towards inward direction and the displacements for Kobe 75% and Kobe 100% occurred towards outward. For El Centro 100% the increase of the residual displacements was linear along the wall height and reached 6 mm at the top. For Kobe 100% the maximum residual displacement recorded was -4 mm.

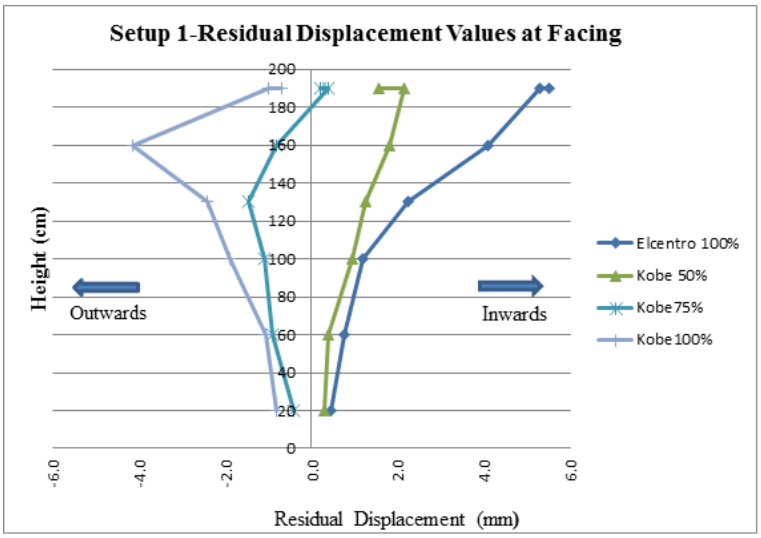

Figure 4.26. Residual Relative Displacements at Facing of Setup 1.

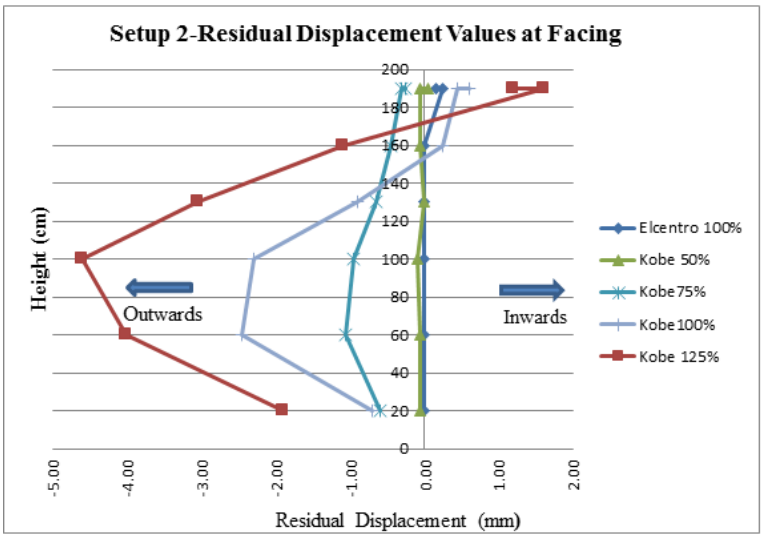

Figure 4.27. Residual Relative Displacements at Facing of Setup 2.

Figure 4.27 shows the relative residual displacements occurred during base excitations at the facing of Setup 2. Kobe 100% and Kobe 125% earthquakes created remarkable outward residual movements. In the figure the bulging behavior occurred at the mid-height of the facing with a displacement value of -4.5 mm for Kobe 125% and the top of the wall made an inwards movement as 1.5 mm.

Figure 4.28 shows the relative residual displacement values at the facing of Setup 3 measured under seismic actions. The residual displacement behavior was quite similar with Setup 2. The bulging behavior of the wall at the mid-height occurred during Kobe 125% earthquake that can be considered as the most remarkable outcome of the graph.

The residual displacements measured at facing of Setup 4 during seismic actions are shown in Figure 4.29. The most outstanding result of the figure is the relatively high negative residual displacement values represented for Kobe 150% earthquake. Significant outward deformation of modular blocks could be regarded as an indication for the beginning of a failure condition at Kobe 150% earthquake.

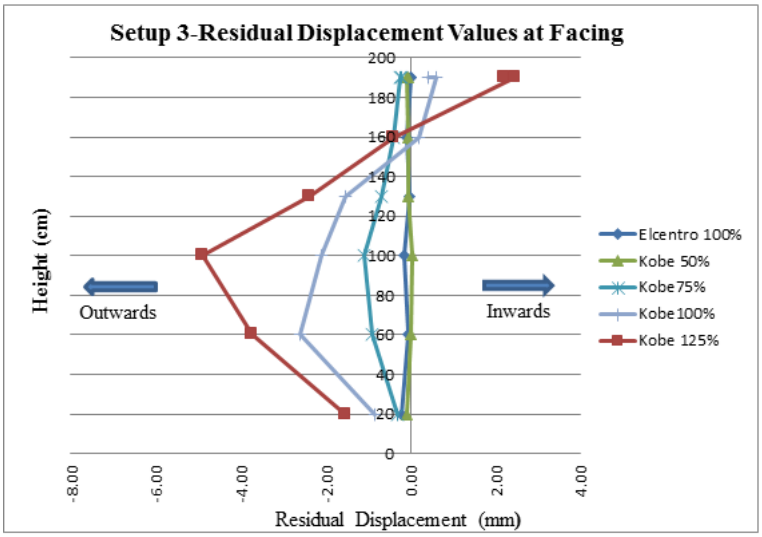

Figure 4.28. Residual Relative Displacements at Facing of Setup 3.

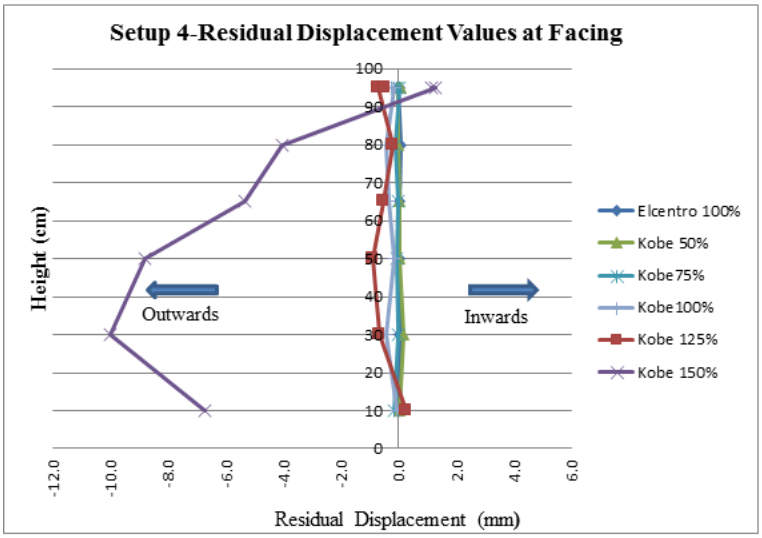

Figure 4.29. Residual Relative Displacements at Facing of Setup 4.

4.3.2. Summary of the Results

According to related tables and figures above, seismic performance of all setups can be evaluated as successful. In the literature, concerning seismic displacements, Wang (2015) determined a 5% displacement to height ratio limit for the seismic deformation permission value of the geogrid reinforced rigid retaining wall. Koseki *et al.*, (1998) and Huang *et al.*, (2011) found out that when slope displacement reached 5% of its height the reinforced slope was undergone a measurable strength deterioration. Ling *et al.*, (2003) reported that the amplitude of lateral displacement exceeding 50 mm was considered as excessive as a conclusion for the seismic performance of reinforced soil. With the help of the steel frame attached to the steel box, relative displacements were measured more precisely and these values of peak relative displacements were smaller than the mentioned limits in the literature.

Considering the distribution of inward and outward movements along the wall height it can be said that the walls behaved almost elastically under all seismic actions, residual displacements were quite smaller comparatively. The largest peak displacements occurred at the top blocks and the distribution almost linearly increased along the wall height for higher base accelerations. No significant residual displacement value

was recorded and no failure of the facing was observed under earthquake motions. All in all, wall facing displacements increased in both directions with increasing base input excitation as expected.

For Setup 1 wall with dry sand backfill, inward movement of the wall was greater than outward movement for the first two seismic actions. This behavior can be explained with the following: the backfill was a medium-dense backfill and duringthe first two seismic loads the sand was compacted, settlement occurred and the wall moved inwards. This condition is also promoted with observed excessive settlement values and the residual displacement behavior of the wall for these two earthquakes. For the third action Kobe 75% the wall seemed to be stiffened, the behavior was almost similar to cohesive backfill counterpart of it as Setup 2 and 3. For the Kobe 100% although potential failure conditions had been started the wall behaved almost elastically where the blocks tended to move to the outwards direction and had larger displacement values than inwards direction. Residual displacements were smaller compared to the peak displacements and the top blocks' residual and peak displacements tended to turn inwards. This behavior can be related with the significantly high acceleration values measured for inward direction at top. The most important outcome is that; peak relative displacements in both directions were bigger than the corresponding displacement values of the walls with cohesive backfill under same base input displacements.

For Setup 2 and Setup 3 it can be said that any significant effect of reinforcement length was not observed. Behaviors of the walls for peak and residual displacements were almost identical but shorter reinforcement length of Setup3 led to a little bit more front wall deformations. Up to Kobe 100% (0.94g) earthquake, the distribution of peak displacements was constant. After this value, the values increased linearly along the wall height and they seemed as elastic; although the outward displacements were a little bit higher, walls moved as same amounts in both directions and residual displacements were quite smaller compared to peak displacements. General displacement behavior character of the model walls can be summarized as following. The outward movement tends to increase gradually along the wall height but the inwards movement reached its peak values at the top of the wall. Then, positive values became smaller at the

bottom and mid heights where they become equal with negative direction at top. So, relative displacement gap between these opposite directions was closed at the top. This behavior is consistent with the fact that related acceleration amplification values for the positive direction increased significantly higher than negative direction. This displacement generation may be related with wall inclination. However, this situation also affected the residual displacement values with the same tendency. Although the residual displacement values were small compared to peak displacement values (30-35 mm) residual displacement (4-5 mm, they were smaller than the 20% of the peak values at most) configuration along the wall height is a key parameter for the potential failure type.

As a result of this mentioned peak displacement behavior, the residual displacement of the top blocks were inwards and the maximum residual values were observed at the mid of the wall. This swelling behavior at the mid of the discrete facing was also observed in the study of Huang (2000) and in that study this convex shape deformation of the facing (bulging) ended up with a concave settlement profile. The maximum values measured almost after the reinforced zone which can be related with the cracks developed in the beginning of unreinforced zone in this study. To conclude, this residual deformation behavior can be related with the potential failure mechanism occurred in the reinforced zone (internal) which led to a bulging (swelling) shape in the mid of the wall.

For Setup 4 which was the half scaled identical of Setup2, it was observed that up to Kobe 125% earthquake any significant peak displacements were not developed in both directions. But during the Kobe 150% earthquake there was a great movement in the outward direction. Negative peak displacement values were measured as three times of Kobe 125% displacement values (while the displacements in positive directions are 1.2 times of that earthquake). This peak displacement occurred during Kobe 150% earthquake, also resulted with a deep and wide tension crack formed at the end of reinforced zone. Also 10 mm residual displacement was measured for outward direction where the peak negative displacement was 18.7 mm which was the greatest residual/peak displacement ratio among the walls. Formation of the residual

displacement resembled the behavior of Setup2 and Setup3 with a bulging shape at the middle. Residual displacements of the top blocks were inwards for Kobe 150% and as a note almost no residual displacement was recorded up to Kobe 150%. In the study of Güler and Selek (2014), ½ scaled and ¼ scaled models of the prototype were tested and when the displacement results of the model walls with sand backfill were enhanced to the prototype (displacement values were multiplied by two and four respectively) it was found out that the ¼ scaled values resulted in higher displacement values than the ½ scaled models. According to this outcome scaled models were said to be on the safe side. But this study is in contradiction with the results of that previous study. As an example, for 125% earthquake, peak displacement values were five times smaller for outward direction and 6-7 times smaller for inwards. This means that when the displacement results were enlarged considering prototype, still the ¼ scaled model wall would create lower displacement values. This result makes scaled models unreliable because they were acting more rigid than expected and this situation is an outcome of the cohesive characteristic of the backfill.

4.4. Reinforcement Stress Results

In this chapter, strain measurements from four wall configurations, calculated tensile stresses and potential failure plane locations predicted from these values are investigated. First of all a calibration study is reported to compare the strain results recorded in the strain gauges and actual strains on geogrid reinforcements. Then the strain results after construction period and during seismic actions are presented. The peak tensile stress results and their distribution along the reinforcement are investigated to find out whether the reinforcement design is sufficient. And this distribution indicates the location of potential failure surface running through an active zone and a resistant (backfill) zone. As it was illustrated before, three of reinforcement layers could be monitorized with strain gages. Gages were not located with equal spaces along the geogrid, alternatively a group of gages were placed close to each other near the front wall on the bottom geogrid layer where they were grouped at the end of reinforcement on the top reinforcement. This configuration was preferred to detect the peak tensile strain more precisely with the idea argued in the study of Başbuğ (2011)

and points were selected according to theory of Rankine failure conditions. The details of configuration generated according to that idea was illustrated in Section 3.4., Figure 4.30 to Figure 4.32.

4.4.1. Calibration Study

The method for placement of strain gauges and how they bonded to geogrids are reported in Section 3.3 in details. Using silicone for strain gauge attachment performed well in the study of Ling *et al.*, (2005) where the calibration results of PET geogrid with silicone and epoxy adhesives, were reported. A calibration study also made to observe whether the strain gauges attached to the geogrid can give similar strain results with the strain graph given by the manufacturer. Fortex GG 40x40 geogrid's load-strain graph was previously reported but for that study which mobilized smaller strains during seismic action, a more detailed (up to 1.5%) strain-load graph was illustrated in Figure 4.30. In that figure, it can be seen 4 geogrid samples used during tensile stress strain standard tests. Average elasticity modulus obtained from this graph upto 1% strain is 570 kN/m.

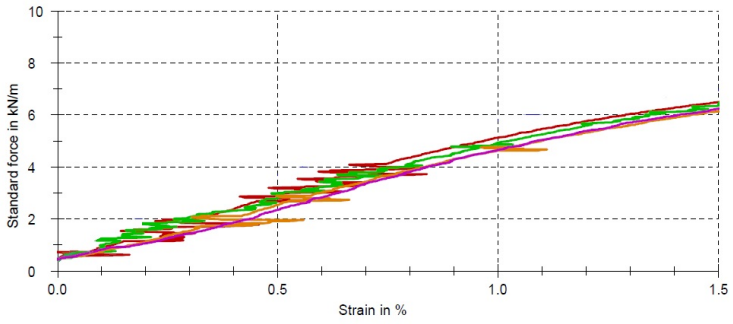

Figure 4.30. Tensile Strain vs. Tensile Load Graph for Fortex GG-40x40 up to 1.5% Strain (Istanbul Teknik Engineering and Industry Co.).

Setup for calibration experiments was established with reference to ASTM D4595, two strain gauges were attached to the center line strand of a 25 cm wide by 50 cm long geogrid. Test setup is shown in Figure 4.31 and Figure 4.32 sketches the test arrangement more detailed. Two hard wood clamps which had metal plate outside

covers were used to clamp the geogrid sample from bottom and top. The dimensions of the clamps were 40x60x300 mm and they were tightened using three bolts. Three bolts and sandpaper between wood and geogrid surfaces were used to distribute tensile loads uniformly along the width of the specimen. A hook with a weight plate was attached to bottom clamp which was stiff, tightened and acted as a rigid beam. Tension force was applied to specimen by this weight plate, 10 kg weights were placed as uniform loading and strain readings were recorded at every loading step, up to 120 kg. The maximum weight for 25 cm width specimen was calculated as 4.8 kN/m tensile load when scaling law was applied.

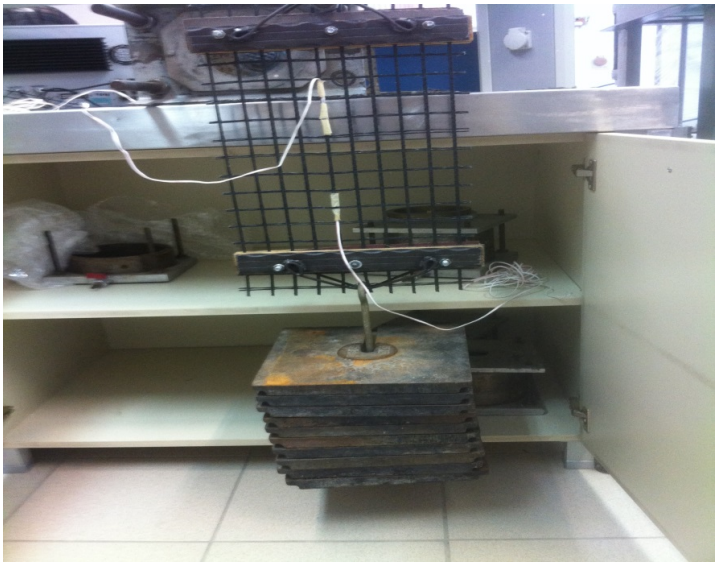

Figure 4.31. View of the Strain Calibration Test Setup.

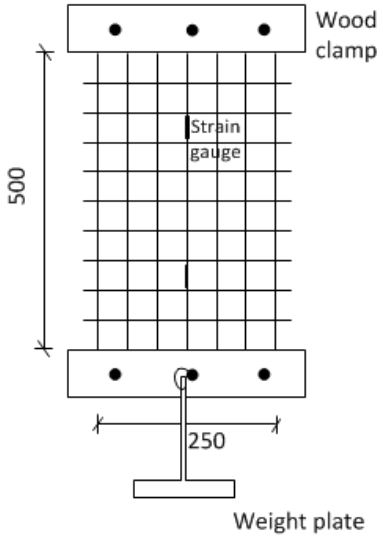

Figure 4.32. Front View Sketch of the Strain Calibration Test Setup.

Results can be seen in Figure 4.33, two strain gauges records are similar to each other (smaller than %1 difference). For clearance of graph time axis of second gauges is shifted 50 seconds but the measurements were recorded simultaneously. As a result, it can be mentioned that strain gages on geogrids gave similar strain results with the standard force vs. strain data in Figure 4.30. For example, strain values measured for strain gauge 1 for 4.8 kN/m are 0.98 %, strain gauge 2 % 0.97 and original geogrid is 1%. Strain values measured for strain gauge 1 for 4.1 kN/m are 0.79 %, for strain gauge 2 is % 0.78 and original geogrid is 0.8%.

As an important note; during this study note negative (-) strain values stand for tension, where positive (+) values mean compression.

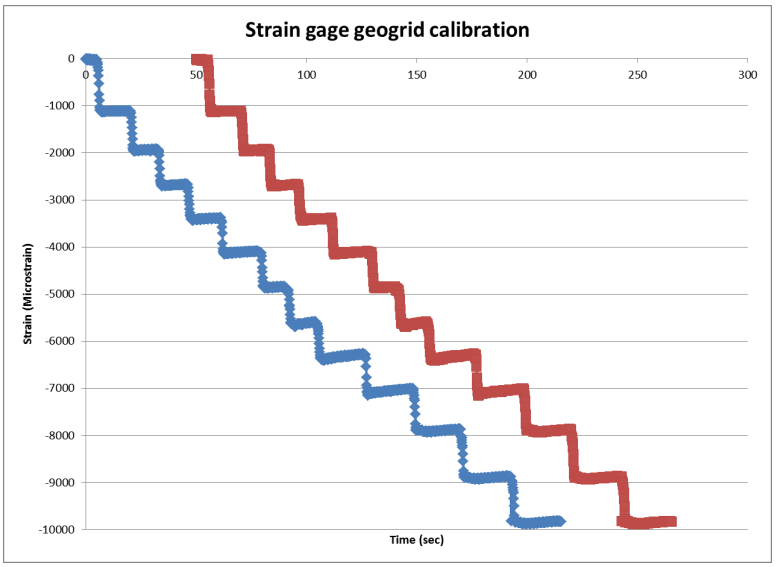

Figure 4.33. Strain Records for Two Gauges for Gauge Calibration Study.

4.4.2. Construction Phase Results

Before recording test results for seismic action, permanent strain values developed on geogrid layers during construction phase were noted down for each setup. These strain values or in other words, tensile stresses were resulted from vertical earth pressure. Stress values calculated from the strain data at the end of construction are the tensile load carried by the reinforcement layers which is the part of the horizontal earth force exerted against facing blocks. Strain values in tension recorded at the end of the

construction phase are given in Table 4.10, as a note for Setup 1 strain gauge 2 and 8 became unserviceable during construction activity.

Table 4.10. Strain Measurements (μs) at the End of Construction Phase.

		Tensile Strains (μs)			
	Strain Gauge No	SETUP1	SETUP2	SETUP3	SETUP4
Top Geogrid	S1	-427	-986	-1332	-411
	S2	0	-1274	-1615	-297
	S3	-1512	-2369	-2256	-877
	S4	-2130	-2062	-2319	-902
	S5	-2031	-1516	-2114	-637
Mid Geogrid	S6	-1652	-1621	-1883	-713
	S7	-2812	-2785	-2056	-822
	S8	0	-2976	-3087	-1237
	S9	-3364	-3412	-3214	-1488
	S10	-3133	-3112	-3817	-1904
Bottom Geogrid	S11	-1209	-1634	-1478	-1113
	S12	-2066	-3660	-3121	-1365
	S13	-2470	-2807	-4121	-912
	S14	-3773	-4141	-4331	-2012
	S15	-3570	-4044	-4180	-2282

As can be seen from the table above, strain values obtained from the model walls were below 1%. Maximum strain values were recorded as 0.4% for Wall 2 and Wall 3. In the study of Bathurst (2002) it was reported that reliable strain levels for the end of construction were determined below 1%.

For all wall configurations top geogrid layer had the lowest strain peak values. Mean values of strains were higher at the middle layer where peak strain values were observed on the bottom reinforcement. The bottom layer had the peak strain values close to the wall facing where the peak values were located on the middle parts of the middle and top geogrid layers. A potential failure surface of internal stability for static case can be drawn by joining the location of peak strain points of the geogrid layers

and the obtained line is consistent with Rankine failure surface. Especially for bottom layer relatively high strains just behind the modular block facing can be attributed to the relative downward movement of the soil behind the facing. In conclusion, mean values and distribution of strain data and related tensile loads acted by reinforcements are key parameters for internal stability design of such wall systems.

For the magnitude of strains, higher values were recorded for Setup 3 with shorter reinforcement length compared to Setup 2, also for bottom and middle layers, peak strain values were a little bit uniformly distributed then the Setup 2. Strains mobilized on the reinforcements of Setup 1 indicated lower values (around %30) than the walls with cohesive backfill this may be attributed to the difference of vertical earth pressures. It is consistent with the situation that, the unit weight of dry sand is 25% lower than cohesive backfill at its optimum moisture content. Peak strain values of Setup 4 were one third of the Setup 2 although it was the half scaled version of Setup 2.

4.4.3. Test Results

Strain test results include the peak and strain values which are listed in Table 4.11 to Table 4.15. Each of four wall configurations were performed with different base excitations and their strain time history plots are given in Appendix C.

Data acquisition system used to collect strain data was activated with a capacity of 200 Hz. same as acceleration and displacement data acquisition system. So displacement time-history and the strain time history plots coincided perfectly. In Figure 4.34 to Figure 4.36, the similarity between front wall displacements and the strain values on the geogrid at the same height can be observed for Setup2, Kobe 125% earthquake. The displacement time history obtained from D15 transducer was comparable in terms of peak displacement and residual displacement values with its corresponding strain values for S5 which was the closest strain gage to the front face at top geogrid reinforcement (Figure 4.34). A similar story can be mentioned for D12 displacement transducer which was at the middle height of the wall and S10 on the mid geogrid layer closest to the wall but tensile residual strain was developed on that gauge where an outward

residual displacement was observed (Figure 4.36). For the bottom geogrid layer three consecutive gauges S15, S14, S13 time history graphs were shown. S15 was the closest gauge to block and also to the toe; highest compressive peak strain was recorded on that region and also a compressive residual strain was observed. S14 had the highest peak tensile strain value and it was the locus point of the potential failure plane on the bottom geogrid. Strain time history of S13 with a tensile residual strain is also illustrated because it presents the most similar behavior with the related displacement history recorded with D10 (Figure 4.35).

As it was stated above during the base excitations compressive strains also occurred on the geogrids additively to the tensile strains and the peak values for both of these strains were highlighted in Table 4.11 to Table 4.15. But only the maximum tensile loads generated on the geogrids were taken into account. Peak tension and compression strain values according to their locations on the bottom, mid or top geogrids are represented in Figure 4.37 to Figure 4.40 for each wall configuration under different base excitations. Residual strain values recorded with these strain gauges are also illustrated in Figure 4.41 to Figure 4.44 and they ended up with compression or tension.

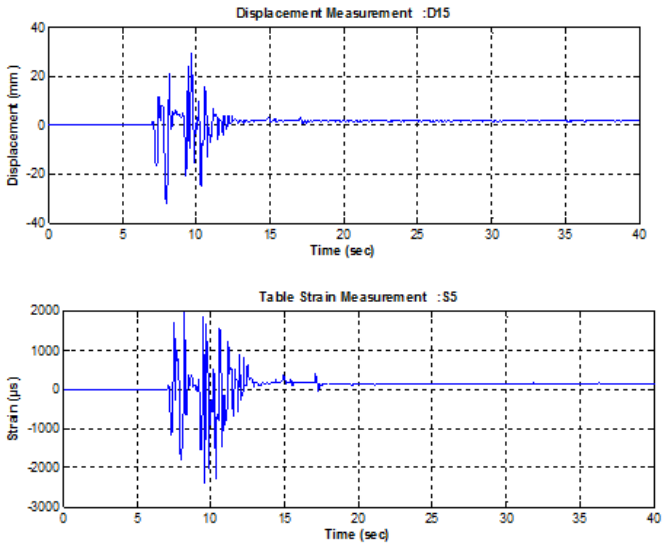

Figure 4.34. Strain and Displacement Time History Results for Top Geogrid Setup 2, Kobe 125% Earthquake.

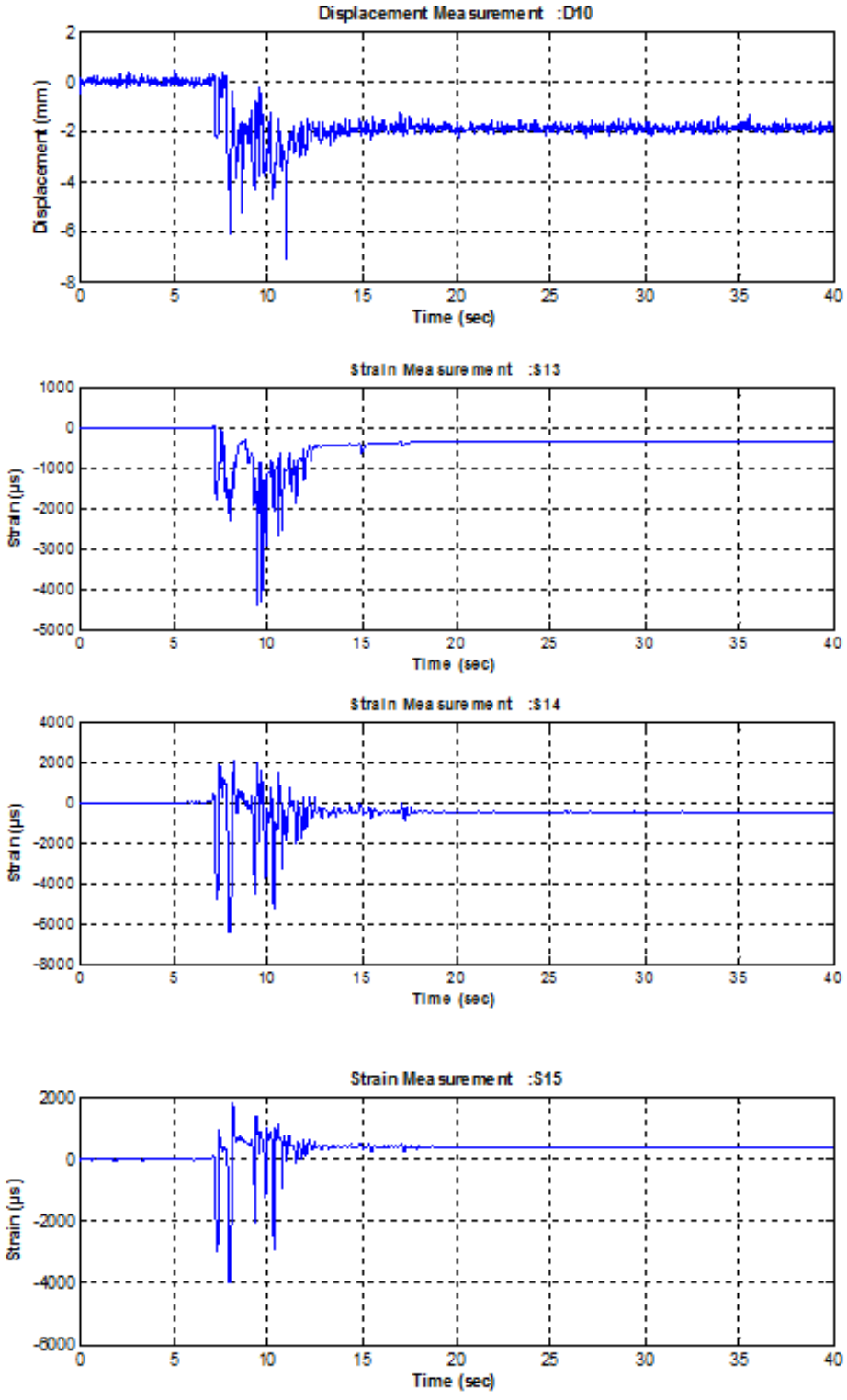

Figure 4.35. Strain and Displacement Time History Results for Bottom Geogrid Setup 2, Kobe 125% Earthquake.

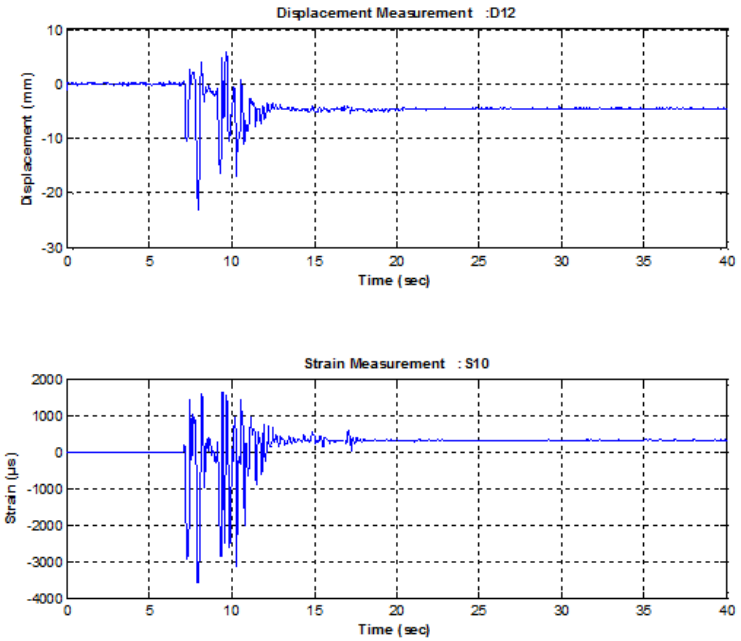

Figure 4.36. Strain and Displacement Time History Results for Mid Geogrid Setup 2, Kobe 125% Earthquake.

In Table 4.11, peak tension and compression strains generated on the reinforcements during the seismic actions and the residual strain values obtained at the end of excitations were reported for Setup 1. Negative values mean tension and positive values mean compression and the strain values are given in micro strains as 10000 μs equals to 1% strain of reinforcement; in all of the following tables. Strain gages S2 and S8 were damaged during construction period so strain data could not be recorded for these gages. For El Centro 100% and Kobe 50% compression strain values were higher that the tension strain values and the difference between the top and bottom reinforcements were negligible, this behavior was consistent with the inwards residual movement of the front facing. Strain values for both compression and tension were increased with increasing amplitude of base excitation likewise the increasing facing displacements. For Kobe 75% highest tension and compression strain values were recorded as -2422 μs and 1543 μs respectively on the mid geogrid. For Kobe 100% earthquake, maximum tension and compression strain values were recorded as -5214 μs and 1879 μs respectively at the bottom geogrid; maximum tensile strains recorded on the mid and top geogrids were -3251 μs and -2091 μs respectively and these values were considerably

lower than the bottom geogrid. Maximum residual strains were -650 μs recorded on the second closest gage (S14) to the facing on the bottom geogrid. Maximum compression residual strain was 710 μs measured on the gage closest to the facing (S15) on the bottom geogrid indicating a compression zone behind the toe.

Table 4.12 includes the peak compression and tension strain values and residual strain values developed on the top, mid and bottom geogrids of Setup 2. For El Centro 100% and Kobe 50% earthquakes insignificant strain values were obtained. For Kobe 75% earthquake, maximum strain values were recorded as -1001 μs and 684 μs on the bottom geogrid. After Kobe 75% earthquake it can be realized that the compression strains were half of the tension strains. Compression strain values reduced one third of the tension strain values on the bottom geogrids for Kobe 125%. On the top geogrids this difference between the compression and tension strain values were closed, for Kobe 100% earthquake compression strain values became equal and slightly higher than the tensile strain values.

Also in Table 4.12 it can be seen that; for Kobe 100%, 1378 μs and -3502 μs were the maximum measured strain values on the bottom geogrid and it can be seen that they are significantly lower than the results of the Setup 1 at the same seismic motion. It was mentioned that the cohesive backfill performed better than the dry backfill according to the peak displacement values measured as 20.40 mm and -34.60 mm for Setup 1 and 12.69 mm and -13.22 mm for Setup 2. But with this incomparable displacement results a conclusion could not be drawn for the performance geogrids working with cohesive backfill. Because lower displacements and consecutively lower strains were measured. The cause of this situation was probably the cohesive characteristic of the soil although the shear strength values obtained from triaxial tests were not so much different under these vertical stresses. For Kobe 125% earthquake, 2125 μs and -6436 μs, were the maximum measured strain values on the bottom geogrid. The peak displacement values during Kobe 125% earthquake for Setup 2 were 0.49 mm and -7.05 mm, 5.76 mm and -23.00 mm, 29.13 mm and -32.42 mm for bottom, mid and top blocks respectively. These displacement values are more comparable with the results of the Setup 1 for Kobe 100% earthquake measured as 0.87 and -3.13 mm, 7.90 mm

and -10.77 mm, 20.40 mm and -34.60 mm for bottom, mid and top blocks respectively. These displacement values were getting closer after the mid height of the wall and almost same at the wall top. For Setup 2 during Kobe 125% motion, -2373 μs, -3585 μs and -6436 μs were the recorded maximum tensile strain values for top, mid and bottom geogrids respectively. For Setup 1 during Kobe 100% earthquake, -2091 μs, -3951 μs and -5214 μs were the recorded maximum tensile strain values for top, mid and bottom geogrids respectively. It is obvious that especially for top of the wall, Setup 2 had almost equal and even slightly higher tensile loads on the reinforcements than Setup 1 for these closer displacement values. And this result would be an evidence for the fact that geogrids can perform with cohesive backfills as well as granular backfills.

Table 4.13 reports the peak compression and tension strain values and residual strain values measured on the top, mid and bottom geogrids of Setup 3. Compressive and tensile strain values on the geogrids were almost same with the Setup 2, and likewise the highest strains generated on bottom geogrids and lowest were generated on top geogrids. The ratio of difference between compressive and tensile strain values for top, mid and bottom geogrids were similar with Setup 2. For Kobe 100% earthquake, 1259 μs and -3391 μs and for Kobe 125% earthquake, 2564 μss and -6953 μs were the maximum measured strain values on the bottom geogrid. These strain values were slight higher than Setup 2 consistent with the difference of relative displacement values between these two setups. The maximum compressive strain recorded was 275 μs and the maximum strain recorded was -640 μs on the bottom geogrid during Kobe 125% earthquake, these values were approximately one tenth of the corresponding peak compression and tension strain values.

In Table 4.14, peak tension and compression, residual strain values measured on the reinforcements during the seismic excitation were reported for Setup 4. Up to Kobe 125% earthquake, generated strain results were insignificant; the maximum strain value recorded was 0.6% for Kobe 100% earthquake. For Kobe 125% earthquake maximum strain values were measured as 959 μs on mid geogrid and -1315 μs on bottom geogrid. Compression strain values were half of the tension strain values on bottom geogrid but they were equal to or higher than tension strain values on top geogrids. For Kobe

150% earthquake maximum strain values were measured as 2805 μs on top geogrid and -3222 μs on mid geogrid. For Kobe 150% compression strain values were highest on mid geogrids and they were almost equal for top and bottom geogrids. This result was completely indifferent with the previous test setups but consistent with the shape of the remarkable outward movement of the facing at this motion. At Kobe 150% earthquake, maximum compressive strain value recorded as 430 μs on bottom geogrid and this value was one fourth of the peak strain. And maximum tensile strain value recorded as -340 μs on bottom geogrid and this value was one tenth of the corresponding peak tensile strain. For Kobe 125% and Kobe 100%, recorded tensile strain values were approximately one fourth and third of the related results of Setup 2. This outcome was compatible with the ratios of peak displacement values of Setup 2 and Setup 4 which was almost one sixth.

Table 4.11. Peak Tension, Compression and Residual Strain Values for Setup 1 During Seismic Actions.

	Strain Gauge No →	S1	S2	S3	S4	S5	S6	S7	S8	S9	S10	S11	S12	S13	S14	S15
El Centro 100%	Compression Strain (μs)	386	0	327	62	199	222	252	0	401	277	33	237	234	99	346
	Tension Strain (μs)	-38	0	-90	-94	-3	-91	-217	0	-246	-167	-126	-74	-91	-177	-129
	Residual Strain (μs)	125	0	5	-30	115	-5	-95	0	-70	-40	-60	-60	220	-90	-50
Kobe 50%	Compression Strain (μs)	204	0	336	64	412	178	402	0	715	767	85	339	643	870	780
	Tension Strain (μs)	-180	0	-274	-147	-227	-308	-324	0	-513	-635	-186	-249	-462	-580	-415
	Residual Strain (μs)	-35	0	-60	-70	70	15	-60	0	-30	125	-65	-100	-60	140	350
Kobe 75%	Compression Strain (μs)	233	0	782	1022	823	109	467	0	1223	1543	381	425	613	1056	1405
	Tension Strain (μs)	-423	0	-1233	-819	-657	-564	-1053	0	-2422	-1917	-662	-720	-1356	-1858	-2122
	Residual Strain (μs)	-70	0	-255	-190	-105	-180	-290	0	-40	275	-345	-150	-370	-220	340
Kobe 100%	Compression Strain (μs)	365	0	794	1167	906	335	923	0	1348	1092	383	992	701	1879	1618
	Tension Strain (μs)	-1137	0	-1556	-2091	-1460	-951	-3951	0	-3112	-2325	-1064	-2522	-3917	-5214	-4440
	Residual Strain (μs)	-220	0	-300	-230	-140	-290	-440	0	-115	-420	-640	-345	-270	-650	710

Table 4.12. Peak Tension, Compression and Residual Strain Values for Setup 2 During Seismic Actions.

	Strain Gauge No →	S1	S2	S3	S4	S5	S6	S7	S8	S9	S10	S11	S12	S13	S14	S15
El Centro 100%	Compression Strain (μs)	88	40	30	38	174	89	130	95	162	131	20	40	3	161	121
	Tension Strain (μs)	-21	-39	-30	-51	-90	-39	-118	-78	-144	-111	-41	-60	-398	-121	-90
	Residual Strain (μs)	-5	-20	-20	0	20	-5	-35	-20	-50	10	0	-20	-10	-50	-15
Kobe 50%	Compression Strain (μs)	53	64	68	94	128	51	89	70	103	114	81	110	2	159	88
	Tension Strain (μs)	-58	-80	-66	-85	-135	-81	-158	-108	-126	-207	-103	-115	-271	-232	-159
	Residual Strain (μs)	10	-40	-35	-25	-20	-5	-10	-40	-10	-45	-25	-45	-5	-125	-25
Kobe 75%	Compression Strain (μs)	48	127	37	235	427	162	205	335	249	441	113	463	3	684	504
	Tension Strain (μs)	-112	-193	-203	-335	-496	-213	-327	-523	-411	-704	-310	-641	-1011	-837	-589
	Residual Strain (μs)	-15	-45	-115	-60	-55	-20	-80	-105	-50	-80	-45	-75	-210	-165	110
Kobe 100%	Compression Strain (μs)	123	1129	274	1066	1410	922	899	777	1047	1201	261	858	17	1378	1262
	Tension Strain (μs)	-550	-1109	-811	-920	-1352	-884	-1720	-1296	-1466	-2107	-1017	-1815	-2425	-3502	-2764
	Residual Strain (μs)	-45	-115	-135	70	105	-20	-175	-180	-35	50	130	-50	-260	-345	260
Kobe 125%	Compression Strain (μs)	580	1755	686	2055	2016	966	1092	1195	1384	1640	319	1238	28	2125	1803
	Tension Strain (μs)	-618	-1968	-1594	-1814	-2373	-1210	-1683	-2578	-3085	-3585	-1279	-2085	-4406	-6436	-4021
	Residual Strain (μs)	-55	-210	150	265	175	-65	-190	-280	65	325	-160	-90	-330	-460	365

Table 4.13. Peak Tension, Compression And Residual Strain Values For Setup 3 During Seismic Actions.

	Strain Gauge No →	S1	S2	S3	S4	S5	S6	S7	S8	S9	S10	S11	S12	S13	S14	S15
El Centro 100%	Compression Strain (μs)	26	49	77	138	134	35	34	98	58	140	48	71	73	150	24
	Tension Strain (μs)	-30	-46	-91	-107	-121	-23	-56	-139	-39	-130	-39	-60	-100	-122	-160
	Residual Strain (μs)	-10	-10	0	-35	25	-10	-5	-35	10	-25	-20	-20	-25	-70	-125
Kobe 50%	Compression Strain (μs)	80	81	107	161	129	50	48	121	127	167	17	92	45	179	157
	Tension Strain (μs)	-65	-85	-86	-172	-144	-135	-111	-154	-171	-204	-115	-176	-115	-288	-236
	Residual Strain (μs)	-10	-5	-45	-20	5	-70	-65	-80	-30	-100	-25	-60	-40	-140	-45
Kobe 75%	Compression Strain (μs)	59	174	131	273	466	171	228	302	350	425	18	368	132	361	522
	Tension Strain (μs)	-102	-337	-230	-504	-469	-275	-431	-548	-466	-649	-456	-646	-665	-1156	-730
	Residual Strain (μs)	-10	-90	-55	35	80	-85	-150	-115	-65	-95	-210	-185	-160	-220	105
Kobe 100%	Compression Strain (μs)	410	979	1089	1426	1843	1136	836	1061	1118	1909	43	1263	967	1259	1301
	Tension Strain (μs)	-244	-1077	-874	-1236	-1542	-945	-1427	-1515	-2245	-3431	-1207	-3136	-1946	-3391	-3804
	Residual Strain (μs)	-20	-130	65	140	175	-55	-215	-190	-260	-170	-510	-420	-290	-330	135
Kobe 125%	Compression Strain (μs)	377	1652	1607	2193	2427	1249	1295	1476	1574	1815	205	1354	1255	2564	2290
	Tension Strain (μs)	-315	-1814	-1588	-1901	-2670	-1305	-2500	-3120	-2166	-3434	-1226	-4436	-2722	-6953	-5058
	Residual Strain (μs)	-10	-170	-65	40	205	-20	-265	-180	40	150	-290	-410	-290	-640	275

Table 4.14. Peak Tension, Compression and Residual Strain Values for Setup 4 During Seismic Actions.

	Strain Gauge No →	S1	S2	S3	S4	S5	S6	S7	S8	S9	S10	S11	S12	S13	S14	S15
El Centro 100%	Compression Strain (μs)	27	49	83	121	148	90	72	51	77	108	18	60	68	111	134
	Tension Strain (μs)	-13	-66	-48	-88	-72	-71	-50	-57	-61	-122	-32	-109	-55	-148	-101
	Residual Strain (μs)	-5	-5	-15	-40	10	5	-10	-15	25	15	0	-30	-15	20	50
Kobe 50%	Compression Strain (μs)	28	71	110	78	134	102	56	78	66	136	38	69	67	106	94
	Tension Strain (μs)	-26	-60	-44	-40	-75	-90	-77	-60	-48	-123	-60	-63	-100	-115	-80
	Residual Strain (μs)	2	-5	-30	-20	-5	4	-5	2	2	4	-10	-15	-20	-45	-5
Kobe 75%	Compression Strain (μs)	81	133	102	174	241	96	150	119	198	248	70	119	169	138	194
	Tension Strain (μs)	-46	-108	-94	-131	-169	-159	-110	-180	-154	-222	-124	-204	-234	-146	-181
	Residual Strain (μs)	-5	-25	-45	-55	-30	-5	-30	-95	30	90	-35	-70	-120	-65	-20
Kobe 100%	Compression Strain (μs)	130	226	382	419	479	192	283	165	478	430	175	142	246	384	232
	Tension Strain (μs)	-186	-344	-318	-450	-418	-256	-361	-333	-432	-555	-463	-424	-631	-582	-326
	Residual Strain (μs)	20	-110	-85	-90	110	-30	-150	-3	45	110	-190	-60	-175	-140	-30
Kobe 125%	Compression Strain (μs)	370	340	460	770	934	357	407	754	959	653	243	508	431	772	815
	Tension Strain (μs)	-430	-410	-475	-608	-880	-620	-840	-1035	-1252	-945	-661	-1060	-870	-1168	-1315
	Residual Strain (μs)	-15	-75	40	120	210	-120	-220	-180	45	130	-220	-95	-30	110	145
Kobe 150%	Compression Strain (μs)	1293	1521	1216	2451	2805	1222	1147	1414	1055	477	1153	1649	1839	1957	1337
	Tension Strain (μs)	-1208	-1422	-1753	-1859	-2311	-2186	-1615	-1827	-2740	-3222	-1676	-2030	-2855	-1844	-2448
	Residual Strain (μs)	125	130	270	180	320	-240	-120	250	60	-340	-180	270	230	330	430

Figure 4.37 illustrates the peak compression and tension strain values for Setup 1 during base excitations for top, mid and bottom geogrids. Horizontal axis stands for the distance of the strain gages from the front facing. Locations of the gages were different of every setup and they were also changed between bottom, mid and top geogrids. The gap seen for top and mid geogrids signifies the damaged strain gages which cannot record strain data. It can be seen from the figures the location of maximum strain values developed close to facing on bottom geogrids but maximum strain locations moved to the mid of the geogrids for upper layers.

Figure 4.38 shows the distribution of compressive and tensile strains along the reinforcement length for top, mid and bottom geogrids of Setup 2. The characteristic of the distribution can be summarized as: for bottom geogrids strain values had higher values and they formed a more peaked curve. For compressive strains two remarkable maximum points were observed for top and bottom geogrids. Strain values developed on the mid and top geogrids increased linearly from the end of the geogrid toward the facing in a smooth manner. For tensile strains they always reached the maximum on the closest gage to the facing.

Distribution of compressive and tensile strains along the reinforcement for Setup 3 measured during the seismic actions is illustrated in Figure 4.39. The distribution trend of the strains was almost similar with the Setup 2. But for the tensile strains developed on the bottom and mid geogrids during Kobe 100% and Kobe 125% two maximum points were occurred. Up to Kobe 100% the strain values were so small that a noticeable observation could not be done for the strain distribution.

Figure 4.40 illustrates the distribution of strain values along the geogrids for Setup 4 for each base excitation. The most meaningful observation can be made for Kobe 150% earthquake is that; tensile strain values made two peaks on the bottom geogrid. Tensile strains were increased linearly towards the facing on mid and top geogrid. Compressive strains for mid and bottom geogrid formed a more flat distribution curve but at the top where the compressive strains values were higher than tensile strain values, again there was a linear increase towards facing.

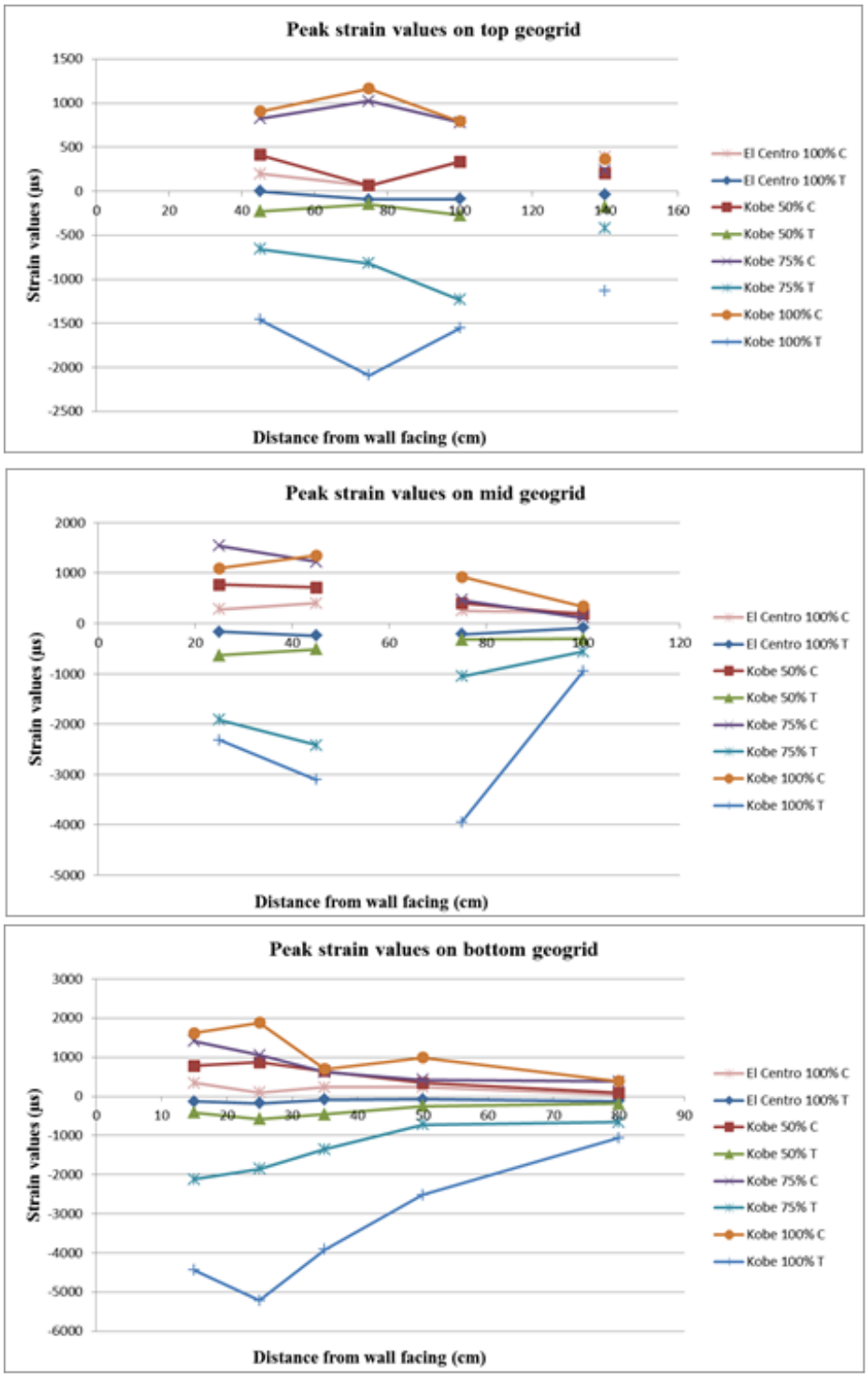

Figure 4.37. Maximum Strains at Top, Mid-height and Bottom Geogrids Layers, Setup 1.

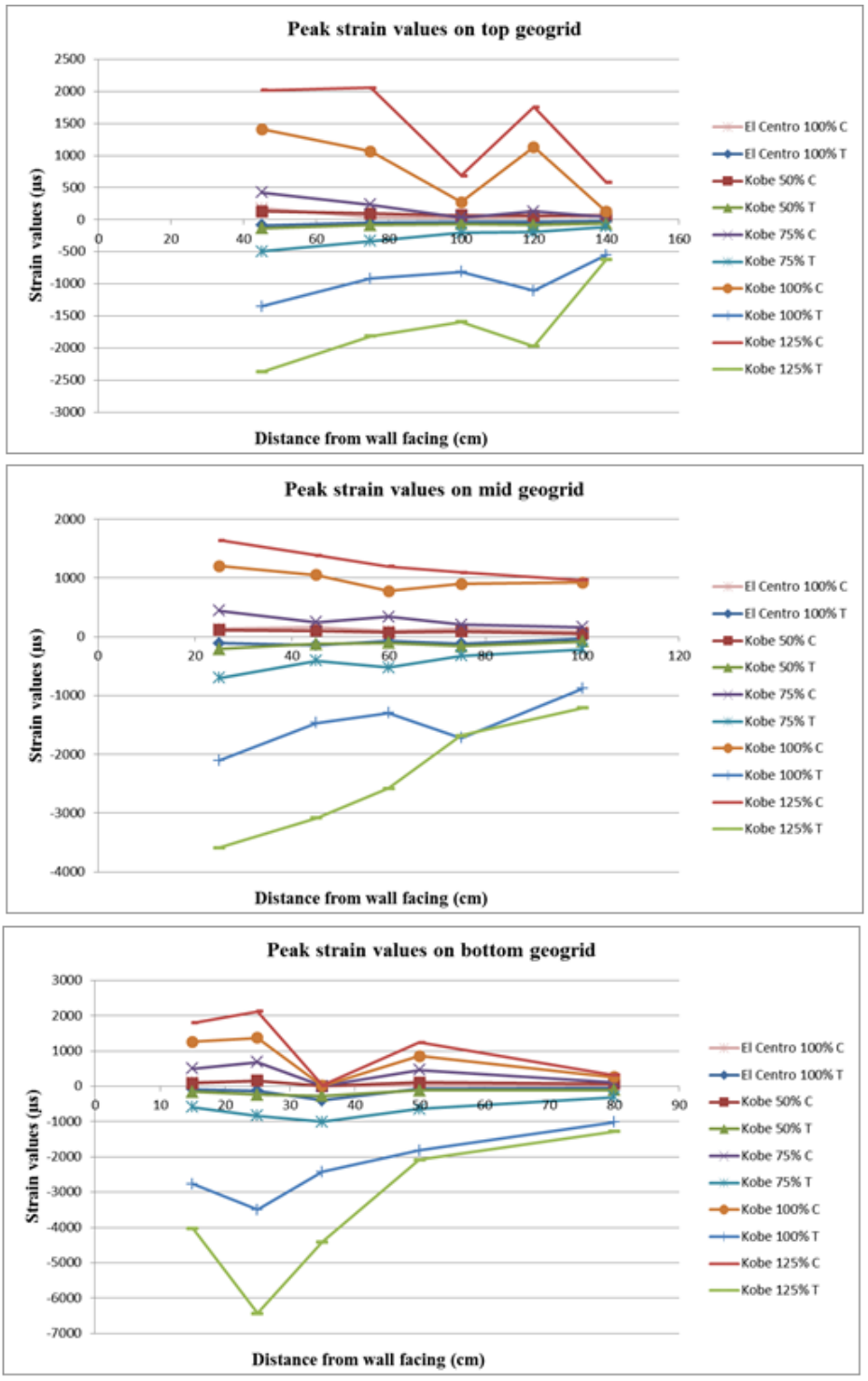

Figure 4.38. Maximum Strains at Top, Mid-height and Bottom Geogrids Layers, Setup 2.

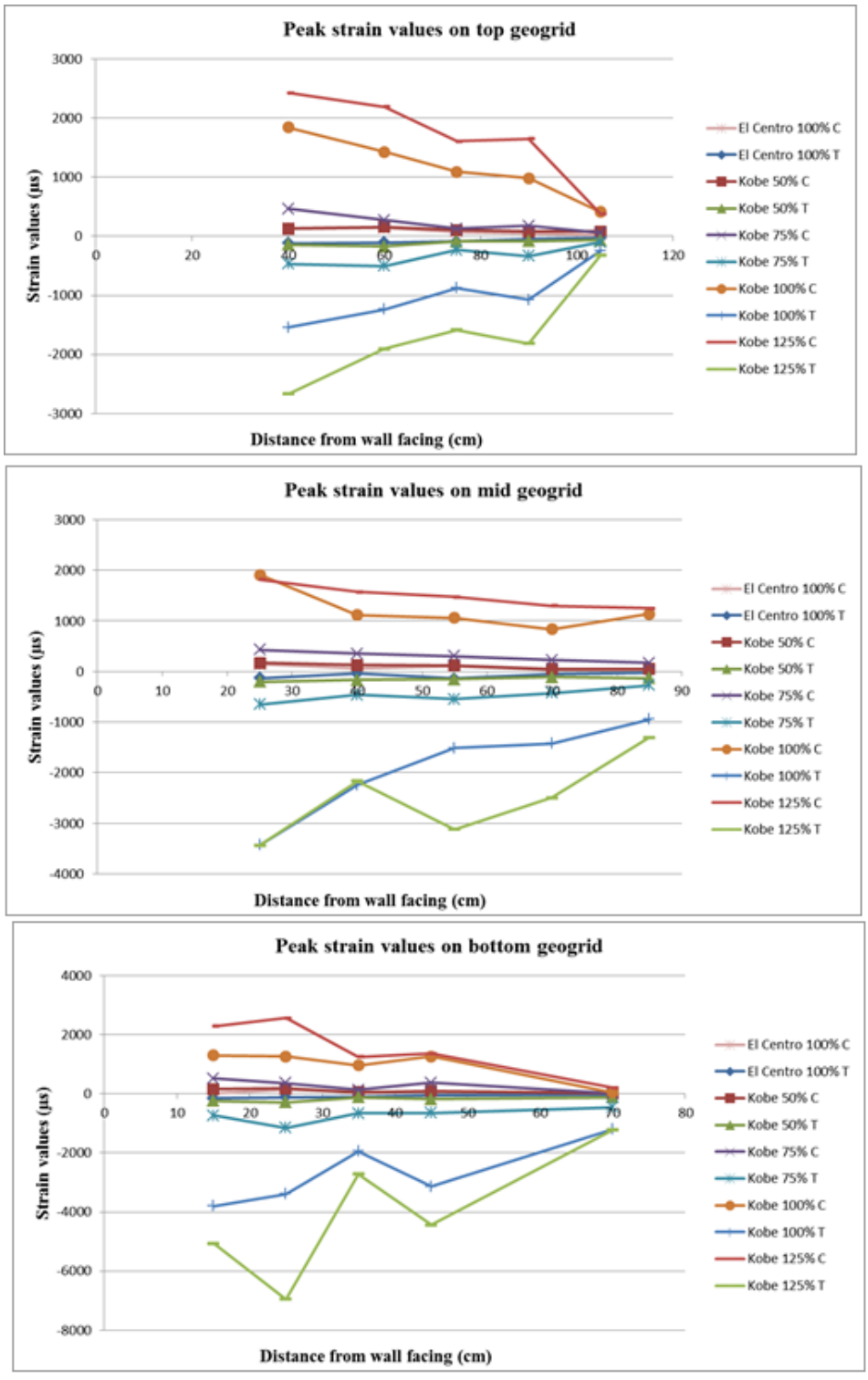

Figure 4.39. Maximum Strains at Top, Mid-height and Bottom Geogrids Layers, Setup 3.

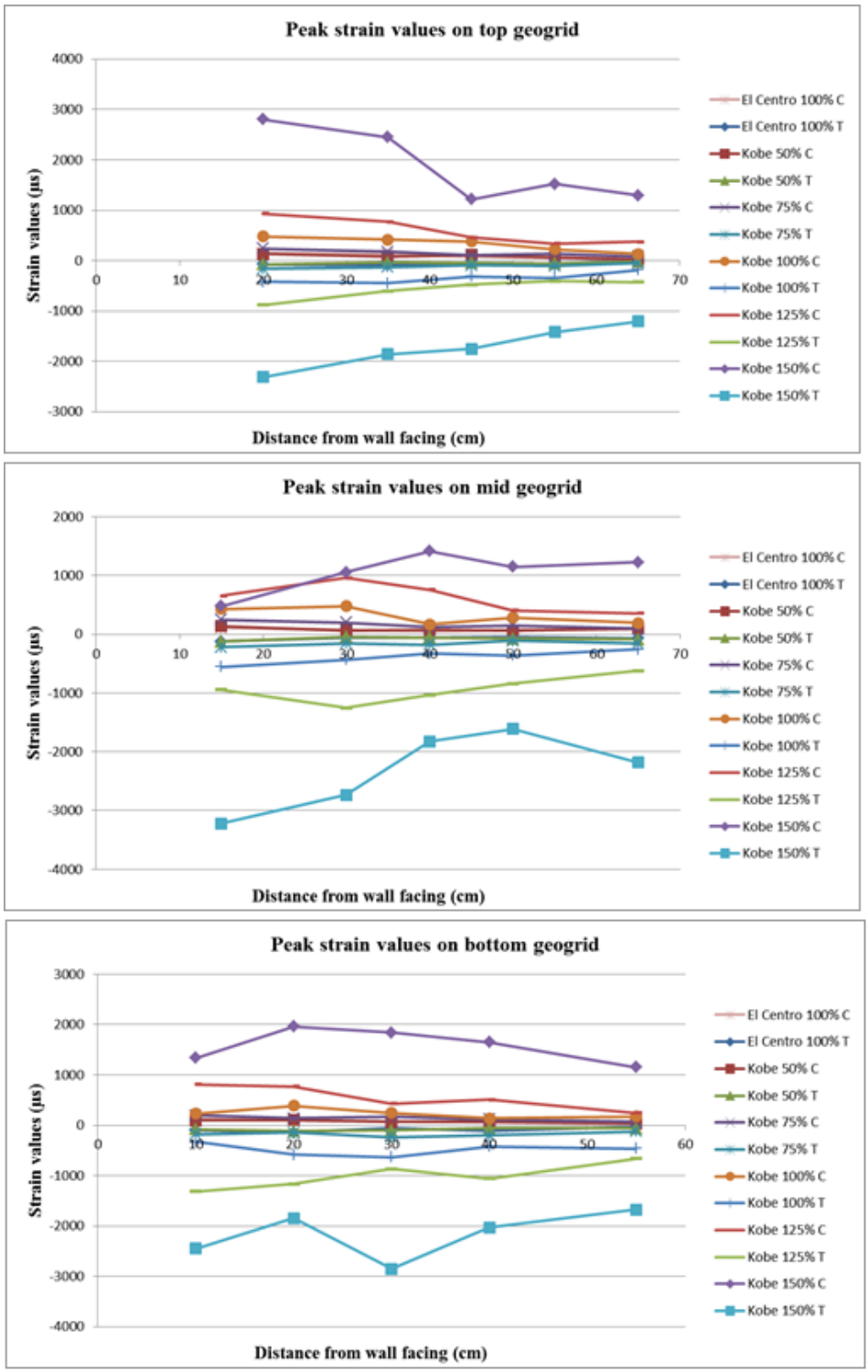

Figure 4.40. Maximum Strains at Top, Mid-height and Bottom Geogrids Layers, Setup 4.

Figure 4.41 illustrates the residual strain values measured on top, mid and bottom geogrids at the end of base excitations for Setup 1. Damaged strain gages are the

cause of the gaps on the lines of top and mid geogrids. For Kobe 100% the highest residual compressive strain was on the bottom geogrid at the closest gage to the facing. Afterwards the residual strain values turned to tension after that gage on the same bottom geogrid. For Kobe 75% the trend of bottom geogrid was similar but the peak values were lower than Kobe 100%. For these two excitations residual strain values on mid and top geogrid were all in tension.

Residual strain values measured on top, mid and bottom geogrids at the end of base excitations for Setup 1 are shown in Figure 4.42. For Kobe 125% and Kobe 100% residual strains on the gage closest to the facing were in compression and the gage next to it made a peak residual strain in tension, on the bottom geogrid. On the top geogrid, for Kobe 125% and Kobe 100%, the residual strains were in compression for the first three gages then residual tensile strains were developed at the end of reinforcement.

Figure 4.43 illustrates the residual strain values measured on top, mid and bottom geogrids at the end of base excitations for Setup 3. The trend for Kobe 100% and Kobe 125% earthquakes were similar with Setup 2. The most remarkable difference between the this setup and Setup 2 was that, for Kobe 100% and Kobe 75% the residual strains on the mid geogrid were totally in tension.

Figure 4.44 illustrates the residual strain values measured on top, mid and bottom geogrids at the end of base excitations for Setup 4. For Kobe 150% earthquake the residual strains were in compression on the top and bottom geogrids. Mid geogrid had a peak in compression at the middle gage but tensile strains were developed at the beginning and at the end of the reinforcement. For Kobe 125% earthquake, compression strains were dominant on the first half of the reinforcement then the strain values turned in tension on the next half of the reinforcement towards the end for the top, mid and bottom geogrids. Seismic excitations up to Kobe 100% did not remain significant residual strains on the geogrids.

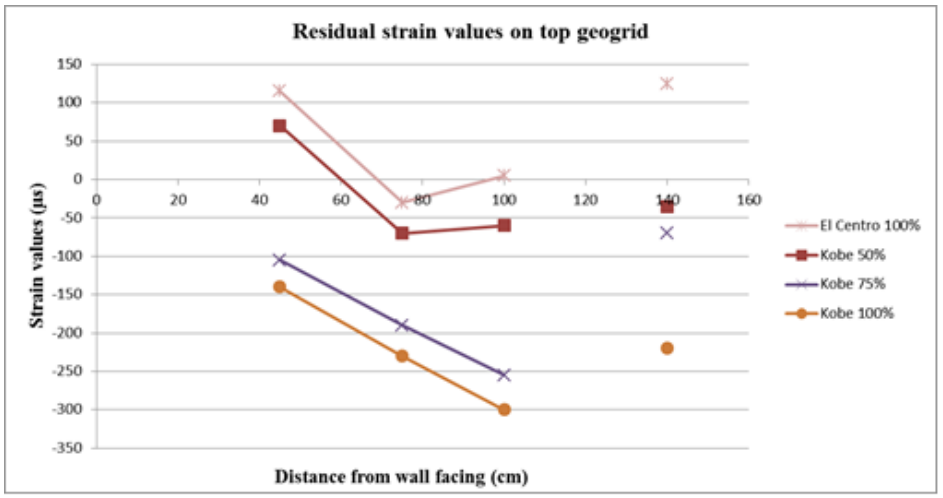

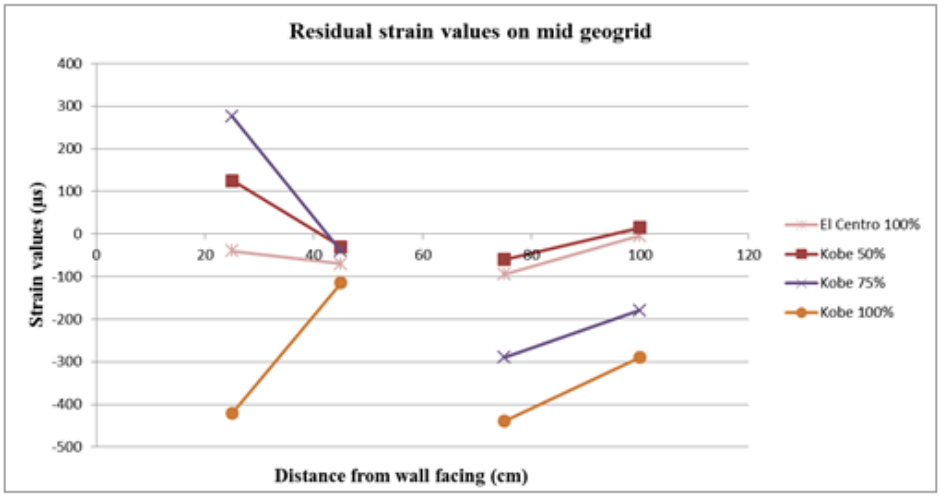

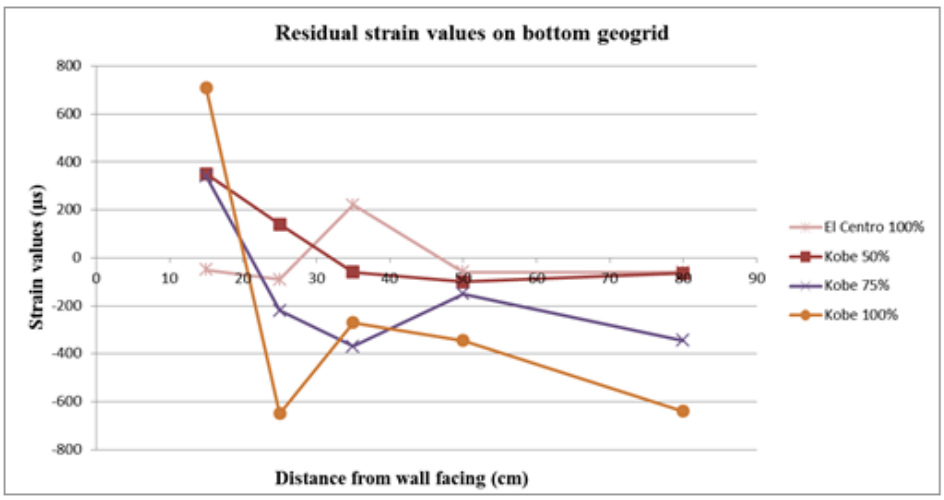

Figure 4.41. Residual Strains at Top, Mid-height and Bottom Geogrids Layers, Setup 1.

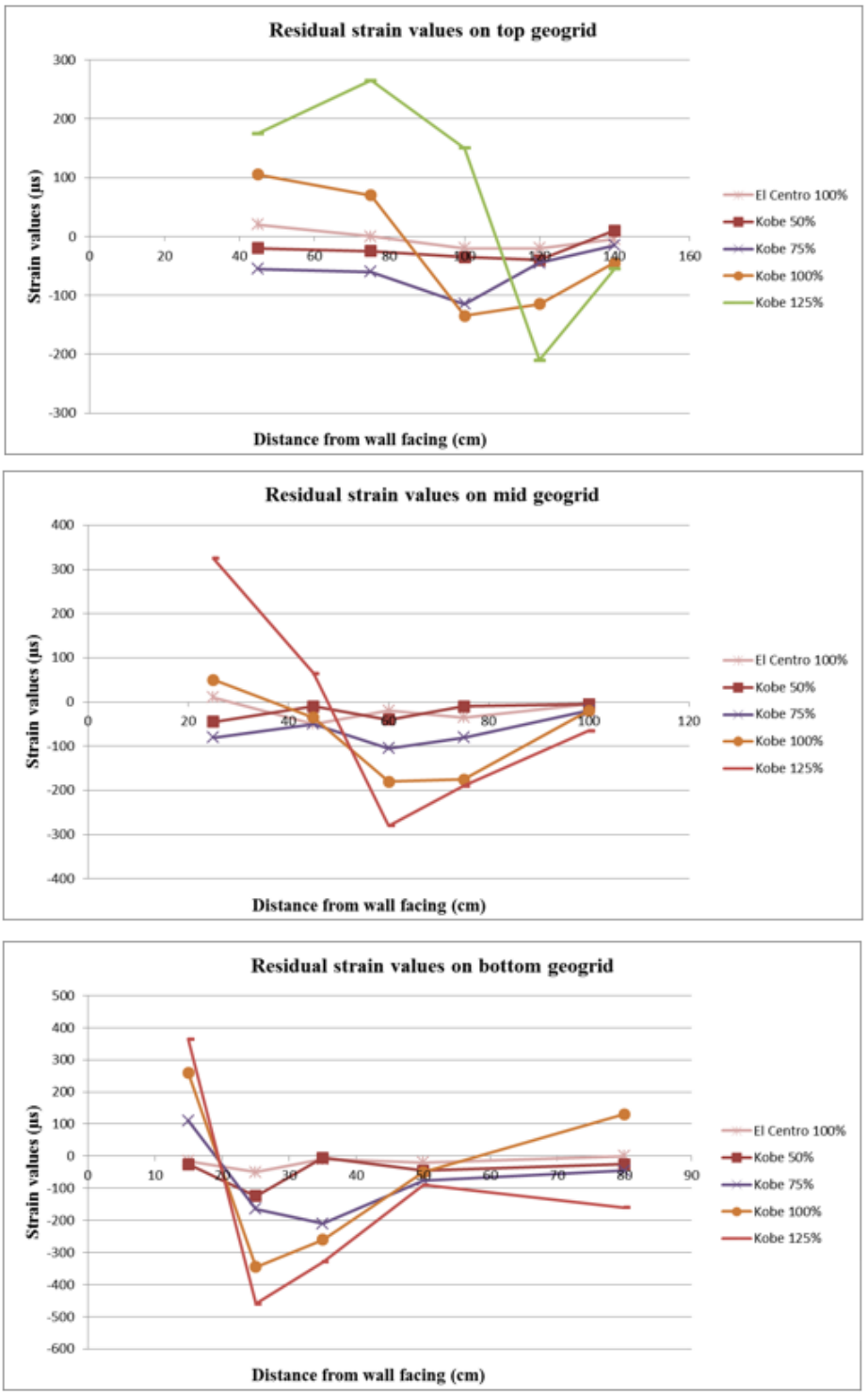

Figure 4.42. Residual Strains at Top, Mid-height and Bottom Geogrids Layers, Setup 1.

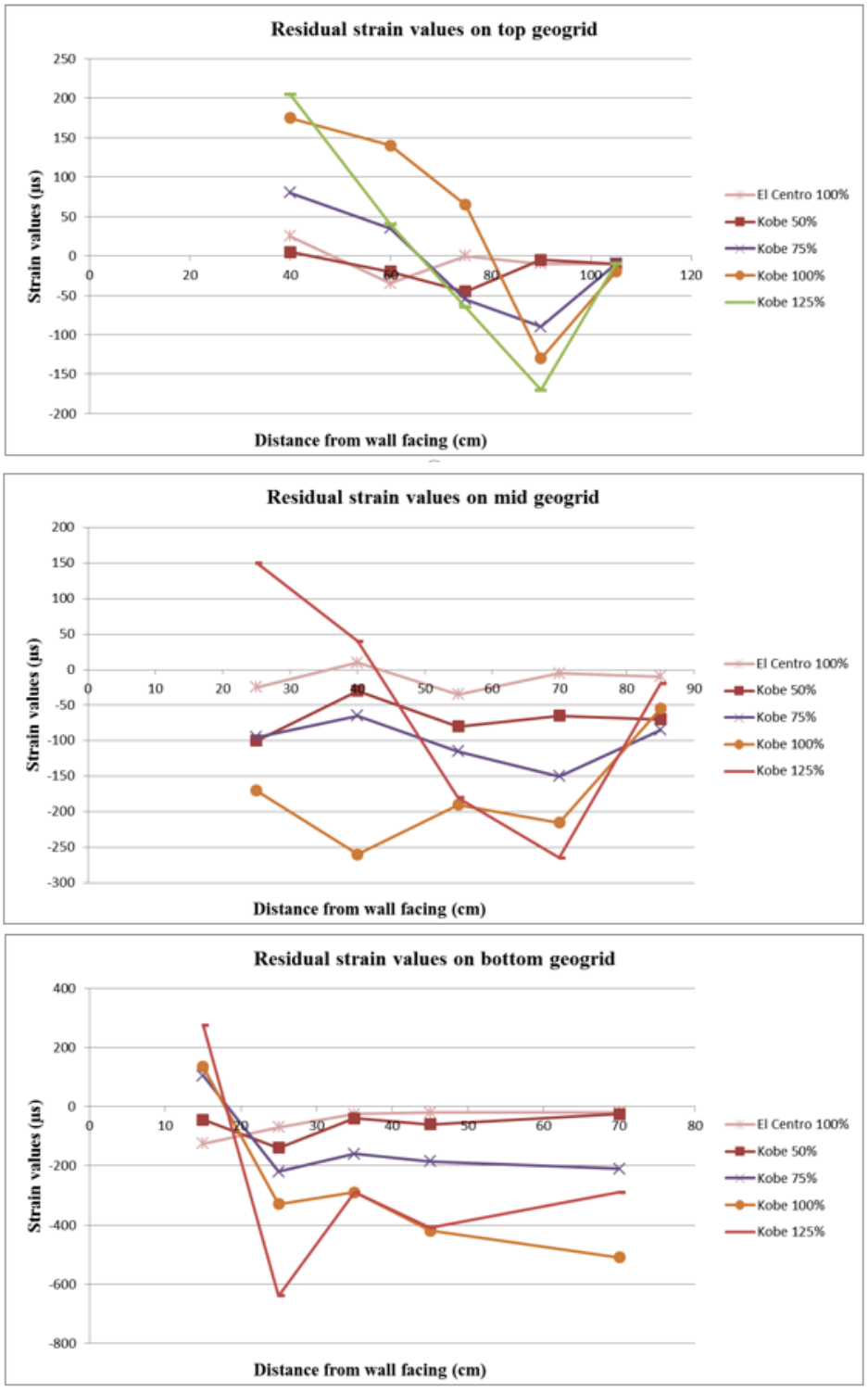

Figure 4.43. Residual Strains at Top, Mid-height and Bottom Geogrids Layers, Setup 1.

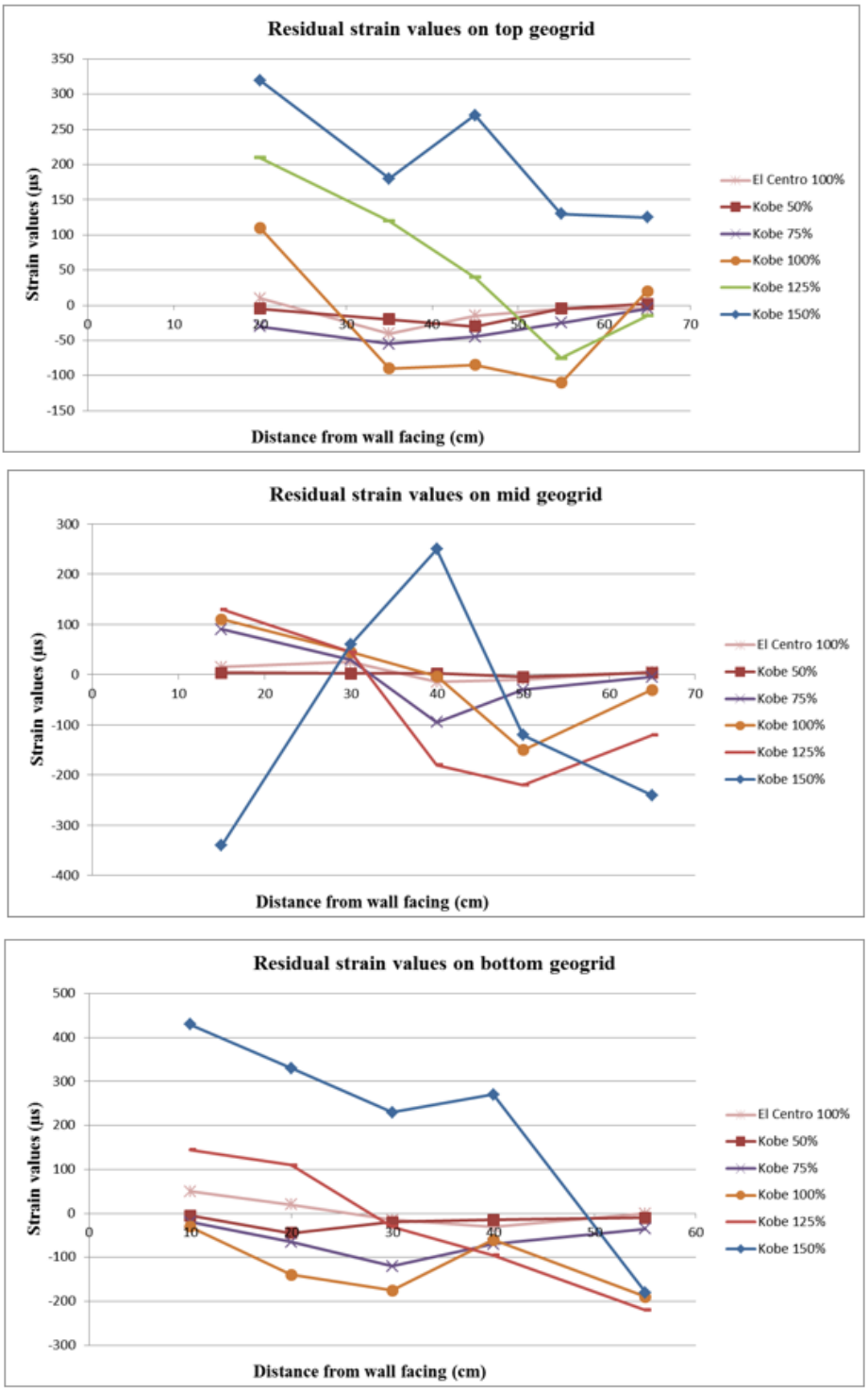

Figure 4.44. Residual Strains at Top, Mid-height and Bottom Geogrids Layers, Setup 1.

Stresses, especially in tension, developed on the geogrids are more important for design purposes in engineering aspect, strain results are just the measured quantities

used to obtain reinforcement loads. But the developed stress values were so small that it would be difficult to investigate the behavior of geogrids considering the differences between setups and seismic actions.

Tensile strains measured on the geogrids were converted to tensile loads according to their elastic modulus and the results are given in Table 4.15 to Table 4.18 for four wall configurations. Because mean and peak values of tensile loads and their distribution among the reinforcement are key parameters to find out the performance of the reinforcement for internal stability check. Measured tensile load values from these tests and corresponding calculated design tensile loads with proposed design methods in NCMA and FHWA can be compared. These comparisons can be regarded as a feedback for the current design regulations. In the tables tensile loads are given in kN/m; the elastic modulus was taken as 570 kN/m obtained from manufacturer's sheet (up to 1% strain limit) and validated with the calibration tests reported in Section 4.4.1. The maximum developed tensile loads were compared with the limit results stated in the literature. It should be kept in mind that these tensile load values indicated the dynamic effects because the data loggers were set to zero after construction phase, static effects were not induced in these tensile loads.

Table 4.15 represents the tensile loads developed on the top, mid and bottom geogrids of Setup 1 during seismic actions. It can be seen from the table that tensile load values increased with increasing amplitude of seismic action. For Kobe 75% maximum tensile load was generated at mid geogrid as 1.38 kN/m and the average values were close to bottom geogrid. For Kobe 100% earthquake, maximum tensile load was 2.97 kN/m on the bottom geogrid and this value was higher than the measured peak tensile loads on the mid and top geogrids as 1.77 kN/m and 1.19 kN/m respectively.

Table 4.16 represents the tensile loads developed on the top, mid and bottom geogrids of Setup 2 during base excitations. For Kobe 100% maximum tensile loads calculated for the bottom, mid and top geogrids were 2.00 kN/m, 1.20 kN/m and 0.77 kN/m respectively and these values 50% percent lower than the Setup 1 with sand backfill. For Kobe 125% earthquake, 3.67 kN/m, 2.04 kN/m and 1.35 kN/m were

the maximum tensile loads on the bottom, mid and top geogrids respectively. It was observed that the tensile loads increased from bottom to top geogrid.

Tensile loads calculated for top, mid and bottom geogrids of Setup 3 during base excitations were given in Table 4.17. For Kobe 100% maximum tensile loads calculated for the bottom, mid and top geogrids were 2.17 kN/m, 1.96 kN/m and 0.88 kN/m respectively. These values were close to each other and approximately one fourth of the results of Setup 2. For Kobe 125% earthquake, 3.96 kN/m, 1.96 kN/m and 1.52 kN/m were the maximum tensile loads on the bottom, mid and top geogrids respectively. Tensile load values obtained from bottom geogrids were higher than the values of mid and top geogrids.

Table 4.18 presents the tensile loads calculated for top, mid and bottom geogrids of Setup 4 during base excitations. For Kobe 125% maximum tensile loads calculated for the bottom, mid and top geogrids were 0.75 kN/m, 0.71 kN/m and 0.50 kN/m respectively and these values 50% percent lower than the Setup 1 with sand backfill. For Kobe 125% earthquake 1.63 kN/m, 1.84 kN/m and 1.32 kN/m were the maximum tensile loads on the bottom, mid and top geogrids respectively. Dissimilarly the maximum tensile loads were developed on the mid geogrid.

Table 4.15. Maximum Tensile Loads on Geogrids for Setup 1 for Seismic Loads.

	Tensile Loads (kN/m)			
Strain Gauge No	El Centro 100 %	Kobe 50 %	Kobe 75 %	Kobe 100 %
S1	0.02	0.1	0.24	0.65
S2	0	0	0	0
S3	0.05	0.16	0.7	0.89
S4	0.05	0.08	0.47	1.19
S5	0	0.13	0.37	0.83
S6	0.05	0.18	0.32	0.54
S7	0.12	0.18	0.6	2.25
S8	0	0	0	0
S9	0.14	0.29	1.38	1.77
S10	0.1	0.36	1.09	1.33
S11	0.07	0.11	0.38	0.61
S12	0.04	0.14	0.41	1.44
S13	0.05	0.26	0.77	2.23
S14	0.1	0.33	1.06	2.97
S15	0.07	0.24	1.21	2.53

Table 4.16. Maximum Tensile Loads on Geogrids for Setup 2 for Seismic Loads.

	Tensile Loads (kN/m)				
Strain Gauge No	El Centro 100 %	Kobe 50 %	Kobe 75 %	Kobe 100 %	Kobe 125 %
S1	0.01	0.03	0.06	0.31	0.35
S2	0.02	0.05	0.11	0.63	1.12
S3	0.02	0.04	0.12	0.46	0.91
S4	0.03	0.05	0.19	0.52	1.03
S5	0.05	0.08	0.28	0.77	1.35
S6	0.02	0.05	0.12	0.5	0.69
S7	0.07	0.09	0.19	0.98	0.96
S8	0.04	0.06	0.3	0.74	1.47
S9	0.08	0.07	0.23	0.84	1.76
S10	0.06	0.12	0.4	1.2	2.04
S11	0.02	0.06	0.18	0.58	0.73
S12	0.03	0.07	0.37	1.03	1.19
S13	0.23	0.15	0.58	1.38	2.51
S14	0.07	0.13	0.48	2	3.67
S15	0.05	0.09	0.34	1.58	2.29

Table 4.17. Maximum Tensile Loads on Geogrids for Setup 3 for Seismic Loads.

	Tensile Loads (kN/m)				
Strain Gauge No	El Centro 100 %	Kobe 50 %	Kobe 75 %	Kobe 100 %	Kobe 125 %
S1	0.02	0.04	0.06	0.14	0.18
S2	0.03	0.05	0.19	0.61	1.03
S3	0.05	0.05	0.13	0.5	0.91
S4	0.06	0.1	0.29	0.7	1.08
S5	0.07	0.08	0.27	0.88	1.52
S6	0.01	0.08	0.16	0.54	0.74
S7	0.03	0.06	0.25	0.81	1.43
S8	0.08	0.09	0.31	0.86	1.78
S9	0.02	0.1	0.27	1.28	1.23
S10	0.07	0.12	0.37	1.96	1.96
S11	0.02	0.07	0.26	0.69	0.7
S12	0.03	0.1	0.37	1.79	2.53
S13	0.06	0.07	0.38	1.11	1.55
S14	0.07	0.16	0.66	1.93	3.96
S15	0.09	0.13	0.42	2.17	2.88

Table 4.18. Maximum Tensile Loads on Geogrids for Setup 4 for Seismic Loads.

	Tensile Loads (kN/m)					
Strain Gauge No	El Centro 100 %	Kobe 50 %	Kobe 75 %	Kobe 100 %	Kobe 125 %	Kobe 150 %
S1	0.01	0.01	0.03	0.11	0.25	0.69
S2	0.04	0.03	0.06	0.2	0.23	0.81
S3	0.03	0.03	0.05	0.18	0.27	1
S4	0.05	0.02	0.07	0.26	0.35	1.06
S5	0.04	0.04	0.1	0.24	0.5	1.32
S6	0.04	0.05	0.09	0.15	0.35	1.25
S7	0.03	0.04	0.06	0.21	0.48	0.92
S8	0.03	0.03	0.1	0.19	0.59	1.04
S9	0.03	0.03	0.09	0.25	0.71	1.56
S10	0.07	0.07	0.13	0.32	0.54	1.84
S11	0.02	0.03	0.07	0.26	0.38	0.96
S12	0.06	0.04	0.12	0.24	0.6	1.16
S13	0.03	0.06	0.13	0.36	0.5	1.63
S14	0.08	0.07	0.08	0.33	0.67	1.05
S15	0.06	0.05	0.1	0.19	0.75	1.4

4.4.4. Summary of the Results

Before starting evaluation of the test results summarized in above tables and graphs it should be noted that, shakings were applied to a set up consecutively which ended up with a stiffer soil backfill because of this earthquake compaction, but this effect is ignored for the following outcomes.

Tensile strain values and corresponding tensile loads compared with reinforcement strength are the parameters to determine the reinforcement sufficiency. By this aspect it can be said that the geogrids performed well because the maximum tensile strains observed were in the range of 0.6-0.7% for Kobe 125% earthquakes of Setup 2 and Setup 3 which could create really low stress values. It was also below the ultimate limit state value of 3% reinforcement strain used in the K-stiffness method for granular soils reinforced with extensible reinforcement layers, stated in the study of Bathurst *et al.*, (2008). As it was expected; both compressive and tensile strain values increased with the increasing base excitation amplitudes.

Tensile strains were observed together with opposite compressive strains during base excitation indicating the generation of compression and tension zones inside the backfill because of the wave propagation pressure. Compressive strain formation has importance to understand behavior of structure. It was stated that outward and inward movements were almost equal especially for Setup2 and Setup3 and strain distribution time history data followed that displacement trend. Compression strain values were observed as high as tensile strain values on the geogrids; for Setup 1 during El Centro 100% and Kobe 50% compressive strain values were considerably higher. That result is consistent with the peak and residual inward movement which created higher compressive pressures towards the backfill. Generally El Centro earthquake created rationally higher compressive strains because of the waveform of that excitation, for all wall configurations. For Setup 2 and Setup 3 general trend was compressive strain values were higher at top geogrid sometimes higher than tensile values. It can be explained by higher peak inward movement and inward residual displacements at top blocks of facing. For mid reinforcements compressive strain values reached half of the tensile

strain values where at the bottom geogrid, they could just reach one third. For Setup 4 base excitations with lower amplitudes (Kobe 50% and Kobe 75%) created higher compressive strains. This was again in agreement with their displacement behavior but when an overall consideration was made, strain distribution was said to be similar to Setup 2. As an important point, peak tensile and compressive strains were observed generally at the same or very close strain gauges which can also be related with the propagation of pressure waves.

Residual strains were observed both in compression and tension at the end of base excitations and these values may indicate an important sign for the behavior of the structure. These strains should not be evaluated just as the permanent deformations remained at the end of seismic action. Because in that view they are not so meaningful while the reinforcements were in the elastic region and they could still perform if the excitation continued. These residual strains also reflected the latest condition of the backfill in terms of tension and compression zones developed in the soil. Transitions between these permanent zones may be an evidence for the potential failure plane. But it is not a strong evidence because the ratio of residual and peak strain values were about 1/10 for Setup 2 and Setup 3 for Kobe 125% and Kobe100% earthquakes. Although they reached half of the peak strain values at lower amplitude seismic loads, these values can't be regarded as meaningful pressure zones when the level of the measured stress values and the capacity of the geogrid were considered together. As another indication, distribution of residual strain values along the geogrid was consistent with an estimated failure wedge obtained from the residual displacement values of the front facing. These alternative potential failure planes generated according to the probable residual compression tension transition zones are illustrated in Figure 4.54. These possible failure planes can't be drawn for all wall configurations but some of them were observed obviously like Kobe 125% earthquake of Setup 2. It also had an evidence that a tension crack was observed at the top surface of backfill at the point where this possible failure line ended. And compressive residual strains were recorded at the strain gage closest to facing on the bottom geogrid, where a residual compression zone was expected just behind the fixed toe of the wall.

Due to stepwise application of seismic excitations, strain values on the geogrids increased especially on bottom geogrid layers, while the top reinforcement always experienced the lowest tensile stresses. The maximum peak and average strains were observed on the bottom geogrid layer. The difference between bottom and middle geogrid layers decreased with decreasing base acceleration amplitude for average strain values. In the study of Matsuo *et al.*, (1998), for the model walls with discrete facings, the increase in both the earth pressure acting on the wall and the tensile force in the geogrid reinforcement were significant at the bottom of the wall. The behavior that strain values increased from bottom to top, can be explained by the high overburden stresses at the bottom of the wall. Also the mid-height of the wall also experienced large increases of strain values because of the higher peak and residual outwards displacement values.

For the distribution of strain values among the reinforcement, it was observed that bottom layer had a more apparent peaked curve. And the mid and bottom layers had generally a linear increase trend towards the facing for strain values along the reinforcement. For the bottom layer the peak strains occurred at very close distance to the facing. Restraining effect due to reinforcement may be another cause for this, apart for the high overburden stresses developed at the wall base, this explanation was also reported by Ling *et al.*, (2005). And for all reinforcement layers low strain values were measured on strain gauges generally at the end of reinforcement which were far from the critical potential failure plane. But when potential failure planes are viewed it can be seen that they formed in the reinforced zone close to facing especially for model walls with cohesive backfills.

Reinforcement layers in Setup 3 experienced higher tensile and compressive strains compared to Setup 2, because shorter reinforcements were exposed to higher tensile loads to sustain the internal stability. And also slightly higher outward and inward displacements of the facing of Setup 3 compared to Setup 2 could be a cause for higher strain values.

Strain values measured on geogrid layers of Setup1 and Setup 2 can be compared

in order to comprehend the influence of backfill material. For Setup 1 tensile strains for Kobe 100% earthquake reached the values of 5200 μs where the same seismic action created 3500 μs as the maximum tensile strain on the bottom geogrid layer of Setup 2. On the same geogrid layer 6400 μs tensile strain was generated for Kobe 125% earthquake for Setup 2. It was mentioned that the cohesive backfill performed better than the dry backfill according to the peak displacement values measured as 20.40 mm and -34.60 mm for Setup 1 and 12.69 mm and -13.22 mm for Setup 2 during Kobe 100% earthquake. In the model with cohesive backfill lower displacements and consecutively lower strains were measured. And with this incomparable displacement results the performance geogrids could not be directly determined. Peak displacement values of Setup 1 for Kobe 100% earthquake and Setup 2 for Kobe 125% earthquake were more comparable for the mid upper part of the wall. And it can be seen that Setup 2 had almost equal even slightly higher strain values compared to Setup 1 for these closer displacement values. And this result could confirm that, geogrid reinforcement with cohesive backfill could perform as well as it was in sand backfill.

In Appendix D, peak strain values for compression and tension are illustrated according to their locations on the geogrid. These strain values were obtained from time history graphs; four instants on time axis were determined for both directions (eight in total) where the strain values reached a peak (top four peak values) during the seismic excitation. These simplified time history graphs drawn according to gauge locations for bottom, mid and top geogrids lead us to have an opinion about the distribution of peak strains along the geogrid during the whole duration of the seismic action. Location of the peak tensile and compression strains were obtained from these graphs. Potential internal failure surface was formed by joining the locus points of these peak strain values. Peak tensile strain locations were considered primarily. Where the maximum compressive strains had another locus point or the tensile strains made a secondary peak, this point was also considered as secondary potential failure line. In the previous study of Başbuğ (2011) the locus points of the tensile loads were joined to obtain failure plane.

Locations of the potential surface planes were determined as they were illustrated

in Figure 4.46 to Figure 4.57 for top three base excitation amplitudes of each wall configuration. The failure surface plane can be regarded as a separation line between the active and passive zones occurred in the backfill during failure. Active zone is the wedge standing between this line and facing; shear stresses on the reinforcements are directed towards the wall face in front of this line and the shear stresses directed away into the backfill behind this line. In this study the lines regarded as the potential failure plane were the lines indicating the critical locations of reinforcements for internal stability calculations, predicted to be the potential failure plane if an internal failure had occurred in the reinforced zone.

Figure 4.56, Figure 4.57 and Figure 4.48 illustrate the potential failure surfaces of Setup 1, for Kobe 50%, Kobe 75% and Kobe 100% earthquakes. In wall configurations there may be more than one possible failure plane according to strain distribution along the reinforcements. For Setup1; Kobe 50% earthquake's second possible failure case and Kobe 100%'s more apparent potential failure case was seemed to mobilize like the condition described in two wedge theory. But for Kobe 75% earthquake, potential failure line option was seemed to be close to and parallel to facing. The two-wedge failure mechanism shown in Figure 4.45 has been adopted to analyze geosynthetic-reinforced retaining walls. The two-wedge failure mechanism, illustrated in Figure 4.51 is a method used to analyze the stability of geosynthetic-reinforced retaining walls and it is preferred because it is practical and suitable for geosynthetic-reinforced soil problems (Organ *et al.*, 1994). The vertical inter-wedge boundary and the case that base of the lower wedge intersects the toe of the wall, can be considered as the only constraints of the two-wedge failure mechanism. (Ismeik and Güler, 1998). Also Matsuo *et al.*, (1998) reported in their study that, shaking table tests have demonstrated that a "two-wedge" mode exists for most GRS wall with granular backfills under strong seismic loading. Finally it can be said that the determination of potential surface planes for Setup 1 is in agreement with these statements from literature.

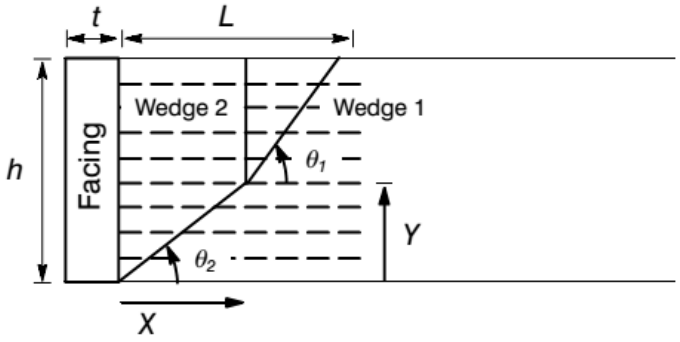

Figure 4.45. Two-wedge Failure Mechanism for Geosynthetic-reinforced Retaining Walls. (Ismeik and Güler, 1998).

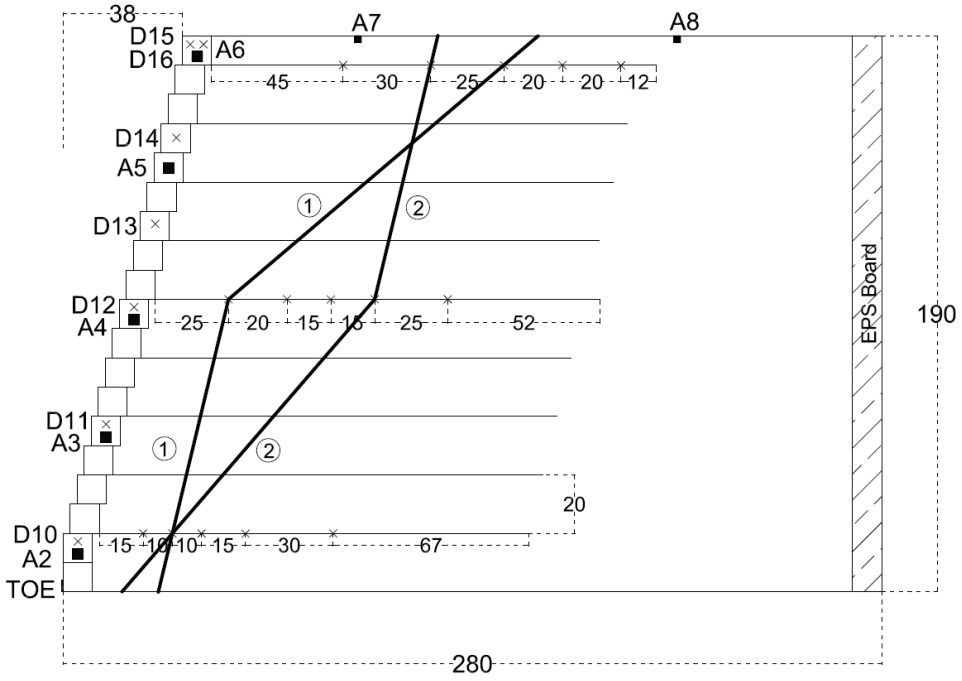

Figure 4.46. Potential Failure Planes for Setup 1 Kobe 50%.

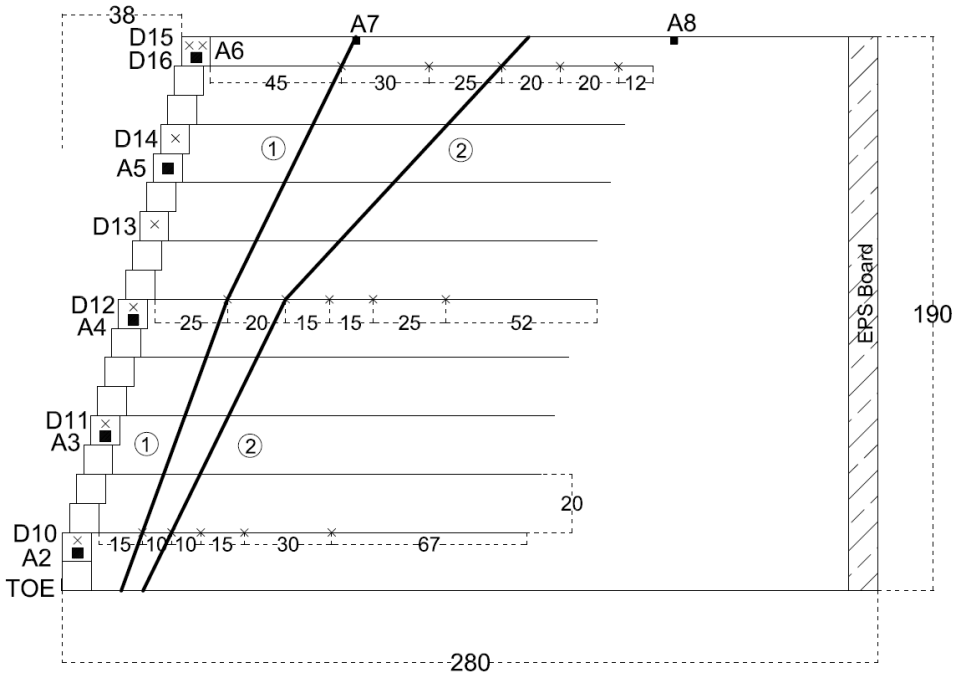

Figure 4.47. Potential Failure Planes for Setup 1 Kobe 75%.

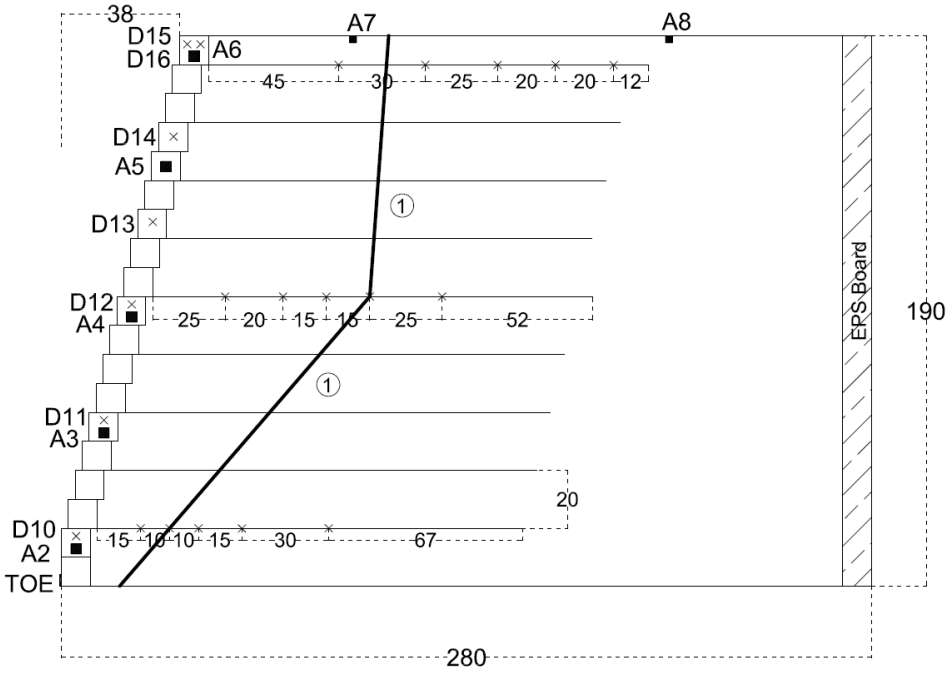

Figure 4.48. Potential Failure Planes for Setup 1 Kobe 100%.

Figure 4.49, Figure 4.50 and Figure 4.51 show the potential failure surfaces of Setup 2, for Kobe 75%, Kobe 100% and Kobe 125% earthquakes. Figure 4.52, Figure 4.53 and Figure 4.54 illustrate the potential failure surfaces of Setup 3, for Kobe 75%,

Kobe 100% and Kobe 125% earthquakes. Setup 2 and Setup 3, which behaved similar for wall displacements also experienced similar strain distribution on the reinforcements which was utilized as an indication for potential failure plane location. For Kobe 75% possible failure plane would form parallel to and close to the facing. With increasing amplitude of the excitation (Kobe 100% and Kobe 125%) the possible failure plane tended to move away from the facing, which means an increase in the area of active zone wedge and an increase for the coherent body of the reinforced soil. At the base, the potential failure plane always intersected the bottom geogrid at a point close to toe of the wall but in the upper parts of the wall, line moved away from the facing into the backfill. For Setup 2; Kobe 125% and Kobe 100% earthquakes an alternative possible failure surface line is added just in Figure 4.51. Because this surface could be determined apparently just for these two earthquakes and this line was defined as the transition zone between the residual compression and tension strains generated in the soil. The idea behind this alternative plane was mentioned above should not be ignored: although the residual values were very small compared to peak values, their consistency with residual displacements and the importance of residual strain values in terms of permanent stress zones at the end of the tests were remarkable.

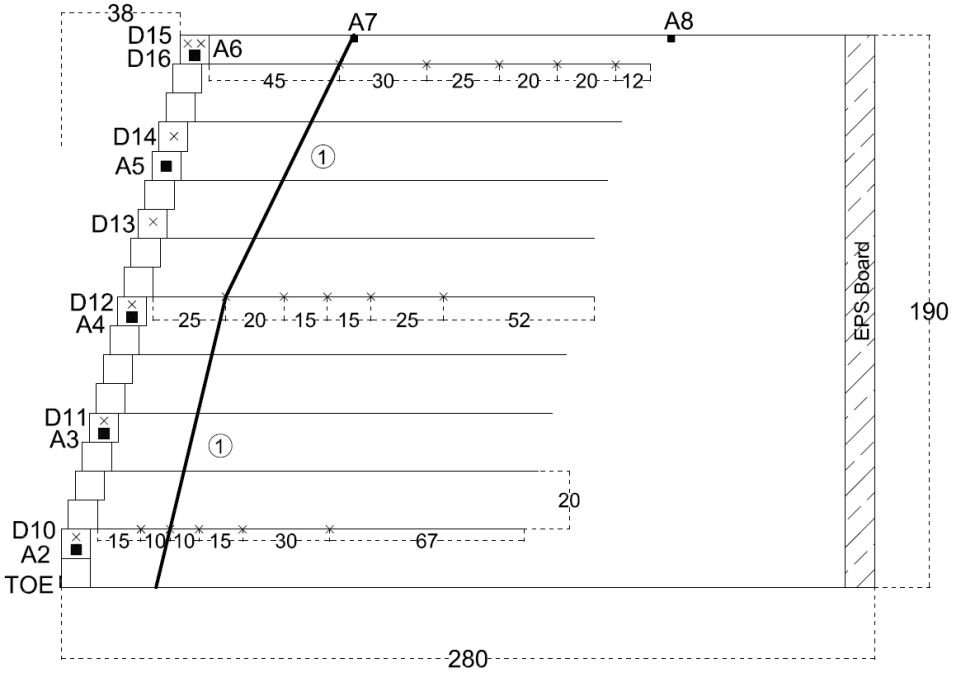

Figure 4.49. Potential Failure Planes for Setup 2 Kobe 75%.

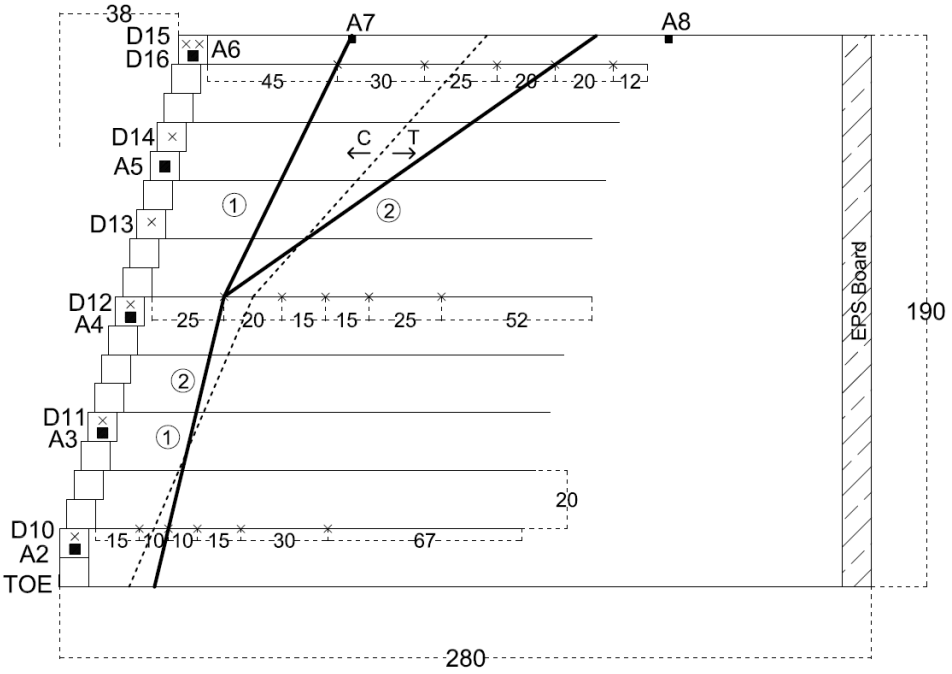

Figure 4.50. Potential Failure Planes for Setup 2 Kobe 100%.

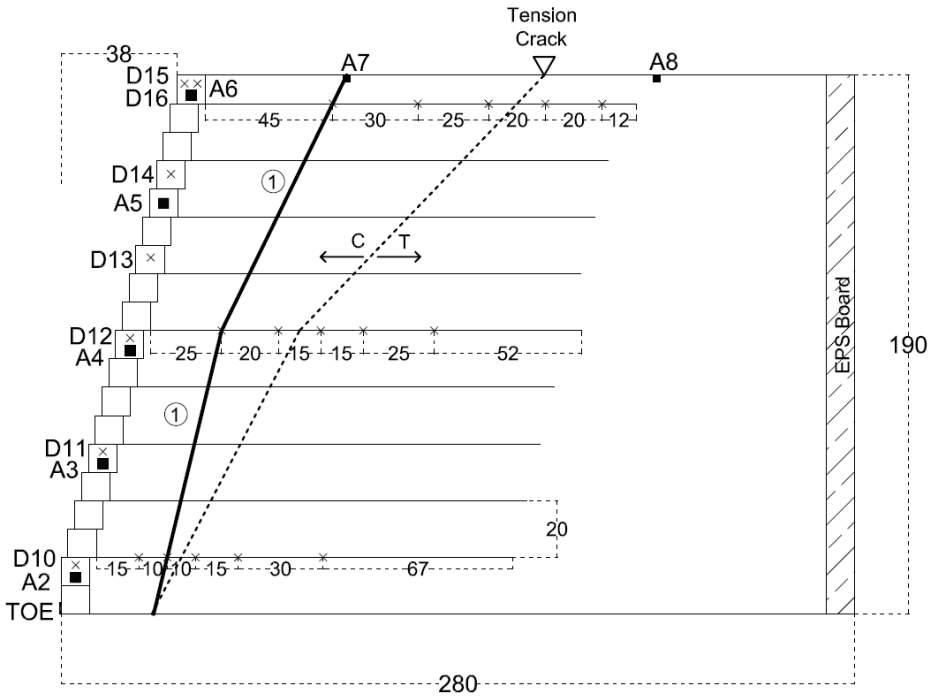

Figure 4.51. Potential Failure Planes for Setup 2 Kobe 125%.

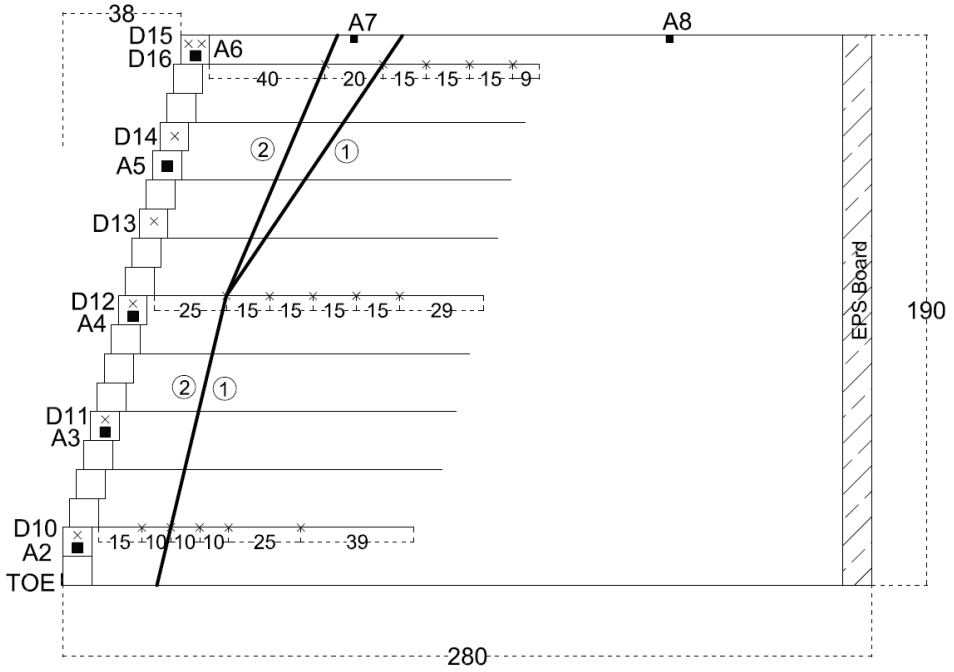

Figure 4.52. Potential Failure Planes for Setup 3 Kobe 75%.

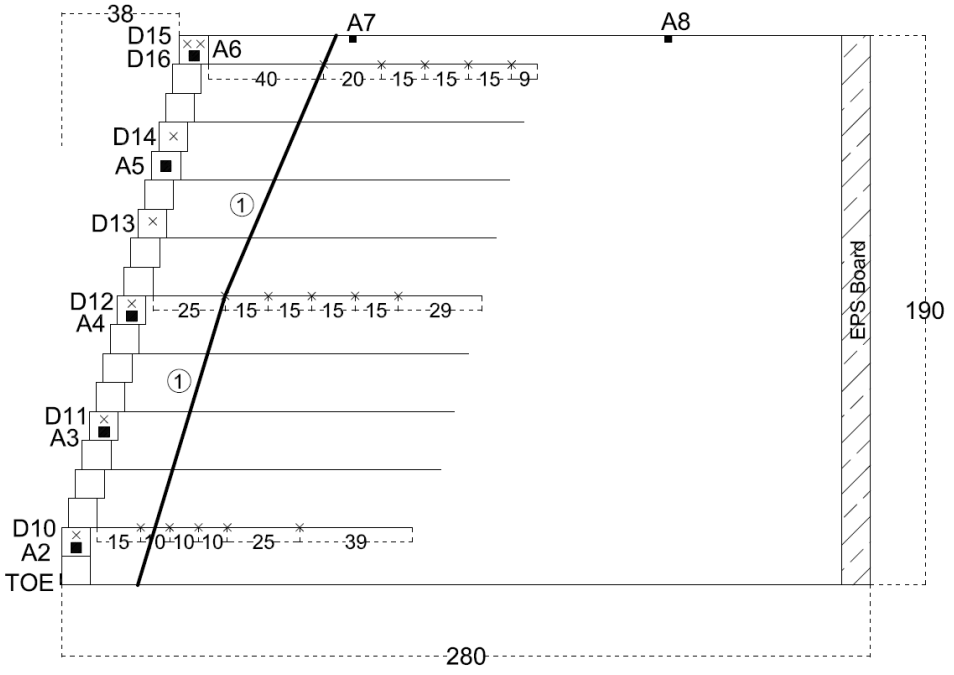

Figure 4.53. Potential Failure Planes for Setup 3 Kobe 100%.

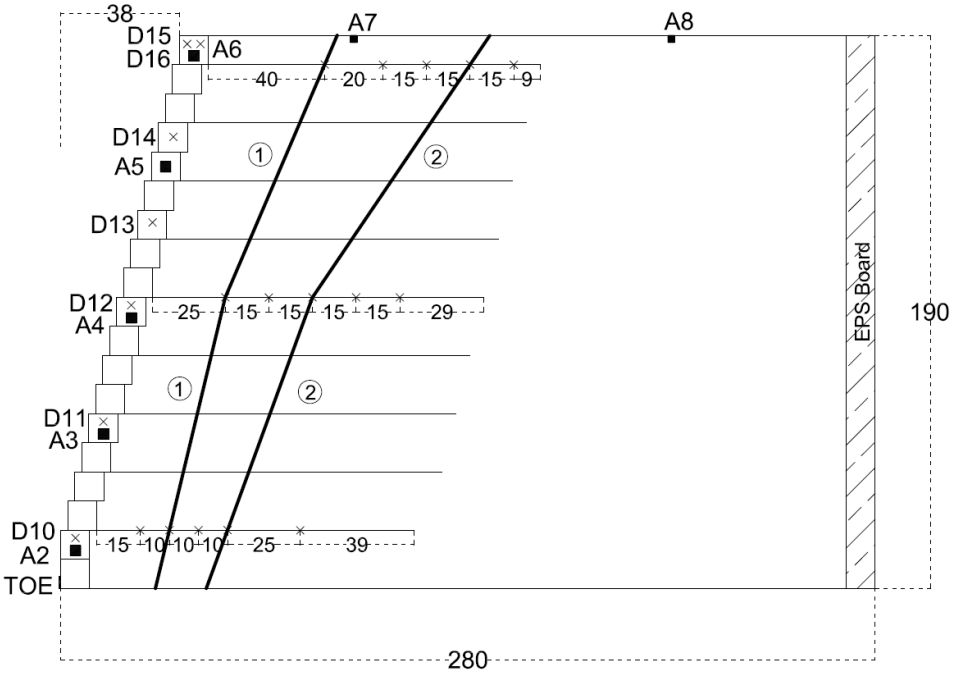

Figure 4.54. Potential Failure Planes for Setup 3 Kobe 125%.

Figure 4.55, Figure 4.56 and Figure 4.57 illustrate the potential failure surfaces of Setup 4, for Kobe 100%, Kobe 125% and Kobe 150% earthquakes. For Setup 4, Kobe 100% earthquake had a similar potential failure plane with Setup 2 parallel to facing, only difference of Kobe 125% motion was that the possible failure plane would pass from the back part of the top geogrid. Kobe 150% had potential failure indications as the significant residual outward movement of the front facing and wide tension cracks were formed on the top of backfill at unreinforced zone. So the reinforced zone was seemed to behave like a coherent body. And as a note, the secondary potential failure plane option can be evaluated as a two-wedge failure condition.

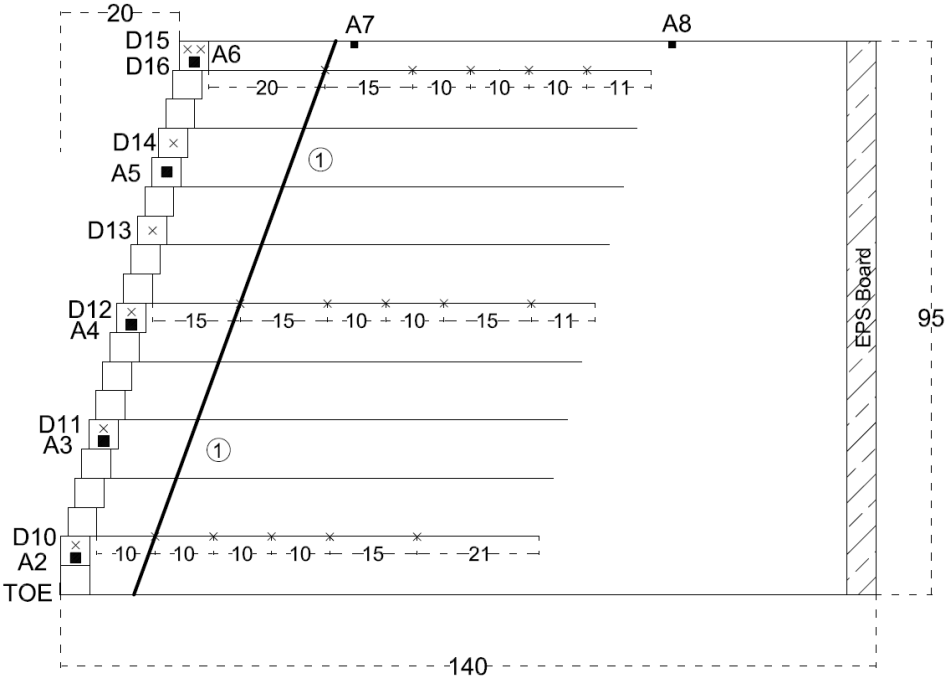

Figure 4.55. Potential Failure Planes for Setup 4 Kobe 100%.

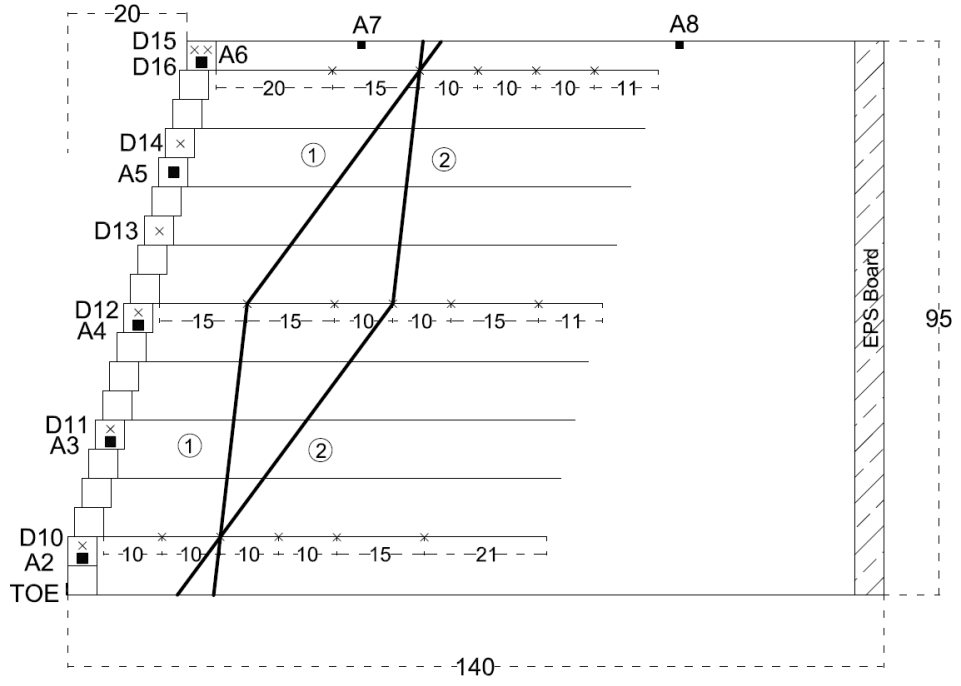

Figure 4.56. Potential Failure Planes for Setup 4 Kobe 125%.

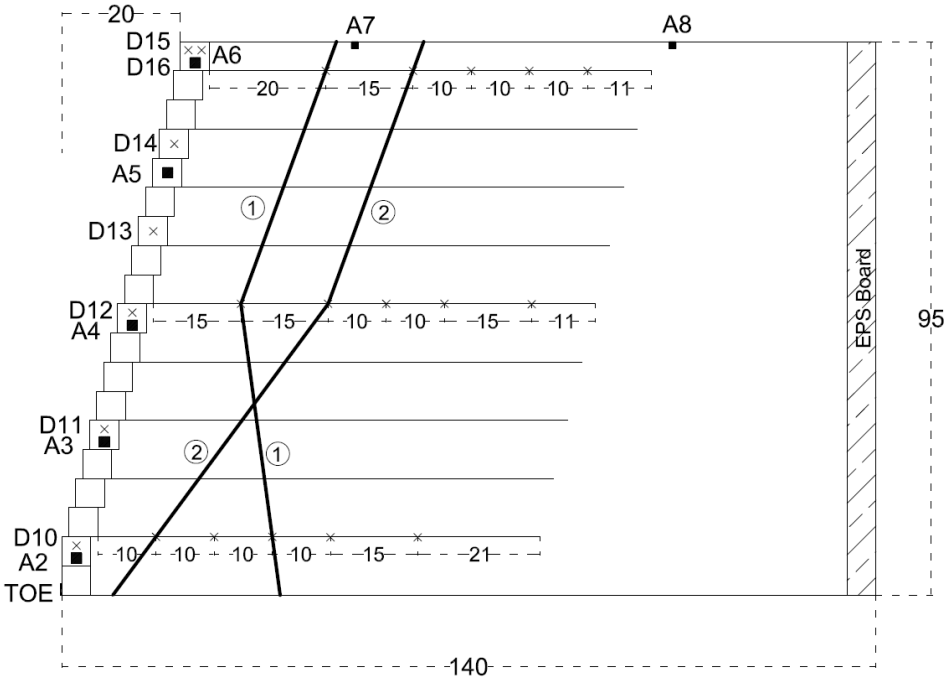

Figure 4.57. Potential Failure Planes for Setup 4 Kobe 150%.

4.5. Visual Observations

In this chapter; visual observations after application of each base excitation are given. No failure was observed considering the front facing deformations even under extreme seismic loads. Toppling of top rows of modular blocks did not occur because they were grouted in order to work as a coherent body. As a conclusion, it can be said that an apparent indication of failure was not observed and all model wall configurations performed well according to this observation.

After final seismic excitations (Kobe 100% for Setup 1, Kobe125% for Setup 2 and Setup 3 and Kobe 150% for Setup 4) surface settlements were measured for backfills of all wall configurations. Before the tests, the initial height difference between the top of the surface backfill and EPS board was obtained and after the last seismic loading final measurements were taken referred to EPS board. For Setup 1 a heave was also observed in the mid part of the top surface and related with this heave there were great surface settlements occurred behind the top blocks around 4 cm and in front of the back side EPS board 11 cm surface settlement was observed, initial depth was 6 cm final

depth was 17 cm as illustrated in Figure 4.5. This observation was an indication for a total settlement of medium-dense dry sand backfill and after each seismic excitation the backfill became denser ended up with a heave in the mid.

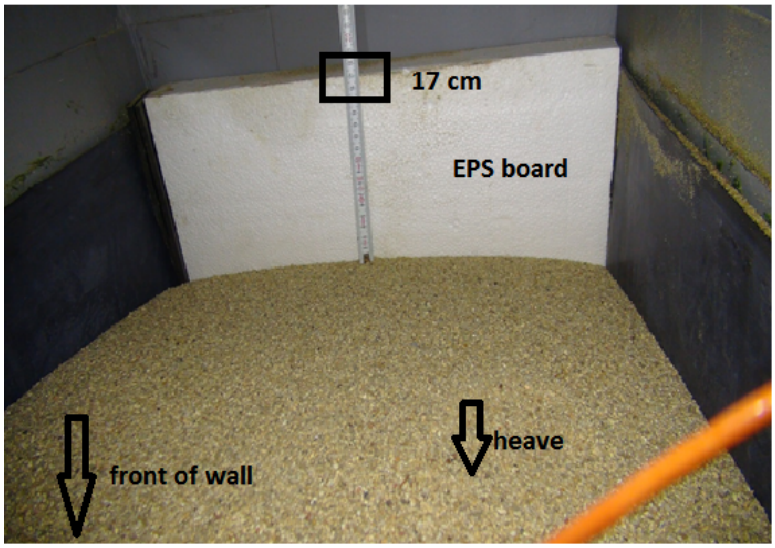

Figure 4.58. Surface Settlement for Setup 1 Including the View of Heave.

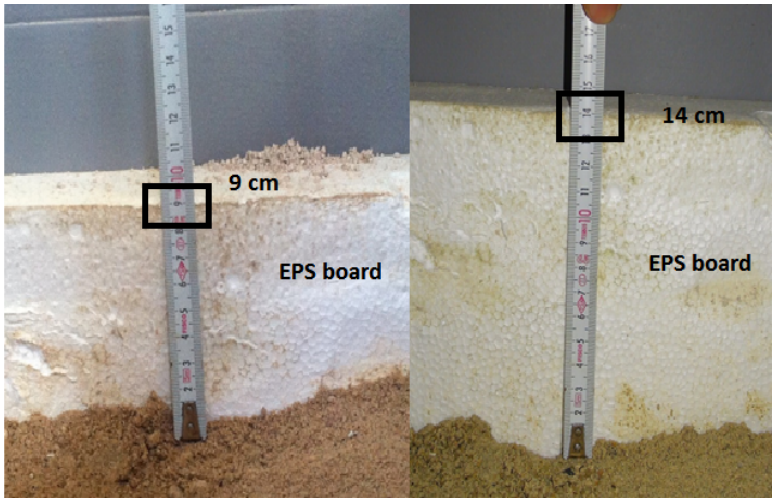

Figure 4.59. Surface Settlement Measurements in Front of EPS board for Setup 3.

For Setup 2 and Setup 3 similar surface settlements were observed after the final base excitation; 4.5 cm and 5 cm average settlements were measured in front of EPS board as the initial and final depth measurements were shown in Figure 4.59. No settlement or separation was observed behind the top modular blocks, that observation is consistent with the inwards residual deformation of top blocks.

For Setup 4 similar observations were obtained with previous models but the surface settlement was measured as 3 cm in front of EPS which was relatively high compared to Setup 2.

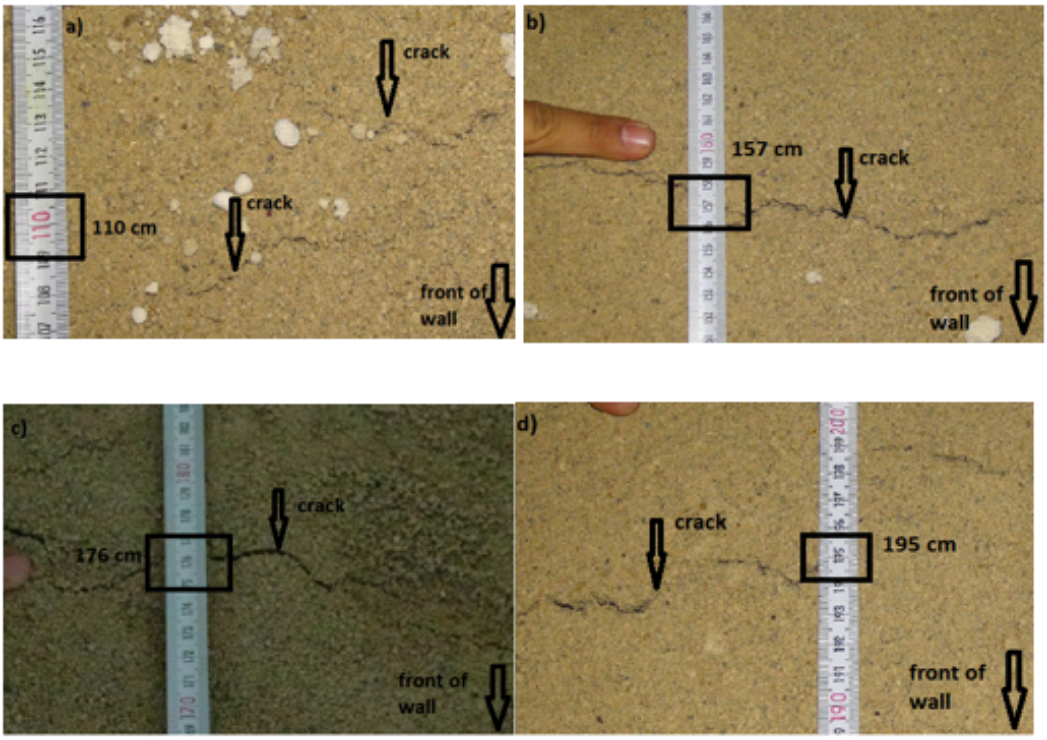

Figure 4.60. Tension Cracks Setup 2 a) 110 cm, b) 157 cm, c) 176 cm, d) 195 cm.

For cohesive backfills observation of tension cracks is an essential criterion as important as front facing failure, tension cracks were observed on the top surface of the backfill during the final seismic loadings of each wall configuration. It should be noted that before the final seismic excitations top surfaces were checked and no apparent crack was observed. For Setup 2 as illustrated in Figure 4.60, tension cracks were observed at 110 cm, 157 cm, 176 cm and 195 cm distances from the facing. A slight crack at 110 cm coincided with the end of compression-tension alternative possible failure plane as it was mentioned in Section 4.4. For Setup 2 the reinforcement ended at 152 cm and the cracks developed in the unreinforced zone.

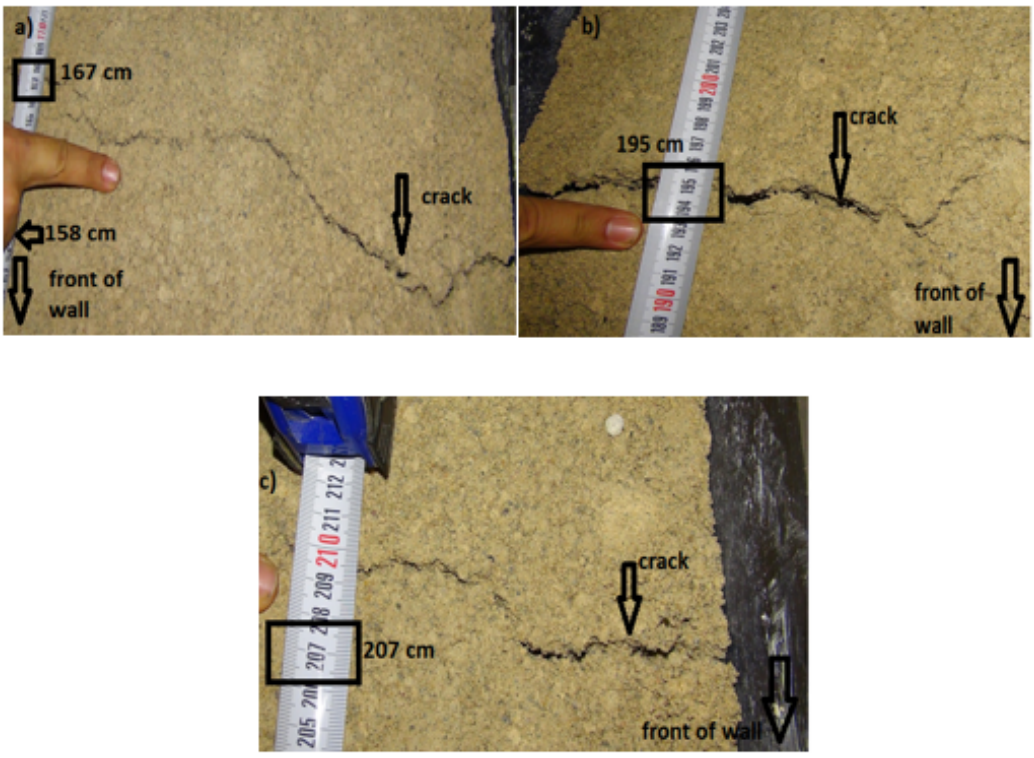

Figure 4.61. Tension Cracks Setup 3 a) 167 cm, b) 195 cm, c) 207 cm.

Figure 4.61 illustrates the tension cracks developed at the end of final base excitation Kobe 125% earthquake, For Setup 3. Tension cracks were observed at distances 167 cm, 195 cm and 207 cm from the front facing and cracks were more remarkable compared to Setup2. Reinforcement of the model wall ended at 114 cm and the cracks stayed in the unreinforced backfill.

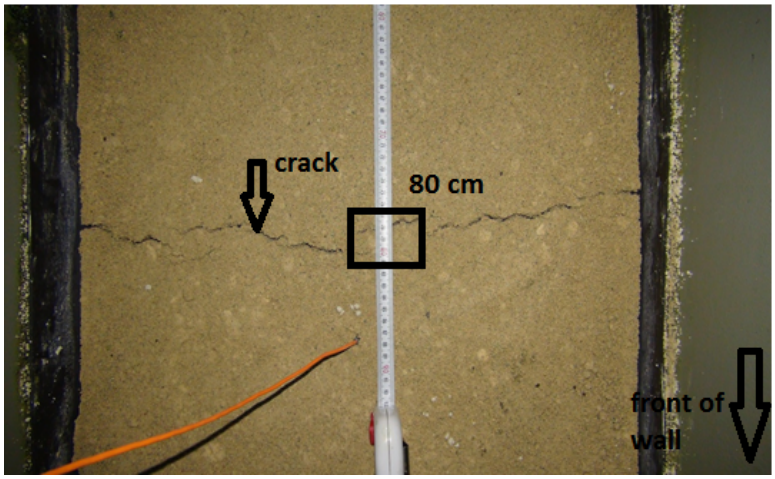

Figure 4.62. Tension Crack for Setup 4 at 80 cm.

Figure 4.62 illustrates the tension crack developed at the backfill surface of Setup 4 during Kobe 150% earthquake. One wide and deep tension crack was observed at a distance of 80 cm from the facing where the reinforcement length was 76 cm.

4.6. Design Tensile Loads

In this chapter, design tensile loads calculated according to FHWA 2001 and 2009 (Federal Highway Administration) and NCMA (National Concrete Masonry Association) regulations are represented. First the procedure of calculations for above stated regulations is explained and then the calculated tensile loads are compared with the measured values during the tests. For static loads all setups were considered but for dynamic case only Setup 1 with granular backfill was regarded for comparison. Tables in Appendix E give the detailed calculation results for the design tensile loads.

4.6.1. Calculation Procedure

The excel sheet referred to NCMA regulations was calculated according to internal stability procedures and Figure 4.63 represents the stress distribution for static load F_{stai} (Equation 4.4), dynamic load F_{dyni} (Equation 4.4) and wall inertial force increment $k_h.\Delta W_i$ components of the total design load F_i of the reinforcement as stated in Equation 4.2. ΔW_i is the weight of the facing block with length L_w and unit weight δ_w in the contributory area S_v of the corresponding reinforcement layer and calculated as in Equation 4.3.

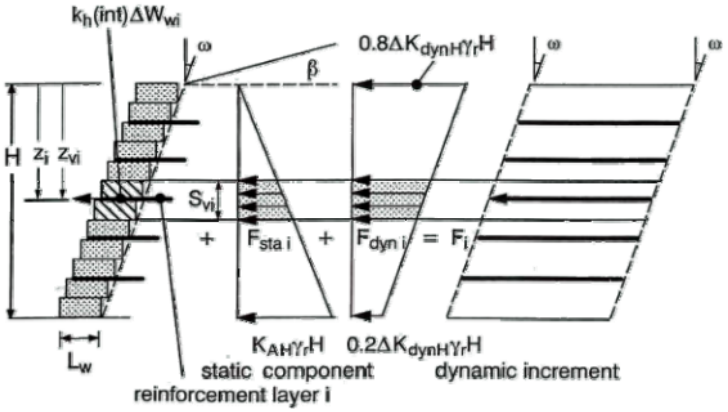

Figure 4.63. Geometry and Stress Distribution to Calculate Reinforcement Loads for Reinforced SRW Structures (Bathurst, 1998).

$$F_i = k_h \Delta W_i + F_{stai} + F_{dyni} \tag{4.2}$$

$$\Delta W_i = S_{vi} L_w \gamma_w \tag{4.3}$$

$$F_{stai} = K_{AH} \gamma_b z_{vi} S_{vi} \tag{4.4}$$

$$F_{dyni} = \left(0.8 - 0.6\frac{z_{vi}}{H}\right) \Delta K_{dynHi} \gamma_b H S_{vi} \tag{4.5}$$

Height of the wall is identified with H and the distance from the crest of the wall to the mid-elevation of contributory is defined with z_{vi}. Vertical component of the static and dynamic forces calculated from the weight of the backfill with bulk unit weight γ_b.

Bathurst and Cai (1995) proposed the total active earth pressure distribution

due to soil self-weight including static and dynamic components as in Figure 4.64. During the calculations of this study horizontal components of the pressures with the coefficients K_{AH} and ΔK_{dynH} were used.

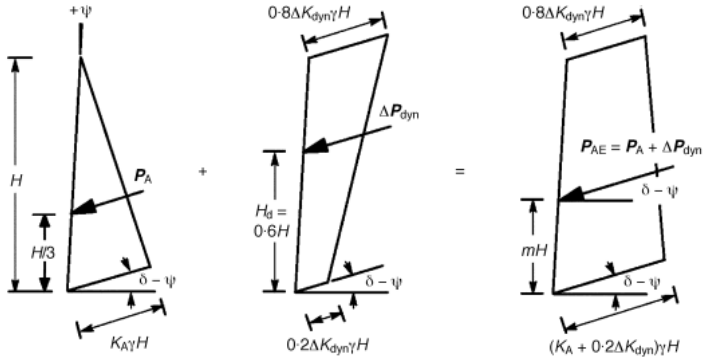

Figure 4.64. Total Earth Pressure Distribution with Static and Dynamic Components (Bathurst and Cai, 1995).

Total active earth pressure under seismic loads P_{AE} developed by the backfill soil is calculated by Equation 4.6. and the corresponding total earth pressure coefficient K_{AE} is calculated by Equation 4.7; where φ is the peak soil internal friction angle, ψ is the wall-slope face inclination (positive in a clockwise direction from the vertical), δ is the mobilized internal friction angle at the back of the wall or back of the reinforced zone (in this study taken as equal to peak soil friction angle assumed as full mobilization), β is the back slope angle and θ is the seismic inertia angle given by Equation 4.8 k_h and k_v are horizontal and vertical seismic coefficients.

$$P_{AE}=\frac{1}{2}(1\pm k_v)K_{AE}\gamma H^2 \tag{4.6}$$

$$K_{AE}=\frac{\cos^2(\phi+\psi-\theta)}{\cos\theta\cos^2\psi\cos(\delta-\psi+\theta)\left[1+\sqrt{\frac{\sin(\phi+\delta)\sin(\phi-\beta-\theta)}{\cos(\delta-\psi+\theta)\cos(\psi+\beta)}}\right]^2} \tag{4.7}$$

$$\theta=\tan^{-1}\left(\frac{k_h}{1\pm k_v}\right) \tag{4.8}$$

In the study of Seed and Whitman (1970) separated the total active earth pressure into static P_A and dynamic components ΔP_{dyn} as in Equation 4.9 and likewise in Equation 4.10, K_A the static active earth pressure coefficient and ΔK_{dyn} incremental dynamic active earth pressure can be obtained. Finally in Equation 4.11 a closed form approximate solution for the orientation of the critical planar surface from the horizontal, α_{AE} is represented. For static case active earth pressure coefficient K_A and failure plane angle α_A can be calculated with the Equation 4.7 and Equation 4.11 by excluding seismic inertia angle, θ from the formulas.

$$P_{AE}=P_A + \Delta P_{dyn} \tag{4.9}$$

$$(1\pm k_v)K_{AE}=K_A+\Delta K_{dyn} \tag{4.10}$$

$$\alpha_{AE}=\phi-\theta+\tan^{-1}\left(\frac{-A_\alpha+D_\alpha}{-E_\alpha}\right) \tag{4.11}$$

where;

$$A_\alpha=\tan^{-1}(\phi-\theta-\beta) \tag{4.12}$$

$$D_\alpha=\sqrt{A_\alpha(A_\alpha+B_\alpha)\,(B_\alpha\,|C|_\alpha+1)} \tag{4.13}$$

$$E_\alpha=1+[|C|_\alpha\,(A_\alpha+B_\alpha)] \tag{4.14}$$

$$B_\alpha=1/\tan(\phi-\theta+\psi) \tag{4.15}$$

$$C_{\alpha} = \tan(\delta + \theta - \psi) \tag{4.16}$$

According to above procedure the application of total active earth pressure PAE to the front segmental facing of the retaining wall is illustrated in Figure 4.65.

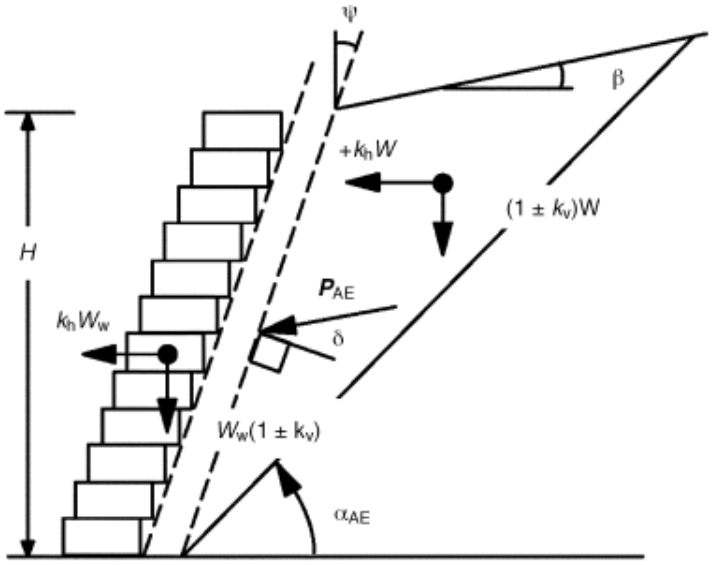

Figure 4.65. Forces in Pseudo Static Analysis of Segmental Retaining Walls (Bathurst *et al.*, 2002).

Horizontal seismic coefficient, k_h for internal stability calculations according to NCMA recommendations was calculated as,

$$k_h = \frac{PGA}{2g} \tag{4.17}$$

In order to calculate design tensile loads according to FHWA recommendations under seismic loading the inertial forces acting horizontally produced by the seismic action were added to existing static forces, T_{max} as in Equation 4.18. As it can be seen in Figure 4.66 dynamic increment in tensile forces T_{md} was caused by the inertia force P_I and it was assumed that the location and the maximum lines (potential failure plane) did not change during seismic loading so α_A was used in dynamic calculations.

To calculate P_I as in Equation 4.19 horizontal seismic coefficient, k_h described

above was used in order to compare with NCMA results and multiplied with W_A, the weight of the active zone. Total dynamic increment load distributed to reinforcements at different elevations as described in Equation 4.20 according to the active reinforcement length at that elevation L_{ai}. In FHWA 2009 recommendations T_{md} is distributed to the reinforcements equally.

$$T_{max}=K_{AH}\,\sigma_v\,S_{vi} \tag{4.18}$$

where K_{AH} is the horizontal earth pressure coefficient calculated for reinforced zone, σ_v is the total vertical including soil self-weight.

$$P_I = A_M\,W_A \tag{4.19}$$

$$T_{md}=P_I\frac{L_{ai}}{\sum_{i=1}^{n} L_{ai}} \tag{4.20}$$

$$T_{total}=T_{max}+T_{md} \tag{4.21}$$

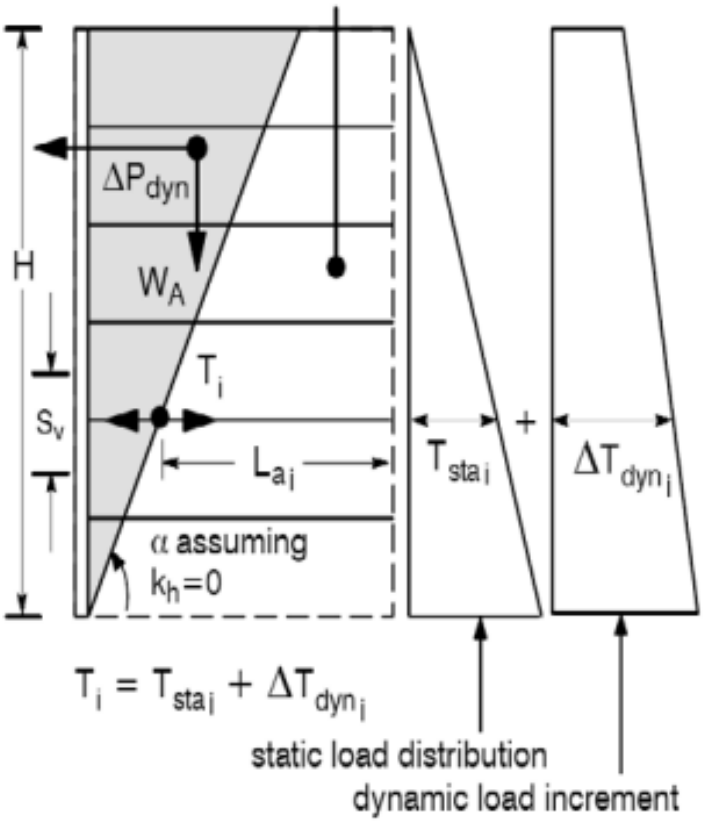

Figure 4.66. Load Distribution and Tensile Loads According to FHWA Method (Bathurst and Alfaro, 1996).

4.6.2. Comparison of Measured and Design Tensile Loads

Measured tensile loads obtained from the strain values on bottom, mid and top geogrids were compared with the design tensile loads calculated according to FHWA (2001 and 2009) and NCMA codes. For static loading all three methods gave the same result and also the results for Setup 2 and Setup3 were same because of the same vertical loads due to soil self-weight stress. The effect of cohesion was not considered in both dynamic and static cases in the design codes, in this study as given in Table 4.20. The alternative static load including cohesion effect was calculated as subtracting the load resulted from cohesion as a uniform cohesive stress distribution along the wall height. And this stress value was calculated by multiplying cohesion value (25 kPa), earth pressure horizontal coefficient (K_{AH}) and reinforcement spacing. Table 4.19 represents the measured static tensile loads after construction (with E=570 kPa). When these

two tables are compared it seems that these values are not consistent with each other especially the cohesion effect creates greater differences between the results. The reason for that may be the calculated ones are the result of a vertical stress distribution due to soil weight where the measured ones include the effects of all construction procedure especially soil compaction procedure.

Table 4.19. Measured Static Tensile Loads.

Tensile Loads (kN/m)					
Strain Gauge No	SETUP1	SETUP2	SETUP3	SETUP4	
S1	0.24	0.56	0.76	0.23	Top
S2	0	0.73	0.92	0.17	
S3	0.86	1.35	1.29	0.5	
S4	1.21	1.18	1.32	0.51	
S5	1.16	0.86	1.2	0.36	
S6	0.94	0.92	1.07	0.41	
S7	1.6	1.59	1.17	0.47	Mid
S8	0	1.7	1.76	0.71	
S9	1.92	1.94	1.83	0.85	
S10	1.79	1.77	2.18	1.09	
S11	0.69	0.93	0.84	0.63	
S12	1.18	2.09	1.78	0.78	Bottom
S13	1.41	1.6	2.35	0.52	
S14	2.15	2.36	2.47	1.15	
S15	2.03	2.31	2.38	1.3	
Average	0.7	0.94	1.1	0.36	Top
	1.25	1.59	1.6	0.7	Mid
	1.49	1.86	1.96	0.88	Bottom

Table 4.20. Calculated Static Design Tensile Loads with NCMA and FHWA.

	SETUP1	SETUP 2 and SETUP 3		SETUP 4	
	w/o cohesion	w/o cohesion	with cohesion	w/o cohesion	with cohesion
Top	0.036	0.09	-1.083	0.022	-0.564
Mid	0.327	0.806	-0.366	0.202	-0.385
Bottom	0.773	1.904	0.438	0.476	-0.257

Dynamic design tensile loads were calculated by NCMA and FHWA for Setup 1 with granular soil backfill. Because the cohesive soils were not considered in these design manuals, design tensile loads were not taken into account for other setups. After construction phase and before each seismic action strain measurements were set to zero so the measured tensile loads were referring the performed dynamic increment only. Design tensile loads were only resulted from dynamic increments; wall inertia forces and static forces were not included. As it can be seen from the tables of Appendix E results from the alternative potential failure plane with angle aAE (considering seismic effect for the potential failure plane angle) were also reported, that is not actually mentioned in FHWA regulations.

Figure 4.67 and Figure 4.68 illustrate the measured and calculated design tensile loads for Kobe 75% and Kobe 100% respectively for Setup 1. Comparison for average and maximum measured tensile loads from top, mid and bottom geogrids and their corresponding calculated design load values with FHWA (2001 and 2009) and NCMA were considered. Only the last two highest seismic actions were considered because the lower ones did not give significant load values.

It can be observed from the figures that maximum measured tensile loads were always higher than FHWA results. But the more important result is that the stress distribution given in NCMA for dynamic load increment was not compatible when it was compared with the measured ones. Because the top geogrids always had lower tensile strains than bottom geogrids during the tests. FHWA (2001) gave better results because it regards a potential failure plane angle which resulted with a potential failure

wedge and effective geogrid length.

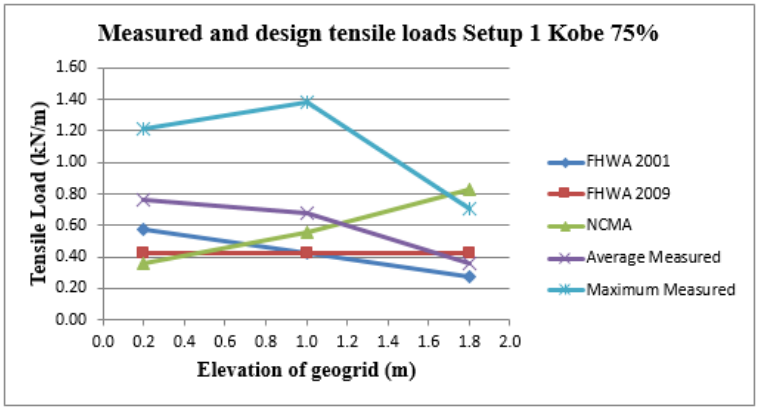

Figure 4.67. Design and Measured Tensile Loads for Setup 1 Kobe 75%.

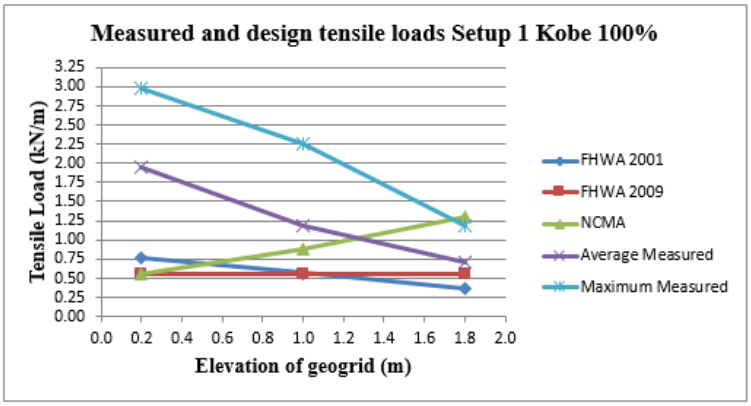

Figure 4.68. Design and Measured Tensile Loads for Setup 1 Kobe 100%.

In the tensile load calculation methodology of both FHWA and NCMA regulations, cohesion effect is not included and the calculation methods are adjusted for granular soils. Without cohesion and with low friction angles, realistic results could not be reached for the calculations of lateral pressure coefficients and potential failure plane angles. Also measured tensile loads were higher on the bottom geogrids inside cohesive backfill soils and that distribution would not be consistent with NCMA recommendations which calculated the lowest tensile load on bottom geogrid layer for seismic loading.

5. CONCLUSION

In this study the seismic performance of geosynthetic reinforced retaining walls with cohesive backfills were investigated. The results obtained from the four shaking table tests performed for three 1/2 scaled and 1/4 scaled model walls were evaluated to investigate the effects of backfill type (one granular backfill Setup 1 was tested as a control sample), the influence of reinforcement length (Setup 2 and Setup 3 were compared) and the scaling effects (Setup 2 and Setup 4 were compared).

Peak acceleration values and corresponding amplification factors represented a great difference between positive and negative directions. It was observed that this tendency had an effect on the relative displacements of the facing especially on the residual displacements. The main reason for that was the accelerations aimed to be applied by the control unit of shaking table were different from the measured accelerations on the shaking table, especially for inward direction.

For all setups the maximum accelerations occurred on the top of the front facing. The amplification factors at the backfill's top surface were lower than the top of the facing. This can be explained by the condition that the soil mass and the facing did not move monolithically where the movement of the interior soil mass was more constrained than the facing. It was observed that the amplification factors in the reinforced zone were larger than those in the backfill soil. This can be attributed to the lower stiffness of the backfill zone since loose soils have better damping characteristics.

The amplification factors of dry sand backfill wall was greater than the cohesive backfill counterparts for the front wall and this outcome is consistent with the relative displacements of these walls. In this study for cohesive backfills there was an increase for amplification factors after 0.9g for positive direction and 0.6g for negative direction but an incremental amplification increase was observed for every base input excitation. This result was in contradiction with the results of the study of Başbuğ (2011) where they observed an input base acceleration value, 0.56g after which the amplification

factors tended to increase significantly. A critical acceleration threshold (the limit acceleration after that amplification factor does not increase with increasing input acceleration) was not observed in this study. This may be caused by the fact that large soil shear deformations did not occur in the backfill which could have causing softening and strength degradation.

Amplification factors recorded for Setup 3 with 0.6 L/H reinforcement length were slightly higher than the values recorded for Setup 2 with 0.8 L/H reinforcement length. This tendency was also compatible with the influence of reinforcement length on relative displacements of walls. This result is not consistent with the observation of Allen and Bathurst (2002) who stated that the amplification factors increased by increasing the reinforcement length and the global stiffness (sum of the layer stiffness values divided by the height of the wall).

Inward and outward movements along the wall heights indicated that the walls behaved elastically under all seismic actions. The largest peak displacements occurred at the top blocks and the distribution increased almost linearly along the wall height for higher base accelerations. During seismic loading no significant residual displacement value was recorded and no failure condition on the facing was observed. Front facing displacement values increased in both directions with increasing base input motion as expected.

For Setup1, inward movement of the wall was greater than outward movement for the first two seismic actions. This behavior can be explained with the following thought: the backfill was medium-dense sand that compacted during excitation so the wall was moving inwards. Peak relative displacement values in both directions of the dry sand backfill wall were higher than the corresponding displacement values of the walls with cohesive backfill under same base input displacements.

For Setup2 and Setup3 it can be said that reinforcement length did not create a significant effect on wall behavior such as peak and residual displacement values were almost same but Setup3 with shorter reinforcement had slightly higher facing

deformations.

General displacement behavior character of the model walls can be summarized as follows. The outward movement tends to increase gradually along the wall height but the inwards movement reached its peak values at the top of the wall. Positive values were smaller at the bottom and mid heights of the wall where they became equal with negative direction at the wall top. So peak relative displacement gap between these opposite directions was closed at the top. Residual displacement configuration along the wall height could give evidence about the potential failure types although they were relatively small values (4-5 mm) compared to peak displacement values (30-35 mm) (they were smaller than the 20% of the peak values at most). As a result of the mentioned peak displacement behavior, residual displacements of the top blocks were inwards and the peak residual values were observed at the mid of the wall. This residual behavior can be associated with the possible failure mechanism that would occur in the reinforced zone (internal) which induced a bulging (swelling) shape at the mid of the wall.

For Setup 4, up to Kobe 125% earthquake any significant peak displacement values were not observed in both directions but during the Kobe 150% earthquake a large movement has occurred in the outward direction. This setup was the ½ times scaled version of Setup 2 and when the displacement results of the model walls Setup 2 (½ scaled) and Setup 4 (¼ scaled) were enhanced to the prototype (displacement values were multiplied by two and four respectively) it was found out that ¼ scaled model resulted in lower displacement values than the ½ scaled models. Because for example for 125% earthquake, peak displacement values of Setup 4 were five times smaller for outward direction and 6-7 times smaller for inwards than the results of Setup 2. This result made scaled models unreliable because they were acting more rigid than expected and this situation is an outcome of the cohesive characteristic of the backfill.

Tensile and compressive strains were observed together during base excitation indicating that the pressure wave propagation generated compression and tension zones

inside the backfill. For Setup 2 and Setup 3; compressive strain values were higher at top geogrid that can be explained by, higher peak inward movement and inward residual displacements at top blocks of facing. For mid reinforcement compressive strain values reached half of the tensile strains where at the bottom geogrid they could just reach one third.

At the end of base excitation residual strains were observed both in compression and tension reflecting the remaining condition of the backfill in terms of tension and compression zones developed in the soil. The ratio of residual and peak strains were about 1/10 for high amplitude seismic loads and these values can't be regarded as meaningful pressure zones when calculated stress values compared with the capacity of the geogrid, but the transitions between these permanent zones may be an evidence for the potential failure plane. Also at the bottom geogrid, compressive residual strains were observed at the strain gauge closest to facing, where a residual compression zone was expected just behind the fixed toe of the wall.

With increasing amplitude of base excitations strain values increased especially at bottom geogrids, top reinforcements always experienced the lowest tensile forces. The maximum of peak and average strains were observed at the bottom geogrid layer, the difference between bottom and middle geogrid layers decreased with decreasing base acceleration amplitude, for average strain values. While high overburden stresses created strains on bottom geogrids, high tensile strains were generated on mid-height geogrids because of both overburden stresses and higher outward displacement values.

The distribution of strains on the bottom layers created a more apparent peaked curve than at the mid and bottom layers. Mid and bottom geogrid layers had generally a linear increase trend as lower at the end and higher at the facing, for strain values along the reinforcement. Development of high strains at a very close distance to the facing may also have been resulted from reinforcement restraining effect.

Shorter reinforcements were exposed to higher tensile loads for internal stability and also higher outward and inward elastic displacements of front wall. These larger dis-

placements also created higher strains during seismic action. So as a summary, higher strains were recorded in Setup 3 compared to Setup 2. It was mentioned that the cohesive backfill performed better than the dry backfill according to the peak displacement values measured for Setup 1 compared to Setup 2 during Kobe 100% earthquake. In the model with cohesive backfill lower displacements and consecutively lower strains were measured. Therefore it can be stated that the geogrid functioned properly within the cohesive backfill. But with this incomparable displacement results the performance of geogrids could not be directly determined. Setup 1 for Kobe 100% earthquake and Setup 2 for Kobe 125% earthquake had more comparable peak displacement values for the mid upper part of the wall. And it can be seen that Setup 2 had almost equal even slightly higher strain values compared to Setup 1 for these closer displacement values. And this result could confirm that, geogrid reinforcement in cohesive backfill could perform as well as in sand backfill. In this study these lines were accepted as predicted potential failure planes indicating the locations on the reinforcements during a possible internal failure that might occur in the reinforced zone.

Potential internal failure surfaces were formed by joining the locus points of the maximum tensile strain values on the geogrids. Where the maximum compressive strains had another locus point, this point was also considered as secondary potential failure line. In this study these lines were accepted as predicted potential failure planes indicating the critical locations on the reinforcements during a possible internal failure that might occur in the reinforced zone. For Setup1; the potential failure condition described by two wedge theory observed for Kobe 50% and 100% earthquakes. Similar strain distributions and possible failure conditions were observed for Setup 2 and Setup3 consistent with their similar wall displacement behavior. Increase in amplitude of the seismic excitation caused the potential failure plane to move away from the facing, which means an increase in the area of active zone wedge and an increase for the coherent body of the reinforced soil. At the base, the failure plane always intersected the bottom geogrid at a point close to toe of the wall but in the upper parts of the wall failure plane moved away from the facing into the backfill. Setup 4 showed a potential failure behavior similar to the residual outward movement of the front facing. Wide tension cracks were formed on the backfill surface at unreinforced zone during

Kobe 150%. The reinforced zone tended to move as a coherent body according to the observed potential failure plane.

Finally measured tensile loads were compared with design tensile loads calculated according to FHWA and NCMA for all setups considering static loads. But for dynamic case only Setup 1 with granular backfill was considered for comparison, because effect of cohesion was not taken into account in these design manuals. For static case, measured and calculated stress values were not consistent. Calculated tensile stresses were result of the vertical stress distribution due to soil weight where the measured stresses indicated the effects of all construction procedure especially soil compaction procedure. For dynamic loading, results calculated by FHWA (2001) were better than the other methods although maximum measured tensile loads were always higher than FHWA results. The stress distribution among the geogrid layers obtained from NCMA calculations was totally different from the measured results. Quite higher strain values were measured on bottom geogrids compared to top geogrids during seismic motions where the NCMA accepted an exactly opposite stress distribution condition.

As the most outstanding result it can be said that; the model walls with cohesive backfill performed well under seismic loading conditions when compared with granular backfills and checked with the limit design values described in previous studies and codes. This result is a general comment made according to the evaluations of acceleration amplifications results, peak and residual displacement results, strain and tensile load results on geogrids and resulting potential failure planes and conditions.

APPENDIX A: ACCELERATION TIME HISTORY GRAPHS OBTAINED FROM THE TESTS

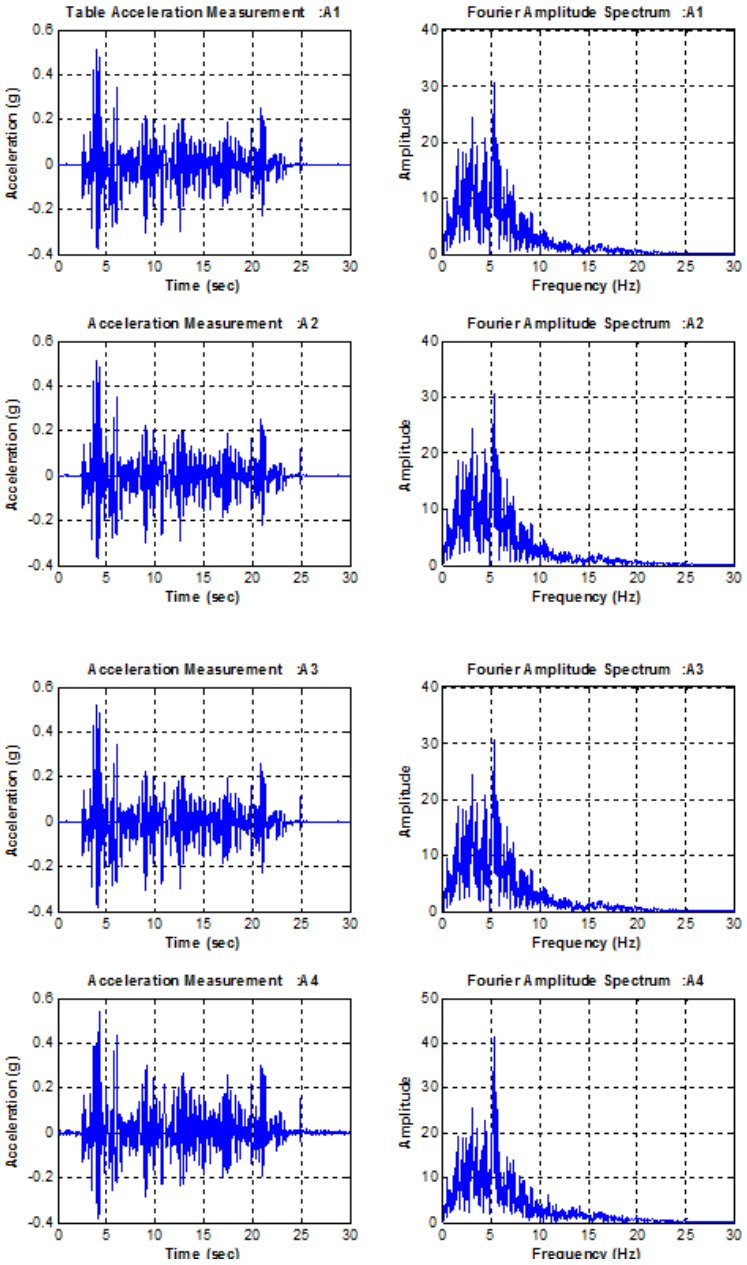

Figure A.1. Acceleration Time History Graphs for Setup 1 El Centro 100%.

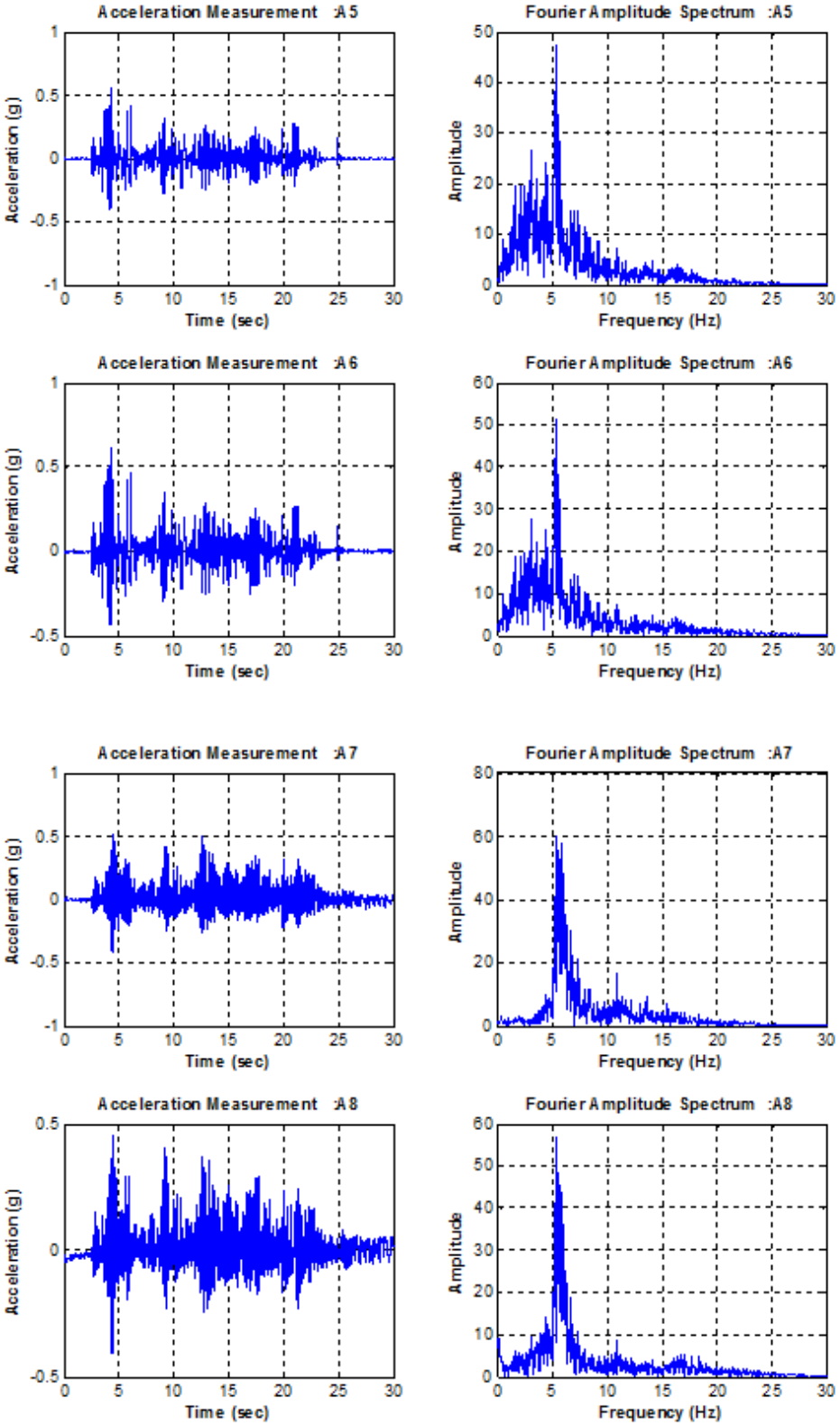

Figure A.2. Acceleration Time History Graphs for Setup 1 El Centro 100%.

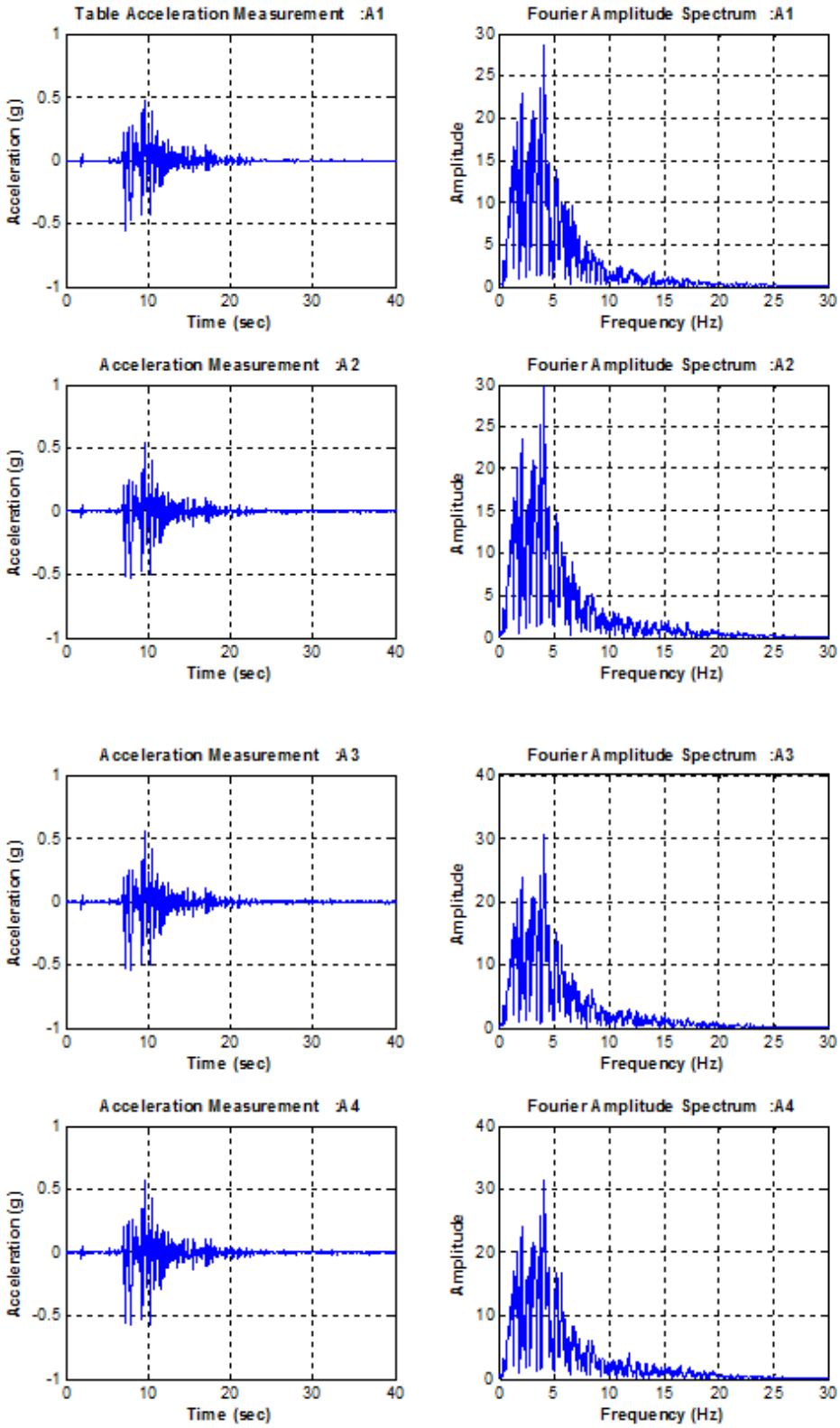

Figure A.3. Acceleration Time History Graphs for Setup 1 Kobe 50%.

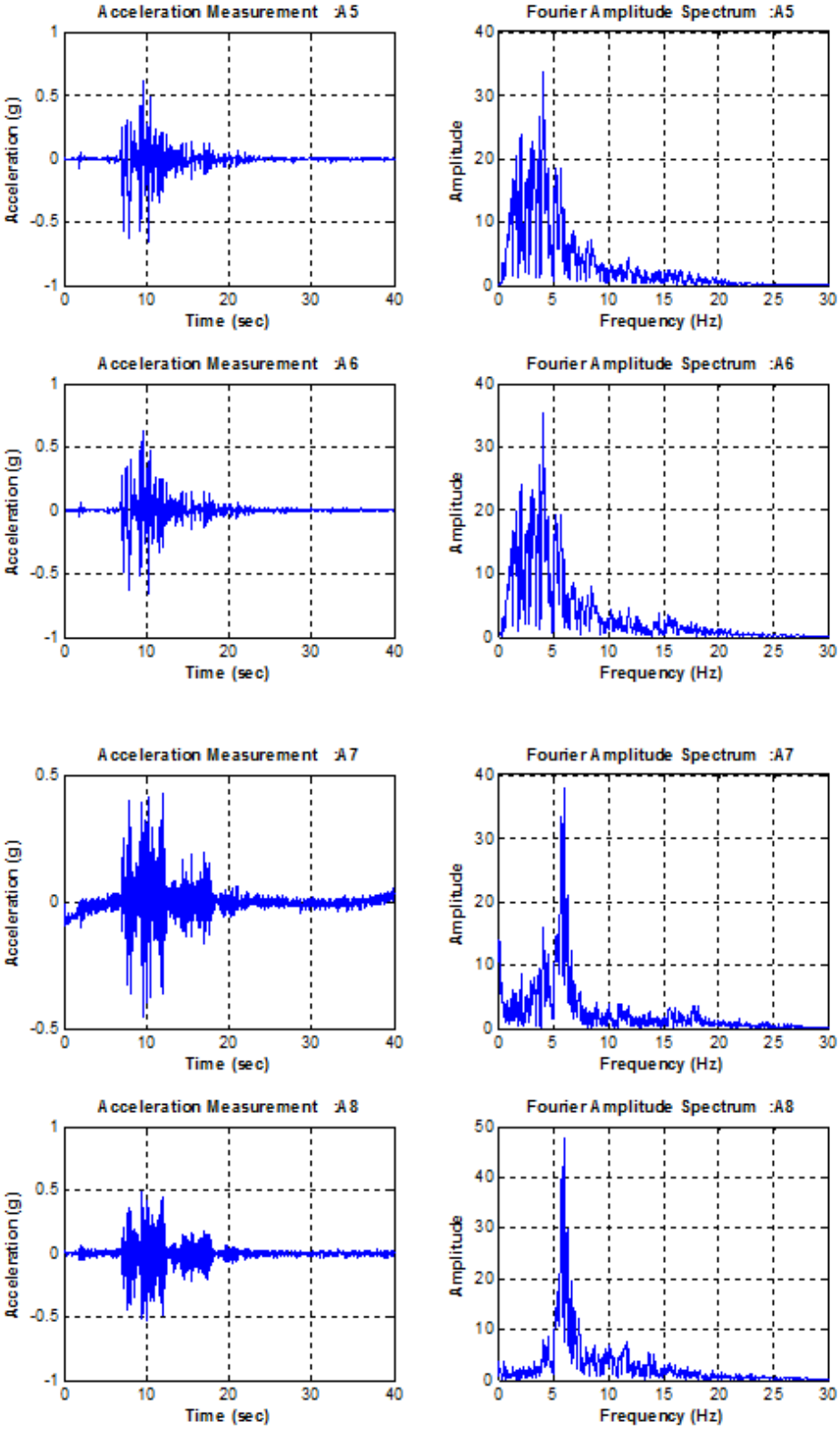

Figure A.4. Acceleration Time History Graphs for Setup 1 Kobe 50%.

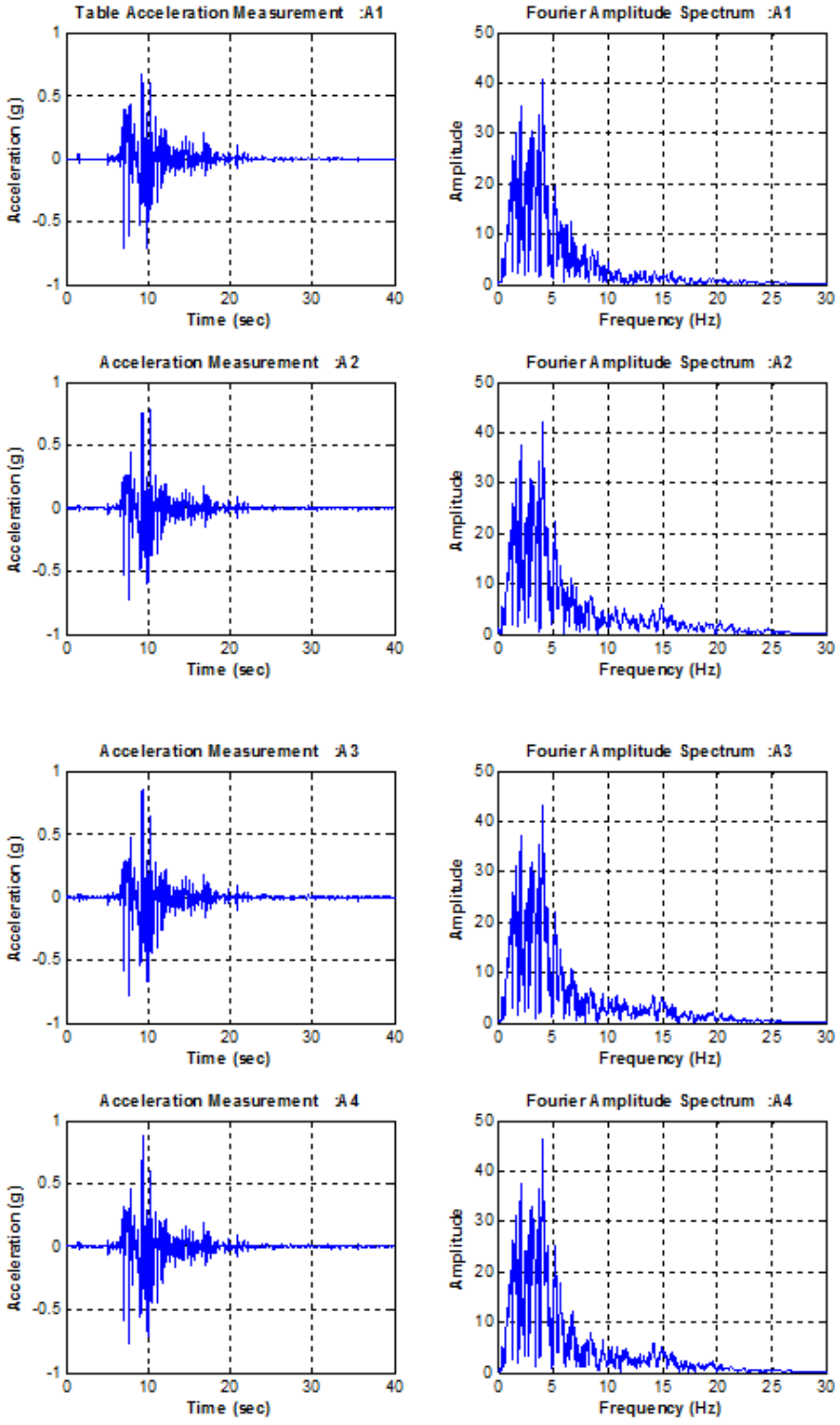

Figure A.5. Acceleration Time History Graphs for Setup 1 Kobe 75%.

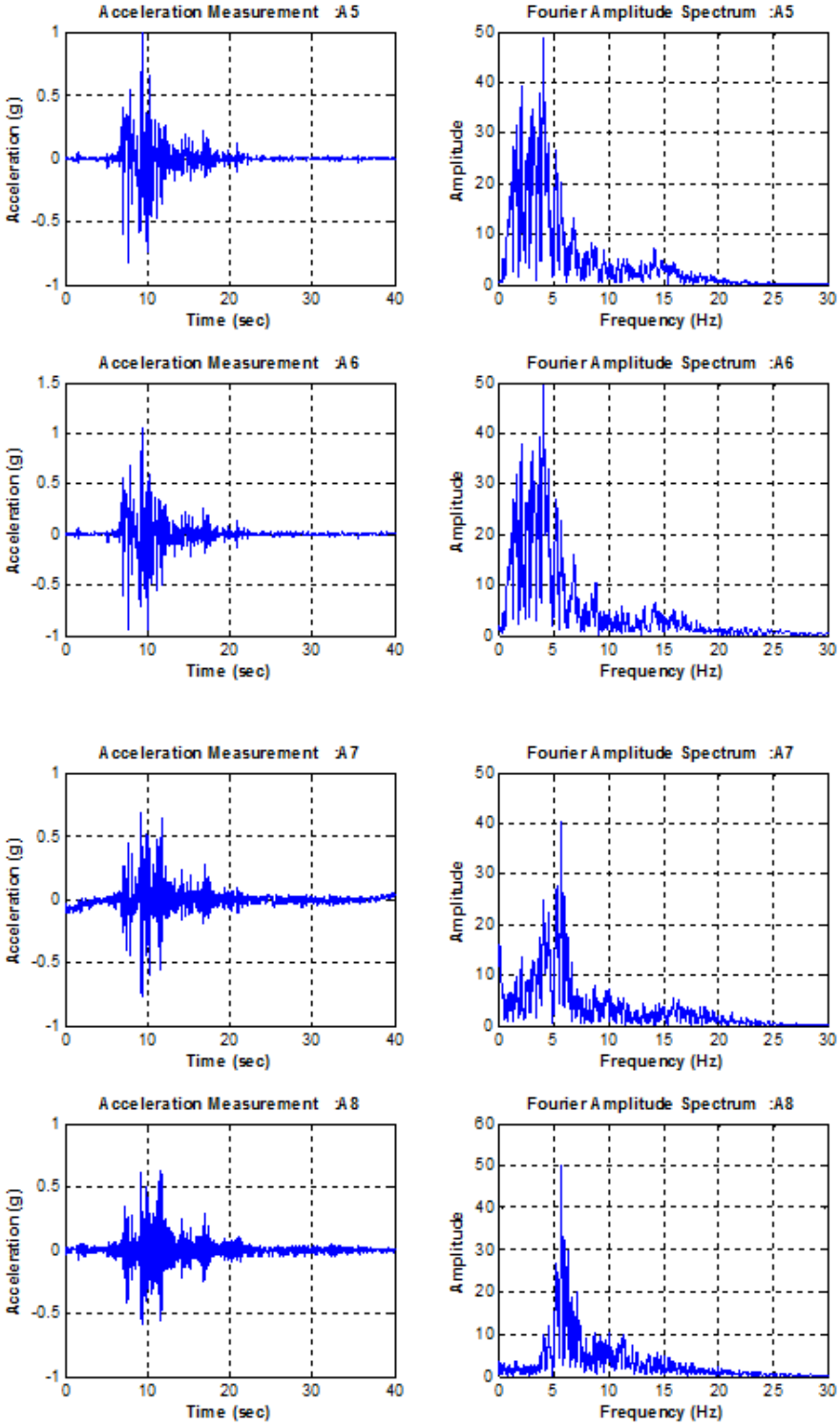

Figure A.6. Acceleration Time History Graphs for Setup 1 Kobe 75%.

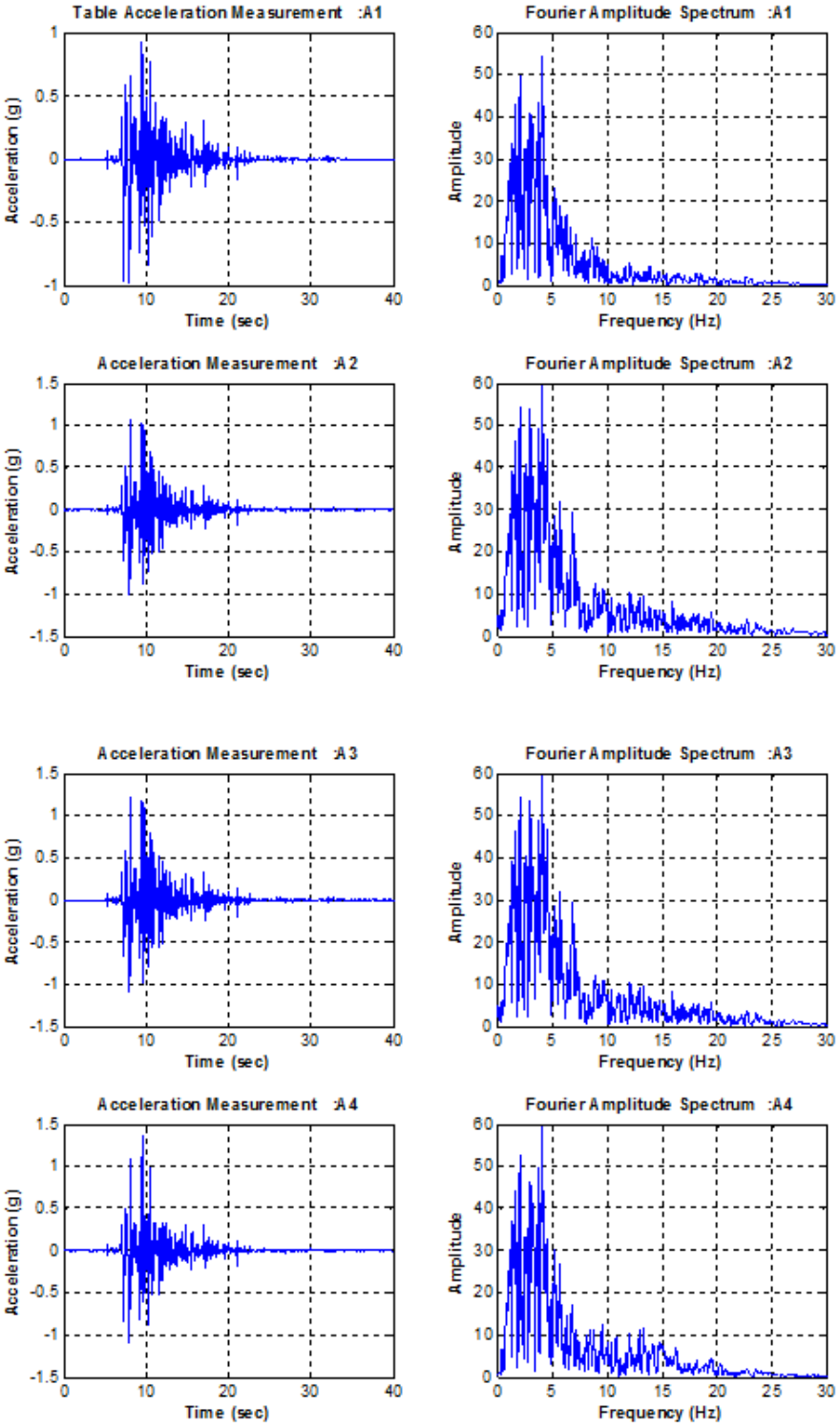

Figure A.7. Acceleration Time History Graphs for Setup 1 Kobe 100%.

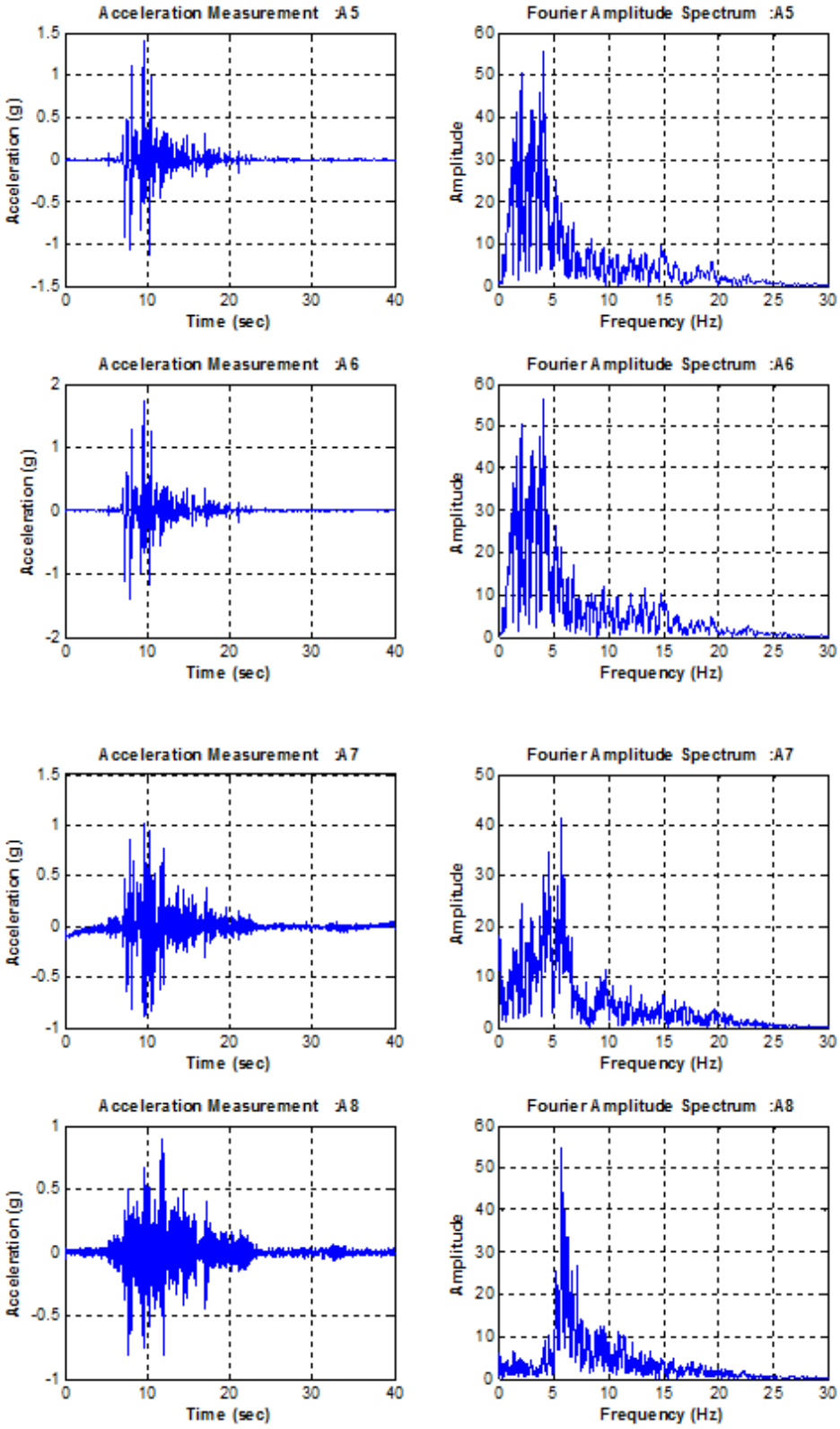

Figure A.8. Acceleration Time History Graphs for Setup 1 Kobe 100%.

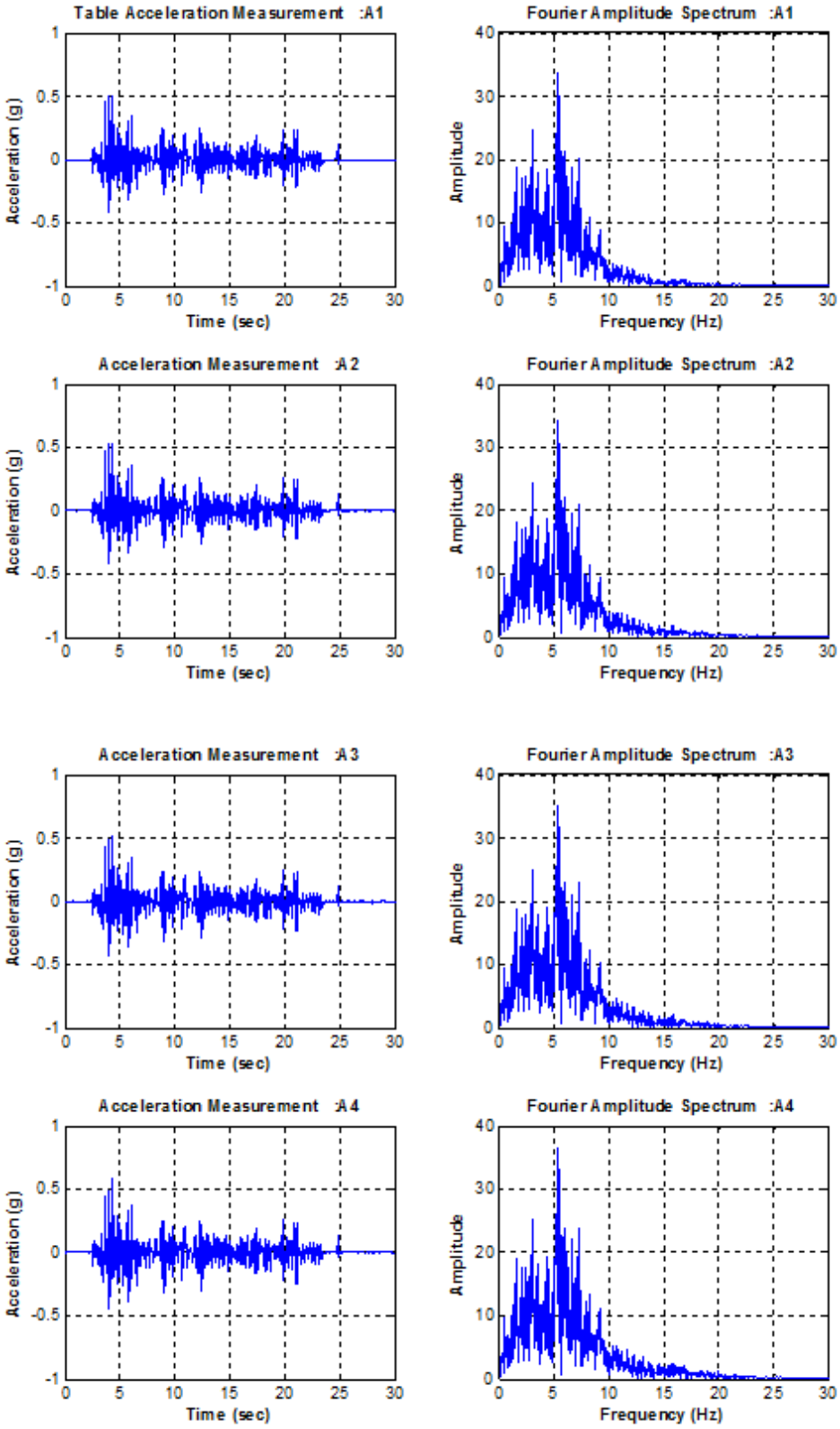

Figure A.9. Acceleration Time History Graphs for Setup 2 El Centro 100%.

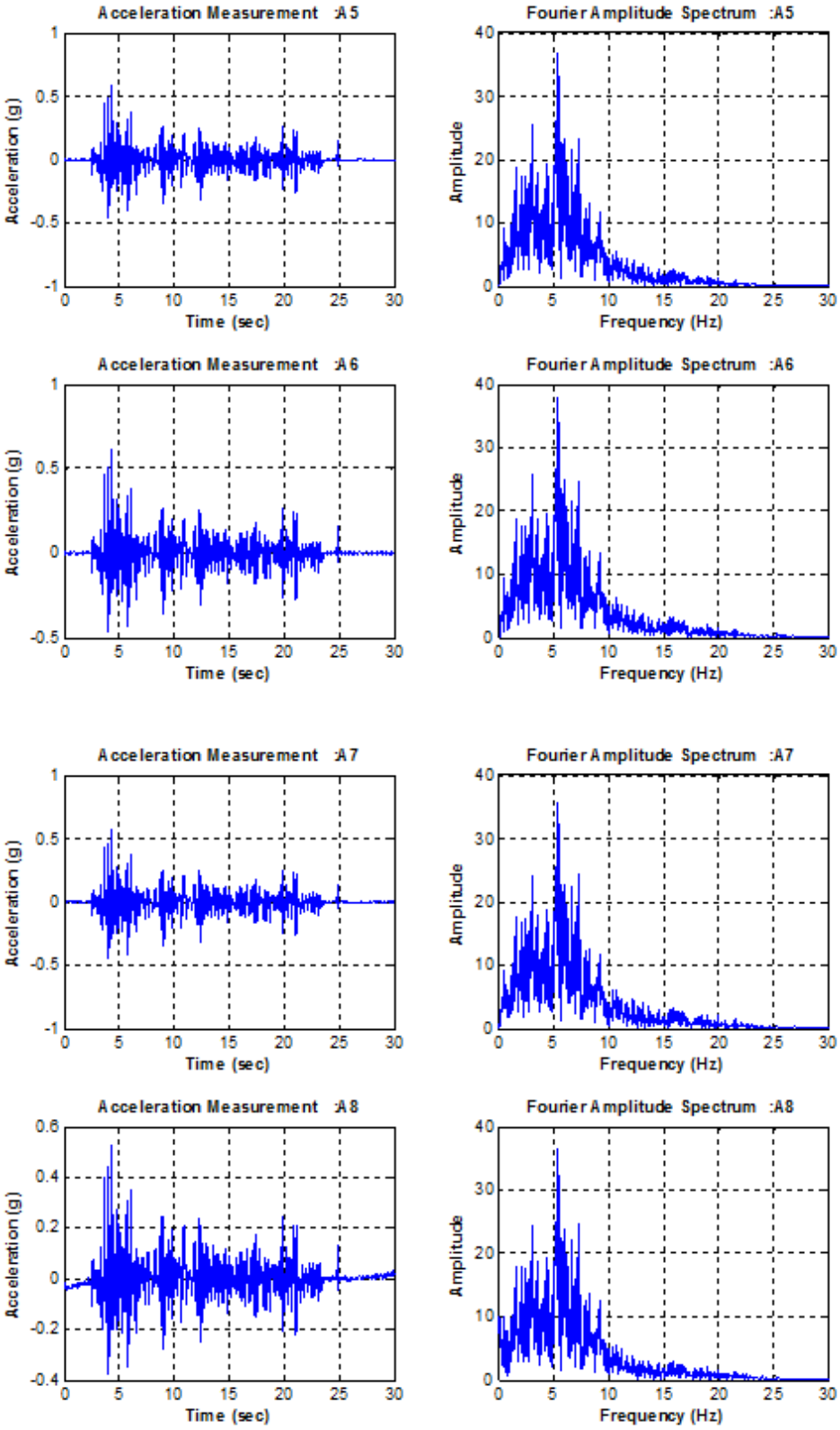

Figure A.10. Acceleration Time History Graphs for Setup 2 El Centro 100%.

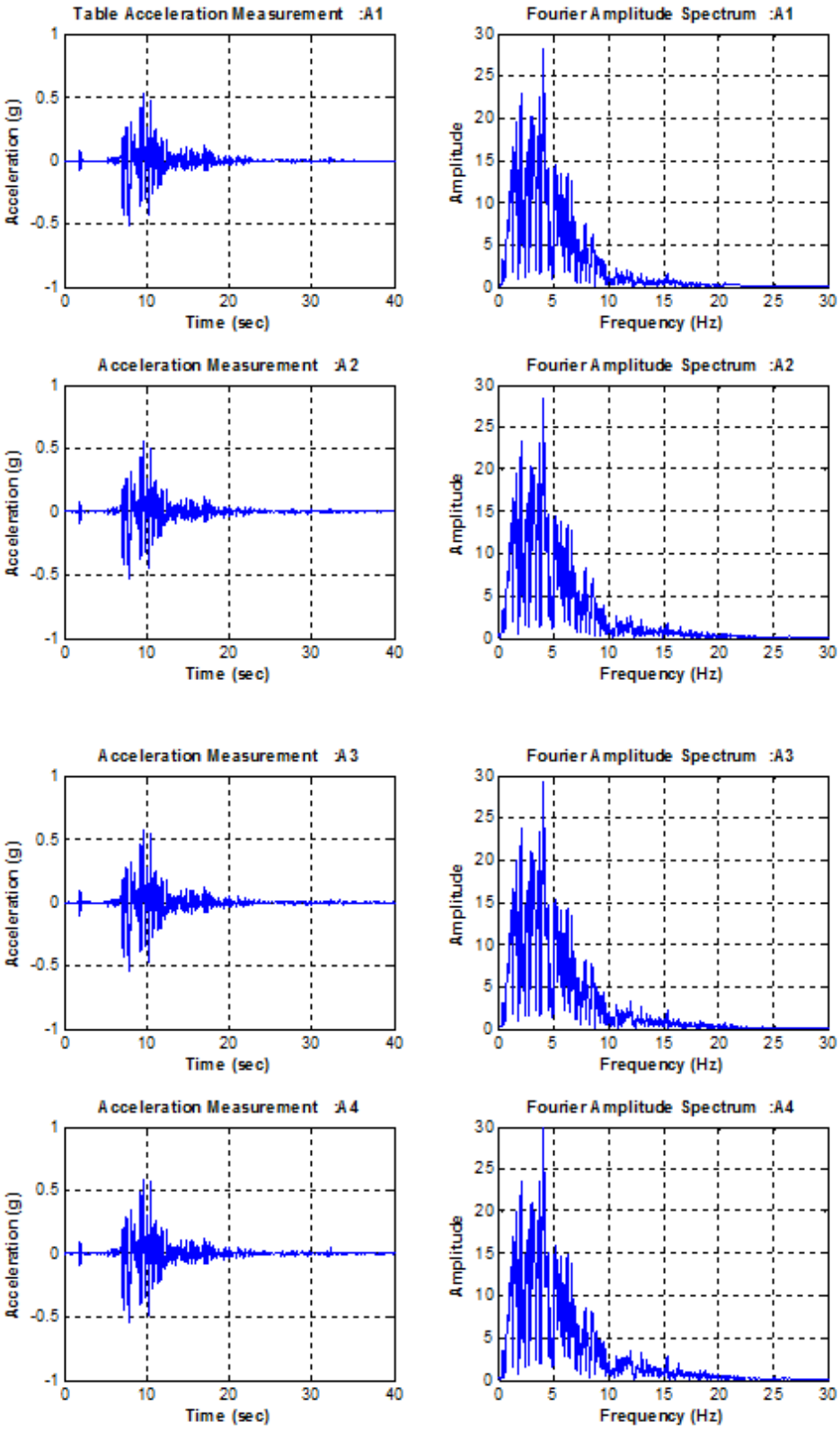

Figure A.11. Acceleration Time History Graphs for Setup 2 Kobe 50%.

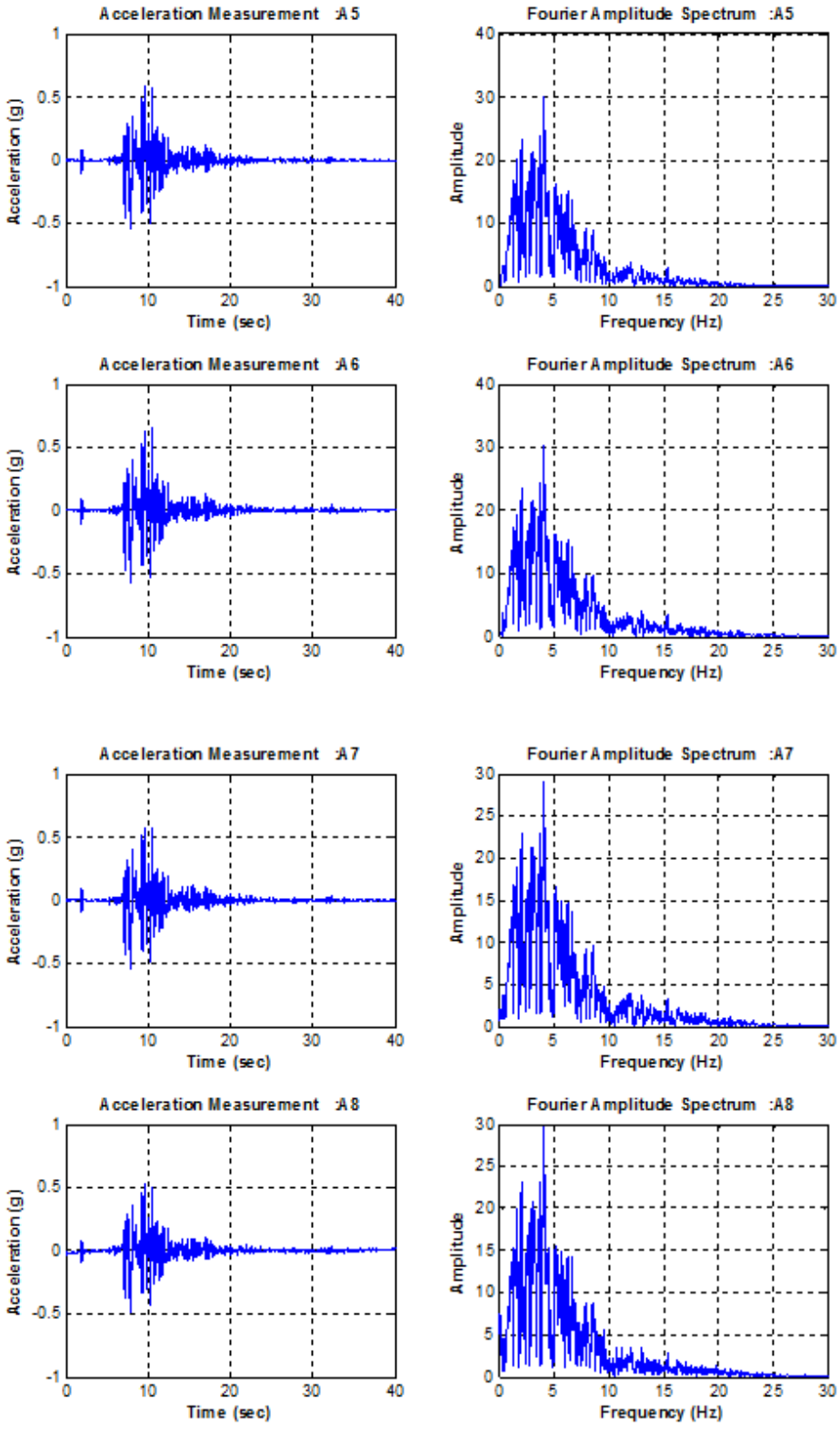

Figure A.12. Acceleration Time History Graphs for Setup 2 Kobe 50%.

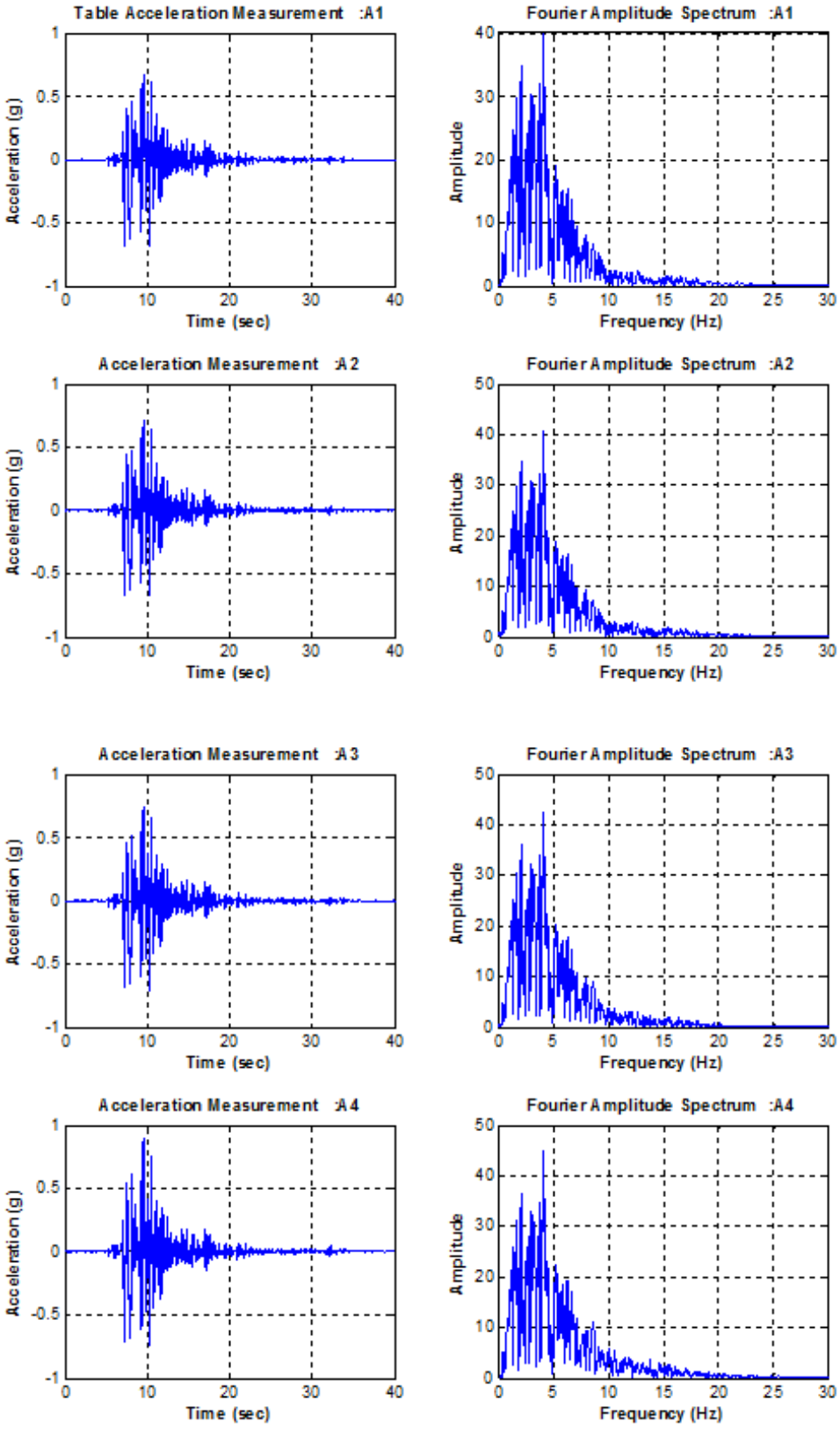

Figure A.13. Acceleration Time History Graphs for Setup 2 Kobe 75%.

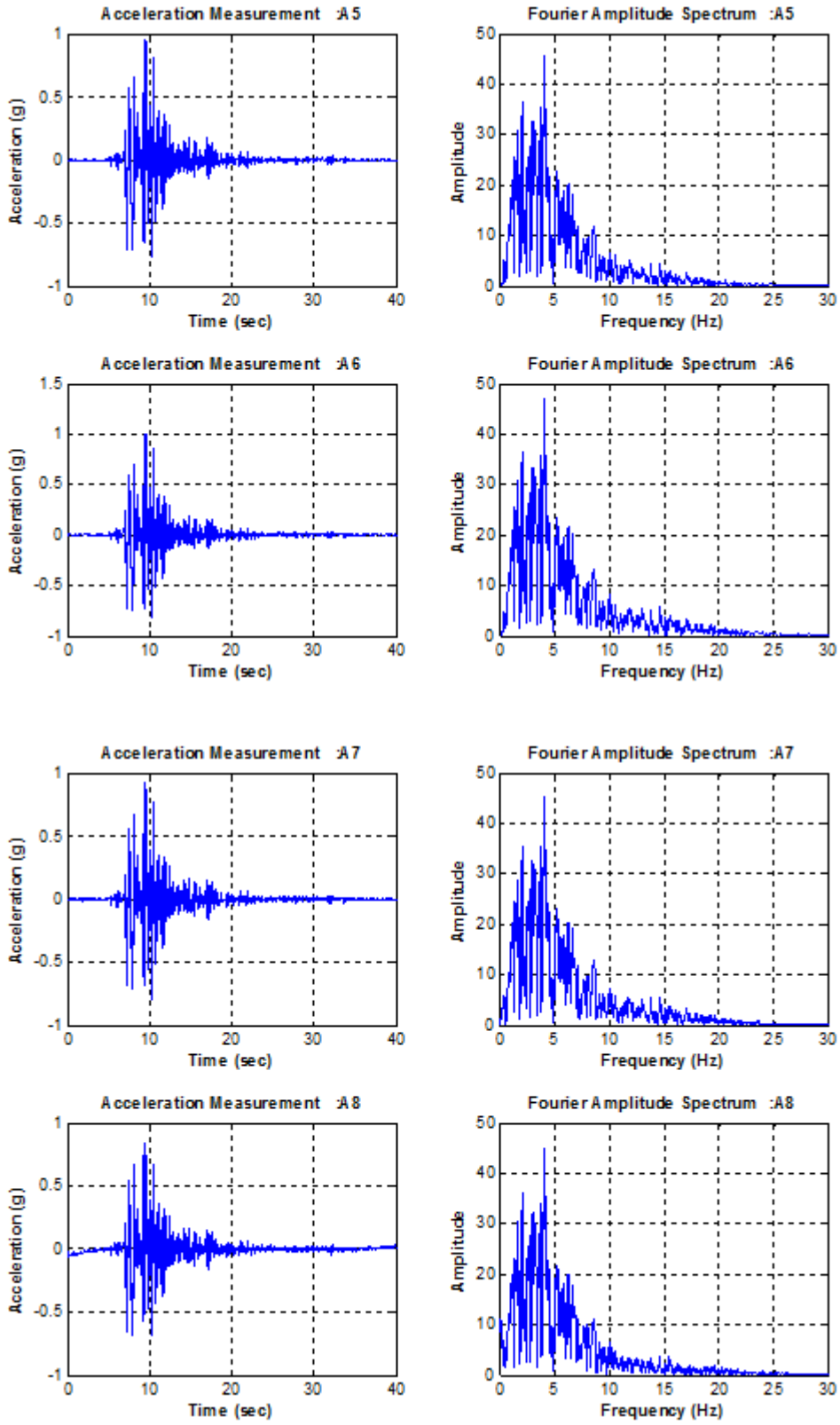

Figure A.14. Acceleration Time History Graphs for Setup 2 Kobe 75%.

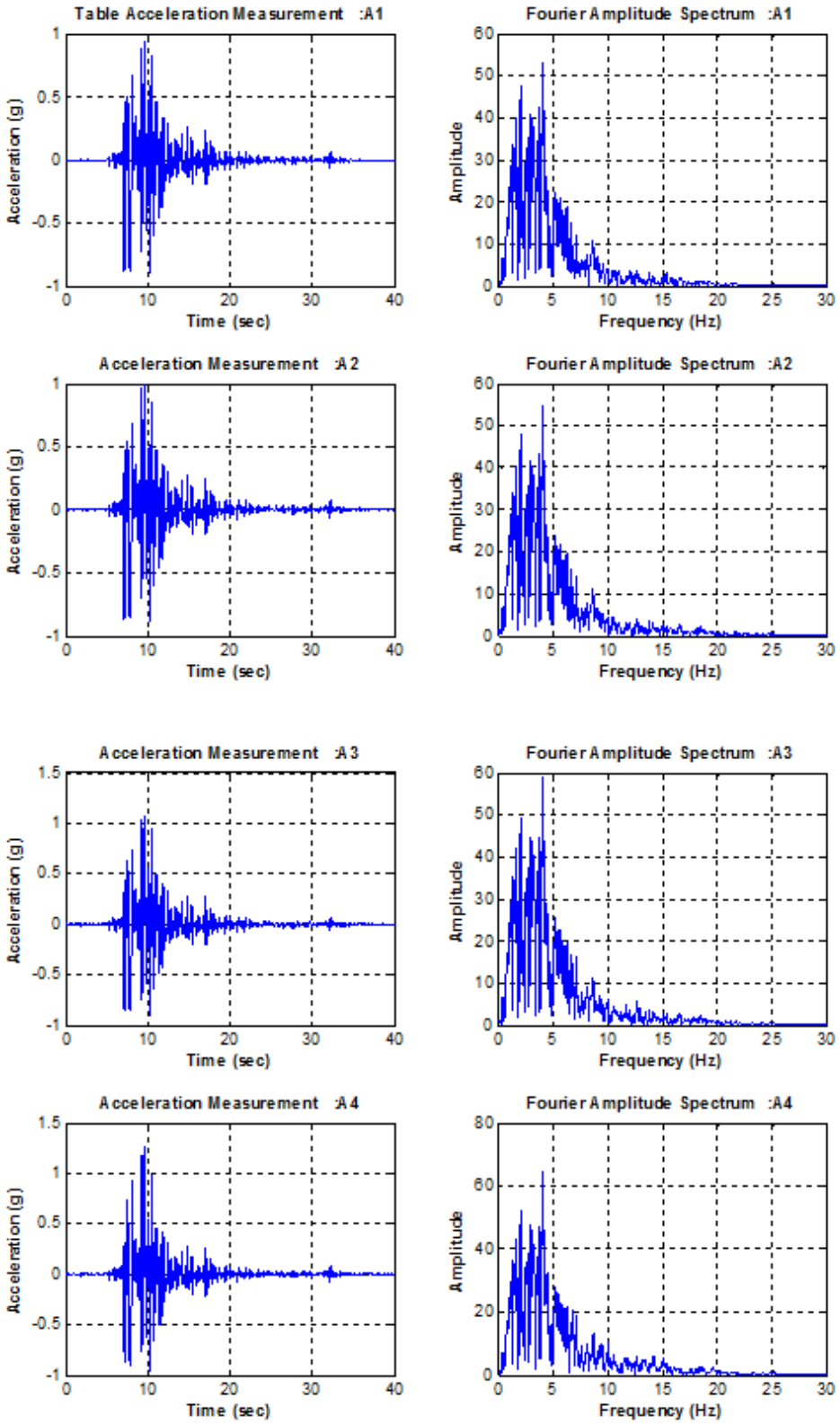

Figure A.15. Acceleration Time History Graphs for Setup 2 Kobe 100%.

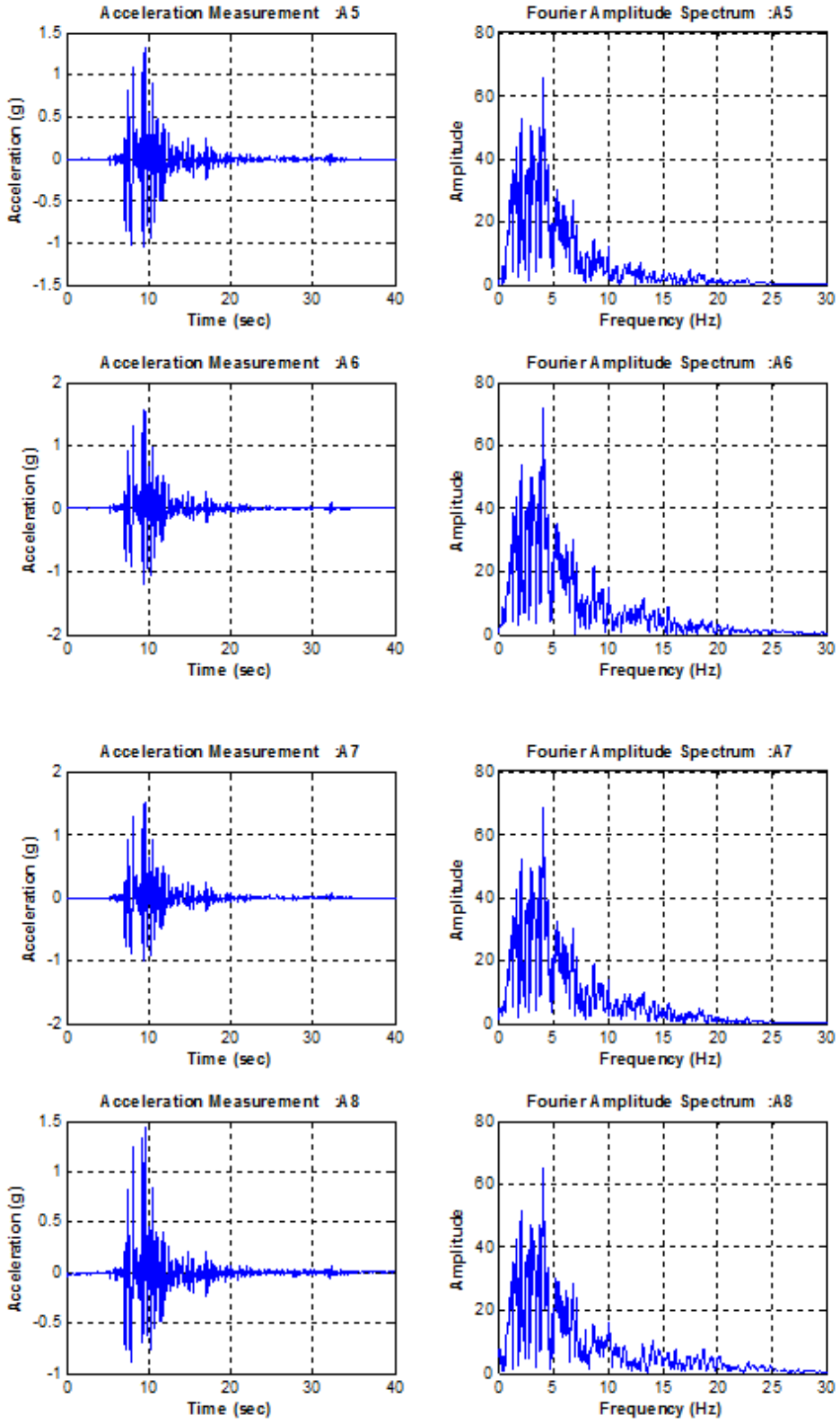

Figure A.16. Acceleration Time History Graphs for Setup 2 Kobe 100%.

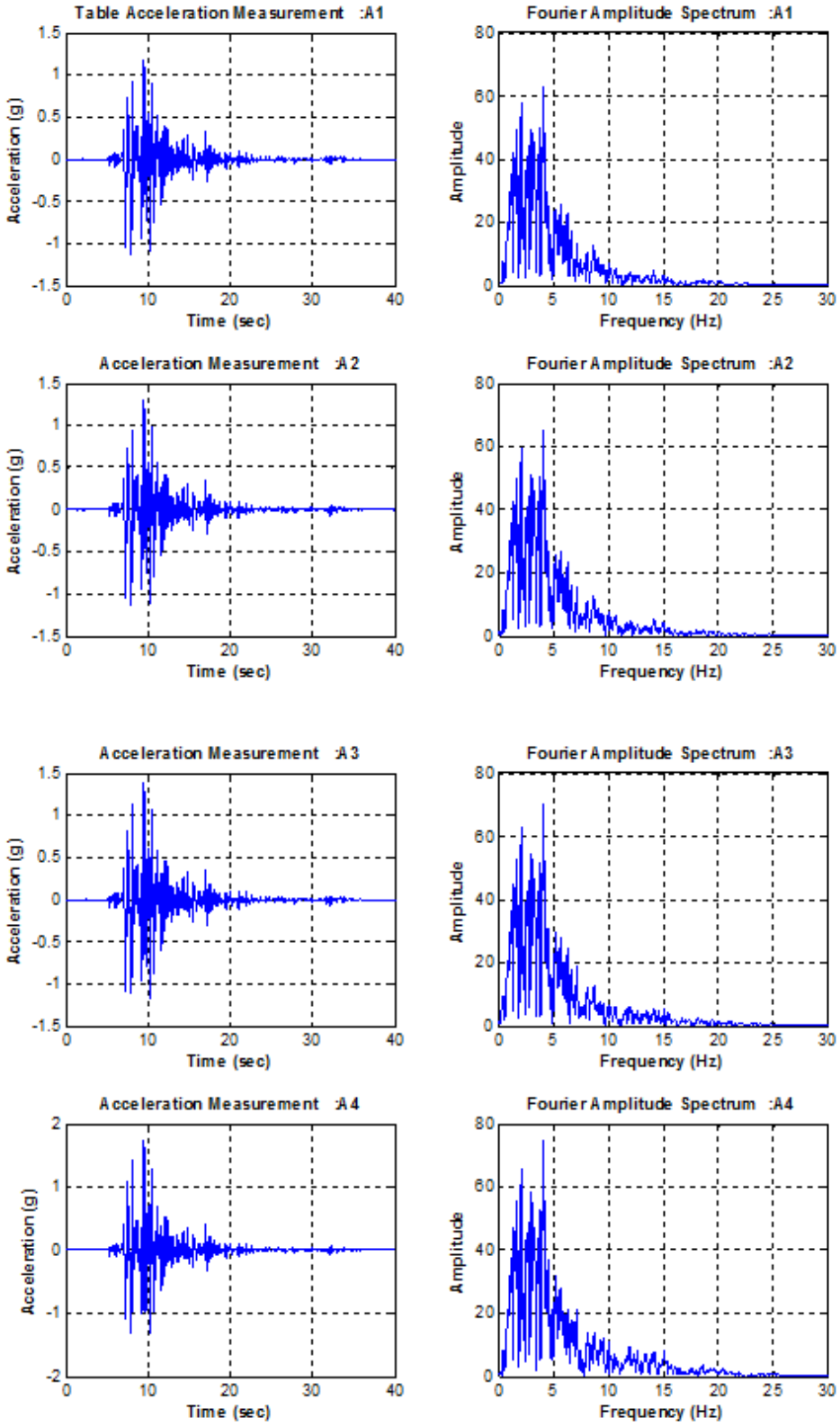

Figure A.17. Acceleration Time History Graphs for Setup 2 Kobe 125%.

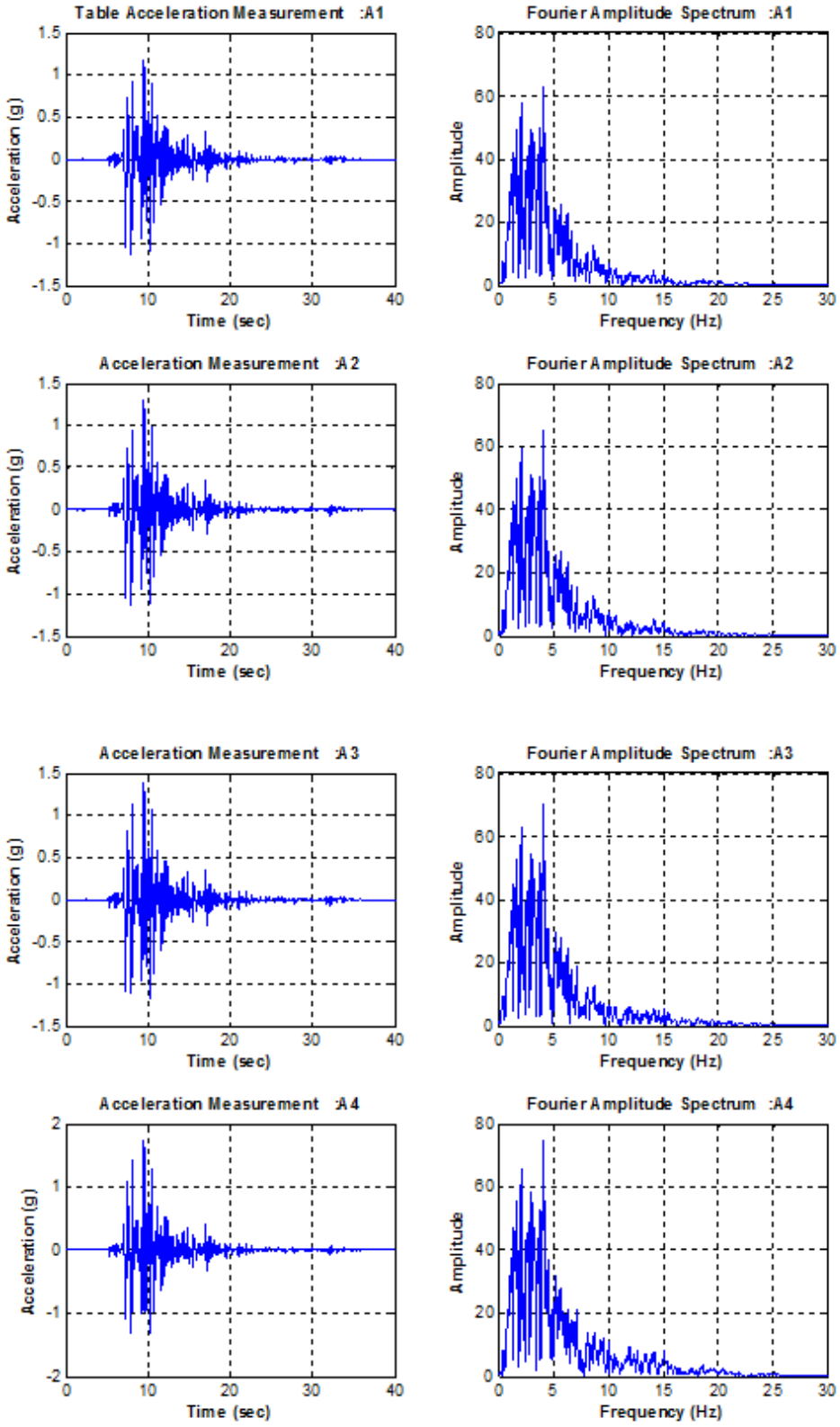

Figure A.18. Acceleration Time History Graphs for Setup 2 Kobe 125%.

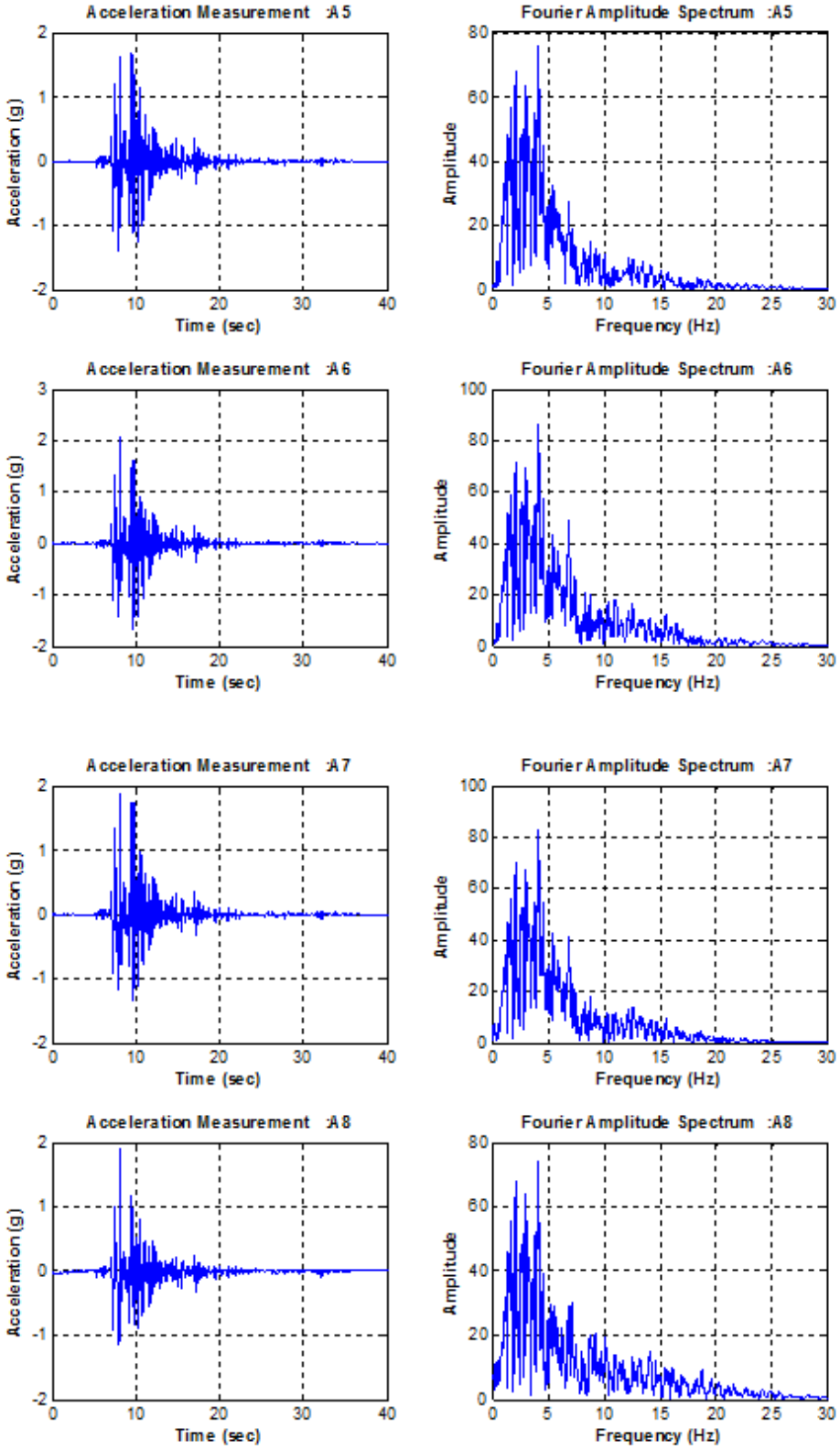

Figure A.19. Acceleration Time History Graphs for Setup 2 Kobe 125%.

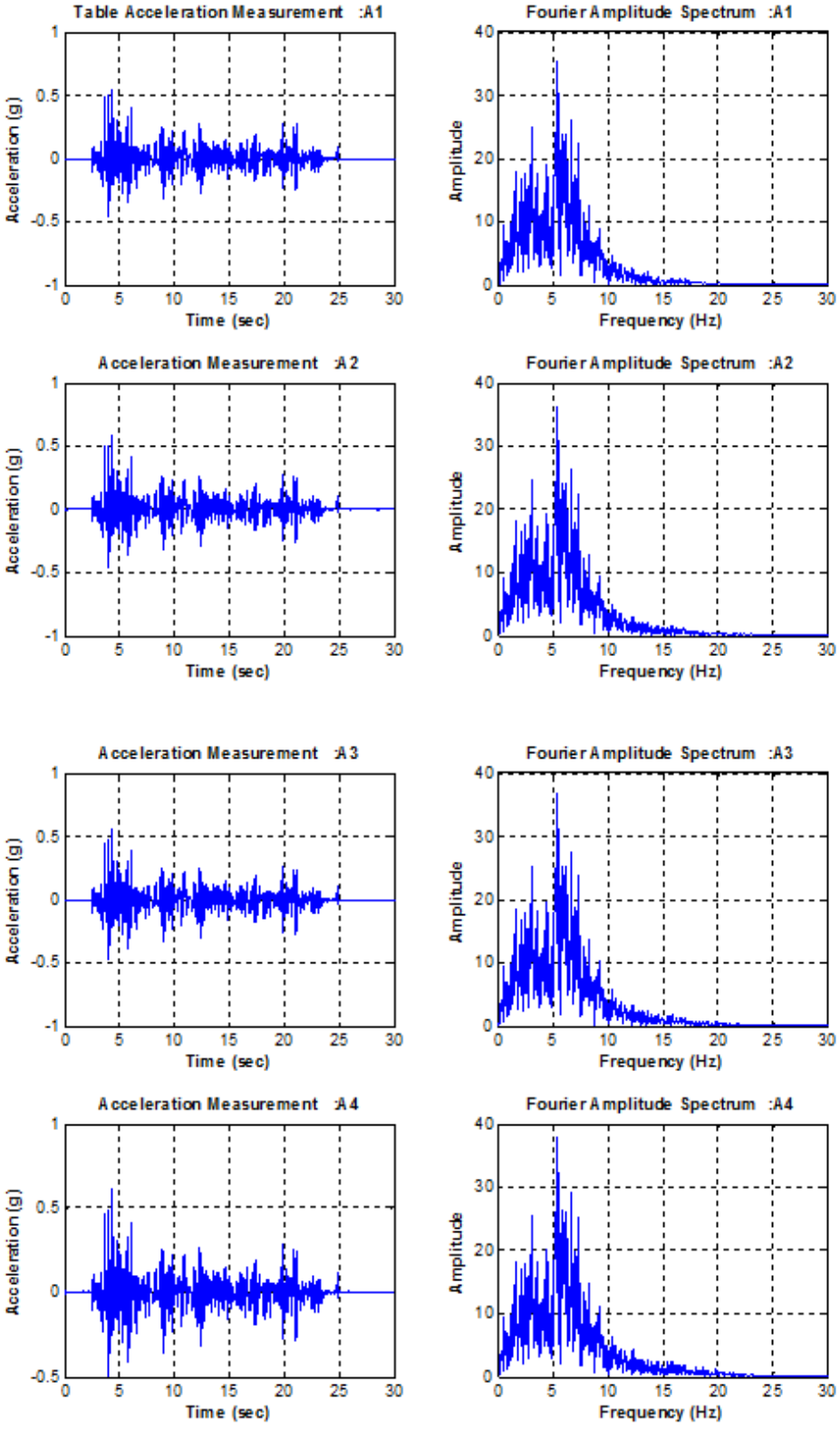

Figure A.20. Acceleration Time History Graphs for Setup 3 El Centro 100%.

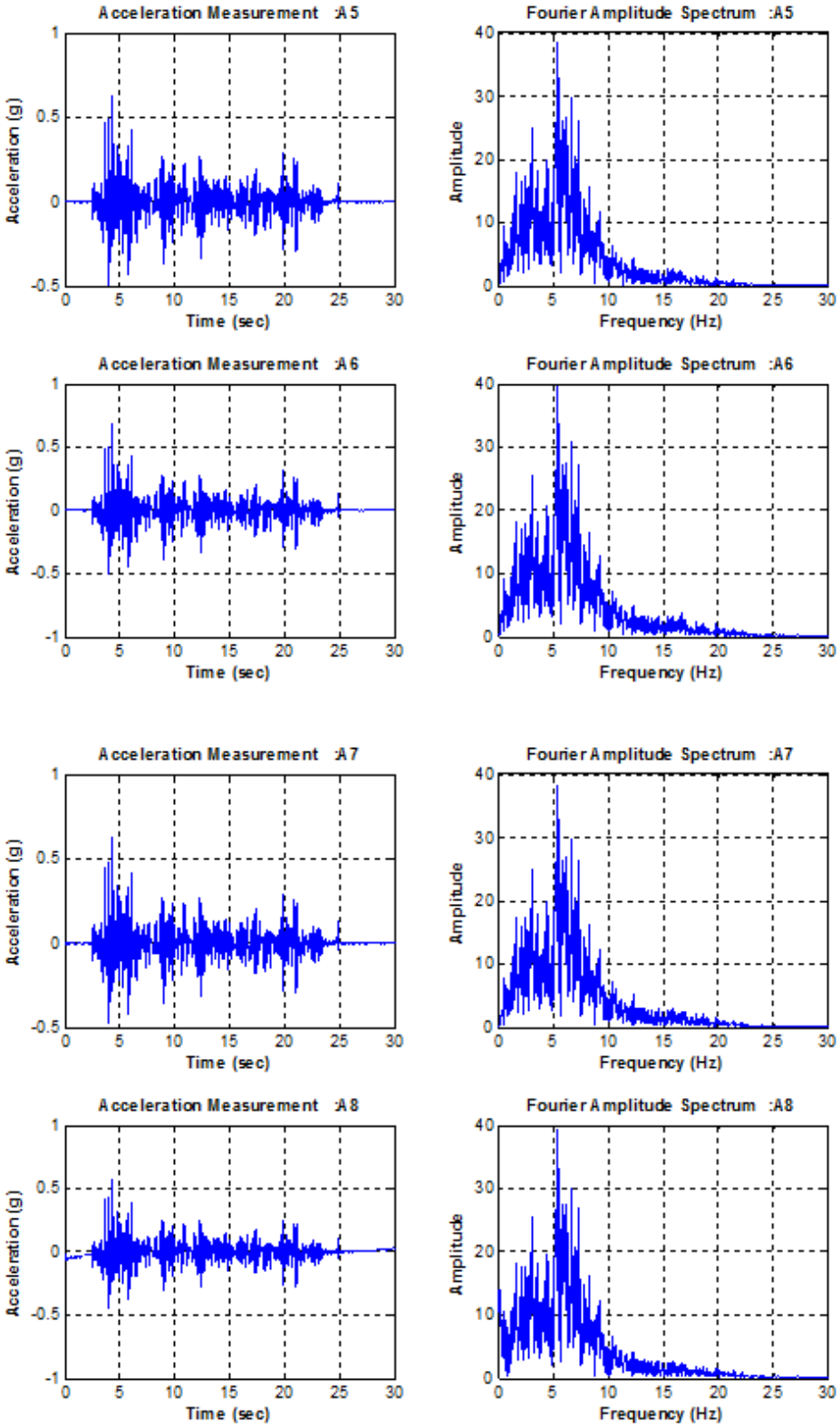

Figure A.21. Acceleration Time History Graphs for Setup 3 El Centro 100%.

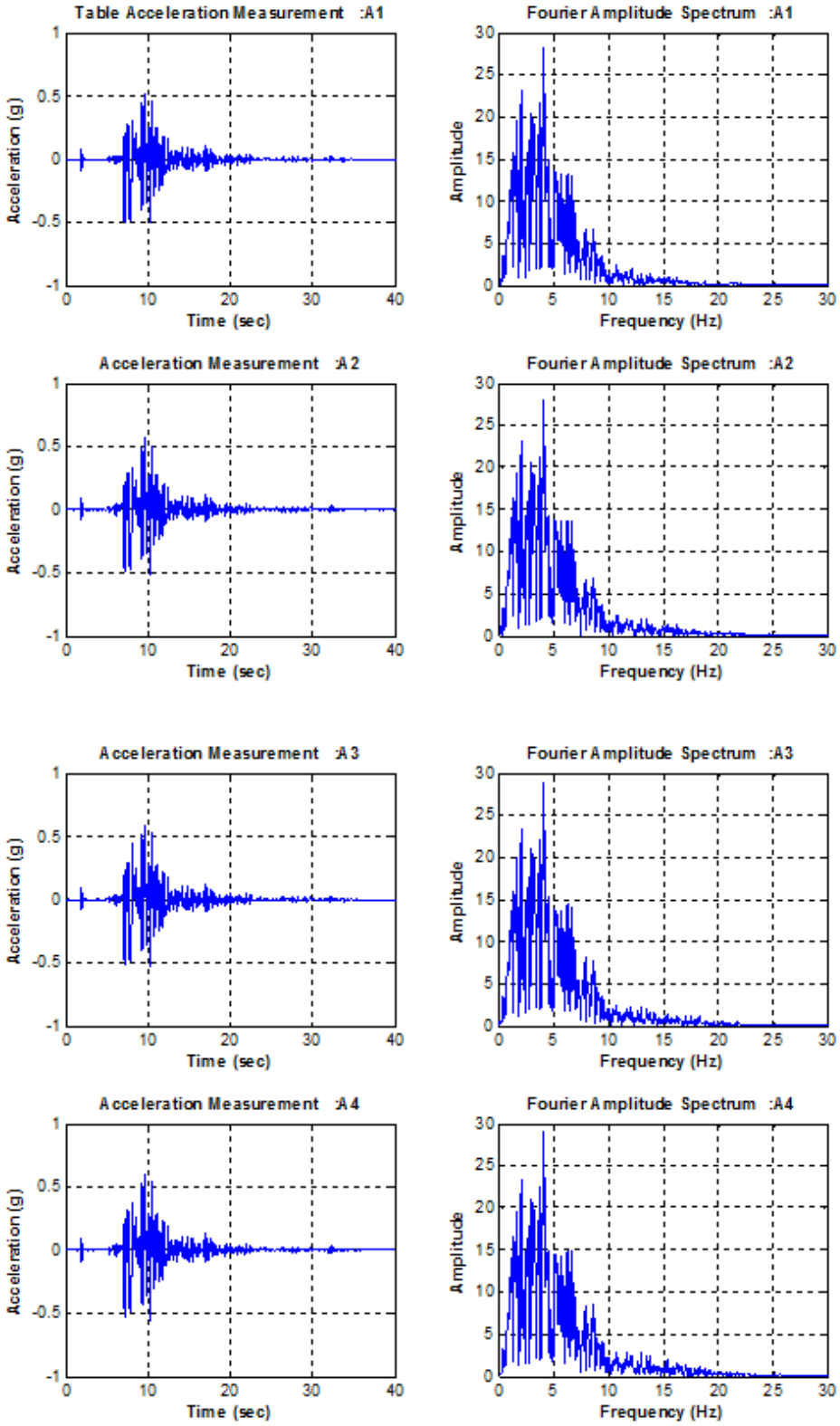

Figure A.22. Acceleration Time History Graphs for Setup 3 Kobe 50%.

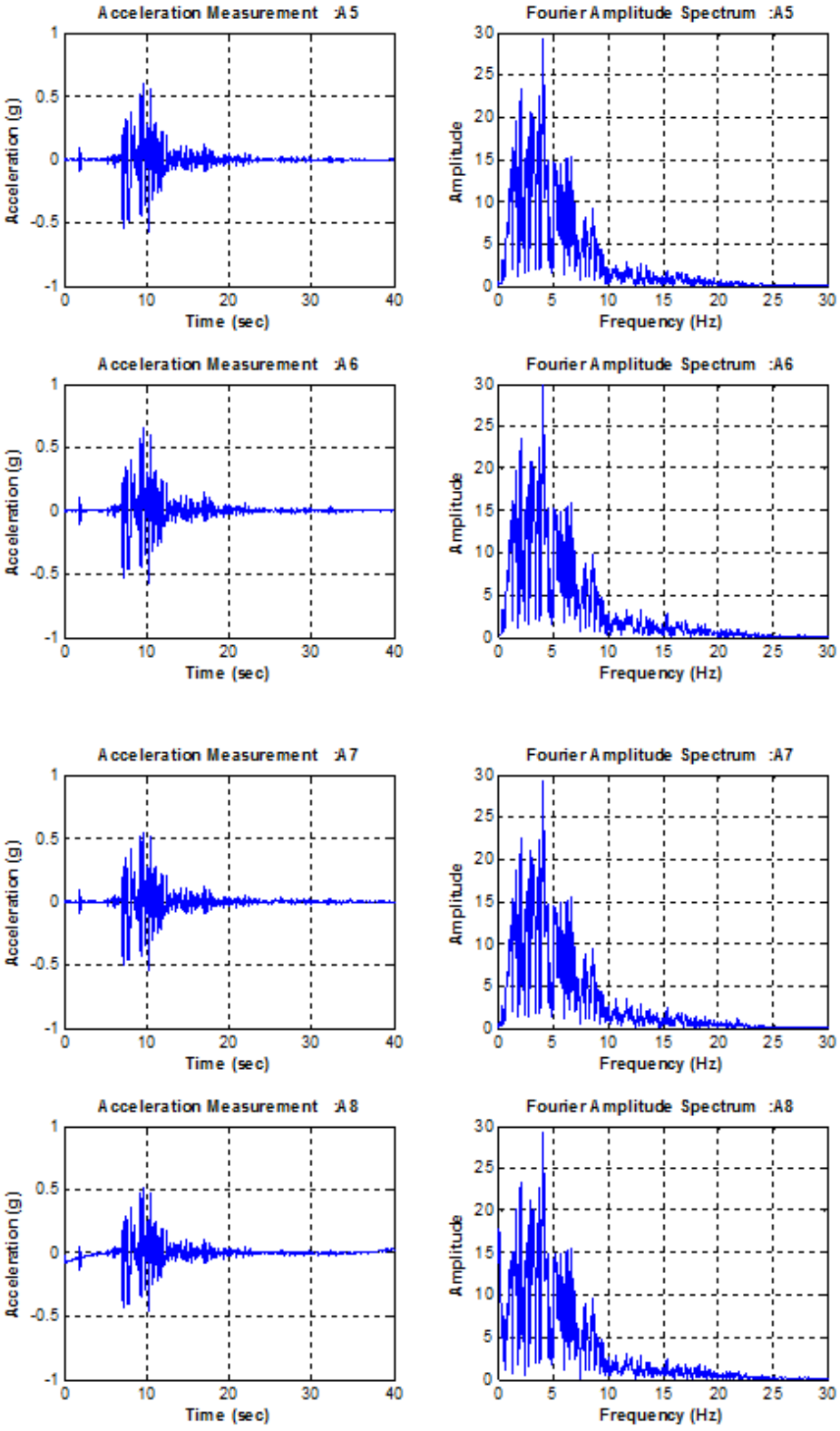

Figure A.23. Acceleration Time History Graphs for Setup 3 Kobe 50%.

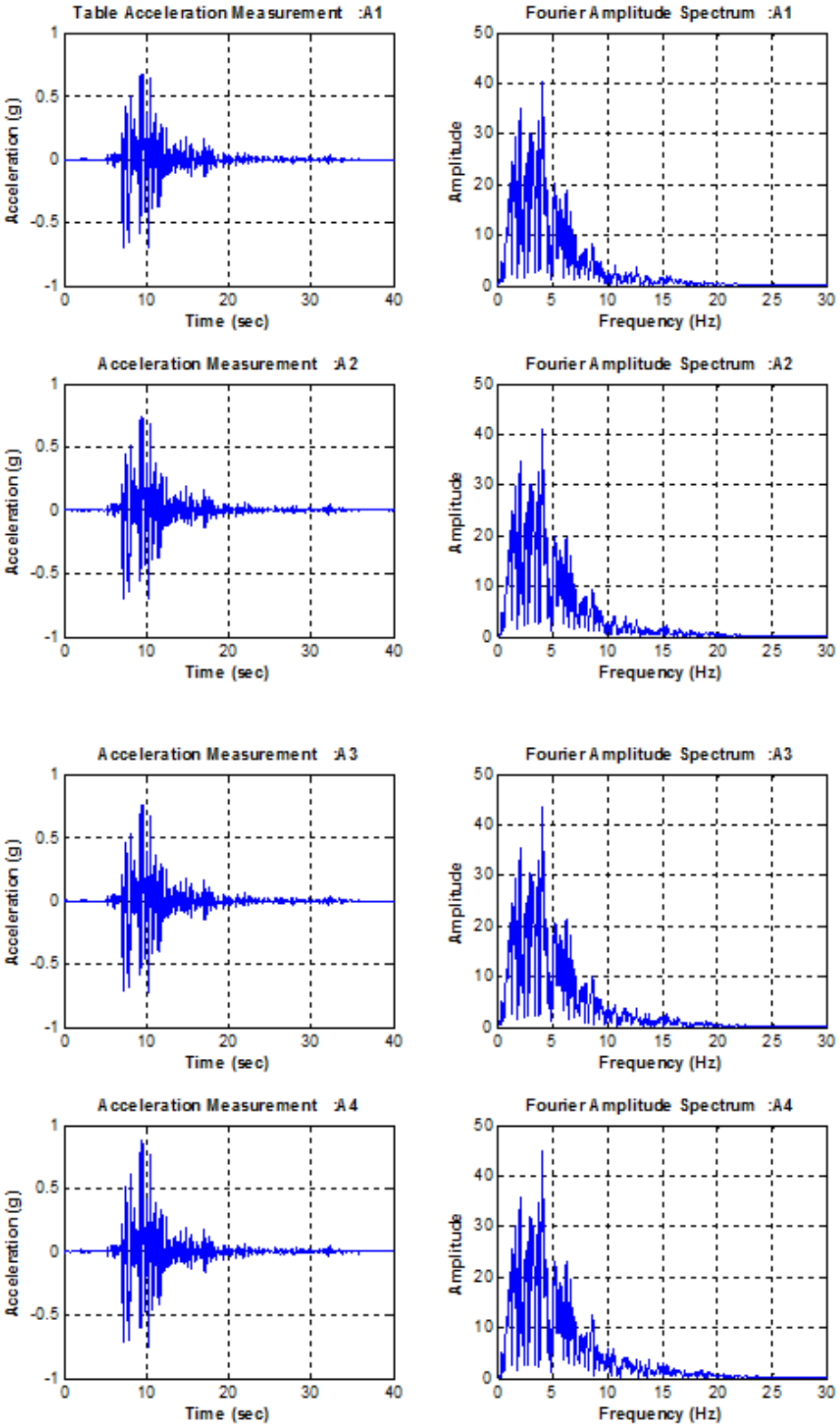

Figure A.24. Acceleration Time History Graphs for Setup 3 Kobe 75%.

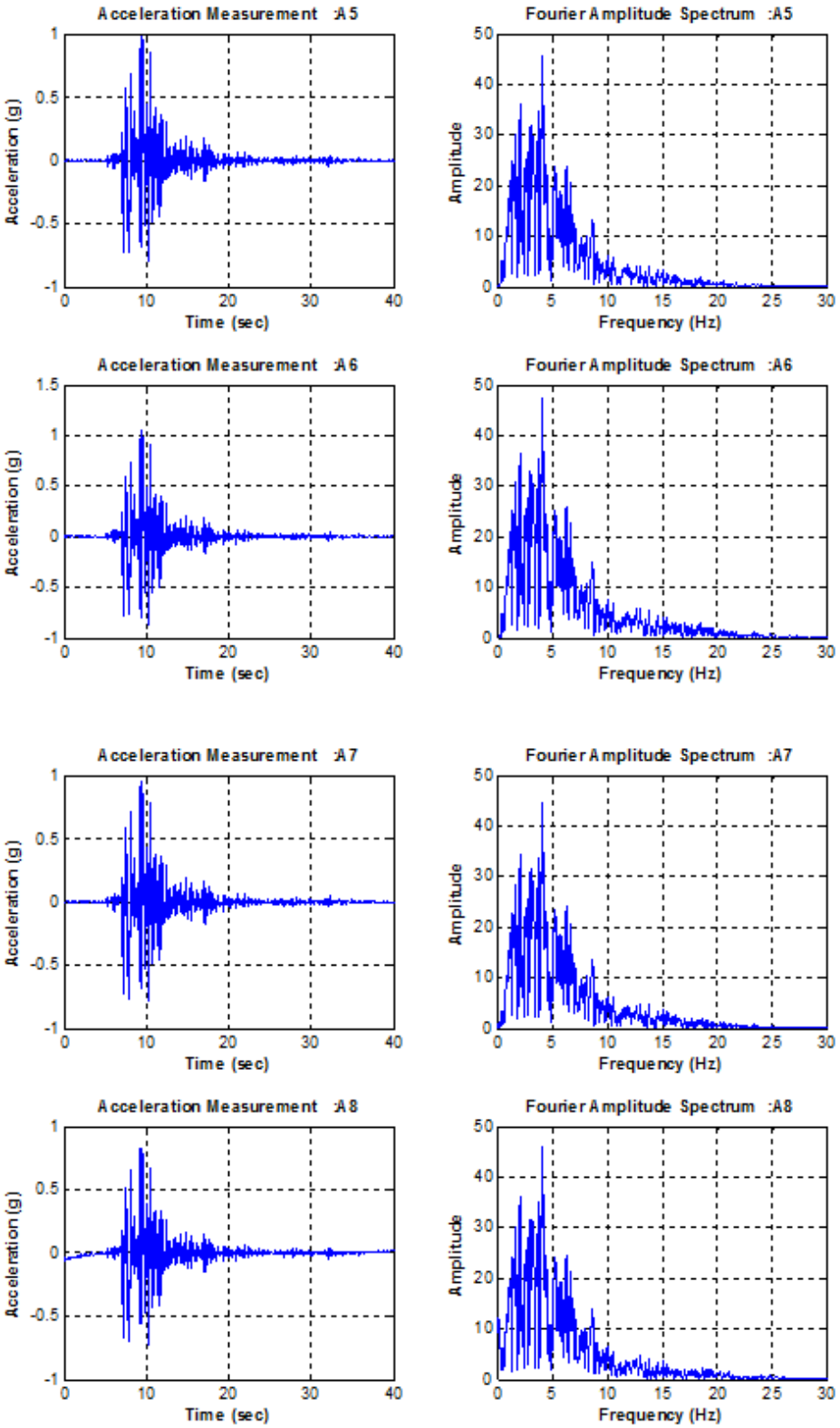

Figure A.25. Acceleration Time History Graphs for Setup 3 Kobe 75%.

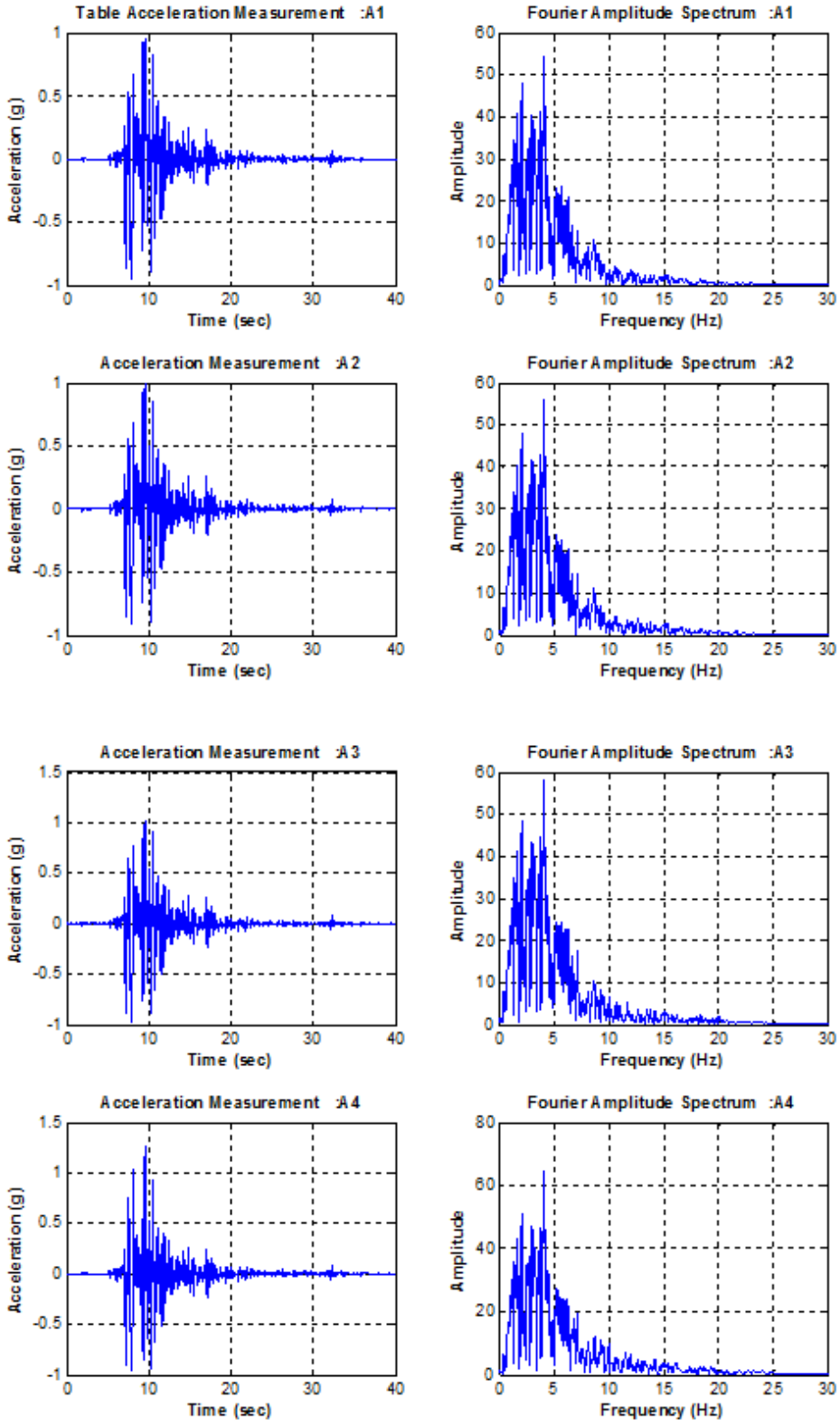

Figure A.26. Acceleration Time History Graphs for Setup 3 Kobe 100%.

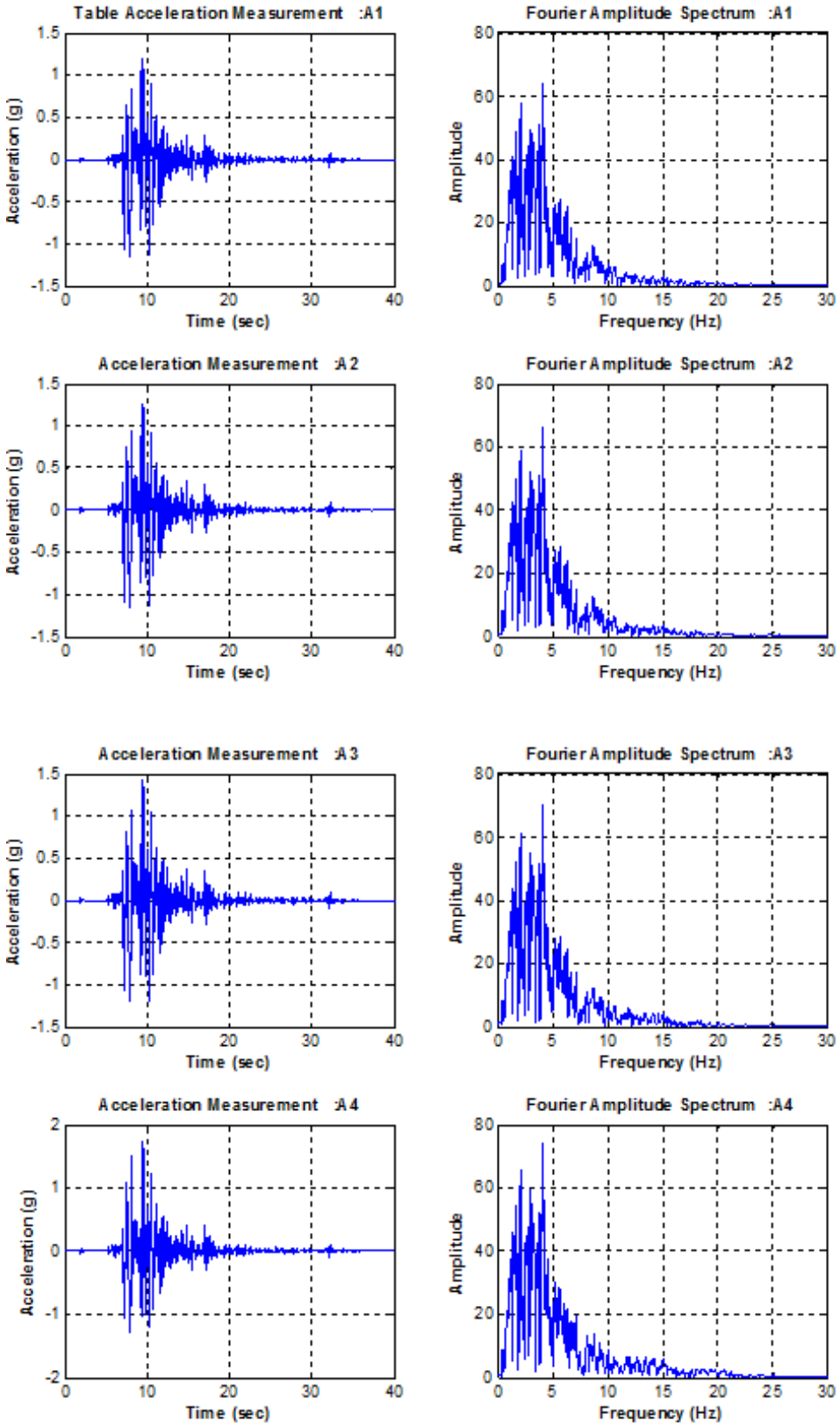

Figure A.27. Acceleration Time History Graphs for Setup 3 Kobe 125%.

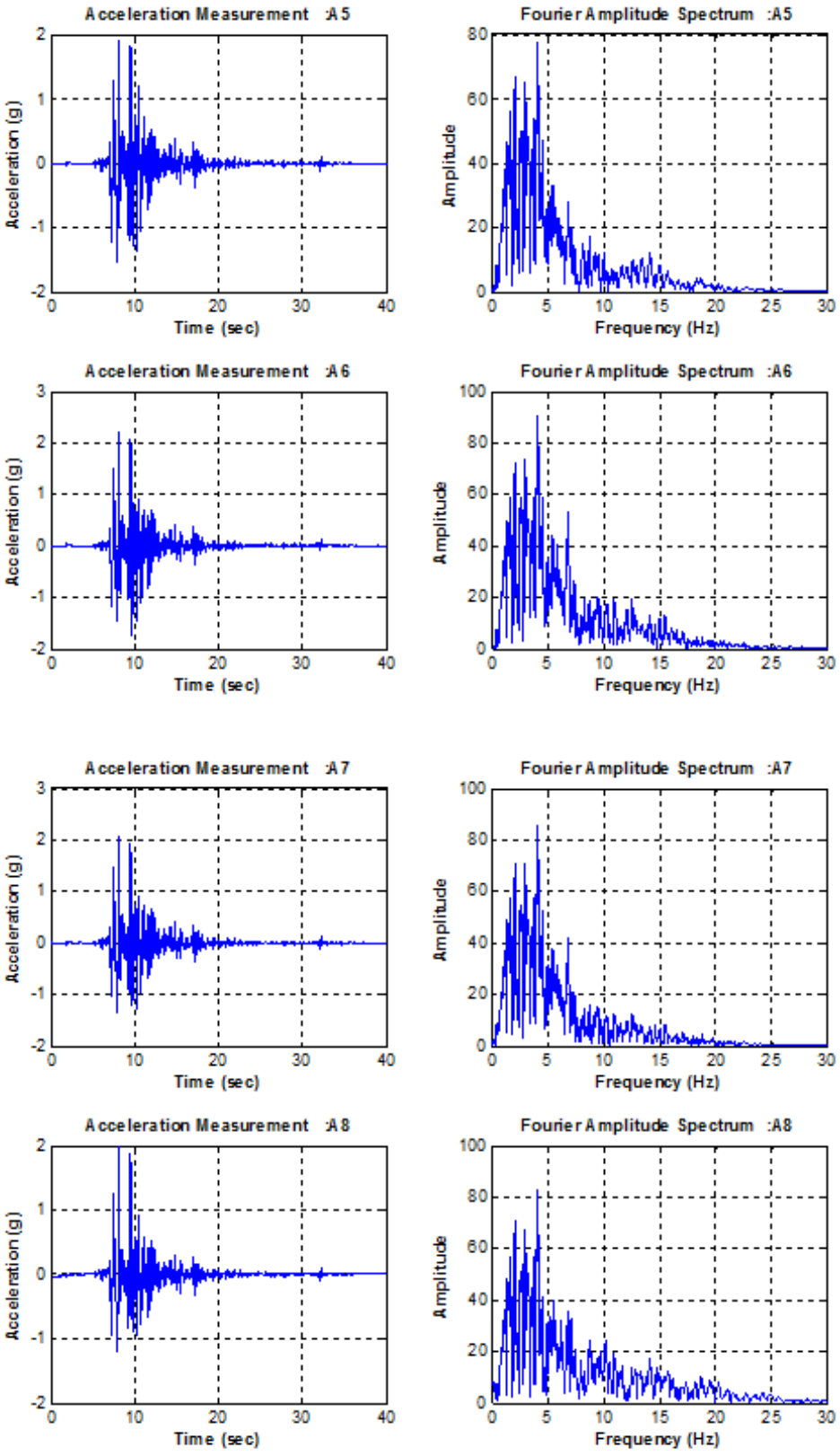

Figure A.28. Acceleration Time History Graphs for Setup 3 Kobe 125%.

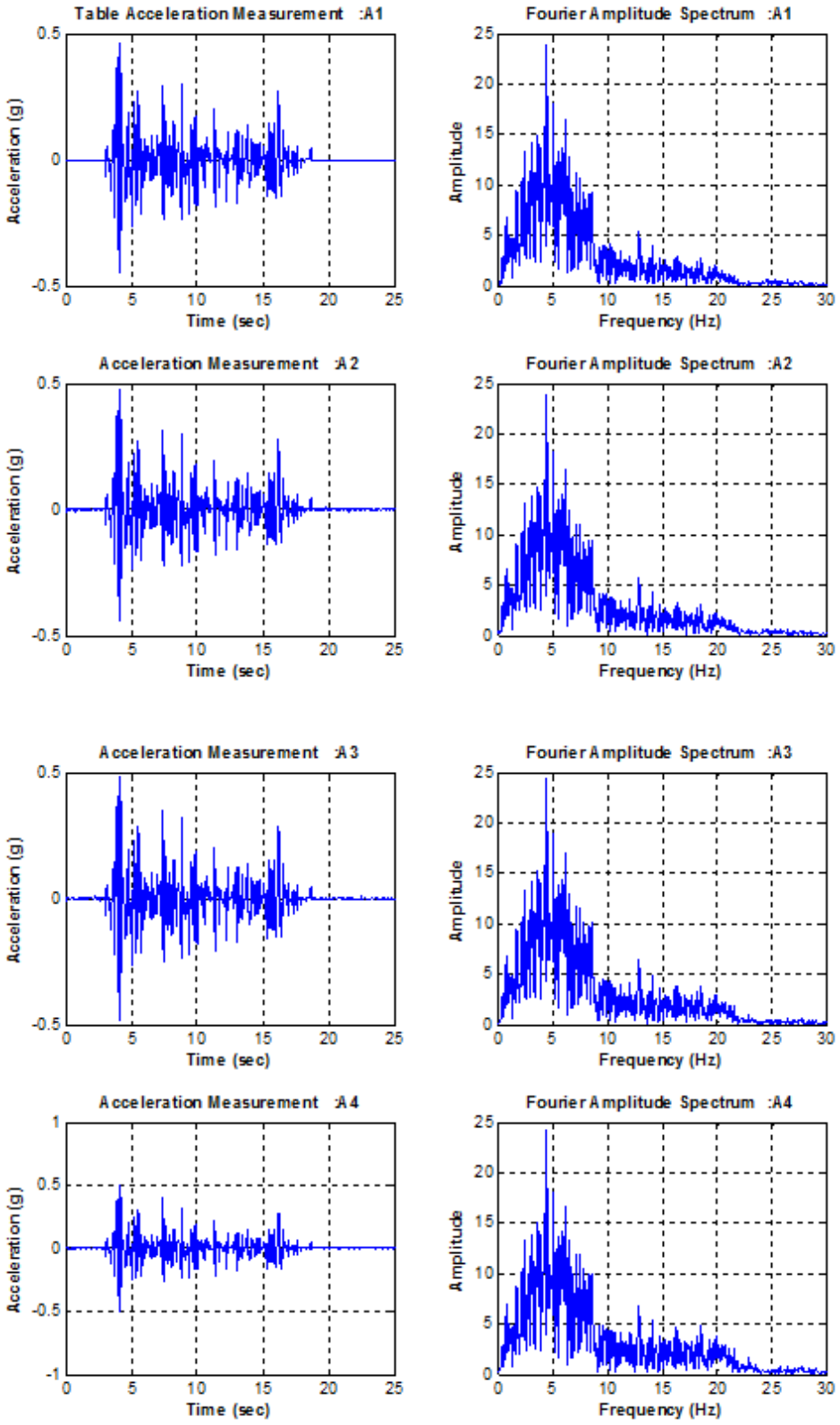

Figure A.29. Acceleration Time History Graphs for Setup 4 El Centro 100%.

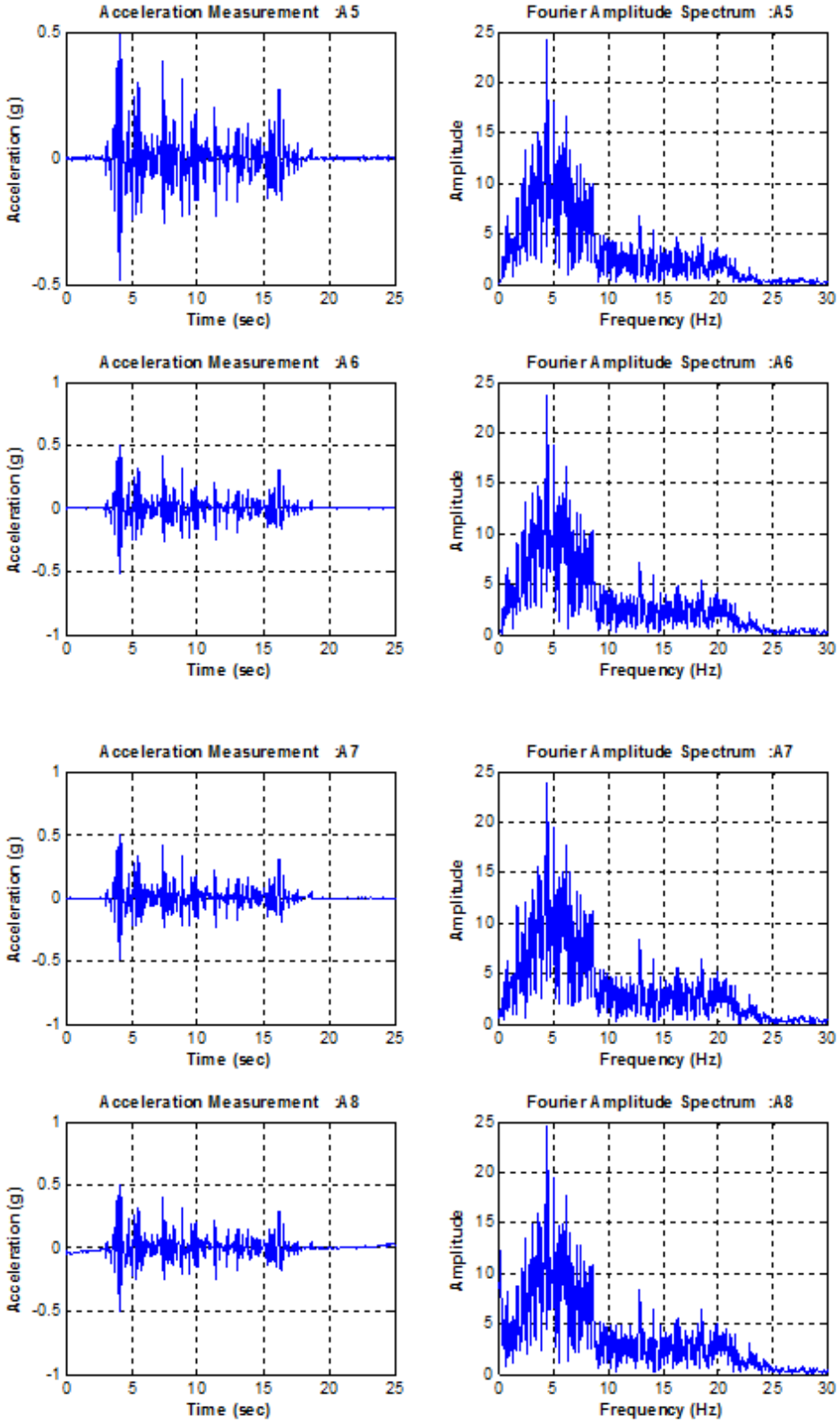

Figure A.30. Acceleration Time History Graphs for Setup 4 El Centro 100%.

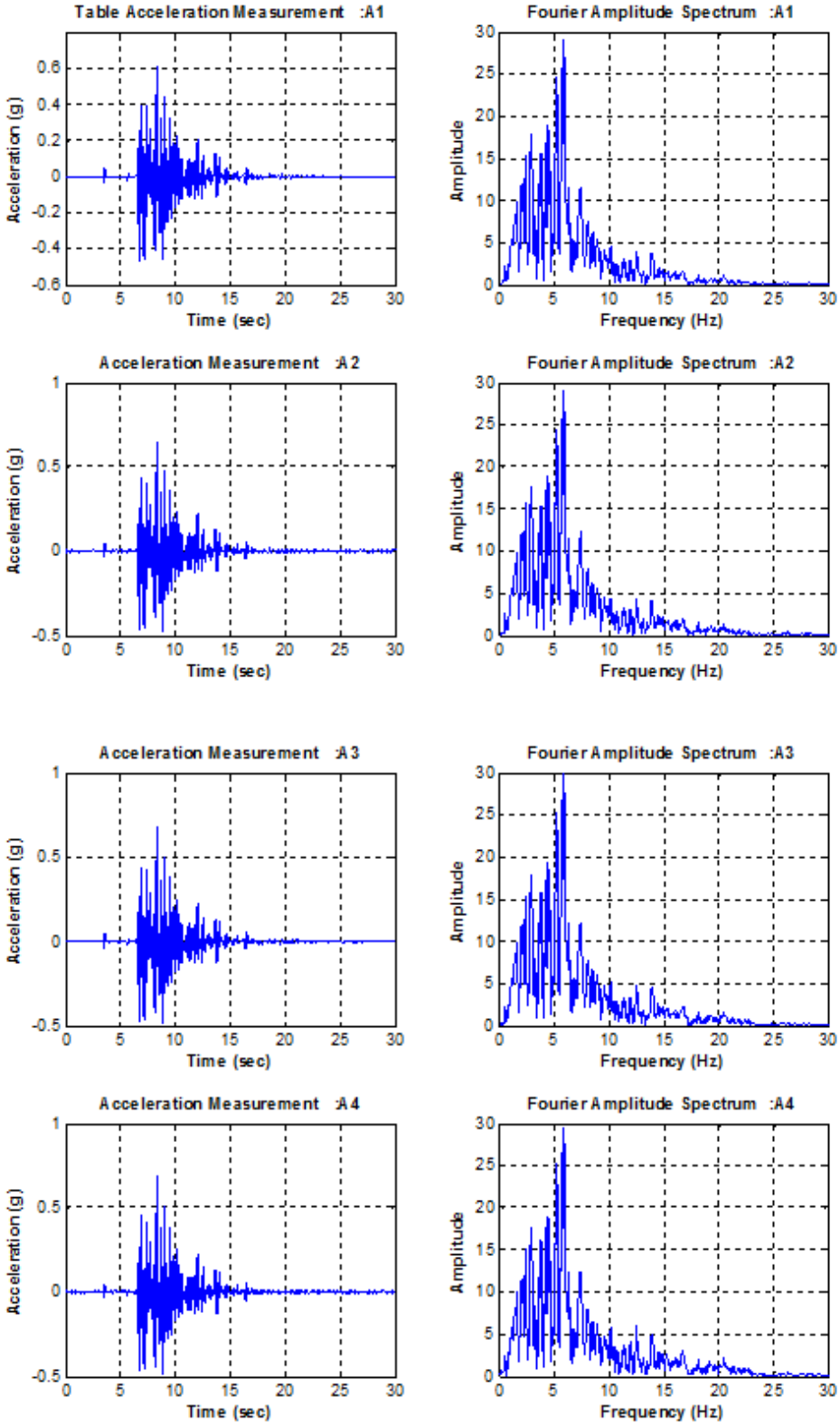

Figure A.31. Acceleration Time History Graphs for Setup 4 Kobe 50%.

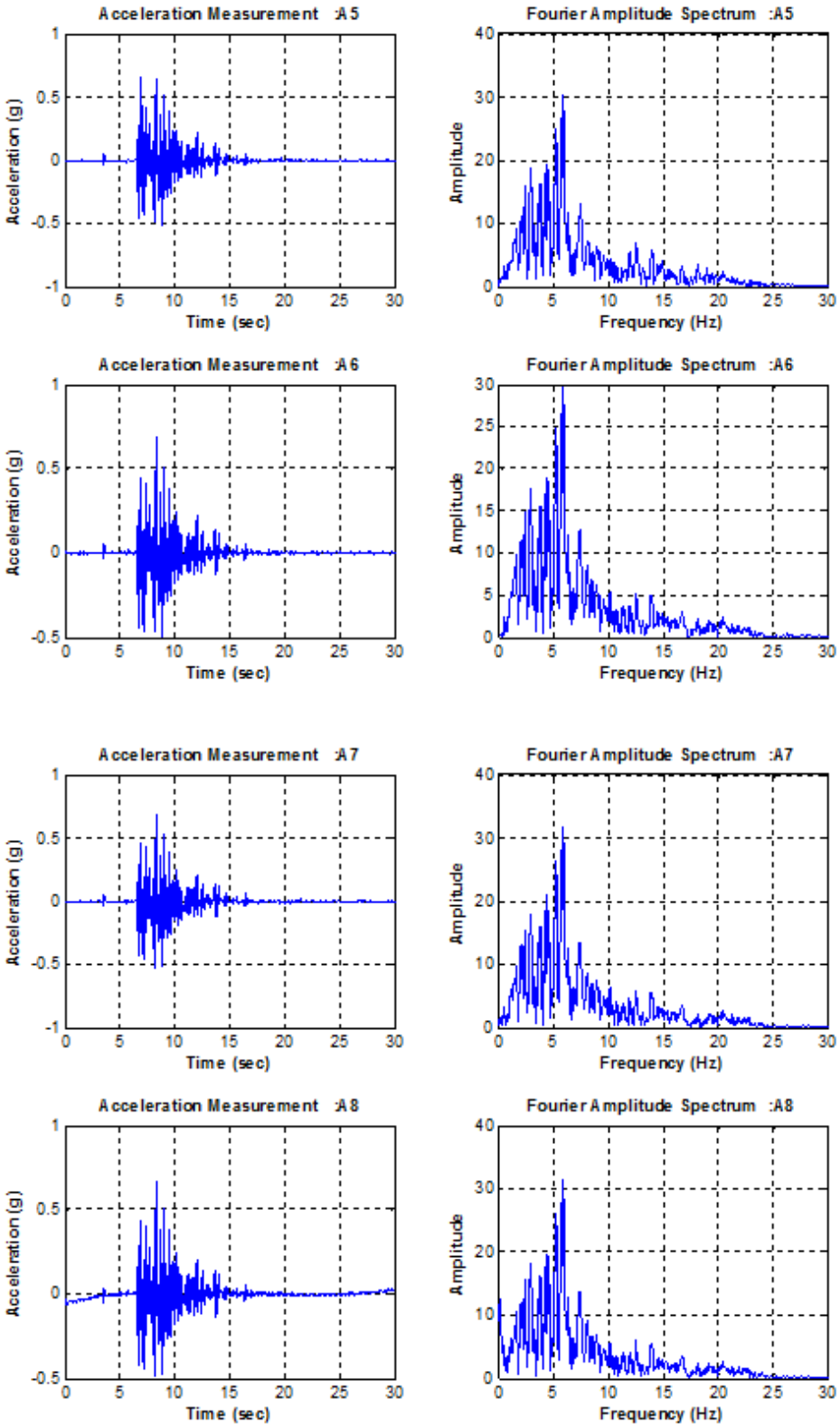

Figure A.32. Acceleration Time History Graphs for Setup 4 Kobe 50%.

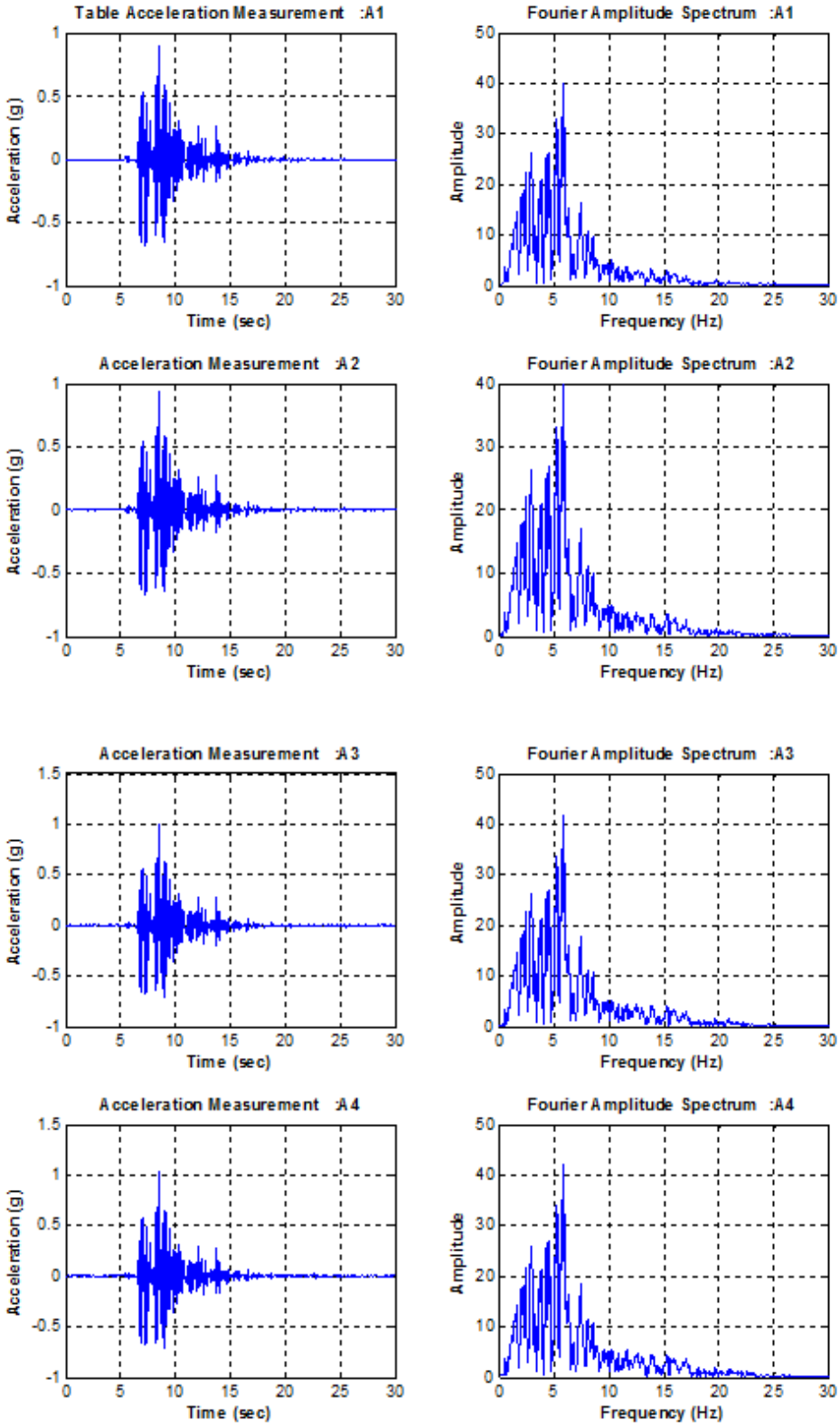

Figure A.33. Acceleration Time History Graphs for Setup 4 Kobe 75%.

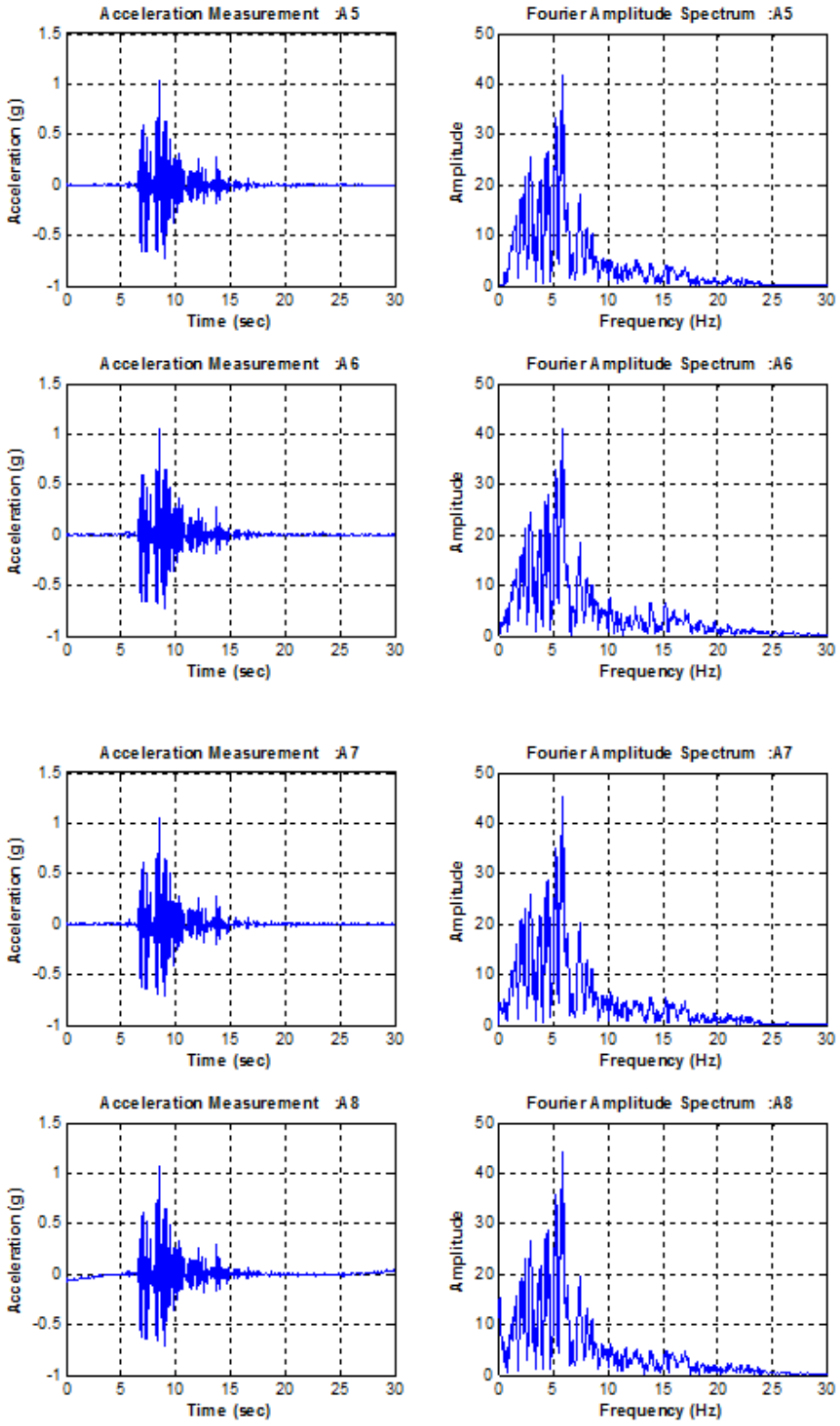

Figure A.34. Acceleration Time History Graphs for Setup 4 Kobe 75%.

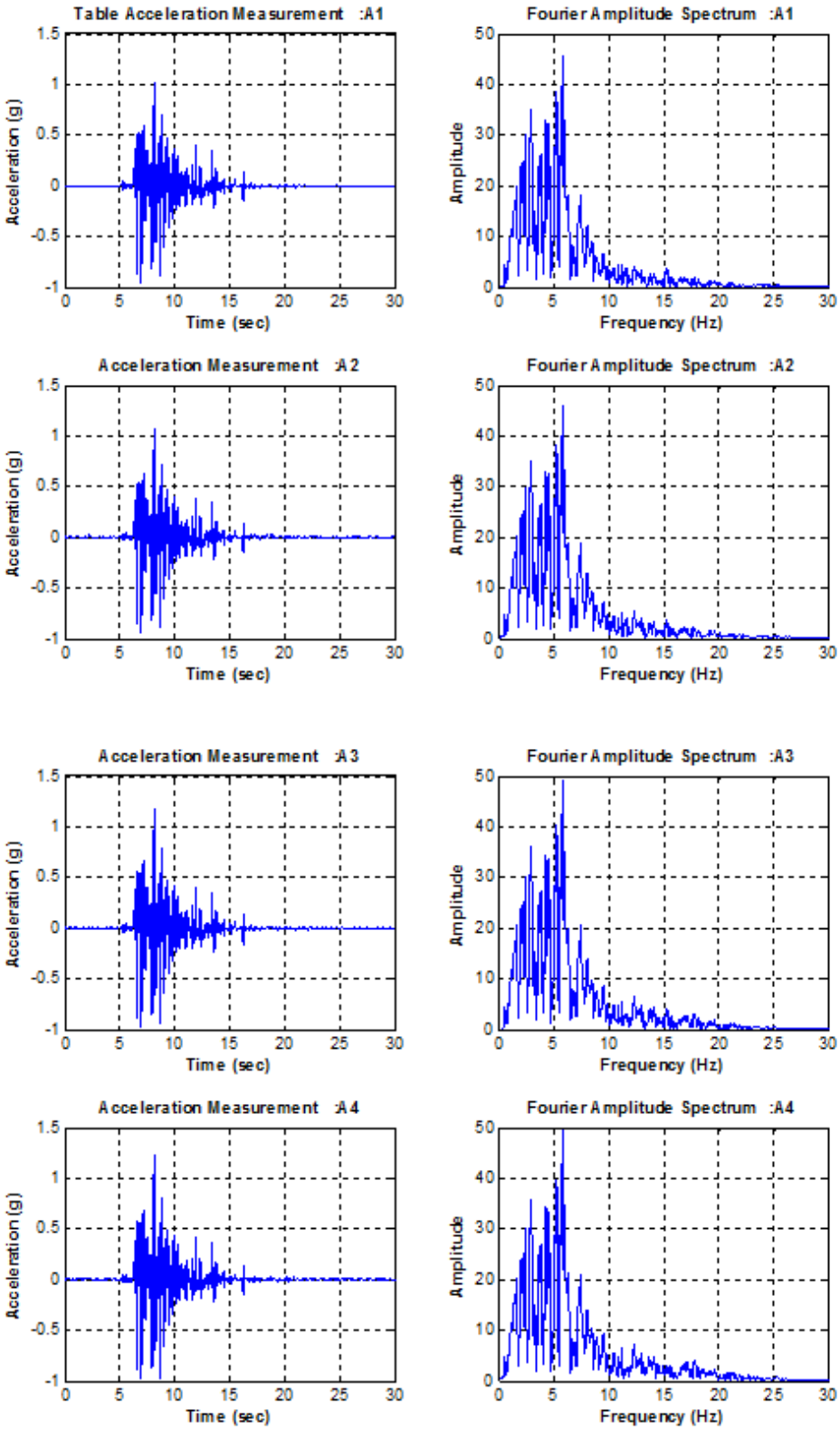

Figure A.35. Acceleration Time History Graphs for Setup 4 Kobe 100%.

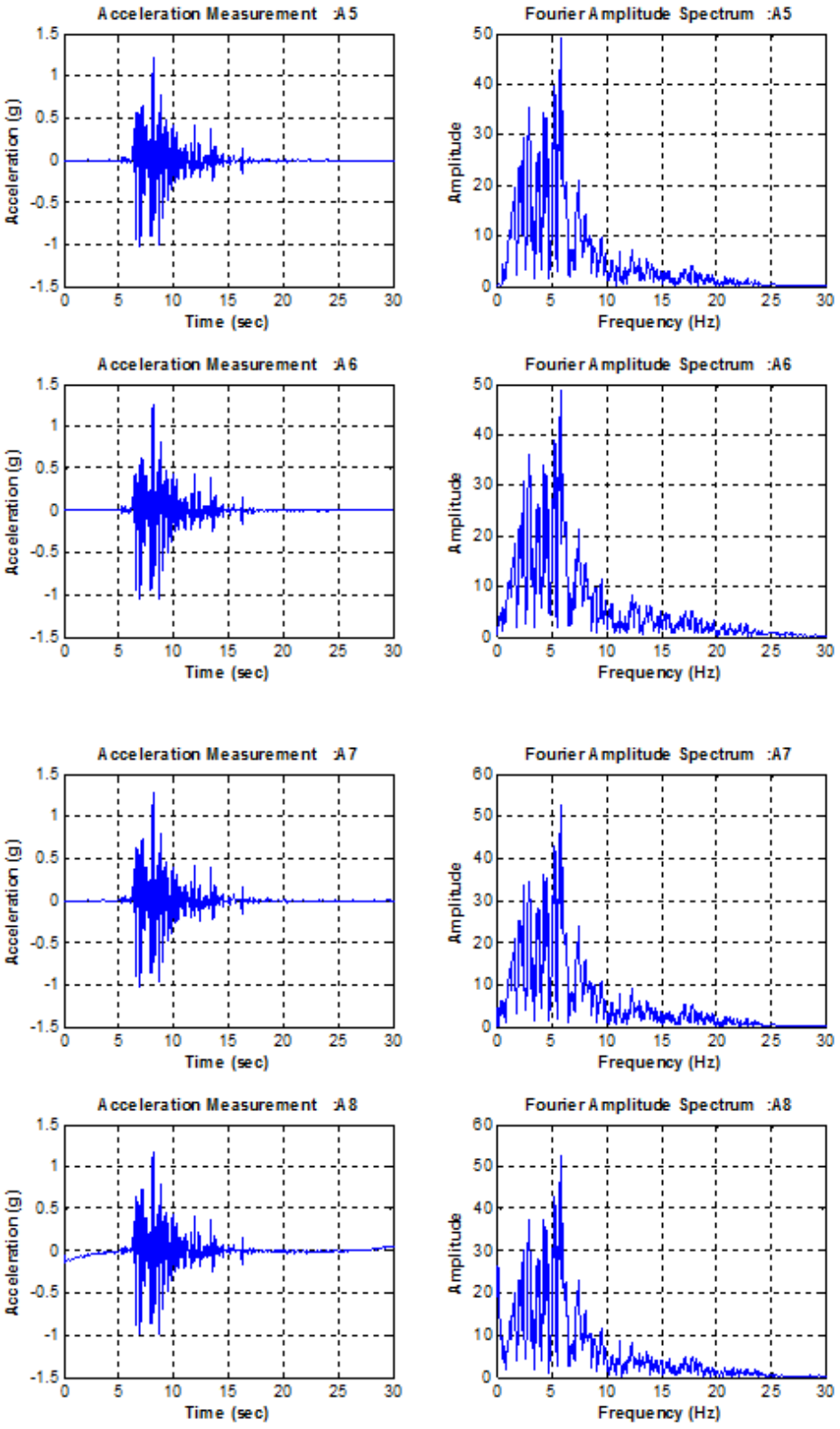

Figure A.36. Acceleration Time History Graphs for Setup 4 Kobe 100%.

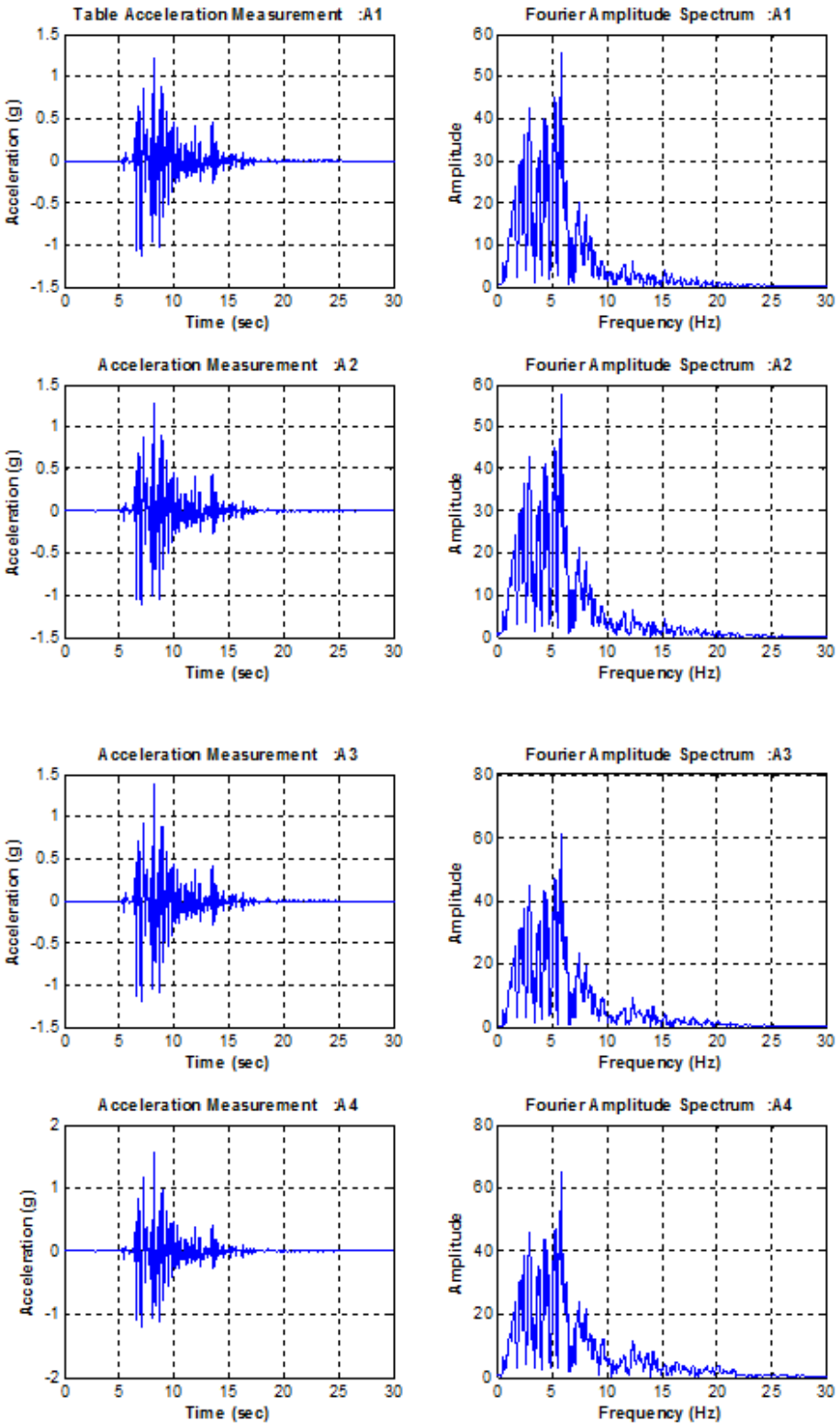

Figure A.37. Acceleration Time History Graphs for Setup 4 Kobe 125%.

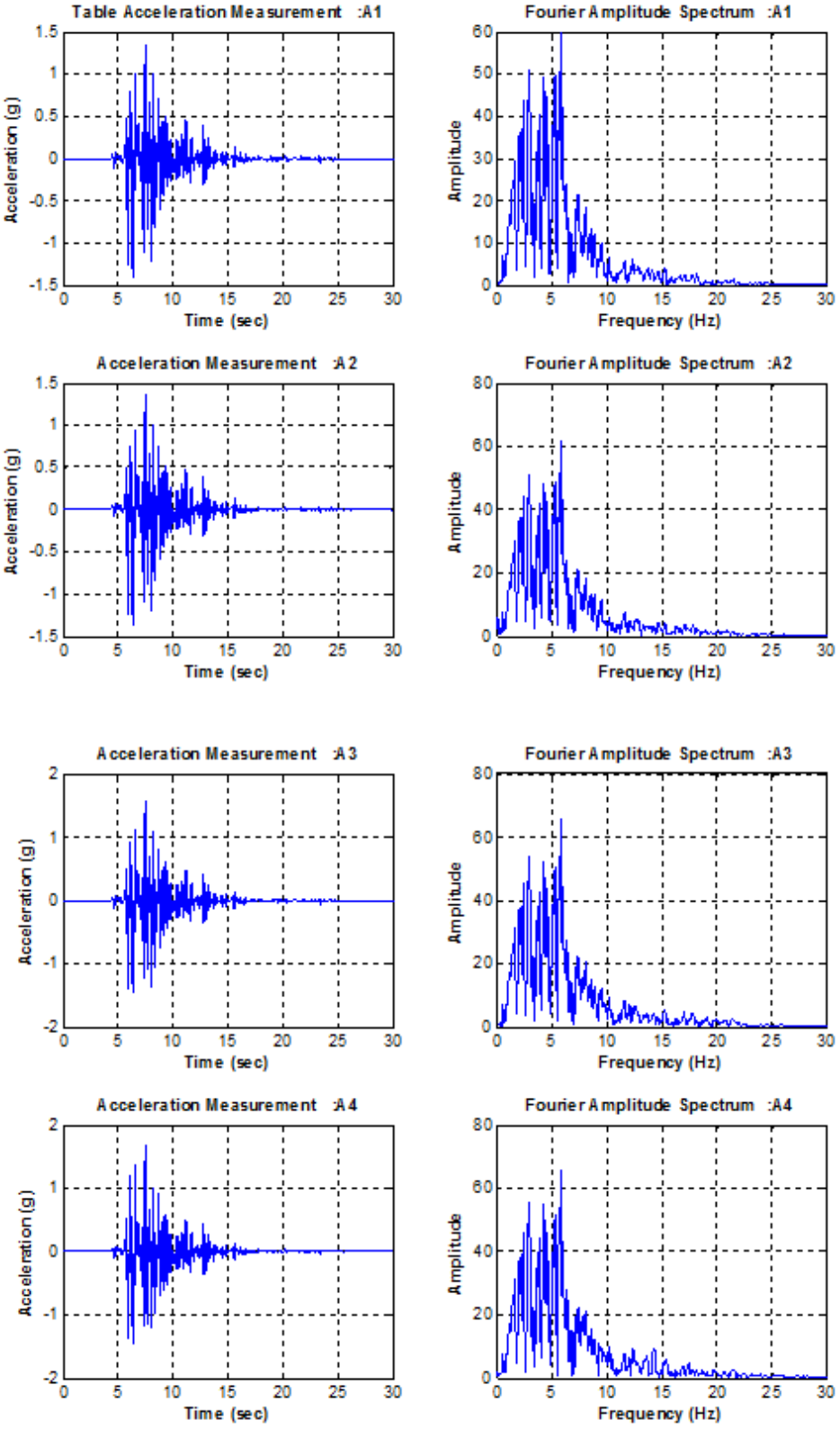

Figure A.38. Acceleration Time History Graphs for Setup 4 Kobe 125%.

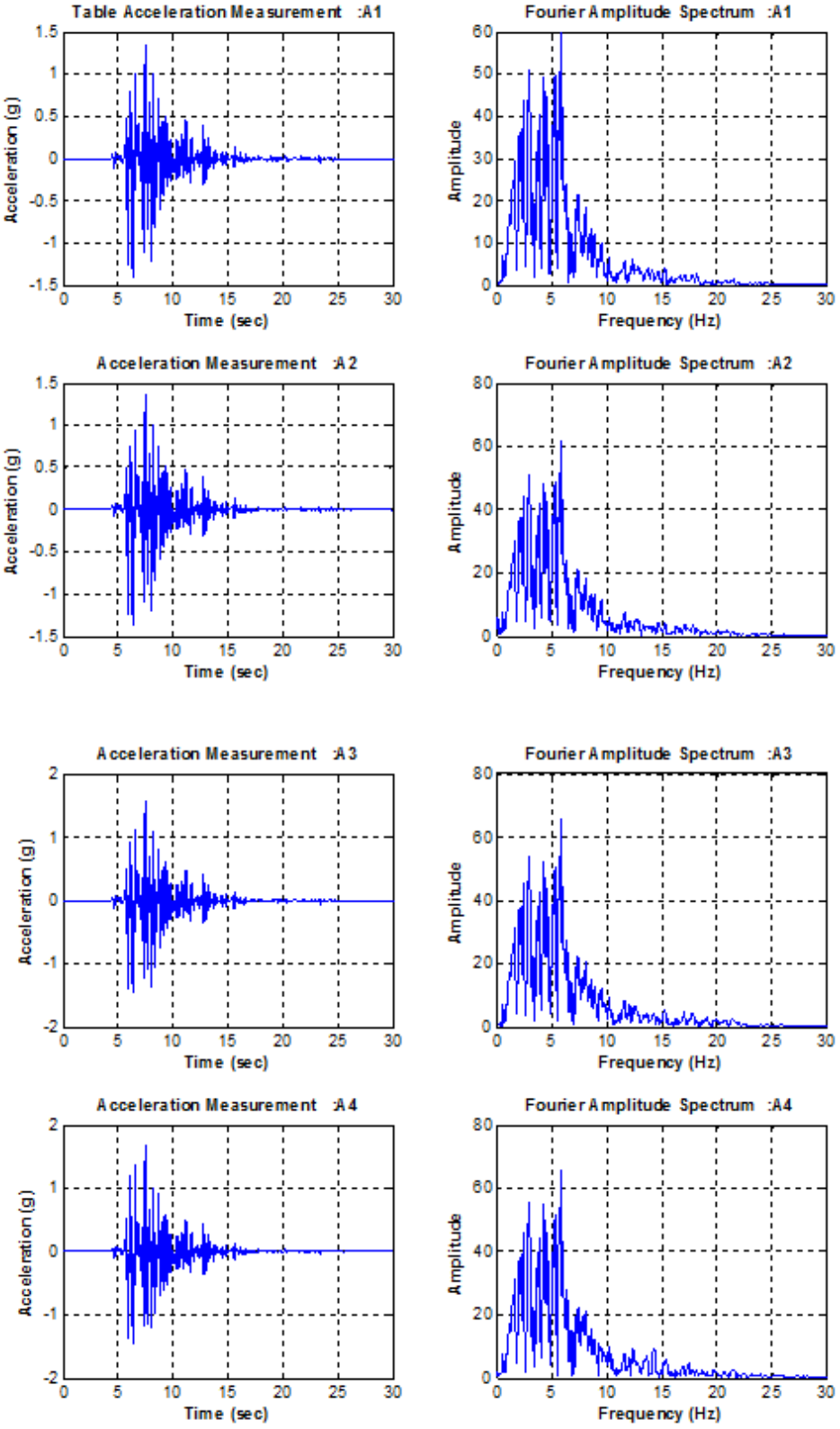

Figure A.39. Acceleration Time History Graphs for Setup 4 Kobe 150%.

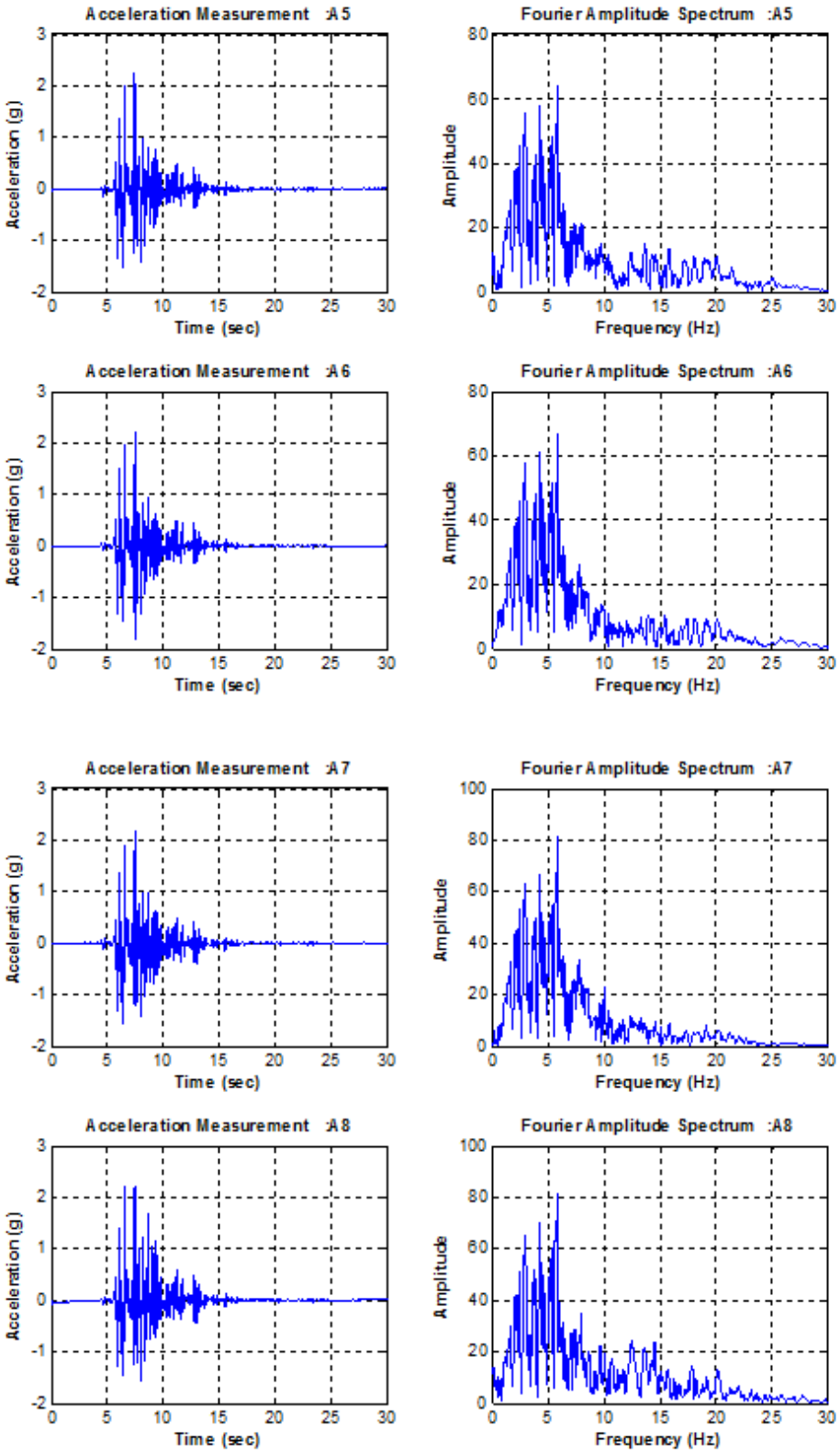

Figure A.40. Acceleration Time History Graphs for Setup 4 Kobe 150%.

APPENDIX B: DISPLACEMENT TIME HISTORY GRAPHS OBTAINED FROM THE TESTS

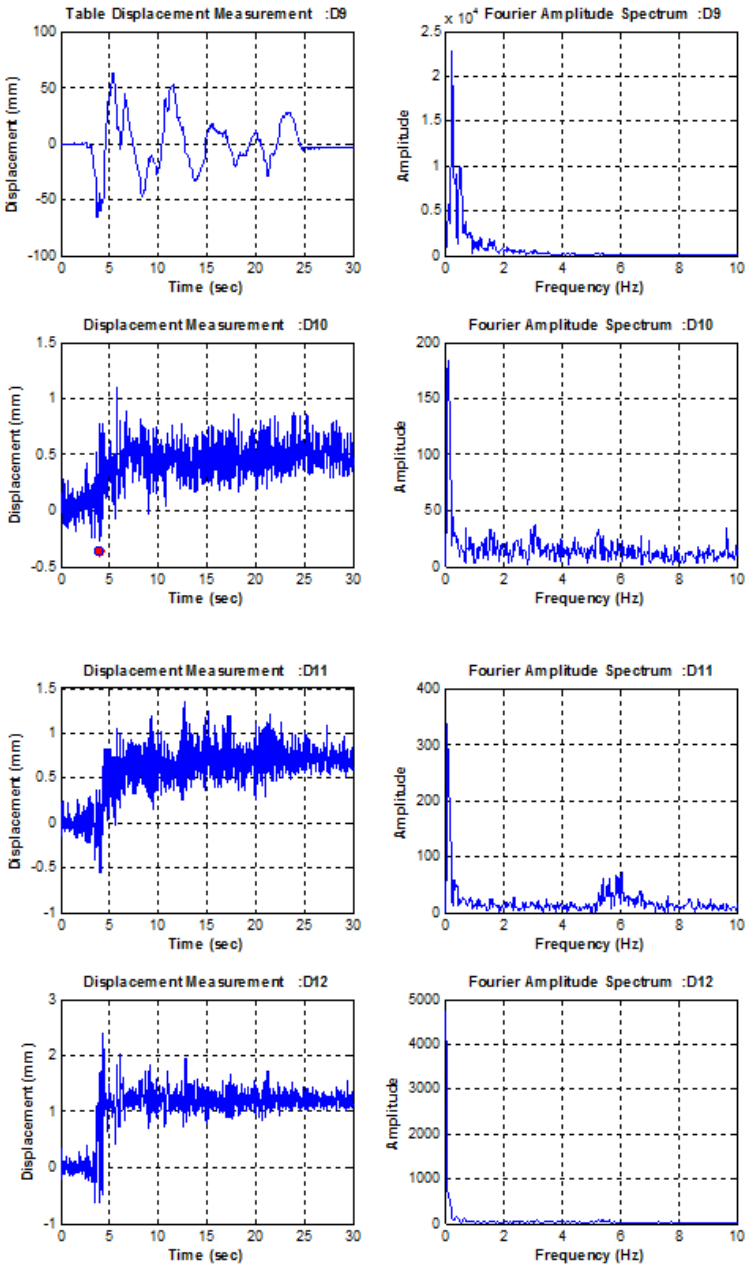

Figure B.1. Displacement Time History Graphs for Setup 1 El Centro 100%.

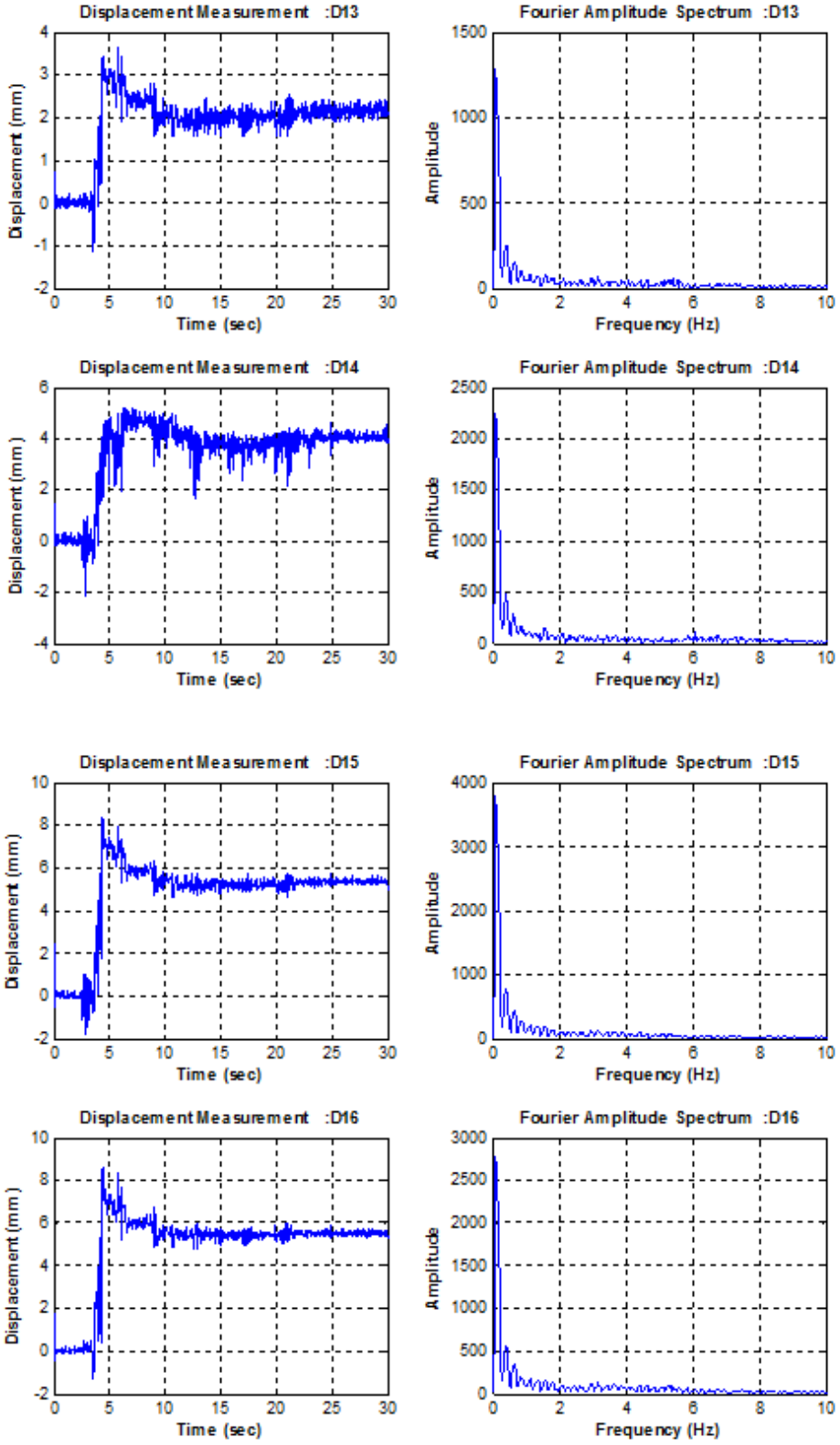

Figure B.2. Displacement Time History Graphs for Setup 1 El Centro 100%.

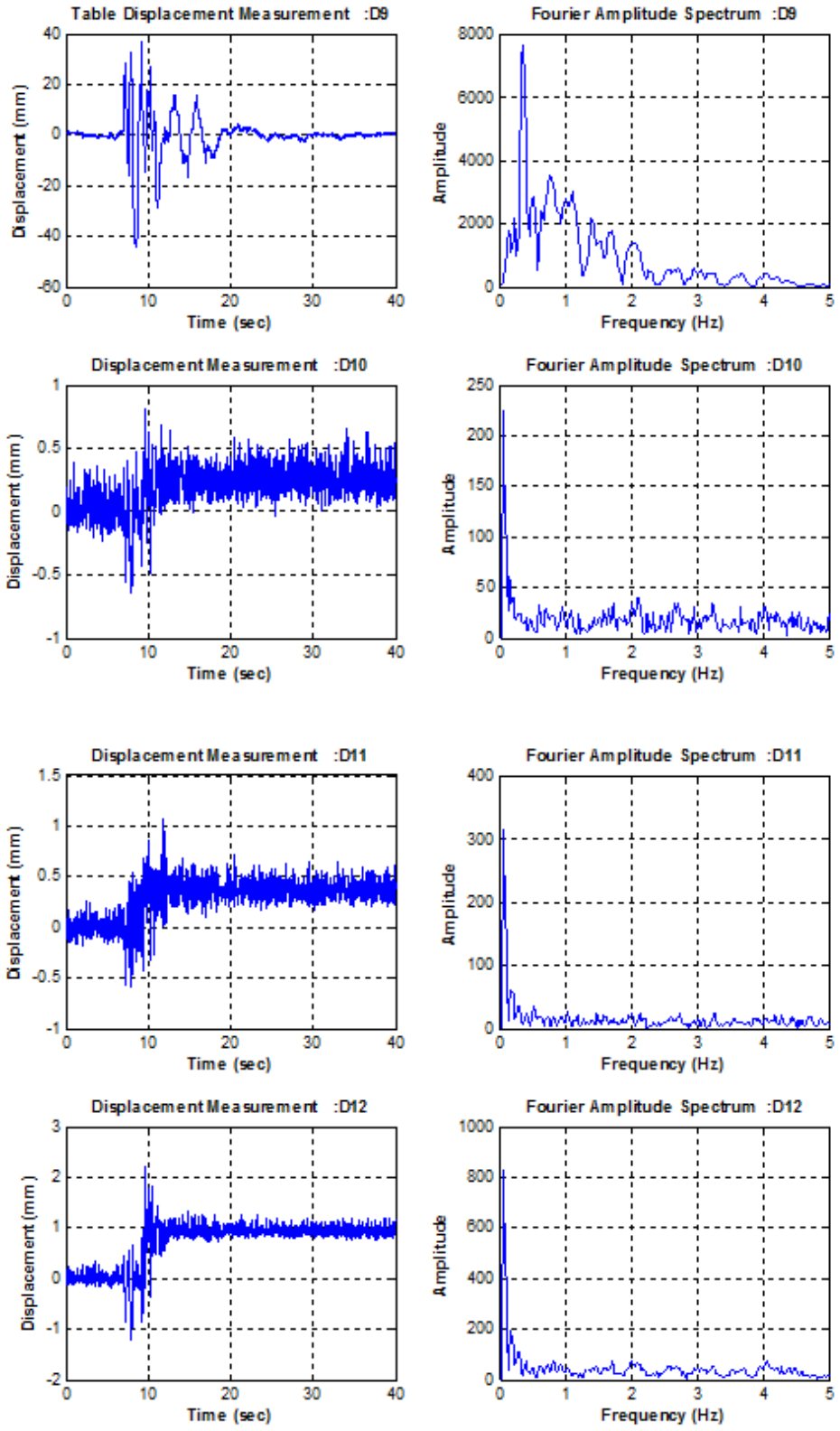

Figure B.3. Displacement Time History Graphs for Setup 1 Kobe 50%.

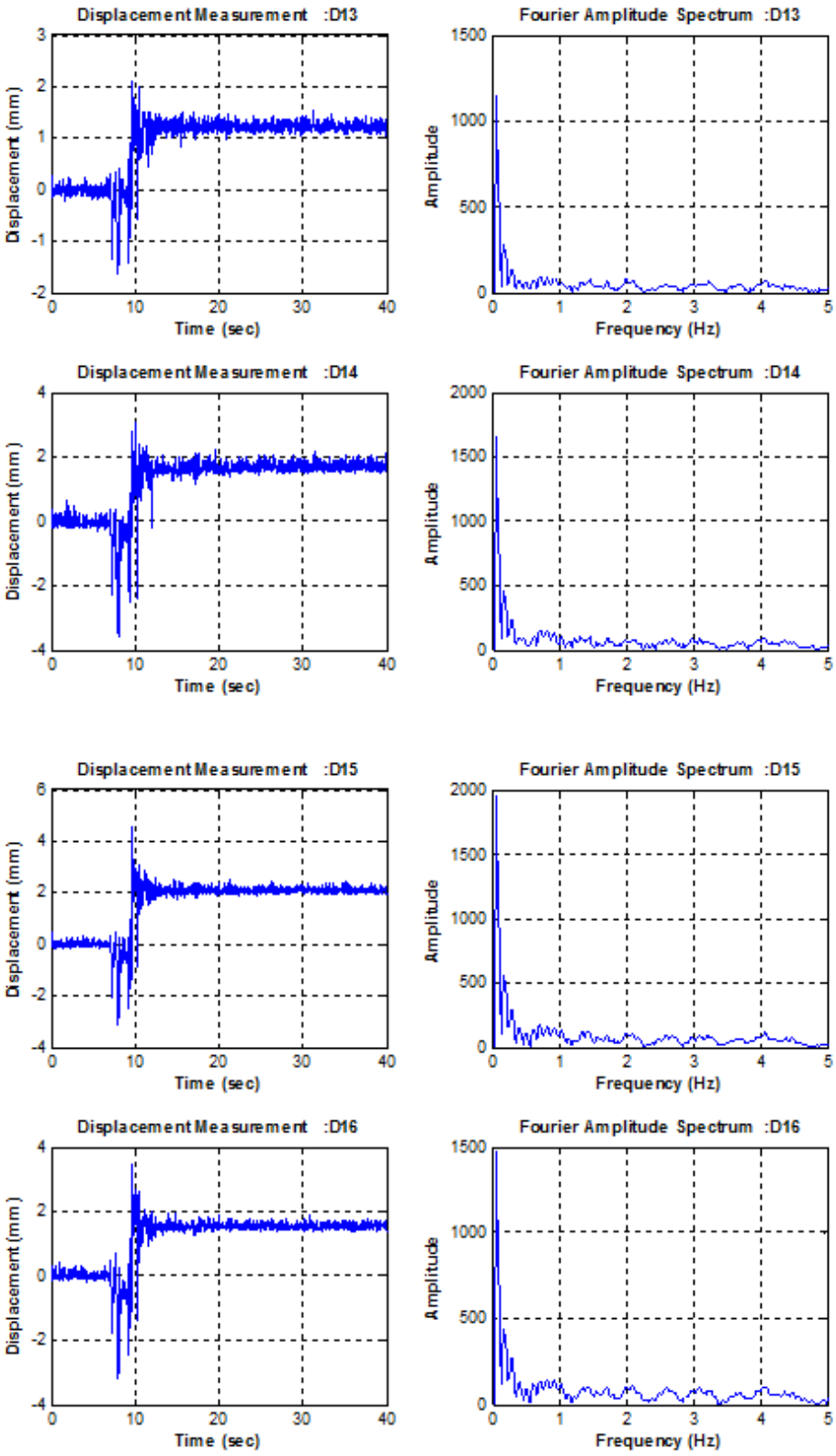

Figure B.4. Displacement Time History Graphs for Setup 1 Kobe 50%.

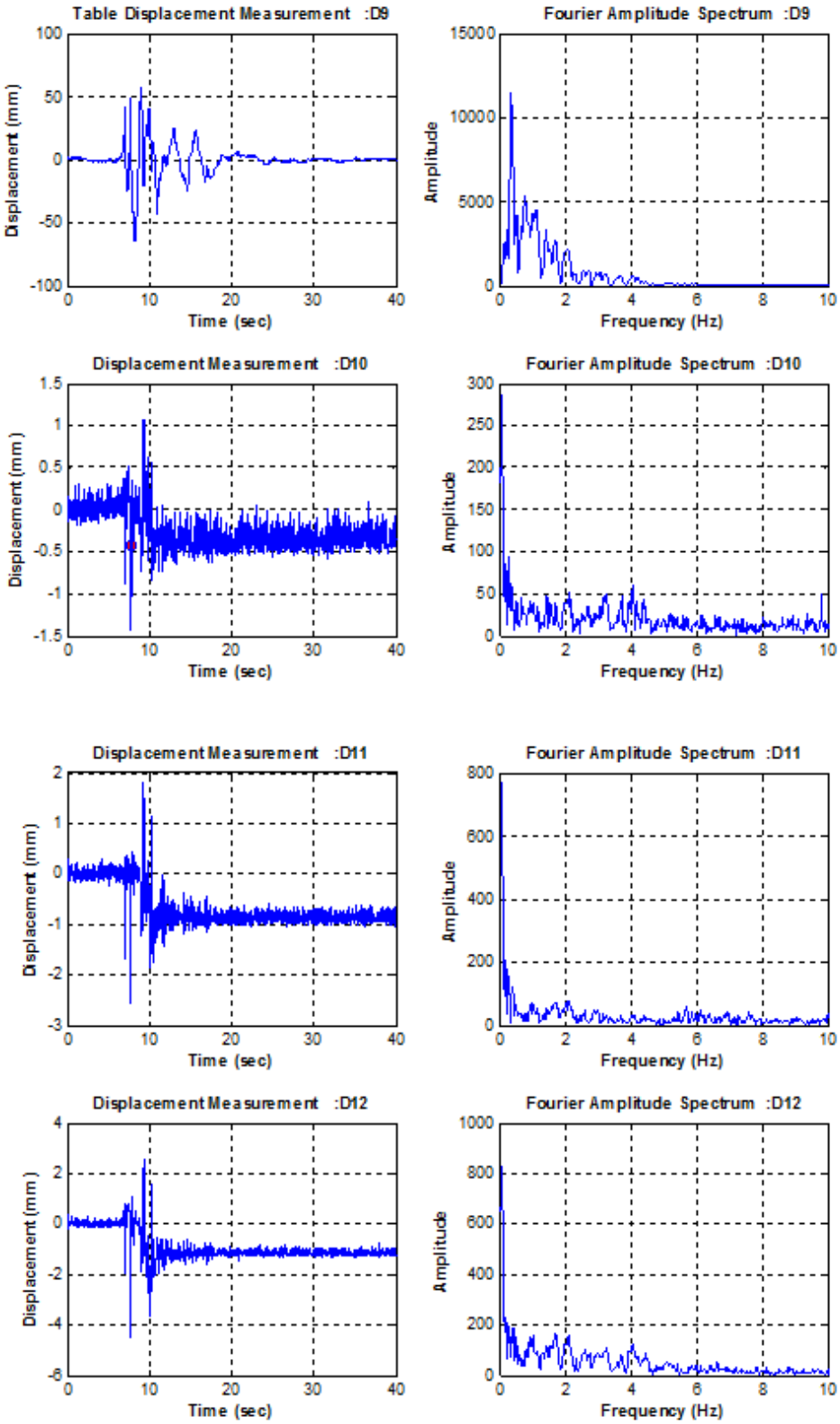

Figure B.5. Displacement Time History Graphs for Setup 1 Kobe 75%.

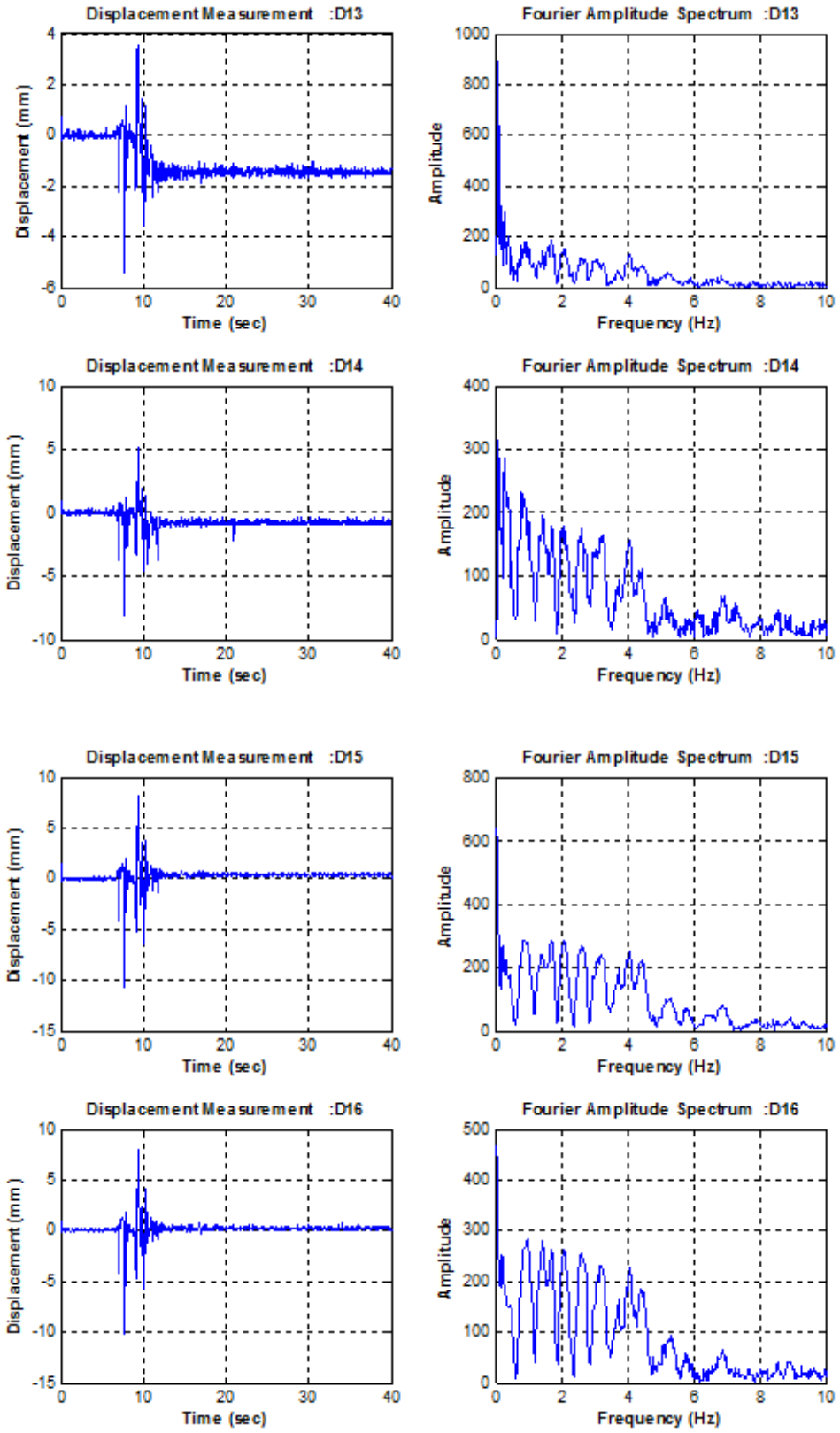

Figure B.6. Displacement Time History Graphs for Setup 1 Kobe 75%.

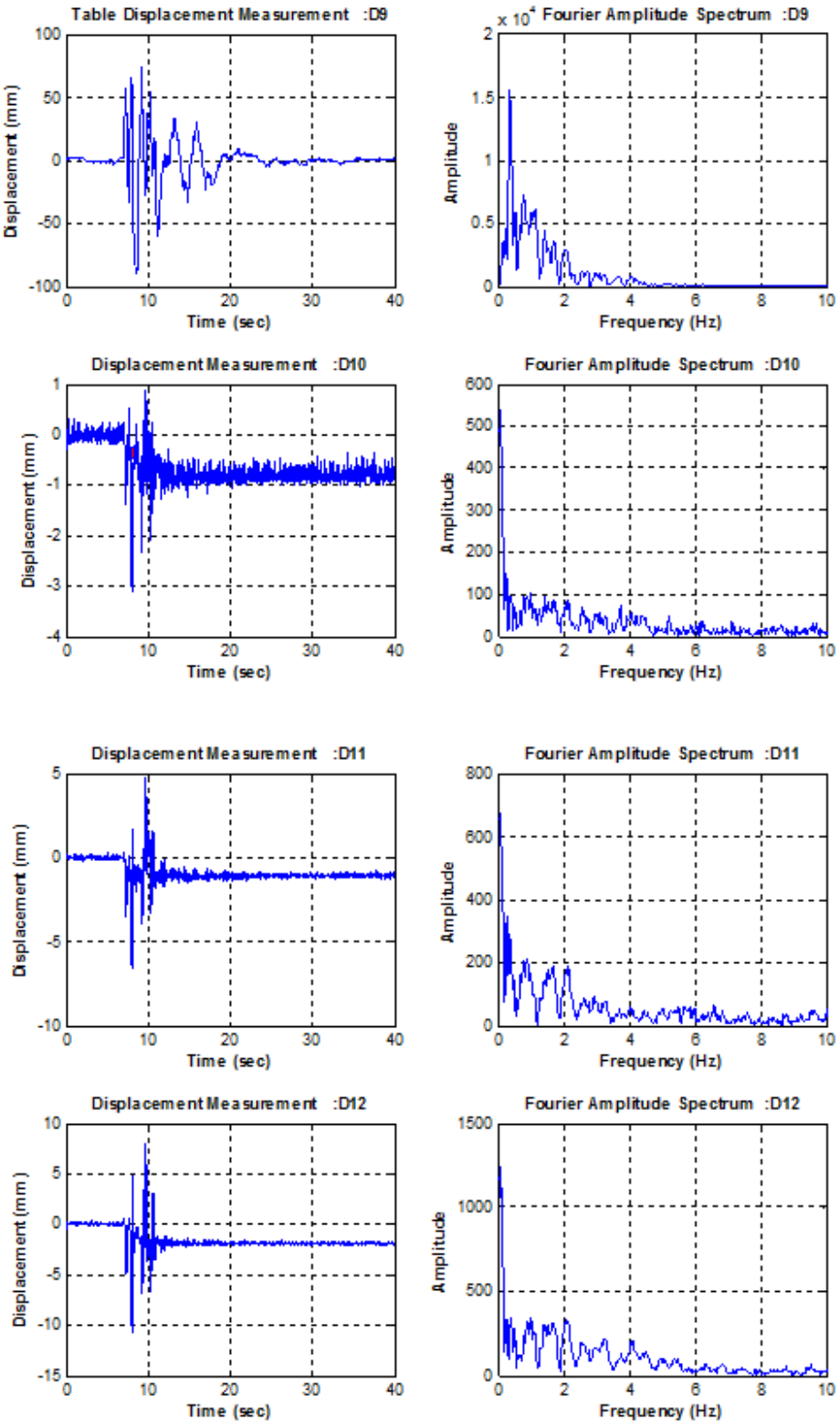

Figure B.7. Displacement Time History Graphs for Setup 1 Kobe 100%.

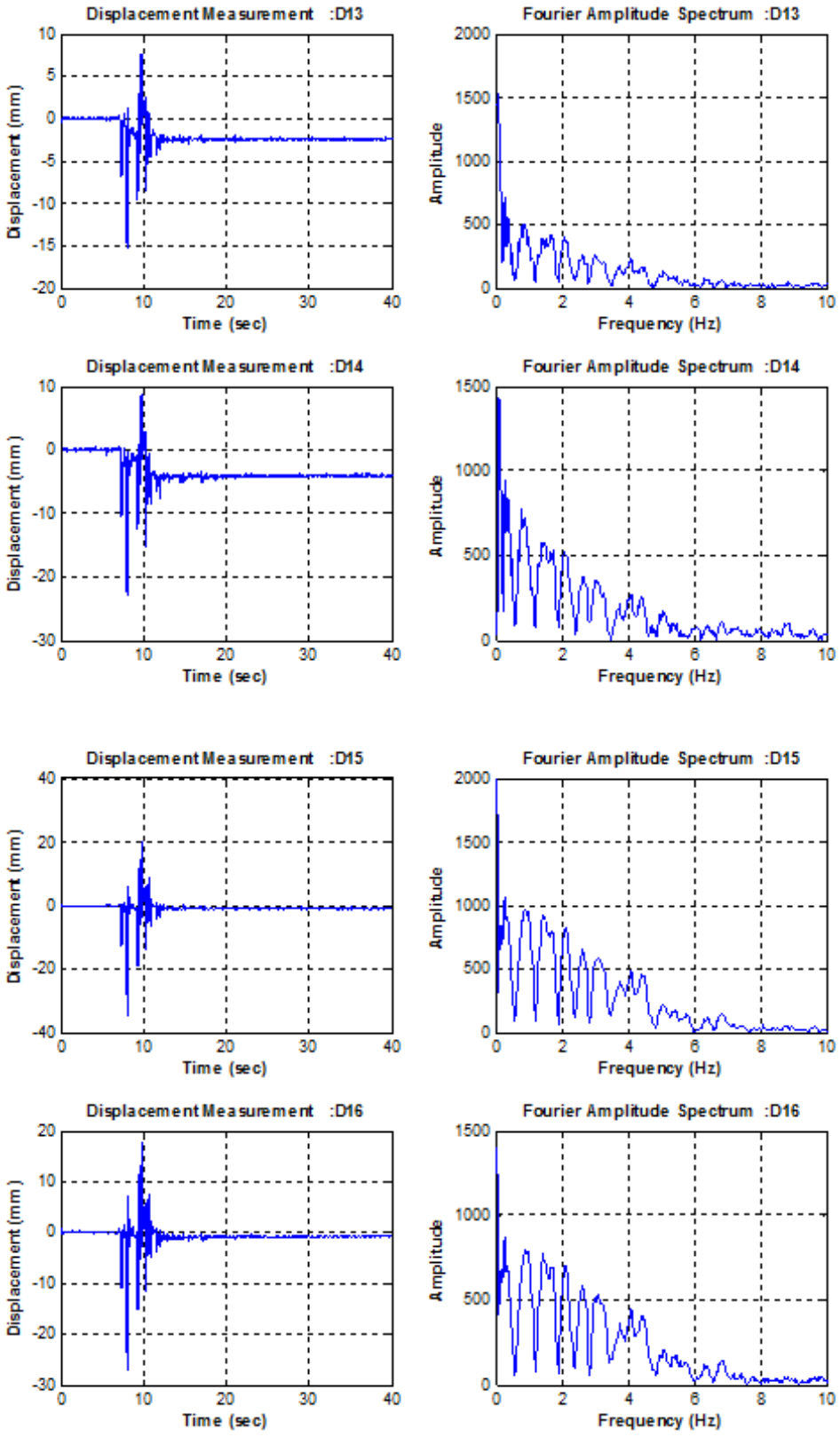

Figure B.8. Displacement Time History Graphs for Setup 1 Kobe 100%.

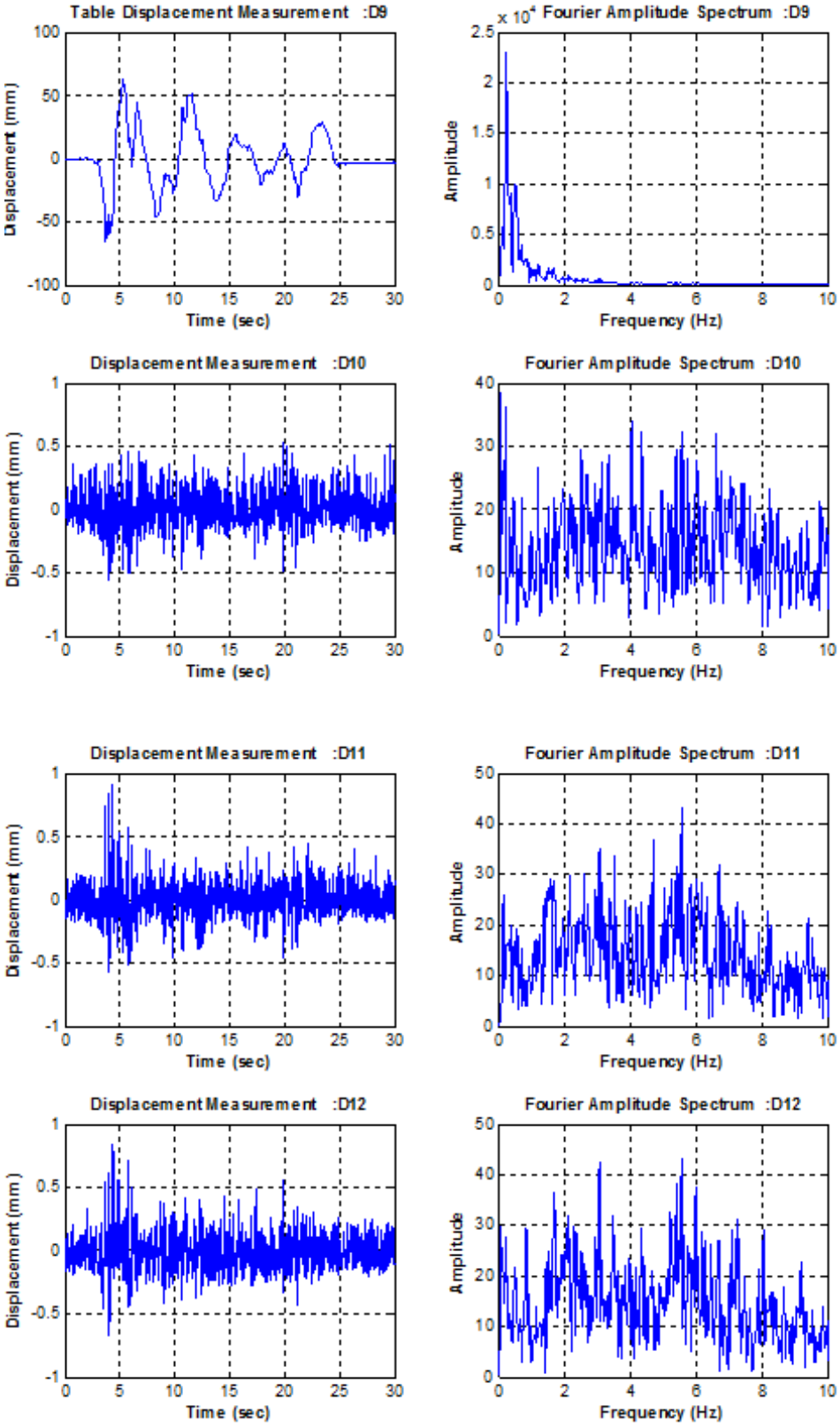

Figure B.9. Displacement Time History Graphs for Setup 2 El Centro 100%.

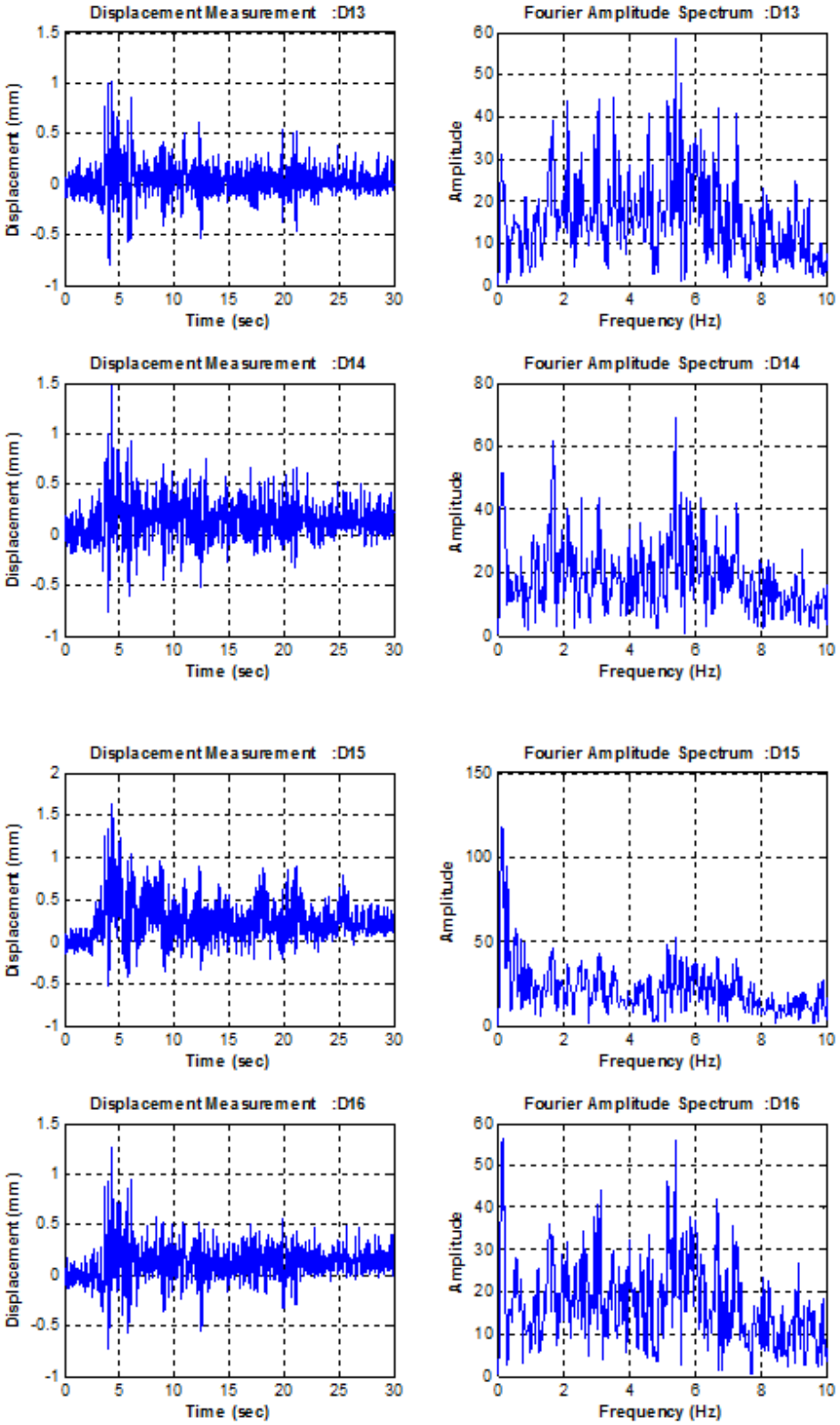

Figure B.10. Displacement Time History Graphs for Setup 2 El Centro 100%.

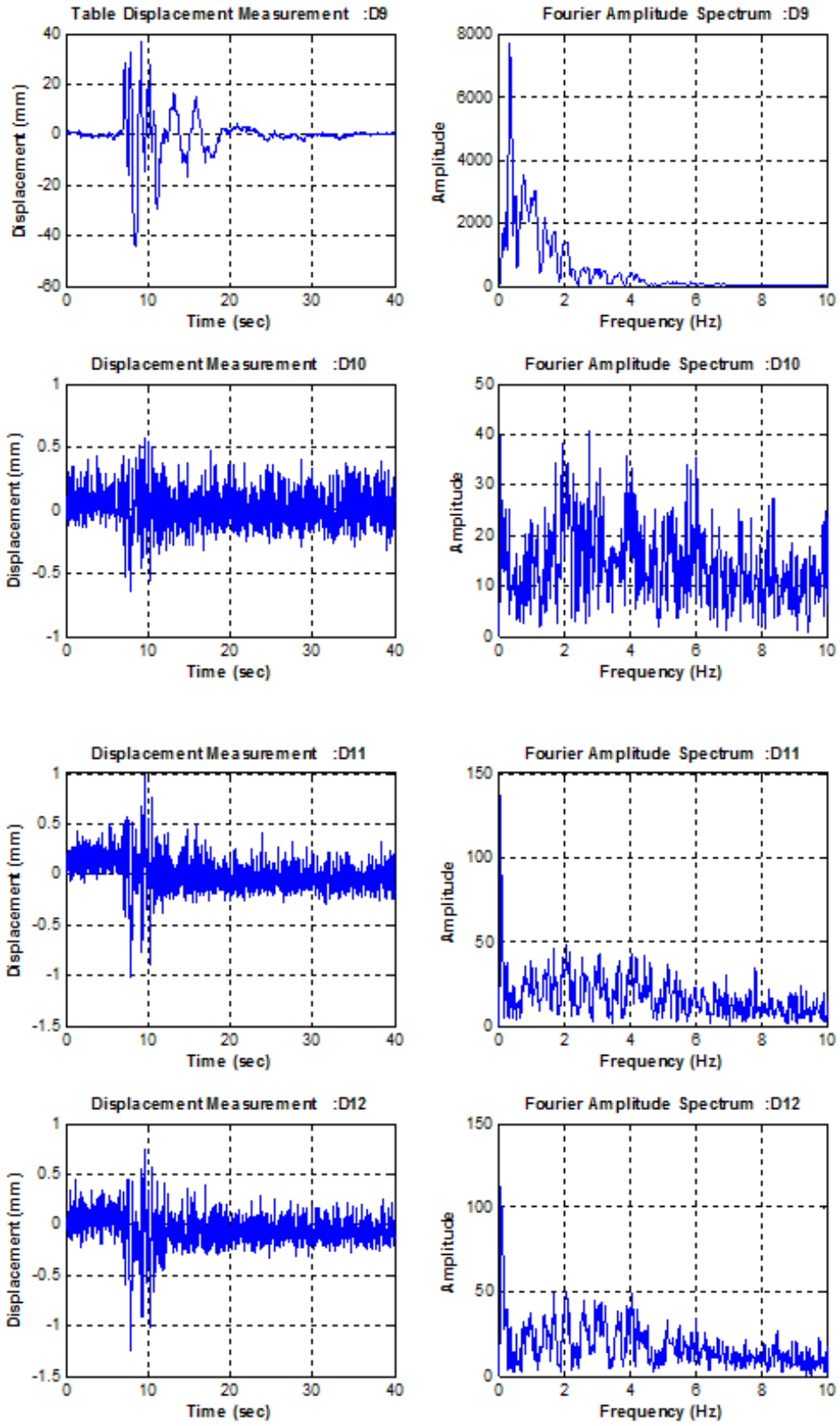

Figure B.11. Displacement Time History Graphs for Setup 2 Kobe 50%.

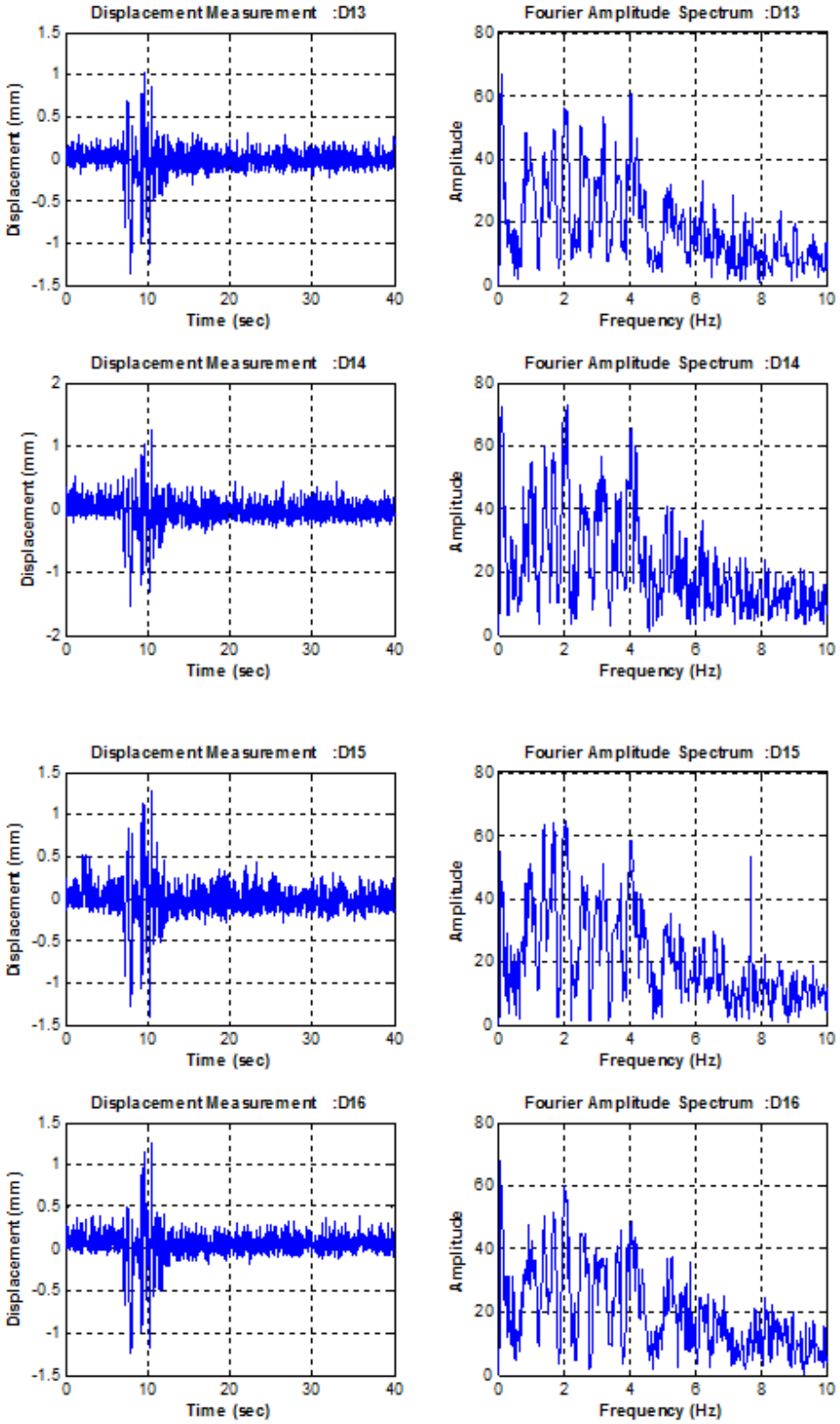

Figure B.12. Displacement Time History Graphs for Setup 2 Kobe 50%.

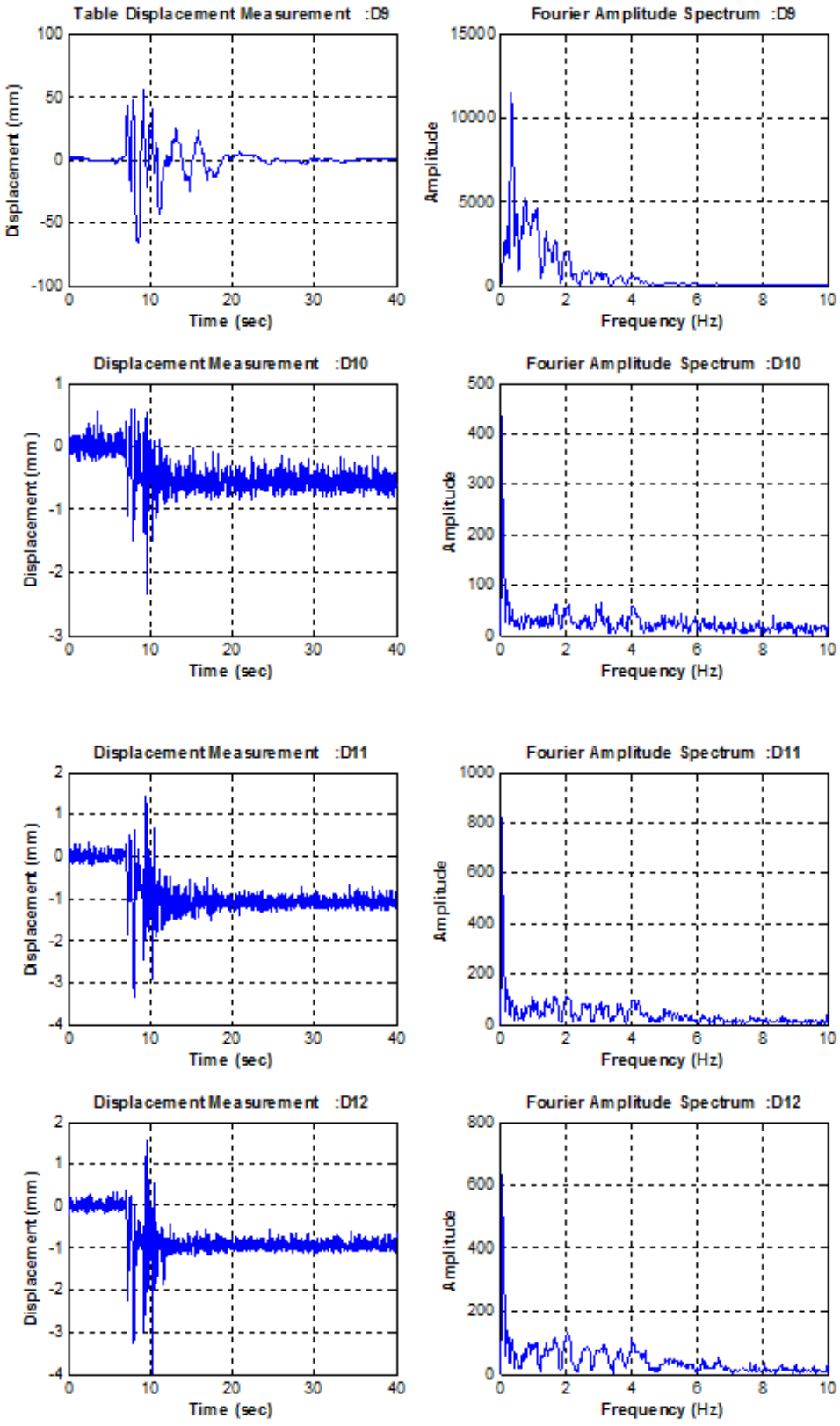

Figure B.13. Displacement Time History Graphs for Setup 2 Kobe 75%.

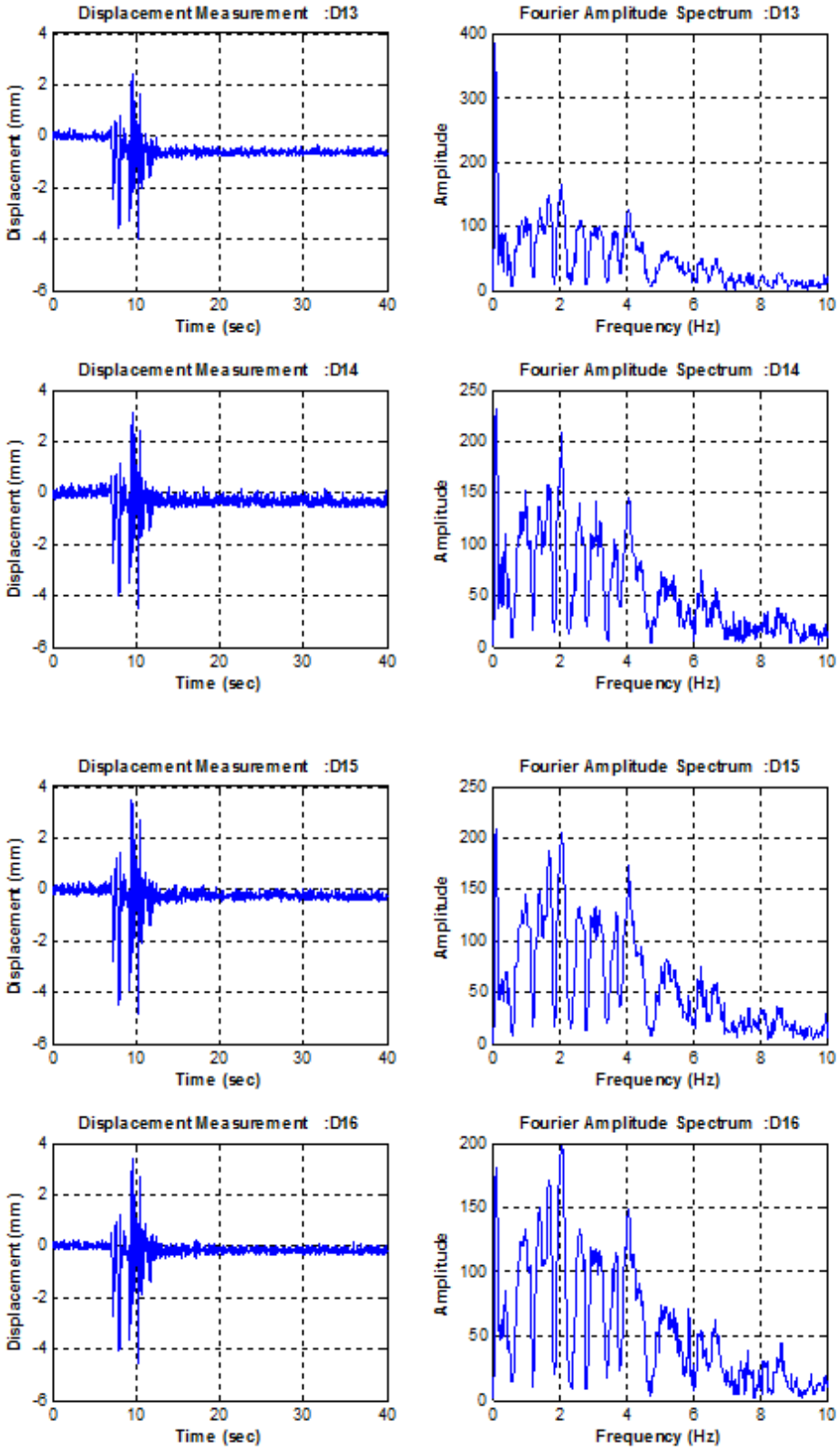

Figure B.14. Displacement Time History Graphs for Setup 2 Kobe 75%.

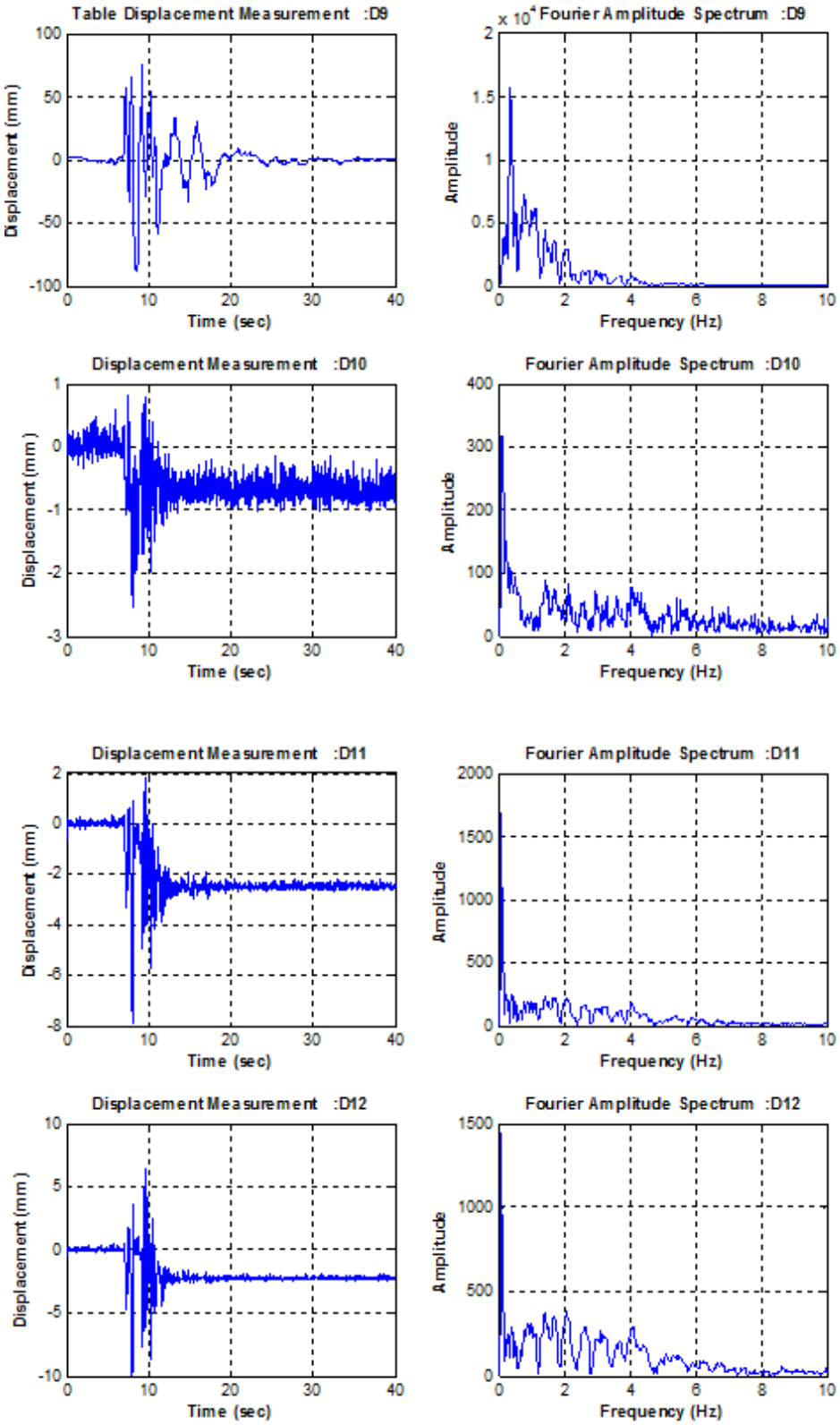

Figure B.15. Displacement Time History Graphs for Setup 2 Kobe 75%.

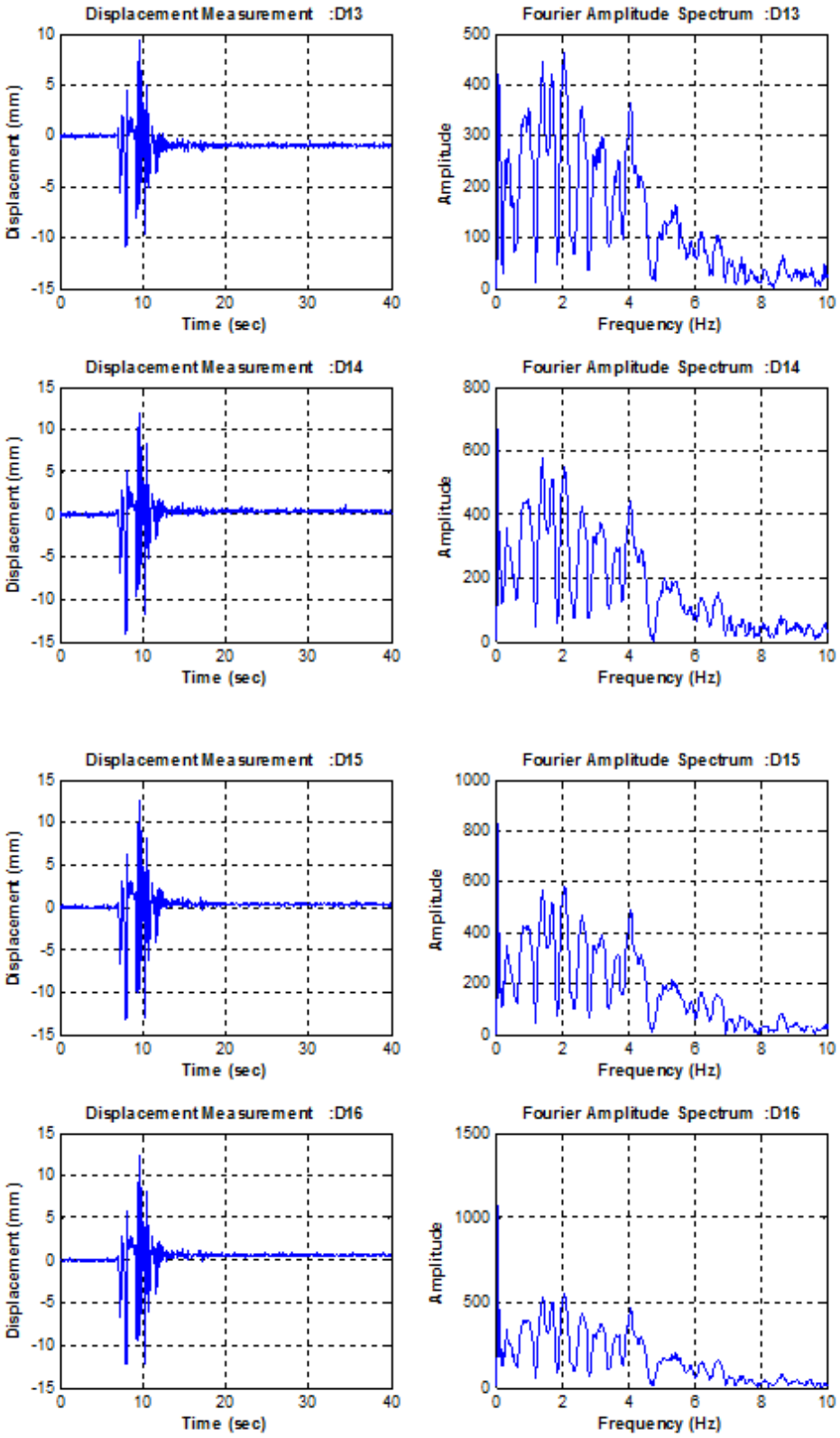

Figure B.16. Displacement Time History Graphs for Setup 2 Kobe 100%.

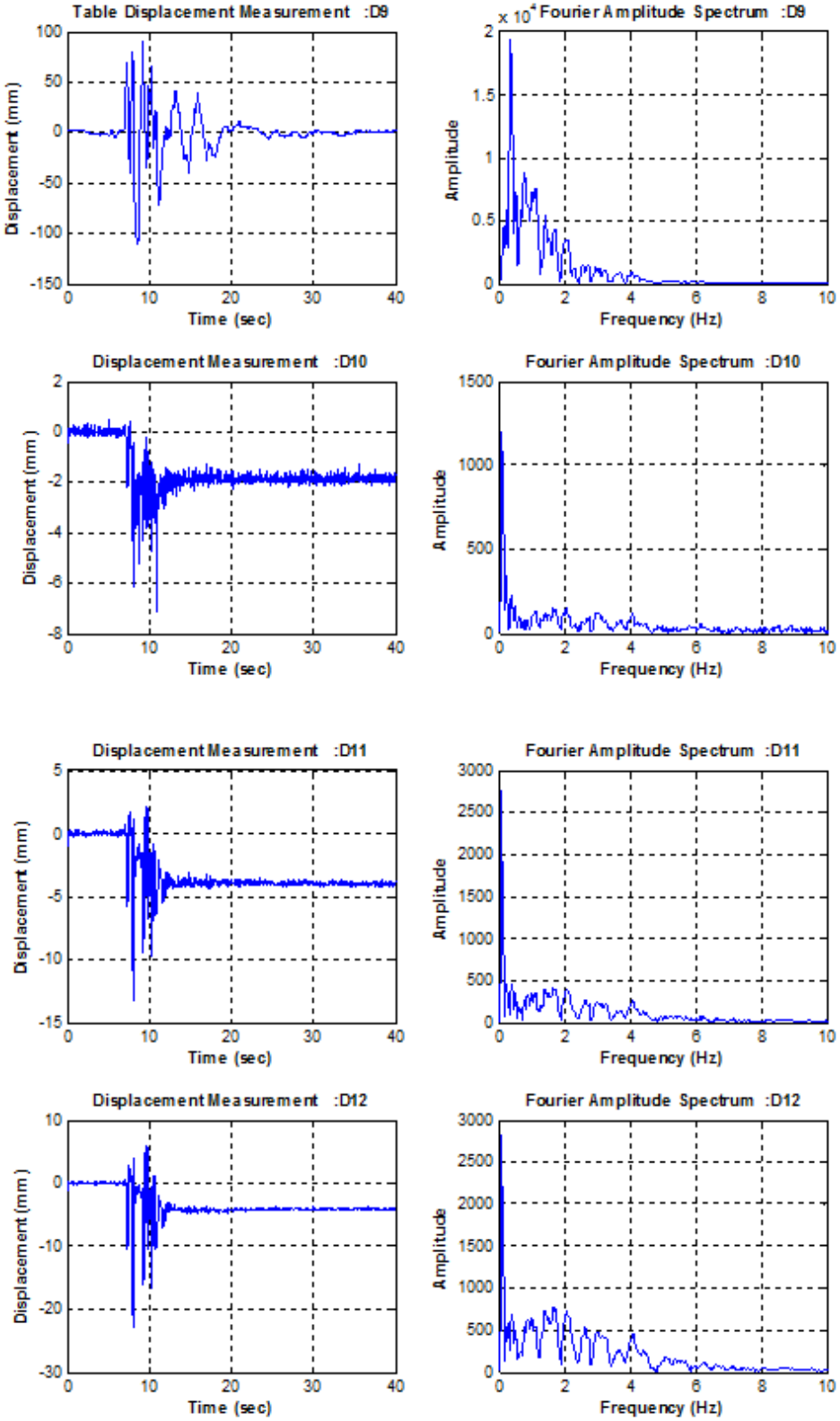

Figure B.17. Displacement Time History Graphs for Setup 2 Kobe 125%.

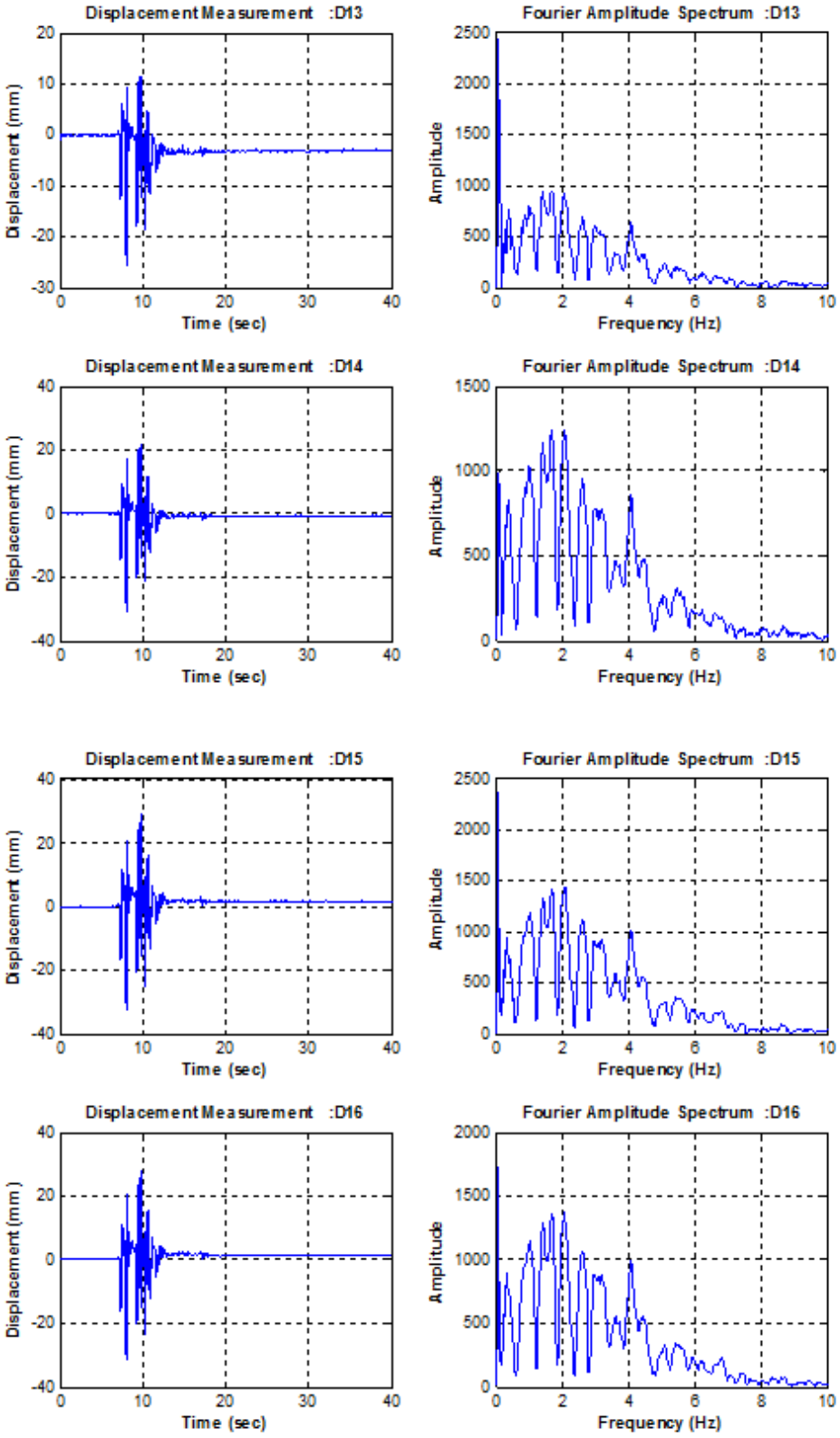

Figure B.18. Displacement Time History Graphs for Setup 2 Kobe 125%.

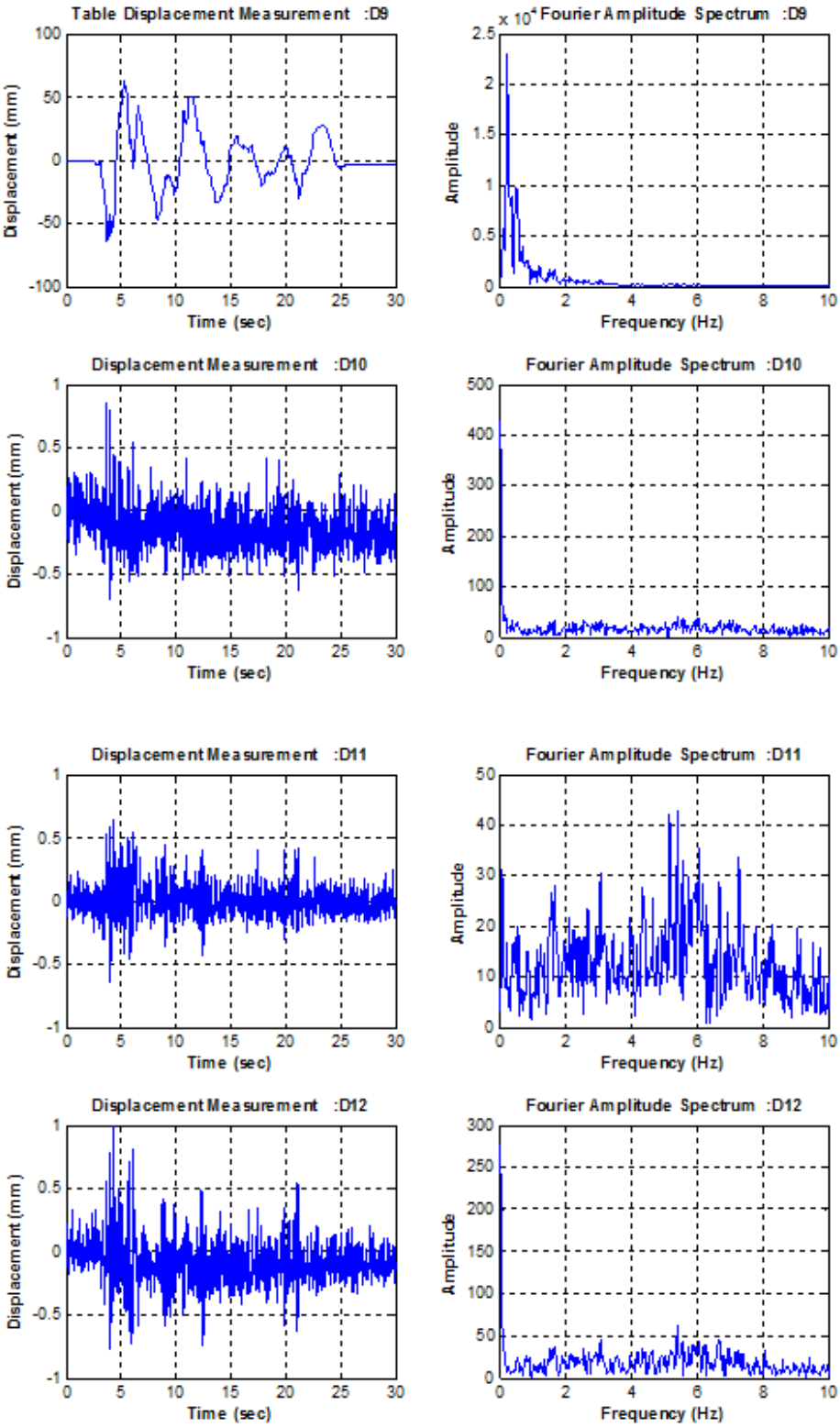

Figure B.19. Displacement Time History Graphs for Setup 3 El Centro 100%.

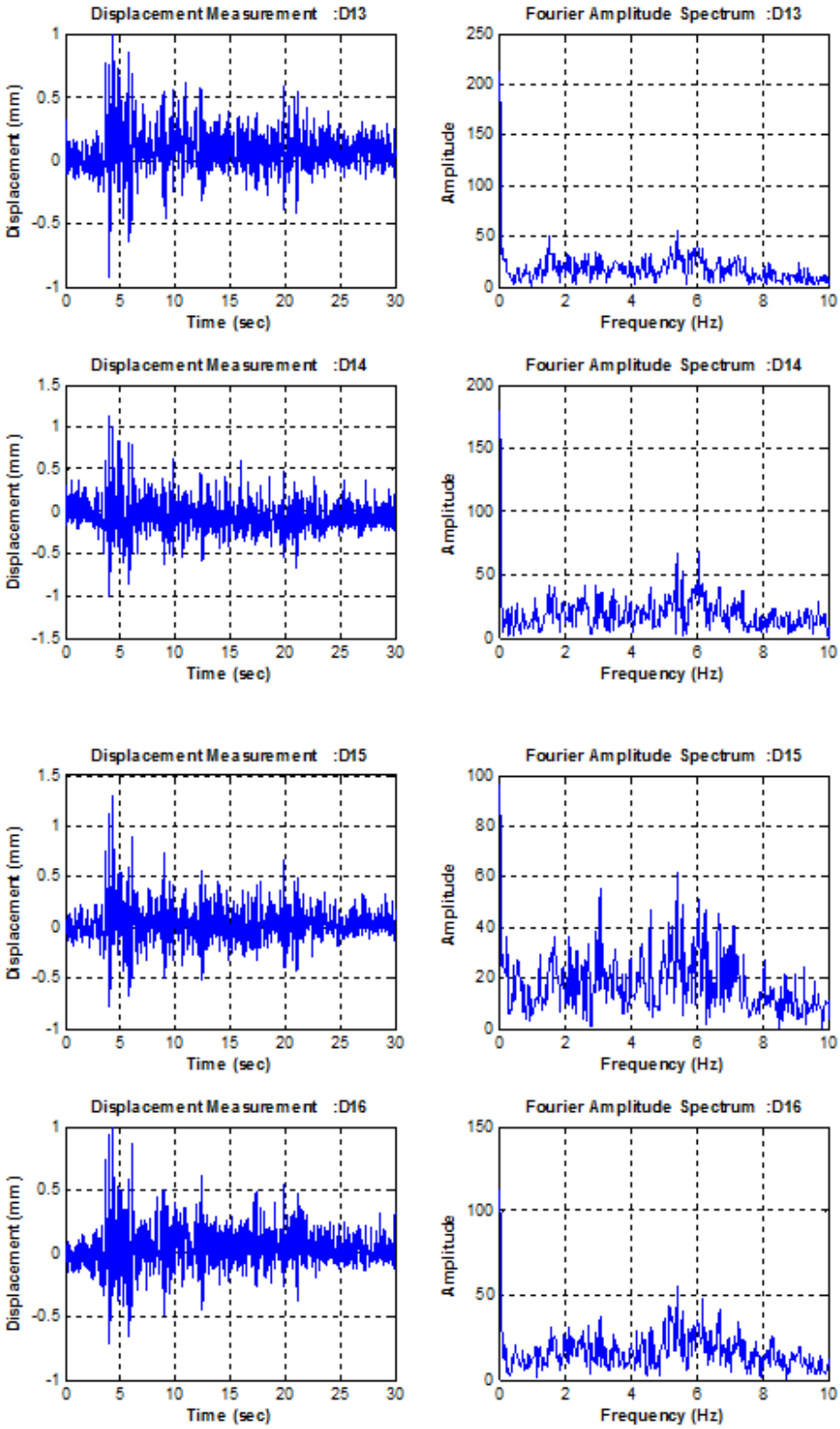

Figure B.20. Displacement Time History Graphs for Setup 3 El Centro 100%.

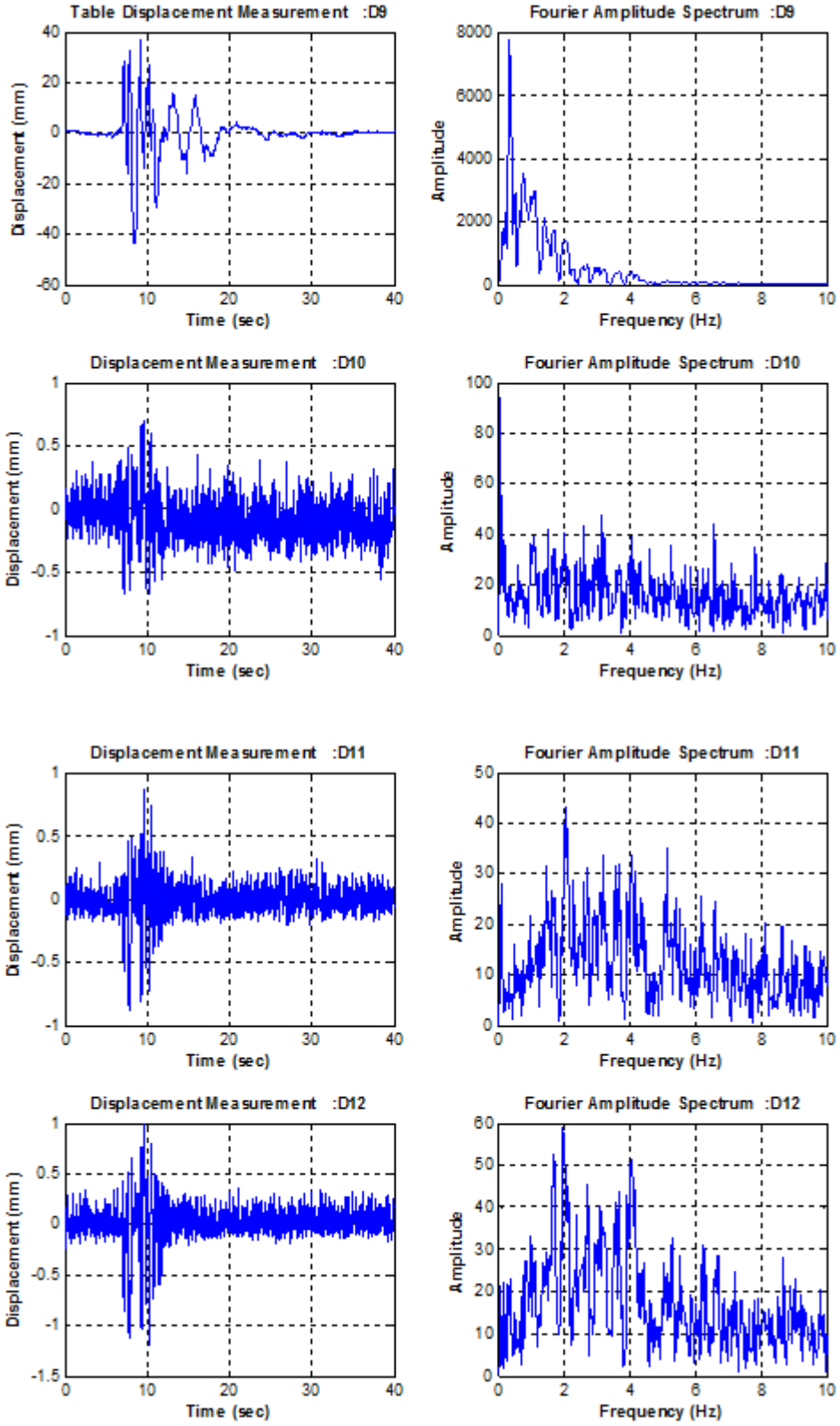

Figure B.21. Displacement Time History Graphs for Setup 3 Kobe 50%.

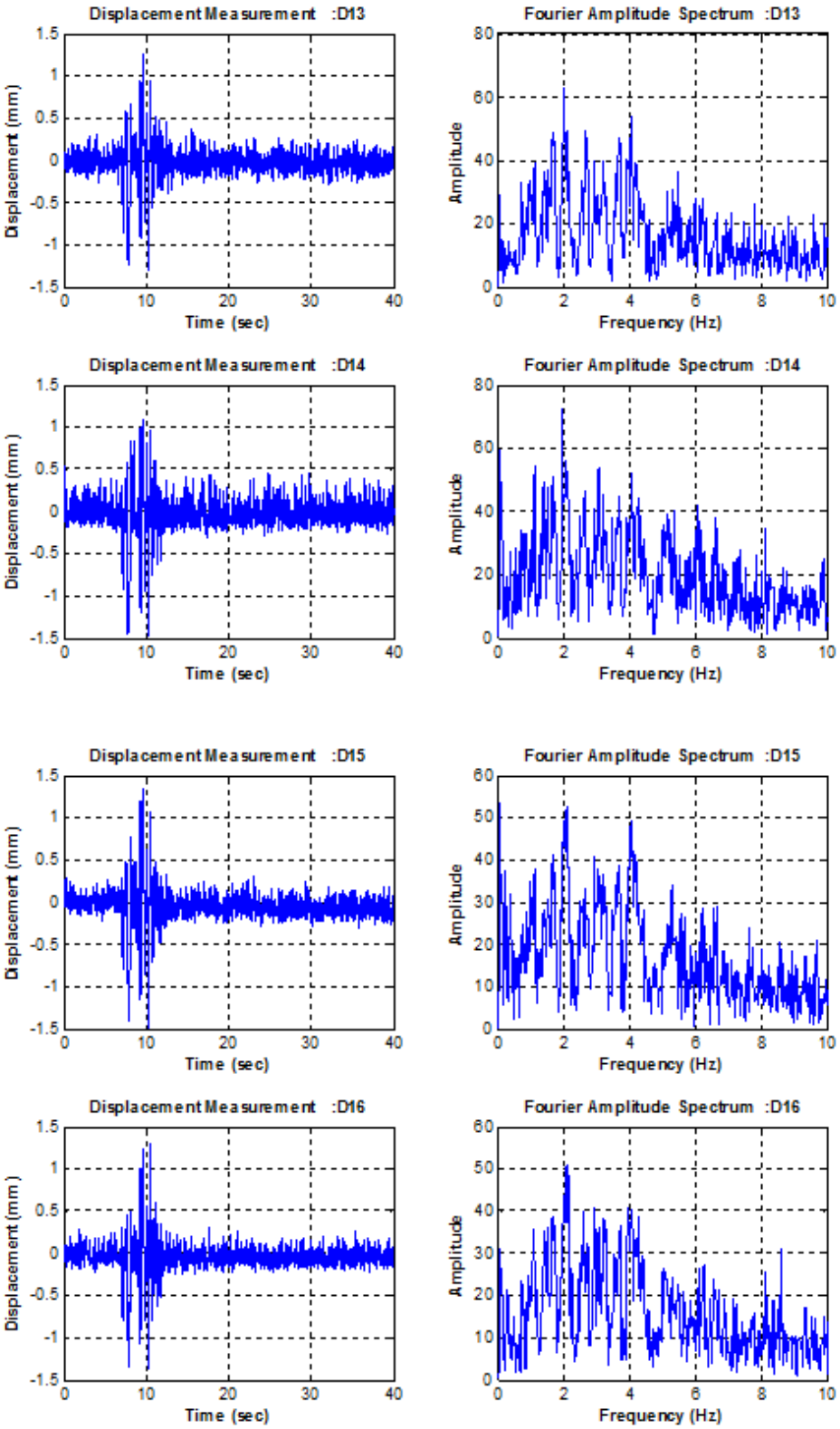

Figure B.22. Displacement Time History Graphs for Setup 3 Kobe 50%.

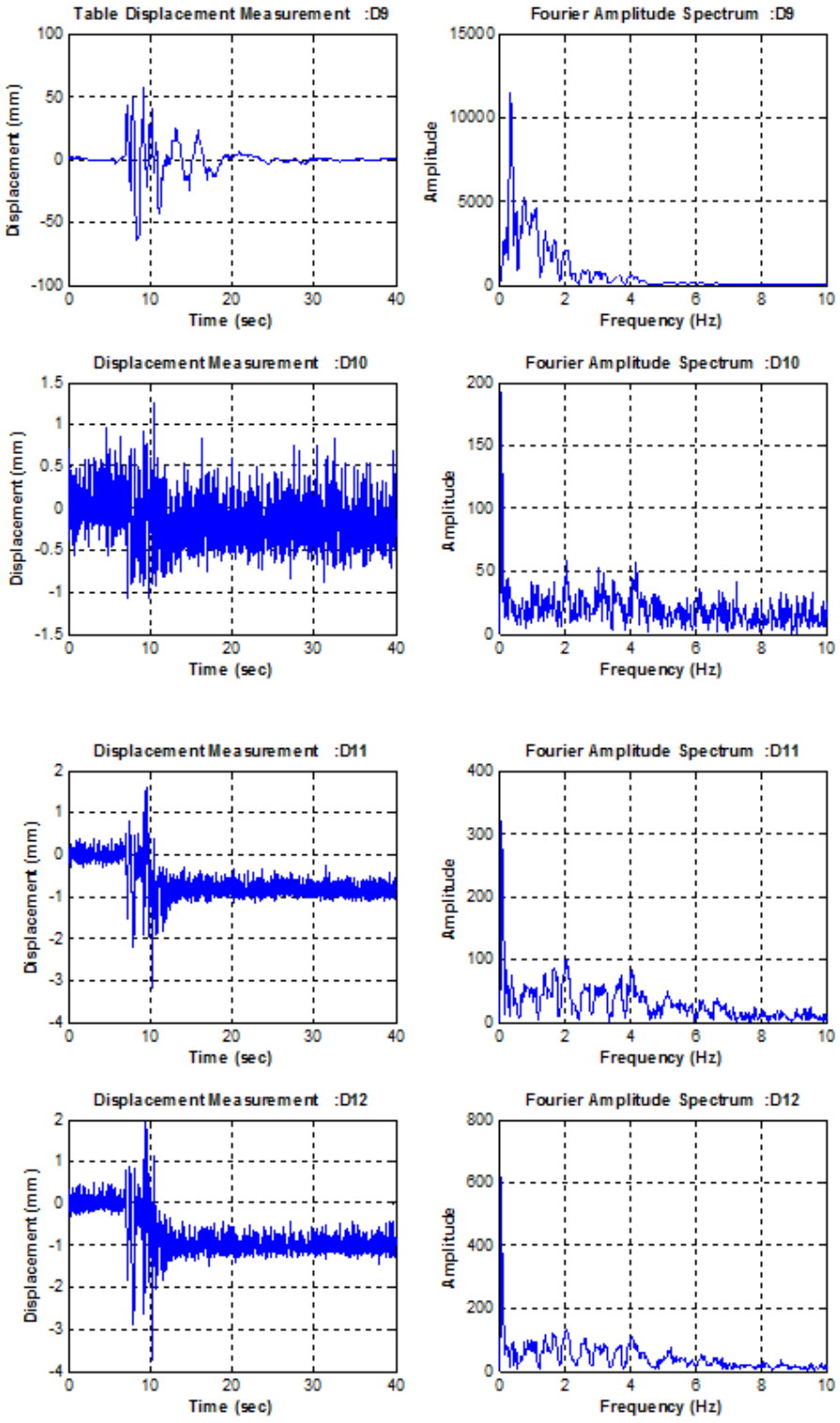

Figure B.23. Displacement Time History Graphs for Setup 3 Kobe 75%.

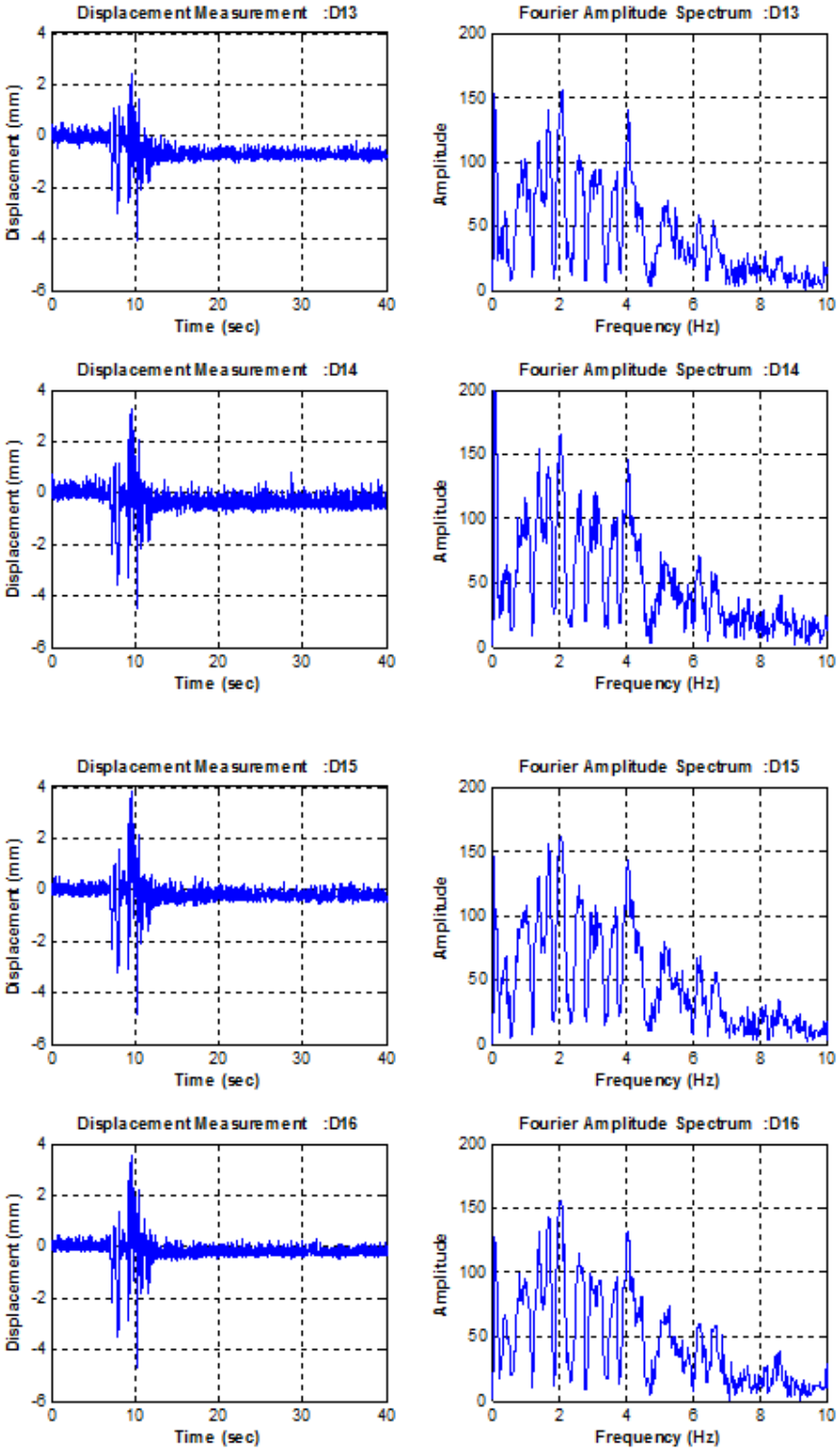

Figure B.24. Displacement Time History Graphs for Setup 3 Kobe 75%.

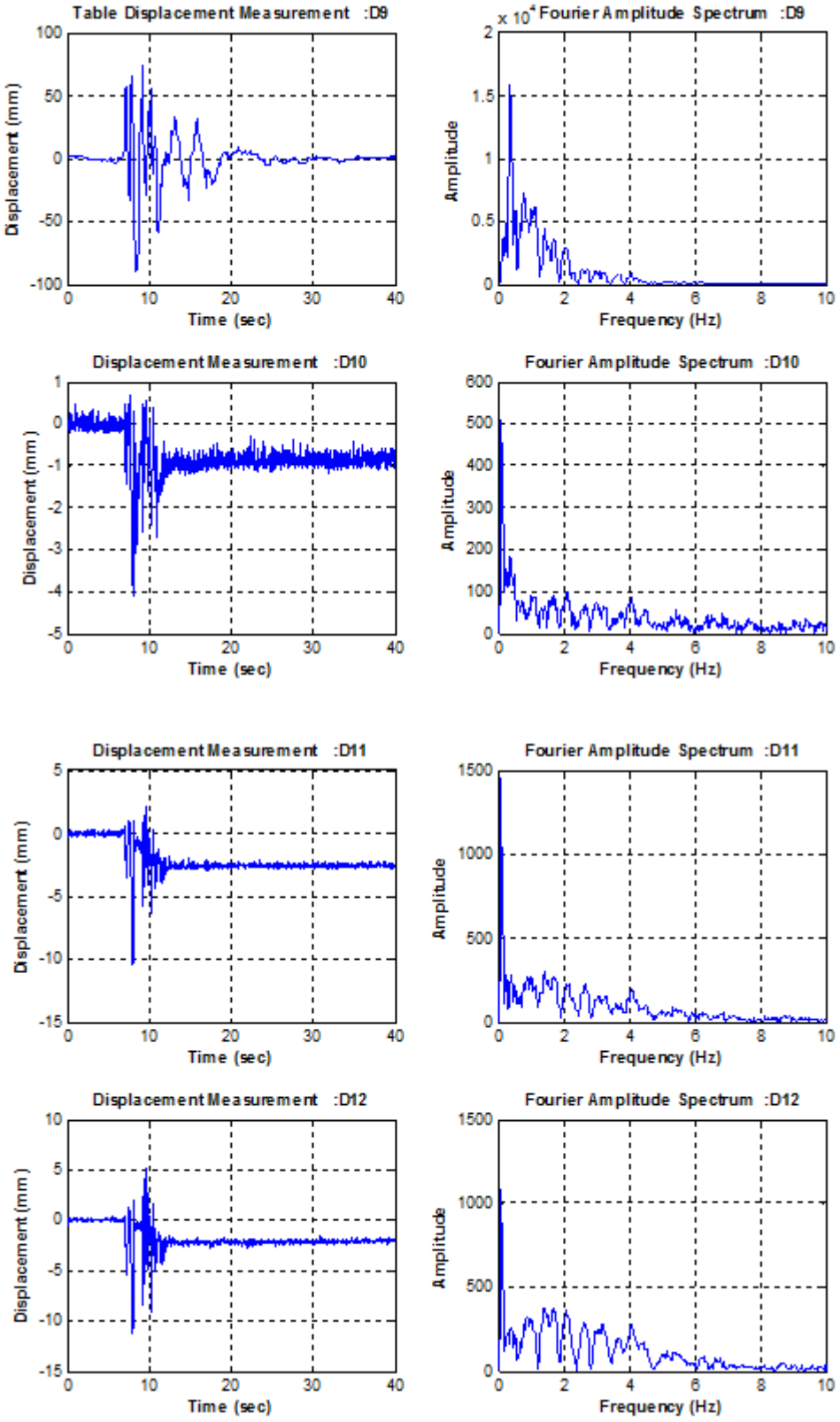

Figure B.25. Displacement Time History Graphs for Setup 3 Kobe 100%.

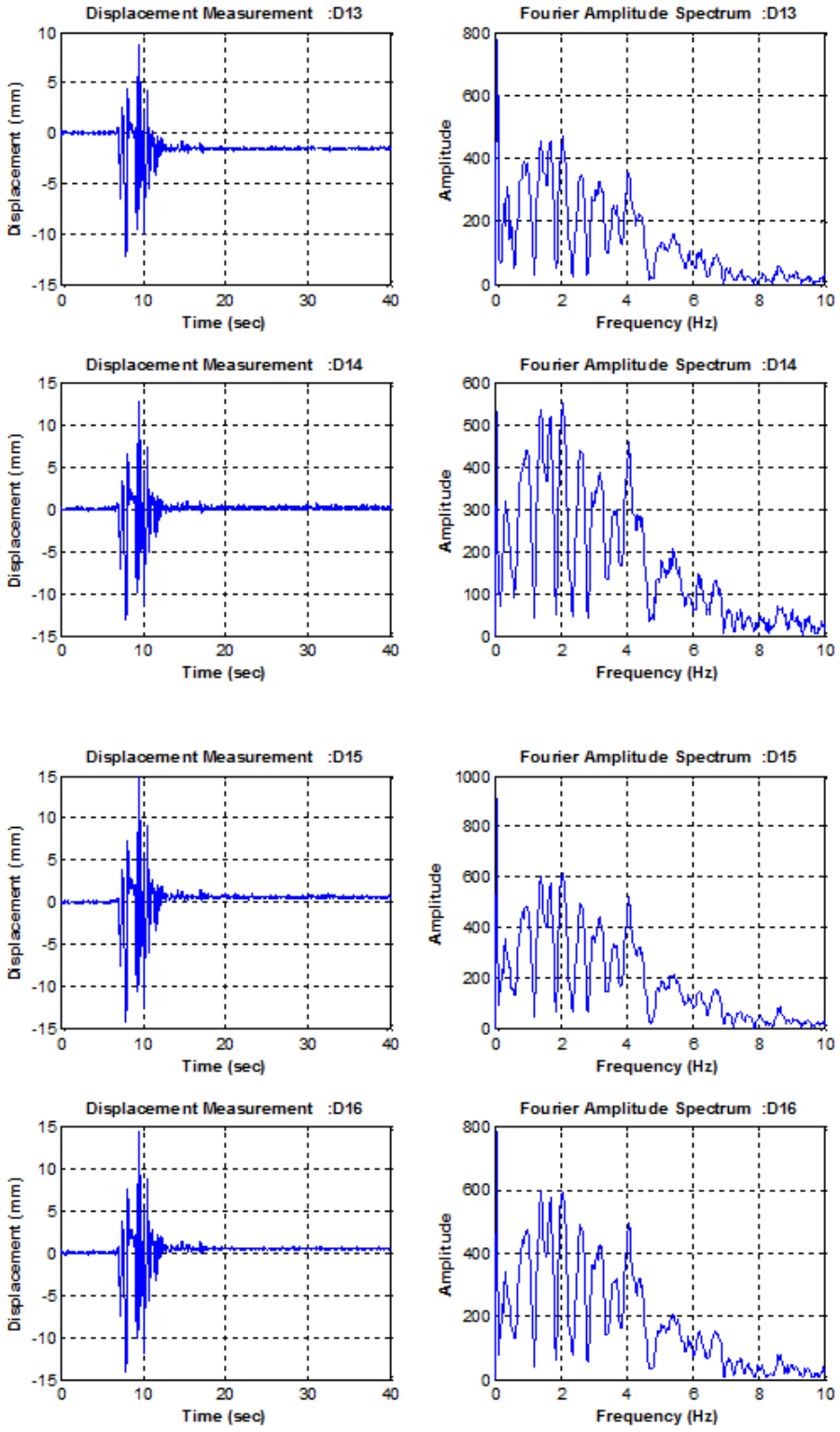

Figure B.26. Displacement Time History Graphs for Setup 3 Kobe 100%.

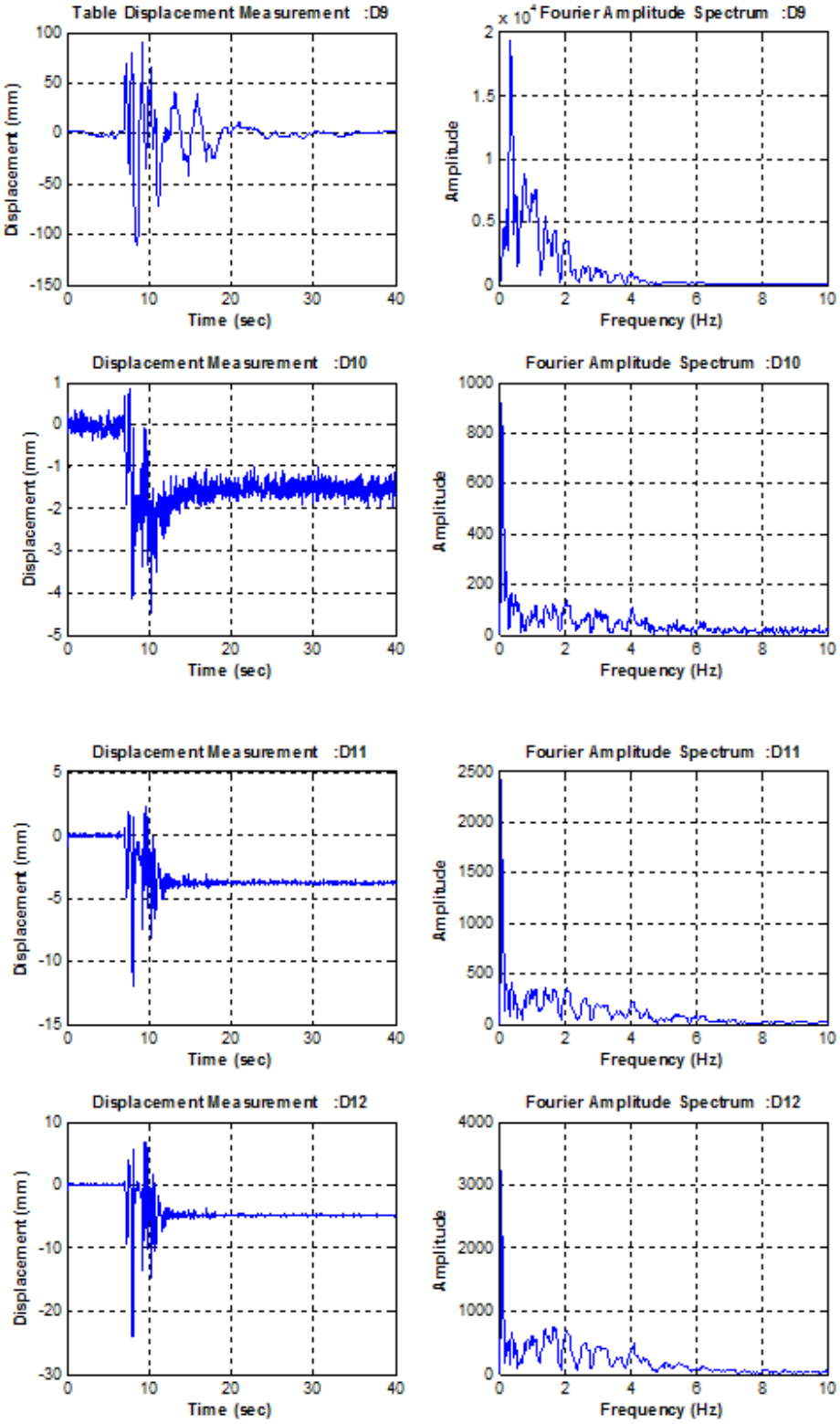

Figure B.27. Displacement Time History Graphs for Setup 3 Kobe 125%.

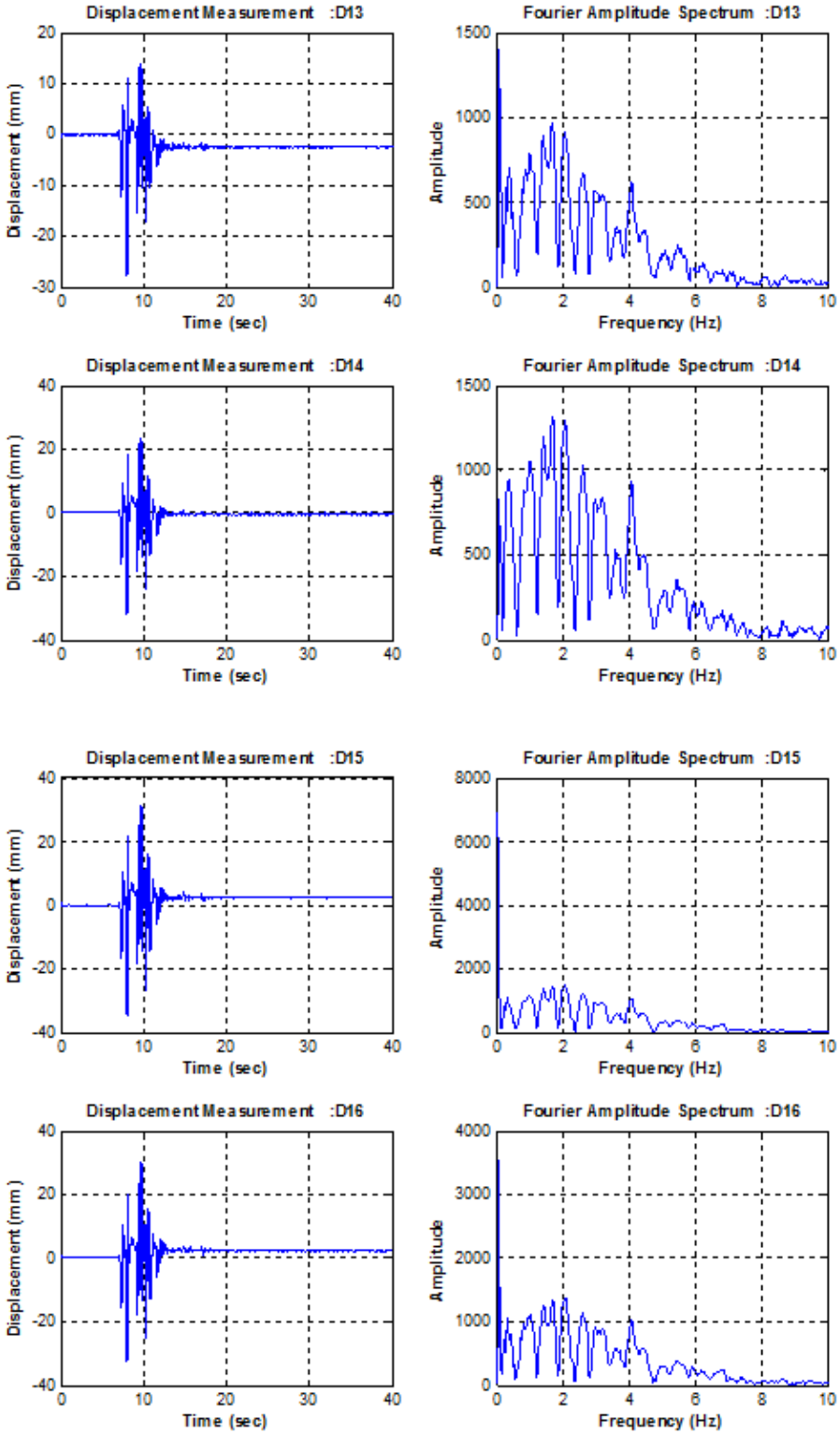

Figure B.28. Displacement Time History Graphs for Setup 3 Kobe 125%.

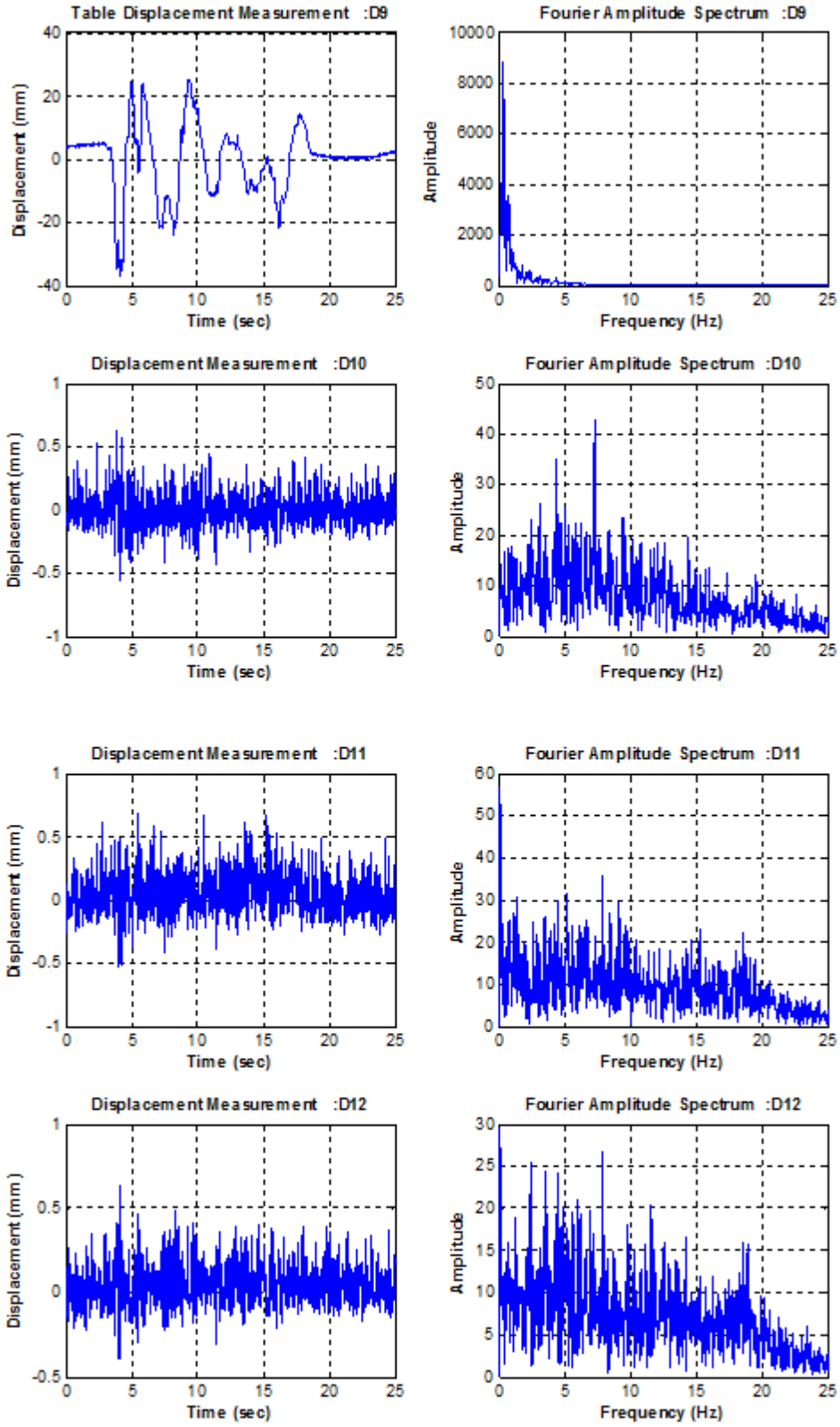

Figure B.29. Displacement Time History Graphs for Setup 3 Kobe 100%.

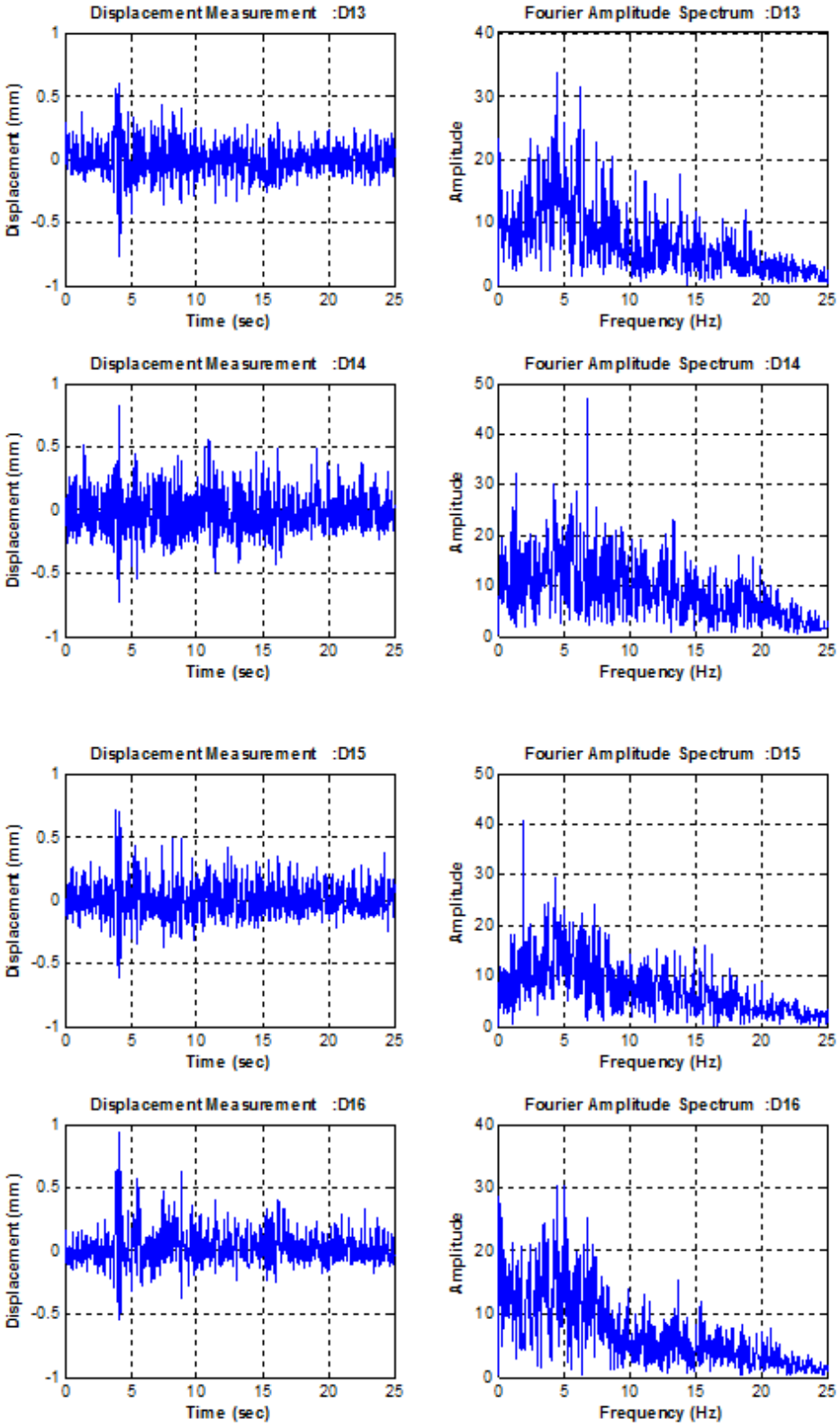

Figure B.30. Displacement Time History Graphs for Setup 4 El Centro 100%.

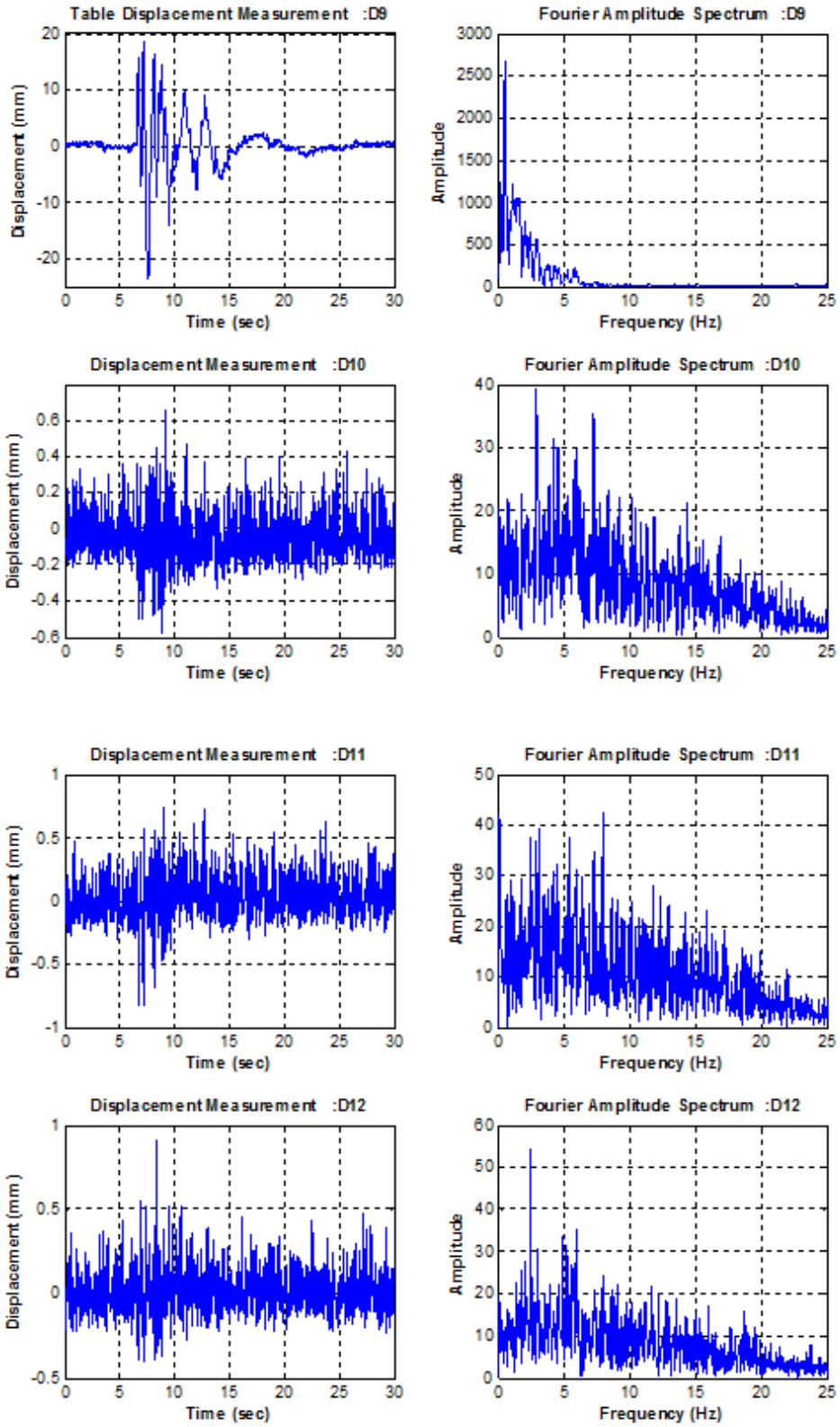

Figure B.31. Displacement Time History Graphs for Setup 4 Kobe 50%.

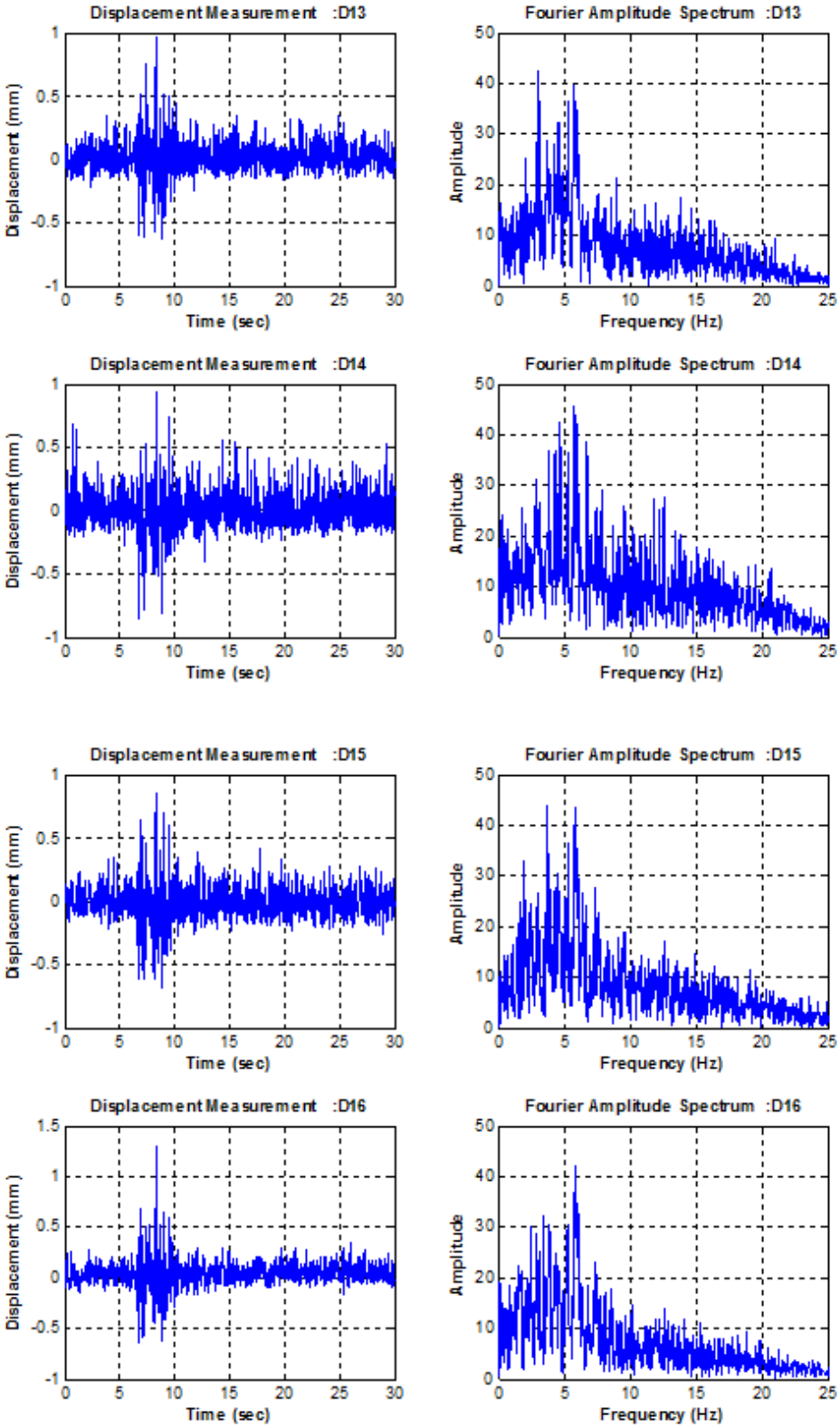

Figure B.32. Displacement Time History Graphs for Setup 4 Kobe 50%.

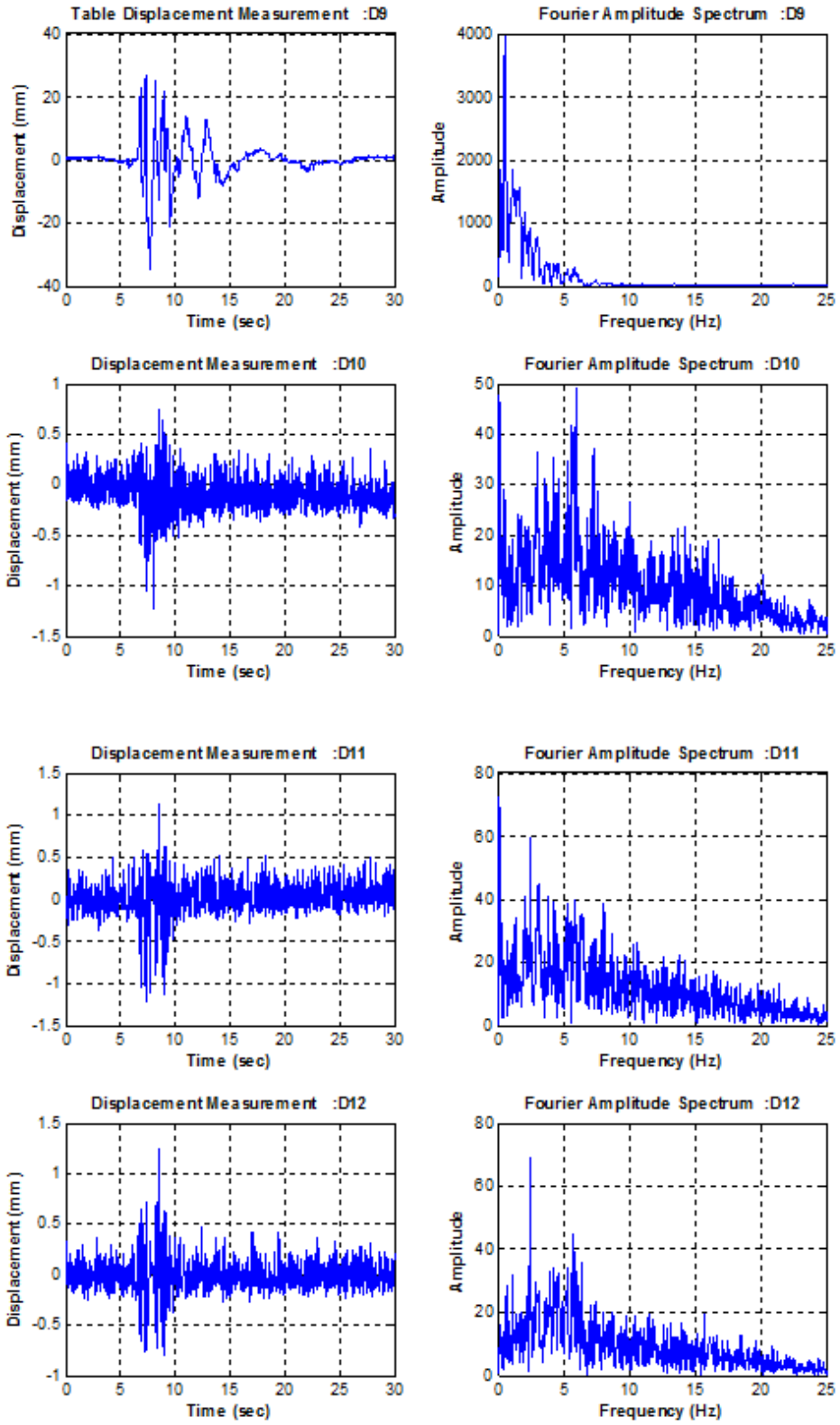

Figure B.33. Displacement Time History Graphs for Setup 4 Kobe 75%.

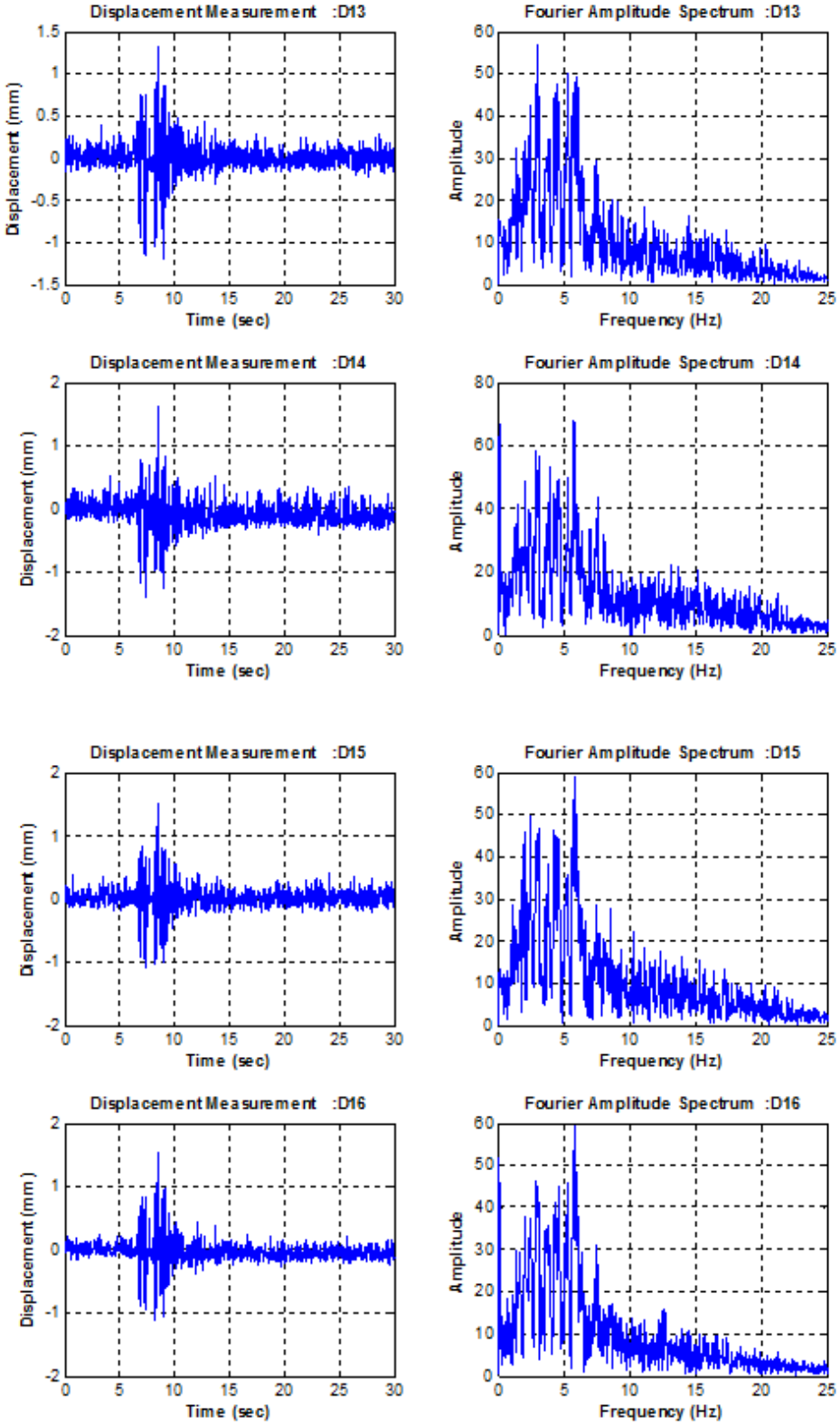

Figure B.34. Displacement Time History Graphs for Setup 4 Kobe 75%.

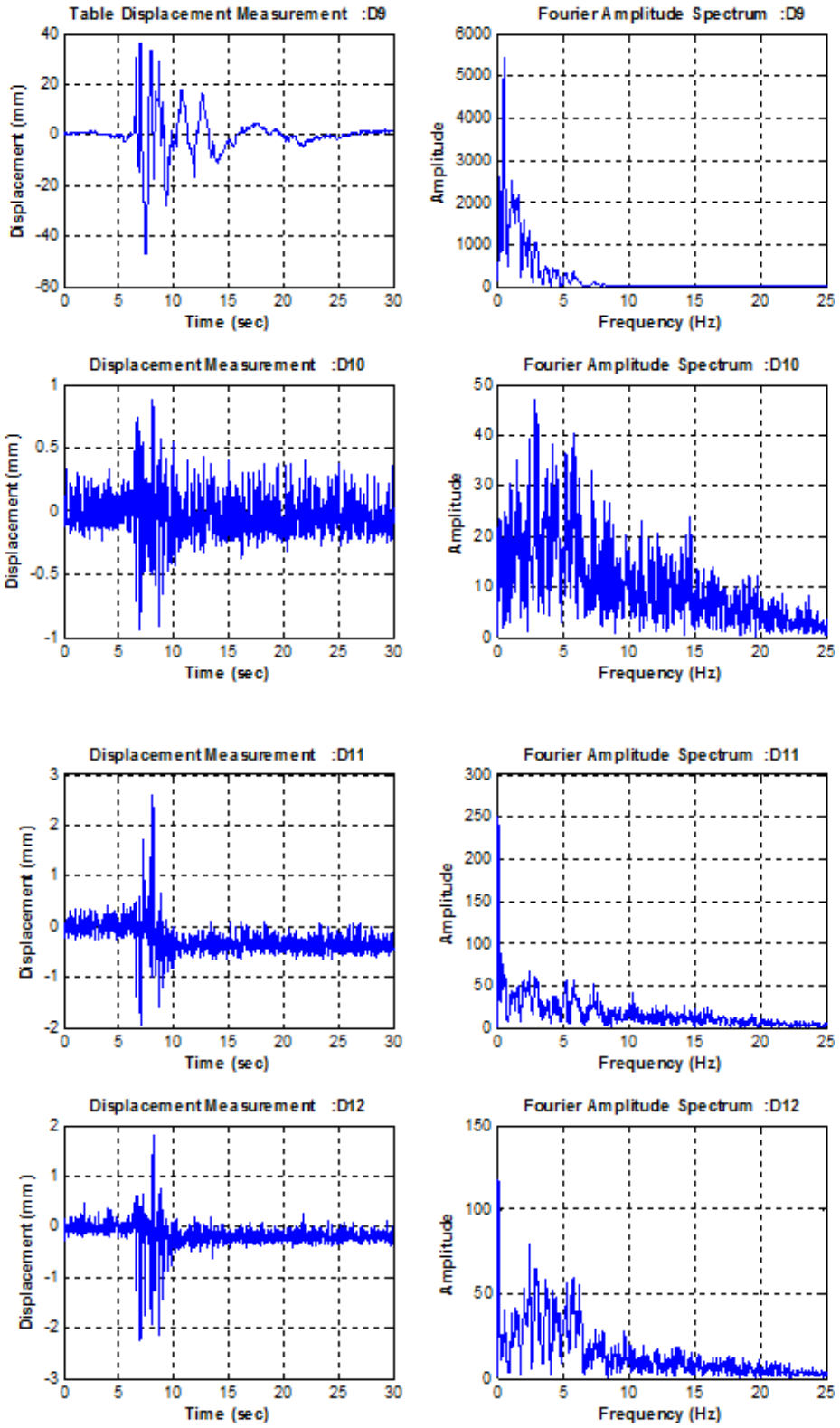

Figure B.35. Displacement Time History Graphs for Setup 4 Kobe 100%.

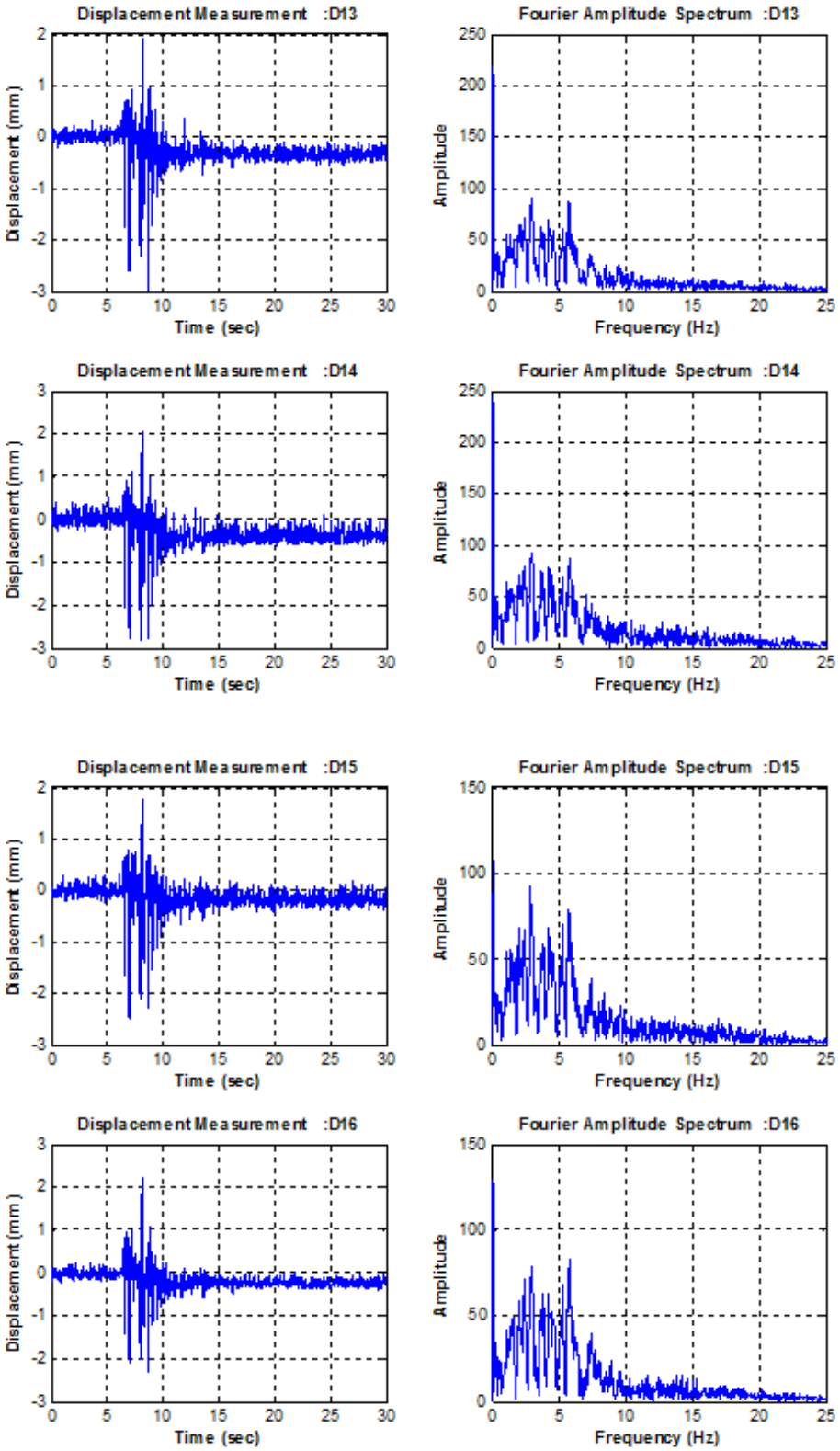

Figure B.36. Displacement Time History Graphs for Setup 4 Kobe 100%.

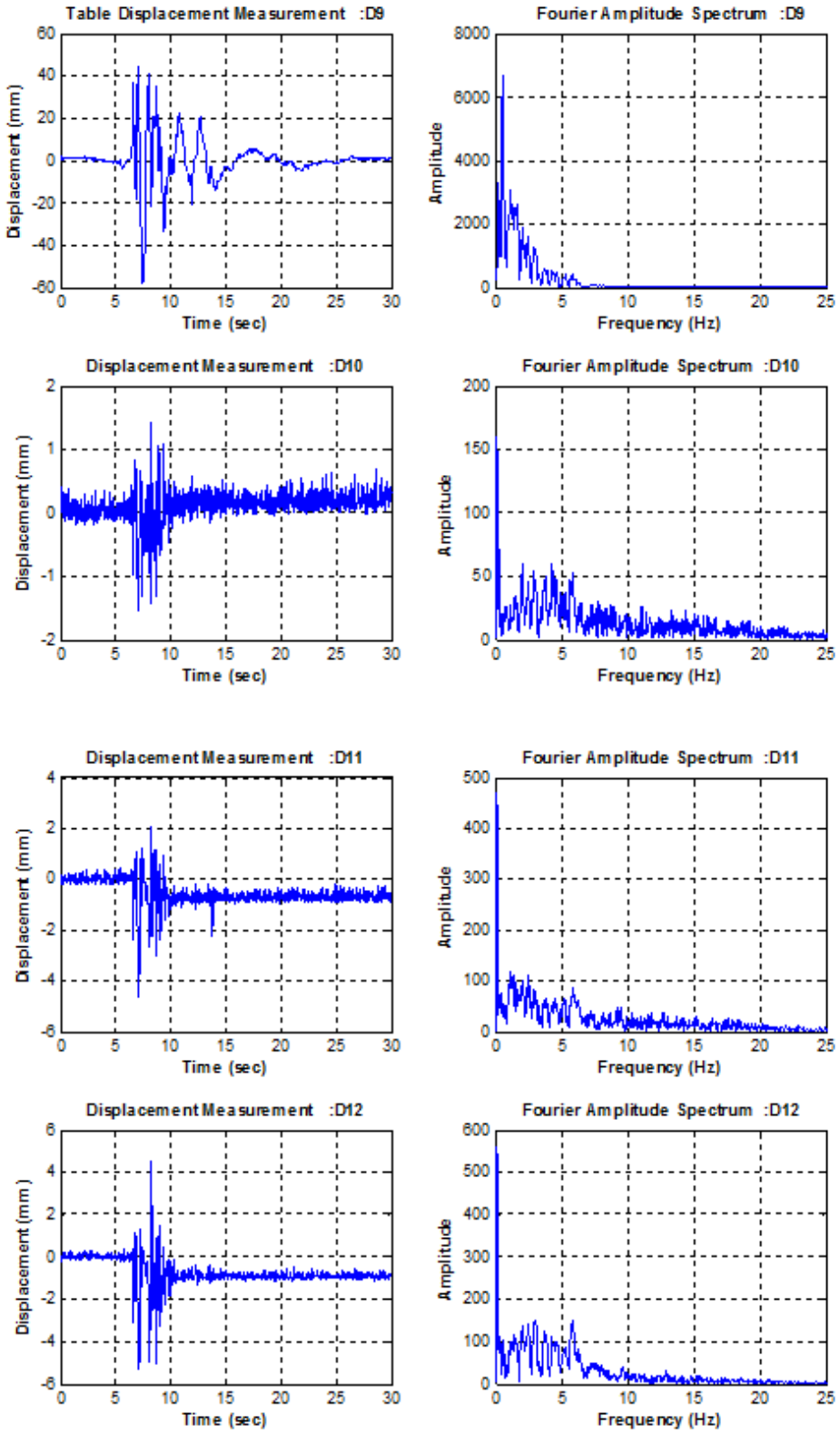

Figure B.37. Displacement Time History Graphs for Setup 4 Kobe 125%.

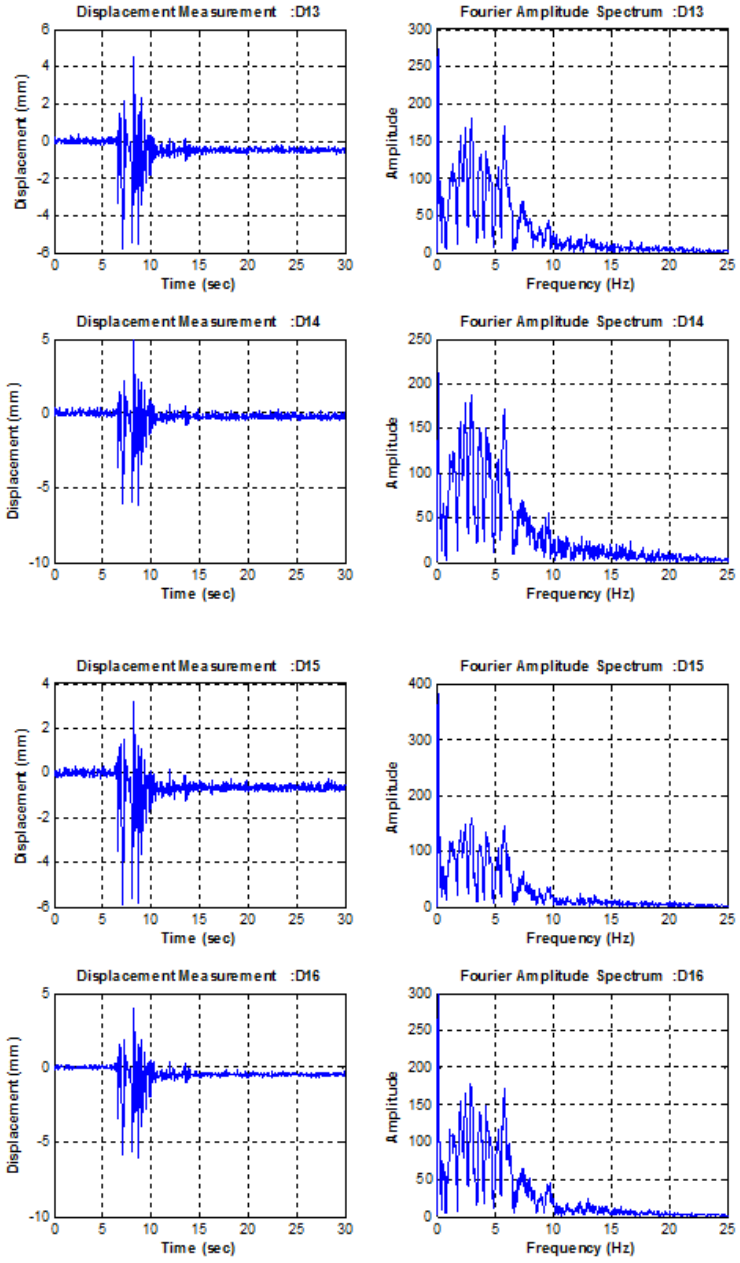

Figure B.38. Displacement Time History Graphs for Setup 4 Kobe 125%.

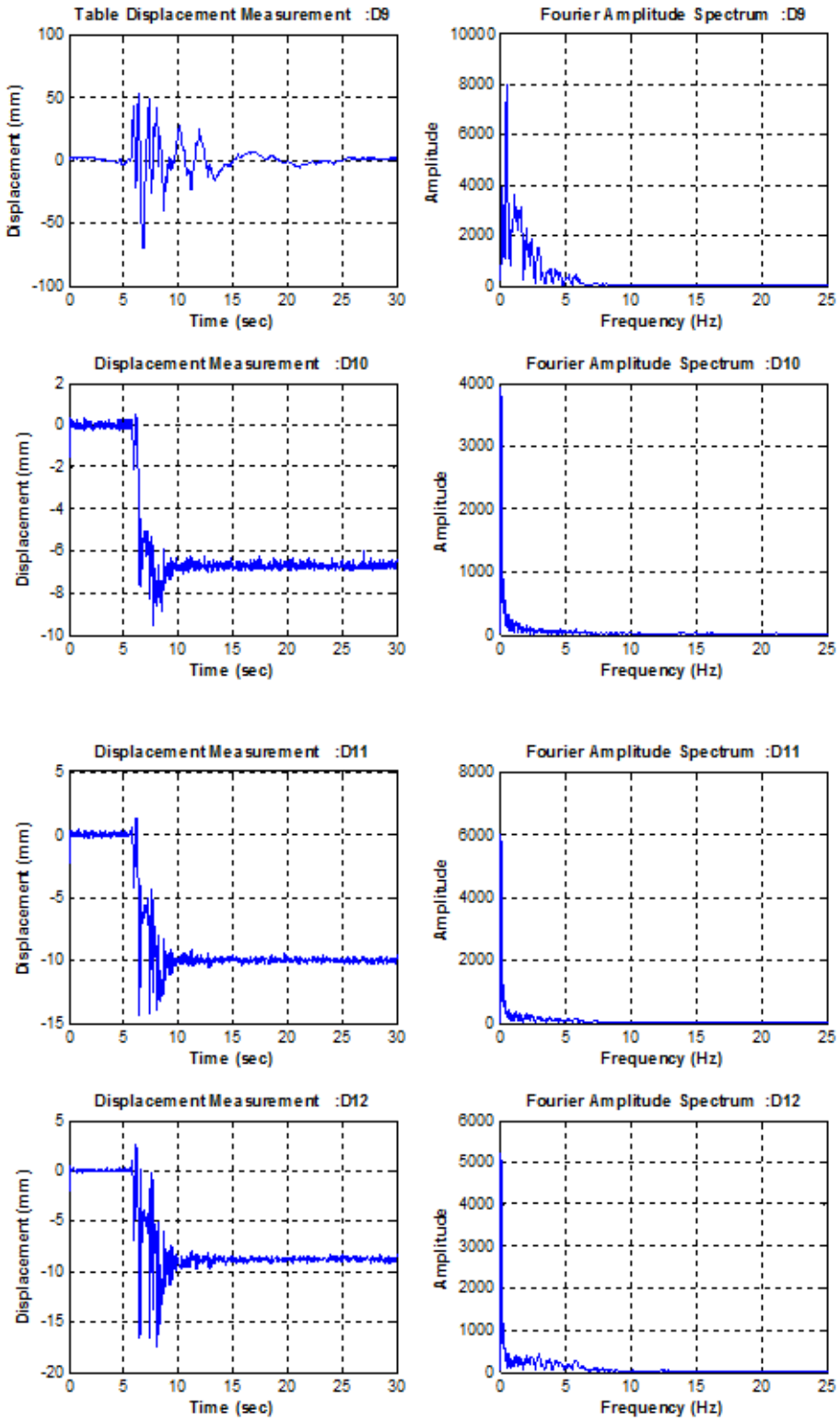

Figure B.39. Displacement Time History Graphs for Setup 4 Kobe 150%.

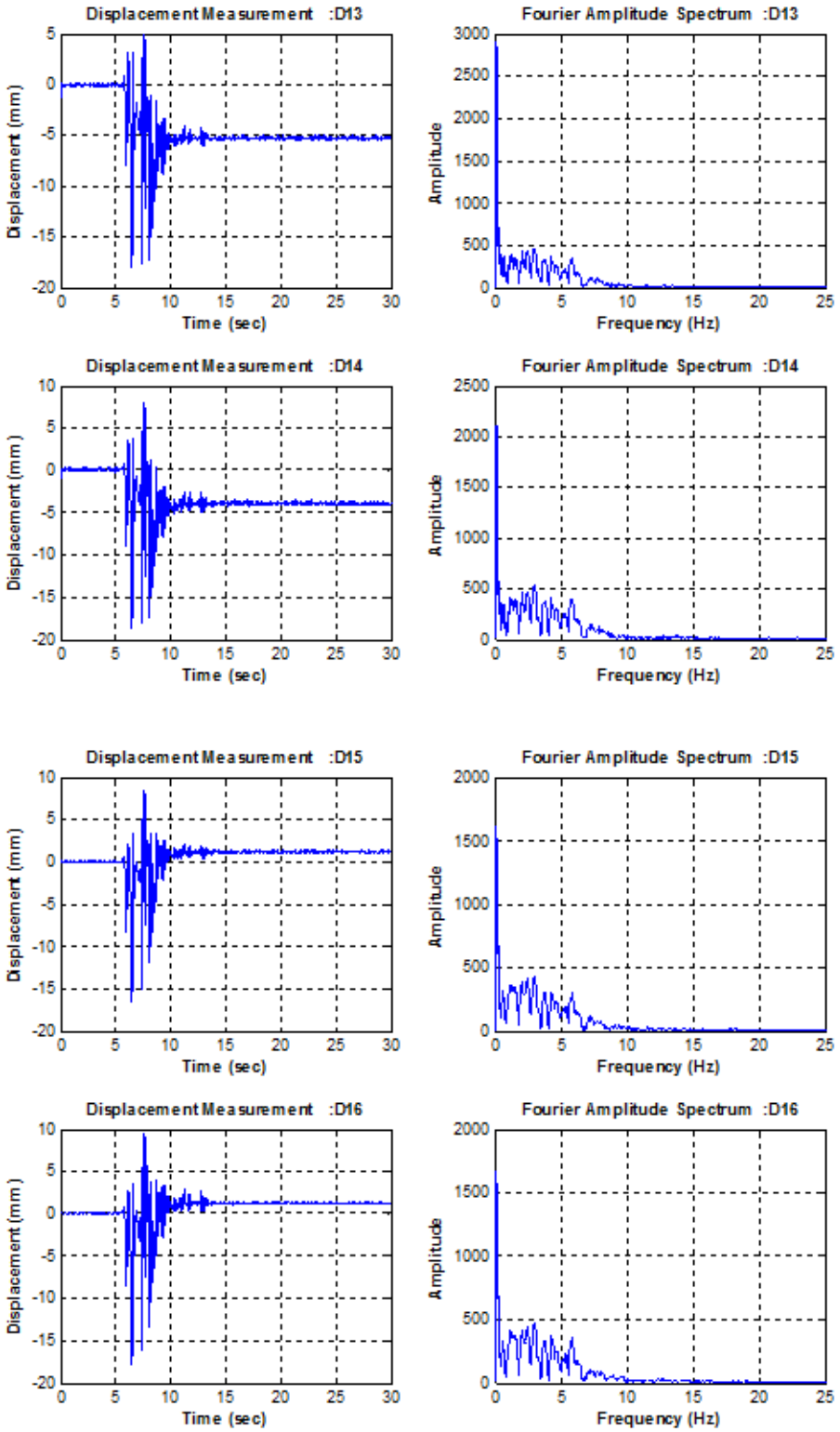

Figure B.40. Displacement Time History Graphs for Setup 4 Kobe 150%.

APPENDIX C: STRAIN TIME HISTORY GRAPHS OBTAINED FROM THE TESTS

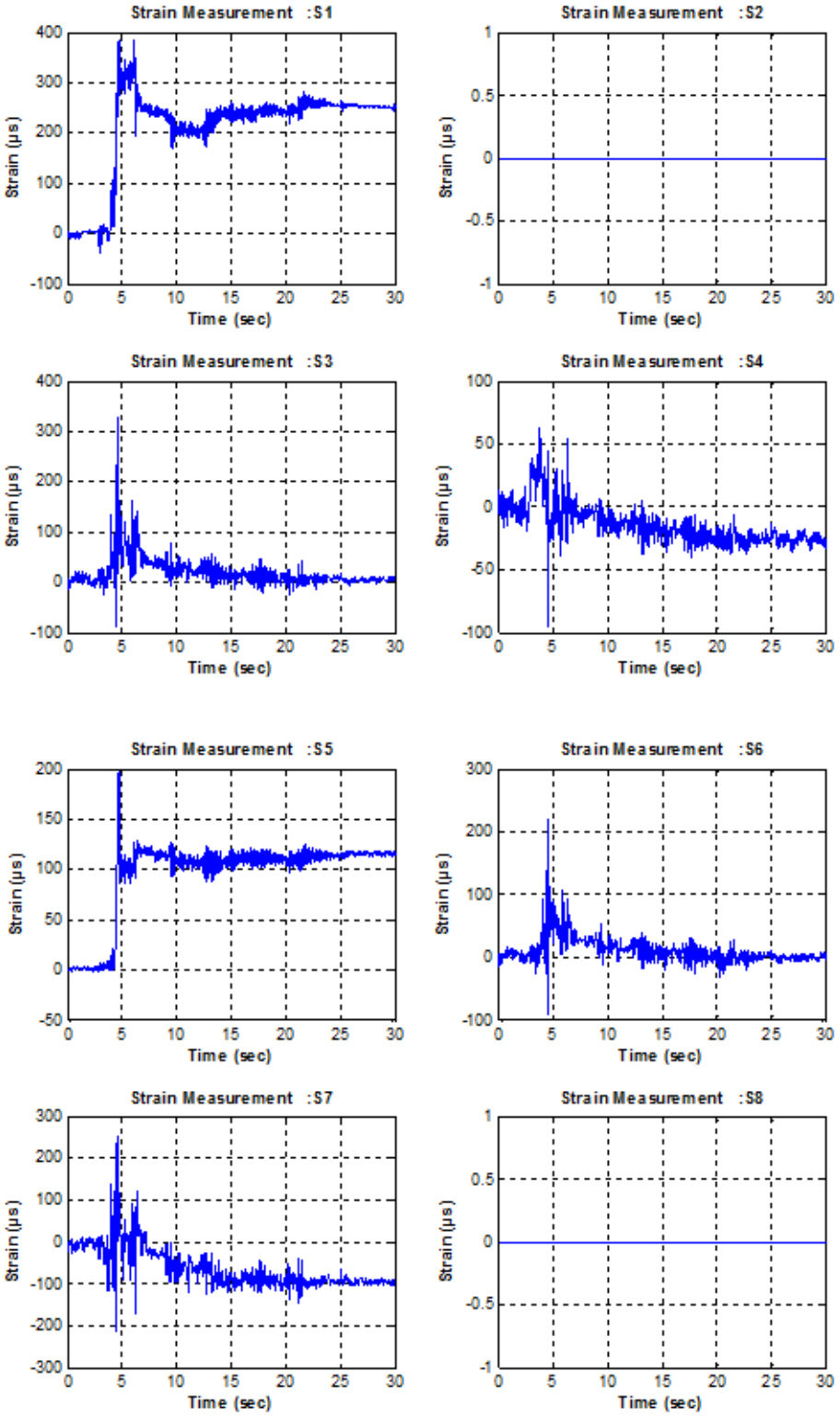

Figure C.1. Strain Time History Graphs for Setup 1 El Centro 100%.

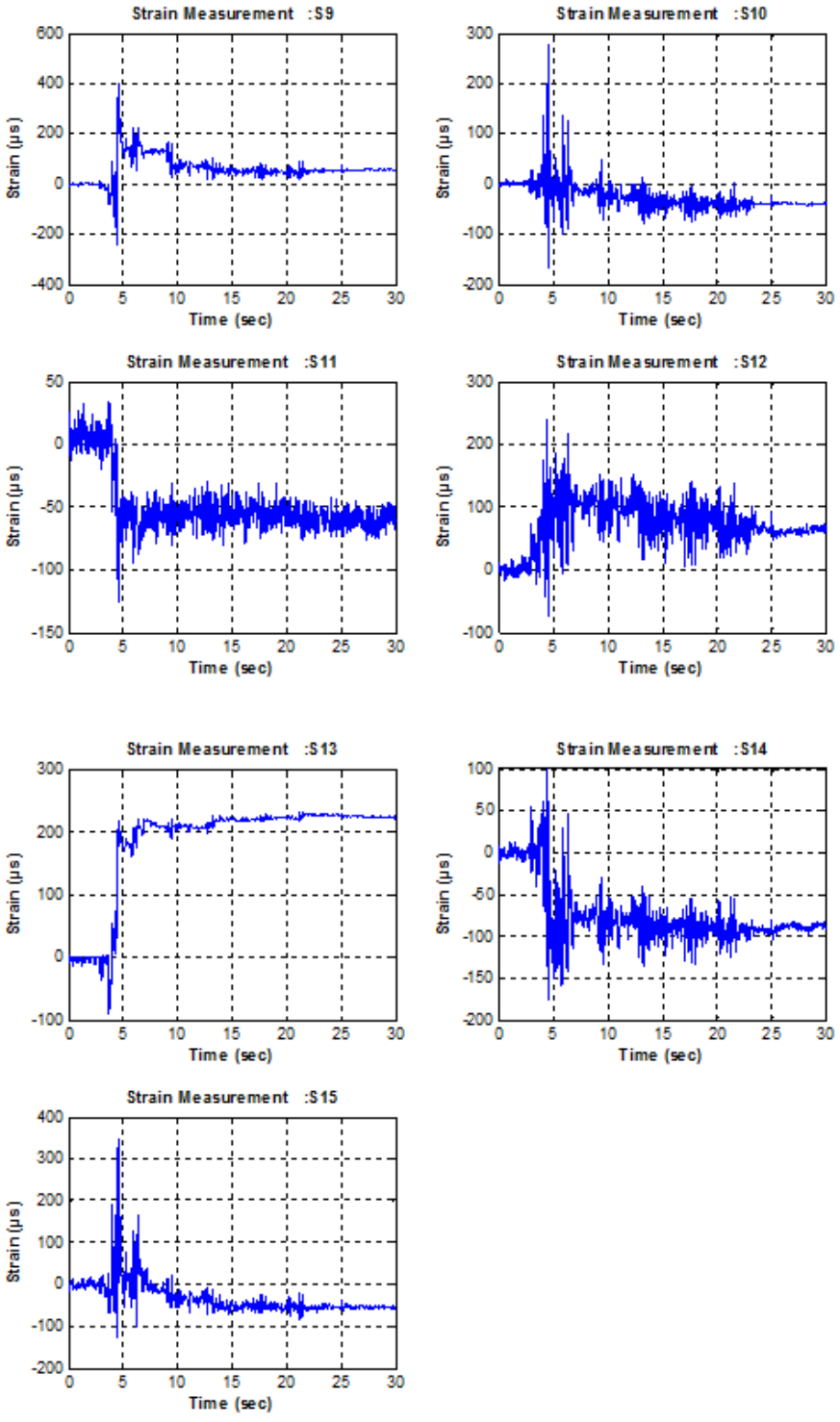

Figure C.2. Strain Time History Graphs for Setup 1 El Centro 100%.

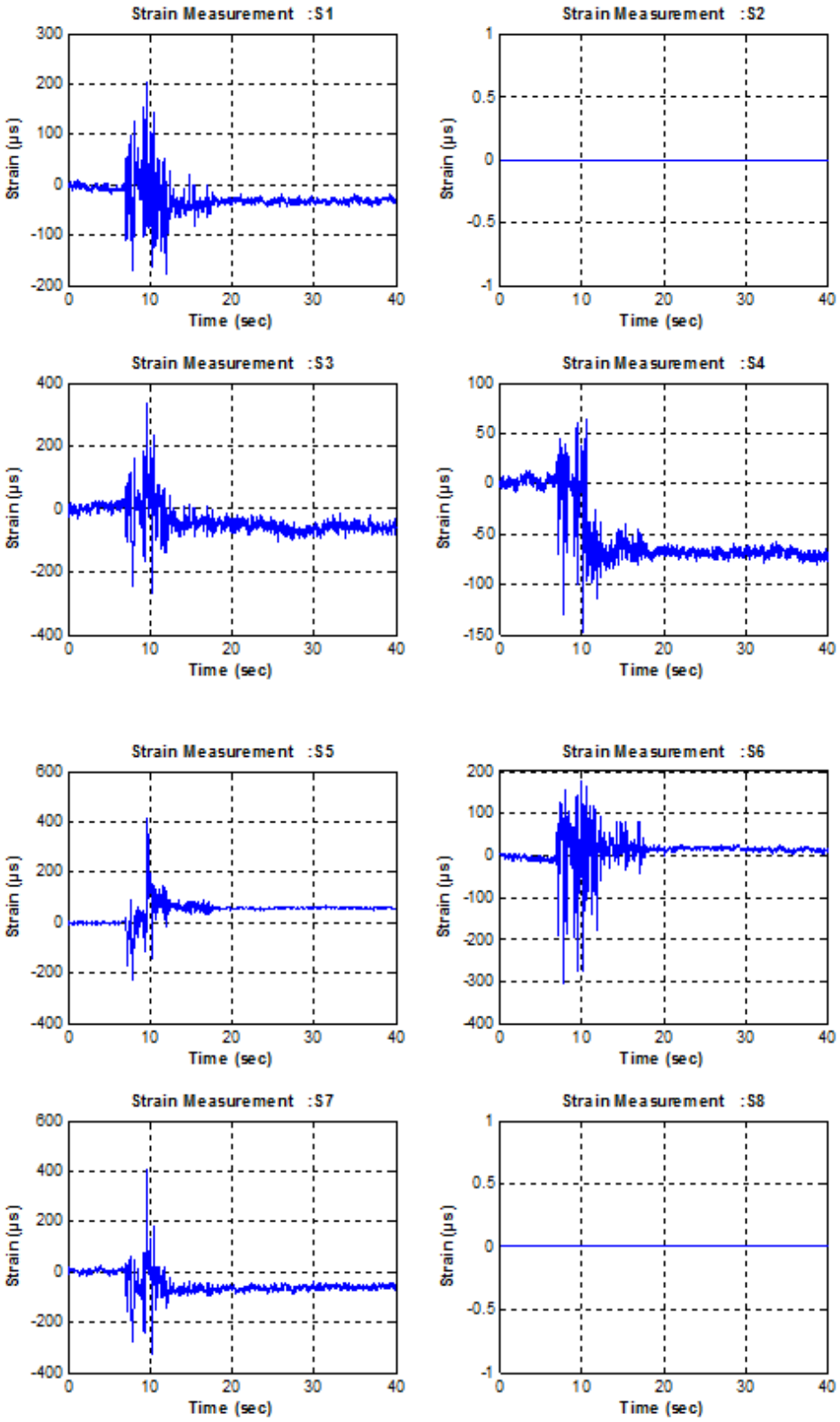

Figure C.3. Strain Time History Graphs for Setup 1 Kobe 50%.

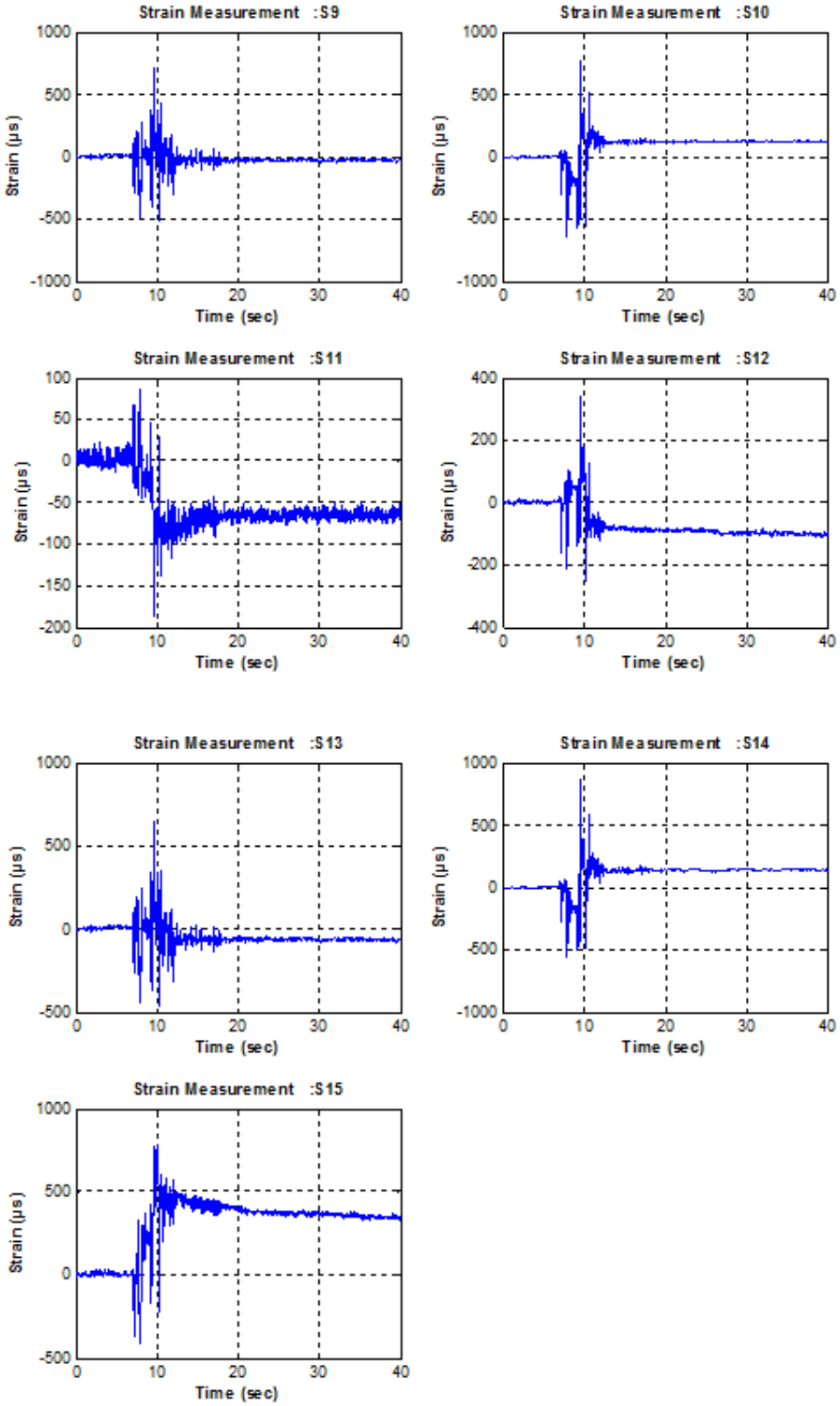

Figure C.4. Strain Time History Graphs for Setup 1 Kobe 50%.

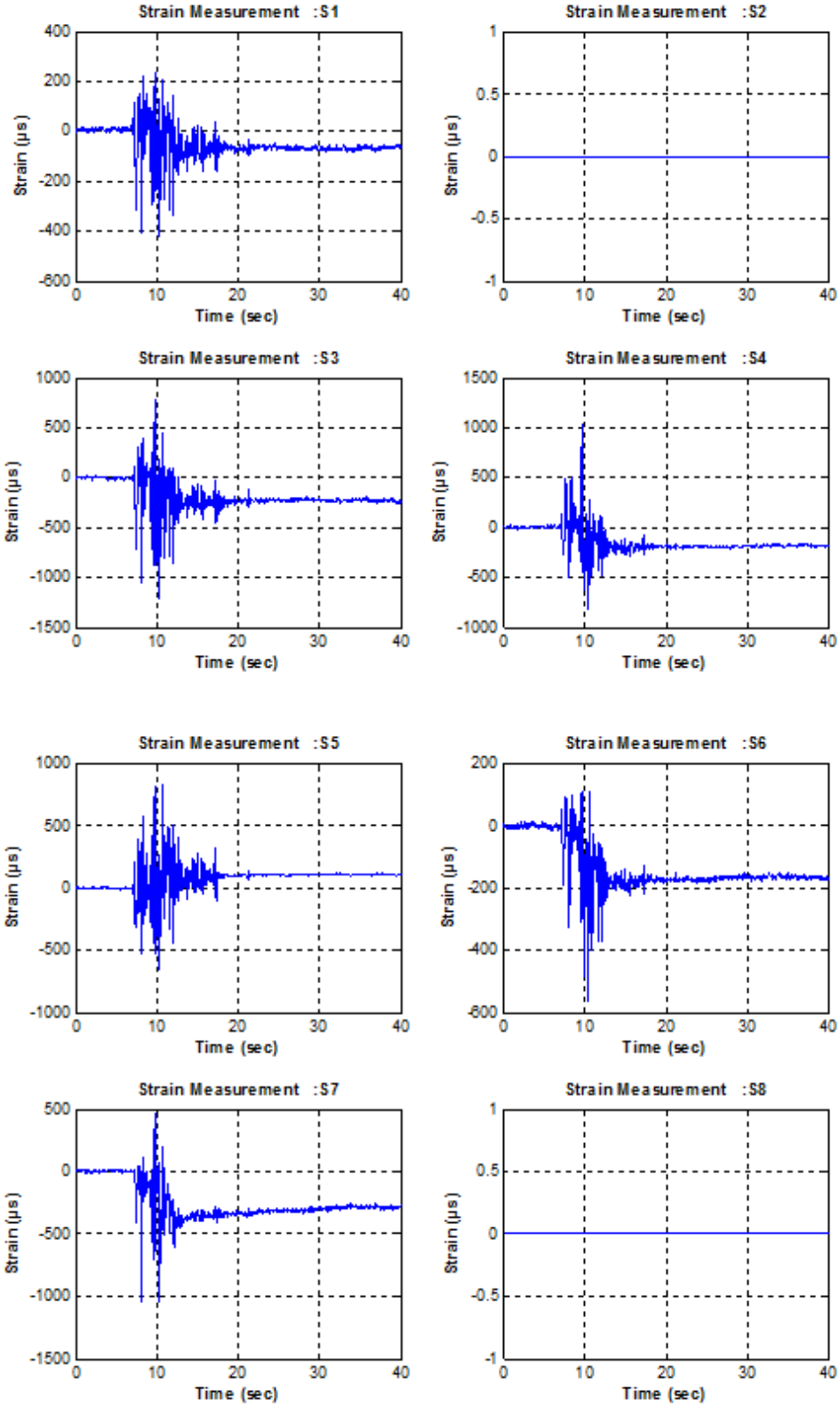

Figure C.5. Strain Time History Graphs for Setup 1 Kobe 75%.

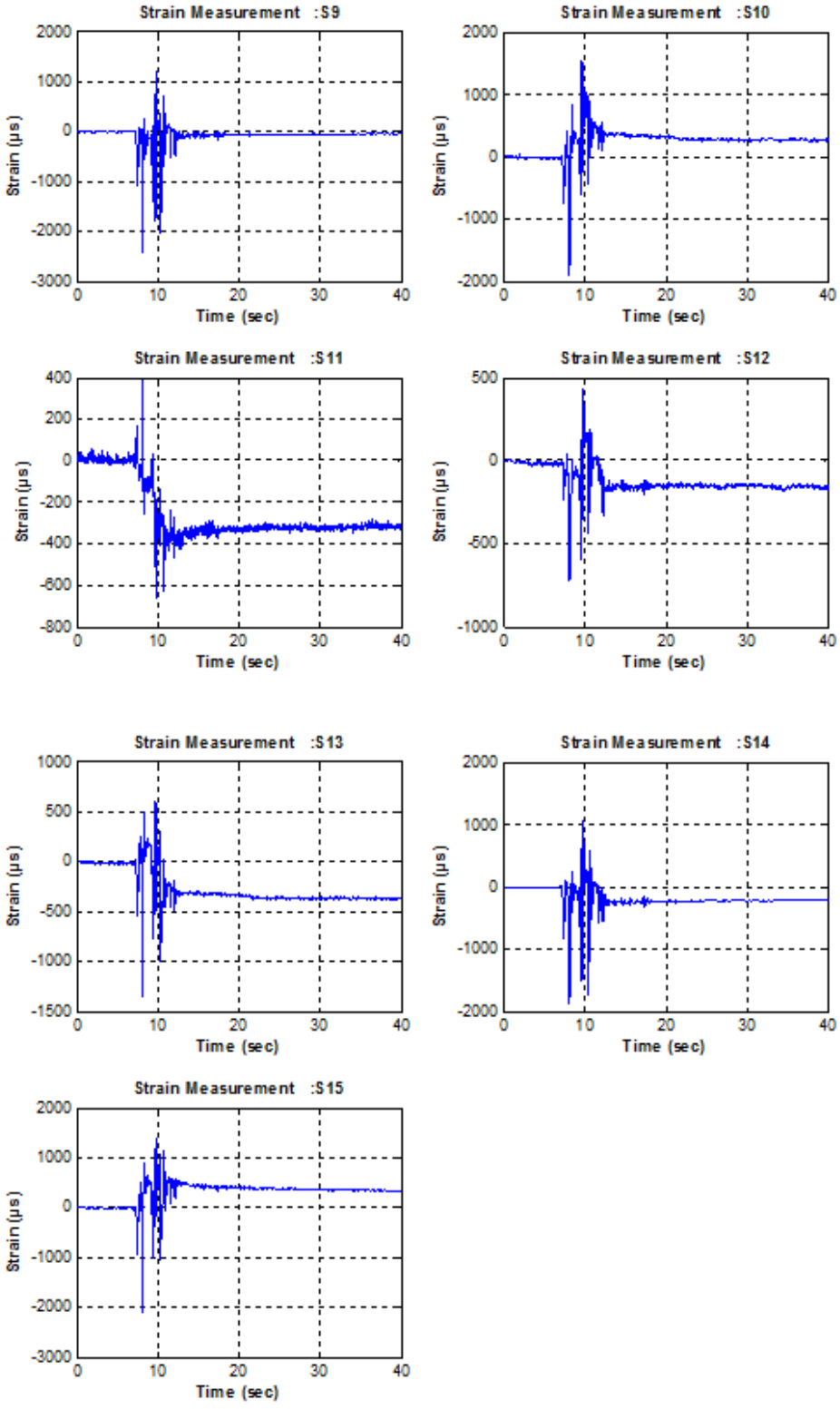

Figure C.6. Strain Time History Graphs for Setup 1 Kobe 75%.

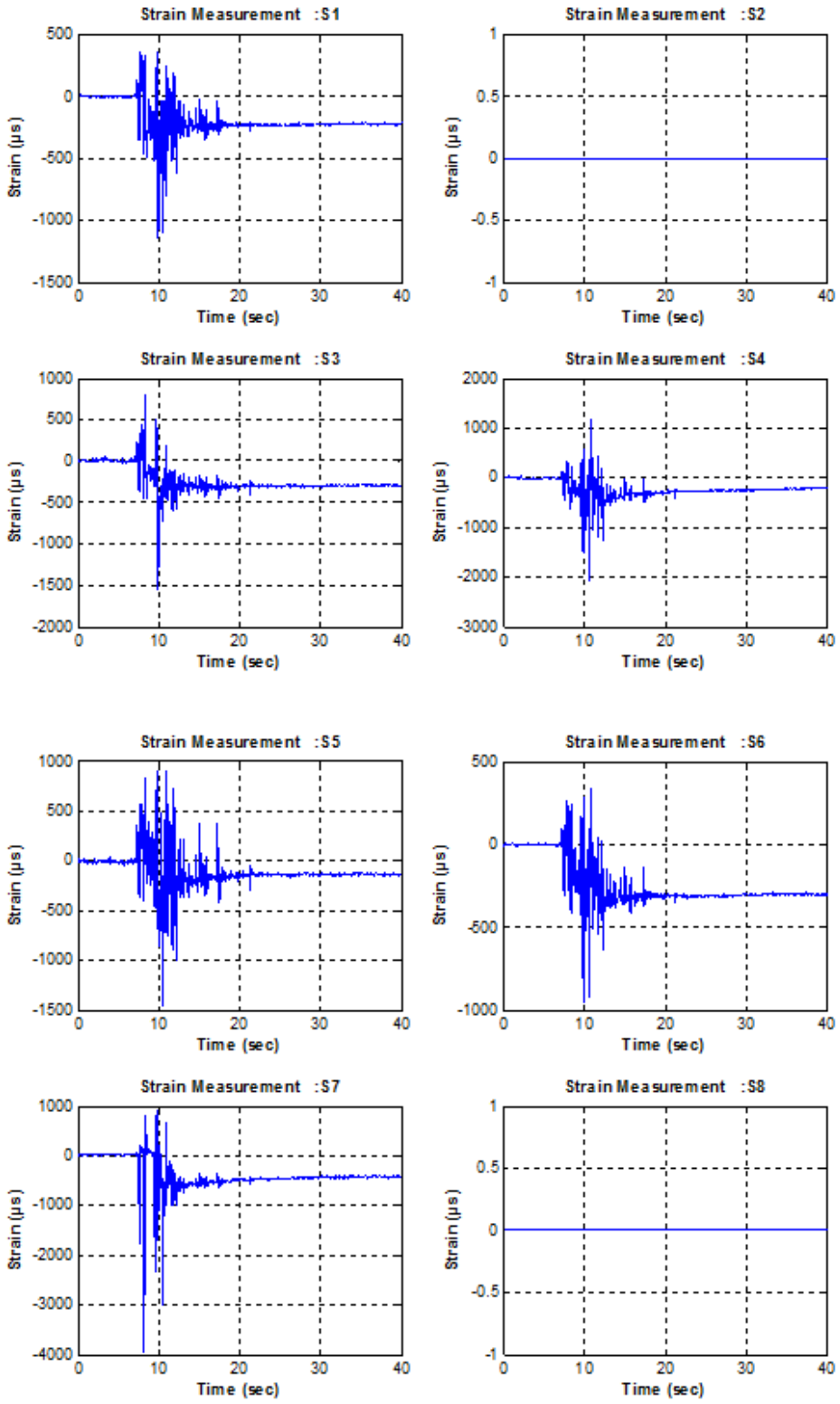

Figure C.7. Strain Time History Graphs for Setup 1 Kobe 100%.

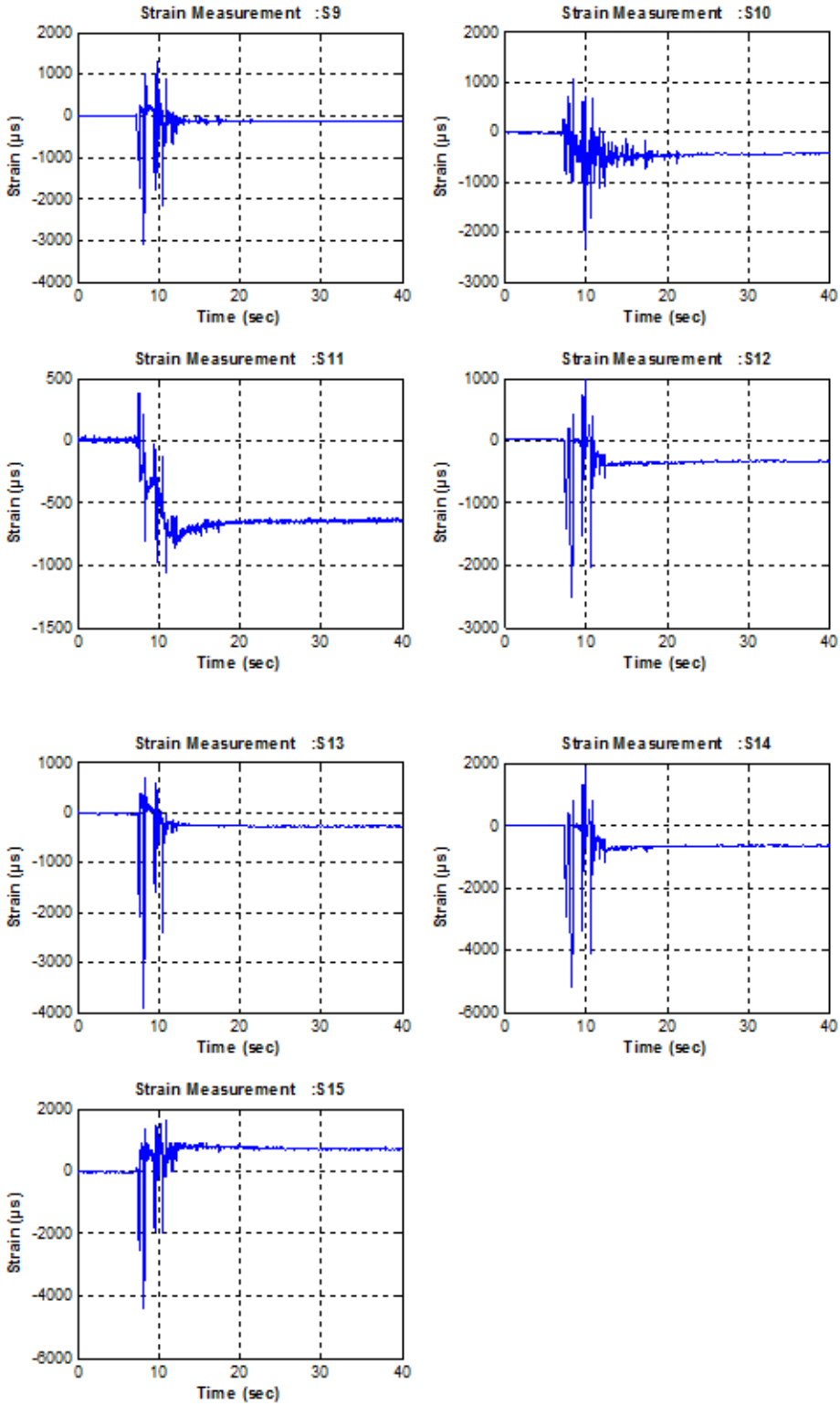

Figure C.8. Strain Time History Graphs for Setup 1 Kobe 100%.

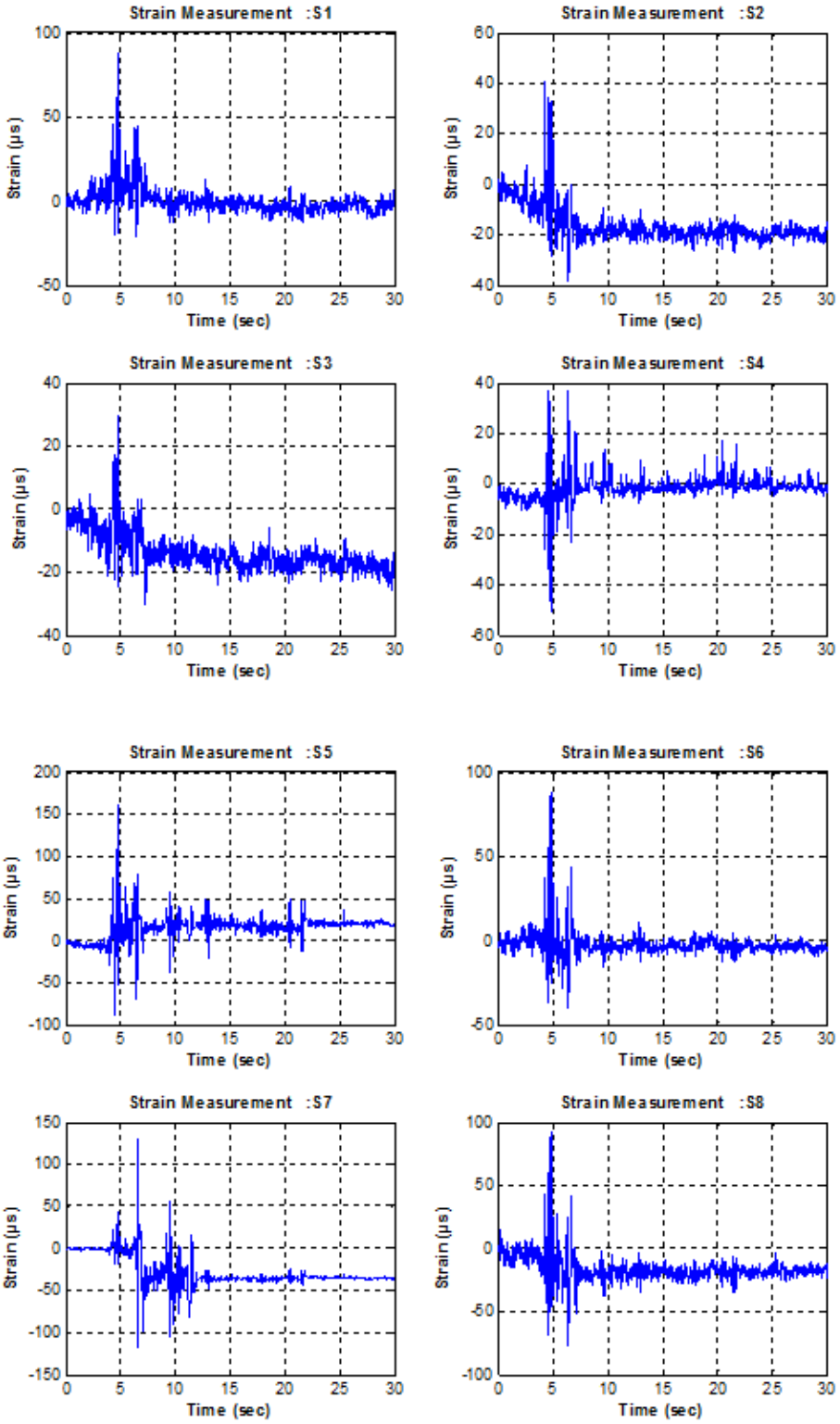

Figure C.9. Strain Time History Graphs for Setup 1 Kobe 100%.

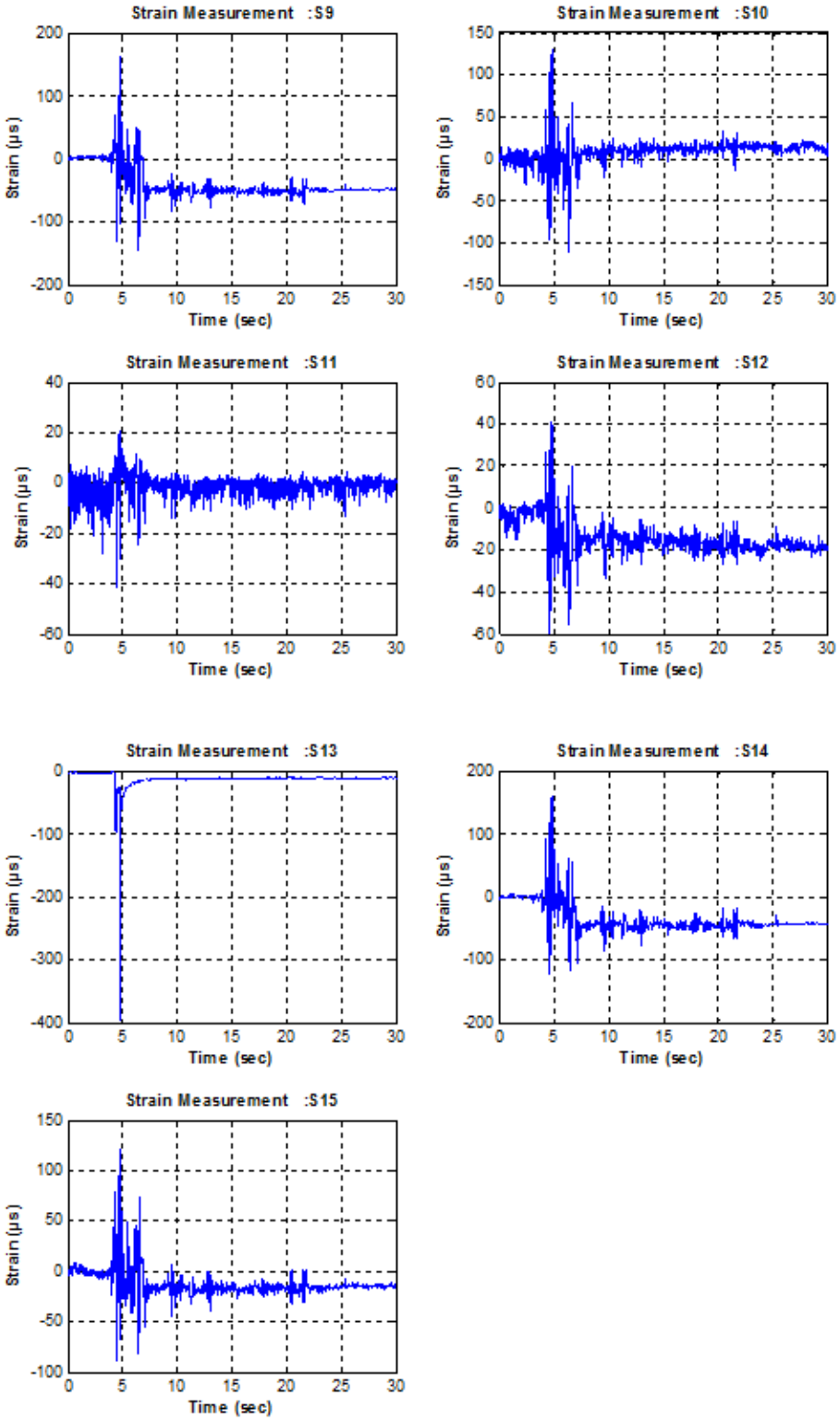

Figure C.10. Strain Time History Graphs for Setup 2 El Centro 100%.

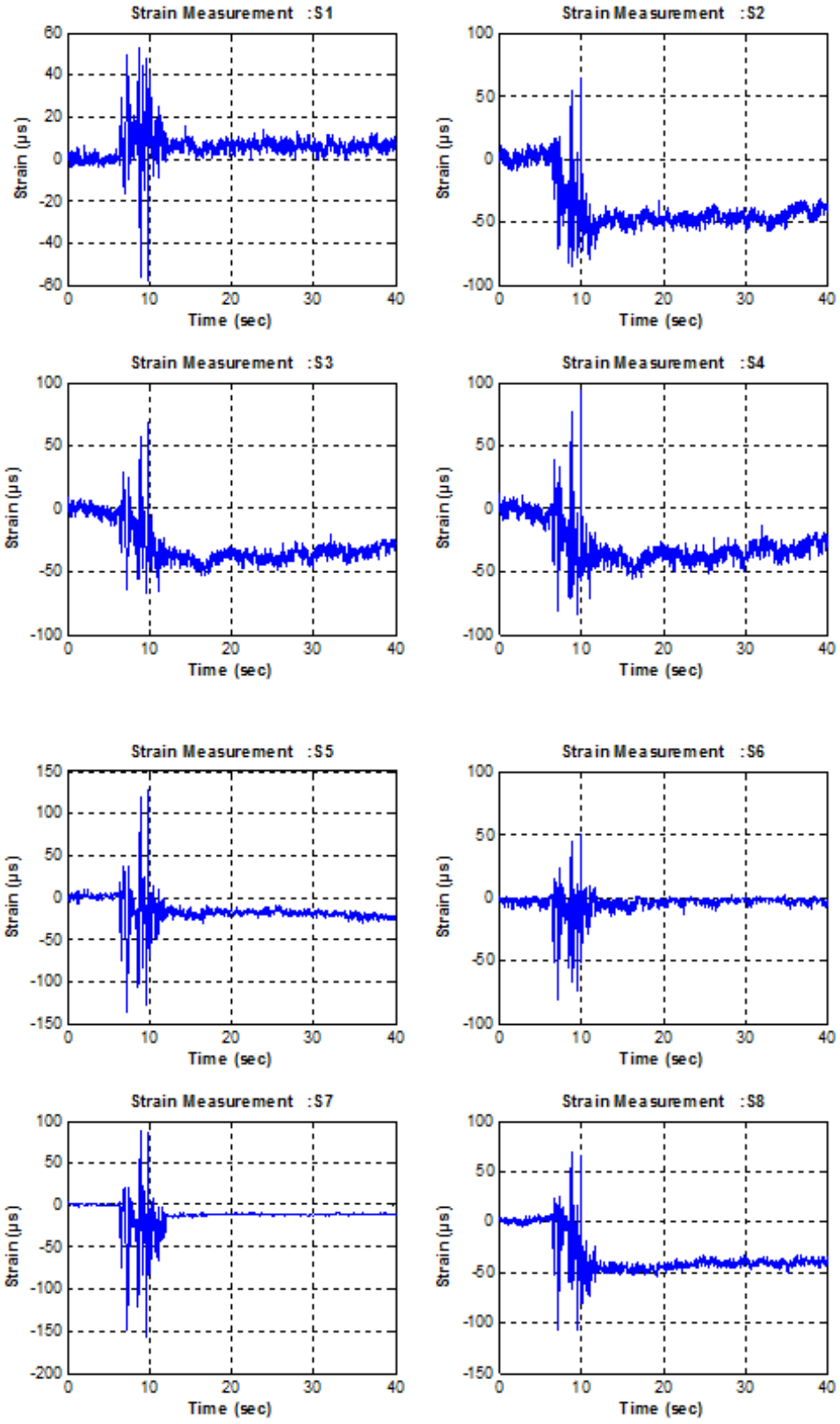

Figure C.11. Strain Time History Graphs for Setup 2 Kobe 50%.

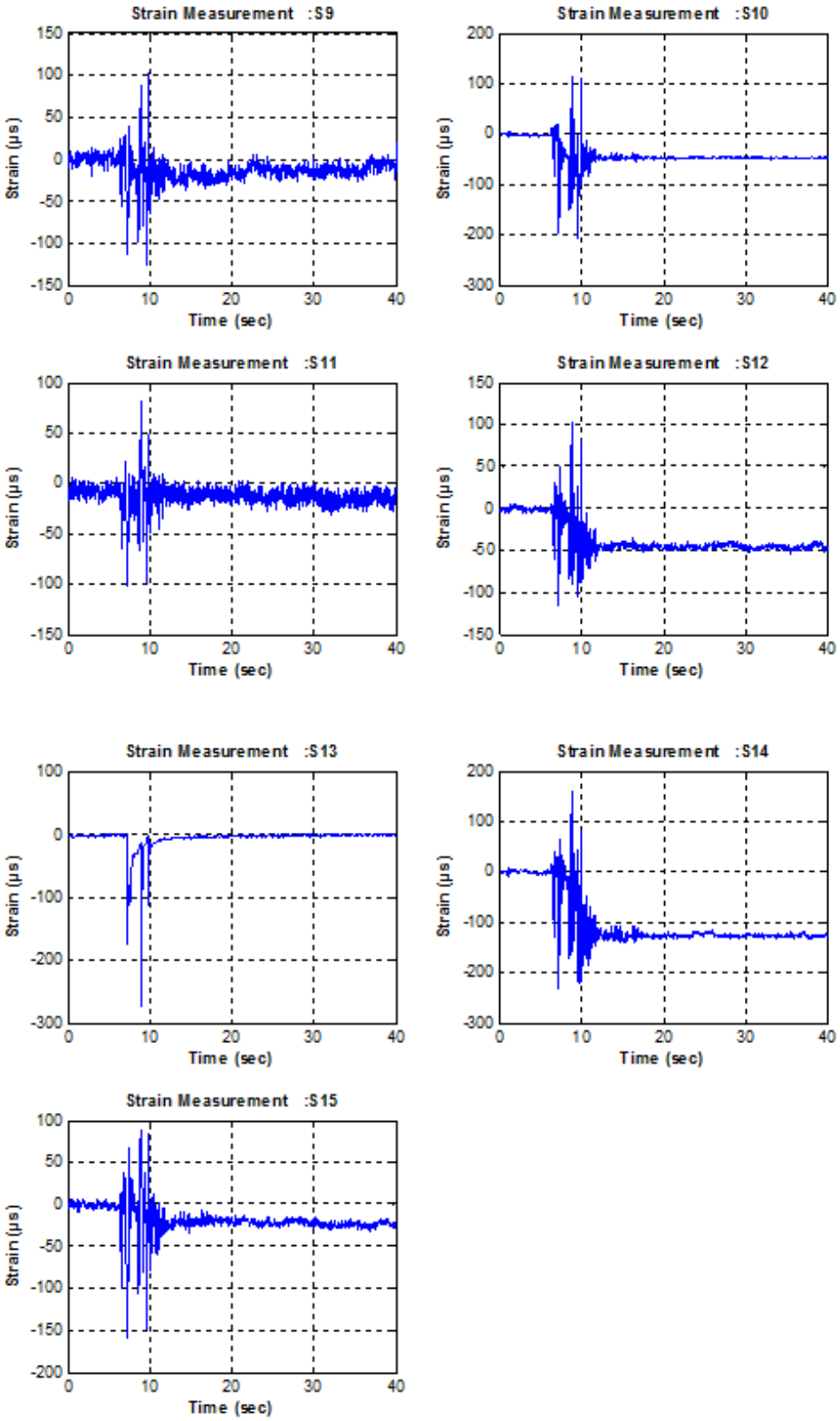

Figure C.12. Strain Time History Graphs for Setup 2 Kobe 50%.

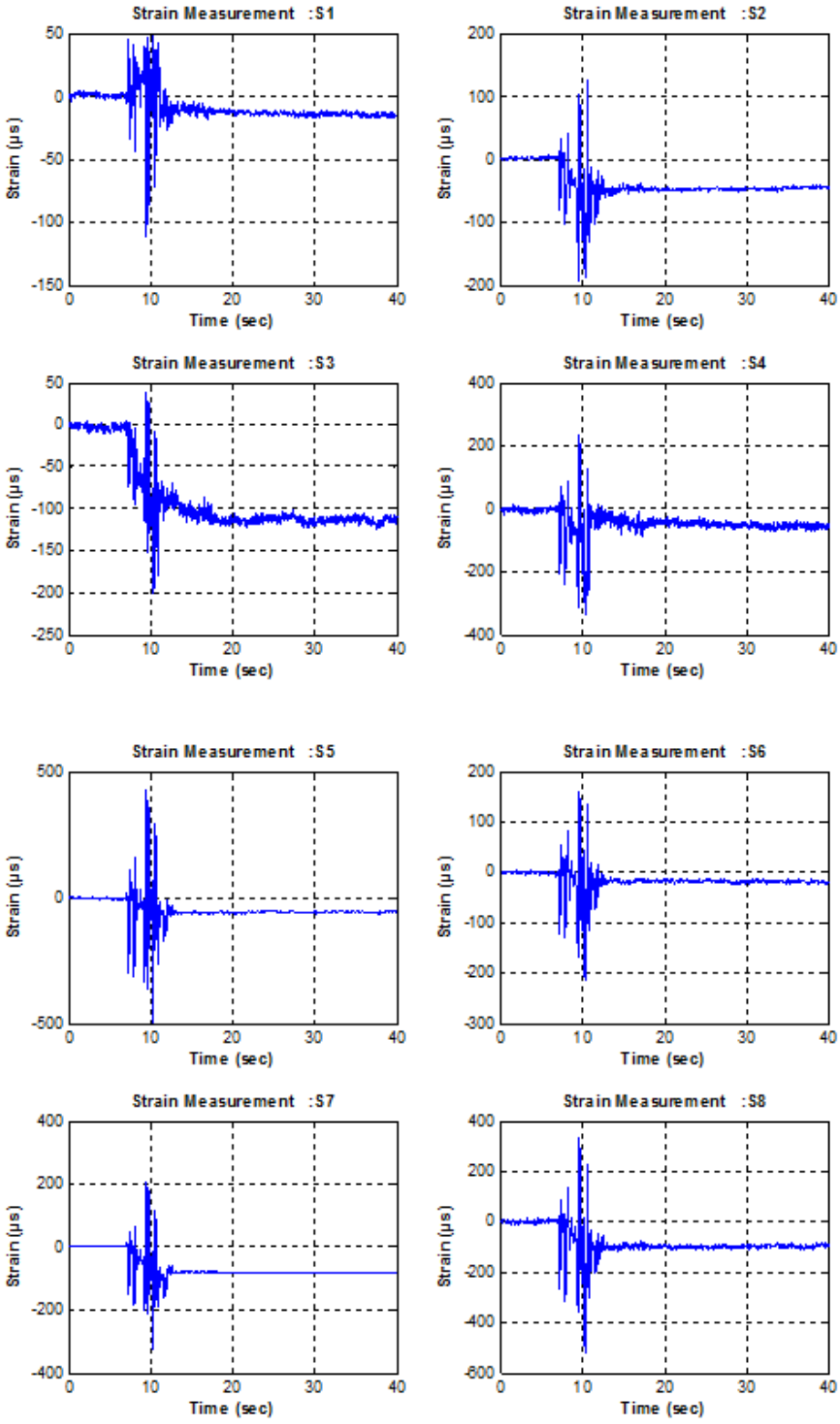

Figure C.13. Strain Time History Graphs for Setup 2 Kobe 75%.

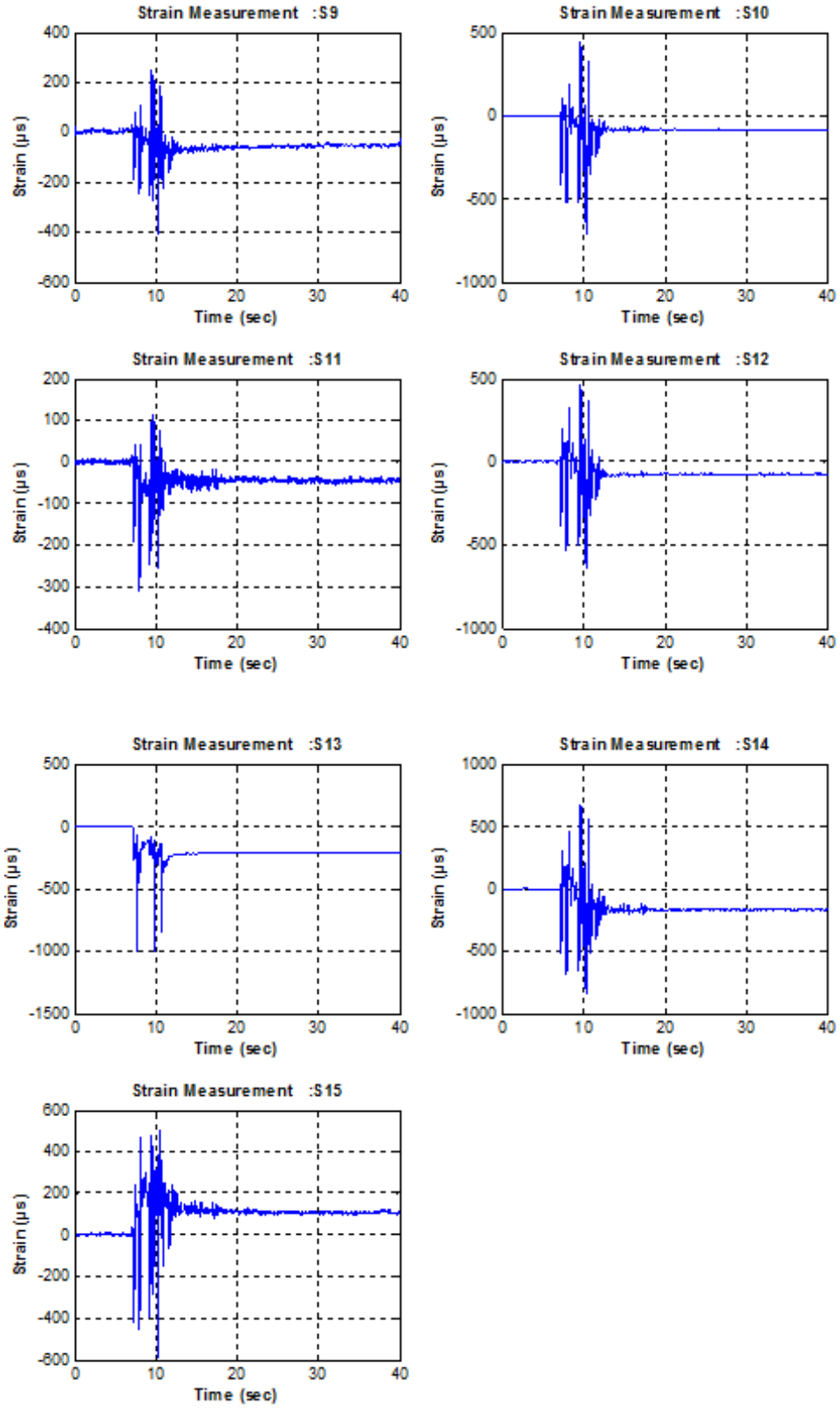

Figure C.14. Strain Time History Graphs for Setup 2 Kobe 75%.

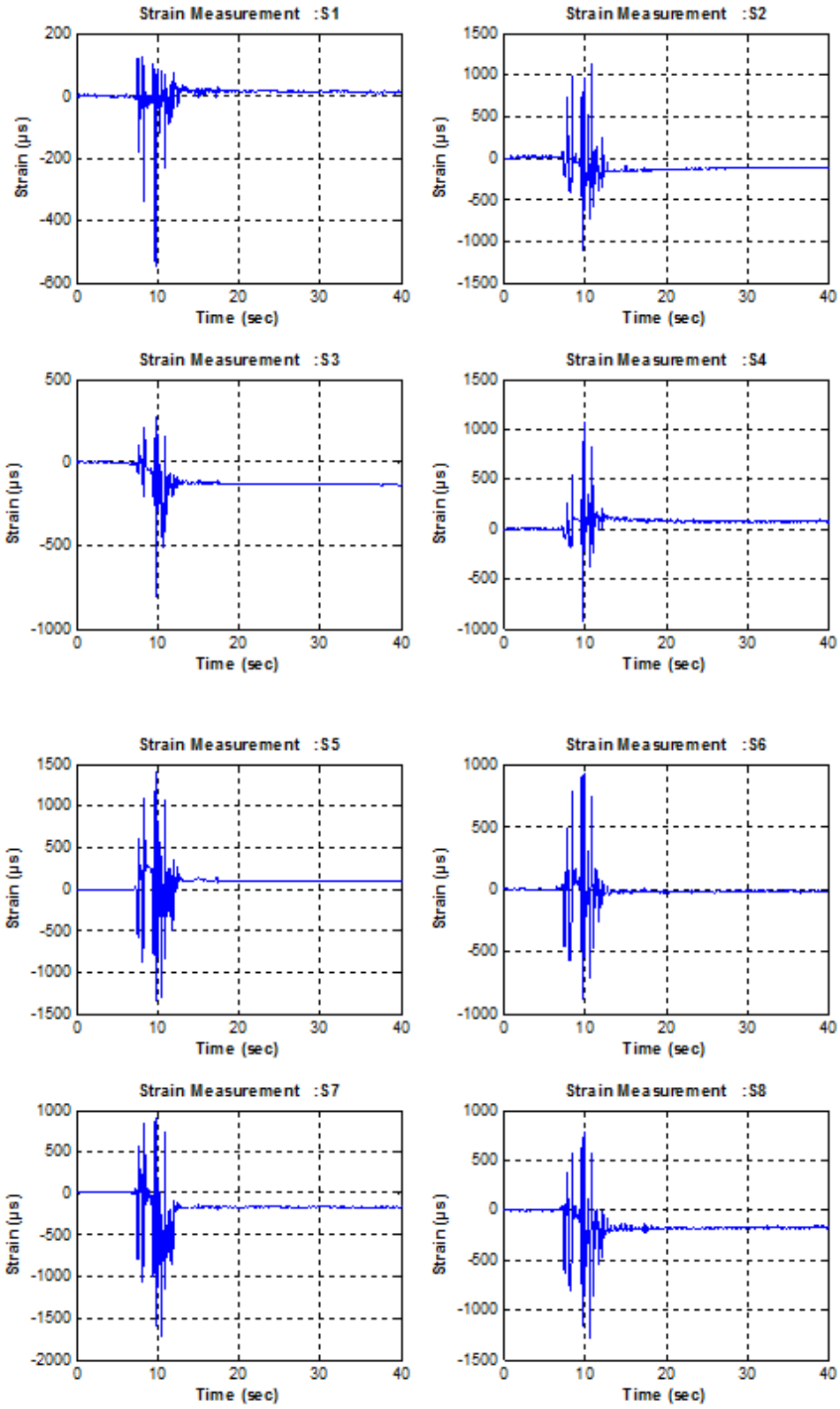

Figure C.15. Strain Time History Graphs for Setup 2 Kobe 100%.

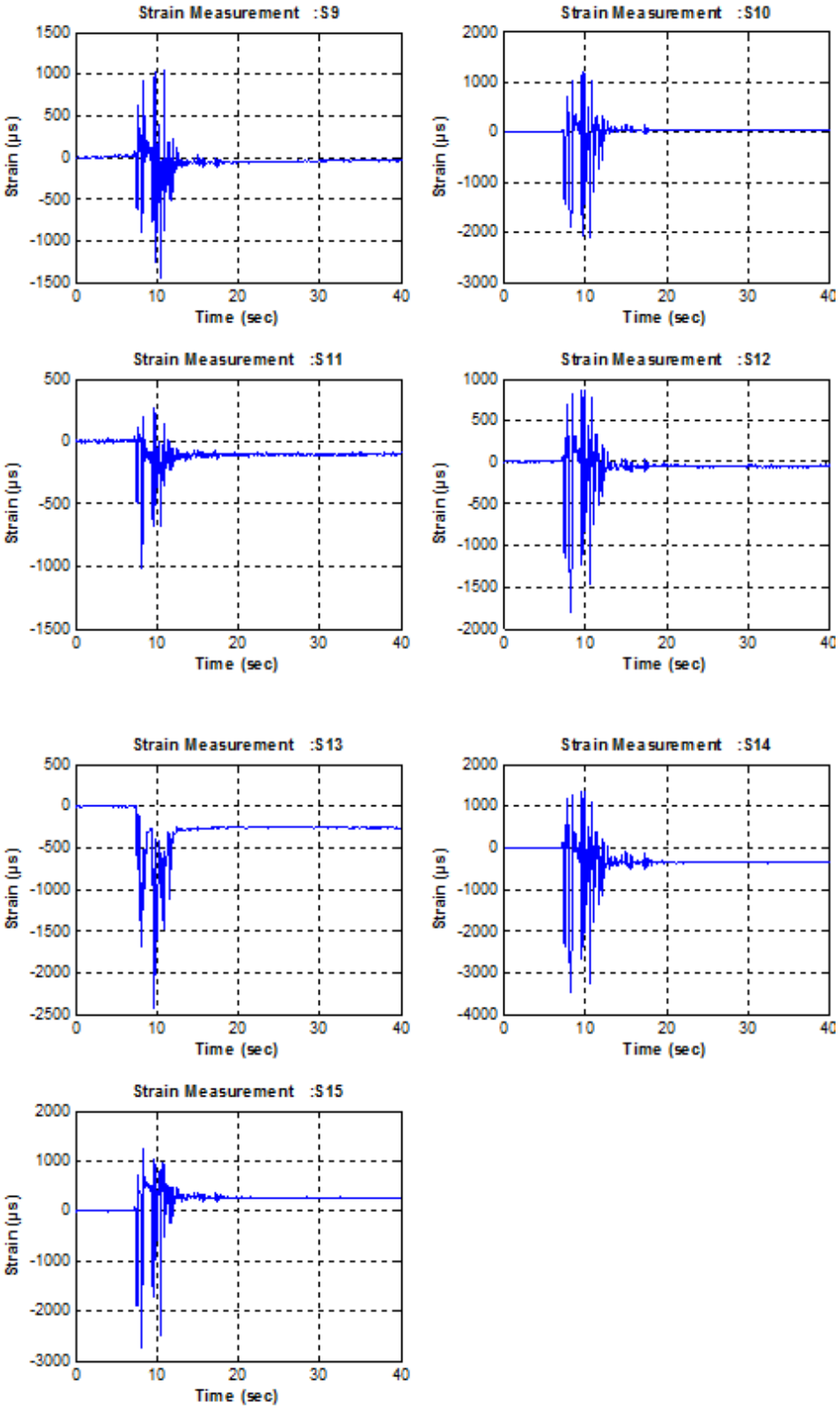

Figure C.16. Strain Time History Graphs for Setup 2 Kobe 100%.

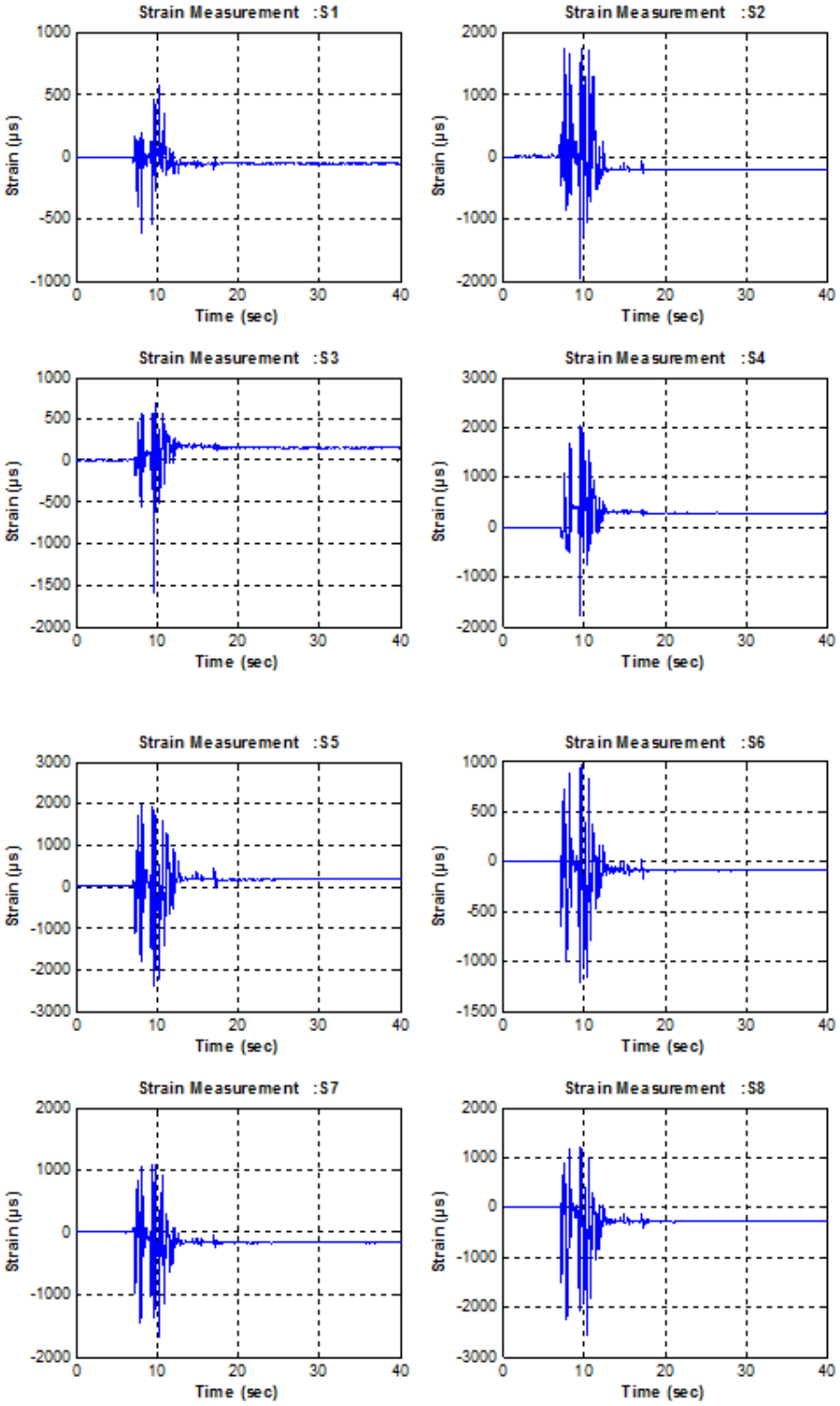

Figure C.17. Strain Time History Graphs for Setup 2 Kobe 125%.

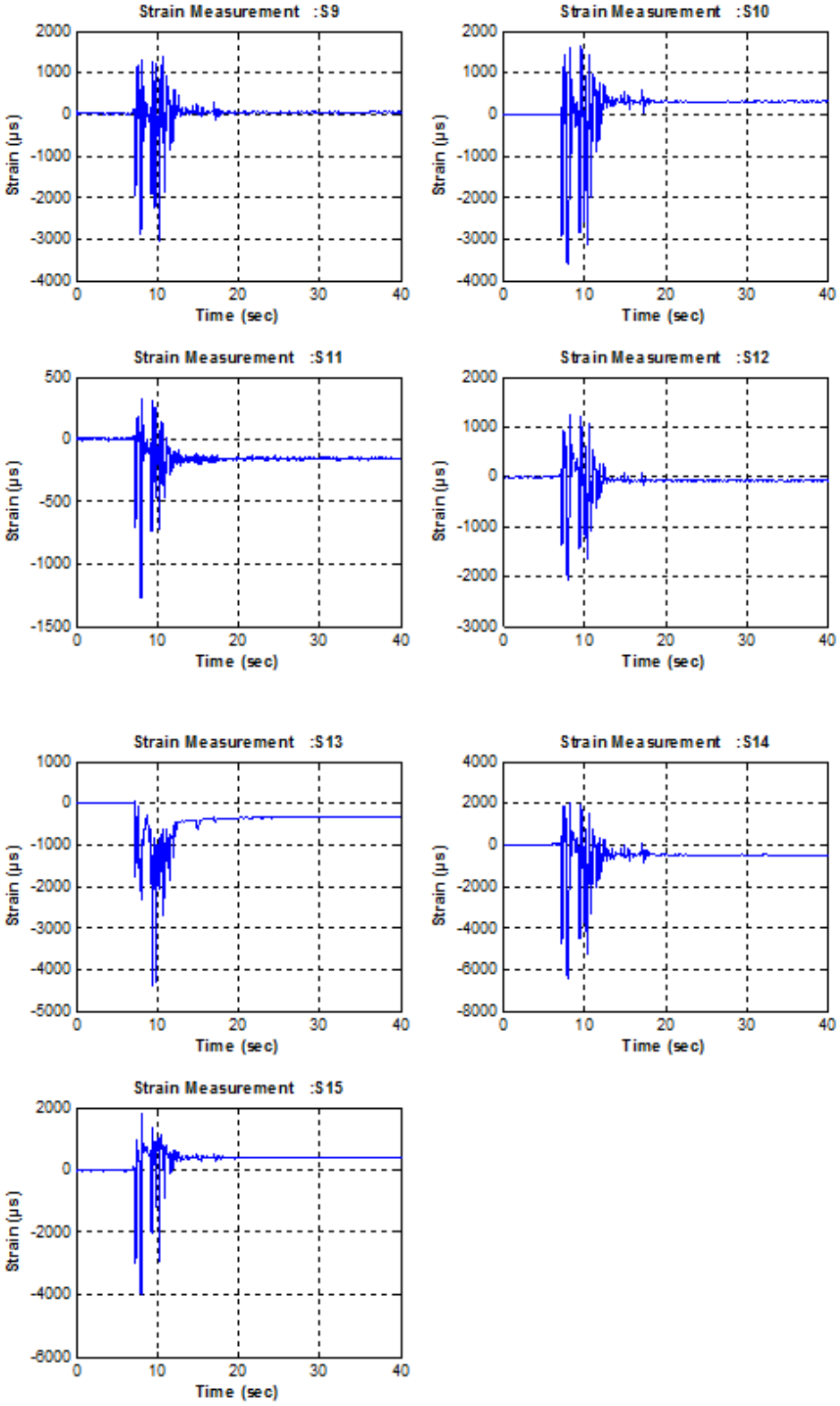

Figure C.18. Strain Time History Graphs for Setup 2 Kobe 125%.

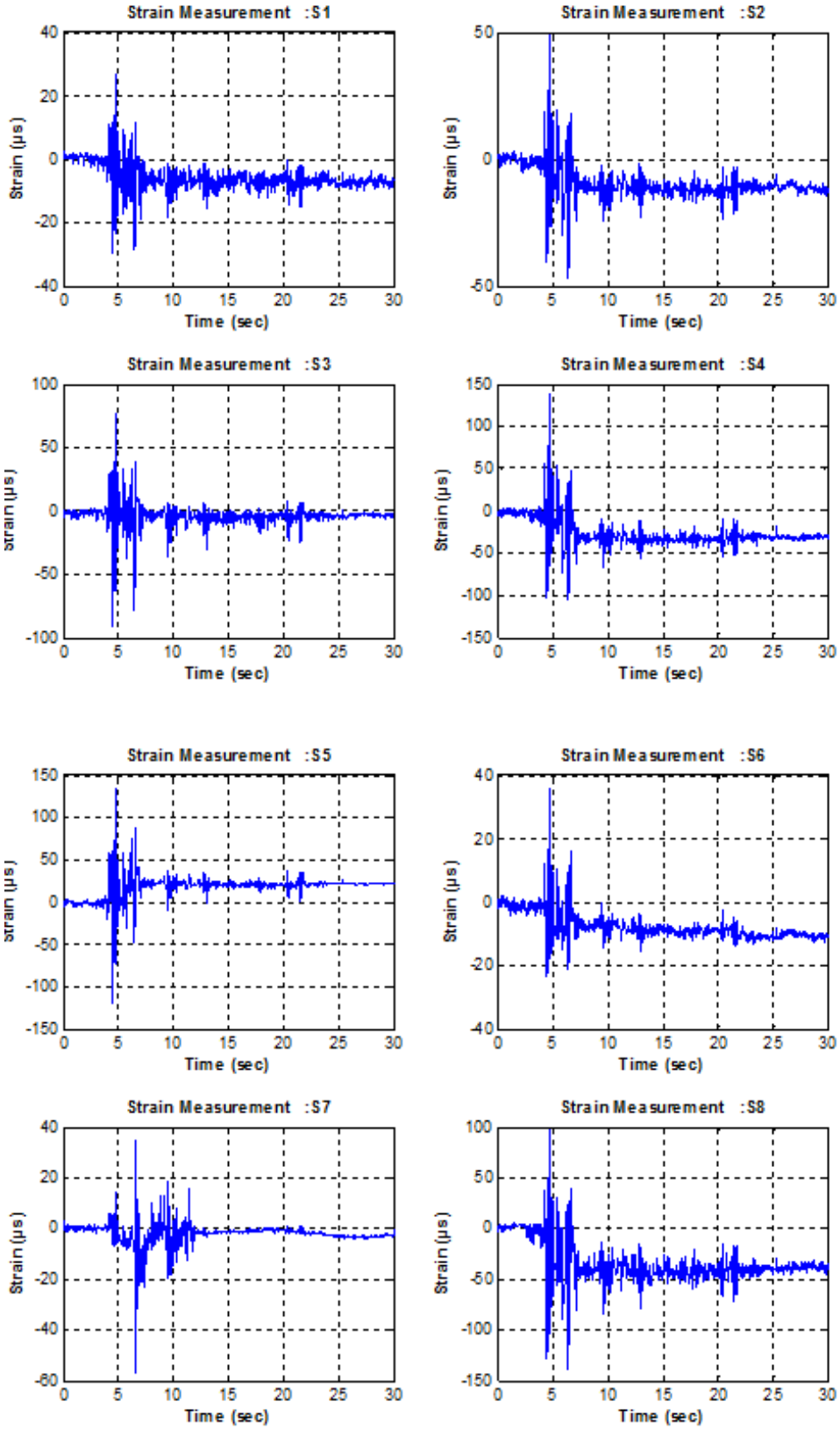

Figure C.19. Strain Time History Graphs for Setup 3 El Centro 100%.

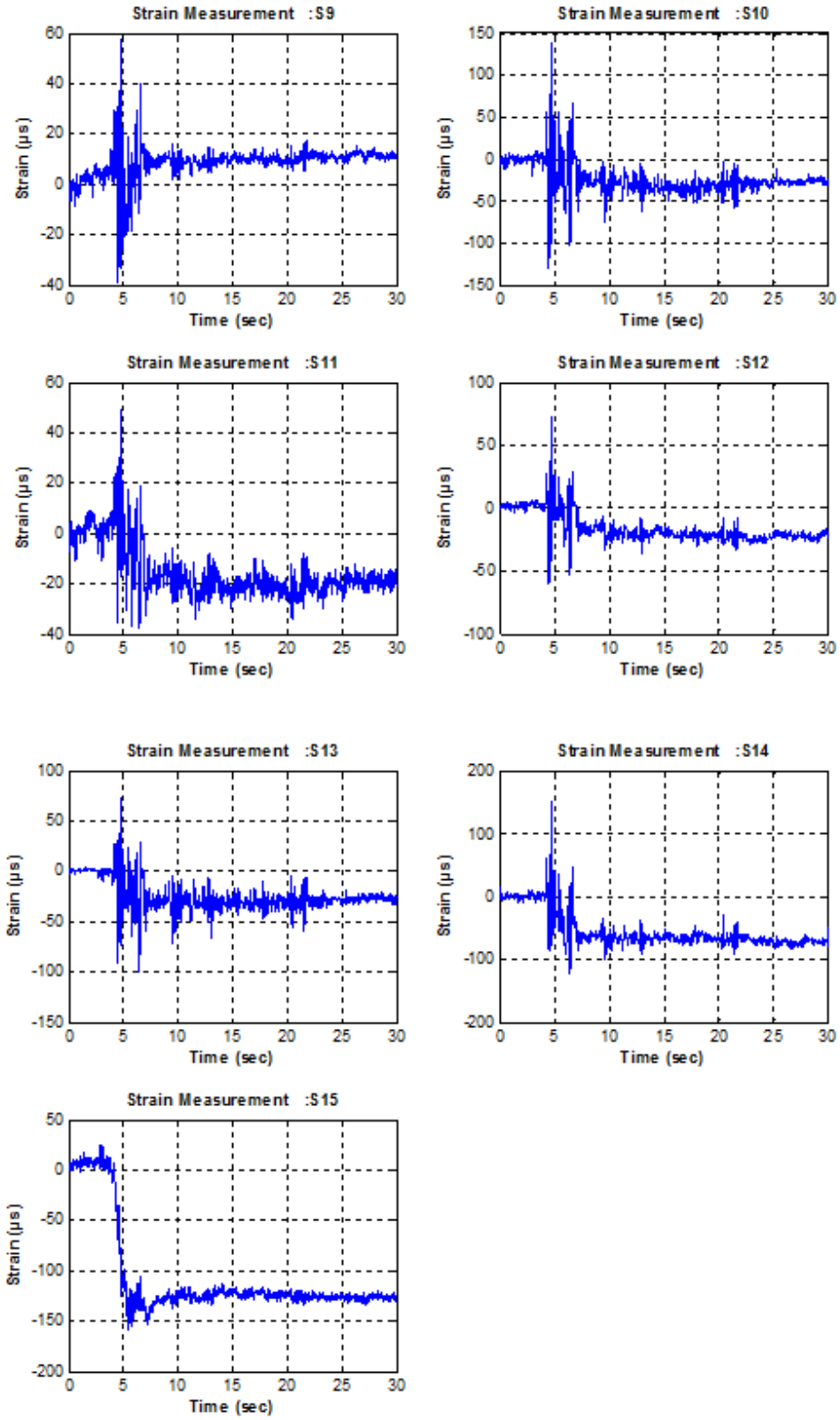

Figure C.20. Strain Time History Graphs for Setup 3 El Centro 100%.

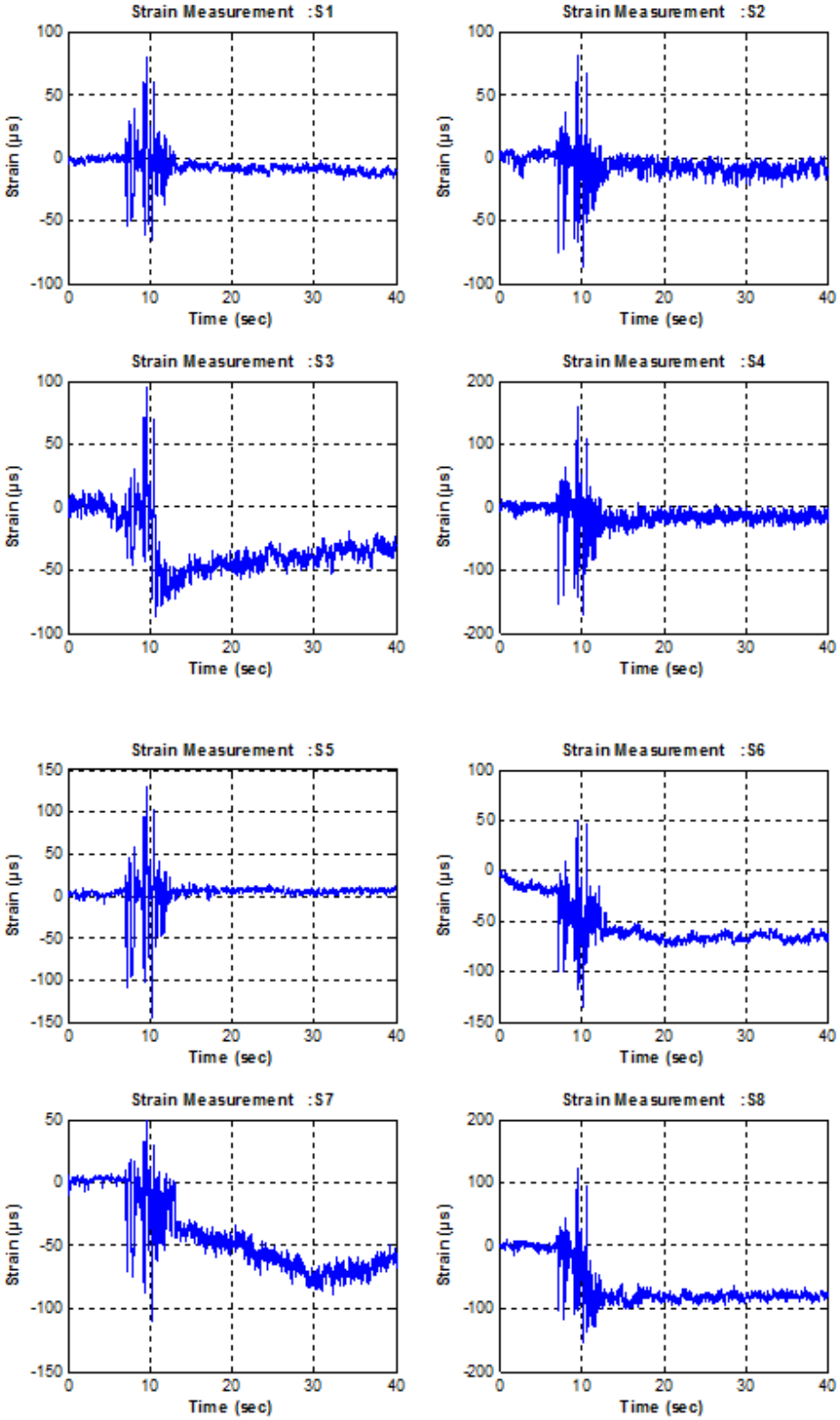

Figure C.21. Strain Time History Graphs for Setup 3 El Centro 50%.

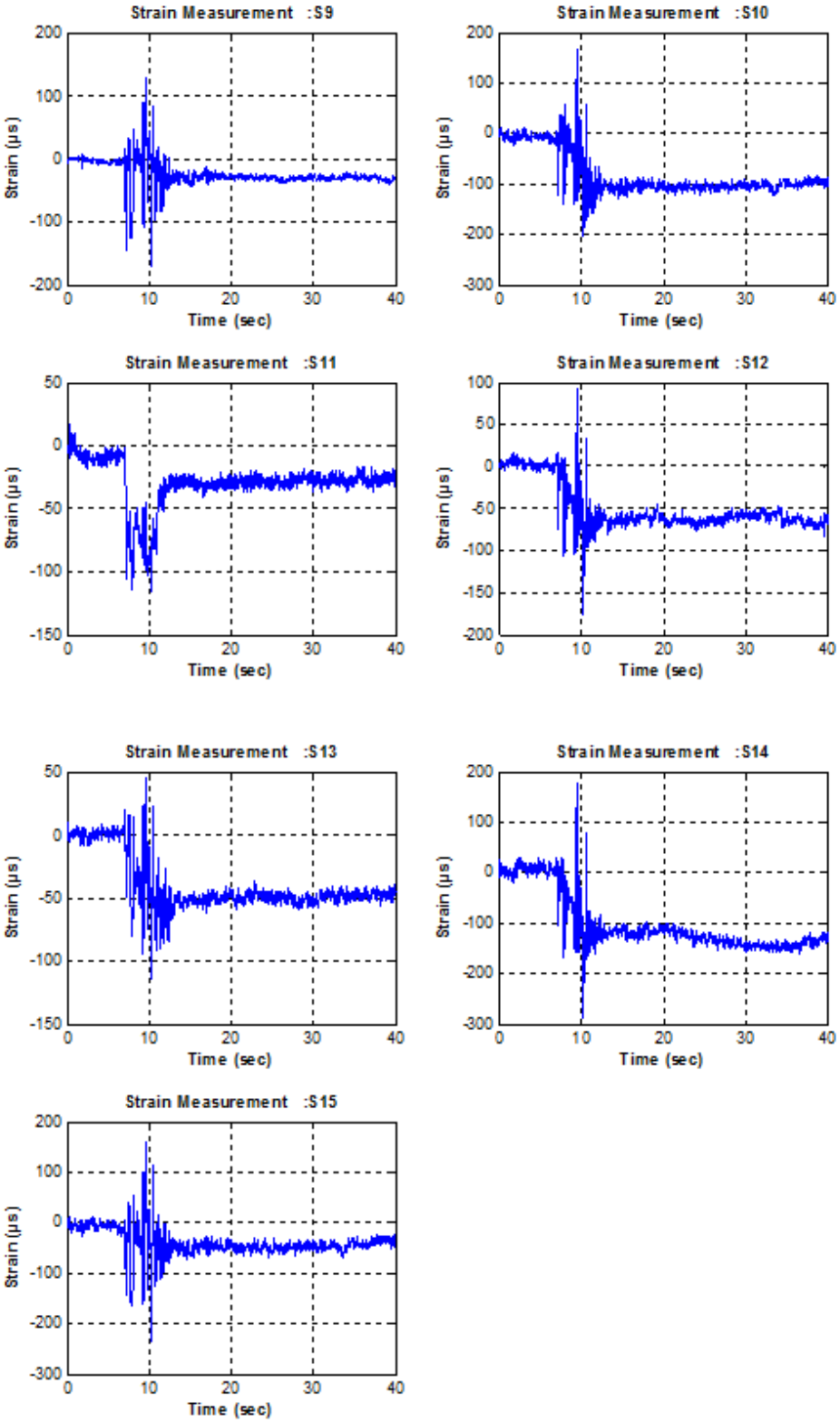

Figure C.22. Strain Time History Graphs for Setup 3 Kobe 50%.

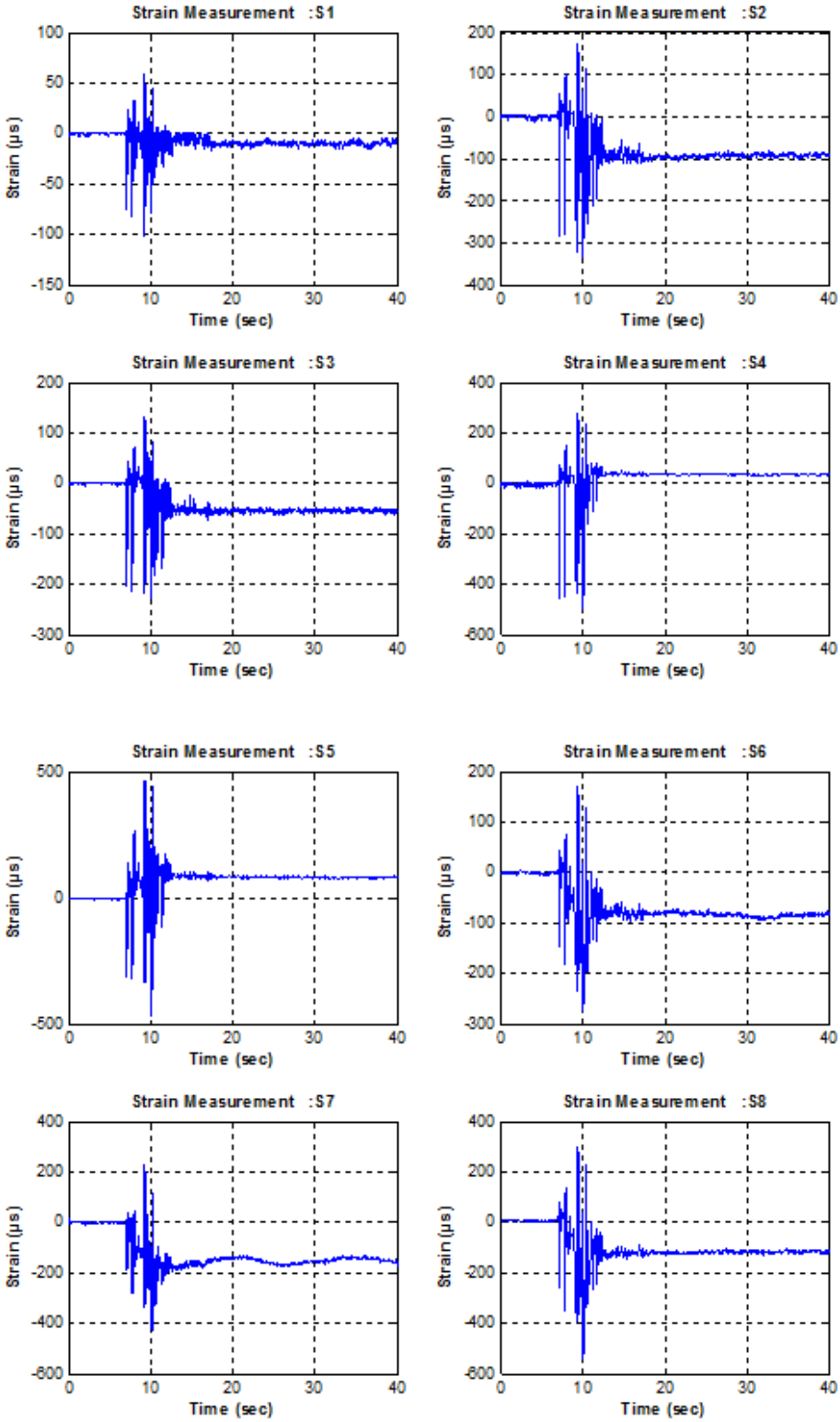

Figure C.23. Strain Time History Graphs for Setup 3 Kobe 75%.

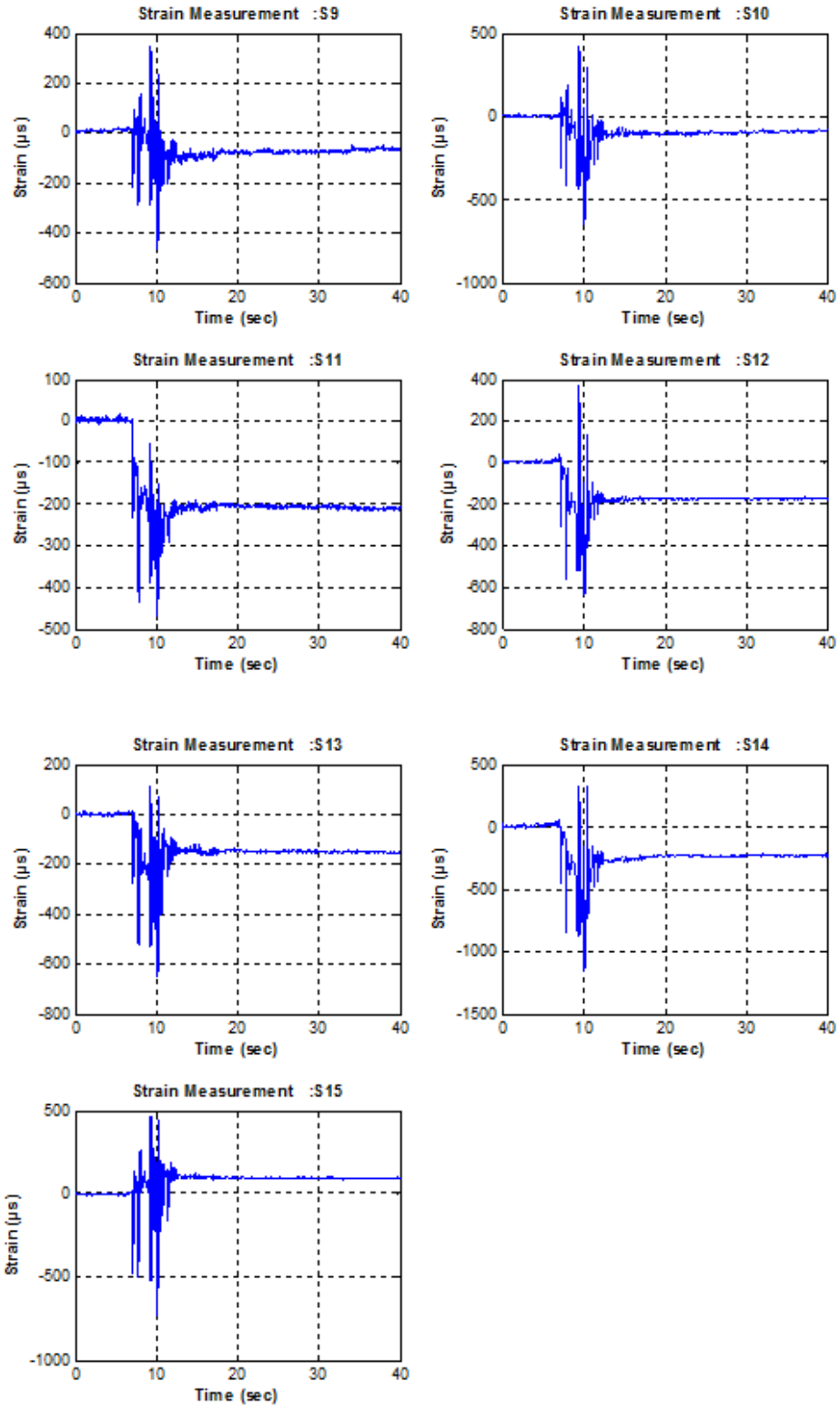

Figure C.24. Strain Time History Graphs for Setup 3 Kobe 75%.

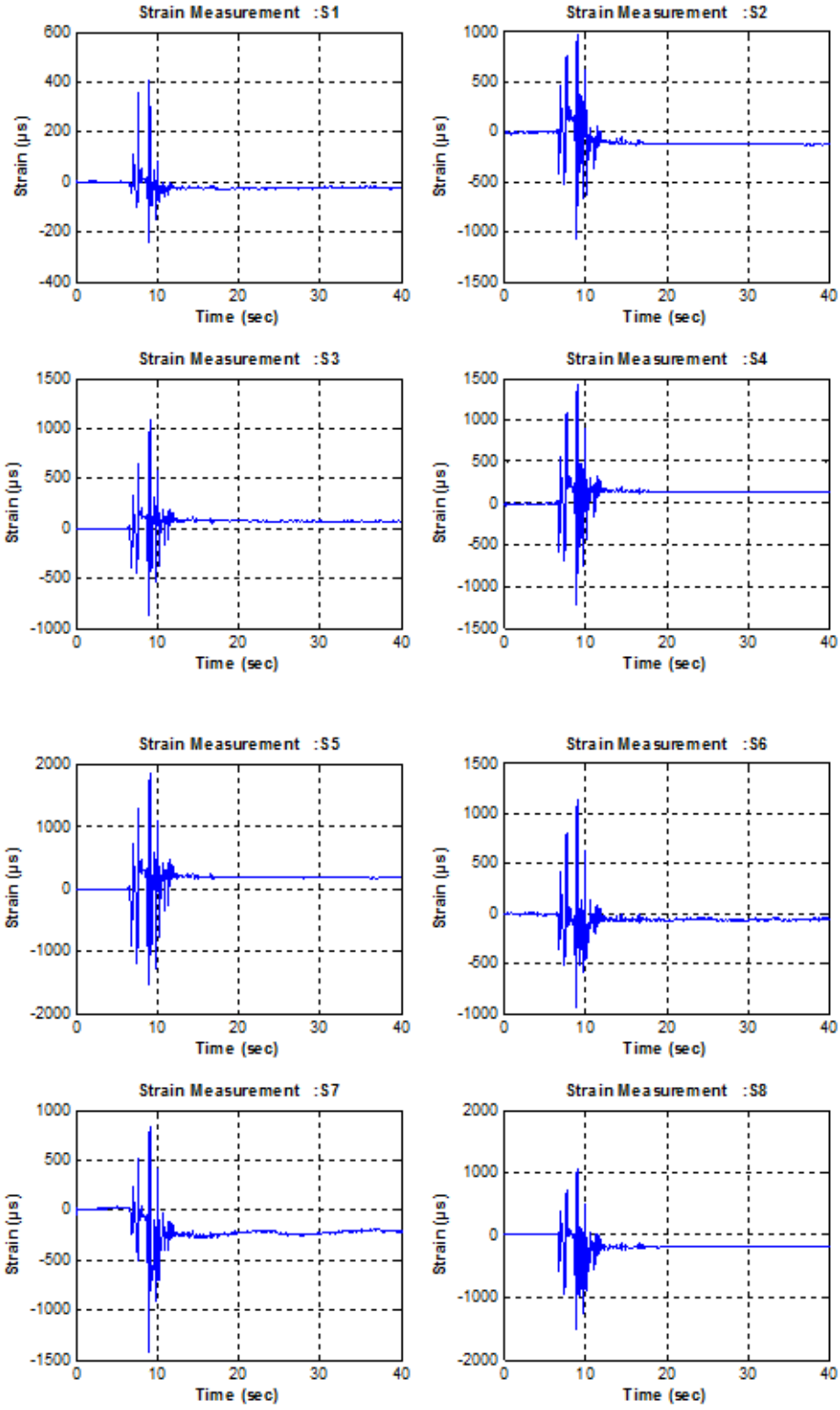

Figure C.25. Strain Time History Graphs for Setup 3 Kobe 100%.

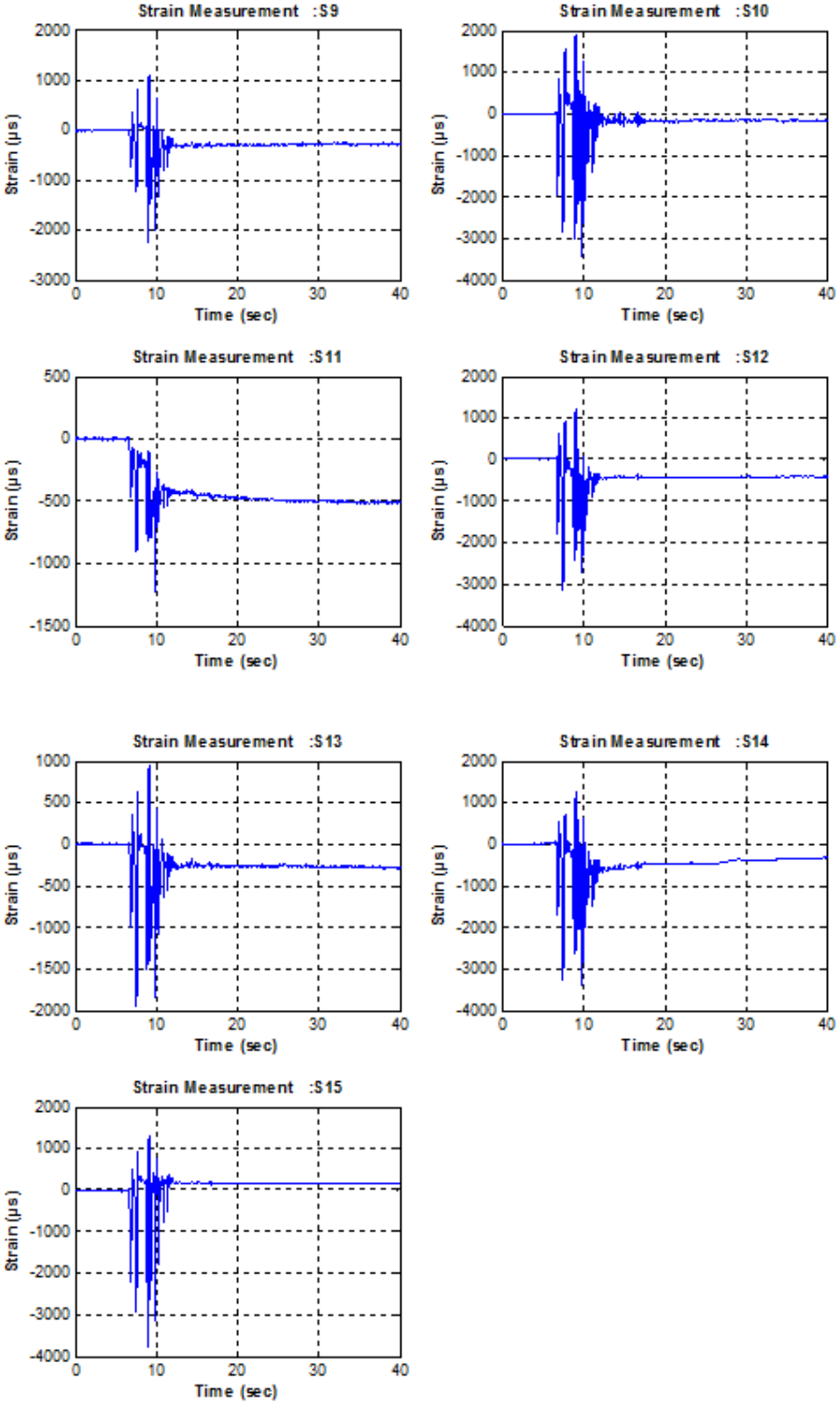

Figure C.26. Strain Time History Graphs for Setup 3 Kobe 100%.

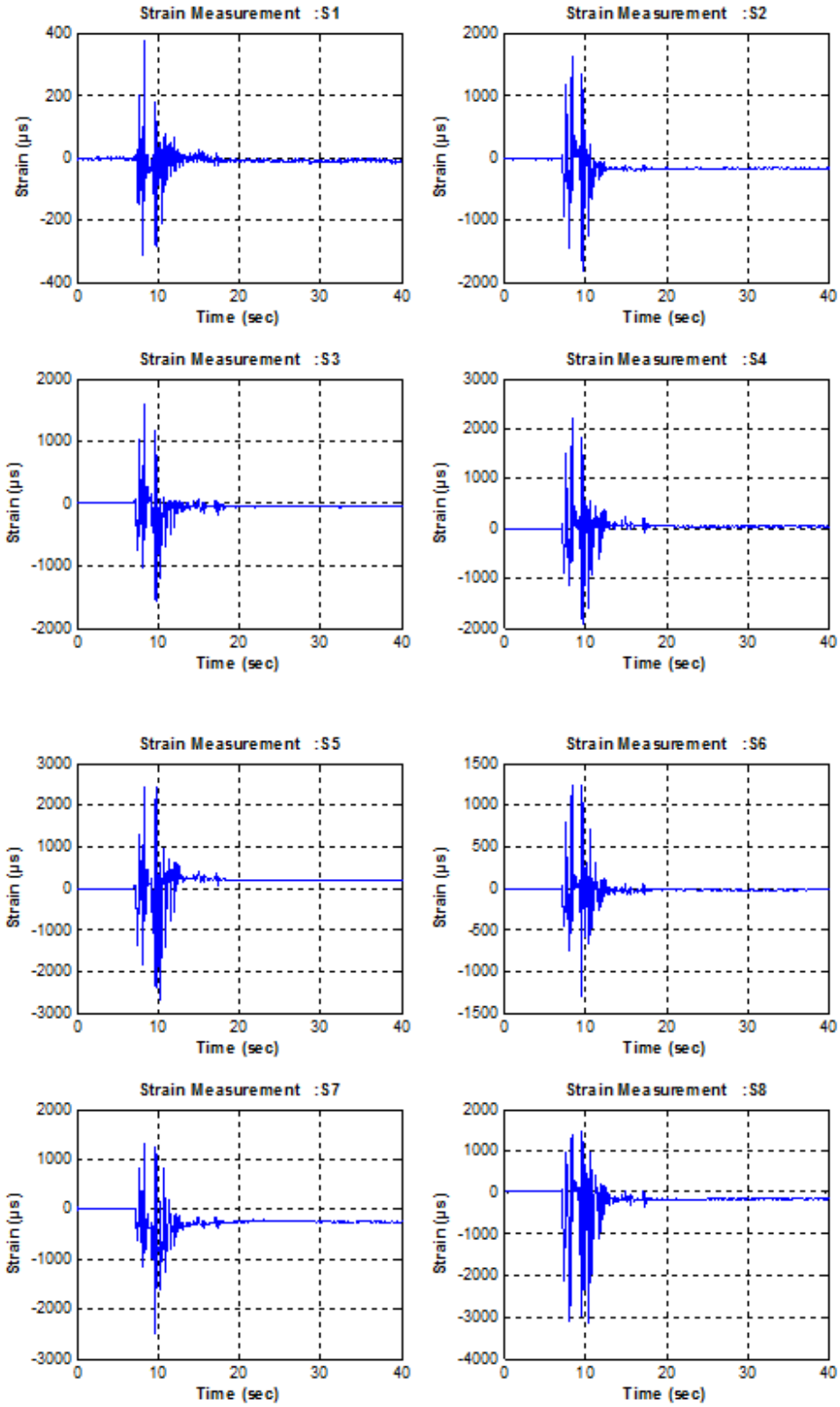

Figure C.27. Strain Time History Graphs for Setup 3 Kobe 125%.

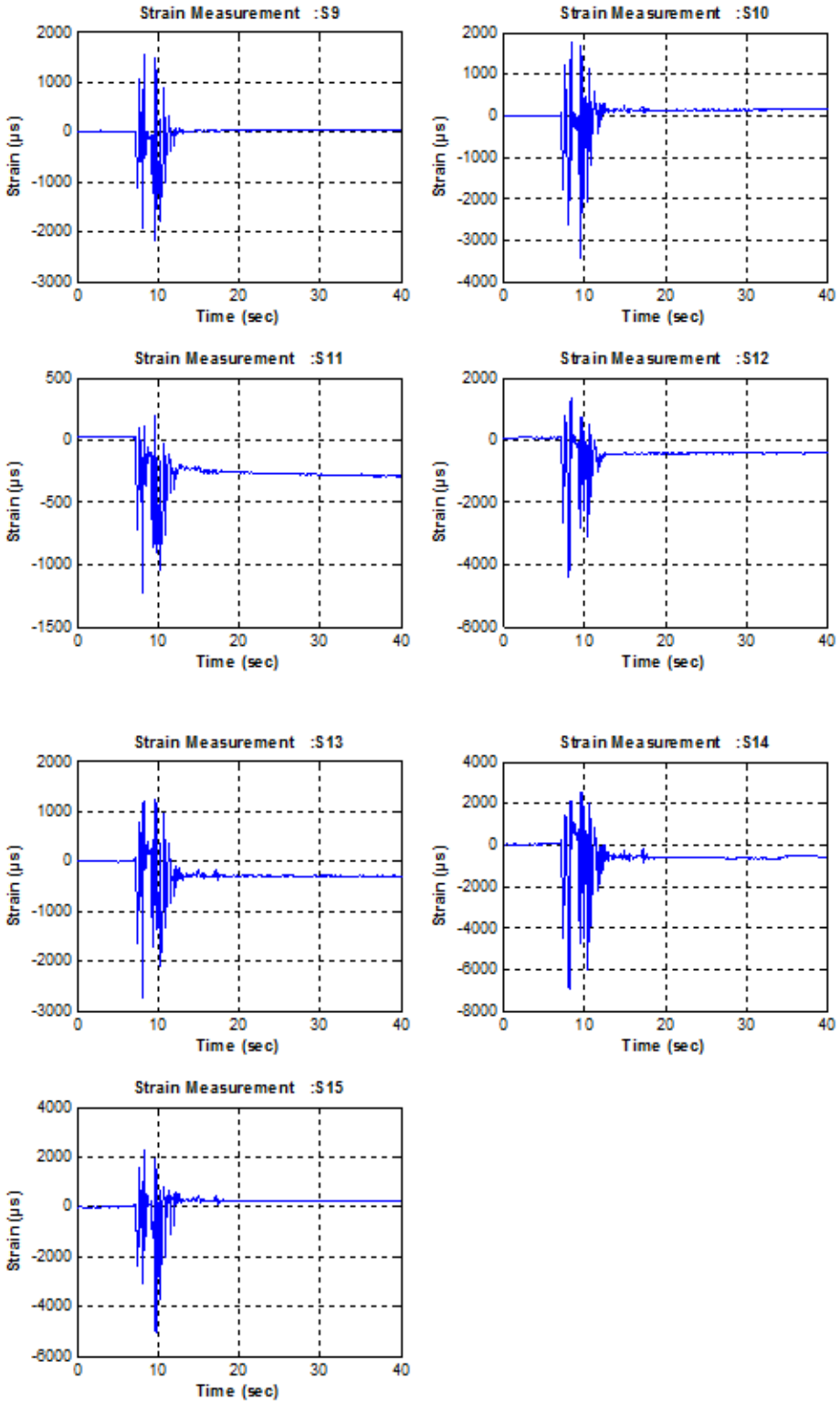

Figure C.28. Strain Time History Graphs for Setup 3 Kobe 125%.

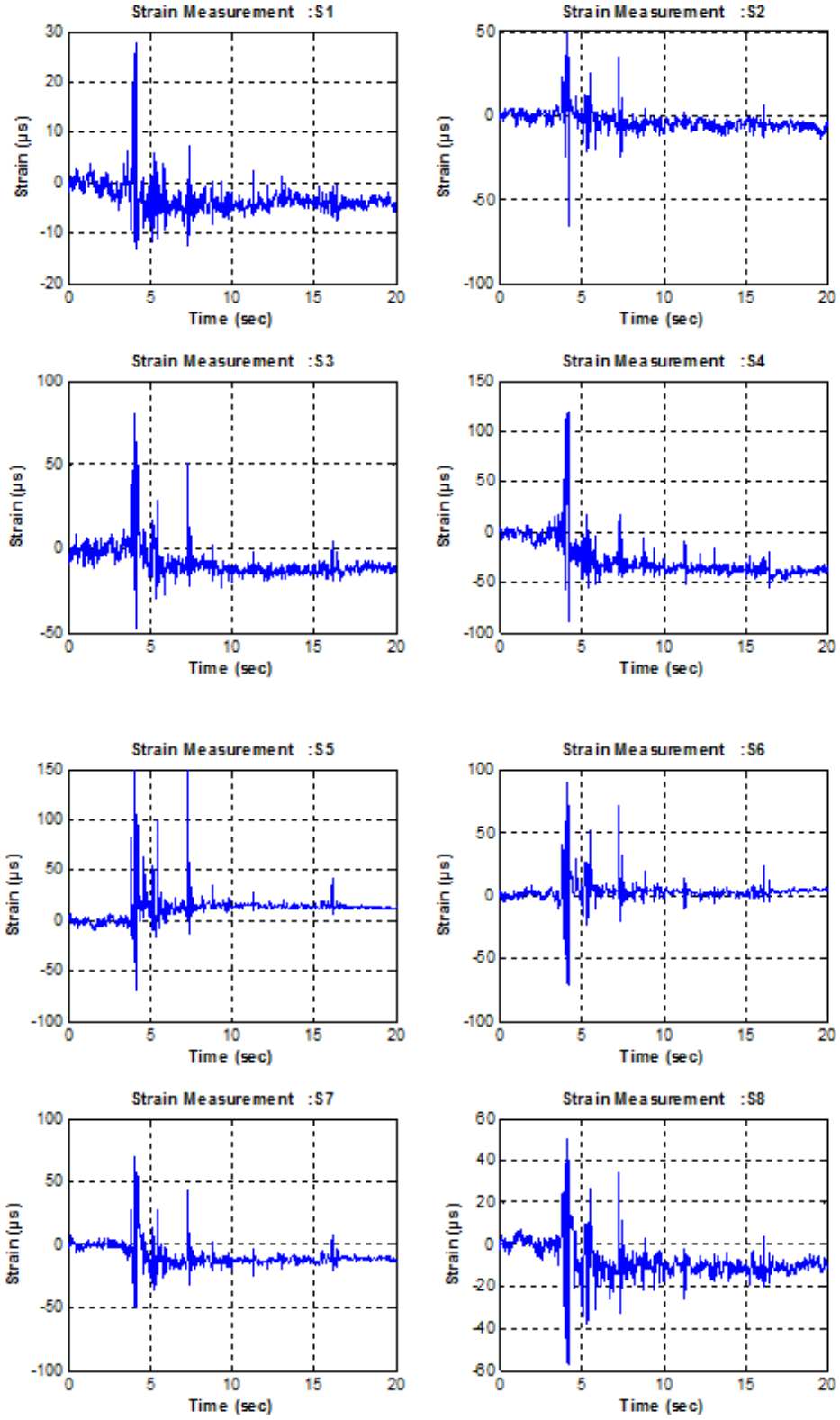

Figure C.29. Strain Time History Graphs for Setup 4 El Centro 100%.

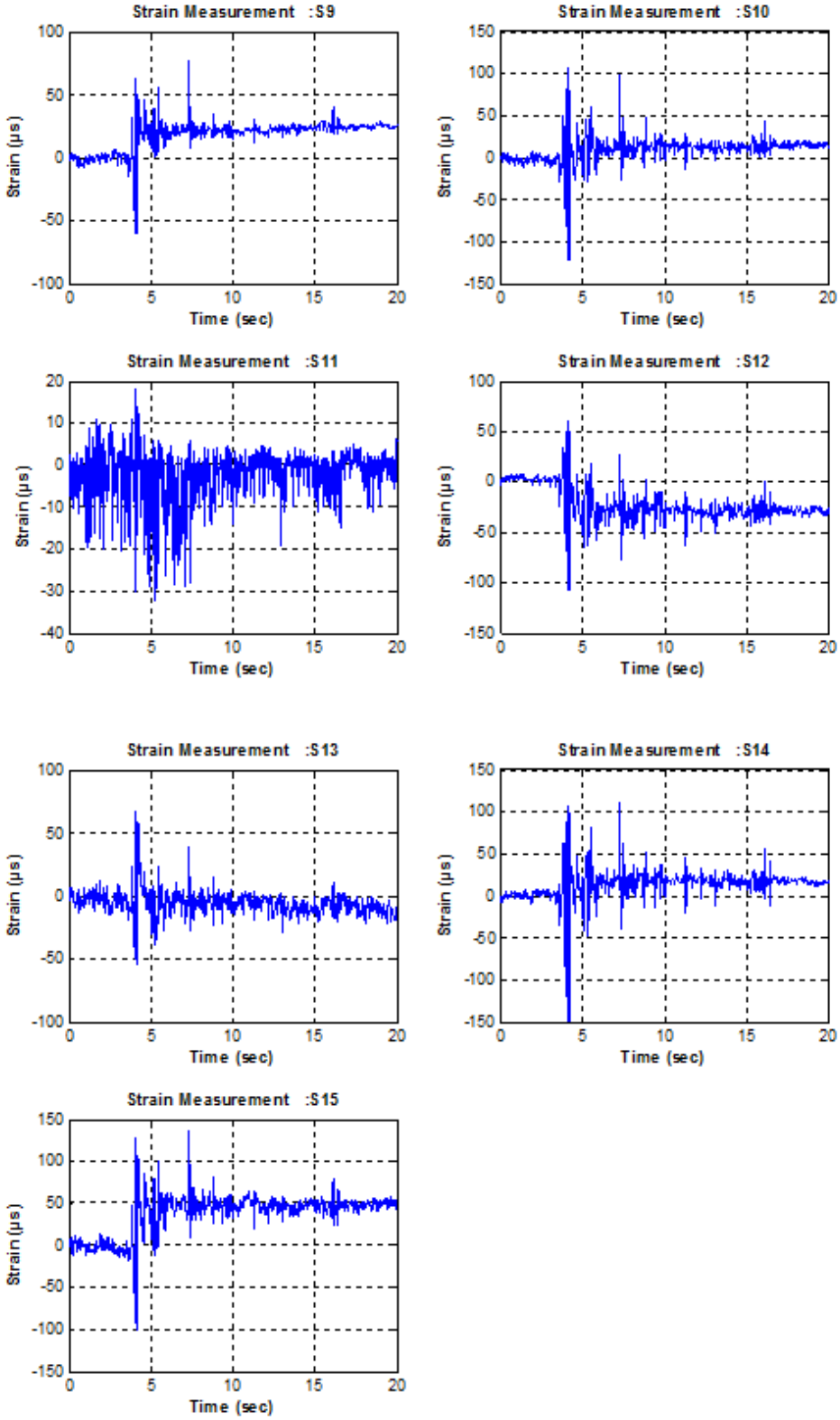

Figure C.30. Strain Time History Graphs for Setup 4 El Centro 100%.

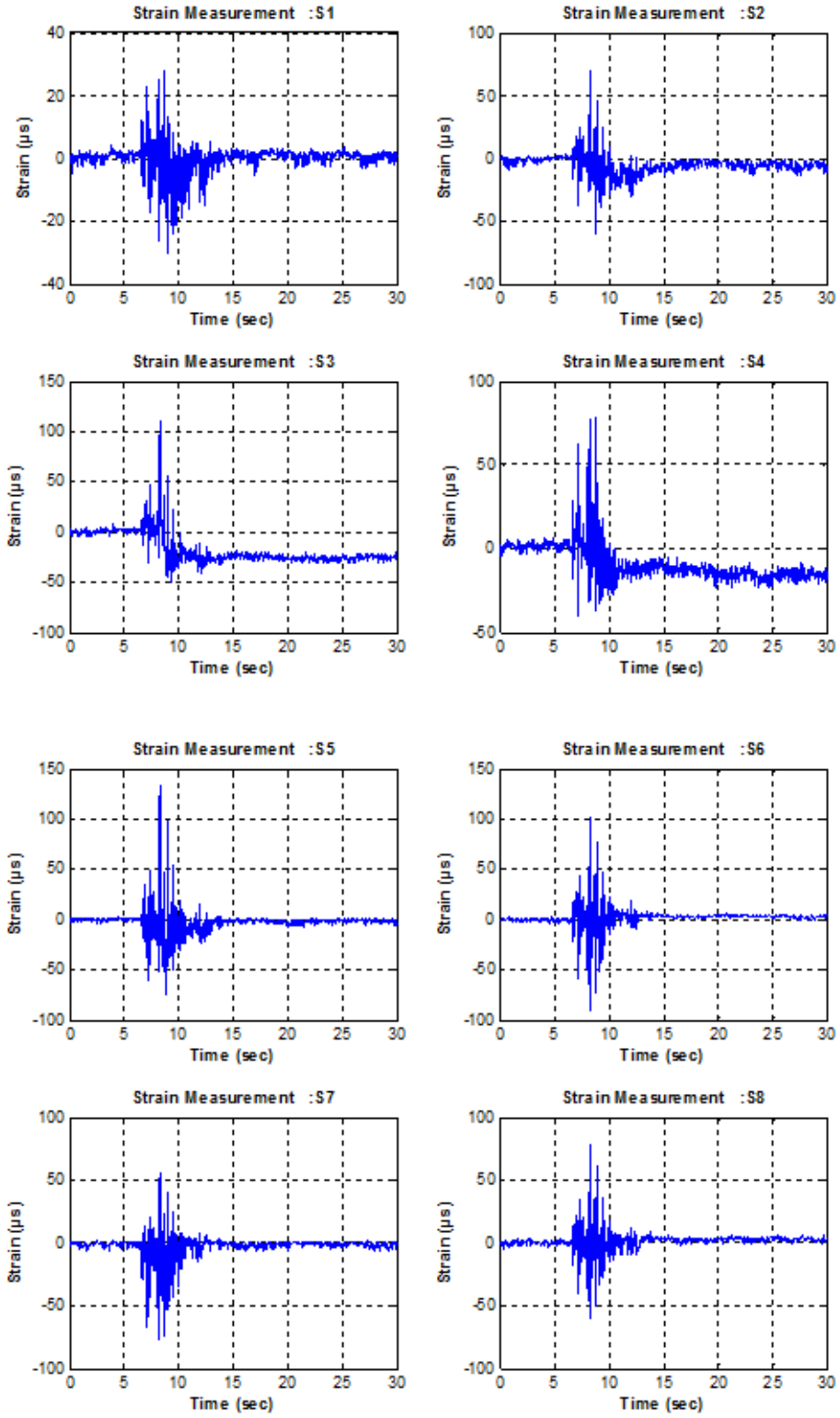

Figure C.31. Strain Time History Graphs for Setup 4 Kobe 50%.

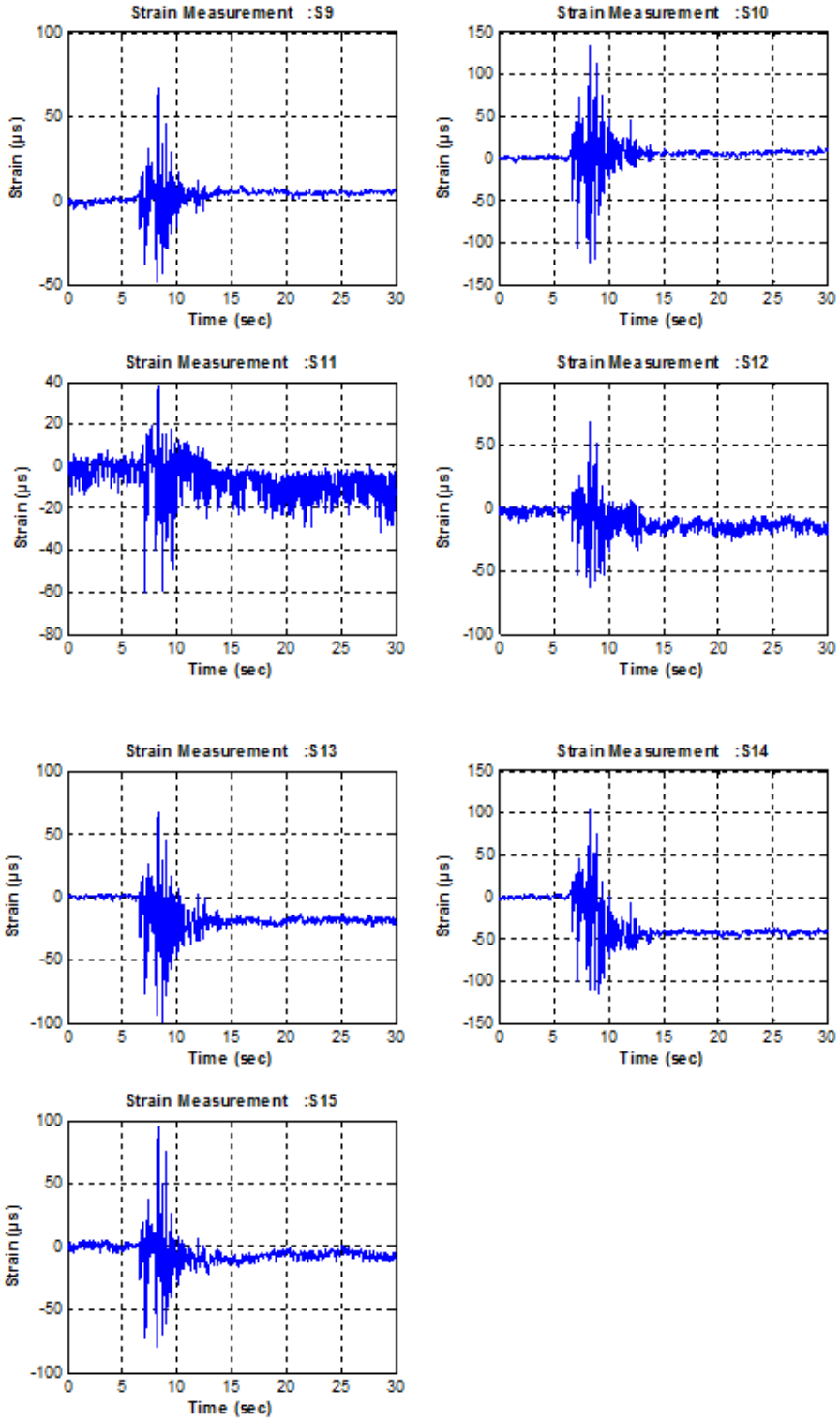

Figure C.32. Strain Time History Graphs for Setup 4 Kobe 50%.

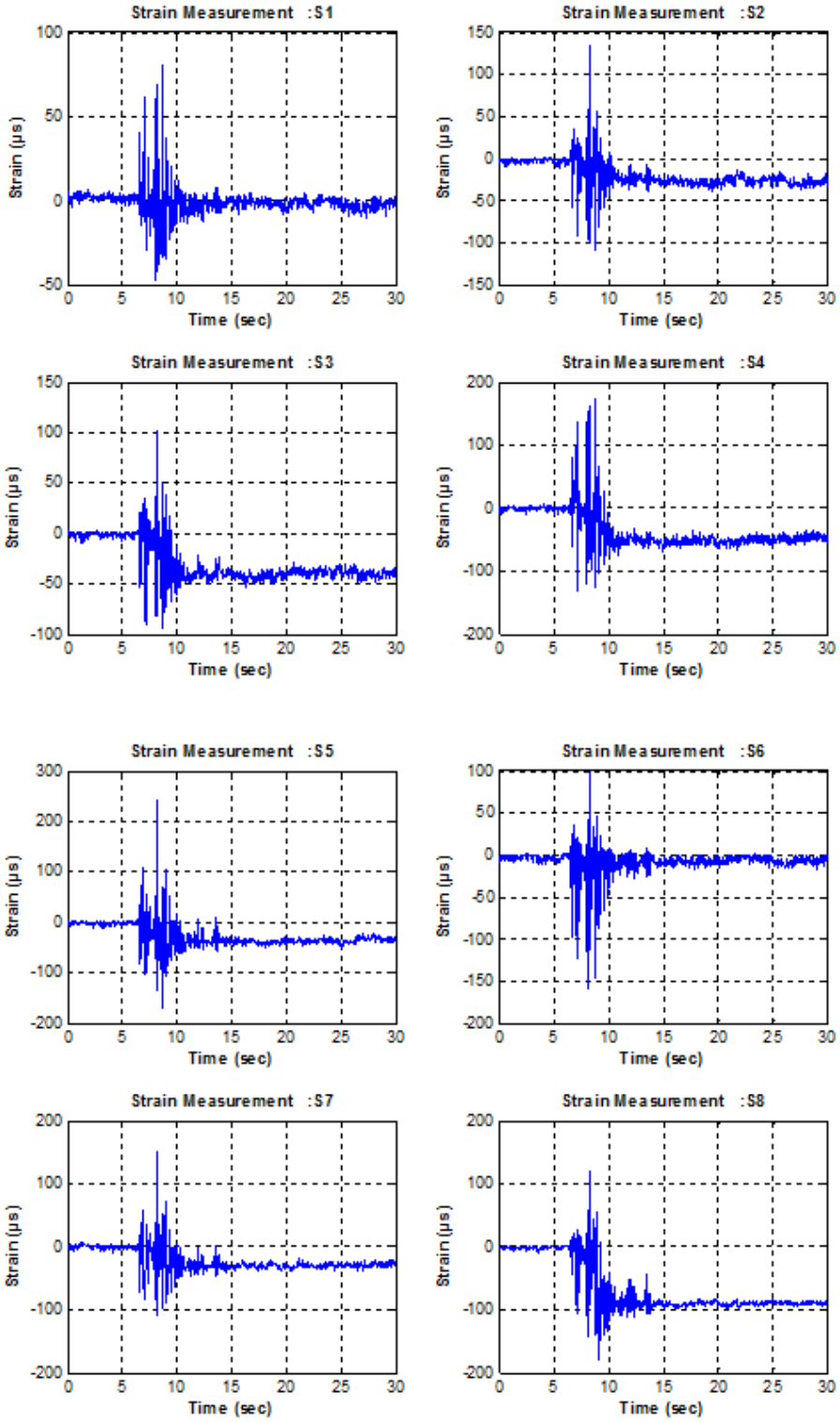

Figure C.33. Strain Time History Graphs for Setup 4 Kobe 75%.

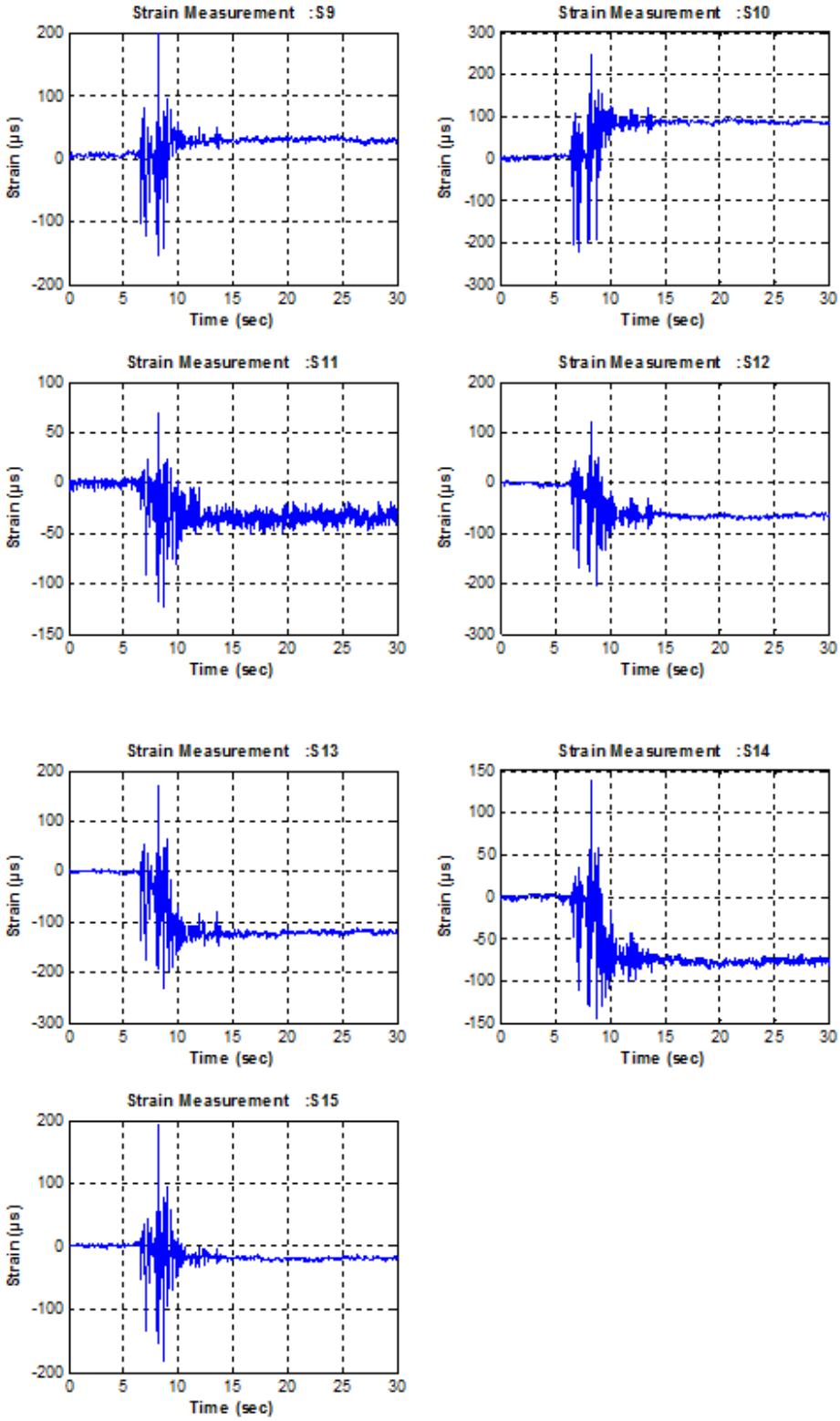

Figure C.34. Strain Time History Graphs for Setup 4 Kobe 75%.

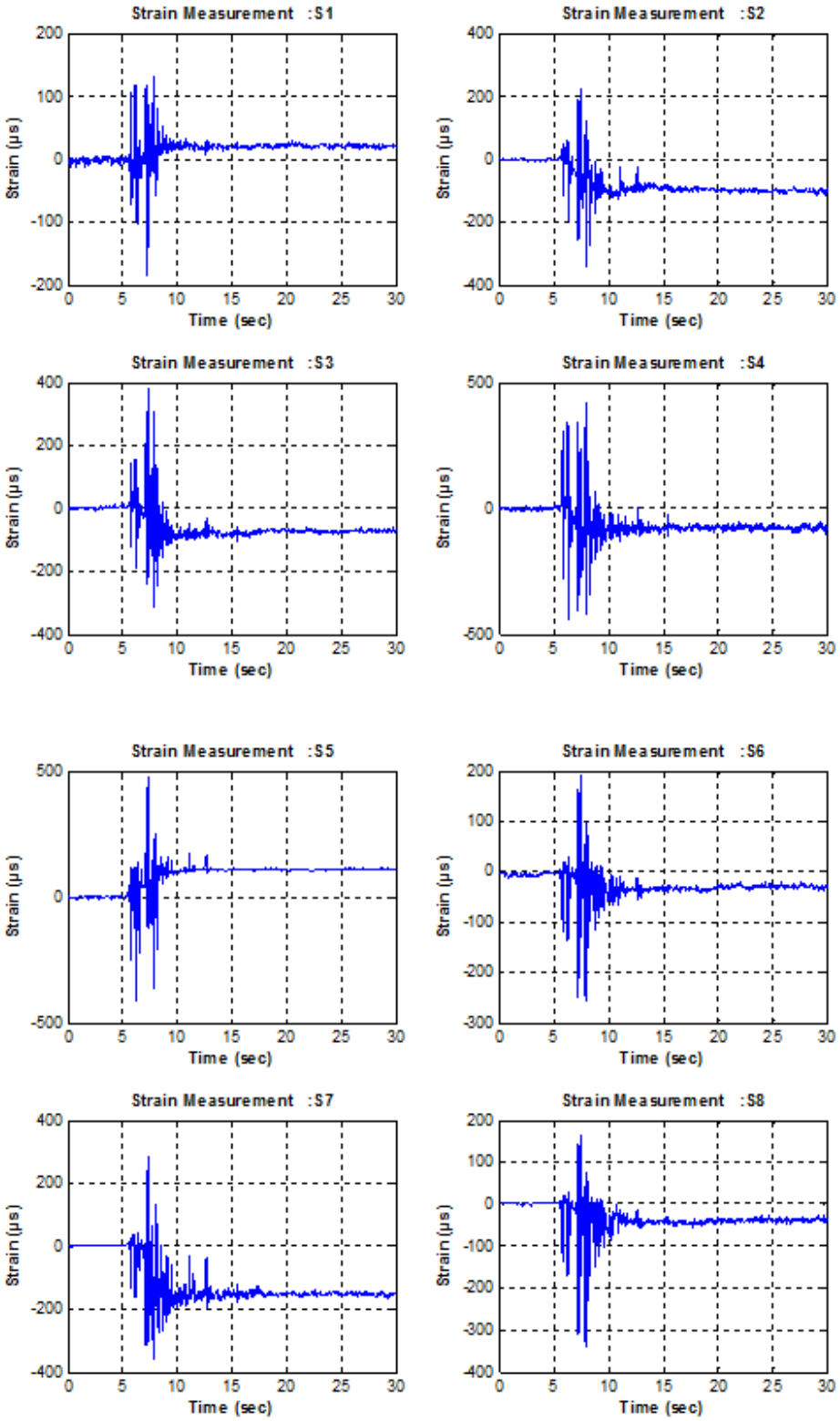

Figure C.35. Strain Time History Graphs for Setup 4 Kobe 100%.

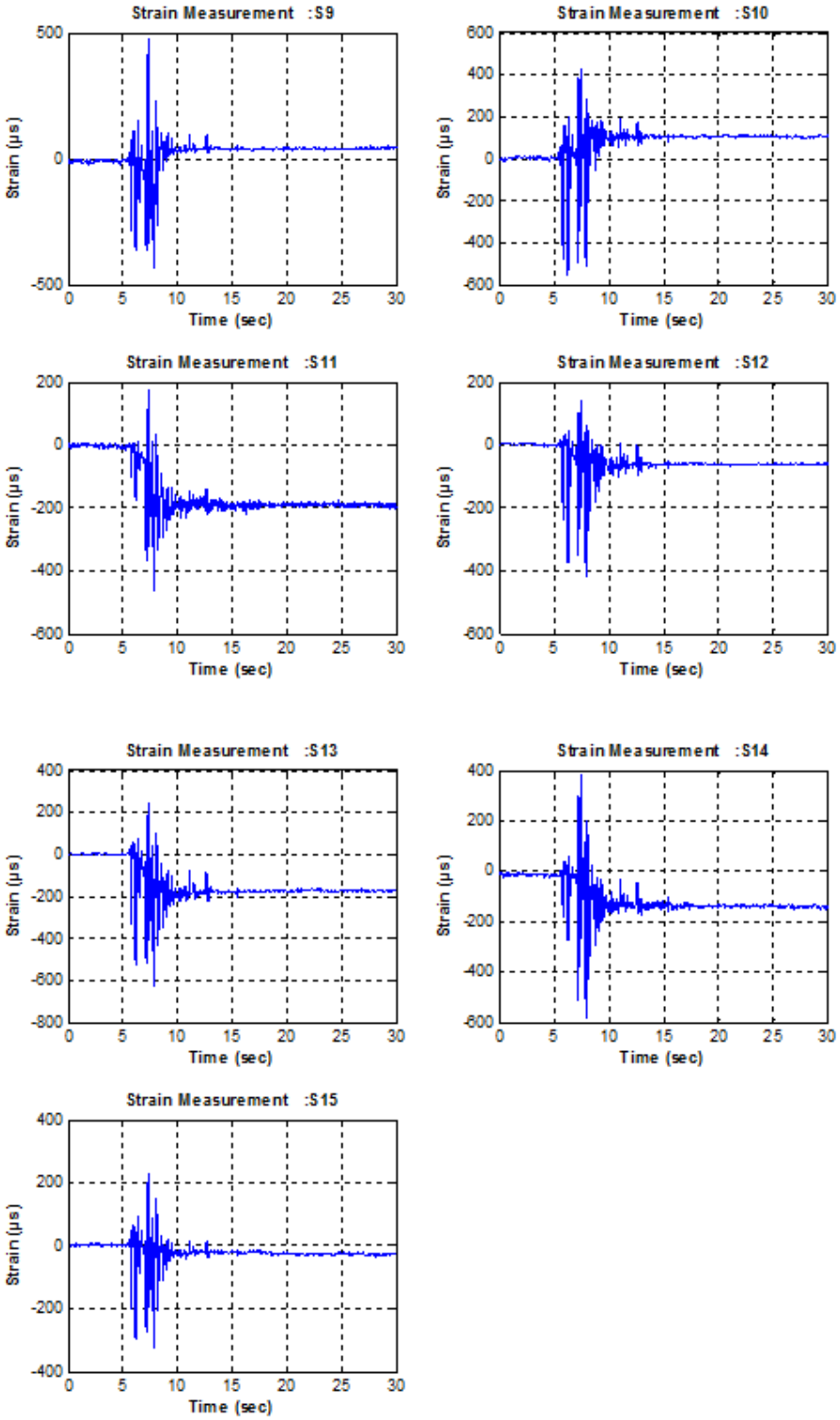

Figure C.36. Strain Time History Graphs for Setup 4 Kobe 100%.

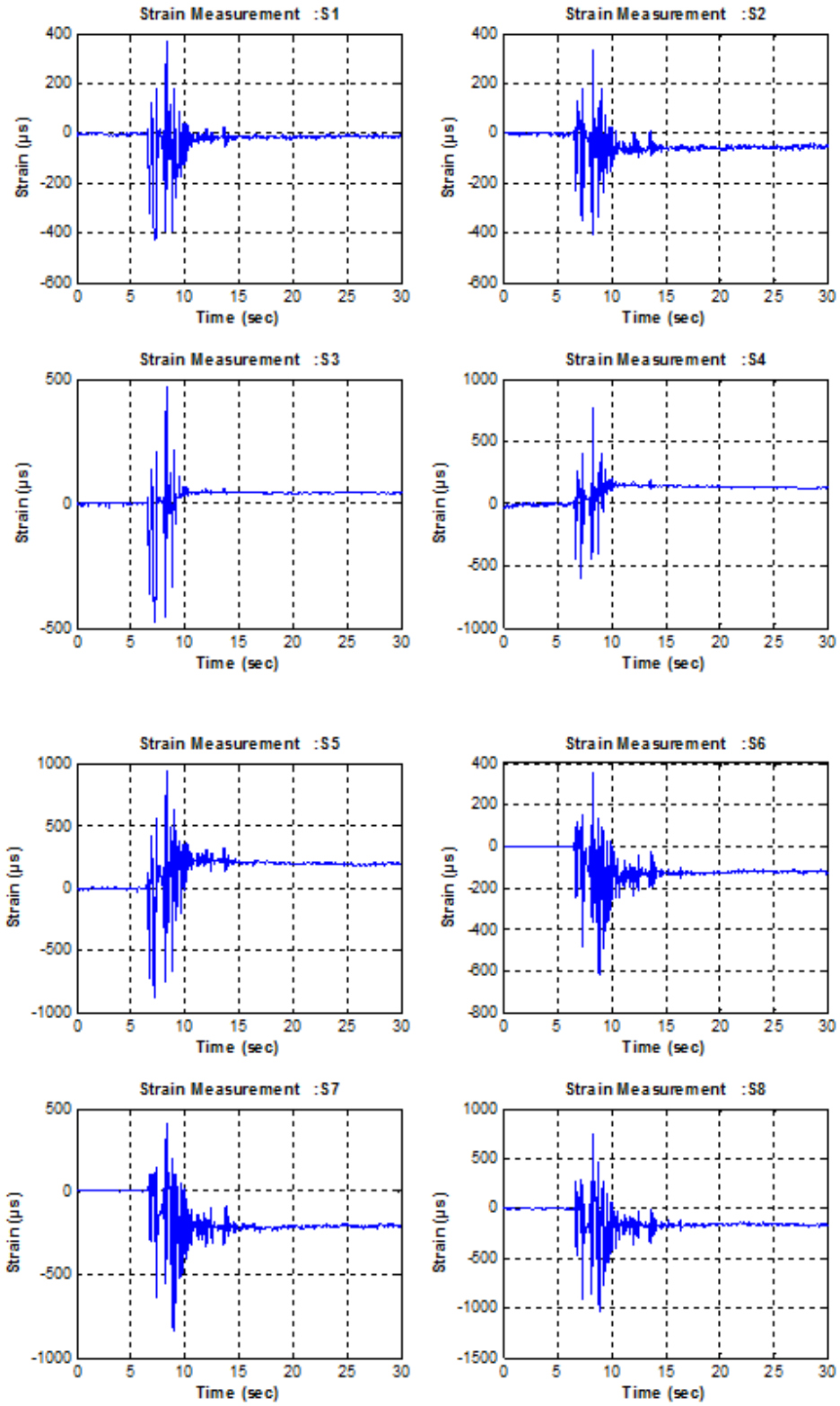

Figure C.37. Strain Time History Graphs for Setup 4 Kobe 125%.

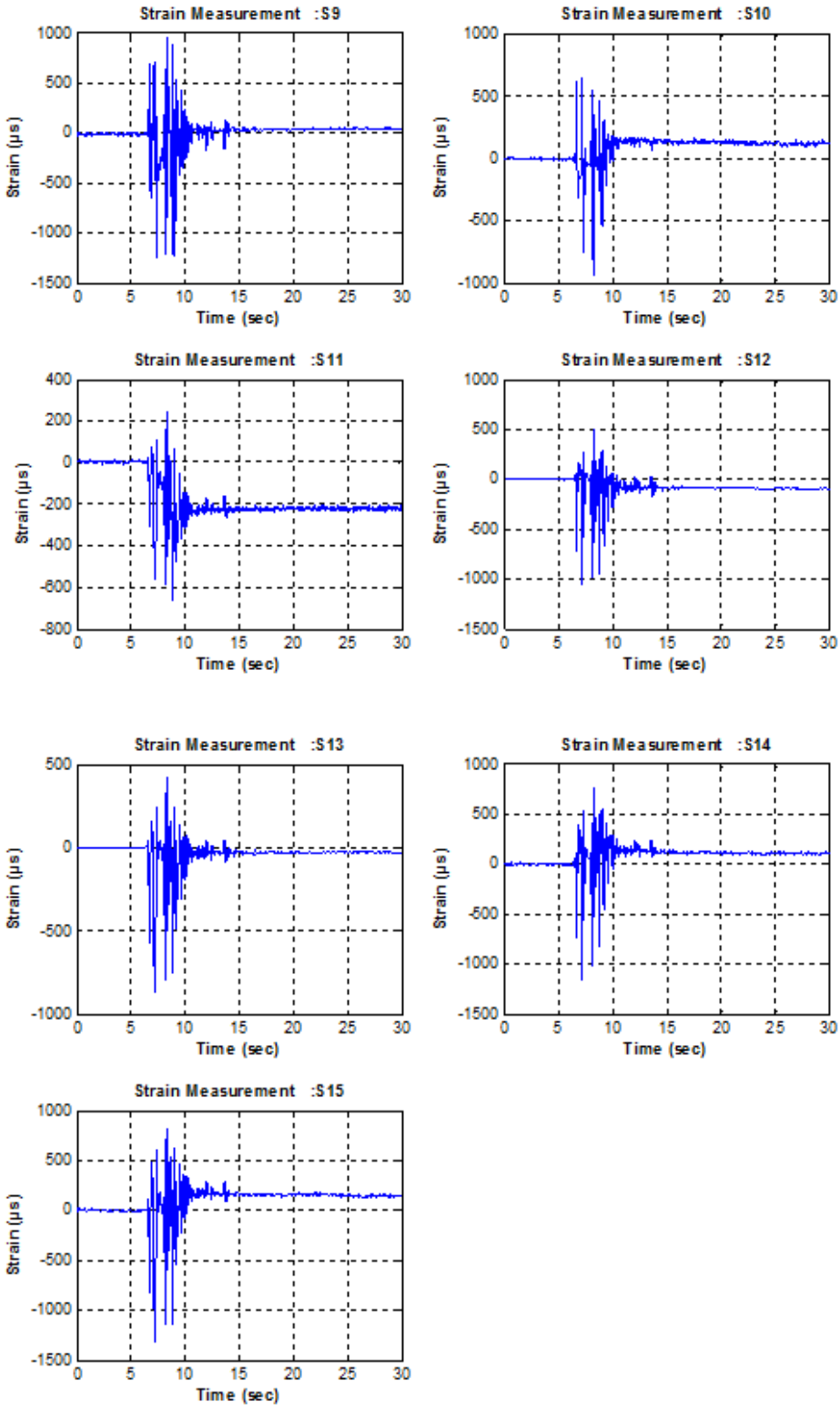

Figure C.38. Strain Time History Graphs for Setup 4 Kobe 125%.

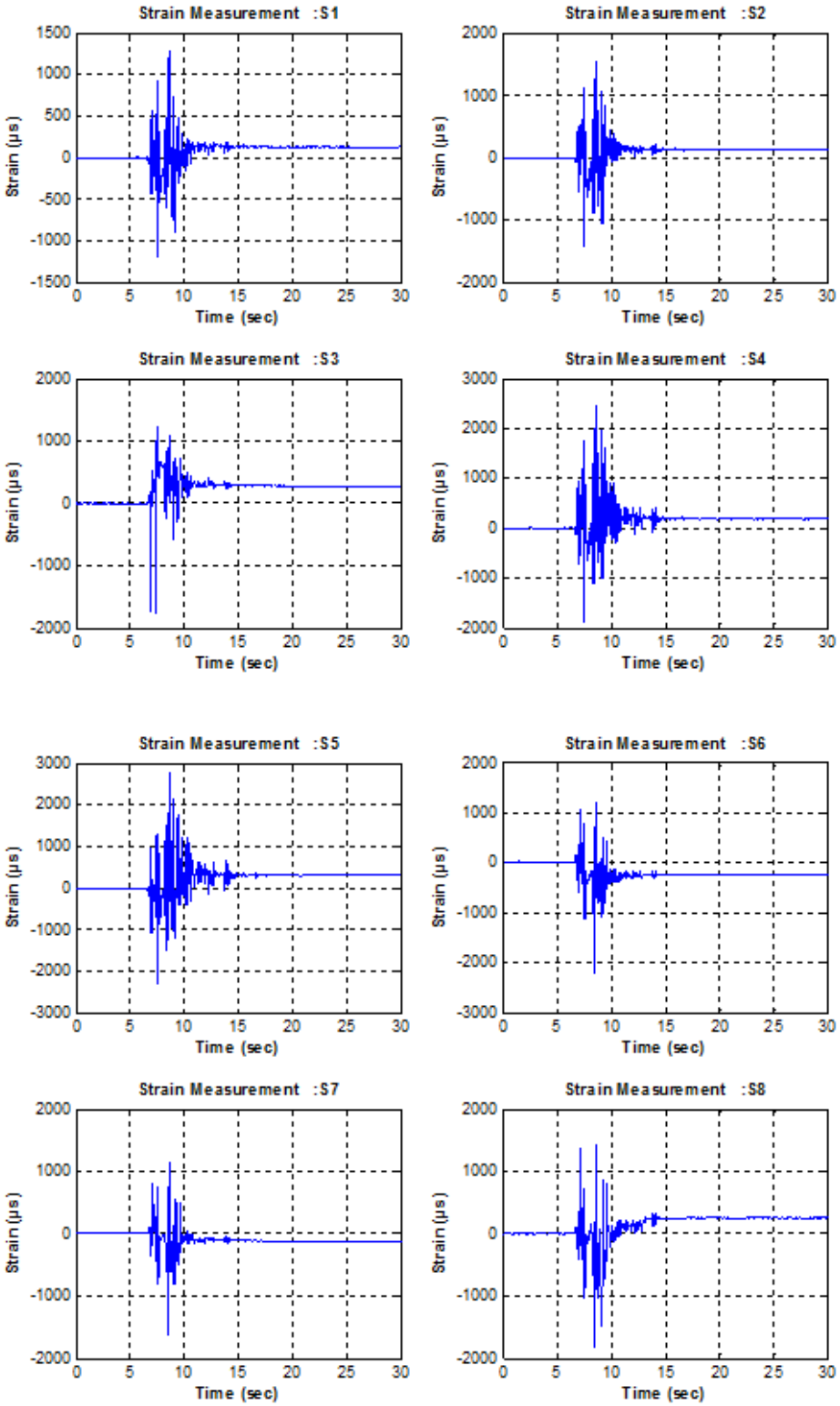

Figure C.39. Strain Time History Graphs for Setup 4 Kobe 150%.

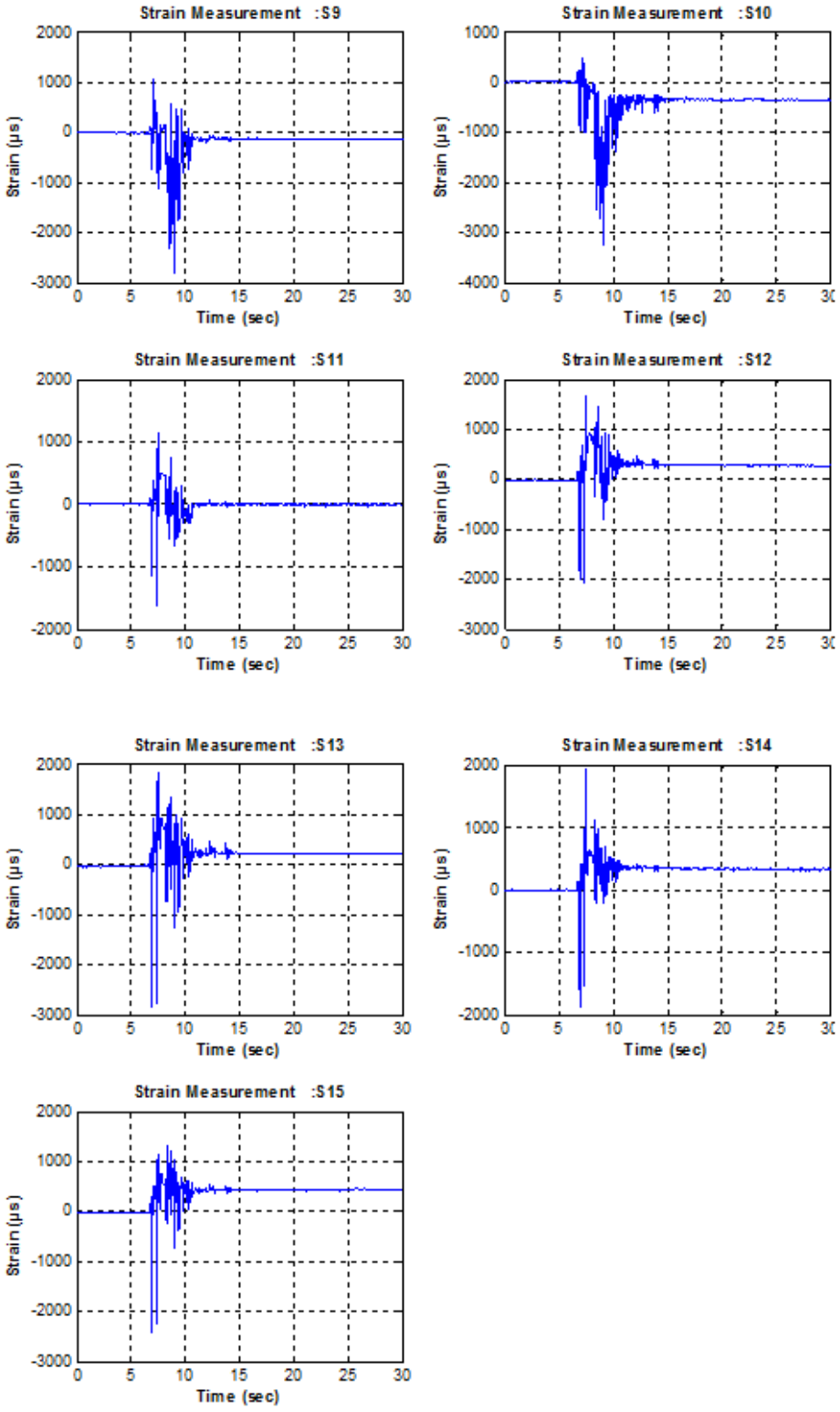

Figure C.40. Strain Time History Graphs for Setup 4 Kobe 150%.

APPENDIX D: STRAIN VERSUS TIME PEAK RESULTS ON TOP, MID AND BOTTOM GEOGRIDS

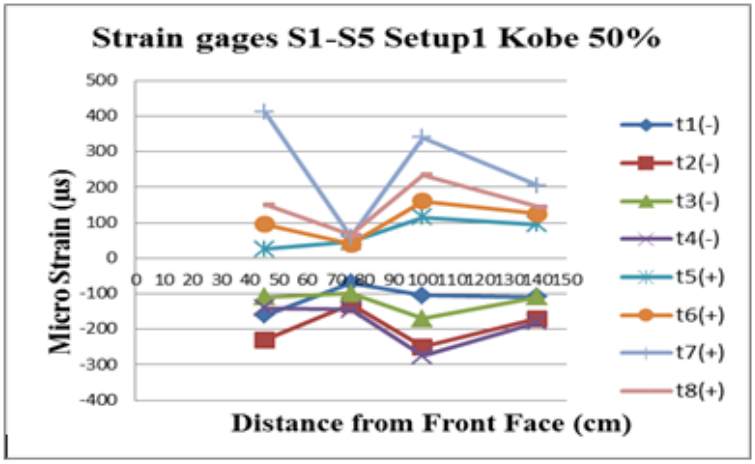

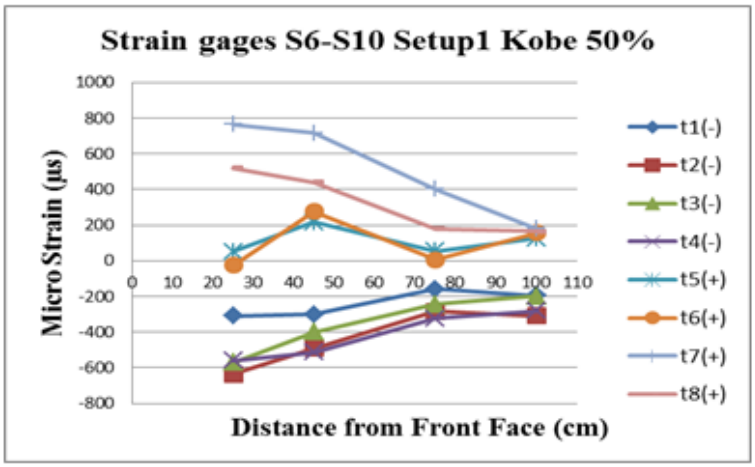

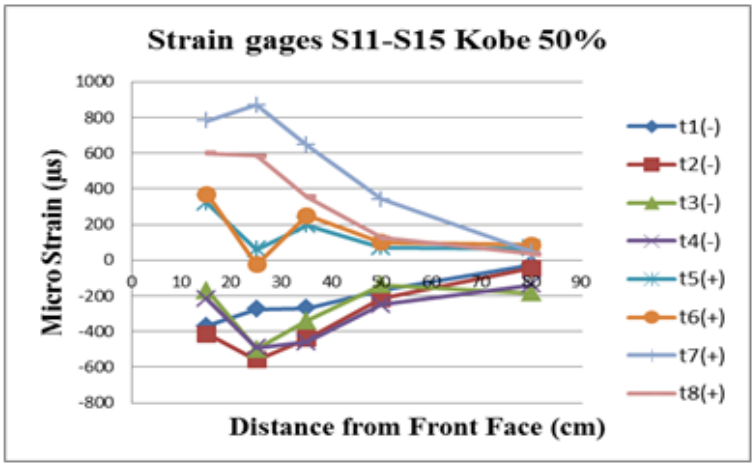

Figure D.1. Strain Time Peaks for Compression and Tension for Setup 1 Kobe 50%.

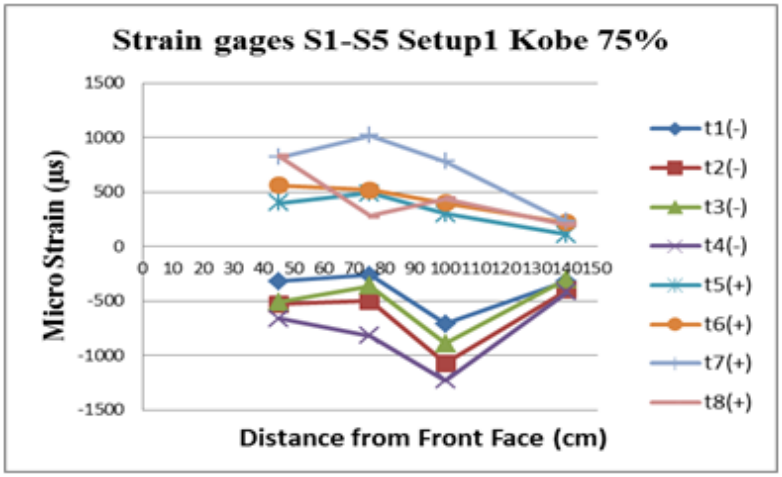

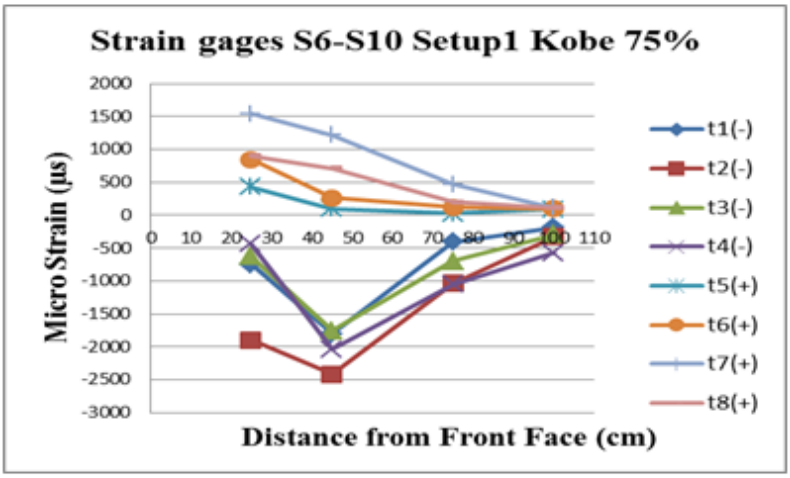

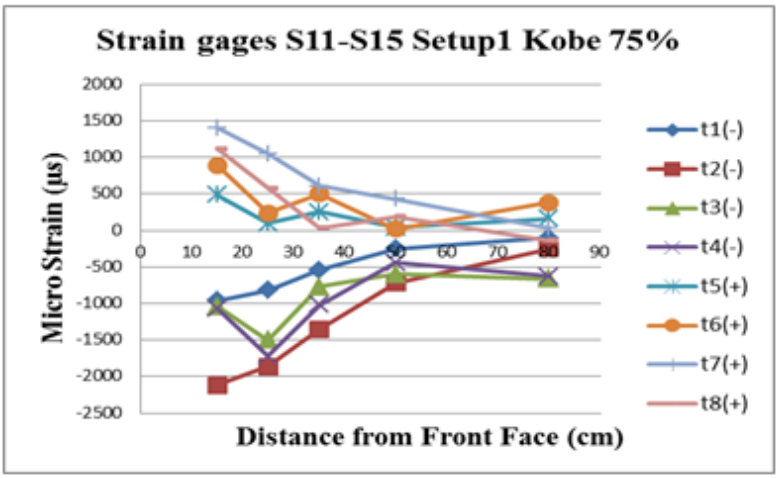

Figure D.2. Strain Time Peaks for Compression and Tension for Setup 1 Kobe 75%.

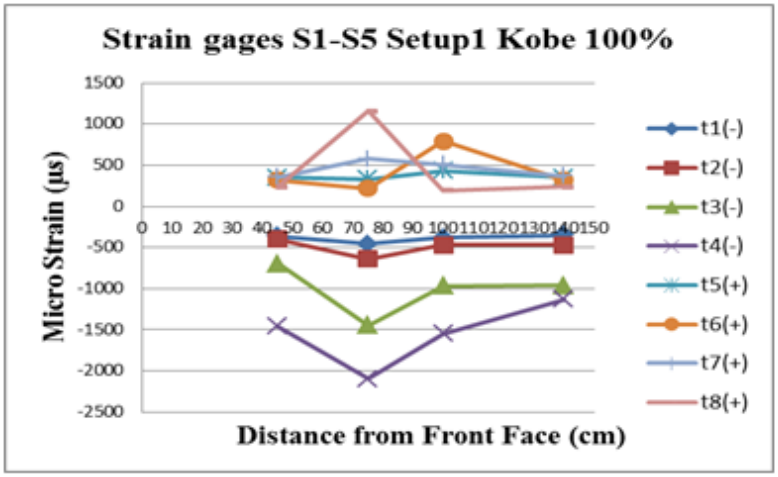

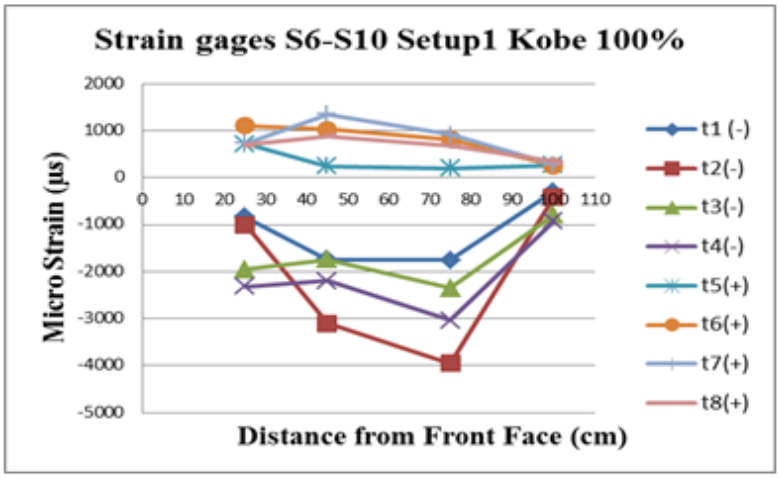

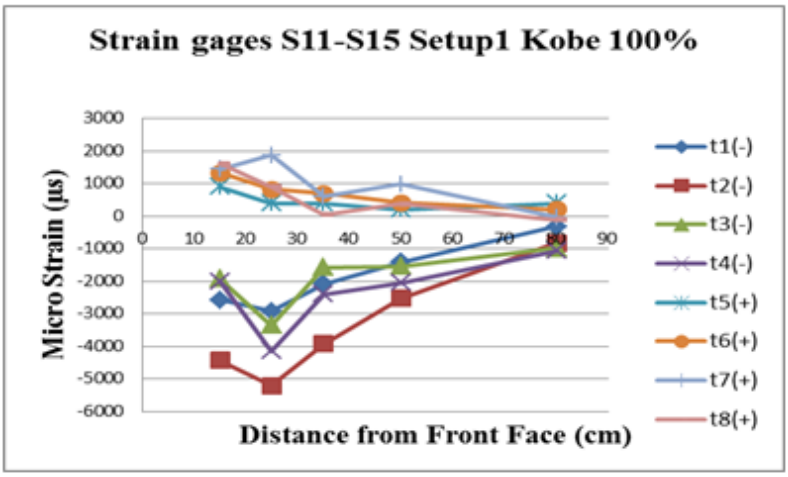

Figure D.3. Strain Time Peaks for Compression and Tension for Setup 1 Kobe 100%.

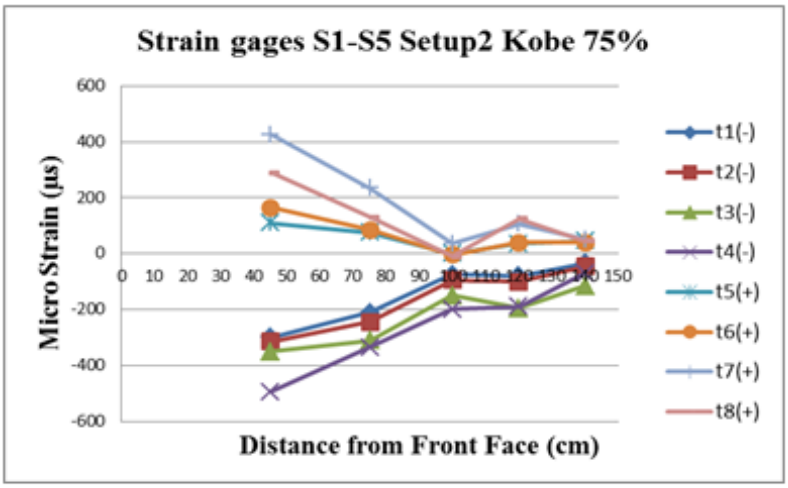

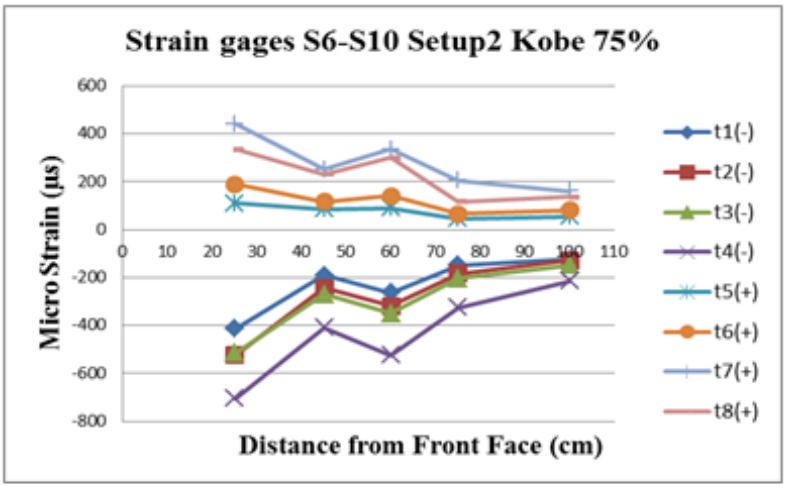

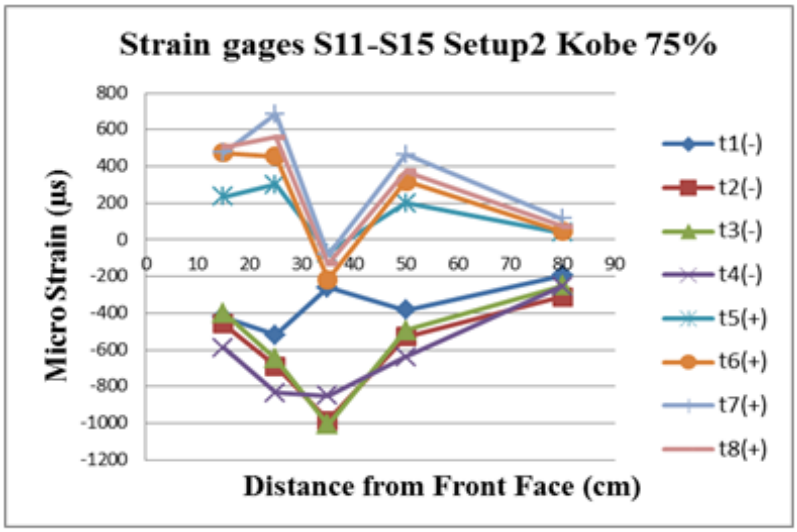

Figure D.4. Strain Time Peaks for Compression and Tension for Setup 2 Kobe 75%.

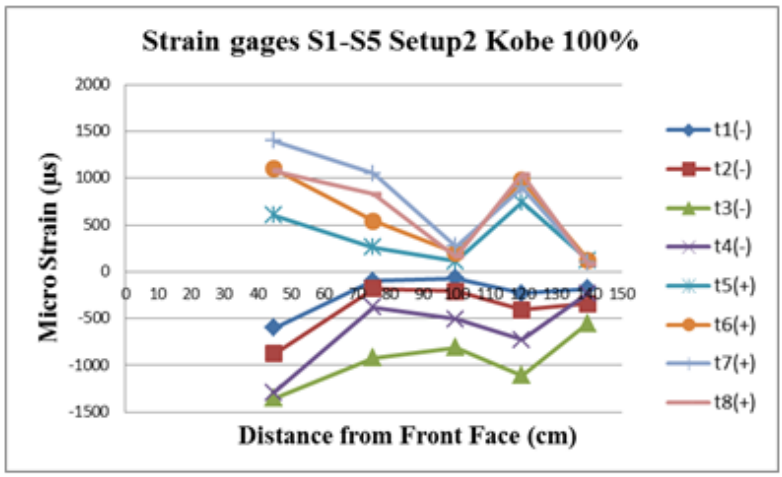

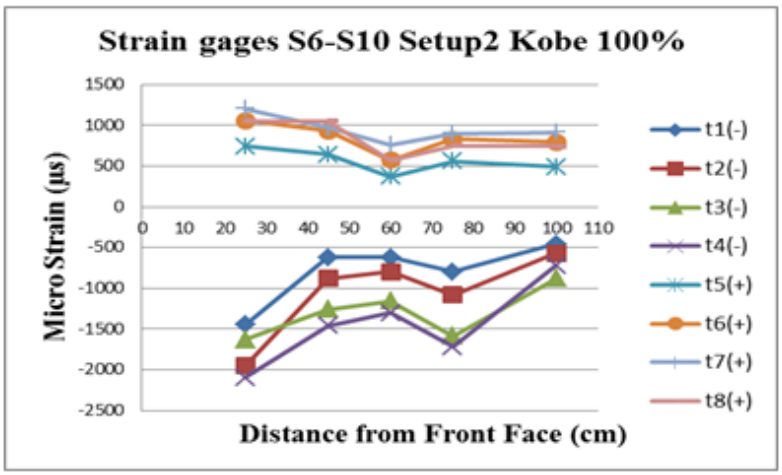

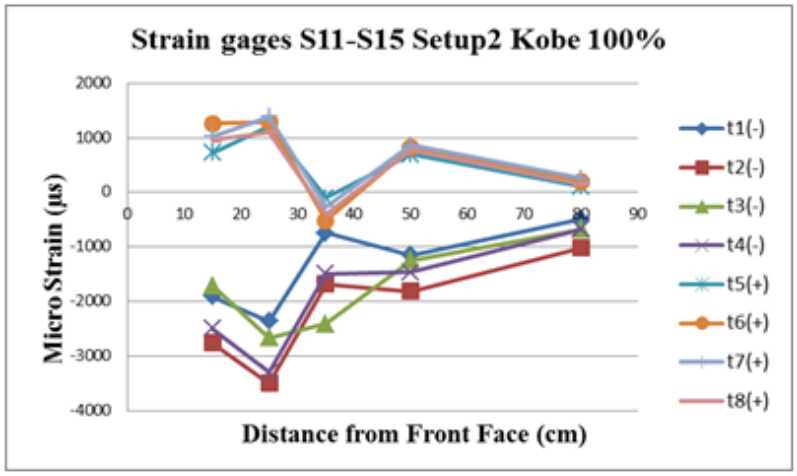

Figure D.5. Strain Time Peaks for Compression and Tension for Setup 2 Kobe 100%.

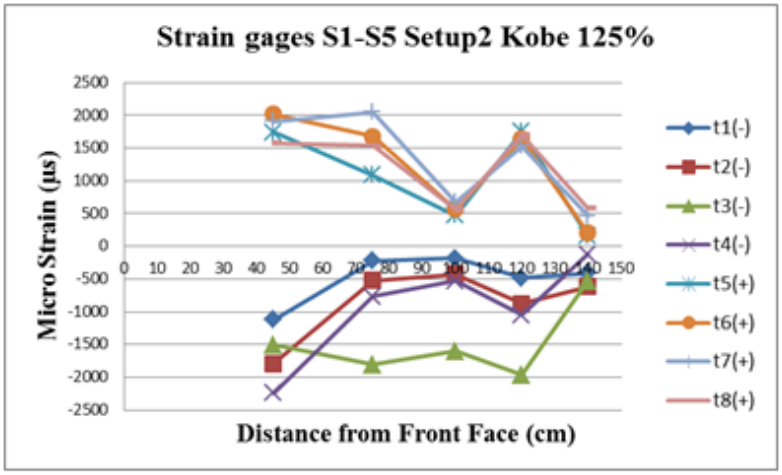

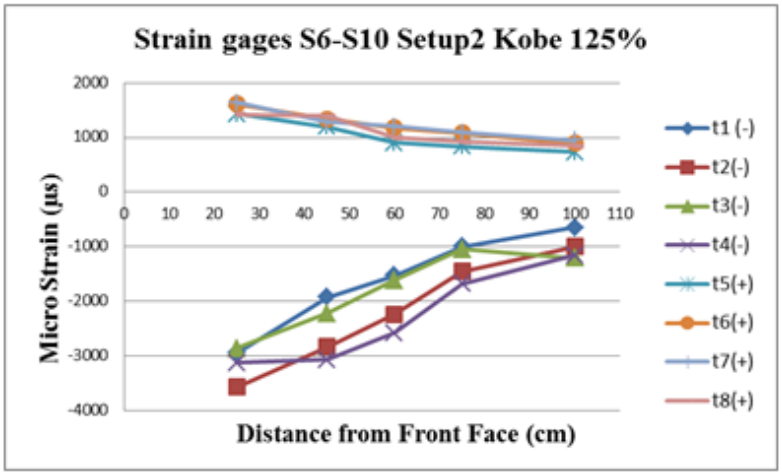

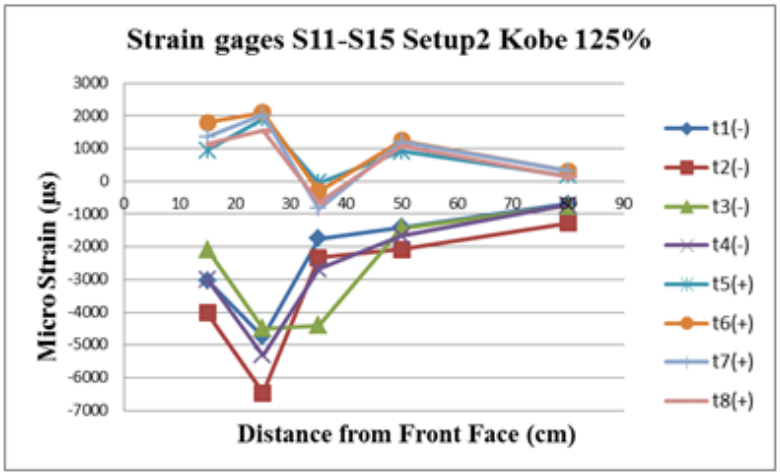

Figure D.6. Strain Time Peaks for Compression and Tension for Setup 2 Kobe 125%.

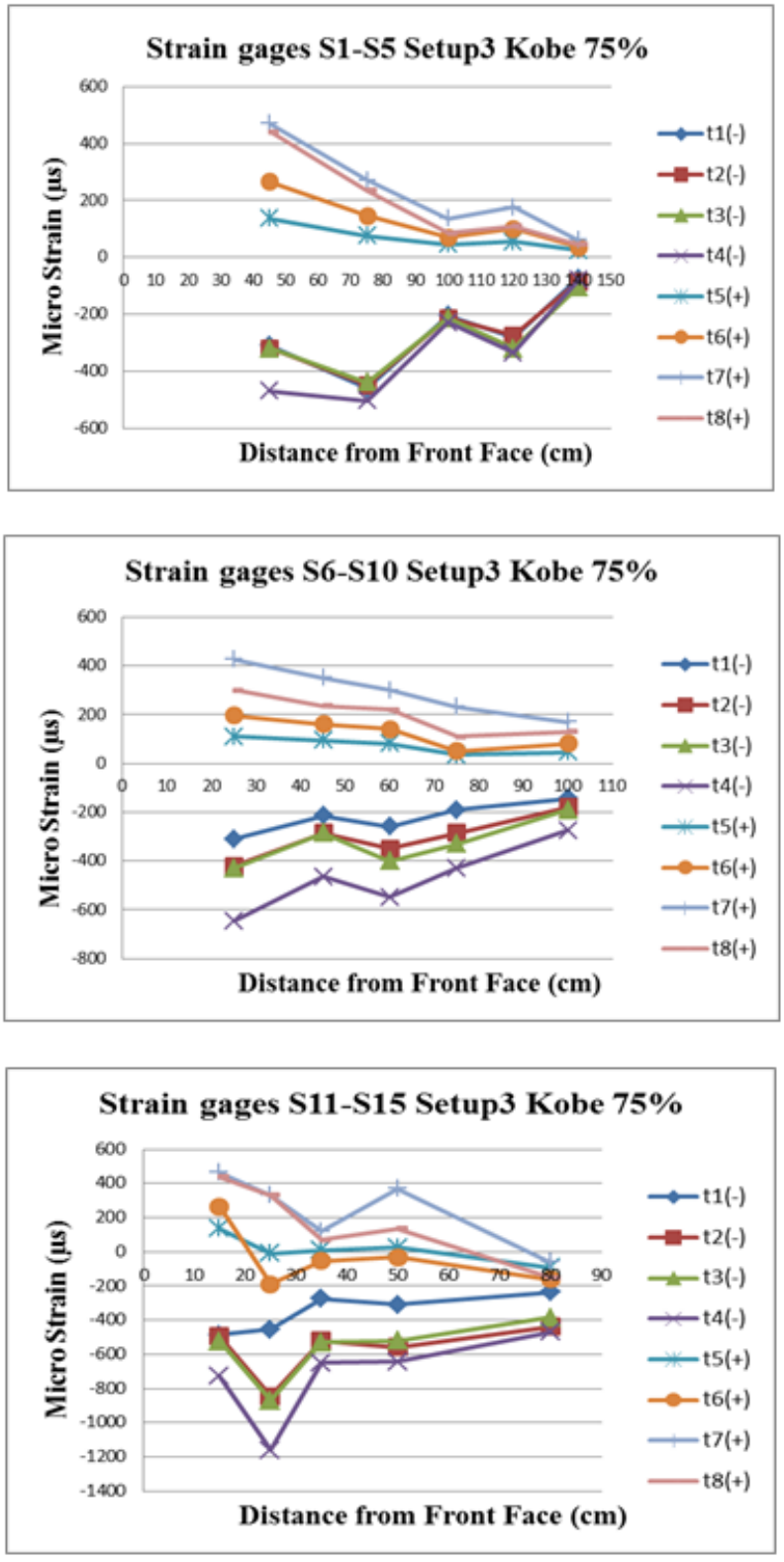

Figure D.7. Strain Time Peaks for Compression and Tension for Setup 3 Kobe 75%.

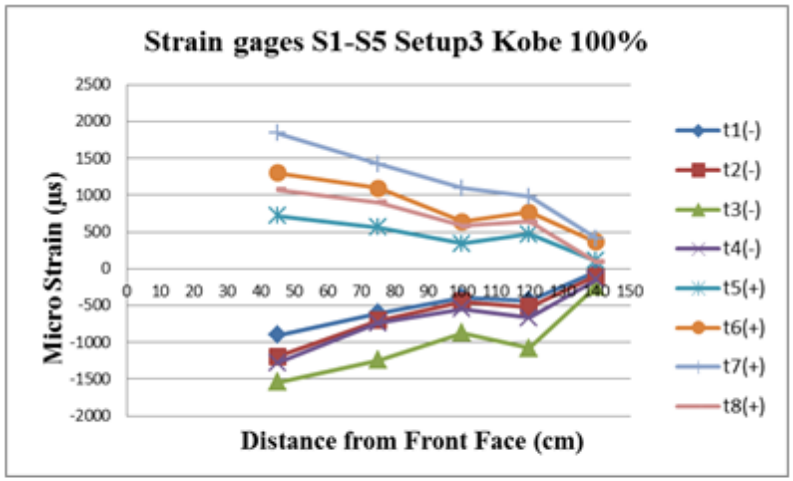

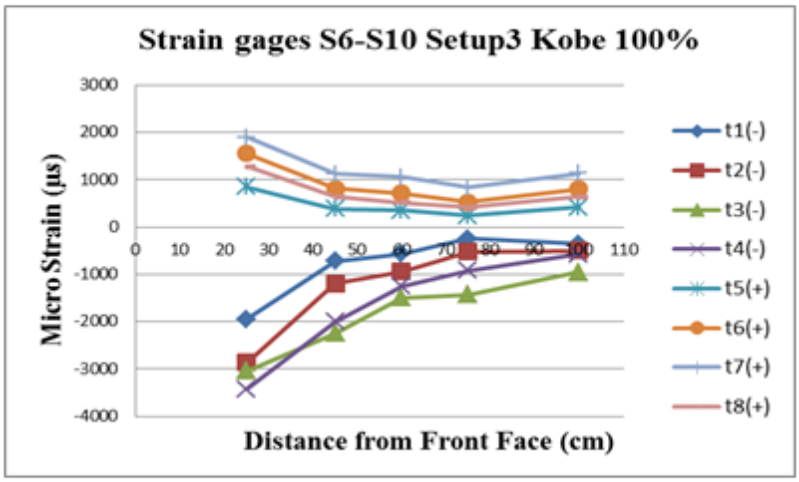

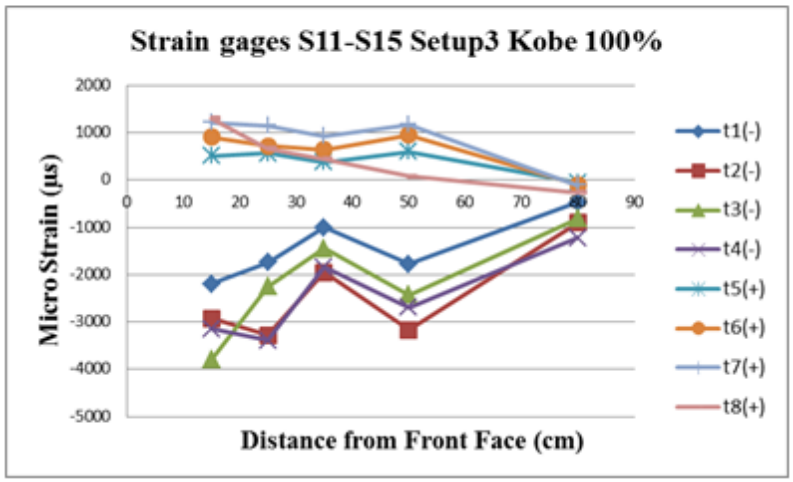

Figure D.8. Strain Time Peaks for Compression and Tension for Setup 3 Kobe 100%.

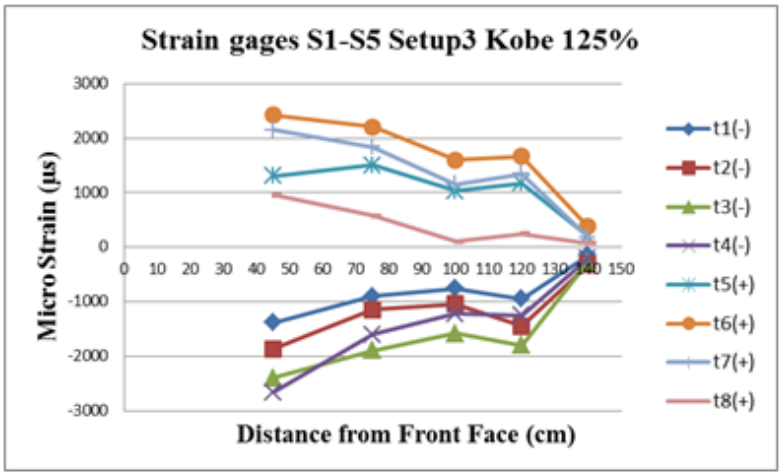

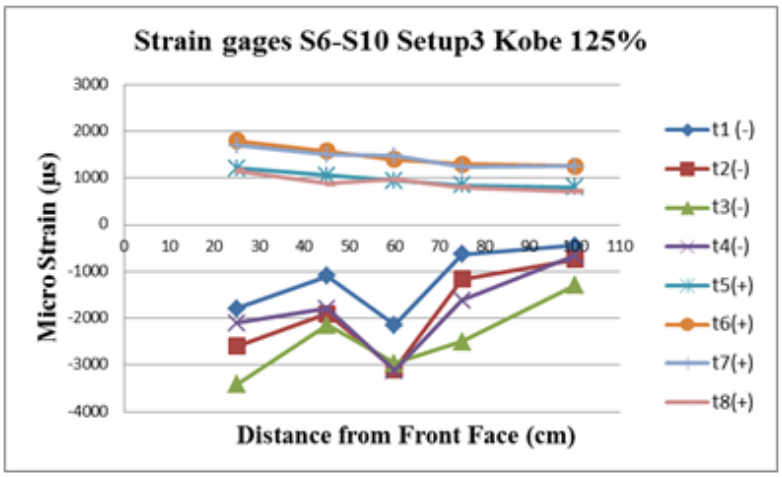

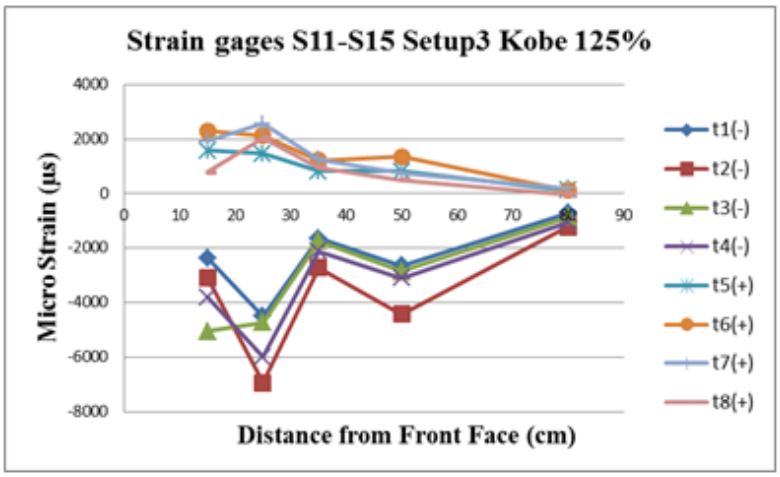

Figure D.9. Strain Time Peaks for Compression and Tension for Setup 3 Kobe 125%.

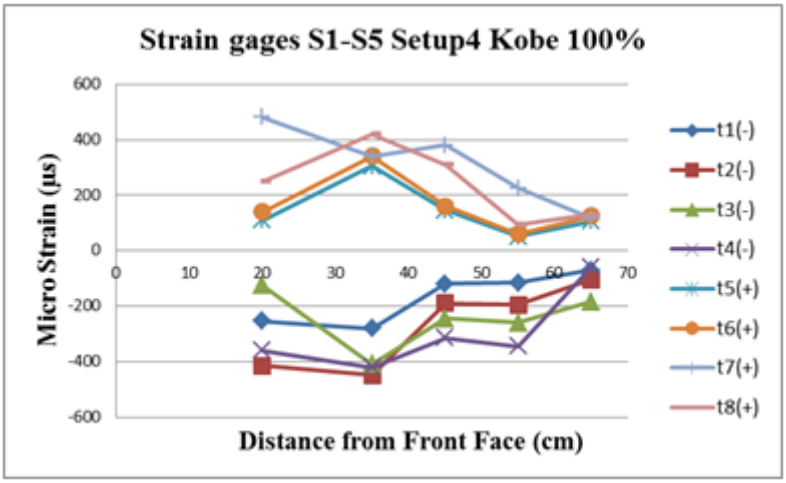

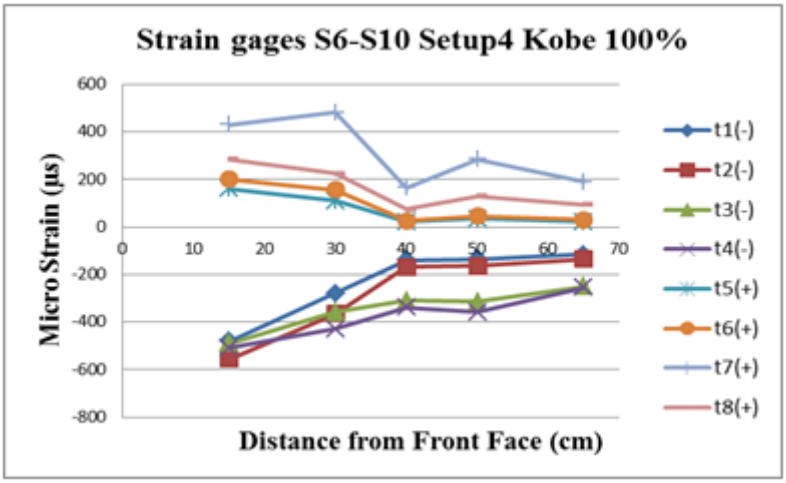

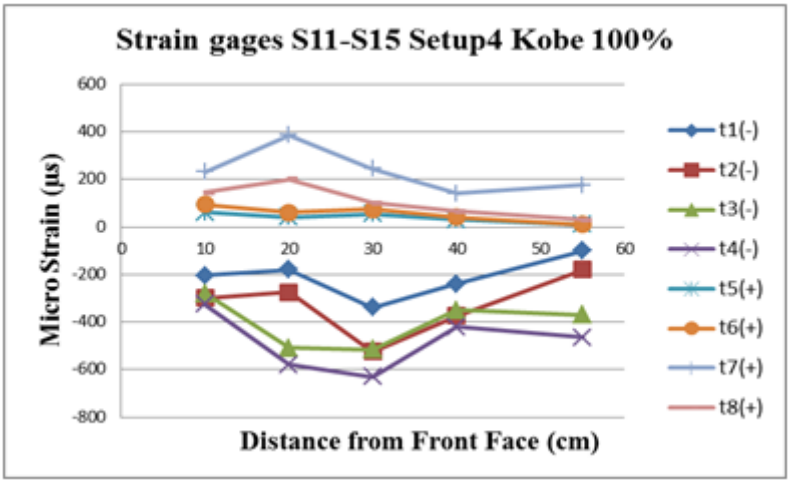

Figure D.10. Strain Time Peaks for Compression and Tension for Setup 4 Kobe 100%.

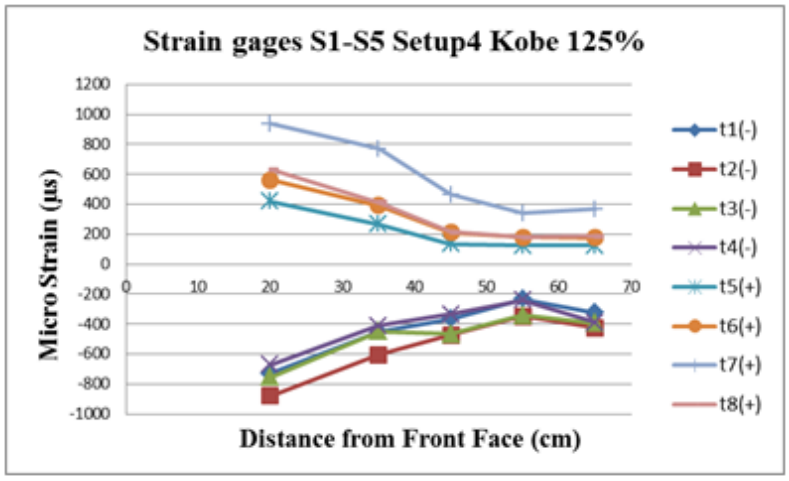

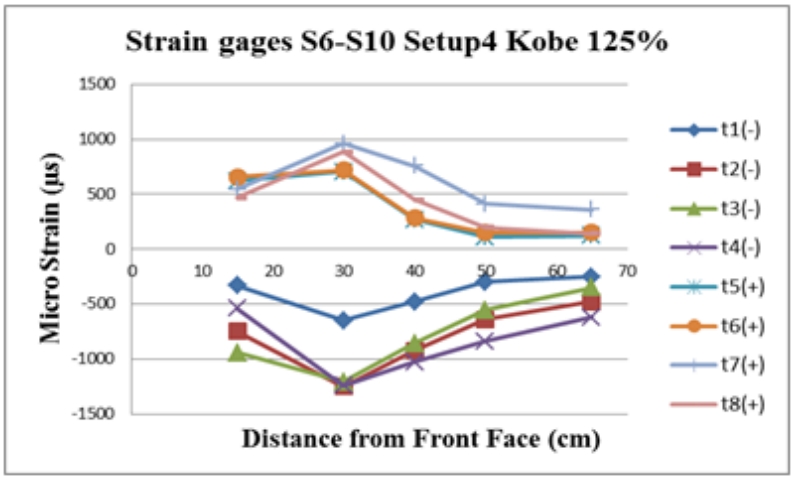

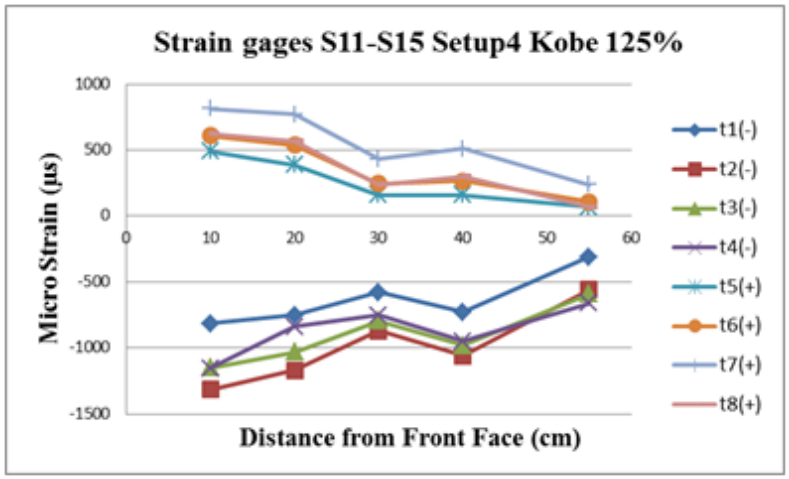

Figure D.11. Strain Time Peaks for Compression and Tension for Setup 4 Kobe 125%.

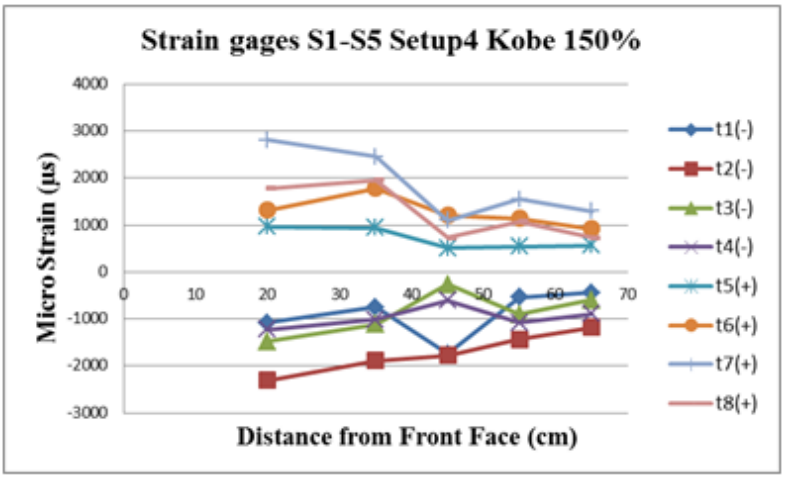

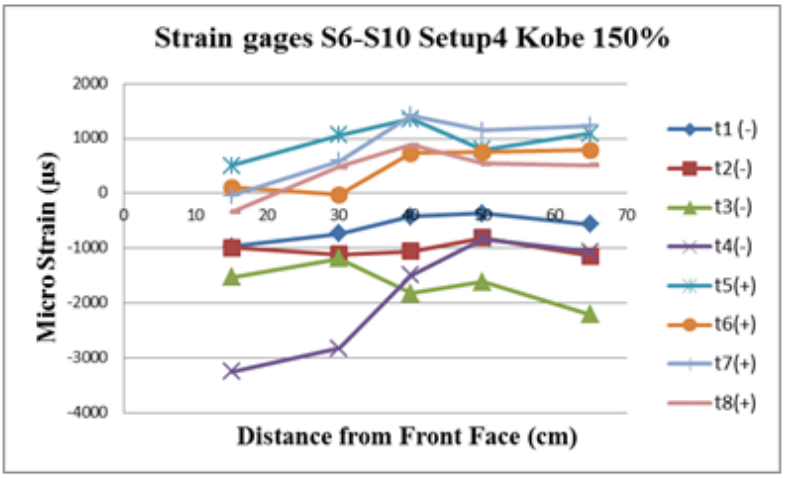

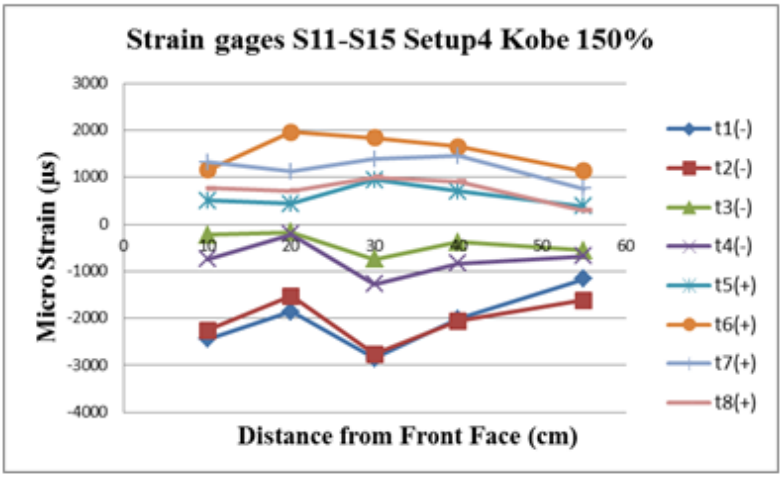

Figure D.12. Strain Time Peaks for Compression and Tension for Setup 4 Kobe 150%.

APPENDIX E: DESIGN TENSILE LOADS ACCORDING TO NCMA AND FHWA GUIDELINES

Table E.1. Calculation of Tensile Loads on Geogrids at Different Elevations According to NCMA Regulations for Setup 1 Kobe 75%.

PGA hor.(g)	0.6		K_A	0.131	
k_h	0.3		K_{AE}	0.337	
φ (internal friction^o)	39.0		ΔK_{dyn}	0.205	
δ (interface friction^o)	39.0				
ψ (wall inclination^{o}0)	13.0		K_{AH}	0.118	
θ (seismic inertia^o)	16.7		K_{AEH}	0.303	
β (backfill slope^o)	0		ΔK_{dynH}	0.185	
c (kPa)	0				
L (m)	1.52				
H (m)	1.90				
γ_s backfill (kN/m^3)	15.40				
Block width (m)	0.1				
$\gamma_{\|c\|}$ block (kN/m^3)	23				
Layer Number i	Elevation (m)	Z_v (i) (m)	S_v (i) (m)	F_{sta} (i) (kN/m)	F_{dyn}(i) (kN/m)
1	0.2	1.70	0.25	0.773	0.356
2	0.4	1.50	0.2	0.546	0.353
3	0.6	1.30	0.2	0.473	0.421
4	0.8	1.10	0.2	0.400	0.489
5	1	0.90	0.2	0.327	0.557
6	1.2	0.70	0.2	0.255	0.626
7	1.4	0.50	0.2	0.182	0.694
8	1.6	0.30	0.2	0.109	0.762
9	1.8	0.10	0.2	0.036	0.830

Table E.2. Calculation of Tensile Loads on Geogrids at Different Elevations According to NCMA Regulations for Setup 1 Kobe 100%.

PGA hor.(g)	0.8		K_A	0.131	
k_h	0.4		K_{AE}	0.455	
φ (internal friction^o)	39.0		ΔK_{dyn}	0.324	
δ (interface friction^o)	39.0				
ψ (wall inclination^{o}0)	13.0		K_{AH}	0.118	
θ (seismic inertia^o)	21.8		K_{AEH}	0.409	
β (backfill slope^o)	0		ΔK_{dynH}	0.291	
c (kPa)	0				
L (m)	1.52				
H (m)	1.90				
γ_s backfill (kN/m^3)	15.40				
Block width (m)	0.1				
$\gamma_{\|c\|}$ block (kN/m^3)	23				
Layer Number i	Elevation (m)	Z_v (i) (m)	S_v (i) (m)	F_{sta} (i) (kN/m)	F_{dyn}(i) (kN/m)
1	0.2	1.70	0.25	0.773	0.560
2	0.4	1.50	0.2	0.546	0.556
3	0.6	1.30	0.2	0.473	0.663
4	0.8	1.10	0.2	0.400	0.771
5	1	0.90	0.2	0.327	0.878
6	1.2	0.70	0.2	0.255	0.986
7	1.4	0.50	0.2	0.182	0.094
8	1.6	0.30	0.2	0.109	0.201
9	1.8	0.10	0.2	0.036	0.309

Table E.3. Calculation of Tensile Loads on Geogrids at Different Elevations According to FHWA Regulations for Setup 1 Kobe 75%.

PGA hor.(g)	0.6		K_A	0.131	
k_h	0.4		K_{AE}	0.337	
φ (internal friction^o)	39.0		ΔK_{dyn}	0.205	
δ (interface friction^o)	39.0			0.118	
ψ (wall inclination^{o}0)	13.0		K_{AH}	0.303	
θ (seismic inertia^o)	16.7		K_{AEH}	0.185	
β (backfill slope^o)	0		ΔK_{dynH}		
c (kPa)	0				
α_A (failure plane angle^o	55.4		L(m)	1.52	
α_{AE} (failure plane angle^o	40.9		H(m)	1.90	
			γ_s backfill (kNm^3	15.40	
			Block width (m)	0.1	
			γ_s backfill (kNm^3	23.0	
W_A (with blocks) (kN)	12.73	for α_A			
P_I (kN)	3.82				
W_A (with blocks) (kN)	25.68	for α_A			
P_I (kN)	7.70				

					for α_A			for α_{AE}		
						FHWA 2001	FHWA 2009		FHWA 2001	FHWA 2009
Layer Number i	Elevation (m)	Z_v (i) (m)	S_v(i)(m)	T_{max} (kN/m)	L_e (i)(m)	T_{md}(kN/m)	T_{md}(kN/m)	L_e(i)(m)	T_{md} (kN/m)	T_{md}(kN/m)
1	0.2	1.70	0.25	0.773	1.43	0.571	0.424	1.34	1.868	0.856
2	0.4	1.50	0.2	0.546	1.34	0.534	0.424	1.15	1.609	0.856
3	0.6	1.30	0.2	0.473	1.25	0.497	0.424	0.97	1.351	0.856
4	0.8	1.10	0.2	0.400	1.15	0.461	0.424	0.78	1.092	0.856
5	1	0.90	0.2	0.327	1.06	0.424	0.424	0.60	0.834	0.856
6	1.2	0.70	0.2	0.255	0.97	0.388	0.424	0.41	0.575	0.856
7	1.4	0.50	0.2	0.182	0.88	0.351	0.424	0.23	0.317	0.856
8	1.6	0.30	0.2	0.109	1.79	0.315	0.424	0.04	0.058	0.856
9	1.8	0.10	0.2	0.036	0.70	0.278	0.424	0.00	0.000	0.856

Table E.4. Calculation of Tensile Loads on Geogrids at Different Elevations According to FHWA Regulations for Setup 1 Kobe 100%.

PGA hor.(g)	0.8		K_A	0.131
k_h	0.4		K_{AE}	0.455
φ (internal friction^o)	39.0		ΔK_{dyn}	0.324
δ (interface friction^o)	39.0			0.118
ψ (wall inclination^{o}0)	13.0		K_{AH}	0.409
θ (seismic inertia^o)	21.8		K_{AEH}	0.291
β (backfill slope^o)	0		ΔK_{dynH}	
c (kPa)	0			
α_A (failure plane angle^o	55.4		L(m)	1.52
α_{AE} (failure plane angle^o	35.0		H(m)	1.90
			γ_s backfill (kNm^3	15.40
			Block width (m)	0.1
			γ_s backfill (kNm^3	23.0
W_A (with blocks) (kN)	12.73	for α_A		
P_I (kN)	5.09			
W_A (with blocks) (kN)	33.30	for α_A		
P_I (kN)	13.32			

					for α_A			for α_{AE}		
						FHWA 2001	FHWA 2009		FHWA 2001	FHWA 2009
Layer Number i	Elevation (m)	Z_v (i) (m)	S_v(i)(m)	T_{max} (kN/m)	L_e (i)(m)	T_{md}(kN/m)	T_{md}(kN/m)	L_e(i)(m)	T_{md} (kN/m)	T_{md}(kN/m)
1	0.2	1.70	0.25	0.773	1.43	0.761	0.566	1.28	4.171	1.480
2	0.4	1.50	0.2	0.546	1.34	0.712	0.566	1.04	3.390	1.480
3	0.6	1.30	0.2	0.473	1.25	0.663	0.566	0.80	2.610	1.480
4	0.8	1.10	0.2	0.400	1.15	0.614	0.566	0.56	1.830	1.480
5	1	0.90	0.2	0.327	1.06	0.566	0.566	0.32	1.049	1.480
6	1.2	0.70	0.2	0.255	0.97	0.517	0.566	0.08	0.269	1.480
7	1.4	0.50	0.2	0.182	0.88	0.468	0.566	0.00	0.000	1.480
8	1.6	0.30	0.2	0.109	1.79	0.419	0.566	0.00	0.000	1.480
9	1.8	0.10	0.2	0.036	0.70	0.371	0.566	0.00	0.000	1.480

REFERENCES

American Association of State Highway and Transportation Officials, 1996, *Standard Specifications for Highway Bridges*, American Association of State Highway and Transportation Officials, Washington, DC.

Allen, T.M. and R.J., Bathurst, 2002, "Soil Reinforcement Loads in Geosynthetic Walls at Working Stress Conditions", *Geosynthetics International*, Vol. 9, pp. 525-566.

Allen, T.M. and R.J., Bathurst, 2002, "Observed Long-Term Performance of Geosynthetic Walls and Implications for Design", *Geosynthetics International*, Vol. 9, pp. 567-606.

Başbuğ, E., 2011, Dynamic Behavior of Geogrid Reinforced Segmental Block Walls under Earthquake Loads, Ph.D. Thesis, Boğaziçi University.

Bathurst, R.J. and Z., Cai, 1995, "Pseudo-Static Seismic Analysis of Geosynthetic Reinforced Segmental Retaining Walls", *Geosynthetics International*, Vol. 2, No. 5, pp. 787-830.

Bathurst, R.J., Z., Cai and M.J. Pelletier, 1996, "Seismic Design and Performance of Geosynthetic Reinforced Segmental Retaining Walls", *Proceedings of the 10th Annual Symposium of the Vancouver Geotechnical Society*, Vancouver, British Columbia, Canada, 1996.

Bathurst, R.J., and K., Hatami, 1998, "Seismic Response Analysis of a Geosynthetic-Reinforced Soil Wall" *Geosynthetics International*, Vol. 5, No. 1-2, pp. 127-166.

Bathurst, R.J., D., Walters, N., Vlachopoulos, P., Burgess and T.M., Allen, 2000, "Full Scale Testing of Geosynthetic Reinforced Walls: Invited Keynote Paper", *Advances in Transportation and Geoenvironmental Systems using Geosynthetics Geo-Denver 2000*, Denver, CO, USA, August 2000, American Society of Civil

Engineering Special Publication No. 103, pp. 201-217.

Bathurst, R.J., K., Hatami and M.C. Alfaro, 2002, "Geosynthetic Reinforced Soil Walls and Slopes: Seismic Aspects", *Geosynthetics and Their Applications (S.K. Shukla Ed.)*, Thomas Telford, Vol. 1, pp. 327-392.

Bathurst, R.J., Y., Miyata, A., Nernheim and T.M., Allen, 2008, "Refinement of K-stiffness method for Geosynthetic Reinforced Soil Walls", *Geosynthetics International*, Vol. 15, No. 4, pp. 269-295.

Boyle, S.R., 1995, *Deformation Prediction of Geosynthetic Reinforced Soil Retaining Walls*, Ph.D. Thesis, University of Washington, Seattle.

Cai, Z. and R.J., Bathurst, 1996, "Seismic-induced Permanent Displacement of Geosynthetic Reinforced Segmental Retaining Walls", *Canadian Geotechnical Journal*, Vol. 33, pp. 937-955.

El-Emam, M. and R.J., Bathurst, 2004, "Experimental Design, Instrumentation and Interpretation of Reinforced Soil Wall Response Using a Shaking Table", *International Journal of Physical Modelling in Geotechnics*, Vol. 4, No. 4, pp. 13-32.

El-Emam, M., R.J., Bathurst and K., Hatami, 2004, "Numerical Modeling of Reinforced Soil Retaining Walls Subjected to Base Acceleration", *13th World Conference on Earthquake Engineering*, Vancouver BC, 2004.

El-Emam, M. and R.J., Bathurst, 2005, "Facing Contribution to Seismic Response of Reduced Scale Reinforced Soil Walls", *Geosynthetics International*, Vol. 12, No. 5, pp. 215- 238.

El-Emam, M., and R.J., Bathurst, 2007, "Influence of Reinforcement Parameters on the Seismic Response of Reduced-Scale Reinforced Soil Retaining Walls", *Geotextiles and Geomembranes*, Vol. 25, No. 1, pp. 33-49.

Federal Highway Administration, 2001, "Mechanically Stabilized Earth Walls and Re-

inforced Soil Slopes Design and Construction Guidelines", *Federal Highway Administration*, Washington, DC.

Federal Highway Administration, 2009, "Design and Construction of Mechanically Stabilized Earth Walls and Reinforced Soil Slopes", *Demonstration Project 82*, Federal Highway Administration, Washington, DC.

Goodings, D.J., 1990, "Research on Geosynthetics in Reinforced Cohesive Soil Retaining Walls at the University of Maryland", *Geotechnical News*, Vol. 1, pp. 23-25.

Güler, E. and A.K. Enünlü, 2009, "Investigation of Dynamic Behavior of Geosynthetic Reinforced Soil Retaining Structures under Earthquake Loads", *Bulletin of Earthquake Engineering*, Vol. 7, pp. 737-777.

Güler, E., M., Hamderi and M.M., Demirkan, 2007, "Numerical Analysis of Reinforced Soil-Retaining Wall Structures with Cohesive and Granular Backfills", *Geosynthetics International*, Vol. 14, No. 6, pp. 330-345.

Güler, E., E., Çiçek, M.M., Demirkan and M., Hamderi, 2012, "Numerical Analysis of Reinforced Soil Walls with Granular and Cohesive Backfills under Cyclic Loads", *Bulletin of Earthquake Engineering*, Vol. 10, No. 3, pp. 793-811.

Güler, E. and Ö., Selek, 2014, "Reduced-Scale Shaking Table Tests on Geosynthetic Reinforced Soil Walls with Modular Facing", *Journal of Geotechnical and Geoenvironmental Engineering*, Vol. 140, No. 6, pp. 1-11.

Hatami, K. and R.J., Bathurst, 2000, "Effect of Structural Design on Fundamental Frequency of Reinforced-Soil Retaining Walls", *Soil Dynamics and Earthquake Engineering*, Vol. 19, pp. 137-157.

Hausmann, M.R., 1990, "Engineering Principles of Ground Modification", *McGraw-Hill*, New York.

Holtz, R.D. and W.F., Lee, 2002, "Internal Stability Analyses of Geosynthetic Rein-

forced Retaining Walls", *Research Report*, University of Washington.

Huang, C.C., 2000, "Investigations of Soil Retaining Structures Damaged During the Chi-Chi (Taiwan) Earthquake", *Journal of the Chinese Institute of Engineers*, Vol. 23, No. 4, pp. 417-428.

Huang, C.C., J.C., Horng, S.Y., Chueh, J.S., Chiou and C.H., Chen, 2010, "Dynamic Behavior of Reinforced Slopes: Horizontal Acceleration Response", *Geosynthetics International*, Vol. 17, No. 4, pp. 207-219.

Huang, C.C., J.C., Horng, S.Y., Chueh, J.S., Chiou and C.H., Chen, 2011, "Dynamic Behavior of Reinforced Slopes: Horizontal Displacement Response", *Geotextiles and Geomembranes*, Vol. 29, pp. 257-267.

Iai, S., 1989, "Similitude for Shaking Table Tests on Soil-Structure-Fluid Model in 1g Gravitational Field", *Port and Harbour Research Institute*, Vol. 27, No. 3.

Ismeik, M. and E., Güler, 1998, "Effect of Wall Facing on the Seismic Stability of Geosynthetic-Reinforced Retaining Walls", *Geosynthetics International*, Vol. 5, No. 1-2, pp. 41-53.

Jones, C.J.F.P., 1997, "Earth Reinforcement and Soil Structures", *Thomas Telford*, London.

Kerisel, J., 1993, "History of Retaining Wall Designs", *Proceeding of Conference of Retaining Structures*, Cambridge, Thomas Telford, London.

Koerner, R.M., 1998, "Designing with Geosynthetics", *4th Edition, Prentice Hall Publication Co.*, Englewood Cliffs, NJ.

Kong, X.J., Y.C.H., Li, D.G., Zou and Y., Zhou, 2009, "Shaking Table Model Tests on Soil Slope Reinforced with Geogrid", *Journal of Hydroelectric Engineering*, Vol. 28, No. 5, pp. 152-157.

Koseki, J. and K., Hayano, 2000, "Preliminary Report on Damage to Retaining Walls Caused by the 1999 Chi-Chi Earthquake", *Bulletin of ERS, Institute of Industrial Science*, Vol. 33, pp. 23-34.

Koseki, J., R.J., Bathurst, E., Güler, J., Kuwano and M., Maugeri, 2006, "Seismic Stability of Reinforced Soil Walls", *8th International Conference on Geosynthetics*, Yokohama, Japan, 18-22 September 2006.

Lee, K.Z.Z., N.Y., Chang and H.Y., Ko, 2010, "Numerical Simulation of Geosynthetic Reinforced Soil Walls under Seismic Shaking", *Geotextiles and Geomembranes*, Vol. 28, No. 4, pp. 317-334.

Leshchinsky, D., H.I., Ling and J.P., Wang, 2008, "Equivalent Seismic Coefficient in Geocell Retention Systems", *Geotextiles and Geomembranes*, Vol. 27, pp. 9-18.

Ling, H.I., 2003, "Chapter 25. A Critical Review of Full-Scale Shaking Table Tests Conducted on Reinforced Soil Retaining Walls", *Reinforced Soil Engineering: Advances in Research and Practice*, Marcel Dekker, New York.

Ling, H.I., H., Liu, V.N., Kaliakin and D., Leshchinsky, 2004, "Analyzing Dynamic Behavior of Geosynehtic-Reinforced Soil Retaining Walls", *Journal of Engineering Mechanics*, Vol. 130, No. 8, pp. 911-920.

Ling, H.I., H., Liu and Y., Mohri, 2005a, "Parametric Studies on The Behavior of Reinforced Soil Retaining Walls under Earthquake Loading", *Journal of Engineering Mechanics*, Vol. 131, No. 10, pp. 1056-1065.

Ling, H.I., Y., Mohri, D., Leshchinsky, C., Burke, K., Matsushima and H., Liu, 2005, "Large-Scale Shaking Table Tests on Modular-Block Reinforced Soil Retaining Walls", *Journal of Geotechnical and Geoenvironmental Engineering*, Vol. 131, No. 4, pp. 465-476.

Ling, H.I., S., Yang, D., Leshchinsky, H., Liu and C., Burke, 2010, "Finite-Element

Simulations of Full-Scale Modular-Block Reinforced Soil Retaining Walls under Earthquake Loading", *Journal of Engineering Mechanics*, Vol. 136, No. 5, pp. 653-661.

Ling, H.I., D., Leshchinsky, Y., Mohri and J.P., Wang, 2012, "Earthquake Response of Reinforced Segmental Retaining Walls Backfilled with Substantial Percentage of Fines", *Journal of Geotechnical and Geoenvironmental Engineering*, Vol. 138, pp. 934-944.

Matsuo, O., T., Tsutsumi, K., Yokoyama and Y., Saito, 1998, "Shaking Table Tests and Analyses of Geosynthetic-Reinforced Soil Retaining Walls", *Geosynthetics International*, Vol. 5, No. 1-2, pp. 97-126.

Mitchell, J.K. and J.G., Zornberg, 1995, "Reinforced Soil Structures with Poorly Draining Backfills Part II: Case Histories and Applications", *Geosynthetics International*, Vol. 2, No. 1, pp. 265-307.

Murata, O., M., Tateyama and F., Tatsuoka, 1994, "Shaking Table Tests on a Large Geosynthetic-Reinforced Soil Retaining Wall Model", *Recent Case Histories of Permanent Geosynthetic-Reinforced Soil Walls, Seiken Symposium*, Tokyo, Japan.

Murray, R.T. and J.B., Boden, 1979, "Reinforced Earth Wall Constructed with Cohesive Fill", *Colloque International sur le Renforcement des Sols*, Vol. 2, pp. 569-577.

NCMA, 2010, *Seismic Design Of Segmental Retaining Walls*, TEK 15-9A, National Concrete Masonry Association, Herndon, Virginia.

Nakamura, K., Y., Tamura, F., Tatsuoka, K., Iwasaki and H., Yamauchi, 1988, "Roles of Facings in Reinforcing Steep Clay Slopes with a Non-Woven Geotextile", *Proceedings of the International Geotechnical Symposium on Theory and Practice of Earth Reinforcement*, Fukuoka Kyushu, Japan, October 1988, pp. 553-558.

Nishimura, J., T., Hirai, K., Iwasaki, Y., Saito and M., Morishima, 1996, "Earthquake Resistance of Geogrid-Reinforced Soil Walls Based On A Study Conducted Following The Southern Hyogo Earthquake", *International Symposium on Earth Reinforcement, IS-Kyushu'96*, Fukuoka, Kyushu, Japan, pp. 439-444.

Race, R. and H., del Cid, 2001, "Seismic Performance of Modular Block Retaining Wall Structures during the January 2001 El Salvador Earthquake", I*nternational Geosynthetics Engineering Forum 2001*, Taipei, Taiwan.

Rowe, R. K. and S. K., Ho, 1992, "Keynote lecture: A review of the behavior of reinforced soil walls", *Proceedings of the International Symposium on Earth Reinforcement Practice*, Vol. 2, pp. 801-829.

Sandri, D., 1994, "Retaining Walls Stand up to the Northridge Earthquake", *Geotechnical Fabrics Report*, Vol. 12, No. 4, pp. 30-31.

SSeed, H.B. and R.V., Whitman, 1970, "Design of Earth Retaining Structures for Dynamic Loads", *Proceedings of the American Society of Civil Engineering Specialty Conference: Lateral Stresses in the Ground and Design of Earth Retaining Structures*, Ithaca, New York.

Sego, D.C., E.A., Scott, E.A., Richards and Y., Liu, 1990, "Performance of a Geogrid in a Cohesive Soil Test Embankment", *Proceedings of Fourth International Conference on Geotextiles, Geomembranes and Related Products*, The Hague, Netherlands, May 1990.

Segrestin, P. and M. J., Bastick, 1988, "Seismic Design of Reinforced Earth Retaining Walls - The Contribution of Finite Element Analysis", *Theory and Practice of Earth Reinforcement: Proceedings of the International Geotechnical Symposium on Theory and Practice of Earth Reinforcement, IS-Kyushu'88*, Fukuoka, Japan, Balkema, Rotterdam.

Srilatha, N., G., Madhavi Latha and C.G., Puttappa, 2013, "Effect of Frequency on

Seismic Response of Reinforced Soil Slopes in Shaking Table Tests", *Geotextiles and Geomembranes*, Vol. 36, No. 2, pp. 27-32.

Tatsuoka, F. and H., Yamauchi, 1986, "A Reinforcing Method for Steep Clay Slopes Using a Non-woven Geotextile", *Geotextiles and Geomembranes*, Vol. 4, No. 3-4, pp. 241-268.

Tatsuoka, F., O., Murata, M., Tateyama, K., Nakamura, Y., Tamura, H.I., Ling, K., Iwasaki and H., Yamauchi, 1990, "Reinforcing Steep Clay Slopes with a Non-woven Geotextile", *Proceedings of the International Reinforced Soil Conference, Glasgow*, Scotland, September 1990.

Tatsuoka, F., J., Koseki and M., Tateyama, 1997b, "Performance of Reinforced Soil Structures During the 1995 Hyogo-Ken Nanbu Earthquake", *Earth Reinforcement*, Vol. 2, pp. 973-1008.

Tatsuoka F., J., Koseki, M., Tateyama, Y., Munaf and K., Horii, 1998, "Seismic Stability against High Seismic Loads on Geosynthetic-Reinforced Soil Retaining Structures. Keynote Lecture", P*roceedings of the 6th International Conference on Geosynthetics*, Atlanta, Georgia.

Wang, L., G., Chen and S., Chen, 2015, "Experimental Study on Seismic Response of Geogrid Reinforced Rigid Retaining Walls with Saturated Backfill Sand", *Geotextiles and Geomembranes*, Vol. 43, pp. 35-45.

Watanabe, K., Y., Munaf, J., Koseki, M., Tateyama and K., Kojima, 2003, "Behaviors of Several Types of Model Retaining Walls Subjected to Irregular Excitation", *Soils and Foundations*, Vol 43, No. 5, pp. 13-27.

Wolfe, W.E., K.L., Lee, D., Rea and A.M., Yourman, 1978, "The Effect of Vertical Motion on the Seismic Stability of Reinforced Earth Walls", *Proceedings of the American Society of Civil Engineering Symposium on Earth Reinforcement*, Pittsburgh, Pennsylvania.

Wu, G., 1994, *Dynamic soil-structure interaction: Pile Foundations and Retaining Structures*, Ph.D. Thesis, University of British Columbia, Vancouver.

Yang, K.H., W.Y., Hung and E.Y., Kencana, 2013, "Acceleration-Amplified Responses of Geosynthetic-Reinforced Soil Structures with a Wide Range of Input Ground Accelerations", *2013 GeoCongress: Stability and Performance of Slopes and Embankments III.*, San Diego, California.

Zarnani, S. and R.J., Bathurst, 2007, "Experimental Investigation of EPS Geofoam Seismic Buffers using Shaking Table Tests", *Geosynthetics International*, Vol. 14, No. 3, pp. 165-177.